ACTA TECHNICA

ACADEMIAE SCIENTIARUM HUNGARICAE

ADIUVANTIBUS

L. GILLEMOT, GY. HEVESI, K. P. KOVÁCS,
K. SZÉCHY, G. TARJÁN

REDIGIT

A. GELEJI

TOMUS 51 FASCICULI 1—2

AKADÉMIAI KIADÓ, BUDAPEST

1965

ACTA TECHNICA

A MAGYAR TUDOMÁNYOS AKADÉMIA MŰSZAKI TUDOMÁNYOK OSZTÁLYÁNAK KÖZLEMÉNYEI

SZERKESZTŐSÉG ÉS KIADÓHIVATAL: BUDAPEST V., ALKOTMÁNY U. 21.

Az Acta Technica német, angol, francia és orosz nyelven közöl értekezéseket a műszaki tudományok köréből.

Az Acta Technica változó terjedelmű füzetekben jelenik meg, több füzet alkot egy kötetet.

A közlésre szánt kéziratok a következő címre küldendők:

Acta Technica
Budapest V., Nádor u. 7.

Ugyanerre a címre küldendő minden szerkesztőségi és kiadóhivatali levelezés.

Az Acta Technica előfizetési ára kötetenként belföldre 80 forint, külföldre 110 forint. Megrendelhető a belföld számára az „Akadémiai Kiadó"-nál (Budapest V., Alkotmány utca 21. Bankszámla 05-915-111-46), a külföld számára pedig a „Kultúra" Könyv- és Hírlap Külkereskedelmi Vállalatnál (Budapest I., Fő utca 32. Bankszámla: 43-790-057-181) vagy annak külföldi képviseleteinél és bizományosainál.

Die Acta Technica veröffentlichen Abhandlungen aus dem Bereiche der technischen Wissenschaften in deutscher, französischer, englischer oder russischer Sprache.

Die Acta Technica erscheinen in Heften wechselnden Umfanges. Mehrere Hefte bilden einen Band

Die zur Veröffentlichung bestimmten Manuskripte sind an folgende Adresse zu senden:

Acta Technica
Nádor u. 7.
Budapest V.
Ungarn

An die gleiche Anschrift ist auch jede für die Schriftleitung und den Verlag bestimmte Korrespondenz zu richten.

Abonnementspreis pro Band: 110 Forint. Bestellbar bei dem Buch- und Zeitungs-Außenhandels-Unternehmen »Kultúra« (Budapest I., Fő utca 32. Bankkonto Nr. 43-790-057-181) oder bei seinen Auslandsvertretungen und Kommissionären.

ACTA TECHNICA

Tomus 51

INDEX

Imre Rázsó 1904—1964 Имре Ражо 1904—1964 271

Ferenc Ratkovszky 1900—1965 Ференц Ратковски 1900—1965. 273

Ács, E.: Communication Methods Using Codes Carrying Address and Contents or Address only — Verfahren der Nachrichtenübertragung mit Koden, welche die Adresse und den Inhalt oder nur die Adresse tragen — Méthodes de communications avec codes adresses et informations ou codes adresses seulement — *Ач, Э.:* Методы связи с использованием кодов, несущих адрес и содержание или только адрес 451

Balázs, Gy.: Berechnung der vom Schwinden des Betons herrührenden Kräfte in Stahlbetonelementen — Analysis of Forces Due to Shrinkage — Calcul des contraintes intérieures dues au retrait du béton — *Балаж, Д.:* Расчет внутренних сил бетона, возникающих от его усадки 309

Batta, I.: Calculation of Water Hammer Phenomena by Automatic Sequence Controlled Digital Computers, I. — Wasserstoßberechnung mit Hilfe einer programmgesteuerten, digitalen Rechenmaschine, I. — Calcul du coup de bélier par calculatrice électronique digitale à programme, I. — *Батта, И.:* Расчет водяного удара при помощи цифровой электронной вычислительной машины программного управления, I. 3

Bujdosó, E.—Czoboly, E.—Magyary, F.: The Determination of the Distribution Coefficient of Zinc with Radioisotope Zn^{65} by the Zone Melting of Aluminium — Bestimmung des Verteilungskoeffizienten von Zink mittels des Radioisotops Zn^{65} beim Zonenschmelzen des Aluminiums — Détermination du coefficient de distribution du zinc avec isotope Zn^{65}, au raffinement par zone fondue de l'aluminium — *Буйдошо, Э.—Цоболь, Э.—Мадяри, Ф.:* Определение коэффициента распределения цинка при помощи изотопа Zn^{65} в процессе зонной плавки алюминия 63

Forgó, L.: Problems of Deaeration in Heat Exchangers Consisting of Steam-Heated Parallel Tubes — Probleme der Entlüftung von Wärmeaustauschern aus dampfgeheizten parallel geschaltenen Röhren — Problèmes de désaération des échangeurs à rangées de tubes parallèles chauffés à la vapeur — *Форго, Л.:* Проблемы обезвоздушивания теплообменников, собранных из параллельно соединенных и отпаливаемых паром труб 223

Geszti, P. O.—Póka, Gy.: Impedances Seen by Distance Relays in a General Case — Der allgemeine Fall der Distanzerfassung durch Schutzrelais — Le cas général de la perception par les protections à distance — *Гести, П. О.—Пока, Д.:* Восприятие дистанционных защит в общем случае 403

Haas, A.: Stationary Temperature Distribution in Thermometer Protecting Tubes — Die stationäre Temperaturverteilung in Schutzrohren von Thermometern — La distribution stationnaire des températures dans les gaines protectrices des thermomètres — *Хаас, А.:* Распределение установившейся температуры защитных трубок термометров 291

Haszpra, O.: The Problem of the Quadratic Weir. Proportional Flow Measurement without the Disturbance of the Free Watersurface — Das Problem des quadratischen Überfalls. Wassermengenmessung ohne Unterbrechung der freien Oberfläche — Le problème du déversoir quadratique. Mesure de débit par courant dérivé, sans rupture de la surface libre — *Хаспра, О.:* Проблема квадратичного водослива. Замер количества воды побочного потока без нарушения свободной поверхности 121

Hoffmann, A.: Analysis of the Effect Exerted by a Variable Heat-Transfer Coefficient upon the Heating Process Carried out with a Cylindrical Body. I. — Analyse des Einflußes eines veränderlichen Wärmeübergangskoeffizienten auf den Anwärmevorgang beim Erhitzen eines zylindrischen Körpers — Examen de l'effet du coefficient variable de la transmission de chaleur dans le chauffage des corps cylindriques — *Хоффманн, А.:* Исследование влияния переменного коэффициента теплопередачи при нагреве цилиндрического тела, I. 163

Hornung, A.: Die Standzeitsfragen der Schleifscheiben — The Problem of the Determination of the Toollife of Grinding Wheels — Les problèmes de la détermination de la durée des meules — *Хорнунг, А.:* Вопросы определения срока службы шлифовального круга 211

Horváth, J.: Ausbildung achsensymmetrischer Belastung in der Umgebung von Strecken mit Rundprofil — The Development of Centrally Symmetric Loads Around Mine Entries of Circular Cross Section — La formation d'états de contraintes symétriques par rapport à l'axe autour de galeries de mine de section circulaire — *Хорват, Й.:* Возникновение осесимметричных нагрузок вокруг горных выработок круглого сечения 193

Huszár, I.—Bodor, J.: The Computation of the Forces of the Commutator Riser — Berechnung des Kräftespiels einer Kommutatorfahne — Calcul du jeu de forces des talons de commutateurs — *Хусар, И.—Бодор, Я.:* Расчет работы коллекторного петушка 149

Huszár, I.—Csizmadia, L.: Three-dimensional Photoelastic Investigation of a Twisted Bar — Räumliche photoelastische Untersuchung eines verdrehten Stabes — Photoélasticimétrie tridimensionnelle d'une barre tordue — *Хусар, И.—Чизмадиа, Л.:* Изучение креченной штанги пространственным оптическим путем 381

Kaliszky, S.: Structural Analysis of Buildings with Vertical, Thin Walled Load Carrying Elements, Affected by Horizontal Forces — Statische Berechnung von durch Horizontalkräfte belasteten Gebäuden mit Tragwänden — Calcul statique de bâtiments à murs porteurs chargés par des forces verticales — *Калиски, Ш.:* Статический расчет зданий с несущими стенами, подверженными горизонтальным нагрузкам 133

Kisbocskói, L.—Stvrteczky, F.: Calculation of Factors Influencing the Output Characteristics of Fluid Couplings — Berechnung des Einflusses der leistungsverändernden Faktoren auf die Kennwerte der hydrodynamischen Kupplungen — Calcul de l'influence des différents facteurs sur la puissance de l'accouplement hydrodynamique — *Кишбочкои, Л.—Штертецки, Ф.:* Расчет факторов, влияющих на параметры характеристики мощности гидромуфт 469

Petrasovits, G.: Soil Stabilization Experiments with Plastics — Bodenverfestigungsversuche mit Kunstharzen — Essais de stabilisation du sol par résines synthétiques — *Петрашович, Г.:* Опыты укрепления грунта искусственными смолами 431

Roboz, P.—Kovách, A.: Mass Spectrometric Studies of Additive Materials Evaporating from Tungsten Produced by Powder Metallurgical Treatment — Massenspektrometrische Untersuchung von aus pulvermetallurgisch hergestelltem Wolframverdampfenden Zusätzen — Examen par le spectromètre de masse des additifs s'évaporant du tungstène produit par la métallurgie des poudres — *Робоз, П.—Ковач, А.:* Масс-спектроскопический анализ добавок, испаряющихся из металлокерамического вольфрама 277

Stvrteczky, F.—Szabó, Á.: The Influence of the Blade-Breadth on the Characteristics of Centrifugal Pumps with Open Type Impellers — Einfluß der Schaufelbreite auf die Gestaltung der Charakteristik-Kurven von Zentrifugalpumpen mit offenem Laufrad — L'influence de la largeur d'aube sur les caractéristiques des pompes centrifuges à roue ouverte — *Штвертецки, Ф.—Сабо, А.:* Влияние ширины рабочего колеса центробежных насосов с полуоткрытой лопастной решеткой на вид кривых 31

Szántó, I. S.: Recent Developments of Line Profile Analysis Used in X-Ray Metallography — Über eine neue Methode der Linienprofilanalyse in der Röntgen-Metallographie — Une nouvelle méthode d'analyse radiographique de la distribution de l'intensité diffractée en métallurgie — *Санто, И. С.:* О новом методе анализа профилей линий в рентгеновском металловедении 251

Tóth, L.: Die Berechnung des Verformungswiderstandes prismatischer Körper beim Zusammendrücken ihrer parallelen Flächen — Calculation of the Deformation Resistance of Prismatic Bodies Compressed by Parallel Plates — Le calcul de la résistance à la déformation des corps prismatiques comprimés par plaques parallèles — *Тот, Л.:* Расчет сопротивления деформации при сжатии призматических тел между параллельными плоскостями 105

Tóth, L.: Die Wirkung des Schmierens beim Stauchen von Metallen — The Influence of Lubricants on the Deformation of a Compression Test Piece — L'influence de la lubrification dans le gonflement des métaux — *Тот, Л.:* Влияние смазки при высадке металлов 327

Tóth, L.—Vincze, E.: Solution of Kármán's Differential Equation for Rolling with the Aid of Infinite Power Series — Die Lösung der Kármánschen Differentialgleichung des Walzvorganges durch unendliche Potenzreihen — Résolution, par séries de puissances infinies, de l'équation différentielle de Kármán se rapportant au processus de laminage — *Тот, Л.—Винце, Е.:* Решение дифференциального уравнения прокатки по Карману с помощью бесконечных экспоненциальных рядов 45

Varga, J.—Sebestyén, Gy.—Schalnew, K. K.—Tschernawskij, B. A.: Untersuchung des Maßstabeffektes der Kavitationserosion— Investigation of the Influence of the Scale Effect on the Erosion by Cavitation — Examen de l'effet d'échelle de l'érosion de cavitation — *Варга, Й.—Шебештьен, Д.—Шальнев, К. К.—Чернявский, Б. А.:* Исследование воздействия на масштаб кавитационной эрозии 361

Vasvári, F.: The Phenomena Arising with the Cavitation Processes — Kavitation als elektrische Erscheinung — La cavitation comme phénomène électrique — *Вашвари, Ф.:* Кавитация как электрического явление 81

Visy, Z.: Moment Calculation of Continuous Reinforced Concrete Beams on Three Supports by Introducing Economical Condition — Die Berechnung der Momente von Stahlbeton-Durchlaufträgern auf drei Stützen unter der Einführung der Wirtschaftlichkeitsbedingung — Calcul des moments des poutres à trois appuis avec introduction de la condition d'économie — *Виши, З.:* Расчет момента трехопорных железобетонных балок, нагруженных постоянной и временной нагрузками, с введением условия экономичности 347

Замбо, Я.: Проблема определения горизонтов в горно-промышленных предприятиях — *Zambó, J.:* The Problem of Division into Stages in Mining Plants — Das Problem der Aufteilung auf Sohlen in Bergbaubetrieben — Le problème de la division en étages dans les exploitations minières 421

ACTA TECHNICA

ACADEMIAE SCIENTIARUM HUNGARICAE

ADIUVANTIBUS
L. GILLEMOT, GY. HEVESI, K. P. KOVÁCS
K. SZÉCHY, G. TARJÁN

REDIGIT
A. GELEJI

TOMUS 51

AKADÉMIAI KIADÓ, BUDAPEST
1965

CALCULATION OF WATER HAMMER PHENOMENA BY AUTOMATIC SEQUENCE CONTROLLED DIGITAL COMPUTERS*

PART I: BASIC PRINCIPLES, EQUATIONS AND FORMULAE

I. BATTA

ENTERPRISE FOR ESTABLISHMENT OF POWER STATIONS, BUDAPEST

[Manuscript received May 24, 1962]

The methods which have generally been applied up to now for the determination of the hydraulic transients of pipeworks of water and oil supply and hydraulic power utilization are not satisfactory. This paper wishes to present, especially for designers, a general method based on Massau's characteristic theory. The main point of this first part is given by various sets of formulae. Some of the boundary value problems elaborated here are: junction of pipes, multiple branches, throttling and volumetric damping elements, power failure of pumps, turbine load failure under action of a speed governor. The present paper illustrates, how to begin solving a problem and how to design a computer program. The second part to be published in the near future, will contain the complete program of an actual problem, the final results of calculations and comparative experimental results.

List of symbols

a	wave velocity;
d	internal diameter of the pipe;
f	cross sectional area of the pipe;
g	acceleration due to gravity;
h	length spacing, address of total head, loss head (h');
i	time spacing point;
j	length spacing point;
m	dimensionless deviation of the adjusting piston of the governor;
n	speed, polytropic exponent;
q	address of discharge;
t	time;
w	adjustment of the desired value on the governor;
x	length, dimensionless deviation of speed;
y	variable level difference;
z	address of Z;
A	atmospherical pressure head;
F	cross sectional area of the surge tank, or that of the air chamber;
G	limit value of the throttling parameter;
H	total head;
J	momentum of inertiae;
L	homogeneous linear ordinary differential expression;
M	torque;
N	number of the longitudinal spacings on a pipe section;
Q	discharge;
T	constant of time-dimension;
Y	constant level difference;
Z	$= Q\|\mathbf{Q}\|$;
ζ, η	generalized loss factors;
τ	throttling parameter.

* Presented in a concise form at the Conference of Hydraulic Machinery held on January 11—13, 1962, by the Society of Mechanical Engineers in Budapest.

I. Introduction

A non-steady flow phenomenon taking place in long pipelines is called water hammer. The present paper deals with the phenomena, in which it must be considered that the value of the velocity of the propagation of the changes is finite. Examination of the water hammer phenomena is first of all necessary in the case of water and oil lines and the discharge tubes of hydroelectric power stations having great head. The computing method to be discussed permits the determination of the time course of the pressure and the velocity, as well as of all quantities connected with the phenomenon at any point of the pipe line, with the complete exploitation of the accuracy assured by the elementary hydraulic relationships, without the applicability of the procedure being limited by the complexity of computing problem — opposite to the graphical and numerical methods known hitherto. In applications of checking, or iterative nature, the procedure gives assistance, by using experimental data if necessary or possible, to the design and operation works, permitting e.g. to avoid the detrimental pressure peaks and the breaking of the water column. Further it allows the precise analysis of e.g. governing or power failure processes and that of complex pipeworks. Thus, it discloses the main components of safety, the economical design and the proper operation. It is to be emphasized that a given computer program may many times be run by variating the several basic data, whereby the most suitable values of the respective data can be chosen.

By this procedure the numerical and graphical methods, respectively so far used are not superfluous, namely, on the one hand, they are included as a degenerated case and, on the other hand, the more simple methods are evidently suited for solving more simple problems later, besides, for preliminary investigations and to examine the effect of certain secondary components, adoption of the methods used up to now is often advantageous. The computing method to be presented is based on one of the classical solutions of partial differential equations and makes possible to take into consideration the pipe friction losses distributed continuously along the pipeline. The losses may be taken into account, in case of any flow pattern, corresponding to steady conditions. This way of considering the pipe friction losses is, in principle, not satisfactory, but — especially in case of relatively slow changes — cannot be objected to from a practical point of view. In addition the behavior of the non steady viscous and turbulent flow is not properly cleared up as yet, finally this simple consideration of the pipe friction obviously means a progress as against the calculation of the losses in a concentrated form.

The present computing method may be applied in the practice — precisely in the problems it is intended for — owing to the high number of the necessary arithmetic operations, can be done only by computer.

The first part of the study now being published clears up the bases of principle of the procedure including various sets of formulae.

II. Basic equations of the water hammer

Equation of motion:

$$H_x + \frac{1}{fg} Q_t = -\frac{\lambda}{2\,d\,f^2\,g} Z\,, \tag{1}$$

$$Z = Q\,|Q|\,.$$

In the right side of equation (1) the pipe friction loss is expressed. By different functions $\lambda = \lambda(R_e)$ any flow pattern may be considered. Among the variables the right-side of the equation depends on Q.

Equation of continuity:

$$H_t + \frac{a^2}{fg} Q_x = 0\,. \tag{2}$$

Equations (1) and (2) form a hyperbolic system of two partial differential equations of the first order, which may be solved by the theory of characteristics.

III. Solution of the fundamental equations, grid equations, internal points of the pipeline

The fundamental equations (1) and (2) form for the unknowns H_x, H_t; Q_x, Q_t an indefinite system, but completed by the stripe conditions

$$\frac{dH}{dx} = H_x + H_t \frac{dt}{dx} \tag{3}$$

and

$$\frac{dQ}{dx} = Q_x + Q_t \frac{dt}{dx} \tag{4}$$

the system becomes definite.

The characteristic projection lines $t = t(x)$ are those, along which, in knowledge of the line derivatives dH/dx and dQ/dx the partial derivatives H_x, H_t; Q_x, Q_t can not be determined univocally from the system formed by the fundamental equations and the stripe conditions. According to this condition — the so-called condition of direction — the determinant of the coefficients along the characteristic projection line should vanish.

$$\begin{vmatrix} 1 & 0 & 0 & \frac{1}{fg} \\ 0 & 1 & \frac{a^2}{fg} & 0 \\ 1 & \frac{dt}{dx} & 0 & 0 \\ 0 & 0 & 1 & \frac{dt}{dx} \end{vmatrix} = 0,$$

that is

$$\frac{dt}{dx} = \pm \frac{1}{a}, \tag{5}$$

thus, the sets of the characteristic projection curves are sets of straight lines of slope $\pm 1/a$.

The change in H and Q along the projection characteristics x, t results from the so-called condition of compatibility. Namely, the system consisting of the fundamental equations and stripe conditions may only be solved, if the rank of the extended matrix is equal to that of the matrix of the coefficients. Accordingly

$$\begin{vmatrix} -\frac{\lambda}{2\,d\,f^2\,g} Z & 0 & 0 & \frac{1}{fg} \\ 0 & 1 & \frac{a^2}{fg} & 0 \\ \frac{dH}{dx} & \frac{dt}{dx} & 0 & 0 \\ \frac{dQ}{dx} & 0 & 1 & \frac{dt}{dx} \end{vmatrix} = 0,$$

that is

$$\frac{dH}{dx} \pm \frac{a}{fg} \frac{dQ}{dx} + \frac{\lambda}{2\,d f^2\,g} Z = 0. \tag{6}$$

This equation, expressing the change in H and Q along the projection characteristics is Massau's form of the characteristics H, Q. The sign $+$ belongs to the slope $+1/a$, while the sign $-$ to that of $-1/a$. A similar equation was published by GRAY, ASCE 1953, however using this equation for modifying the graphical procedure and especially for constructing the laminar water hammer.

It is to be observed that with $\lambda \equiv 0$ there exists characteristics H, Q which are independent of the plane x, t and these are precisely the equations

of the well-known shock lines. The independence of x, t of the shock lines permits the shock lines to span over an arbitrary distance and time, respectively, and in this case to construct a grid of characteristics consisting of infinitesimal elements becomes unnecessary, and the mesh sizes may also be finite. Nevertheless, in case of $\lambda \neq 0$ taken as the basis of these calculations, the problem is precisely the numerical determination of this grid, consisting of infinitesimal elements. To solve a problem numerically, one must always have a recourse to finite elements, consequently, the above discussions mean that practically in case of $\lambda = 0$, if allowed by the boundary conditions, the length- and time units of the grid may be chosen to be considerably greater as compared to the case $\lambda \neq 0$.

Assuming $\lambda =$ const., with fixed length- and time units $\Delta x = h$, $\Delta t = h{:}a$ equation (6) may be solved by the trapeze rule (Fig. 1). The only important restriction is the necessity of use of the trapeze rule:

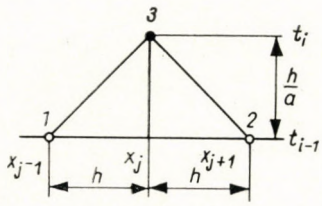

Fig. 1

$$H_3 - H_1 + \frac{a}{fg}(Q_3 - Q_1) + \frac{\lambda h}{4\,d f^2 g}(Z_3 + Z_1) = 0\,, \tag{7}$$

$$H_2 - H_3 - \frac{a}{fg}(Q_2 - Q_3) + \frac{\lambda h}{4\,d f^2 g}(Z_2 + Z_3) = 0\,. \tag{8}$$

These equations may be separately used for calculating the boundary conditions, if the point marked 3 is a right- or left-side boundary point. In internal points H_3 and Q_3 it may be calculated from the known (initial) values belonging to the points 1 and 2 by the formulae obtained by elimination from Eqs (7) and (8):

$$H_3 = \frac{1}{2}(H_1 + H_2) + \frac{a}{2\,fg}(Q_1 - Q_2) + \frac{\lambda h}{8\,d f^2 g}(Z_1 - Z_2)\,, \tag{9}$$

$$Q_3 = \frac{1}{2}\,(Q_1 + Q_2) + \frac{fg}{2\,a}(H_1 - H_2) - \frac{\lambda h}{8\,adf}(Z_1 + 2\,Z_3 + Z_2) \tag{10}$$

From (9) H_3 may directly be computed, (10) yields the value of Q_3 e.g. by iteration. The rapidity of the convergence of the iteration is influenced by the mesh size h.

IV. Initial conditions

The initial conditions correspond to a steady motion or a hydrostatic state. The hydrostatic state is trivial, but the determination of the steady flow demands great care, especially in the case of a complex system of lines. The initial values may be calculated with well-known methods. One must avoid inconsistency between the initial values and the shock equations and the boundary equations. As a starting condition also an intermediate, momentary state of the calculation may figure. A computing problem like this may appear e.g. in connection with a check-walve closing or, for example, if there is a sudden change in the cross sectional area of a surge tank.

V. Boundary conditions

The boundary value problems given do not lay claim to completeness, but due to their diversity they elucidate almost the total field of the water hammer computing problems. The boundary value equations may be adopted without any alteration even if — in case of a short line section — the x, t grid consists purely of boundary points.

1. Junction of two pipe sections

The pipe sections may have different diameters, be of different wave velocities and pipe friction loss coefficients. At the junction a differential throttling may exist.

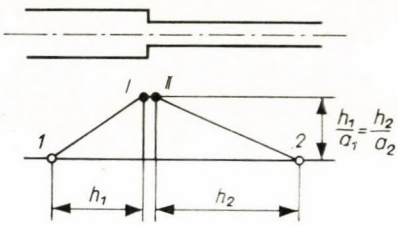

Fig. 2

On the basis of continuity

$$Q_{\mathrm{I}} = Q_{\mathrm{II}} = Q\,, \quad Z_{\mathrm{I}} = Z_{\mathrm{II}} = Z\,.$$

The flow loss appearing at the junction

$$H_{\mathrm{I}} - H_{\mathrm{II}} = \zeta Q^2 + \eta Z\,, \tag{11}$$

where ζ and η are loss factors of suitable dimensions, with signs if necessary.

According to (7) and (8), respectively

$$H_{\mathrm{I}} = H_1 + \frac{a_1}{f_1 g}(Q_1 - Q) - \frac{\lambda_1 h_1}{4 d_1 f_1^2 g}(Z + Z_1),$$
$$H_{\mathrm{II}} = H_2 - \frac{a_2}{f_2 g}(Q_2 - Q) + \frac{\lambda_2 h_2}{4 d_2 f_2^2 g}(Z + Z_2). \tag{12}$$

From equations (11) and (12) H_{I} and H_{II} may be eliminated and from the equation so obtained Q may be determined. After calculating Z, also the values H_{I} and H_{II} may be obtained from Eq. (12).

2. *Junction of many lines in a single point*

All the pipelines of number P may have different diameters. The wave velocities, the pipe friction loss coefficients may also be different.

In the present equations the measurement of the velocity and the pipe length is a positive value towards the junction point.

In the junction, at the instant t_i — at the end of all joining pipelines — the pressure head H is a common value.

The values of the k-th pipeline belonging to the instant t_{i-1} and to the network node beside the junction are designated by k, while the quantities of the junction point referring to t_i are denoted by K.

At the same instant t_i the continuity in the branch point prevails

$$\sum_{K=1}^{P} Q_K = 0. \tag{13}$$

The shock equations for the pipeline sections of number P next to the junction point are as follows:

$$H = H_k + \frac{a_k}{f_k g}(Q_k - Q_K) - \frac{\lambda_k h_k}{4 d_k f_k^2 g}(Z_k + Z_K) \tag{14}$$
$$k, K = 1, 2, \ldots, P.$$

The number of the equations (13) and (14) is altogether $P + 1$, this number is exactly identical to that of the unknowns H and Q_K, consequently, the unknowns may be determined.

3. *The case, when the wave times are incommensurable within a pipework*

Incommensurability is that case, when the pipe sections of the pipework cannot for computing purposes be divided by length units h_k in such a way the grid time unit $\Delta t = h_k/a_k$ should be common for all line sections.

At such times the time unit must be chosen to correspond to the line section probably furnishing the preponderant water hammer effect. To the characteristic grid, however, of all lines sections, which are incommensurable with the main line section from the point of view of the wave times, the irregular mesh elements illustrated in Fig. 3 must be pressed in.

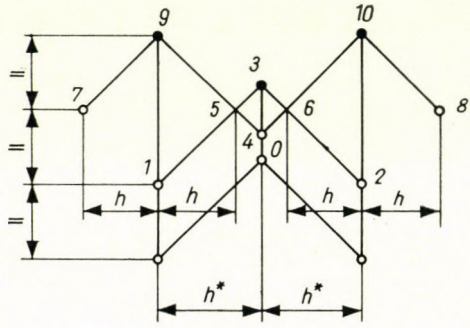

Fig. 3

From the values of points 1 and 2 those belonging to point 3 may be calculated with equations (9) and (10) by substituting $h = h^*$. Thereafter two ways may be chosen. Either the point 4 must be linearly interpolated between 0 and 3 and so the points 9 and 10 may be calculated from points 7 and 8 by Eqs. (7) and (8) — substituting with point 9 the value of $h = h^*$ into (8) and with 10 that of $h = h^*$ into (7) — or the points 5 and 6 must be interpolated between 1—3 and 2—1, respectively, whereby points 5,7—9 and 6,8—10 form regular network elements. In principle the interpolation is permitted only if there are no discontinuities of 0th and 1st order in H and Q on the line section given. From a practical point of view, compromise may be made in the latter case. Calculation by point 4 seems to be more correct as against 5 and 6.

4. *Closing device at the line end*

The closing device either closes, or opens the pipeline. If the closing, or opening is rapid, a suitably short time unit is to be chosen.

According to the condition of discharge into the atmosphere, H_0 is a constant value equal to the geodetic height of discharge. Without limiting the generality, $H_0 = 0$ may be written.

The throttling curves of the closing device may be summarized in the following formulae:

$$\begin{aligned} H_3 &= H_3(Q_3, \tau_3), \qquad 1 \geq \tau \geq G; \\ Q_3 &= Q_3(H_3, \tau_3), \qquad G > \tau \geq 0. \end{aligned} \tag{15}$$

The throttling parameter τ is a function of time. It can be observed that formulae (15) include both the free discharge and the full closing.

It is practicable to apply the shock equation in two forms, too:

$$\begin{aligned} Q_3 &= Q_1 - \frac{fg}{a}(H_3 - H_1) - \frac{\lambda h}{4\,adf}(Z_3 + Z_1), \quad 1 \geq \tau \geq G; \\ H_3 &= H_1 - \frac{a}{fg}(Q_3 - Q_1) - \frac{\lambda h}{4\,df^2 g}(Z_3 + Z_1), \quad G > \tau \geq 0. \end{aligned} \tag{16}$$

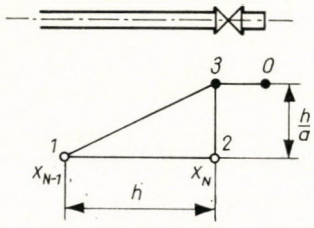

Fig. 4

The system consisting of equations (15) and (16) may be solved e.g. by iteration. The value of G must be so determined that the iteration should be convergent in both phases.

G may be, depending on the nature of the problem, also a fixed value, but it is practicable to build in a preliminary test of convergence in the computing program — corresponding to the approximate method adopted — and accordingly to choose between the two computing methods. The throttling curves — similarly to other empiric functions — may be given tabularly, when the calculation must be performed by interpolation, or — in a wider sense of interpolation — by analytic or sectionally analytic approximate functions.

5. *Closing device in the line*

According to the continuity

$$Q_{\mathrm{I}} = Q_{\mathrm{II}} = Q.$$

The throttling curves of the closing device:

$$H_{\mathrm{I}} - H_{\mathrm{II}} = h'(Q, \tau), \qquad 1 \geq \tau \geq G; \tag{17}$$

$$Q = Q(H_{\mathrm{I}} - H_{\mathrm{II}}, \tau), \qquad G > \tau \geq 0. \tag{18}$$

The shock equations between $I - 1$:

$$Q = Q_1 - \frac{fg}{a}(H_{\mathrm{I}} - H_1) - \frac{\lambda h}{4\,adf}(Z + Z_1) \tag{19}$$

or

$$H_{\mathrm{I}} = H_1 - \frac{a}{fg}(Q - Q_1) - \frac{\lambda h}{4\,df^2 g}(Z + Z_1), \tag{20}$$

and between $II - 2$:

$$Q = Q_2 + \frac{fg}{a}(H_{\mathrm{II}} - H_2) + \frac{\lambda h}{4\,adf}(Z + Z_2) \tag{21}$$

or

$$H_{\mathrm{II}} = H_2 + \frac{a}{fg}(Q - Q_2) + \frac{\lambda h}{4\,df^2 g}(Z + Z_2). \tag{22}$$

That is

$$Q = \frac{1}{2}(Q_1 + Q_2) + \frac{fg}{2\,a}(H_1 - H_2) - \\ - \frac{fg}{2\,a}(H_{\mathrm{I}} - H_{\mathrm{II}}) - \frac{\lambda h}{8\,adf}(Z_1 - Z_2) \tag{23}$$

$$H_{\mathrm{I}} - H_{\mathrm{II}} = H_1 - H_2 - \frac{2\,a}{fg}Q + \frac{a}{fg}(Q_1 - Q_2) - \\ - \frac{\lambda h}{4\,df^2 g}(Z_1 + 2\,Z + Z_2) \tag{24}$$

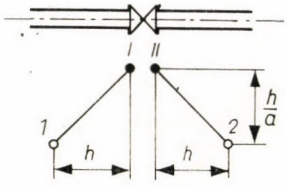

Fig. 5

The calculation must be performed in two parts similarly to the former section.

If $1 \geq \tau \geq G$, from (17) and (23) one must determine $H_{\mathrm{I}} - H_{\mathrm{II}}$ and at the same time from (23) the value of Q, finally from (20) that of H_{I} and from (22) that of H_{II}.

If $G > \tau \geq 0$, one has to calculate from (18) and (24) the value of Q, further from (20) that of H_{I} and from (22) H_{II}.

6. *Air chamber at the line end*

The air chamber works alone in the line after closing the closing device mounted after the pump.

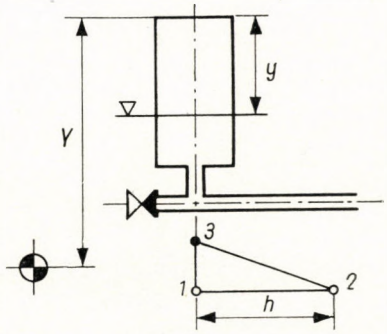

Fig. 6

Continuity:

$$y_3 = y_1 + \frac{h}{2\,aF}(Q_3 + Q_1). \tag{25}$$

Pressure equation:

$$H_3 = H(y_3). \tag{26}$$

The system (25)—(26) is made complete by the shock-equation between points 3 and 2.

Scheme of the iteration cycle:

a) First approximation of y_3 by $Q_3 = Q_1$, from (25);

b) first approximation of H_3 from (26);

c) first approximation of Q_3 from the shock equation.

7. *Air chamber with differential throttling in line*

Continuity:

$$y_b = y_a + \frac{h}{2\,aF}[(Q_{\mathrm{II}} - Q_{\mathrm{I}}) + (Q_{ii} - Q_i)]. \tag{27}$$

The pressure equation is obtained by taking polytropic expansion into account, also hydrostatic considerations and differential throttling:

$$H_b = Y - A - y_b + (H_0 + A - Y + y_0)\left(\frac{y_0}{y_b}\right)^n - \\ - [\zeta (Q_{II} - Q_I) + \eta |Q_{II} - Q_I|] (Q_{II} - Q_I) . \tag{28}$$

Shock equations between $I - 1$:

$$Q_I = Q_1 - \frac{fg}{a}(H_b - H_1) - \frac{\lambda h}{4\, a\, df}(Z_I + Z_1) , \tag{29}$$

and between $II - 2$:

$$Q_{II} = Q_2 + \frac{fg}{a}(H_b - H_2) + \frac{\lambda h}{4\, a\, df}(Z_{II} + Z_2) . \tag{30}$$

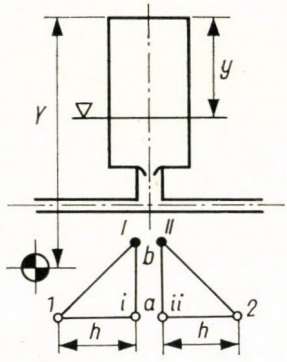

Fig. 7

Scheme of the iteration cycle:

a) Assuming H_b to be constant, the first approximation of Q_I and Q_{II} may be calculated from (29) and (30);

b) first approximation of y_b is given by (27);

c) first approximation of H_b must be calculated from (28).

The cycle is repeated until attaining sufficient accuracy.

8. Reservoir, surge tank

The discharge is constant. Continuity:

$$F \frac{dy}{dt} - Q + Q_0 = 0 ,$$

that is

$$y_3 = y_2 - \frac{h}{aF} Q_0 + \frac{h}{2\,aF} (Q_3 + Q_2). \tag{31}$$

Pressure head at the entrance:

$$H_3 = y_3 + \frac{1}{4 f^2 g} (Z_3 - Q_3^2). \tag{32}$$

The unknowns H_3, Q_3, y_3 are determined by (31) and (32) and by the shock equation between points 3—1.

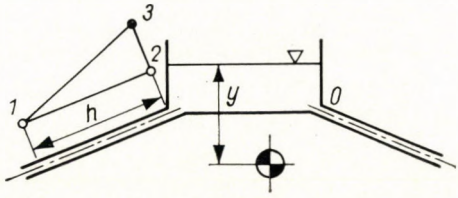

Fig. 8

Variable $Q_0(t)$, or $y(t)$, may be prescribed, further the water hammer may also be considered in the flow-off branch.

9. *Surge tank considered rigid at the end of a closed pipe*

When neglecting the forces of inertiae, the surge tank behaves as a static volumetric damping device similar to an air chamber.

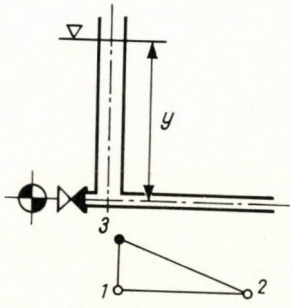

Fig. 9

The overflow return surge tanks changing their cross sectional area by step or breaking, may be computed according to sections. Considering the forces of inertiae — neglecting the elasticity — the following equations are obtained:

Continuity:

$$y_3 = y_1 - \frac{h}{2\,aF}(Q_3 + Q_1). \tag{33}$$

Pressure equation:

$$H_3 = y_3\left[1 - \frac{h}{aFg}(Q_3 - Q_1)\right]. \tag{34}$$

The system (33)—(34) is made complete by the shock equation between points 3—2.

10. Elastic surge tank in line

For characterizing the initial steady state, y and $Q = 0$, the values corresponding to the constant free water level are memorized throughout an interval of suitable length as belonging to some equidistant, or nearly

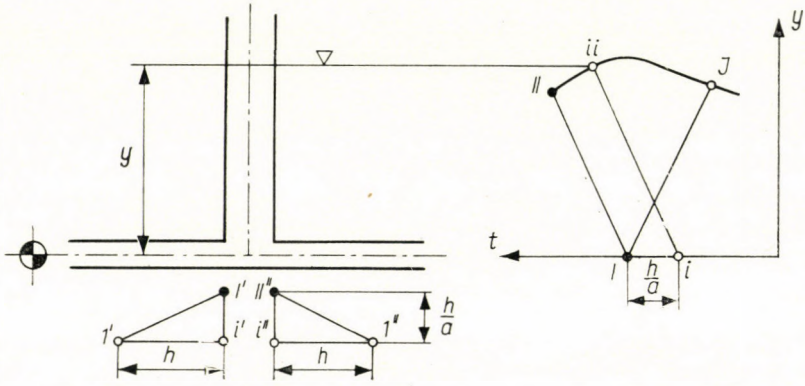

Fig. 10

equidistant time values, together with the respective time value are tabulated many times.

In the further course of calculation the related values of y, Q; t are obtained and may be attached to the end of the table. The calculation advancing, the beginning of the table gradually becomes superfluous.

y, t characteristic between J — I:

$$t_J = t_I - a'\,y_J\,, \tag{35}$$

yielding the values t_J, y_J and Q_J.

y, t characteristic between I — II:

$$t_{II} = t_I + a'\,y_{II}. \tag{36}$$

Shock equation between J — I neglecting the friction:

$$H_{\mathrm{I}} - y_J = \frac{a'}{fg}(Q_{\mathrm{I}} - Q_J). \tag{37}$$

Shock equation between I — II neglecting the friction:

$$y_{\mathrm{II}} - H_{\mathrm{I}} = -\frac{a'}{fg}(Q_{\mathrm{II}} - Q_{\mathrm{I}}). \tag{38}$$

Further the shock equation between points $1'-3'$ and $1''-3''$ may be set down.

Continuity in point $\mathrm{I} \equiv \mathrm{I}' \equiv \mathrm{I}''$:

$$Q_{\mathrm{I}} = Q'_{\mathrm{I}} - Q''_{\mathrm{I}}. \tag{39}$$

Approaching from any direction, the pressure head at the junction is always identical.

Scheme of the iteration cycle.

a) The change may take place either from the direction of point $1'$, or from point $1''$. The shock equation written along the line, assuming H_{I} to be unchanged, yields the first approximation of Q'_{I} and Q''_{I};

b) the continuity equation (39) leads to the first approximation of Q_{I};

c) the first approximation of H_{I} must be computed from the shock equation (37).

The cycle is repeated. After attaining a suitable accuracy, the quantities belonging to point II must be computed. For this, an equation of second degree referring to Q_{II}, obtained from the equation of continuity

$$y_{\mathrm{II}} - y_{ii} = \frac{1}{2F}(Q_{\mathrm{II}} + Q_{ii})(t_{\mathrm{II}} - t_{ii}) \tag{40}$$

of the water level, from (36) and (38), i.e. actually the system (36)—(38)—(40) must be solved.

11. Pump at the line end

There is no closing device or it does not work. The level of the pump well is constant, the losses of the draft pipe and all fittings and armatures are included into the pump characteristics. The speed of the pump reduces because of power failure.

Characteristics of the pump:

$$H = H(Q, n), \tag{41}$$

$$M = M(Q, n). \tag{42}$$

Inertia equation:

$$n_3 = n_1 - \frac{15\,h}{\pi\,aJ}\,(M_3 + M_1). \tag{43}$$

The equations (41), (42), (43) and the shock equations between points 3—2 determine the unknowns Q_3, n_3, H_3, M_3.

It can be observed that the characteristics of the pump given by (41) and (42) permit the calculation, due to the one valued and continuous nature of the functions, of all operational conditions of the pump (two pump-, two turbine- and four brake domains).

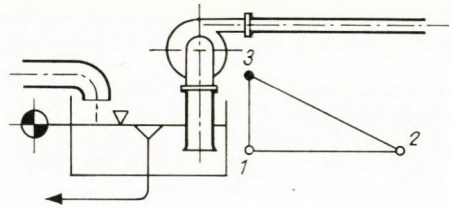

Fig. 11

If in the field of characteristics $\partial H/\partial Q \geq a/fg$ there occurs a jump in the flow along the shock-line, the value of the speed remains unchanged. Fortunately, this statement is only of theoretical importance.

12. Pump, air chamber at the end of the pipeline

Characteristics of the pump:

$$H_3 = H(Q_{\mathrm{III}}, n_3), \tag{44}$$

$$M_3 = M(Q_{\mathrm{III}}, n_3). \tag{45}$$

Equation of inertiae:

$$n_3 = n_1 - \frac{15\,h}{\pi\,aJ}\,(M_3 + M_1). \tag{46}$$

Continuity:

$$Q_{\mathrm{III}} = Q_3 + Q_1 - Q_I - \frac{2\,aF}{h}\,(y_3 - y_1). \tag{47}$$

Pressure equation of the air chamber:

$$y_3 = y(H_3). \tag{48}$$

The system (44)—(48) is completed by the shock equations between 3—2.

The elements of the iteration cycle: n_3 e.g. by $M_3 = M_1$ from (46), H_3 by (44), Q_3 by H_3 from the shock equation, y_3 from (48), Q_{III} from (47), finally M_3 from (45).

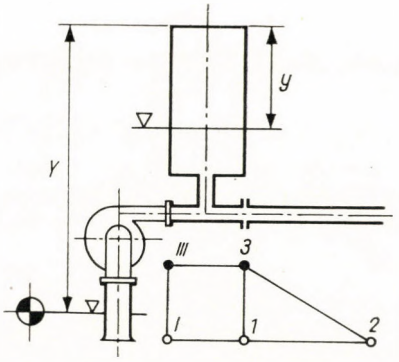

Fig. 12

If $\partial H/\partial Q = 0$, the flow is broken, that is, it runs over the brake-branch of the curve of unchanged speed. This case demands a special treatment but does not disturb the continuity of the water hammer.

13. Pump, closing device at the end of the line

Characteristics of the pump:

$$H_{III} = H(Q_3, n_3), \tag{49}$$

$$M_3 = M(Q_3, n_3). \tag{50}$$

Inertia equation:

$$n_3 = n_1 - \frac{15\,h}{\pi\,aJ}(M_3 + M_1)\,. \tag{51}$$

Throttling curves of the closing device:

$$H_{III} - H_3 = h'(Q_3, \tau_3), \qquad 1 \geq \tau \geq G; \tag{52}$$

$$Q_3 = Q(H_{III} - H_3, \tau_3), \qquad G > \tau \geq 0. \tag{53}$$

The system becomes completed by the shock equation set down between points 3—2. The shock equation is to be solved as is needed for Q_3 and H_3.

The computation is to be performed in two parts by the judicious application of the foregoing. The calculation — in the same way as before — divides

the system in two parts after complete closing. Nevertheless, after complete closing it is possible to calculate separately the closed end pipe section and the closed pump. This separate calculation — especially if the complete closing does not follow at a time spacing point — may also become necessary.

Schematically, the computing cycles consist of the following elements.

Beginning of closing:

a) The first approximation of n_3 by $M_3 = M_1$ is yielded by (51);

b) the first approximation of H_{III} by the first approximation of n_3 is given by (49);

c) the first approximation of H_3 may be calculated from (52);

d) the first approximation of Q_3 is yielded by the shock equation;

e) the first approximation of M_3 is furnished by (50).

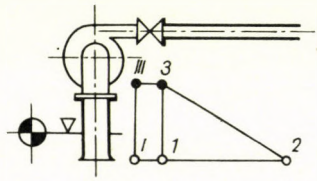

Fig. 13

The second phase of the closing:

a) The first approximation of n_3 by $M_3 = M_1$ from (51);

b) the first approximation of Q_3 by $\tau = \tau_3$, by $H_3 = H_1$ and by $H_{III} = H_I$ from (53);

c) the first approximation of H_3 from the shock equation;

d) the first approximation of H_{III} from (49);

e) the first approximation of M_3 from (50).

14. Pump, closing device, air chamber at the end of the line

Characteristics of the pump:

$$H_{III} = H(Q_{iii}, n_3), \tag{54}$$

$$M_3 = M(Q_{iii}, n_3). \tag{55}$$

Inertia equation:

$$n_3 = n_1 - \frac{15\,h}{\pi\,aJ}\,(M_3 + M_1). \tag{56}$$

Throttling curves:

$$H_{III} - H_3 = h'(Q_{iii}, \tau_3), \qquad 1 \geq \tau \geq G; \tag{57}$$

$$Q_{iii} = Q(H_{III} - H_3, \tau_3), \qquad G > \tau \geq 0. \tag{58}$$

Continuity:

$$Q_{iii} = Q_3 + Q_1 - Q_i - \frac{2\,aF}{h}(y_3 - y_1)\,, \tag{59}$$

$$y_3 = y_1 - \frac{h}{2\,aF}\left[(Q_{iii} - Q_3) + (Q_i - Q_1)\right]. \tag{60}$$

Pressure equation of the air chamber:

$$y_3 = y(H_3), \tag{61}$$

$$H_3 = H(y_3). \tag{62}$$

The system (54)—(62) becomes determined by the shock equation written for points 3—2.

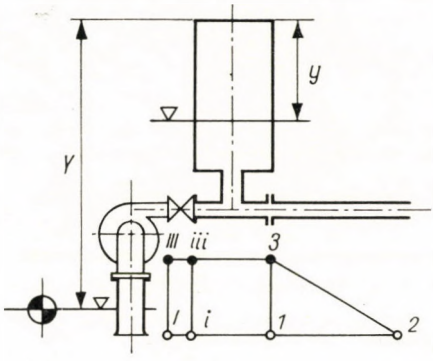

Fig. 14

Scheme of the iteration cycle:

$$1 \geq \tau \geq G$$

n_3 e.g. by $M_3 = M_1$ from (56), H_{III} from (54), H_3 from (57), Q_3 from the shock equation, y_3 from (61), Q_{iii} from (59), M_3 from (55).

$$G > \tau \geq 0$$

y_3 e.g. by $Q_{iii} = 0$ and $Q_3 = Q_1$ from (60), H_3 from (62), n_3 e.g. by $M_3 = M_1$ from (56), Q_3 by H_3 from the shock equation, Q_{iii} from (58), M_3 from (55).

In view of the fact that at a given instant to which a given value τ belongs, the pump with the closing device may be regarded as one unit, the stability of the flow in this case is ensured by the condition $\partial(H - h')/\partial Q < 0$.

15. Pump with a long suction line

Continuity:

$$Q_i = Q_{ii} = Q_a\,;\;\; Q_I = Q_{II} = Q_b\,.$$

Characteristics of the pump, the influence of the suction head neglected:

$$\Delta H = H(Q, n), \tag{63}$$

$$M = M(Q, n). \tag{64}$$

Inertia equation:

$$n_b = n_a - \frac{15\,h}{\pi\,a J}\,(M_b + M_a). \tag{65}$$

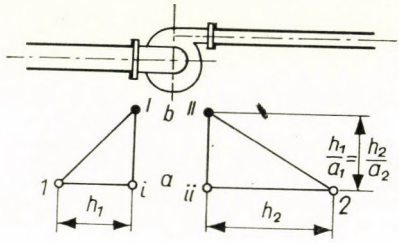

Fig. 15

From the shock equations:

$$H_{\mathrm{II}} - H_{\mathrm{I}} = H\,(Q_b, n_b) = H_2 - H_1 - \frac{a_2}{f_2\,g}\,Q_2 - \frac{a_1}{f_1\,g}\,Q_1 +$$

$$+ \left(\frac{a_2}{f_2\,g} + \frac{a_1}{f_1\,g}\right) Q_b + \tag{66}$$

$$+ \frac{\lambda_2\,h_2}{4\,d_2 f_2^2\,g}\,Z_2 + \frac{\lambda_1\,h_1}{4\,d_1 f_1^2\,g}\,Z_1 + \left(\frac{\lambda_2\,h_2}{4\,d_2 f_2^2\,g} + \frac{\lambda_1\,h_1}{4\,d_1 f_1^2\,g}\right) Z_b\,.$$

Scheme of the iteration cycle:
n_3 e.g. by $M_b = M_a$ from (65), $H_{\mathrm{II}} - H_{\mathrm{I}}$ from (63), Q_b from (66), M_b from (64). Finally H_{II} and H_{I} may be computed on the basis of the separate shock equations.

16. Pump with a long suction line and closing device

Characteristics of the pump:

$$\Delta H = H(Q, n), \tag{67}$$

$$M = M(Q, n). \tag{68}$$

Inertia equation:

$$n_b = n_a - \frac{15\,h}{\pi\,aJ}(M_b + M_a). \tag{69}$$

Throttling curves of the closing device:

$$H_{bb} - H_{bbb} = h'(Q_b, \tau_b), \qquad \tau_b \geq G; \tag{70}$$

$$Q_b = Q(H_{bb} - H_{bbb}, \tau_b), \qquad \tau_b < G. \tag{71}$$

$$\tau_b \geq G$$

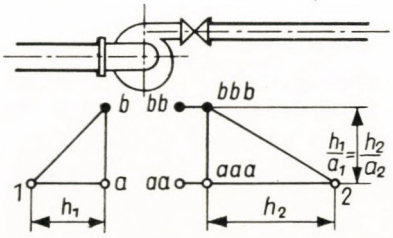

Fig. 16

Scheme of the computing cycle:
n_b e.g. by $M_b = M_a$ from (69), H_{bb} from (67), H_{bbb} from (70), Q_b from the shock equation between points bbb—2, M_b from (68), H_b from the shock equation between 1—b.

$$\tau < G$$

n_b e.g. by $M_b = M_a$ from (69), Q_b by τ_b leaving H_{bb} and H_{bbb} unchanged from (71), H_b and H_{bbb} from the shock equations between points 1 — b and bbb — 2, H_{bb} from (67), M_b from (68).

17. Turbine load failure

It is practicable to give the field of turbine characteristic — as against the pump characteristics — the form of

$$Q = Q(H, n, m), \tag{72}$$

$$M = M(H, n, m); \tag{73}$$

for in the operation domain of the field these functions are one valued, the possibility of the complete closing included.

The shock equation between points 1—3 is to be set down.

Equation of the governor:

$$L_1(m) = L_2(x) + L_3(w). \tag{74}$$

L_1, L_2 and L_3 are linear differential expressions, m is the dimensionless deviation of the adjusting piston being an output quantity; $x = (n - n_0) : n_0$ dimensionless speed deviation, input quantity; w adjustment of the desired value, input quantity.

The load failure should take place with an unchanged adjustment, that is, $L_3(w) = 0$.

If the governor has only a tachometer but no accelerometer, then generally

$$L_2(x) = Tx' + x. \tag{75}$$

This time the inertia equation of the turbine-alternator rotor yields:

$$n_3 = n_2 + \frac{15\,h}{\pi\,aJ}(M_3 + M_2). \tag{76}$$

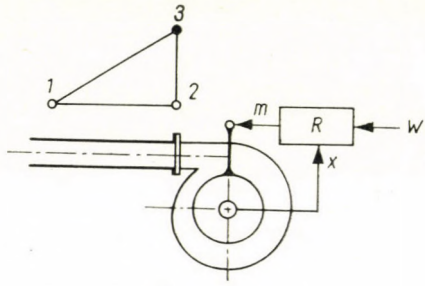

Fig. 17

Scheme of the iteration cycle:

a) First approximation of n_3 by $M_3 = M_2$ from (76);

b) first approximation of $L_2(x)$ by a linear function with the first approximation of n_3 as per (75);

c) first approximation of m_3 by solving (74);

d) first approximation of Q_3 from (72) by $H_3 = H_2$, with the first approximation of n_3 and m_3;

e) computing the first approximation of H_3 by approximating Q_3 from the shock equation;

f) first approximation of M_3 from (73) on the basis of the foregoing.

After repeating the cycle up to sufficient accuracy, the derivatives of m belonging to point 3 must be computed up to the order needed, for the following instant.

With governors provided with an accelerometer, $L_2(x)$ is a differential expression of higher order. As an example, L_2 should be of the fourth order. In this case $L_2(x)$, that is, x or n must be approximated in the interval 2—3 by a polynomial, the degree of which is equal to the order of L_2. In view of

the fact that multi-node differentiating formulae may not be applied generally in the case of hyperbolic differential equations, an interpolation by two multiple nodes is to be made.

The inertia equation of the rotating system is as follows:

$$\frac{dn}{dt} = \frac{30}{\pi J} M. \tag{77}$$

In the equation (77) M is to be given within the interval $t_{i-1} = 0$ and $t_i = h/a$ by a polynomial of the third degree. Assuming both limit values to be known, the limit points are double nodes:

$$M_2 = M(H_2, n_2, m_2);$$

$$M_2' = \left(\frac{\partial M}{\partial H}\right)_2 (H_3 - H_2)\frac{a}{h} + \left(\frac{\partial M}{\partial n}\right)_2 \frac{30}{\pi J} M_2 + \left(\frac{\partial M}{\partial m}\right)(m')_2 \tag{78}$$

and

$$M_3 = M(H_3, n_3, m_3);$$

$$M_3' = \left(\frac{\partial M}{\partial H}\right)_3 (H_3 - H_2)\frac{a}{h} + \left(\frac{\partial M}{\partial n}\right)_3 \frac{30}{\pi J} M_3 + \left(\frac{\partial M}{\partial m}\right)(m')_3. \tag{79}$$

By adopting a Hermitean interpolation formula

$$\begin{aligned} M(t) = M_2 &\left[1 - 3\left(\frac{a}{h}\right)^2 t^2 + 2\left(\frac{a}{h}\right)^3 t^3\right] + \\ &+ M_3\left[3\left(\frac{a}{h}\right)^2 t^2 - 2\left(\frac{a}{h}\right)^3 t^3\right] + \\ &+ M_2'\left[t - 2\frac{a}{h}t^2 + \left(\frac{a}{h}\right)^2 t^3\right] + M_3'\left[-\frac{a}{h}t^2 + \left(\frac{a}{h}\right)^2 t^3\right]. \end{aligned} \tag{80}$$

Hence

$$n = n_2 + \frac{30}{\pi J}\int_0^t M(t)\,dt, \tag{81}$$

that is,

$$\begin{aligned} n_3 = n_2 + \frac{30}{\pi J}\int_0^{h/a} M(t)\,dt = n_2 + \\ + \frac{15\,h}{\pi\,aJ}\left[M_2 + M_3 + \frac{1}{6}\frac{h}{a}(M_2' + M_3')\right]. \end{aligned} \tag{82}$$

Corresponding to the aforesaid:

$$L_2(x) = x_2 + f_1(t)M_2 + f_2(t)M_3 + f_3(t)M_2' + f_4(t)M_3', \tag{83}$$

where $f_p(t)$ ($p = 1, 2, 3, 4$) are functions to be predetermined for the governor.

The iteration steps may be similar to the above ones.

Expression (75) may also be solved according to (83) by a linear approximation of $M(t)$ by a function of second order.

V. Viewpoints of principle of the calculation

1. *Preparation*

For computing the water hammer, the hydraulic model of the system must be determined.

For this the following are needed:

a) Scheme of the system of lines, including the correlations and constructional elements installed;

b) pipe lengths developed;

c) geodetic data;

e) wave velocities;

f) pipe friction loss factors;

g) hydraulic and mechanical characteristics of the constructional elements involved.

Starting out from the given data, all important characteristics of the initial conditions must be calculated. Thereafter, with the aid of an approximate method, the run of the phenomenon must be stated. Already at the approximate determination of the phenomenon — but even more with the accurate calculation — an iteration process may be adopted, not with the purpose of determining the individual numerical values, but consisting of the repeated calculation of the individual sections. In one step of the iteration method mentioned above the characteristics of a group of the sections of the system is to be computed, while the variation in the characteristics of the remaining group on the basis of a preceding step must be considered. In a following step the elements of the group in turn will differ from the foregoing ones. The quantities obtained in the course of the procedure may converge to the system of solution corresponding to the hydraulic and mathematical model chosen. This idea permits, however, to build in approximate methods for considering secondary effects. This procedure may be applied especially when volumetric damping elements are built into the pipework.

After preliminary estimations, the time unit is to be fixed in agreement with the losses, rapidity of the convergence and computer data, and possibly with the commensurability of the sections in view of wave times. Finally all grid- and boundary equations are to be set down with the numerical substitution of the reference data. The computer program must be based on these equations.

2. *Machine program*

As an introduction, the schedule for the calculation of the machine program must be determined, that is, the spacing- and limit points of the individual sections of the pipework must be reasonably numbered and the program must be so established, that the machine should work according to the sequence of the numbering. If there is a fixed-point machine, the basic data, variables and equations must be transformed by suitable scale factors. The initial line of computation is not necessarily a constant time line, but may be e.g. a characteristic line; the essential is merely that it should be out of the domain of the influence of the changes of the boundary values, but it may even attain the limit of the domain of influence if the changes are continuous.

The layout of the program can be illustrated by a simple example. The pipeline should consist of a single section. The constructional elements at the ends (I, II) of the pipeline represent a boundary condition each.

Let $h + j$ ($j = 0, 1, 2, \ldots, N$) be the address of the total head existing momentarily in point j of the pipeline, that is $(h + j) = H_j$, similarly $(q + j) = Q_j$ and $(z + j) = Z_j$.

Let further h_1, h_2; q_1, q_2; z_1, z_2 be the addresses for the temporary storage of the initial values, and h', q', z' the addresses for the transitory storage of the intermediate results. The simbol $\Rightarrow$ means transfer, or setting. In the present example the numerical values computed in succession between the two ends of the line belong to an identical time t_i. The scheme of the program is as follows:

a) Preparation.

b) Calculation of the boundary values I:

$$H_{\mathrm{I}} = H_0 \Rightarrow h', \; Q_{\mathrm{I}} = Q_0 \Rightarrow q', \; Z_{\mathrm{I}} = Z_0 \Rightarrow z'$$

printing.

c) Setting of the transfer orders corresponding to $j = 1$.

d) $(h + j - 1) \Rightarrow h_1$, $(h + j + 1) \Rightarrow h_2$; $(h') \Rightarrow h + j - 1$, similarly for Q and Z, too.

e) As per formulae (9) and (10) the values belonging to the point i, j must be computed and they must be suitably setted in h', q', z'; printing.

f) If $j < N - 1$, after increasing j by 1, jump to *d)* if $j = N - 1$ computing is continued on *g)*.

g) Computing the boundary values II: $H_N \Rightarrow h + N$, $Q_N \Rightarrow q + N$, $Z_N \Rightarrow z + N$; printing.

h) Up to the run of a complete wave, or until a predetermined arbitrary time, after increasing i by 1, jump to *b)*. After reaching the condition signing the end of the total computation, jump to a stop order.

The number of the orders of the program and that of the operations to be performed depend on the order system of the computer.

REFERENCES

1. ALLIÉVI, L.: Allgemeine Theorie über die veränderliche Bewegung des Wassers in Leitungen. Springer Verlag, Berlin 1909.
2. PARMAKIAN, J.: Water Hammer Analysis. Prentice Hall, New York 1956.
3. GRAY, C.: Analysis of Water Hammer by Characteristics. Proceedings of the ASCE (1953), September.
4. SAUER, R.: Anfangswertprobleme bei partiellen Differentialgleichungen. Springer Verlag, Berlin 1952.
5. COLLATZ, L.: Numerische Behandlung von Differentialgleichungen. Springer Verlag, Berlin 1955.
6. HUTAREW, G.: Regelungstechnik. Springer Verlag, Berlin 1955.
7. *Computing Centre of the Hungarian Academy of Sciences* : Programming of the Electronic Computer M 3 (in Hungarian). Budapest 1959.

WASSERSTOSSBERECHNUNG MIT HILFE EINER PROGRAMMGESTEUERTEN, DIGITALEN RECHENMASCHINE; I. TEIL

I. BATTA

ZUSAMMENFASSUNG

Jene Methode, die bisher zur Bestimmung von hydraulischen Transienten von Druckleitungen der Wasser- und Ölversorgung und der Wasserturbinen verbreitet angewandt werden, sind nicht befriedigend. Diese Abhandlung stellt eine sich auf dem Massau'schen Charakteristikenverfahren gründende, allgemeine Methode hauptsächlich den Konstrukteuren zur Verfügung. Der Hauptteil des vorliegenden ersten Absatzes ist eine ziemlich vielfältige Formelsammlung. Eine Auswahl aus den ausgearbeiteten Randwertaufgaben: Anschluß von zwei Rohren, mehrfache Abzweigung, Drosselorgane, Ausgleichsvorrichtungen, Triebkraftausfall von Pumpen, Lastabwurf von geregelten Turbinen. Die vorliegende Abhandlung veranschaulicht, wie man die Lösung einer Aufgabe in Angriffnehmen und ein Berechnungsprogramm zusammenstellen kann. Der zweite Absatz, der in der nächsten Zukunft erscheinen wird, wird das ganze Programm, dessen Berechnungsergebnisse und (zum Vergleich) Versuchsresultate einer konkreten Aufgabe enthalten.

CALCUL DU COUP DE BÉLIER PAR CALCULATRICE ÉLECTRONIQUE DIGITALE À PROGRAMME; Ire PARTIE

I. BATTA

RÉSUMÉ

Les procédés largement employés jusqu'à présent pour la détermination des transitions hydrauliques des systèmes de distribution d'eau et d'utilisation des forces hydrauliques, ainsi que des pipe-lines, ne sont pas satisfaisants. L'auteur se propose d'offrir une méthode générale basée sur le procédé des caractéristiques selon Massau, à l'usage surtout des constructeurs. L'essentiel de cette première partie est formée par un recueil de formules varié. Les problèmes des valeurs limites étudiés par l'auteur se rapportent aux sujets suivants: raccordement des tubes, embranchement multiple, soupapes et robinets, éléments de compensation, arrêt de la force motrice des pompes, arrêt de fonctionnement des turbines avec réglage. L'auteur expose la façon d'aborder un problème et de construire un programme de calcul. La deuxième partie à paraître prochainement contiendra le programme total d'un problème concret, les résultats des calculs et les résultats expérimentaux comparatifs.

РАСЧЕТ ВОДЯНОГО УДАРА ПРИ ПОМОЩИ ЦИФРОВОЙ ЭЛЕКТРОННОЙ-ВЫЧИСЛИТЕЛЬНОЙ МАШИНЫ ПРОГРАММНОГО УПРАВЛЕНИЯ, I

И. БАТТА

РЕЗЮМЕ

Широко применявшиеся до сих пор методы определения гидравлических переходных процессов, возникающих в системах трубопроводов водоснабжения и утилизации гидроэнергии, а также в нефтепроводах, являются неудовлетворительными. Данная работа желает дать общий метод, основывающийся на характеристическом методе Массау, главным образом для проектантов. Основой данной первой части является довольно разнообразный комплекс уравнений. Разработаны следующие задачи: соединение труб, многократные разветвления, дросселирующие органы, уравнивающие элементы, выпад привода насосов, выпад нагрузки турбин при регулировании. Работа дает ответ на вопрос, каким образом необходимо приступить к решению какой-либо задачи и разработать программу расчета. Публикуемая в ближайшем будущем вторая часть будет содержать полную программу некоторой конкретной задачи, конечные результаты расчета и сравнительные опытные результаты.

THE INFLUENCE OF THE BLADE-BREADTH ON THE CHARACTERISTICS OF CENTRIFUGAL PUMPS WITH OPEN TYPE IMPELLERS

F. STVRTECZKY and Á. SZABÓ

DEPARTMENT OF HYDRAULIC MACHINES TECHNICAL UNIVERSITY, BUDAPEST

[Manuscript received December 22, 1962]

Experiments were carried out on impellers having the same size but with different blade breadth. Curves showing the functions of H versus Q and η versus Q respectively, and further curves relating to dimensionless characteristics are plotted in order to reveal the influence of blade breadth. As seen from measuring results made in connection with efficiency maxima, as compared with international standards, an outstanding value could be reached even in the case of deceleration of the average speed at the flow-section preceding the inlet edge of the impeller. As far as a better arrangement of the plotted points is concerned, remarkable influence of an imaginary area, calculated at the breadth belonging to the gravity centre, could be stated.

I. Introduction

The scientific coworkers of the Department of Hydraulic Machines working in the field of pump research have devoted a great deal of their activity to the calculation of pump impellers based on singularities [1—6]. All these calculating methods are characterized by the assumption that the flow in an impeller is two-dimensional. In other words, in these methods the three-dimensional effects, varying with the impeller breadth b are not taken into account.

The measurements as dealt with in this paper were carried out in order to examine by experiments the said influence of dimension b, i.e. the impeller breadth upon the characteristics of the pump.

To carry out measurements, the experiments were made with an impeller (marked VV13) of the VV series developed by the scientific workers of this Department. By turning on a lathe the impeller breadth had been modified step by step. Doing so, two kinds of blades were formed: one type was made with a constant breadth (b = const.), the other one decreasing from the inlet to the outlet edge, ($b_1 > b_2$) showed a conical form (see Fig. 1).

II. Symbols

(See Fig. 2)

D_0 diameter of the suction pipe before the inlet edge of the impeller;
D_1 inlet diameter of the impeller;
D_2 outlet diameter of the impeller;
$A_0 = \frac{D_0^2 \pi}{\pi 4}$;

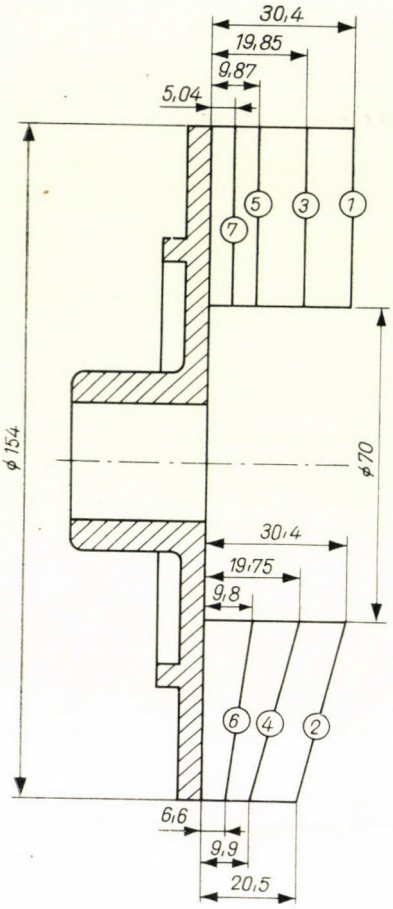

Fig. 1

$A_1 = D_1 \pi b_1$;
$A_{1s} = D_1 \pi b$;
H head of delivery;
P power input;
Q rate of flow;
b impeller breadth;
b_1 blade breadth at inlet circle;
b_2 blade breadth at outlet circle;
$b_{av} = 1/2\,(b_1 + b_2)$ average breadth;
$b_s = b_2 + 1/3\,(b_1 - b_2)$ central breadth (measured at the gravity centre of the conical blade surface, see Fig. 8);
r rounding-off of the pump-cover at the suction side;
x clearance between impeller blade and casing (measured in axial direction);
η pump efficiency;
η_{max} efficiency maximum;
ϱ density of water delivered;
τ power ratio;
φ capacity ratio;
ψ head ratio;
ω angular velocity.

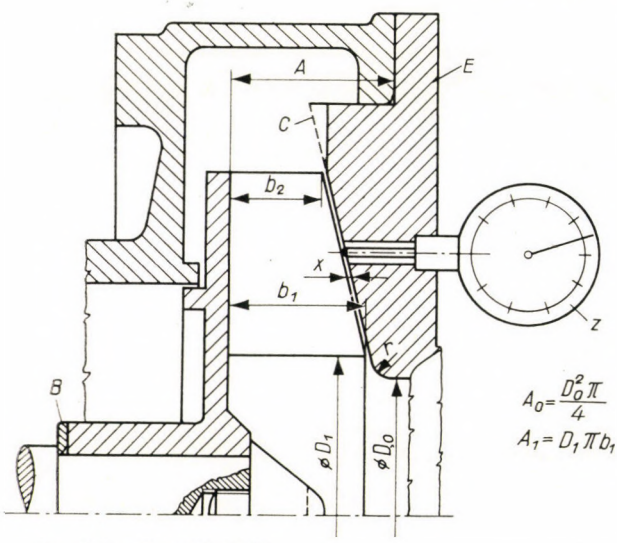

Fig. 2

III. Description of the measuring method

The rate of flow was determined by volumetric measurements. The head was determined by the indication of a differential mercury manometer inserted between the suction side and pressure side, further by the resistance of tube pieces situated between pressure-take-off points and the pipe-ends on the pump, finally by the difference of velocity heads arising from the deviation between the diameter of suction pipe and pressure pipe respectively. The speed was checked by means of a Jaquet-indicator. The dimensions of the impeller used for these experiments were: $D_2 = 154$ mm, $D_1 = 70$ mm, with 3 blades of logarithmic-spiral shape of 15°, made of a 2 mm sheet.

The original breadth of blade was 30,40 mm, consecutively turned down to 5.04 mm. Meridional sections are shown in Fig. 1, numerical breadth values are given in Table I. Blades with constant breadth are shown on the upper part, conical blades on the lower part of Fig. 1. Ciphers which are encircled refer to numeral symbols of the impellers according to Table I (and Table II).

Table I

Impeller dimensions, mm

Identification mark of the impeller	b_1	b_2	b_{av}	b_s
1	30.40	30.40	30.40	30.40
2	30.40	20.50	25.45	23.80
3	19.85	19.85	19.85	19.85
4	19.75	9.90	14.82	13.18
5	9.87	9.87	9.87	9.87
6	9.80	6.60	8.20	7.70
7	5.04	5.04	5.04	5.04

For each one of the impellers, a special shroud-plate E was prepared. In Fig. 2, the pump assembly is shown, including the clearance x and the distance A from the shroud; in addition, in Table II the values of these are given.

The clearance x was measured with an accuracy of 1/100 mm, by means of the indicator gauge Z; the average value of measurements on 4 different points was considered as relevant.

Intentionally, the distance A should be kept invariable, independently of variations of x; thus, the values of the impeller-breadth and of the shroud-

Table II

Assembly dimensions, mm

Identification mark of the impeller	Assembly dimensions		
	x	A	r
1	0.080	48.98	3.5
2	0.035	48.14	4.5
3	0.045	48.00	2.8
4	0.040	47.84	4.5
5	0.055	48.03	3.2
6	0.044	49.34	2.8
7	0.054	48.19	4.5

breadth were specified accordingly. In spite of this, due to machining inaccuracies the A values in Table II vary. For the sake of a possibly greater uniformity of the experiments, an axial shift of the impeller up to about 1 mm was tolerated rather than having variations of the clearance of say 0.1 mm. To this end, shims B of adequate thickness were provided between axle-collar

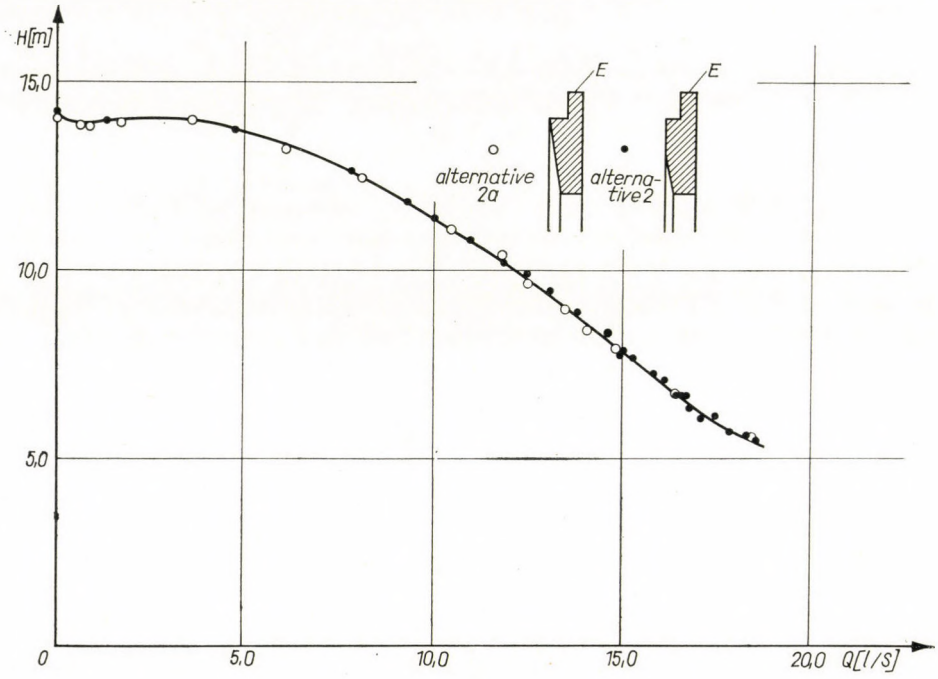

Fig. 3

and wheel-hub by means of which a minimum clearance of 0.5 mm could be arrived at.

In the last column of Table II, values of the rounding-off radius of the shroud are given. According to measurement results as reported below, variations of this radius do not much bear upon the character of the curves.

As illustrated in Fig. 2, the end-point of the conical profile on the inner surface of the shroud-plate at suction side coincides with the outer diameter of the blade and from here the profile continues as a straight line perpendicular to the axis. When testing the impeller marked *2* (according to Table I), another alternative experiment was carried out with a shroud-plate having the form (and mark) *2a*, according to that detailed in Fig. 2, as shown along the dashed line *C*. The characteristic curves H versus Q are delineated in Fig. 3, by plotting the points complying with the results of measurements made on both alternatives. The difference between the two cases does not exceed the normal measuring deviations.

Measurements were made at a speed of 2000 and a geodetic suction head H_{gs} of 1.0 ± 0.1 m.

IV. Measuring results obtained on an impeller with constant blade breadth

In Fig. 4, the curves H versus Q and η versus Q are shown.

As was expected, the diminution of the blade breadth b, the delivered quantity Q decreases. Likewise, with head belonging to zero-delivery and the input-energy decrease too. Efficiency again increases with the decreasing breadth at the first period, and it decreases afterwards; thus, efficiency η, as a function of the breadth b, shows a maximum value.

The impeller No. *3* shows a special feature characterised by an efficiency of 80%. At this point ($\eta_{max} = 80\%$) the corresponding values are: $Q = 10$ l/s; $H = 10.3$ m; n = 2000 r.p.m., and the specific speed $n_q = 35$. In the paper by HAJDU [7] dealing with the best types of pumps produced in the whole world, the highest "standard" efficiency reported for these data is equal to 78.5%. Thus, the efficiency of this impeller No. *3* surpasses this level by 1,5% [7].

For a more conspicuous illustration of changes occurring, curves of the following dimensionless quantities are plotted in Fig. 5.

$$\varphi_s = \frac{2\,Q}{\pi\, D_1^2\, b_s\, \omega}\,;$$

$$\psi = \frac{8\,gH}{D_2^2\, \omega^2}\,;$$

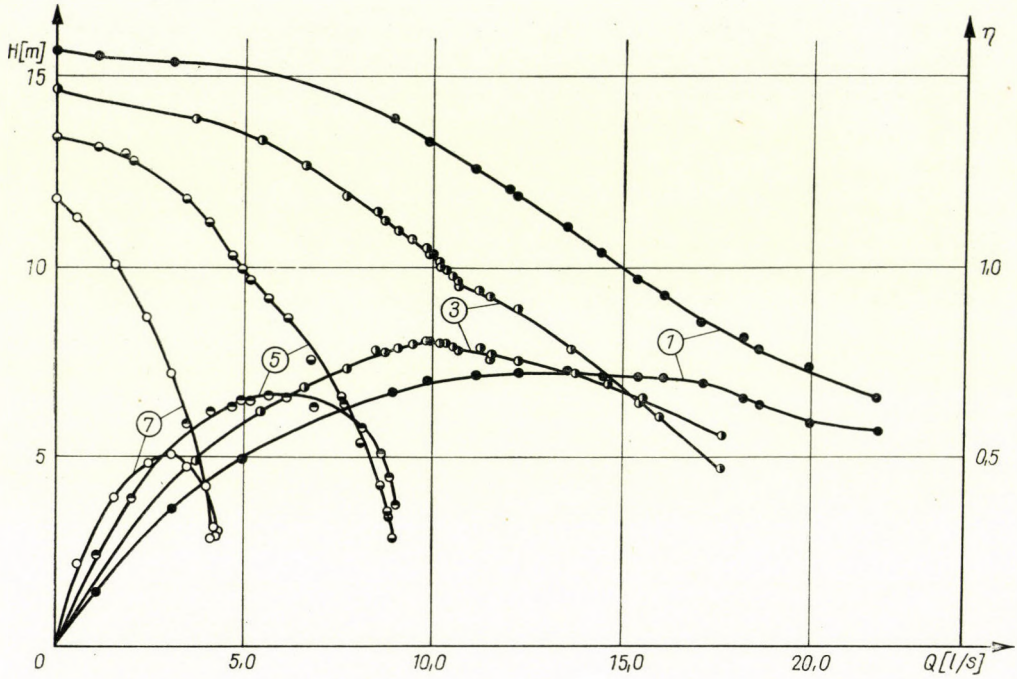
H[m]
15
10
5
0
5,0
10,0
15,0
20,0
Q[l/s]
η
1,0
0,5
1
3
5
7

Fig. 4

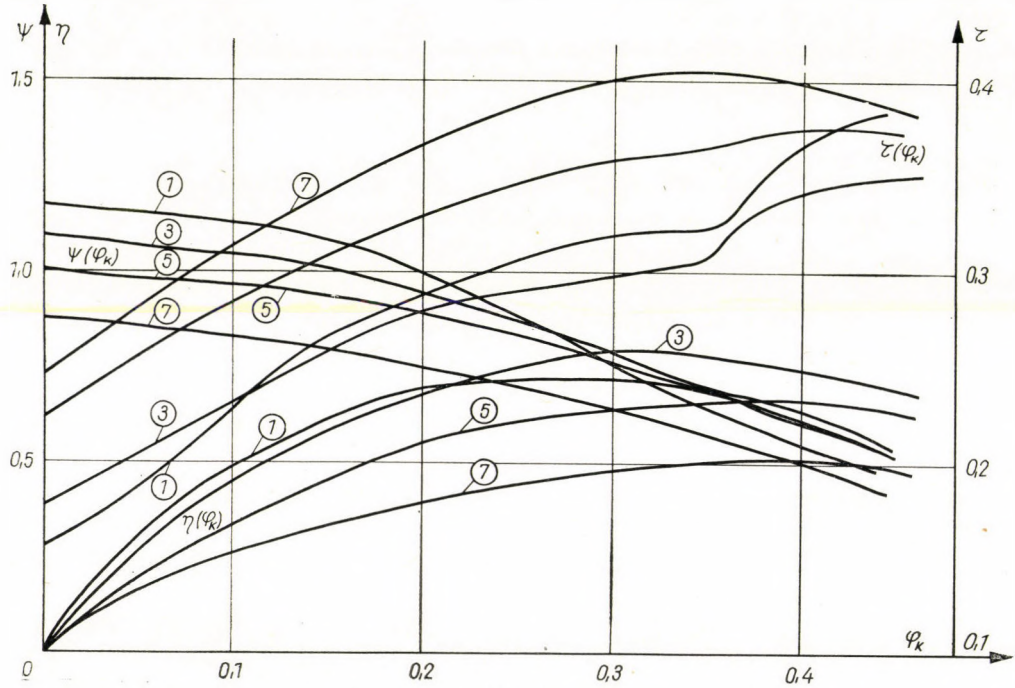
ψ
η
1,5
1,0
0,5
0
0,1
0,2
0,3
0,4
τ
0,4
0,3
0,2
0,1
τ(φk)
ψ(φk)
η(φk)
φk
1
3
5
7

Fig. 5

$$\tau = \frac{1200}{\pi (D_2/D_1)^2 \omega^3 D_1^4 \varrho} \cdot \frac{P}{b_s};$$

$$\eta = \frac{\varphi_s \psi}{\tau}.$$

Al these functions are dimensioned by using the m.kp.s. units system.

As can be seen, the diminution of the blade breadth b generally results in decreasing values of ψ and in increasing values of τ. These increased values of τ are so to say self-evident, because the values of losses independent of delivery as compared to the useful output will increase when the blade-width values b decrease. The same effect can be observed by the sudden decrease of efficiency towards the smaller values of b. The strong decrease of curve ψ (Fig. 5) of the impeller having the lesser blade breadth b, can be regarded as being connected with an important deterioration of the hydraulic efficiency. The sloping down of the ψ curves nearly proportional to the breadth at small φ_s values may be ascribed to some effect exerted by the spiral casing.

V. Measuring results obtained on an impeller of conical shape

By plotting the values Q, H and η as calculated from measuring results the curves H versus Q, and η versus Q are obtained according to Fig. 6.

Experiments were carried out on conical shaped impellers in order to compare the obtained curves with those belonging to impellers of constant blade breadth. As seen from Fig. 1, the meridional section of a conical impeller is obtained by tracing a straight line from the extreme inlet point to the extreme outlet point of the blade belonging to the impeller marked with the next number. (Due to turning operations, some unimportant deviations arose as seen from the values given in Table I and in Fig. 1.) Odd numbers belong to impellers with constant blade-breadth, even numbers serve to mark conical impellers. It follows from what has been said above, that the meridional section line of each conical impeller is located between the meridional section lines of two impellers, marked with an odd number, having a constant blade breadth.

It is advisable to examine any group of three adjacent impellers separately. The respective curves belonging to each group are illustrated in Figs. 7—11, as characteristics of the dimensionless quantitites.

In order to establish a dimensionless relation, the blade breadth b_s as measured at the gravity centre of the conical blade surface will be introduced here. In Fig. 8, in which the impellers numbered *3*, *4* and *5* can be compared, the trend of curves shows that this dimensionless relation is suitable to obtain a coordination of the curves of both the odd-numbered and the even-numbered

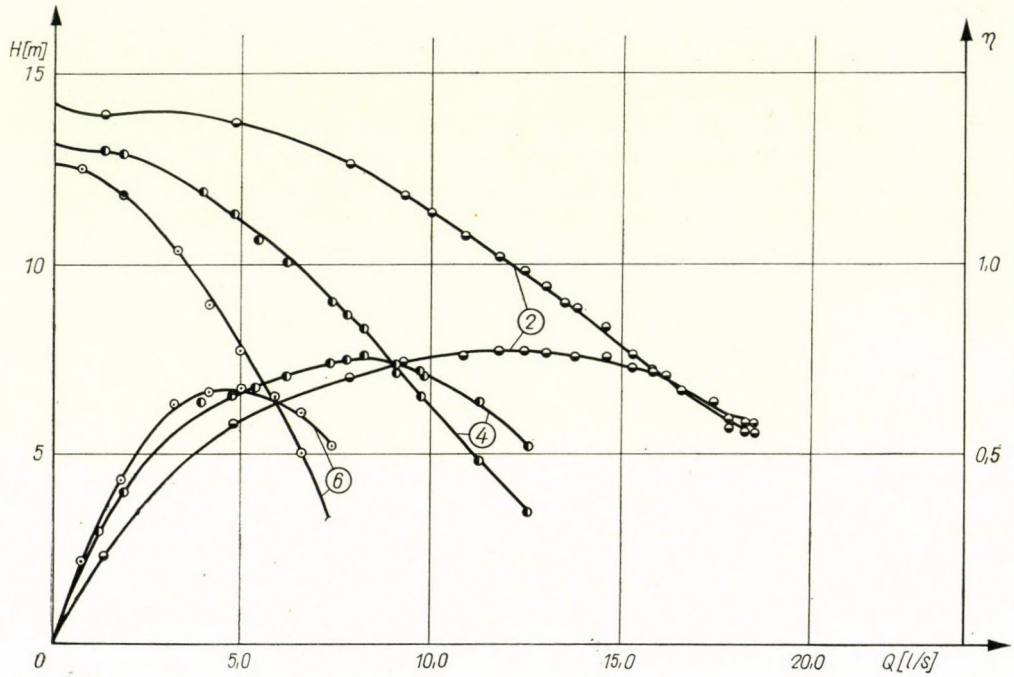
H[m]
15
10
5
0
η
1,0
0,5
5,0
10,0
15,0
20,0
Q[l/s]
2
4
6

Fig. 6

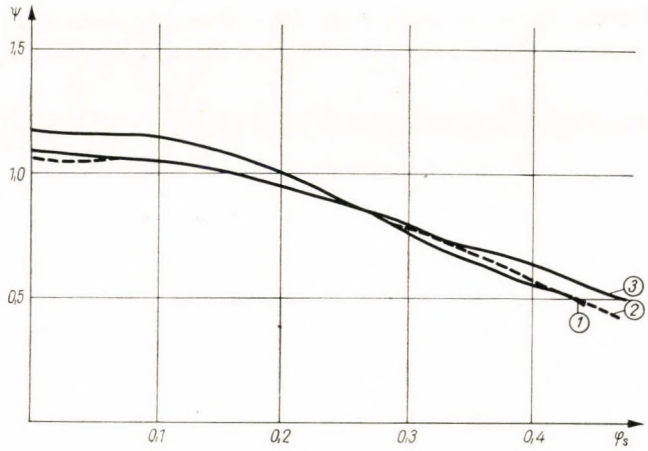
Ψ
1,5
1,0
0,5
0,1
0,2
0,3
0,4
φs
3
2
1

Fig. 7

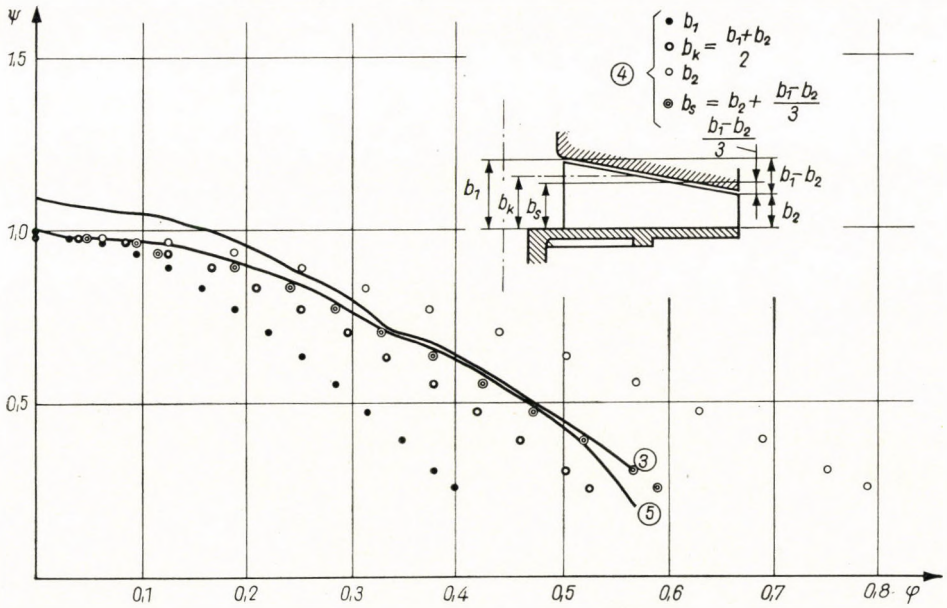
ψ
1,5
1,0
0,5
0,1
0,2
0,3
0,4
0,5
0,6
0,7
0,8
φ
4
• b_1
o $b_k = \frac{b_1+b_2}{2}$
o b_2
◉ $b_s = b_2 + \frac{b_1-b_2}{3}$
$\frac{b_1-b_2}{3}$
b_1
b_k
b_s
b_1-b_2
b_2
3
5

Fig. 8

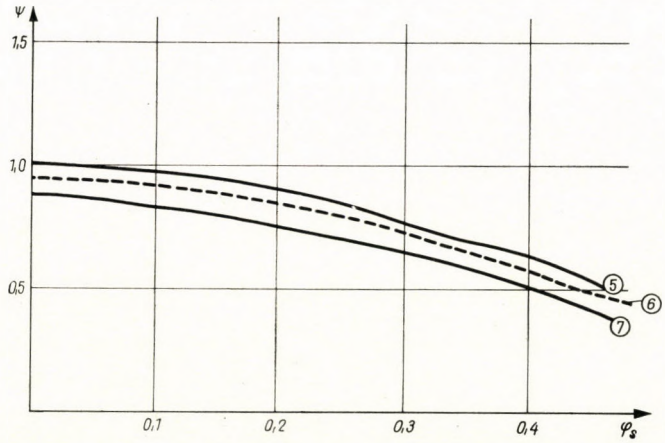
ψ
1,5
1,0
0,5
0,1
0,2
0,3
0,4
φ_s
5
6
7

Fig. 9

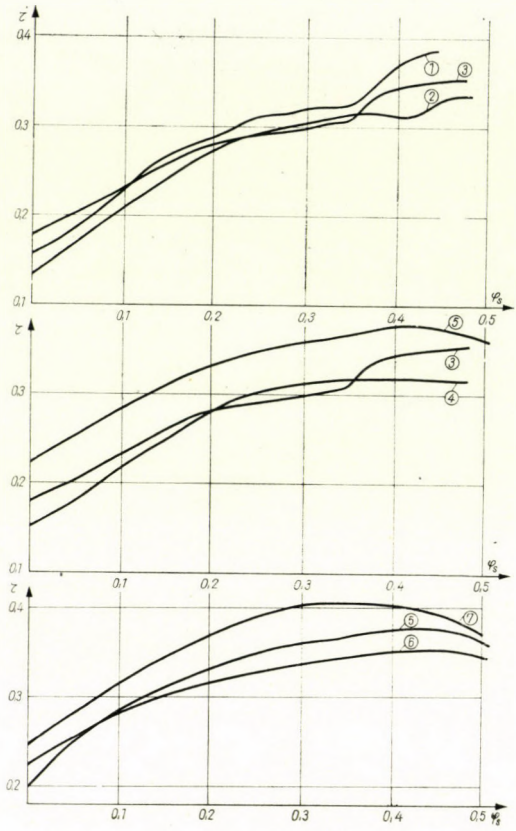

Fig. 10

blades. Namely, in this diagram, those results are plotted that were obtained for the curve $\psi(\varphi)$ belonging to the conical impeller nr. *4* in due consideration of values calculated on the basis of the inlet breadth b_1, the outlet breadth b_2, the central breadth b_s as well as the average breadth b_{av}. Fig. 8 shows full length curves; the curves in the following Figures are drawn by omitting the values belonging to $\varphi > 0.5$ as points having no interest for our investigations.

From this remarkable result obtained by the dimensionless relation based on b_s it seems justified to infer that the blade breadth measured at the gravity centre might be regarded as responsible for the water quantity delivered. Such a statement is in strict opposition to the generally adopted view, according to which the determination of the water quantity delivered depends upon inlet conditions.

As can be seen from Fig. 7—10, the values φ obtained with a conical impeller, and consequently, the values of τ too, are generally smaller than those belonging to impellers with a constant width.

Efficiency correlations are shown in Fig. 11. Obviously, the efficiency curve of a conical impeller runs closely in between the two curves of the adjacent impellers of constant width, with the only exception of the impeller No. *6*.

In the designing practice for pumps, the generally followed trend is characterised by adopting a value of 0.95 ÷ 1 for the ratio of the areas A_1/A_0 according to Fig. 2. As far as flow conditions are concerned, this ratio is re-

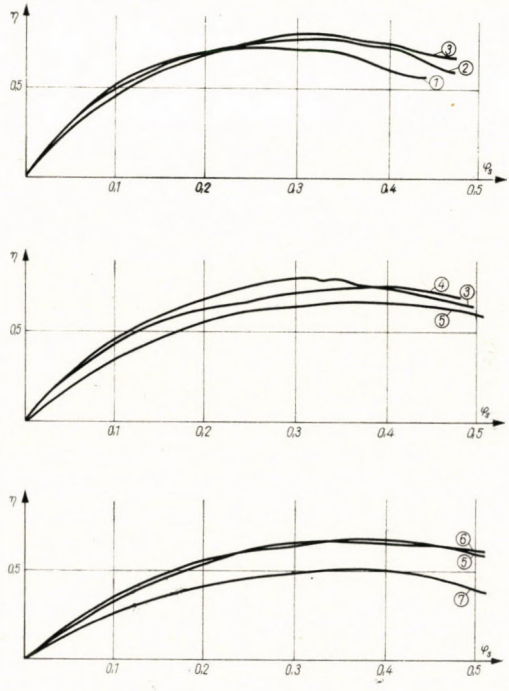

Fig. 11

sponsible for a minute acceleration of the mean flow speed value in the curved section preceding the inlet edge of the impeller.

By plotting the values of efficiency maxima η_{max} in function of the ratio A_1/A_0, according to Fig. 12, the single values show, as compared with the dashed line, a deviation of about $\pm 3\%$. In any case, as seen from the diagram, the ratio A_1/A_0 that belongs to the maximum efficiency, assumes the value of about. 1.5 or, generally speaking, this value is to be found between 1 and 2; in other words, the efficiency of $\eta = 80\%$, outstanding in comparison with international records, could be reached even in connection with the deceleration of the average speed at the flow-section preceding the inlet edge.

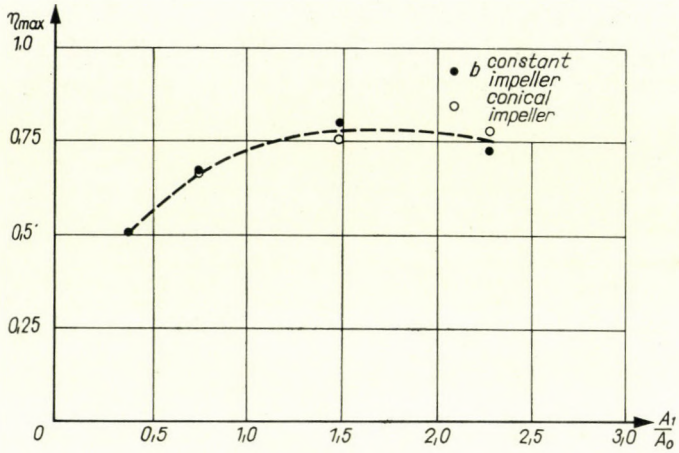

Fig. 12

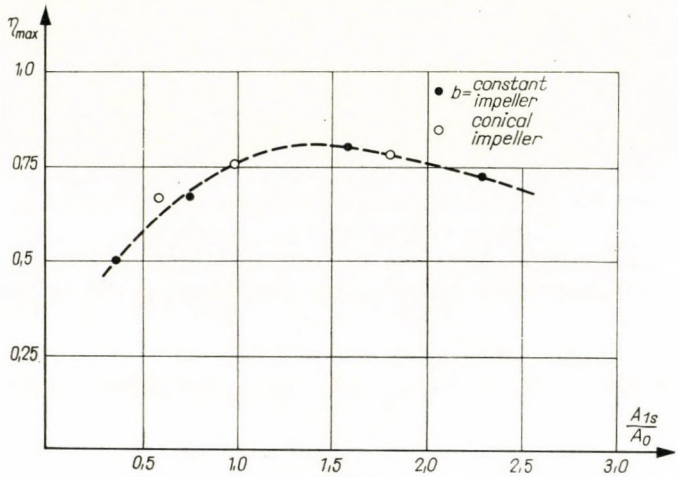

Fig. 13

Attention is to be paid to the fact that the survey data are better arranged, when the imaginary surface

$$A_{1s} = D_1 \pi \cdot b_s$$

is substituted for the original area A_1. The curve of the function $\eta_{max}(A_1/A_0)$ is plotted in Fig. 13.

Acknowledgement

The authors wish to express sincere thanks to A. VERBA for the valuable help he gave by aiding the investigations.

REFERENCES

1. VERBA, A.: Véges lapátvastagságú, radiális átömlésű járókerekek számítása (Computing of Impellers with Finite Blade-Thickness and Radial Flow). Dissertation, 1960.
2. FÜZY, O.: Bestimmung des induzierten Geschwindigkeitsfeldes einer unvollständigen Wirbelquellenreihe. *Periodica Polytechnica, Engineering* **4**, 4 (1960).
3. VERBA, A.: Method of Singularities for Computing the Velocity Distribution in a Radial Impeller. *Acta Techn. Hung.* **1** 1—2. (1961), 4—5.
4. FÜZY, O.: Közel radiális átömlésű járókerekek lapátozásának tervezése (Design of Blade Arrangement in Impellers with Almost Radial Flow). *BME, 1961. évi Tudományos Évkönyv.*
5. FÜZY, O.: Beiträge zur konformen Abbildung eines Schaufelsternes auf ein ebenes Schaufelgitter. *Periodica Polytechnica* **4** (1961).
6. FÜZY, O.: Design of Mixed-Flow Impeller Blades. *Periodica Polytechnica.* **6**, 4 (1962).
7. HAJDU, S.: Örvényszivattyúk hatásfok standardja (Standard Efficiency Values of Centrifugal Pumps). Manuscript.

EINFLUSS DER SCHAUFELBREITE AUF DIE GESTALTUNG DER CHARAKTERISTIK-KURVEN VON ZENTRIFUGALPUMPEN MIT OFFENEM LAUFRAD

F. STVRTECZKY und Á. SZABÓ

ZUSAMMENFASSUNG

Messungen wurden an 7 (darunter 3 kegelförmigen) Laufrädern durchgeführt, welche mit gleichen Dimensionen, aber mit verschiedenen Schaufelbreiten verfertigt worden waren. Die gewonnenen Kurven zeigen die Förderhöhe und den Wirkungsgrad als Funktionen der Wassermenge, und weitere Kurven zeigen den Verlauf der dimensionslosen Kennzahlen, aus welchen der Einfluß der Schaufelbreite klar hervorgeht. Aus einer Analyse der Meßergebnisse bzw. der daraus erhaltenen Wirkungsgrad-Maxima ist es ersichtlich, daß es möglich war, einen den internationalen Standard-Wert übertreffenden Wirkungsgrad auch bei einer Verlangsamung der mittleren Strömungsgeschwindigkeiten vor dem Laufradeintritt zu erzielen. In der Anordnung der Kurvenpunkte konnte man die ausgezeichnete Rolle der fiktiven Fläche konstatieren, die durch die Schwerpunktschaufelbreite definiert worden war.

L'INFLUENCE DE LA LARGEUR D'AUBE SUR LES CARACTÉRISTIQUES DES POMPES CENTRIFUGES A ROUE OUVERTE

F. STVRTECZKY et Á. SZABÓ

RÉSUMÉ

Les auteurs ont effectué des mesures sur des roues de mêmes dimensions ayant des largeurs d'aubes différentes. Les courbes montrent la hauteur d'élévation et le rendement en fonction du débit. D'autres courbes indiquent les caractéristiques sans dimensions, qui font apparaître clairement l'influence de la largeur d'aube. L'analyse des résultats des mesures et des maxima du rendement montre qu'il était possible d'obtenir un rendement dépassant la norme internationale, même quand la vitesse d'écoulement moyenne avant l'entrée de la roue était réduite. Quant à une meilleure disposition des points relevés, on pouvait constater l'influence d'une surface imaginaire, en tenant compte de la largeur d'aube tracée à travers le centre de gravité.

ВЛИЯНИЕ ШИРИНЫ РАБОЧЕГО КОЛЕСА ЦЕНТРОБЕЖНЫХ НАСОСОВ С ПОЛУОТКРЫТОЙ ЛОПАСТНОЙ РЕШЕТКОЙ НА ВИД КРИВЫХ ХАРАКТЕРИСТИК

Ф. ШТВРТЕЦКИ И А. САБО

РЕЗЮМЕ

Проведены замеры семи рабочих колес идентичных размеров (среди них трехконических), но с различной шириной лопаток. Полученные кривые показывают высоту напора и *кпд* в функции количества воды, а также безразмерные показатели. По этим данным видно влияние ширины лопаток. Анализ максимумов *кпд*, полученных на основе данных измерений, показал, что можно было достигнуть *кпд*, превосходящий международный стандарт, даже при замедлении средней скорости перед входом в рабочее колесо. В распределении точек измерения фиктивная поверхность лопаток, определенная шириной лопаток в центре тяжести, играет основную роль.

SOLUTION OF KÁRMÁN'S DIFFERENTIAL EQUATION FOR ROLLING WITH THE AID OF INFINITE POWER SERIES

L. TÓTH
TECHNICAL UNIVERSITY FOR HEAVY INDUSTRIES, MISKOLC
and
E. VINCZE
TECHNICAL UNIVERSITY FOR HEAVY INDUSTRIES, MISKOLC

[Manuscript received January 17, 1963]

After dealing with the basic assumptions of the essential theories concerning the computation of the pressure existing in the rolling process throat, it was pointed out that Kármán's equation describes the static equilibrium of the plastic material. The essence of rolling is the motion of the material processed. The excess force due to motion is interpreted by the properties of the material processed. The solution of Kármán's fundamental equation of the rolling process is given as an infinite power series. In the last part of the treatise the practical application of the solution is shown.

I. Introduction

The first equation used for the computation of forces by rolling, as well as that accurate from the point of view of mechanics was established by KÁRMÁN [1]. Under the conditions given by him, this equation adequately describes the equilibrium of the material standing in the roll throat, while it was assumed, that the material involved was of a perfect plastic type. SIEBEL [2], ZELIKOV [3] and NÁDAI [4] have solved this equation under different conditions and with further simplifications. This is the reason why applied under identical conditions their formulae gave results considerably differing from each other and so it is not possible to tell to what extent the single results differ from the theoretical value. BLAND and FORD [5] corrected this fault. Their solution represents a fairly good approximation where cold rolling is concerned. They were able to give the extent of the maximum percentile difference. TRINKS [6], SIMS [7] and OROWAN [8] have worked out graphical integration methods to solve Kármán's equation.

There are a number of rolling phenomena not covered by Kármán's equation; therefore several new methods were attempted by other investigators. OROWAN [8] has established a general equation of equilibrium; based on an analogy he assumed a distribution of stresses in the rolled body, namely, that of NÁDAY for a material pressed between plane plates that with one another close a small angle, while an additional assumption as to the existence of hypothetical adhesive planes in the case a slip was made. He further extended the validity of the equations which he thought to cover not only the

flow occurring toward the orifice but for the one taking place in the opposite direction. The theory of MICAN [9] was based on similar fundamental principles. KNESCHKE established his theory, beside the theories of equilibrium also on equations describing stresses built up in the viscous material due to motion. GELEJI [11] assumes that besides the internal forces warranting static equilibrium, also excess work has to be done, i.e. additional forces must be present to bring about the motion between the rolls and inhomogeneous compression. According to our opinion the mechanism of rolling is expressed the most lucidly and perspicuously by the last theory.

II. The fundamental equation of rolling

The determination of stresses emerging in the roll throat are to be examined under the following conditions:

a) the roled piecel does not become wider, thus a planar deformation state evolves;

b) the roll does not deform;

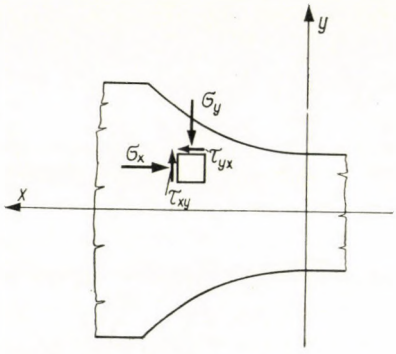

Fig. 1

c) the formed material is homogeneous, with negligible elastic deformation.

Under these conditions the stress distributions are described by the following equations of equilibrium (1) and (2) and determined by the plastic condition (3):

$$\frac{\partial \sigma_x}{\partial x} + \frac{\partial \tau_{xy}}{\partial y} = 0\,, \tag{1}$$

$$\frac{\partial \sigma_y}{\partial y} + \frac{\partial \tau_{xy}}{\partial x} = 0\,, \tag{2}$$

$$(\sigma_x - \sigma_y)^2 + \tau_{xy}^2 = k^2\,. \tag{3}$$

According to Fig. 1 the symbols comprised in the formulae are as follows:

σ_x is the normal stress in direction x;
σ_y is the normal stress in direction y;
τ_{xy} is the stress causing slip;
k is a constant, depending on the nature of the material involved.

In a concrete case the solution may be found with the aid of the external forces acting on the surface of contact, as marginal values of the differential equations. The solution, however, causes great mathematical difficulties even

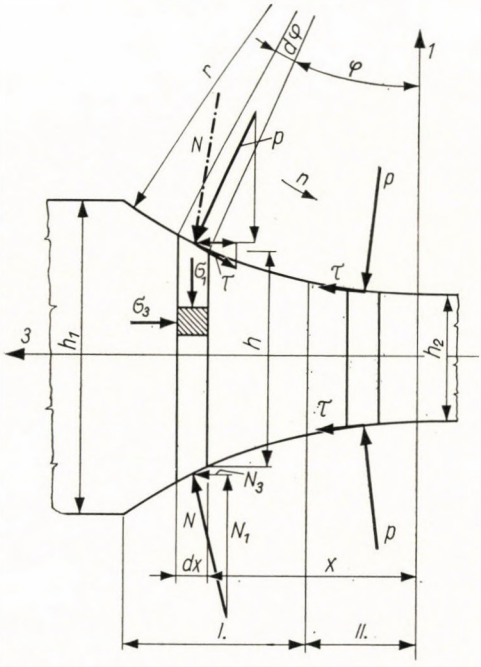

Fig. 2

in the case when marginal conditions are very simple. For this reason the approximate equations suitable for practical engineering are given under marginal conditions these being more adequate to reality by the approximation:

$$\tau_{xy} = 0. \tag{4}$$

This means, that the axes x and y are at the same time main stress directions, thus the volume units $\sigma_x = \sigma_3$ and $\sigma_y = \sigma_1$ are in an unaxial stress state.

As may be seen in Fig. 2, *no* external force *acts* upon the volume unit in the direction of the axis y, thus equation (2) may be written as

$$\sigma_1 - N_1 = 0, \tag{5}$$

while in the direction of axis *2* an external force *does act*, therefore equation (1) can be transformed, thus

$$-\frac{d(\sigma_3 h)}{dx} + 2N_3 = 0 \tag{6}$$

where the quantities comprised in the equations are as follows according to Fig. 2:

N_1 is the stress computed from the component of the external forces acting on the volume unit in direction *1*;

N_3 is the stress computed from the component of the external forces acting on the volume unit in direction *3*;

while equation (3) will be simplified to

$$\sigma_1 - \sigma_3 = k. \tag{7}$$

Further on the existence of a so-called neutral cross section must be assumed, that advances together with the roll. The cross section lying beyond this particular one, either lags behind the roll — in that case when they are in domain *I* or forge ahead of same — if they are in domain *II*. As the frictional force is inversely directed to the relative motion, the values for N_1 and N_2 have to be individually determined for both domains *I* and *II* as well.

According to Fig. 2 in domain *I* for N_1

$$N_1 = (p\cos\varphi + \tau\sin\varphi)\frac{1}{\cos\varphi}, \tag{8}$$

in domain *II*

$$N_1 = (p\cos\varphi - \tau\sin\varphi)\frac{1}{\cos\varphi} \tag{9}$$

may be written.

Analogously to domain *I* the relationship

$$N_3 = (p\sin\varphi - \tau\cos\varphi)\frac{1}{\cos\varphi}, \tag{10}$$

for domain *II*

$$N_3 = (p\sin\varphi + \tau\cos\varphi)\frac{1}{\cos\varphi} \tag{11}$$

can be put down.

By combining equations (8), (9) respectively (10) and (11) the formulae

$$N_1 = (p\cos\varphi \pm \tau\sin\varphi)\frac{1}{\cos\varphi}, \tag{12}$$

$$N_3 = (p\sin\varphi \mp \tau\cos\varphi)\frac{1}{\cos\varphi} \tag{13}$$

result. Thus, in these formulae — and this will also be the case further on to domain *I*, the upper operation symbol, to domain *II* the lower one will apply. According to formulae (5) and (12)

$$\sigma_1 = p \pm \tau \tan \varphi, \tag{14}$$

while relying on formulae (6) and (13) and taking into consideration the relationship

$$dx = r \cos \varphi d\varphi,$$

$$\frac{d(\sigma_3 h)}{d\varphi} = 2 r \cos \varphi (p \tan \varphi \mp \tau) \tag{15}$$

may be written. According to Fig. 2

p represents the radial pressure acting on the roll;
τ the pressure computed from the frictional force acting on the roll.

Assuming that Coulomb's frictional law applies for the domain under investigation, with the frictional factor keeping constant

$$\tau = \mu p. \tag{16}$$

From equations (7), (14), (15) and (16) the formula

$$\frac{d}{d\varphi}\left[(\sigma_1 - k) h\right] = 2 \tau \sigma_1 \frac{\sin \varphi \mp \mu \cos \varphi}{1 \pm \mu \tan \varphi} \tag{17}$$

is obtained suitable for the determination of σ_1.

If k is constant, this equation describes the equilibrium of the material being in a plastic state during the compression of the stationary rolls, i.e. one which makes no rotary movement, wherefrom with adequate simplifications Kármán's equation may be obtained. To enable the material to move in the roll throat, the roll, i.e. the acting external forces in addition must also overcome the resistance of the material against motion. By taking this fact into consideration a distinction can be made between this rolling operation and e.g. the material compression process carried out by two rolls, as equation (17) equally describes the plastic equilibrium also in this case.

The assumption made under (4) involves, as has already been mentioned, the homogeneous compression of the material. Numerous experimental data have proved that by such unaxial stress of the material the strength properties depend on the temperature, the extent of the shaping and the rate of deformation.

In Fig. 3 as an example the actual stress needed to shape a steel with 0.17% C content at 1000° C is shown as a function of the degree of shaping and rate of deformation [12].

On the basis of the figure the mathematical formulation describing the

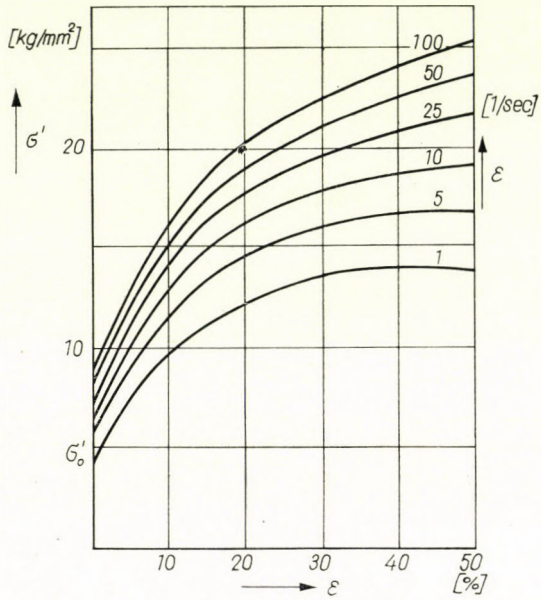

Fig. 3

resistance displayed by the material against unaxial stress as a function of the deformation characteristics is made possible

$$\sigma' = \sigma'_0 + M\varepsilon + N\dot{\varepsilon}. \tag{18}$$

The symbols in the figure are as follows:

σ' represents the actual stress;
ε the degree of shaping;
$\dot{\varepsilon}$ the rate of deformation;
N, M are given parameteres typical for the material processed.

Equation (18) can be used only if the degree and rate of deformation as a function of φ is determined.

From Fig. 4 for the degree of shaping the formula

$$\varepsilon = \frac{h_1 - h}{h_1} = \frac{h_1 - h_2 - 2\,r\,(1 - \cos\varphi)}{h_1} \tag{19}$$

for the rate of deformation the relationship

$$\dot{\varepsilon} = V \frac{\tan \varphi}{[h_2 + 2\,r\,(1 - \cos \varphi)]^2} \tag{20}$$

is obtained.

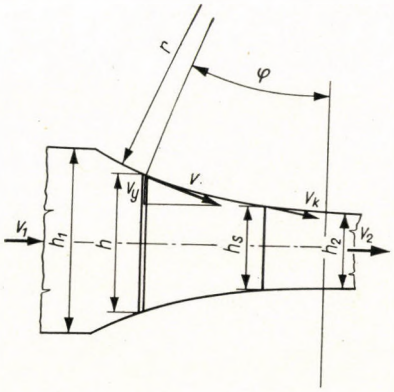

Fig. 4

The symbols in the formulae and in Fig. 4 have the following meaning:

h_1	is the starting height of the rolled piece;
h_2	is the height of the rolled piece after rolling;
h_3	is the height in the neutral cross section;
h	is the height of the rolled piece at angle φ;
r	is the radius of the roll;
v	is the rate of the rolled material;
v_2	is the discharge rate of the material rolled;
v_k	is the rate of the rolled material in the neutral cross section;
V	is the quantity of the material passing through the individual cross sections of the roll during a unit of time namely:

$$V = h_3\, v_k \cos \varphi_3 = h_2\, v_2.$$

According to the theory of Huber—Mises for the planar deformation state also the formula

$$k = \frac{2}{\sqrt{3}}\, \sigma' = \psi \sigma' \tag{21}$$

applies. Equation (17) — of course, together with the equations (18), (19), (20), (21) pertain to same — the fundamental relationship of rolling.

III. Solution of the fundamental relationship of rolling

The solution of the fundamental equation (17) of rolling, in general, meets with great mathematical difficulties. Partly k (a constant typical of the used material) in equation (17) is, as a rule dependent upon φ, the actual

determination of the function is possible only by measurements and shows considerable differences for each material. On the other hand the differential equation cannot — even in case that $k(\varphi)$ = constant — be solved in a closed form. On account of these difficulties the following method is used: According to Fig. 3, with the aid of equations (18), (19), (20), (21) the value of k as a function of φ is determined. From these data the so-called hardening graph could be plotted. If experimental data were available, the hardening graph

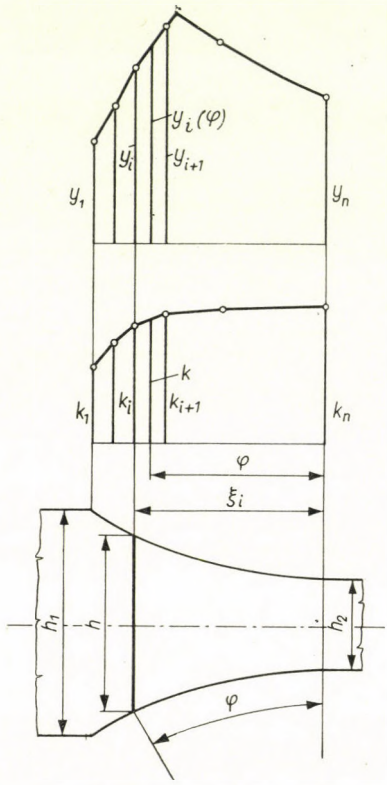

Fig. 5

might naturally be taken on the basis of these. It must be noted that the values obtained with the aid of Fig. 3 through the computation for cold rolling differ from those of the experiment. This is partly due to rolling not being an unaxial forming process. Further to the fact that as generally the plastic equilibrium of a volume part is only possible in case that the elastic zones exist, a certain fraction of the single elementary prisms is in a plastic state, the rest in an elastic one. Now the solutions for the equations (15) and (17) on the basis of Fig. 5 such sections are sought for in which the alteration of $k = k(\varphi)$ *may approximately be considered linear*, i.e. for which

$$k = k(\varphi) = k_i + c_i(\xi_i - \varphi) \tag{22}$$

applies. In this formula

ξ_i is the coordinate of the starting point of the examined section;
c_i is the directional tangent of the hardening graph in the examined section;

$$c_i = \frac{k_{i+1} - k_i}{\xi_i - \xi_{i+1}} .$$

From the equations (17) and (22) the formula

$$\frac{d}{d\varphi}\{[\sigma_{1i} - k_i + c_i(\varphi - \xi_i)]\, h\} = 2\, r\, \sigma_{1i} \frac{\sin\varphi \mp \mu\cos\varphi}{1 \pm \mu\tan\varphi} \tag{23}$$

follows. By the differentiation of the left part of equation (23) and also taking into consideration the relationship

$$h = h_2 + 2r\,(1 - \cos\varphi)$$

the differential equation

$$\frac{d\sigma_{1i}}{d\varphi}[h_2 + 2\,r\,(1 - \cos\varphi)] + c_i[h_2 + 2\,r\,(1 - \cos\varphi)] + \\ + 2\,r\sin\varphi\,[\sigma_{1i} - k_i + c_i(\varphi - \xi_i)] = 2\,r\,\sigma_{1i}\frac{\sin\varphi \mp \mu\cos\varphi}{1 \pm \mu\tan\varphi}$$

is obtained. Where from, after rearrangement the formula

$$\begin{aligned}(a + 1 - \cos\varphi)(\cos\varphi \pm \mu\sin\varphi)\frac{dy_i}{d\varphi} \pm \mu y_i + \\ + a_i\sin\varphi(\cos\varphi \pm \mu\sin\varphi)(\varphi - \xi_i) + \\ + a_i(a + 1 - \cos\varphi)(\cos\varphi \pm \mu\sin\varphi) - \\ - b_i\sin\varphi(\cos\varphi \pm \mu\sin\varphi) = 0\end{aligned} \tag{24}$$

emerges. The symbols used have been as follows:

$$y_i = \frac{\sigma_{1i}}{k_1}, \tag{25}$$

$$a = \frac{h_2}{2\,r}, \tag{26}$$

$$a_i = \frac{c_i}{k_1}, \tag{27}$$

$$b_i = \frac{k_i}{k_1}. \tag{28}$$

The differential equation (24) may be written in an even simpler and more perspicuous form:

$$A(\varphi)\frac{dy_i}{d\varphi} + B(\varphi)\,y_i + C(\varphi)\,(\varphi - \xi_i) + D(\varphi) = 0\,. \tag{29}$$

For the coefficients in question the comparison of equations (24) and (29) gives the following formulae

$$A(\varphi) = (a + 1 - \cos\varphi)(\cos\varphi \pm \mu\sin\varphi), \tag{30}$$

$$B(\varphi) \equiv \pm\,\mu, \tag{31}$$

$$C(\varphi) = a_i \sin\varphi\,(\cos\varphi \pm \mu\sin\varphi), \tag{32}$$

$$D(\varphi) = a_i(a + 1 - \cos\varphi)(\cos\varphi \pm \mu\sin\varphi) - b_i\sin\varphi\,(\cos\varphi \pm \mu\sin\varphi),$$

$$D(\varphi) = a_i\,A(\varphi) - \frac{b_i}{a_i}\,C(\varphi)\,. \tag{33}$$

In the following the coefficients (30), (32) and (33) may be expanded into series proceeding according to the increasing powers of $(\varphi - \xi_i)$. As the functions $\sin\varphi$ and $\cos\varphi$ throughout expand uniformly convergent power series and the coefficients in question are polynomes of the functions $\sin\varphi$ and $\cos\varphi$ the rearrangement and summation of these series [and later on the further operations in equation (29) pertinent to same] will actually be performable in the manner stated below. The formulae for these computations are so chosen *that they may readily be programmed for electronic computers.*

For the coefficient (30) the equations

$$\begin{aligned}
A(\varphi) &= (1 + a - \cos\varphi)(\cos\varphi \pm \mu\sin\varphi) = \\
&= (1+a)\cos\varphi \pm \mu\,(1 + a)\sin\varphi - \frac{1}{2} - \frac{1}{2}\cos 2\,\varphi \mp \\
&\mp \frac{1}{2}\mu\sin 2\,\varphi = (1 + a)\left[\cos\xi_i\cos(\varphi - \xi_i) - \sin\xi_i\sin(\varphi - \xi_i)\right] \pm \\
&\pm \mu\,(1 + a)\left[\sin\xi_i\cos(\varphi - \xi_i) + \cos\xi_i\sin(\varphi - \xi_i)\right] - \\
&- \frac{1}{2} - \frac{1}{2}\left[\cos 2\,\xi_i\cos 2\,(\varphi - \xi_i) - \sin 2\,\xi_i\sin 2\,(\varphi - \xi_i)\right] \mp \\
&\mp \frac{1}{2}\mu\left[\sin 2\,\xi_i\cos 2\,(\varphi - \xi_i) + \cos 2\,\xi_i\sin 2\,(\varphi - \xi_i)\right] = \\
&= (1 + a)(\cos\xi_i \pm \mu\sin\xi_i)\left[1 + \sum_{n=1}^{\infty}\frac{(-1)^n}{(2\,n)!}(\varphi - \xi_i)^{2n}\right] +
\end{aligned}$$

$$+ (1 + a)(\pm \mu \cos \xi_i - \sin \xi_i) \sum_{n=1}^{\infty} \frac{(-1)^{n+1}}{(2n-1)!} (\varphi - \xi_i)^{2n-1} -$$

$$- \frac{1}{2} - \frac{1}{2} (\cos 2\xi_i \pm \mu \sin 2\xi_i) \left[1 + \sum_{n=1}^{\infty} \frac{(-1)^n 2^{2n}}{(2n)!} (\varphi - \xi_i)^{2n} \right] -$$

$$- \frac{1}{2} (\pm \mu \cos 2\xi_i - \sin 2\xi_i) \sum_{n=1}^{\infty} \frac{(-1)^{n+1} 2^{2n-1}}{(2n-1)!} (\varphi - \xi_i)^{2n-1} =$$

$$= (1 + a)(\cos \xi_i \pm \mu \sin \xi_i) - \frac{1}{2} (1 + \cos 2\xi_i \pm \mu \sin 2\xi_i) +$$

$$+ \sum_{n=1}^{\infty} \frac{(-1)^{n+1}}{(2n-1)!} [(1 + a)(\pm \mu \cos \xi_i - \sin \xi_i) +$$

$$+ 2^{2n-2} (\sin 2\xi_i \mp \mu \cos 2\xi_i)] (\varphi - \xi_i)^{2n-1} +$$

$$+ \sum_{n=1}^{\infty} \frac{(-1)^n}{(2n)!} [(1 + a)(\cos \xi_i \pm \mu \sin \xi_i) -$$

$$- 2^{2n-1} (\cos 2\xi_i \pm \mu \sin 2\xi_i)] (\varphi - \xi_i)^{2n},$$

i.e. the equation

$$A(\varphi) = A_0(\xi_i) + \sum_{n=1}^{\infty} A_{2n-1}(\xi_i)(\varphi - \xi_i)^{2n-1} + \sum_{n=1}^{\infty} A_{2n}(\xi_i)(\varphi - \xi_i)^{2n} \tag{34}$$

may be written, where the coefficients can by elementary rearrangement be transformed into the simpler formulae

$$A_0(\xi_i) = (1 + a - \cos \xi_i)(\cos \xi_i \pm \mu \sin \xi_i), \tag{34a}$$

$$\left. \begin{aligned} A_{2n-1}(\xi_i) = \frac{(-1)^{n+1}}{(2n-1)!} [(\pm \mu \cos \xi_i - \sin \xi_i)(1 + \\ + a - 2^{2n-1} \cos \xi_i) \pm \mu 2^{2n-2}], \end{aligned} \right\} \tag{34b}$$

$$\left. \begin{aligned} A_{2n}(\xi_i) = \frac{(-1)^n}{(2n)!} [(\cos \xi_i \pm \mu \sin \xi_i)(1 + \\ + a - 2^{2n} \cos \xi_i) + 2^{2n-1}], \end{aligned} \right\} \tag{34c}$$

$$(n = 1, 2, 3, \ldots).$$

Analogously

$$C(\varphi) = a_i \sin \varphi (\cos \varphi \pm \mu \sin \varphi) = \frac{1}{2} a_i (\sin 2\varphi \mp \mu \cos 2\varphi \pm \mu) =$$

$$= \frac{1}{2} a_i \left\{ \cos 2\xi_i \sum_{n=1}^{\infty} \frac{(-1)^{n+1} 2^{2n-1}}{(2n-1)!} (\varphi - \xi_i)^{2n-1} + \right.$$

$$+ \sin 2\xi_i \left[1 + \sum_{n=1}^{\infty} \frac{(-1)^n 2^{2n}}{(2n)!} (\varphi - \xi_i)^{2n} \right] \mp$$

$$\mp \mu \cos 2\,\xi_i \left[1 + \sum_{n=1}^{\infty} \frac{(-1)^n\, 2^{2n}}{(2\,n)!}\,(\varphi - \xi_i)^{2n}\right] \pm$$

$$\left. \pm \mu \sin 2\,\xi_i \sum_{n=1}^{\infty} \frac{(-1)^{n+1}\, 2^{2n-1}}{(2\,n-1)!}\,(\varphi - \xi_i)^{2n-1} \pm \mu \right\} =$$

$$= \frac{1}{2}\, a_i\,(\sin 2\,\xi_i \mp \mu \cos 2\,\xi_i \pm \mu) +$$

$$+ a_i \sum_{n=1}^{\infty} \frac{(-1)^{n+1}\, 2^{2n-2}}{(2\,n-1)!}\,(\cos 2\,\xi_i \pm \mu \sin 2\,\xi_i)\,(\varphi - \xi_i)^{2n-1} +$$

$$+ a_i \sum_{n=1}^{\infty} \frac{(-1)^n\, 2^{2n-1}}{(2\,n)!}\,(\sin 2\,\xi_i \mp \mu \cos 2\,\xi_i)\,(\varphi - \xi_i)^{2n}$$

that is to say

$$C(\varphi) = C_0(\xi_i) + \sum_{n=1}^{\infty} C_{2n-1}(\xi_i)\,(\varphi - \xi_i)^{2n-1} + \sum_{n=1}^{\infty} C_{2n}(\xi_i)\,(\varphi - \xi_i)^{2n} \tag{35}$$

where the coefficients are given by the formulae

$$C_0(\xi_i) = a_i \sin \xi_i\,(\cos \xi_i \pm \mu \sin \xi_i)\,, \tag{35a}$$

$$C_{2n-1}(\xi_i) = a_i\, \frac{(-1)^{n+1}\, 2^{2n-2}}{(2\,n-1)!}\,(\cos 2\,\xi_i \pm \mu \sin 2\,\xi_i)\,, \tag{35b}$$

$$C_{2n}(\xi_i) = a_i\, \frac{(-1)^n\, 2^{2n-1}}{(2\,n)!}\,(\sin 2\,\xi_i \mp \mu \cos 2\,\xi_i)\,, \tag{35c}$$

$$(n = 1,2,3,\ldots).$$

From the relationships (33), (34), (34a)—(34c), (35), (35a)—(35c) the coefficient $D(\varphi)$ can also be computed.

On the basis of this computation it can be seen that, instead of the differential equation (29), the equation

$$\left.\begin{aligned} &\left[\sum_{m=0}^{\infty} A_m(\xi_i)\,(\varphi - \xi_i)^m\right] \frac{dy_i}{d\varphi} \pm \mu y_i + \left[\sum_{m=0}^{\infty} C_m(\xi_i)\,(\varphi - \xi_i)^m\right](\varphi - \xi_i) + \\ &\qquad + \sum_{m=0}^{\infty} \left[a_i\, A_m(\xi_i) - \frac{b_i}{a_i}\, C_m(\xi_i)\right](\varphi - \xi_i)^m = 0 \end{aligned}\right\} \tag{36}$$

may be written and the constants involved may be interpreted according to the equations (34a)—(34c), (35a)—(35c), (26)—(28). Now the differential equation (36) should be solved by the infinite power series

$$y_i = E_0(\xi_i) + \sum_{m=1}^{\infty} E_m(\xi_i)\,(\varphi - \xi_i)^m\,. \tag{37}$$

The initial condition $\varphi = \xi_i$, $y_i(\xi_i) = y_{i0}$ involves that

$$E_0(\xi_i) = y_{i0}\,. \tag{38}$$

Let us now substitute the function (37) into (36)

$$\left[\sum_{m=0}^{\infty} A_m(\xi_i)\,(\varphi - \xi_i)^m\right]\left[\sum_{m=1}^{\infty} m\,E_i\,(\xi_i)\,(\varphi - \xi_i)^{m-1}\right] \pm$$

$$\pm\,\mu \sum_{m=0}^{\infty} E_m(\xi_i)\,(\varphi - \xi_i)^m + \sum_{m=0}^{\infty} C_m(\xi_i)\,(\varphi - \xi_i)^{m+1} +$$

$$+ \sum_{m=0}^{\infty}\left[a_i\,A_m(\xi_i) - \frac{b_i}{a_i}\,C_m(\xi_i)\right](\varphi - \xi_i)^m = 0$$

hence, by the comparison of the coefficients of the powers with identical exponents the formula

$$(\varphi - \xi_i)^\circ: \qquad A_0(\xi_i)\,E_1(\xi_i) \pm \mu E_0(\xi_i) + a_i\,A_0(\xi_i) - \frac{b_i}{a_i}\,C_0(\xi_i) = 0$$

and generally speaking

$$(\varphi - \xi_i)^m: \qquad \sum_{\nu=1}^{m+1} \nu A_{m+1-\nu}(\xi_i)\,E_\nu(\xi_i) \pm \mu\,E_m(\xi_i) +$$

$$+\,C_{m-1}(\xi_i) + a_i\,A_m(\xi_i) - \frac{b_i}{a_i}\,C_m(\xi_i) = 0 \qquad (m = 1, 2, 3, \ldots)$$

is obtained.

Relying upon the afore stated, for the constants $E_m(\xi_i)(m = 1,2,3, \ldots)$ determining the solution-function (37) the formulae

$$E_1\,(\xi_i) = -\frac{1}{A_0\,(\xi_i)}\left[\pm\,\mu\,E_0(\xi_i) + a_i\,A_0\,(\xi_i) - \frac{b_i}{a_i}\,C_0(\xi_i)\right], \tag{39}$$

$$E_{m+1}(\xi_i) = -\frac{1}{(m+1)\,A_0\,(\xi_i)}\left[\sum_{\nu=1}^{m} \nu A_{m+1-\nu}(\xi_i)\,E_\nu(\xi_i) \pm \mu E_m(\xi_i) + \right.$$

$$\left. +\,C_{m-1}(\xi_i) + a_i\,A_m(\xi_i) - \frac{b_i}{a_i}\,C_m(\xi_i)\right] \tag{40}$$

$$(m = 1, 2, 3, \ldots)$$

suitable for recurrent computations are obtained. Therefore, the solution of the rolling equation is beyond *any interval* (ξ_i, ξ_{i+1}) a function represented by an infinite power row (37), where the coefficients in question may be computed from the formulae (38)—(40), (34a)—(34c), (35a)—(35c), (26)—(28).

From among the double signs in the formulae the upper one concerns domain *I*, the lower one domain *II*. Relying upon these the solution may always be found with the required accuracy.

The convergence of the infinite power row obtained as the solution is not a matter to be thoroughly dealt with here, but it must be noted that the power row converges rather rapidly, so that even in case that the members following the quadratic ones are omitted, the result is still exact enough to meet practical requirements, with an exactitude which extends to two decimal-figures.

IV. Application of the solution

The characteristic data of rolling can be determined only within the measuring accuracy. In addition same have a certain dispersion due to the inhomogeneity of the material processed. This is also supported by the rolling power measurement, as not only the measuring methods, but also the forces involved have some dispersion. Therefore, it is not necessary to strive after an extreme accuracy in the formula of the solution. The degree of exactness sought for in the solution of individual tasks may be given complying with the given circumstances just prevailing.

Hereafter well applicable approximate "quadratic" formulae are given suitable for handling two important practical cases; the relationships may be obtained by taking the first three members of the infinite series that emerged from the preceding computations into consideration and by making use of the approximations

$$\varphi \approx \frac{x}{r};$$

$$\sin \alpha \approx \alpha \approx \frac{l_d}{r}\,;\ \cos \alpha \pm \mu \sin \alpha \approx 1\,;$$

$$\cos 2\,\alpha \pm \mu \sin 2\,\alpha \approx 1\,.$$

a) Assuming "*k*" to be constant (this is practically the case with hot rolling) *for domain I* the equation

$$y = 1 + K_1 (l_d - x) + K_2 (l_d - x)^2 \tag{41}$$

is valid, where the symbols have the following meaning:

$$K_1 = \frac{2}{h_1}\left(\mu - \frac{l_d}{r}\right),$$

$$K_2 = \frac{1}{h_1}\left[(A_1 + \mu)\,K_1 - \frac{1}{r}\right],$$

$$A_1 = \frac{l_d}{r} + \frac{h_2}{2r}\left(\mu - \frac{l_d}{r}\right),$$

$$l_d = \sqrt{r(h_1 - h_2)}\,;$$

while for *domain II:*

$$y = 1 + R_1 x + R_2 x^2 \tag{42}$$

applies with the symbols

$$R_1 = \frac{2\mu}{h_2},$$

$$R_2 = \frac{2}{h_2^2}\left[(\mu^2 + 1)\frac{h_2}{2r} + \mu^2\right].$$

b) If a linear hardening is considered (that is approximately the case with cold rolling) *for domain I* the relationship

$$y = K_0 + K_1(l_d - x) + K_2(l_d - x)^2 \tag{43}$$

may be used, where

$$K_0 = 1 - \frac{\sigma_{\text{breaking}}}{k_1},$$

$$K_1 = \frac{2}{h_1}\left(\mu K_0 + b\frac{h_1}{2r} - \frac{l_d}{r}\right),$$

$$K_2 = \frac{1}{h_1}\left[(A_1 + \mu)K_1 - \frac{b}{r}\left(A_1 + \frac{l_d}{r}\right) + \frac{1}{r}\right],$$

$$A_1 = \frac{l_d}{r} + \frac{h_2}{2r}\left(\mu - \frac{l_d}{r}\right),$$

$$b = \frac{r}{l_d}\left(\frac{k_2}{k_1} - 1\right),$$

$$l_d = \sqrt{r(h_1 - h_2)}$$

and for *domain II* the formula

$$y = R_0 + R_1 x + R_2 x^2 \tag{44}$$

is valid with the symbols:

$$R_0 = \frac{k_2}{k_1} - \frac{\sigma_{\text{drawing}}}{k_1},$$

$$R_1 = \frac{2}{h_2}\left(\mu R_0 - b\frac{h_2}{2r}\right),$$

$$R_2 = \frac{1}{h_2}\left[\mu(a+1)\,R_1 + b\mu\,\frac{h_2}{2\,r^2} + \frac{k_2}{k_1}\,\frac{1}{r}\right],$$

$$a = \frac{h_2}{2\,r}\,.$$

In Fig. 6 the experimental measurement process of SIEBEL and LUEG is shown. The data of the pilot rolling are as follows:

$$r = 90 \text{ mm}, \qquad h_1 = 2 \text{ mm}, \quad h_2 = 1.1 \text{ mm}, \quad \mu = 0.4,$$
$$k_2 = 28.6 \text{ kg/mm}^2, \quad k_1 = 16.8 \text{ kg/mm}^2$$

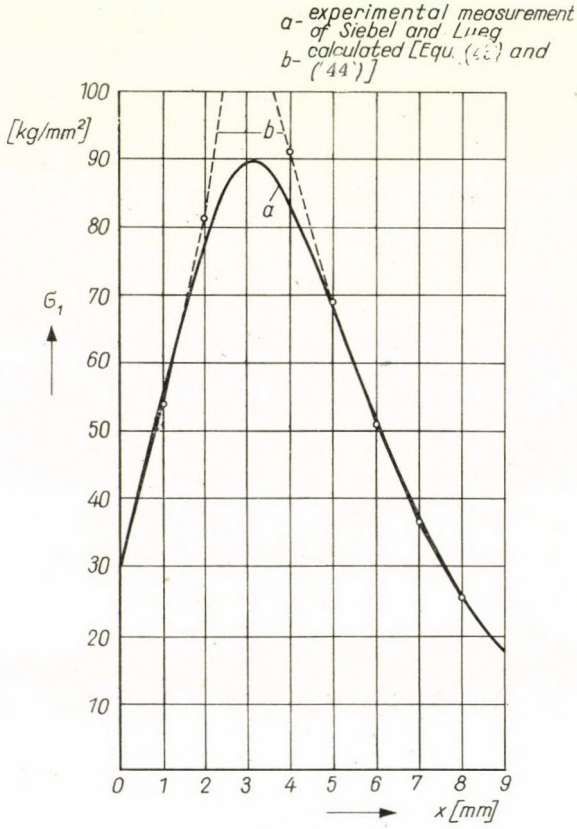

Fig. 6

Graph *b* in Fig. 6 is a theoretical diagram plotted with the data given above. This of course valid being only till adhesion begins. As the figure shows in the case in question the test result is in good accordance with the value obtained from the first 3 members of the infinite series.

By the integration of equation (43) and (44) relatively simple equations describing the powers and moments of the rolling process may be obtained.

REFERENCES

1. KÁRMÁN, TH.: Beitrag zur Theorie der Walzvorganges. *Z. angew. Math. Mechan.* **5** (1925), 139—141.
2. SIEBEL: Die Formgebung im bildsamen Zustande, Düsseldorf 1932.
3. ZELIKOV, A.: Effect of External Friction and Tension on the Pressure of the Metall on the Rolls in Rolling. *Metallurg* (1939), No. 6., 64—76.
4. NÁDAI, A.: The Rolling Process. Paper before Amer. Soc. for Steel Treating (1930), Sept.
5. BLAND, B. A.—FORD, H.: The calculation of Roll Force and Torque in Cold Strip Rolling with Tension. *Proc. Inst. Mech. Engrs.* (1948). 159: 144—159.
6. TRINKS, W.: New Theories on Hot Mill Deformations Obtained by Experimental Rolling. *Blast Furnace and Steel Plant* (1937), 25.
7. SIMS, R.: Calculation of Roll Force and Torque in Cold-Rolling by Grafical and Experimental Methods. *J. Iron St. Inst.* (1954), Sept.
8. OROWAN: The Calculation of Roll Pressure in Hot and Cold Flat Rolling. *Proc. I. Mech. E.* (1943), 150, 4, 140—167.
9. MICAN, G. S.: A New Theory of Hot Rolling. *Iron Steel Engr.* (1954), May, 55—77.
10. KNESCHKE, A.: Zur hydrodynamischen Theorie der Warmwalzens. *Archiv für Eisenhüttenwesen* (1958), 29: 11—22.
11. GELEJI, A.: Bildsame Formung der Metalle in Rechnung und Versuch, Berlin 1960.
12. SIMS, R.: The Calculation of Roll Force and Torque in Hot Rolling Mills. *Proc. Inst. Mech. Engrs.* (1955), 169: 123—163.
13. SIEBEL—LUEG: Untersuchungen über Spannungsverteilung in Walzspalt. *Mitt. Kaiser-Wilhelm. Inst. Eisenforsch.*, Düsseldorf (1933), 15.

DIE LÖSUNG DER KÁRMÁNSCHEN DIFFERENTIALGLEICHUNG DES WALZVORGANGES DURCH UNENDLICHE POTENZREIHEN

L. TÓTH und E. VINCZE

ZUSAMMENFASSUNG

Nach Schilderung der den wichtigsten Theorien zur Berechnung des im Walzspalt auftretenden Druckes zugrundegelegten Grundannahmen wird auf den Umstand hingewiesen, daß die Gleichung von Kármán das statische Gleichgewicht des bildsamen Materials beschreibt. Wesentlich für den Walzvorgang ist die Bewegung des Werkstoffes zwischen den rotierenden Walzen. Die als Folge der Bewegung auftretende zusätzliche Kraft wird auf die Beschaffenheit des verarbeiteten Materials zurückgeführt. Die Lösung der Fundamentalgleichung von Kármán über den Walzvorgang wird in Form einer unendlichen Potenzreihe angegeben. Im Schlußteil der Abhandlung wird die praktische Anwendung der Lösung erörtert.

RÉSOLUTION, PAR SÉRIES DE PUISSANCES INFINIES, DE L'ÉQUATION DIFFÉRENTIELLE DE KÁRMÁN SE RAPPORTANT AU PROCESSUS DE LAMINAGE

L. TÓTH et E. VINCZE

RÉSUMÉ

Après un aperçu des hypothèses fondamentales des principales théories se rapportant au calcul de la pression produite dans l'emprise, l'étude montre que l'équation de Kármán décrit l'équilibre statique de la matière plastique. Le processus de laminage consiste essentiellement dans le cheminement de la matière entre les cylindres animés d'un mouvement de rotation. La force supplémentaire se produisant par suite du mouvement s'explique, selon l'auteur, par les propriétés de la matière. La résolution de l'équation fondamentale de Kármán se rapportant au laminage est présentée sous forme d'une série de puissances infinie. La dernière partie de l'étude traite des applications pratiques de cette solution.

РЕШЕНИЕ ДИФФЕРЕНЦИАЛЬНОГО УРАВНЕНИЯ ПРОКАТКИ ПО КАРМАНУ С ПОМОЩЬЮ БЕСКОНЕЧНЫХ ЭКСПОНЕНЦИАЛЬНЫХ РЯДОВ

Л. ТОТ и Е. ВИНЦЕ

РЕЗЮМЕ

Работа после изложения основных предположений важнейших теорий расчета давления, возникающего в калибре, показывает, что т. н. уравнение Кармана описывает статическое равновесие пластичного материала. Суть процесса прокатки заключается в движении материала между вращающимися прокатными валками. Дополнительные силы, возникающие в процессе движения, объясняются свойствами самого материала. Решение уравнения прокатки по Карману дается в форме бесконечных экспоненциальных рядов. В последней части работы рассматривается практическое применение решения.

THE DETERMINATION OF THE DISTRIBUTION COEFFICIENT OF ZINC WITH RADIOISOTOPE Zn^{65} BY THE ZONE MELTING OF ALUMINIUM

E. BUJDOSÓ,*—E. CZOBOLY**—F. MAGYARY*

[Manuscript received January 30, 1963]

Aluminium bars of 99.99% purity alloyed with Zn^{65} radioisotope were zone refined by various velocities and melted zone length conditions. The distribution of activity in the material originally containing 0.0044% Zn^{65} radioisotope was examined by means of continuously registering measuring equipment. On basis of the observed activity distribution curves both the effective distribution coefficient of the zinc as well as the value of δ/D valid for the given equipment were established. Finally data of the optimal zone melting process were determined in respect to zinc and to contaminations having similar distribution coefficients.

I. Introduction

Several publications have appeared in the last years dealing with the zone melting method developed by W. G. PFANN [1] [2] and his collaborators, and gave an account of the results obtained by employing this method. Still there is rather a great gap between theoretical considerations and practical realisation. The greatest difficulty in this case is the previous determination of the distribution of impurities after zone melting, i.e. the determination of the number of passes required for producing the desired separation. According to preference the distribution passes of zone melting may be determined by several methods. The method of calculation was elaborated both by N. W. LORD [3] and H. REISS [4] while J. L. BIRMAN [5] and R. W. HAMMING [6] proposed approximating methods. However, all these calculations are very complicated and lengthy. Moreover, all equations are only valid under those conditions which may hardly be fulfilled in many cases.

For example, a completely uniform distribution of the impurities in the liquid, i.e. a perfect diffusion in the melted zone is assumed. Moreover, it is assumed that k_0 is a constant this being valid only in the case of linear liquid-solid curves of the equilibrium diagram. Finally, in the case of metals having good thermal conductivity the uniformity of the zone length can only be ensured with difficulty because the length of the zone is shorter in the middle of the bar than at the two ends due to the two directional reduction of heat.

* Research Institute for Non-Ferrous Metals, Budapest.
** Institute of the Mechanical Technology on the Technical University, Budapest.

To conclude, the greatest difficulty arises from the fact that the k distribution coefficient which serves as the base of the calculations is unknown. By reason of the advance of the crystallisation front the impurities at the interface are enriched and the concentration of this layer may exceed the average C_1 concentration. Instead of the ideal state as shown by dotted line in Fig. 1 the state indicated by the unbroken-line shall be realised. Thus

$$C_s' = k_0 C_1 > C_s = k_0 C_1.$$

This relation may also be given as follows

$$C_s' = k C_1$$

where $k > k_0$. According to the theory suggested by BURTON—PRIM—SLICHTER [7]

$$k = \frac{k_0}{k_0 + (1 - k_0)\, e^{-v\delta/D}}$$

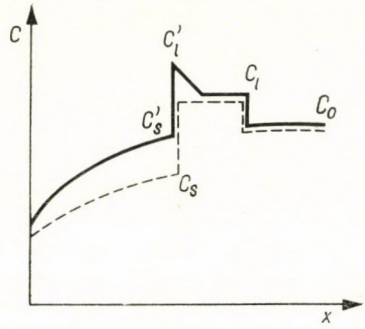

Fig. 1. Distribution of solute in a partly zone melted specimen. Idealised case: dotted line; true case: unbroken line

where k is the real distribution coefficient, v is the velocity of the crystallisation front advance, δ is the thickness of the layer where material transfer takes place only by diffusion, without flow, D is the diffusion coefficient. The values of δ and D are usually unknown, though for a given material and equipment are nearly constant. In the different solutions $D = 10^{-5} \div 10^{-4}$ cm²/sec, while $\delta = 10^{-3} \div 10^{-1}$ cm, dependent on the mixing. Consequently the value of k depends on the speed, too. At small velocities the value of k increases, thus the zone melting process is less effective. The optimal value can only be determined by circumspect calculations where the uncertainty of some ranges — which result from the fact of not having the δ/D value — is not permissible.

The purpose of our investigations was the experimental determination of δ/D value for one of the impurities of aluminium with the zone melting equipment which is the property of the Institute of the Mechanical Technology at the Technical University of Budapest. In addition our aim was to calculate the optimal parameters of zone refining in regard to this equipment, assisted by the above given value.

Our measurements were performed similarly to those of D. GELLI and N. ROBBA [12] wit halloyed Zn^{65} radioisotope. This method has the following advantages:

a) The impurity distribution can be continuously determined in the whole length of the bar;

b) the process is of non-destructive type, thus in case of several meltings the impurity distribution can be determined after each pass;

c) a radioisotope of high specific activity enables the exact determination of trace impurities which could hardly be performed by chemical analysis or spectrometry.

II. Experimental equipment and method of measurements

1. Activity measuring assembly

The measuring equipment constructed in the Isotope Laboratory of the Research Institute for Non-Ferrous Metals comprises the following parts (Fig. 2): lead-shield; scaler of 64; fast-counting ratemeter; timer; MAW compensograph; driving equipment for moving the Al-bar.

To determine the distribution of activity a continuous method by means of the driving equipment, the ratemeter, the lead-shield and the compensograph was used. However, the results were also controlled by measurements at 10 mm steps, during the preliminary experiments, with a scaler.

In order to reduce the background as well as to measure the impulses originating only in a narrow section of the Al-bar a lead-shield provided with 30×16 mm aperture (Fig. 3) was applied. The CTC-5 type GM-tube of 375 V operating point was placed in the middle of the lead-shield. Its optimal position was determined by measurement series. The tube joins the base with drive screws. The pulse number was measured by different spacing of the GM-tube aperture. After optimal position had been determined the tube remained in this same position during all further measurements. The bar was moved at a constant uniform speed before the aperture by means of the driving equipment. The resulting impulses were integrated by the ratemeter which gave a signal proportional to the counting rate (pps) at the output of the instrument. This altered from 0 to 80 V conform to the 0—100 pps, that was reduced by means of voltage divider to 50 mV. Thereafter it was carried to the compen-

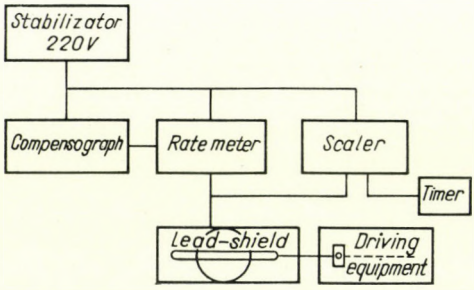

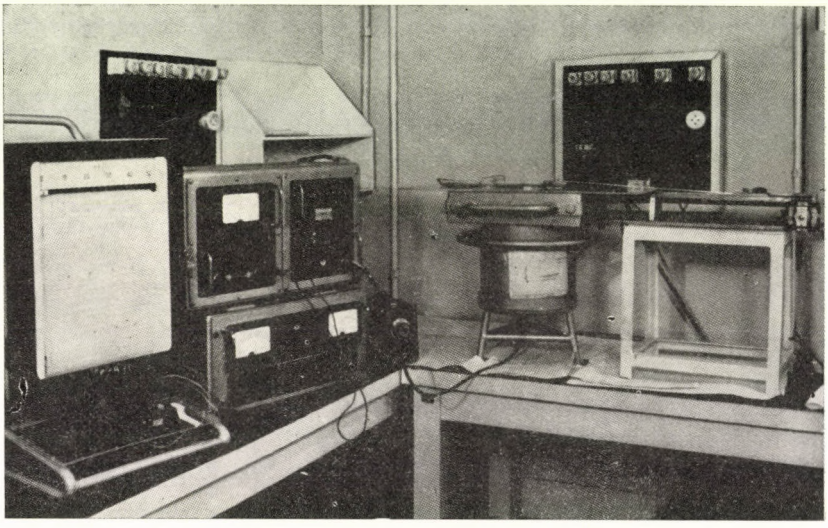

Fig. 2. Outline and photograph of the activity measuring equipment

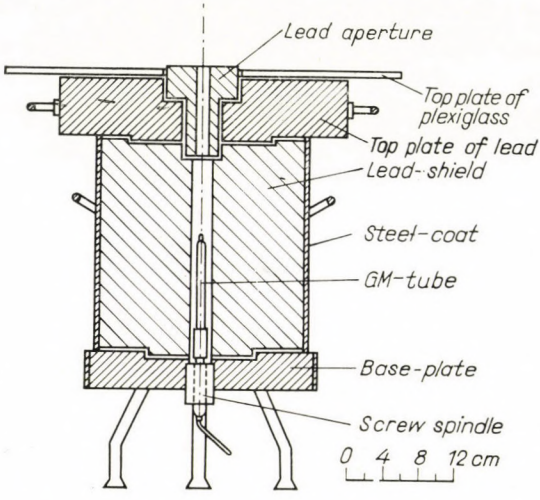

Fig. 3. Sectional view of the lead-shield

sograph where the values of activity distribution were obtained as registered on a strip 25 cm in width. The time constant of the ratemeter was 20 sec, the speed of the driving equipment was 1332 mm/h and the speed of the strip on the compensograph was 1200 mm/h.

The statistical percentual error of the instrument as a function of counting speed was also determined. Hereby it became possible to select a counting rate at which the error of measurements was less than 5 per cent.

2. *Zone melting equipment*

The equipment (Fig. 4) consists of 3 units: high frequency generator; the material to be refined with the graphit boat and quartz tube; the driving equipment.

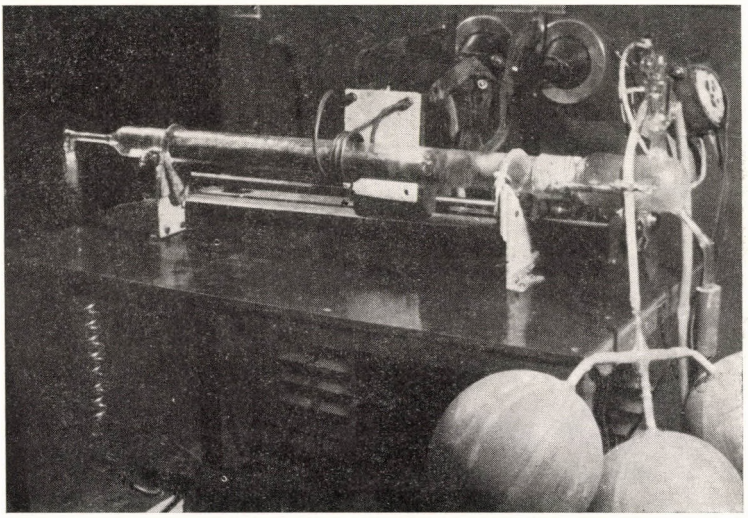

Fig. 4. Photograph of the zone melting equipment

The high frequency generator supplies the energy required for the zone melting. The data of the high frequency generator used in the process were as follows:

anode current	1.2 A;
voltage	4—4.5 kV;
frequency	400 kHz.

The metal placed into a graphit boat was put in a transparent quartz tube having a 50 mm diameter and 1 m length. This was filled with argon gas in order to avoid oxidation. The tube was surrounded by the high frequency coil movable by the driving equipment at varying speed. Different coils were used to produce melted zones of different length; their data are given in Table I.

Table I

Characteristic measurements of coils used in zone melting

Mark of coil	*d* [mm]	*D* [mm]	*n*	*b* [mm]	Note
I	7.5	50	3.5	7.5	Flat, spiral coil
II	7.5	50	3.5	35	Multiturn cylindrical coil
III	7.5	70	6.5	120	

Where *c* diameter of copper tube as conductor,
d inside diameter of coil,
n number of turns,
b length of coil.

III. Experiments

1. Determination of purity of the Zn^{65} radioisotope

Before beginning our zone melting experiments we examined the purity of the Zn^{65} radioisotope.

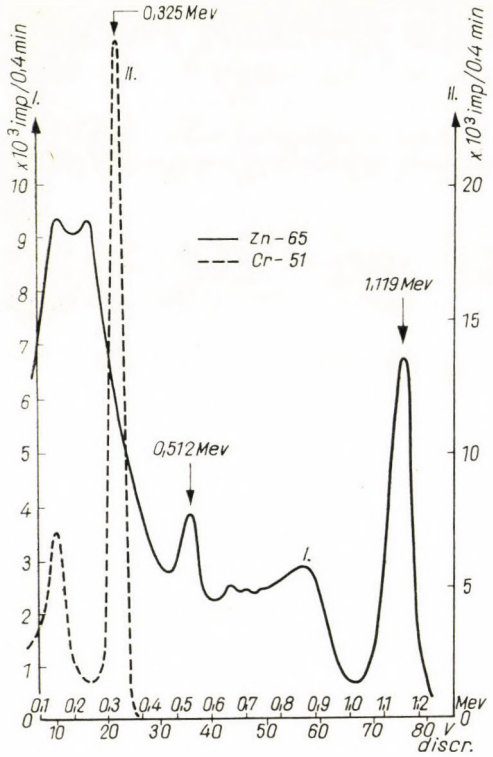

Fig. 5. Gamma-spectra of Cr^{51} and Zn^{65} standard isotopes

The radioactive preparations often contain more or less active or inactive contaminations which originate together with the radioisotopes and their separation cannot be perfecly achieved. Though the mass of these impurities is very low yet their activity may be considerable. These active impurities could falsify the measurements of our experiments, if e.g. their behaviour differs from that of zinc. Therefore, especially great care is to be paid when analysing the active impurities of the zinc isotope used. Gamma-spectrometric

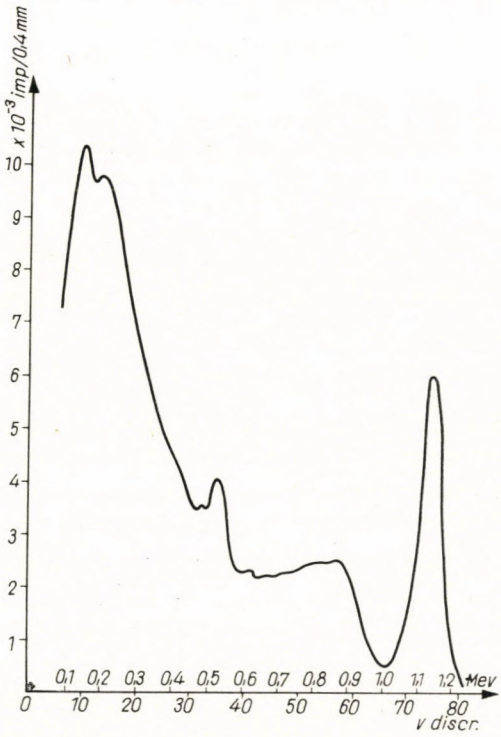

Fig. 6. Gamma-spectra of the Zn^{65} isotope used

measurements were performed for that purpose. The measurements were carried out by means of Siemens GS—DMZ one channel gamma-spectrometer with a NaJ(TI) crystal of 44 mm diameter and 44 mm height.

First of all the Gamma-spectra of Cr^{51} and Zn^{65} standard isotopes were determined, increasing the voltage of the discriminator per volt (Fig. 5). The values of the discriminator were calibrated by the 0.325 MeV photopeak of the Cr^{51} isotope, the 1.118 MeV photopeak of the Zn^{65} isotope as well as the 0.512 MeV gamma line of the Zn^{65} isotope. The latter originates from the annihilation of positrons of 0.325 MeV energy.

The Zn^{65} radioisotope used for the investigations was compared with the standard sample. The form of the curve obtained is almost exactly the same (Fig. 6) as the energy distribution of the standard.

The observed minimal deviation may be due to the difference in the geometry and size of both sources.

On the basis of thes eresults we may state that the radioisotopes used for our investigations were free from active contaminations. So in reality it was the distribution of zinc that was followed in our experiments.

2. *Preparation of the alloy*

The alloying of the isotope was carried out according to the results of the preliminary investigations. The specific activity of the radioisotope used was 197 mc/g. The master alloy consisted of 306.6 g aluminium of 99.99% purity and 0.187 g Zn^{65} isotope. This was added to 3920.0 g aluminium of 99.99% purity. Thus the concentration of radioactive zinc was 0.0044%. From this mass altogether we obtained 9 bars suitable for zone melting, each containing about 3.1 mc Zn^{65} radioisotope on the day when prepared.

3. *Zone refining*

The aim of our study was to examine the effect of the main factors which influences the success of zone refining as well as to determine their optimal values on this base. These factors are the length of the zone and the travel rate — their effect on the impurity distribution becomes evident from the afore-mentioned.

The first series of measurements concerned the influence of zone length. Each of the specimens were melted 3 times by means of the coils specified in Table I. The zone length provided by the coils, the velocity and other data are collected in Table II. It is to be mentioned that it was impossible to assure a constant zone length as a consequence of the good thermoconductivity of aluminium, and so the zone was shorter in the middle of the specimen than at its ends. Therefore, the length and position of the zones were measured every 15 minutes during the melting time and the data were represented in time-length coordinate systems. One of these diagrams is represented for example in Fig. 7, this being determined during the first melting of specimen No. 2. (See data in Table II.) Using these diagrams it was possible to establish that both the mean zone length and the real zone length at every position as well as the real rate of solidification front advance by graphical differentiation of the curve *a*. This shows considerable deviation from the velocity of the coil (curve *d*); that can also be seen from the figure.

The later calculations were based on the real velocity obtained from the diagram.

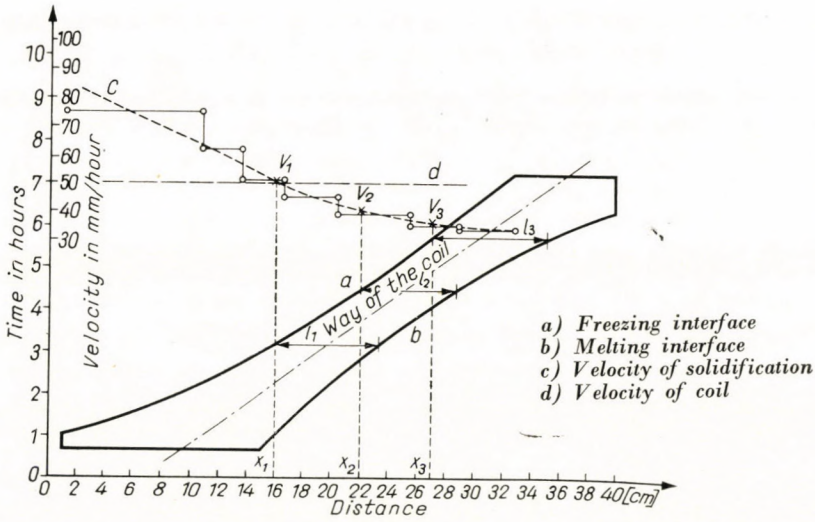

Fig. 7. Change of zone length depending on the position in the specimen. Curve "C" represents the velocity of freezing versus distance, determined by graphical method

During the following experiments the travel rate of the coil was altered, while the mean zone length remained unvaried. Data of these series are also shown in Table II.

Table II

Data of zone melting process, applied in refining the various specimens

Mark of Al-bar	Mark of coil	Time of zone melting, h	Velocity of coil, mm/h	Mean zone length, cm
1	I	7	50	60
2	II	7	50	80
3	III	7	50	140
4	II	14	25	80
5	II	3	116	80

4. *Measurements of activity*

The distribution of activity was determined after each pass by the continuous method described above. These data are given in Figs. 8a—e.

The activity data of one bar, used as a standard sample, were determined by measurements lasting half an hour in addition to the diagram of each bar. Thus, we succeeded in compensating the alterations of the instruments which could have falsified the results of the measurements of the experimental work lasting several months. The curves represented in the figure are normal-

ized to the most frequently occurring activity levels (I_0) by multiplying the factor

$$f = \frac{I_0}{I_m}$$

where I_m is the intensity of the standard obtained by each measurement. This correction also eliminates the decrease of intensity resulting from the half-life.

Considering that during the experiments only the distribution and not the quantity of the indicator had changed, we used this fact to control the accuracy and reliability of our measurements. In every case the areas under the activity distribution curves and under that of the standard were determined with a planimeter. The measurements are exact only in that case when the rates of these values are constant. The values of (T distribution)/(T standard) are given in Table III and as can be seen they are nearly constant.

Table III

The ratio of the areas under the activity distribution curves of zone refined specimens to that of the standard after various passes

Mark of bar	Number of passes			
	1	2	3	4
1	10.9	9.3	9.4	—
2	10.0	9.8	8.5	—
3	10.5	9.1	9.3	—
4	9.8	11.2	9.3	—
5	10.7	9.2	9.4	9.6

IV. Discussion of the results

A comparison of Figs. 8a, b an dc shows that coil III, which produces the longest melted zone, is the most effective as can be expected based on the relationships known from the literature. Curve 3 in Fig. 8c — which may be well approached by a straight line — however, shows that the maximal purity obtainable with this coil is generally attained after 3 passes. Thus a coil producing a shorter zone is necessary for further refining.

We determined by every single pass the related values of k and v at 3—3 places. This was done with the aid of the intensity curves (see Fig. 8b, d and e) and curves representing the rate of crystallisation in function of length (see Fig. 7).

On the time-length diagram of the nth pass we assigned three intersects: x_1, x_2, x_3. The length of melted zones (l_1, l_2, l_3) as well as the rates of crystallisa-

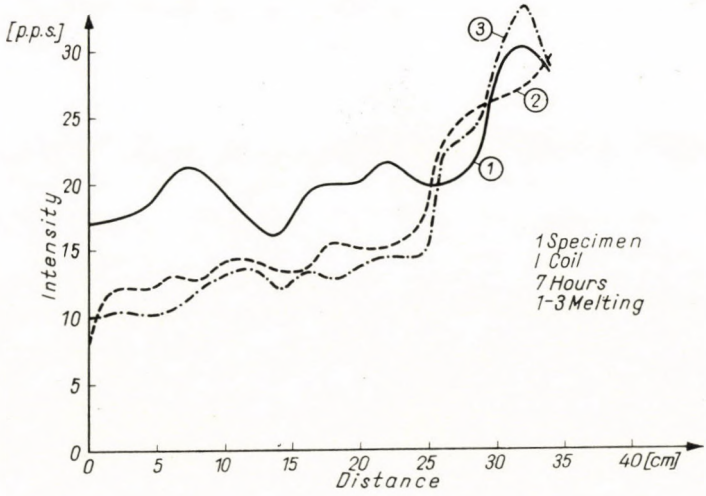
[p.p.s.]
Intensity
Distance
[cm]
1 Specimen
I Coil
7 Hours
1-3 Melting

Fig. 8a

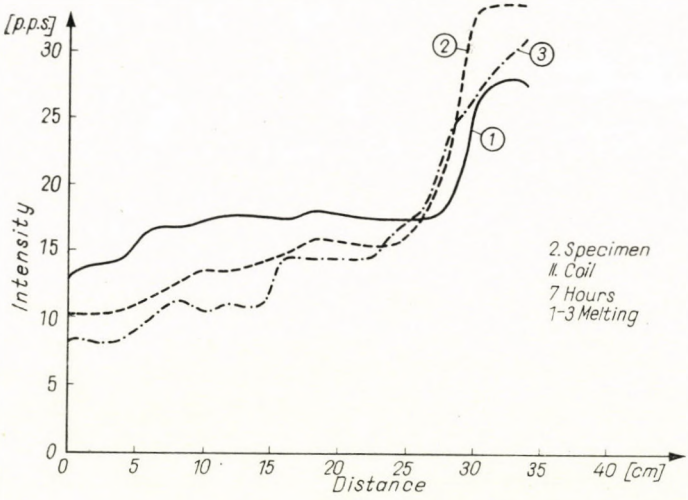
[p.p.s.]
Intensity
Distance
[cm]
2. Specimen
II. Coil
7 Hours
1-3 Melting

Fig. 8b

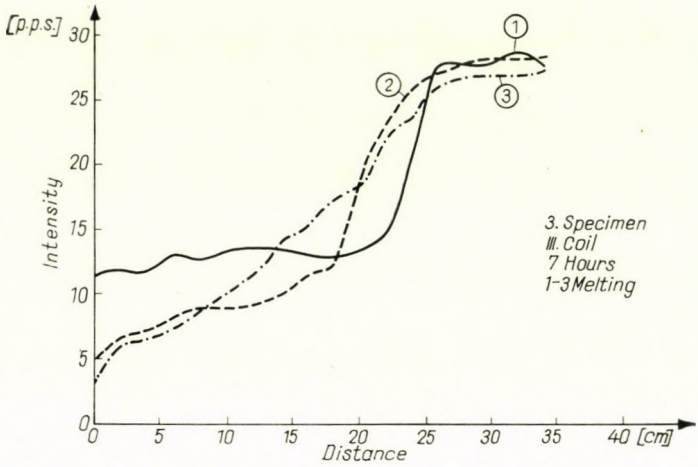
[p.p.s.]
Intensity
Distance
[cm]
3. Specimen
III. Coil
7 Hours
1-3 Melting

Fig. 8c

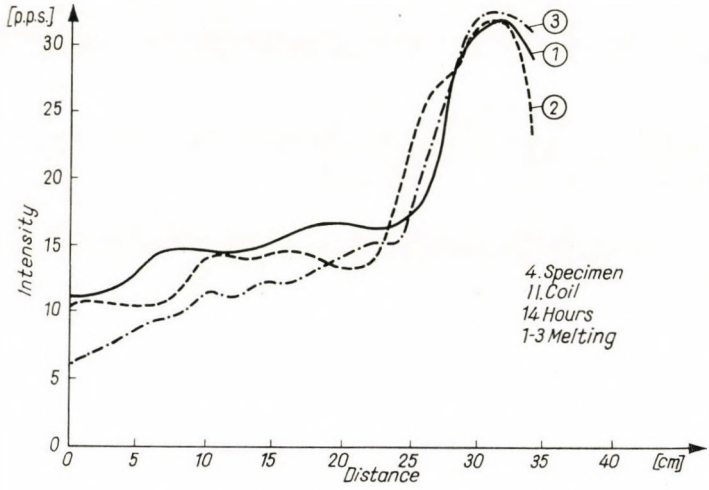
[p.p.s.]
Intensity
Distance
[cm]
4. Specimen
II. Coil
14 Hours
1-3 Melting

Fig. 8d

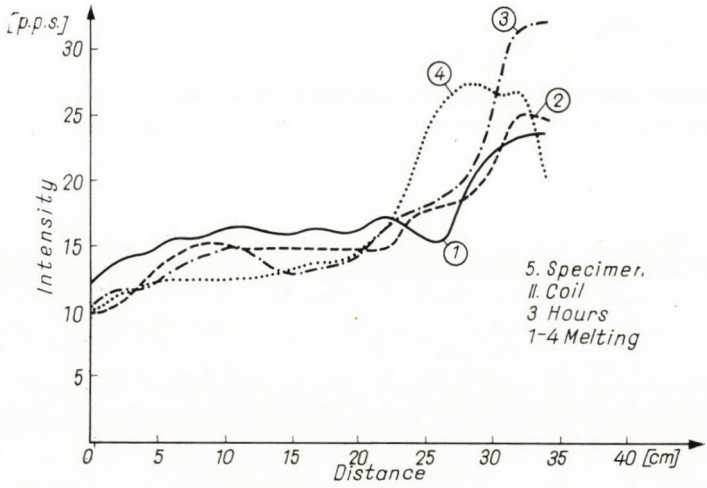

Fig. 8e

Fig. 8a—e. Distribution of Zn^{65} isotope determined by activity measurements after each pass. The mark of coil used, the time of one pass and number of passes are given in the figures

tion (v_1, v_2 and v_3) referring to the intersects were determined (see Fig. 7). Following this the $x_1 + l_1$, $x_2 + l_2$ and $x_3 + l_3$ intersects were assigned on the nth intensity curve obtained, by measuring before the pass and the areas below these values were determined by planimetry, namely,

$$\int_0^{x_i+l_i} I_{n+l}(x)\,dx\,.$$

Similarly the areas below the curve $n + l$ measured after the pass were planimetered between limits 0 to x_1, x_2 and x_3 intersects

$$\int_0^{X_i} I_{n+l}(x)\,dx\,.$$

The difference between the two areas divided by the length of the melted zone gives the momentary concentration of the liquid (C_l). Dividing this value with the concentration of the then crystallizing phase $[(C_s = I_{n+l}(x_i)]$ the sought for factor k can be obtained:

$$K = \frac{C_s}{C_l} = \frac{l \cdot I_{n+l}(x_i)}{\int_0^{x_i+l_i} I_n(x)\,dx - \int_0^{X_i} I_{n+l}(x)\,dx}\,.$$

The Burton—Prim—Slichter equation rearranged and logarithmized gives the following:

$$\log\left(\frac{1}{k}-1\right)=\log\left(\frac{1}{k_0}-1\right)-v\frac{\delta}{D}\log e$$

i.e. the $\log(1/k-1)$ value plotted against velocity (v) a straight line is to be obtained the slope of which is $-\delta/D \log e$ and which intersects at $\log(1/k_0-1)$ value the ordinate ($v=0$).

The values of $\log(1/k-1)$ referring to the different ones of velocity (v) are shown in Fig. 9. Regarding the deviation of the points the line was determined by the method of least squares. Thus the value of k_0 and δ/D taking the probable error into consideration is

$$k_0 = 0.55 \pm 0.12,$$

$$\delta/D = (446 \pm 90)\ \text{sec} \cdot \text{cm}^{-1}.$$

The correlation coefficient of the measurements was 0.88 showing a rather good connection between the measured values.

By means of these values the k in function of both $v\delta/D$ and v were plotted (Fig. 10) according to W. G. PFANN [6]. Applying these as well as the nomogram reported by PFANN (Fig. 11) we determined the number of passes required to achieve relative solute concentration 0.2 at different k values, that is to say the travel rate referring to these values.

On the basis of these data the determination of the time necessary for the whole process, is also possible (see Table IV).

Table IV

Various times required to reduce the relative concentration at the beginning of the specimen to 0.2 when choosing different travel rates

Real distribution, coefficient k	Number of passes, n	Travel rate [mm/hr]	Time of one pass, $t = L/v$ ($L = 350$ mm) [hour]	Refinement time, $I = n \cdot t$ [hour]
0.55	3.7	0	∞	∞
0.6	4.7	17	20.6	$\sim$97
0.65	6.3	37	9.4	$\sim$60
0.7	8.6	56	6.5	$\sim$56
0.75	12.5	76	4.6	$\sim$57
0.8	18.0	103	3.4	$\sim$61

As can be seen from the table the optimal velocity to obtain the relative solute concentration of 0.2 is 60 mm/h. In this case $k \cong 0.7$, the number of passes required is $n = 9$ and the process time is about 56 hours.

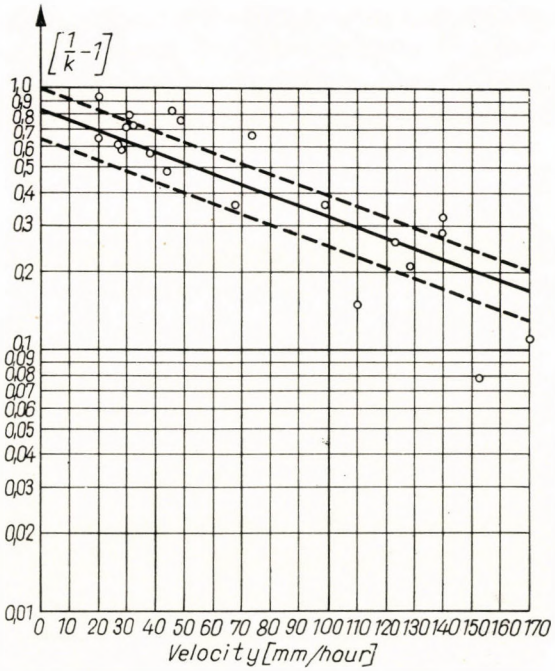

Fig. 9. **The measured values of log [(1/k) — 1] plotted against the velocity of solidification**

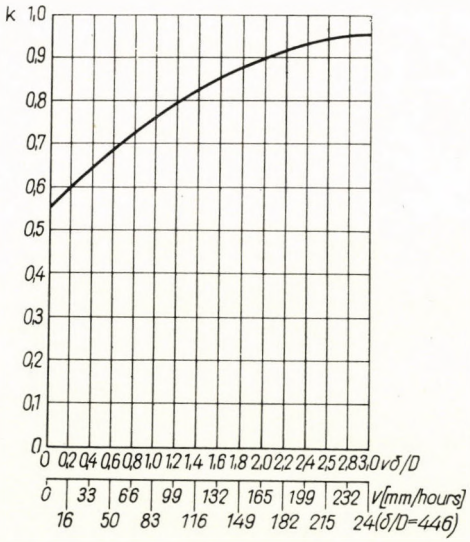

Fig. 10. **The true distribution coefficient as a function of freezing velocity**

The optimal velocity depends on the equipment, too. Nevertheless the result obtained is in good agreement with the data (70 mm/h) published by D. GELLI and M. ROBBA [12] who estimated the optimal velocity from the shape of the intensity curves.

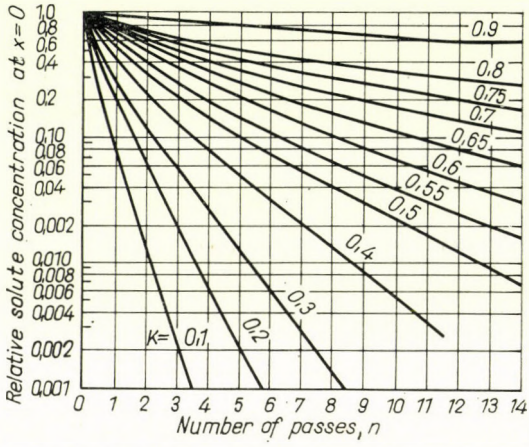

Fig. 11. Relative solute concentration at the beginning of the specimen as a function of the number of passes, for various values of the distribution coefficient [6]

V. Conclusions

Summarizing it may be stated that the optimal parameters of zone refining with the used equipment from the viewpoint of Zn contamination as well as from those of the alloying components, whose distribution coefficient (k_0) is not very different from that of zinc (i.g. Cu, Si, Ca, Li) is the following:

Three passes with coil III, subsequent passes with coil II. The number of passes required depends on the desired purity. It is advisable to adjust the travel rate of the coil so as to assure a constant crystallisation velocity of 60 mm/h.

REFERENCES

1. PFANN, W. G.: *Trans. AIME* **194** (1952), 747.
2. PFANN, W. G.—READ, W. T.: *Trans. AIME* **194** (1952), 747 Appendix.
3. LORD, N. V.: *Trans. AIME* **197** (1953), 1531.
4. REISS, H.: *Trans. AIME* **200** (1954), 1053.
5. BIRMAN, J. L.: *J. Appl. Phys.* **26** (1955), 1195.
6. PFANN, W. G.: Zone Melting. New York, London 1958.
7. BURTON, J. A.—PRIM, R. C.—SLICHTER, W. P.: *J. Chem. Phys.* **21** (1953), 1987.
8. MONTARIOL, F.—REICH, R.—ALBERT, P.—CHAUDRON, G.: *Compt. rend.* **238** (1954), 7 : 815.
9. ALBERT, P.—LE HERICY, J.: *Compt. rend.* **242** (1956), 1612.
10. DEMLER, A. W.: *Trans. AIME* **206** (1956), 958.
11. KUNZLER, J. E.—WERNICK, J. H.: *Trans. AIME* **212** (1958), 856.
12. GELLI, D.—ROBBA, M.: *Allumino* **30** (1961), 3.

BESTIMMUNG DES VERTEILUNGSKOEFFIZIENTEN VON ZINK MITTELS DES RADIOISOTOPS Zn^{65} BEIM ZONENSCHMELZEN DES ALUMINIUMS

E. BUJDOSÓ, E. CZOBOLY und F. MAGYARY

ZUSAMMENFASSUNG

Mit Zn^{65} Radioisotop legiertes Reinstaluminium (99,99% Al) wurde mit dem Zonenschmelzverfahren bei verschiedenen Geschwindigkeiten und Zonenlängen gereinigt. Die Aktivitätsverteilung des ursprünglich 0,0044% Zn^{65} Radioisotop enthaltenden Materials wurde mit kontinuierlich messendem Meßgerät geprüft. Auf Grund der beobachteten Aktivitätsverteilungskurven wurde der wahre Verteilungskoeffizient des Zinks und der für die gegebene Einrichtung gültige δ/D Wert bestimmt. Weiterhin wurde der optimale Parameter des Zonenschmelzverfahrens in Bezug auf Zink und andere Verunreinigungen mit ähnlichen Verteilungskoeffizienten festgestellt.

DÉTERMINATION DU COEFFICIENT DE DISTRIBUTION DU ZINC AVEC ISOTOPE Zn^{65}, AU RAFFINEMENT PAR ZONE FONDUE DE L'ALUMINIUM

E. BUJDOSÓ .E .CZOBOLY et F .MAGYARY

RÉSUMÉ

Des barres d'aluminium d'une pureté de 99,99%, alliées avec l'isotope radioactif Zn^{65} ont été raffinées par la méthode de la zone fondue à différentes vitesses et longueurs de zone en fusion. La distribution de l'activité dans la matière ayant contenu originalement 0,0044% d'isotope radioactif Zn^{65} a été étudiée avec un appareil d'enregistrement continu. A la base des courbes d'activité obtenues, les auteurs ont calculé le coefficient de la distribution effective du zinc, ainsi que la valeur δ/D valable pour l'appareil donné, et déterminé enfin les conditions optima de raffinement par la méthode de la zone fondue pour le zinc et autres impuretés de coefficient de distribution similaire.

ОПРЕДЕЛЕНИЕ КОЭФФИЦИЕНТА РАСПРЕДЕЛЕНИЯ ЦИНКА ПРИ ПОМОЩИ ИЗОТОПА Zn^{65} В ПРОЦЕССЕ ЗОННОЙ ПЛАВКИ АЛЮМИНИЯ

Э. БУЙДОШО, Э. ЦОБОЛЬ и Ф. МАДЬЯРИ

РЕЗЮМЕ

Алюминиевые стержни чистотой 99,99 %, меченные радиоактивным изотопом Zn^{65}, подвергались зонной плавке с различной скоростью продвижения зоны и различной длиной расплавленной зоны. В стержне, содержащем 0,0044 % Zn^{65}, непрерывно регистрировалось распределение активности. По полученным кривым распределения были вычислены истинный коэффициент распределения примеси Zn, значение δ/D, характерное для данной установки, и определены наиболее оптимальные технологические данные зонной очистки алюминия от примесей, коэффициенты распределения которых равны или близки к коэффициенту распределения цинка.

THE PHENOMENA ARISING WITH THE CAVITATION PROCESSES

F. VASVÁRI
TECHNICAL UNIVERSITY, BUDAPEST

[Manuscript received February 14, 1963]

The revision and development of the results obtained with material structure tests, discussed in literature, seem to prove the identity of the damage in the inception period (early phase) caused by water impact, cavitation and spark machining. Comparing these experiences with the theory of the formation of lightning strokes and of spark machining seems to prove that at the beginning of the initial destructions also electric phenomena have a role, both in the case of water impacts and with cavitation.

I. Introduction

In the course of further elaborating the series of experiments [1—3] recently realized, new observations could be made by comparing the colloid-replica electron micrograph of photomicrograph made on surfaces eroded by jet impact and magnetostriction equipments in the initial stage of the destruction.

II. Initial destructions produced by jet impact equipment on metal specimens

(Duration of the stress exposure 5—20 seconds, number of impacts 500—1000)

To begin with, an interesting microscopic comparison can be made between the records made on the guide vane of a mine pump damaged with cavitation (Fig. 1) and on the specimens eroded by jet impact equipment (Fig. 2). The eroded characteristics of the guide vane caused by cavitation in the pump service and those of the jet impact specimens made on different metals — cast iron, brass, copper — are nearly the same. Figs. 3 and 4 are photomicrographs of the cross section of specimens eroded by jets showing a typical cavitation damage.

On Fig. 3 the deviation of the crystallites partly towards the inner part of the material, partly outwardly seems to justify the phenomenon of alternating pressure and suction assumed by Reiner [4]. On record 4 one recognizes the internal material scatter caused by fluid penetration observed by Poulter [5]. The records 5 and 6 verify the folding and crystallite gliding phenomena observed by Plesset and Ellis [6], as well as by Novotny [7], which may be seen both with specimens eroded by magnetostriction and also by jet impact.

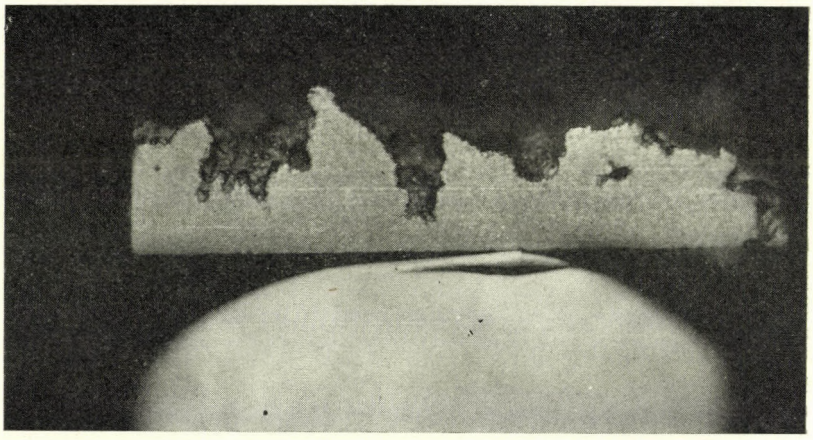

Fig. 1. Cross-section of a guide vane part (cast iron) 12.5 ×

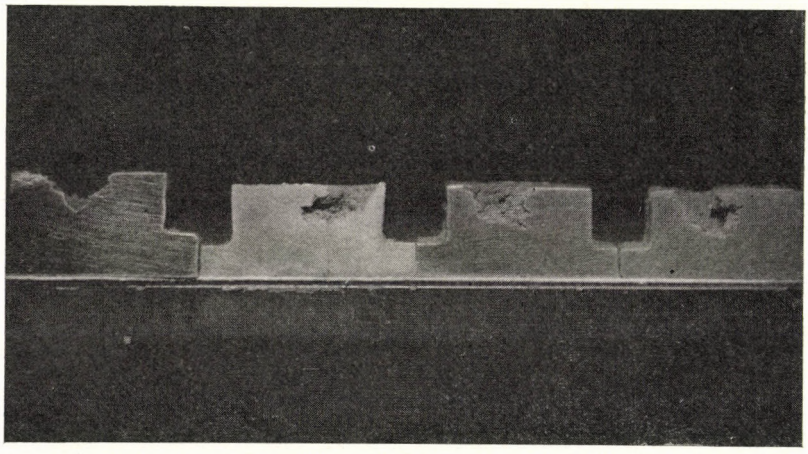

Fig. 2. Cross-sections of specimens eroded by jet impact (cast iron, Al, Sr, Br) 1.5 ×

III. Observations made on specimens eroded by a magnetostriction equipment

(By a frequency of 6500 and an amplitude of 0.084 mm)

In Fig. 7 specimens slightly eroded by a magnetostriction equipment are illustrated, showing annealing colours caused by heat. The specimens were made of electrolytic copper, already presenting annealing colours at 120 °C. Attention was called to the heat phenomena arising with the cavitation tests by ERDMANN—JESNITZER [8] and WHEELER [9].

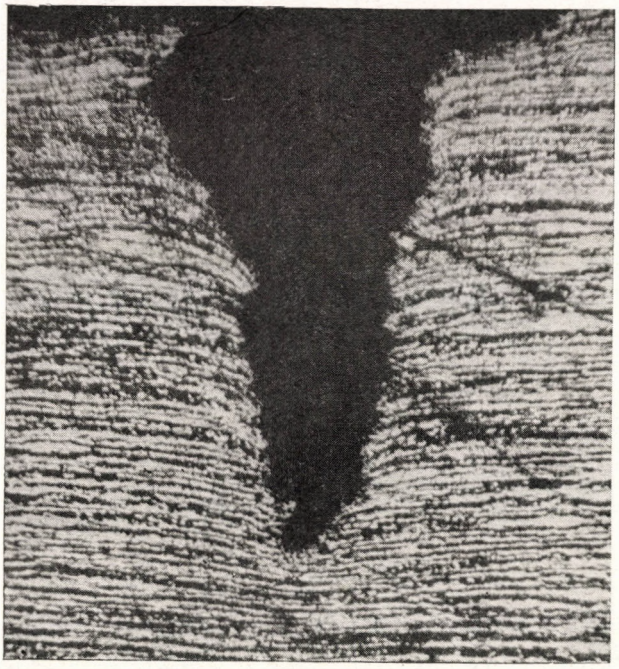

Fig. 3. Crater of a specimen eroded by jet impact (Sr 67) 500 ×

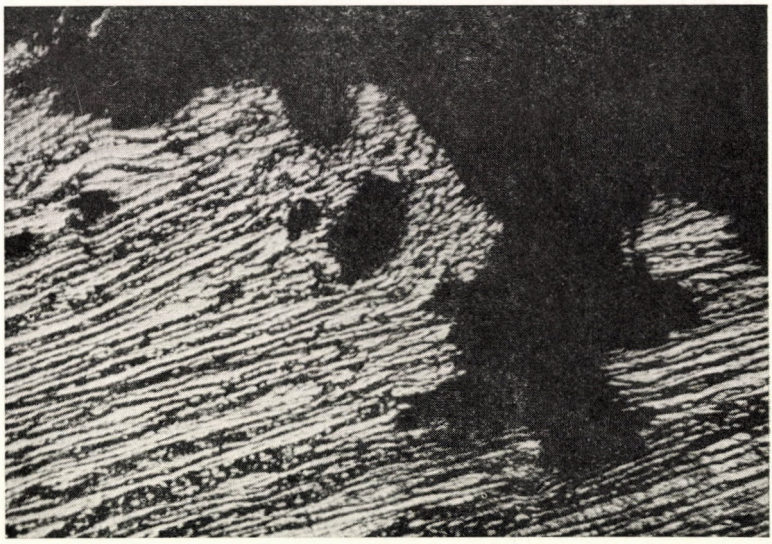

Fig. 4. Internal ruptures of a specimen eroded by jet impact (Sr 67) 500 ×

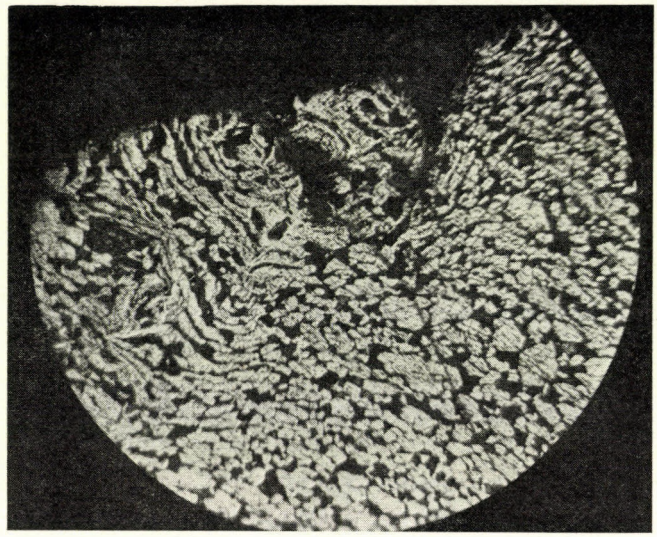

Fig. 5. Crystallite fold due to jet impact (Sr 67) 500×

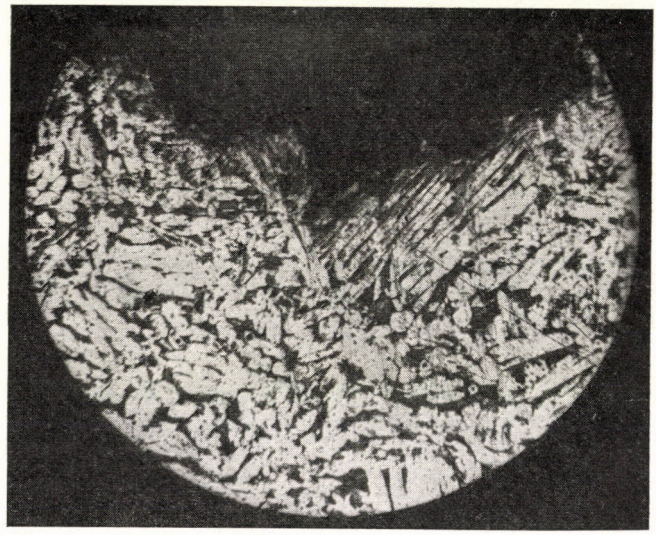

Fig. 6. Crystallite glidings caused by jet impact (Sr 67) 500×

The microscopic records 8 and 9 show craters and melting phenomena due to destruction by magnetostriction of pure gold and electrolytic copper, justifying CREWDSON's [10], RAYLEIGH's [11], P. DE HALLER's [12] and KREEN's [13] calculations and assumptions, respectively, as well as our own calculations [2], [3] referring consequently to the high temperatures.

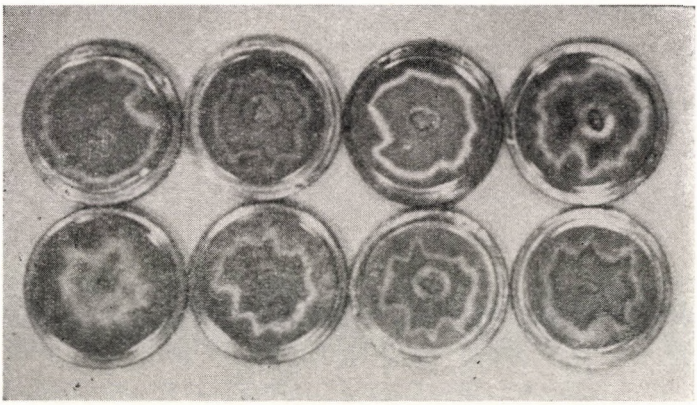

Fig. 7. Surfaces of specimens eroded by magnetostriction with annealing colours (Cu) 1.5 ×

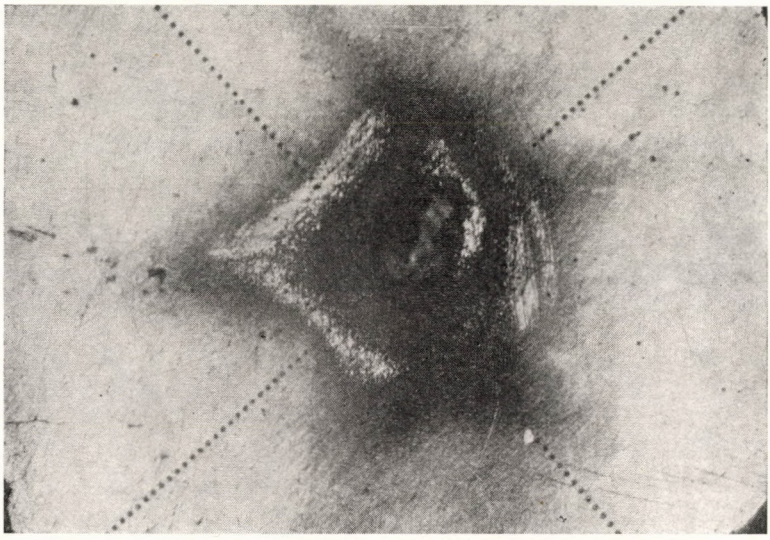

Fig. 8. Crater of a surface eroded by magnetostriction (gold) 7 ×

IV. Test on the initial phase of the jet inmpact and magnetostrictive attack based on colloid-identation and electron-microscopic records

The records 10 and 11 illustrate the formation of circular cracks caused by jet impact on cast iron specimens. Characteristic are the shell-like holes.

Fig. 12 is a microscopic record on the initial period of jet-impact erosion of a copper specimen, and Fig. 13 that of a specimen for a short time eroded by magnetostriction; one may observe identical, circular crack

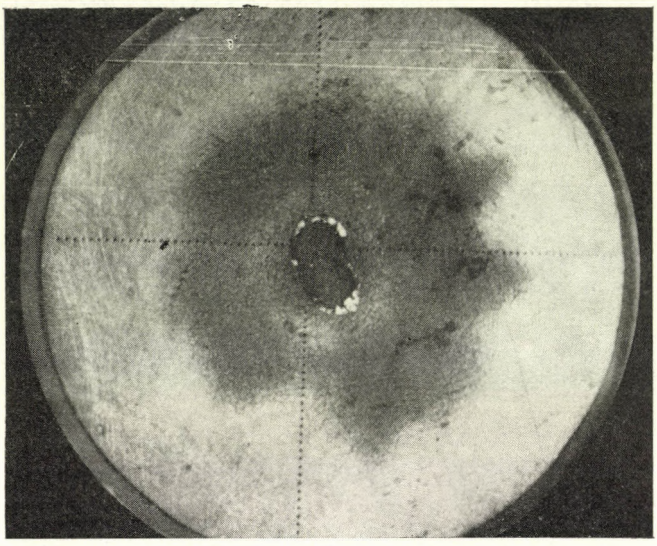

Fig. 9. Crater surface eroded by magnetostriction with phenomena due to heat (Cu) 7×

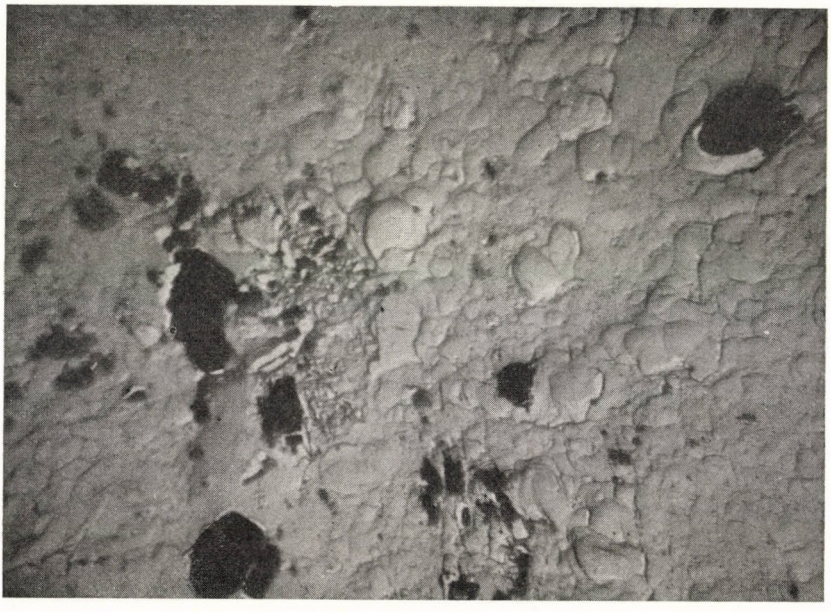

Fig. 10. Surface eroded by jet impact with bubble traces (cast iron) 4800×

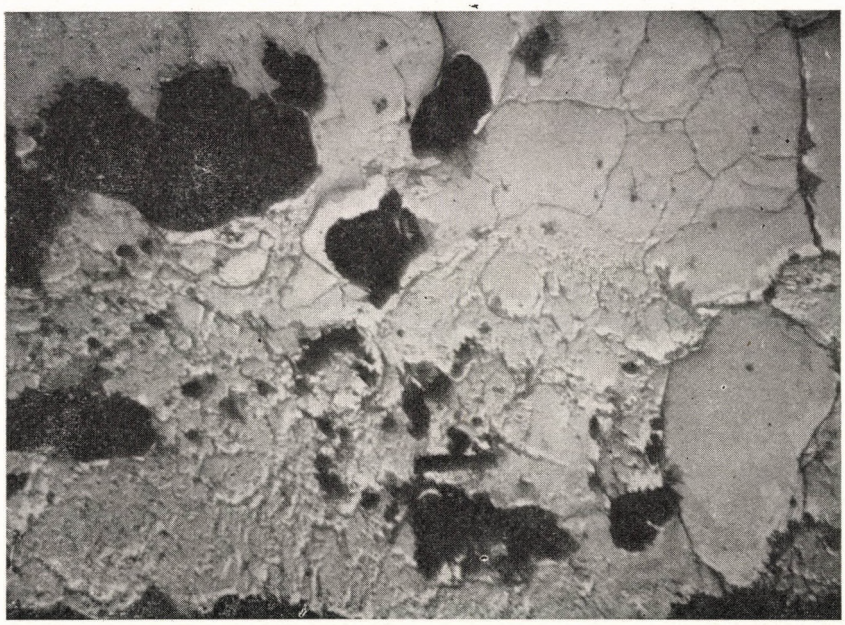

Fig. 11. Surface eroded by jet impact with crystallite periphery indentations (cast iron) 4800 ×

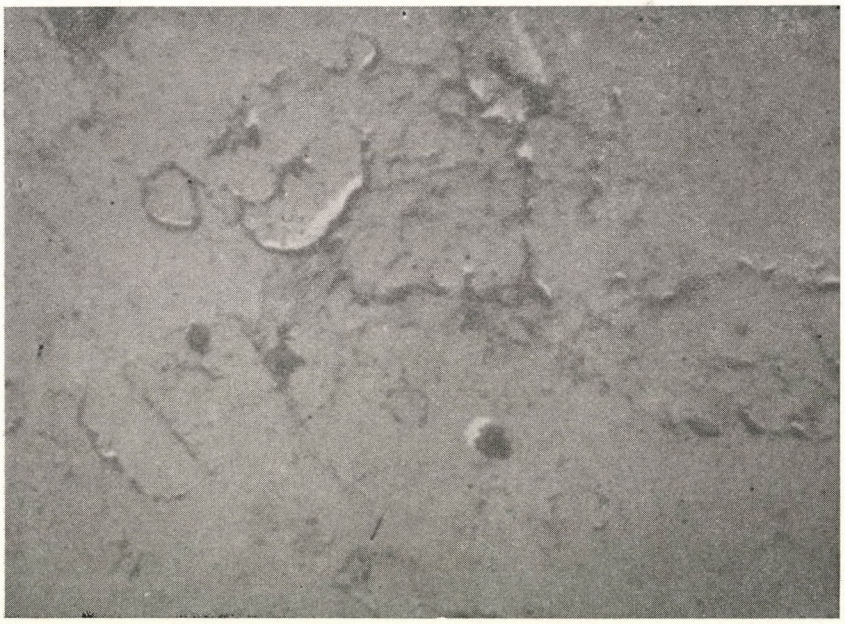

Fig. 12. Surface eroded by jet impact with circular cracks (Cu) 10 000 ×

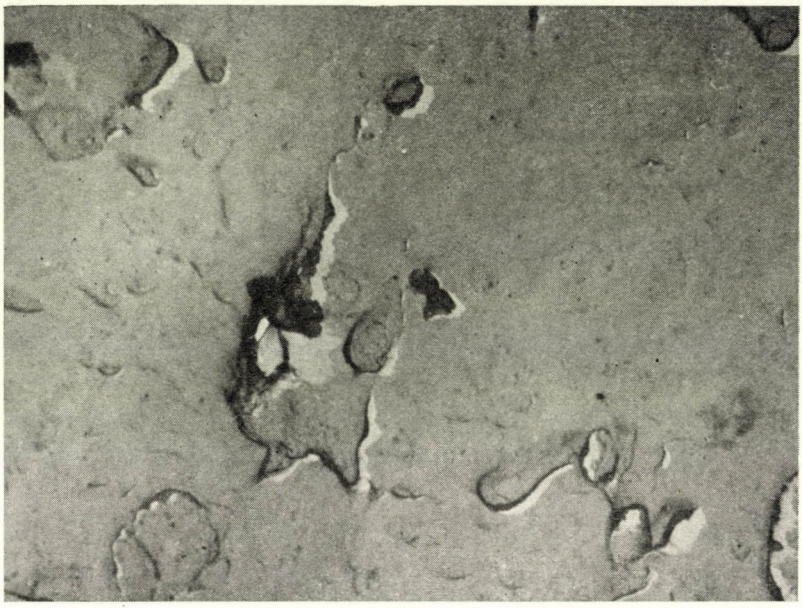

Fig. 13. Surface eroded by magnetostriction with circular cracks (Al) 10 000 ×

Fig. 14. Surface eroded by jet impact with rough cracks (Al) 10 000 ×

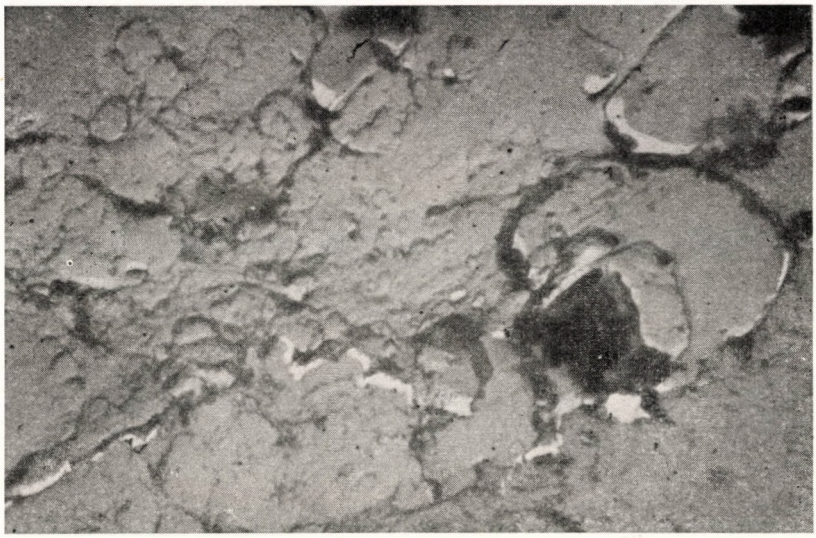

Fig. 15. Surface eroded by magnetostriction with crack- and bubble-traces (Cor 5) 10 000 ×

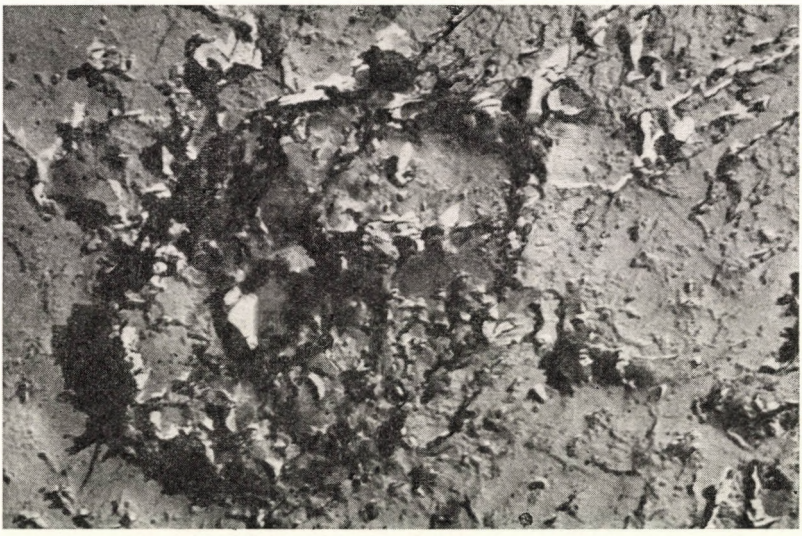

Fig. 16. Indentation in the concentric crater of hardened steel (0.5% C) surface eroded by magnetostriction, 12 600 ×

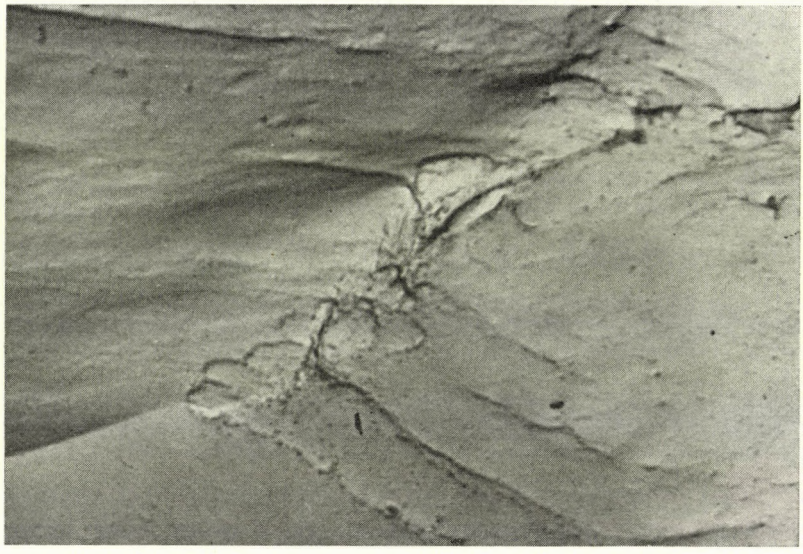

Fig. 17. Surface eroded by jet impact with cold shut lines and bubble traces (Br) 12 600 ×

traces. The cracks are nearly the same as illustrated in Figs 14 (Al) and 15 (Cor 5) on metal surfaces somewhat more eroded. On the records one recognizes well that the initial circular cracks are increasing and widen into rougher cracks. The record (Fig. 16) on the hardened steel (0.5% C) eroded with magnetostriction, where a series of concentric curves can be seen in the middle of a crater about to break off, is interesting, too.

The electron-micrograph of Fig. 17 clearly shows the cold deformation occurring due to a jet impact. Nevertheless, in the corners of the lines referring to this circumstance, also circular bubble traces are present [14].

If the cracks are compared in orders of magnitude, three kinds of phenomena may be observed both with the jet-impact and with the magnetostrictive destruction:

a) With jet impacts, we find on the surfaces eroded circular cracks of 0.2 ÷ 2.0 microns diameter and other crack traces of 0.1 micron width;

b) with malleable materials one may observe corrugation and slip lines;

c) with greater tensile strength materials one may see cracks on the crystallite grains (followed later by through-cracks on the crystallites).

With the specimens eroded by magnetostriction:

a) there appear circular cracks of about 0.05 ÷ 1.0 micron diameters on the eroded surfaces and the material cracks around the crater to about 0.05 micron caused by local heating and repeated impacts.

b) These local cracks become unified along the chrystallite peripheries to cracks of about 0.1 micron width, further stresses increase these cracks to $0.6 \div 1.0$ micron.

c) With the magnetostrictive destruction the dimension of the cracks in the more resistant materials is less than 0.01 micron. The more resistant the material is, the smaller cracks appear, which in some material structures may even be seamed on a later heat effect.

As a result of a comparison of records 12, 13, 14 and 15, justified by identical characteristics of the cracks, the formation of the initial stage of the destruction may primarily be attributed in case of jet impacts and magnetostrictive destruction, to the collapse of bubbles. This phenomenon is analogous both with the jet impacts and the magnetostrictive damage.

At the same time a great difference appears by the deviation in the orders of magnitude of the power impulse effects. This may be explained by the circumstance that while with the magnetostrictive destruction the collapse of the bubble after suction takes place at an increased pressure, in the case of the jet impact the whole surface is constantly stressed by the impact pressure, consequently, the collapse of the bubble ensues quicker than with the magnetostrictive destruction.

The mechanical impulse effect arising whenthe bubble collapses has been many times calculated since RAYLEIGH. The majority of the experts are in agreement on the question that for eroding alloys of extremely high cavitational resistance, the mechanical effect alone is not sufficient. Consequently, other additional effects also have a role. The experience that by *cathodic protection* destruction is delayed (increasing the incubation time), but not completely hindered, supports this supposition.

V. Summary of the mechanism of the cavitation destruction

In the literature many ideas explaining the mechanism of the destruction were published. The majority of these is valid, when pointing to the single factors having an eroding effect.

On the basis of the magnetostrictive and jet impact destruction tests effected on about 600 specimens, involving also hardness tests with small load stresses on the eroded surfaces and on their cross-sections before and after the destruction, for clearing up the changes taking place in hardness due to destruction, the factors to be considered must be completed by the following. (Note that the specimens were of different surface fineness.)

a) The high temperatures to be observed on the surfaces of the material (records 8, 9);

b) identity of destruction on the surface of the material caused by jet impacts and magnetostriction (Figs. 14, 15);

c) shape of the eroded cavities: the conic, deep craters, indicating the presence of a power impact effect directed from inwards to outwards (Fig. 3);

d) the cross-sectional shape of the destructions, where the cavity formation may be demonstrated below the eroded surface (Fig. 4).

Taking into account the aforesaid and the experiences published in literature, the mechanism of the jet impact and magnetostrictive destruction may be taken as follows:

The destruction is established as a result of the mutual effect of the solid material, fluid and gas which is present, so that the following phases of the process are simultaneously proceeding, too:

A) With the magnetostrictive destruction the bubbles formed by the fluid surface caused by the pressure difference and collapsing under the effect of the pressure, are penetrated by the accelerating jet above the bubbles, as a result of which gas (steam) is pressed between the water and the surface of the material. The more eroded the surface is, the more intense and great is the destruction. In case of a jet impact there is also air in the jet which is similarly pressed in between the material and the fluid at the moment of impact.

B) Due to the rapid decrease in the bubble diameter (this being the function of the pressure), it is so intensively heated that the water steam (gas) involved decomposes, which can result in a further heat development (atomous oxygen and hydrogen may be present).

C) On the common effect of the hot gas and water impact, respectively, the surface of the material becomes locally heated, consequently, the ionized gas present may penetrate more intensively into the crystal lattice of the material structure.

D) The crystal structure stressed by the magnetostrictive jet impact is subjected to an elastic deformation. With the jet impact a cold deformation also appears.

E) Under the effect of the gases there *(B)*, the surface of the material is also subjected to a chemical reduction promoted by the high temperature and the ionic action, too *(C)*.

F) The temperature difference between the crystal grains *(C)*, the mechanical stress difference *(D)* and chemical difference *(E)*, respectively, to which is also contributed the crystal lattice and the inhomogeneity of other contaminations, lead to a potential difference on the surface of the attacked material, as a result of which galvanic currents are starting through the water leading to the further chemical corrosion of the material. This may be delayed by cathodic protection.

G) The chemical change *(E)* results in the hardening, embrittlement of the surface, cracked on the effect of the repeated impacts *(C)*, at the same time the gases on the border of the tiny cracks are pressed by the jet impact into the already existing cracks. The high-pressure gas separates the hard parts of the surface eroded by the cracks, this being promoted by the elastic reaction of the internal crystal structure which was pressed *(D)*.

Below the separating crystals the material structure becomes looser, internal cavities may be formed, this being by the carbide separation, or -solution caused by the heat in the material structure, leaving behind cracks along the crystal periphery, or — in the words of AKIMOV [15] and WEAVER [16] — caves (micro-cavities, uniting into cracks).

Through the already broken surface along the crystallite peripheries and through the heated up crystallites, respectively, the gas may penetrate more intensively upon the eff ectof the water impact. The gas penetrated, i.e. the gas expanding between the grains, leads on the effect of heating to the crystal structures rapid splitting-off.

H) With materials of non-oxidating surface, on the effect of repeated impacts, the chrystallites start swinging elastically, this leading to fatigue failures. Through the cracks caused by former, the gas penetration ensues according to phase *(G)*.

I) With inhomogeneous materials, the gas penetrates through the softer connective tissues and causes the crater-like explosion of the more rigid granules.

The circumstance that where air is led into the cavitation place, the destruction becomes reduced, seems to contradict the effect of the gas pressure directing to the material structure. Probably, in case of *cavitation* the introduced air pocket decreases the dimension of the bubble and at the same time its heating, too, so it cannot press so intensively the gas into the less heated surface. Nevertheless, with *jet impacts* the magnitude of the impact is always constant (independent of the air quantity).

The phases of the destruction mechanism appear with different intensities in the different materials and this is the reason, why the measuring values referring to the intensity of the destruction cannot be unambiguously correlated either with the tensile strength, or with the endurance limit, with the surface micro- or macrohardness, with the degree of fineness of the crystal structure, nor with corrosion resistance, the electric and thermal conductivity and with the gas penetrability as these influence the resistance to destruction to different degrees depending on the type of the material. It should be mentioned, however, that with the individual materials one could find relations between the measure of destruction and the Brinell-hardness and the erosion, as well as the endurance limit, but these results are valid only for some materials. So e.g. in case of stainless steels, with the type 18/8, COLOMBIER and

HOCHMANN[17] found as the most appropriate the features of α and γ shapes austenitic crystals. The excellent cavitation resistance of the well-known stainless steel 18/8 is, owing to the precise observance of the alloying elements, for a slight change in the percentage value of these elements causes an unbalancing in the equilibrum of the two phases (α-phase and γ-phase, respectively) resulting in the loss of the steel tenacity and leading to brittleness. The presence of the microcavities originating from the solution at the crystallite peripheries is also a consequence of the former.

Accordingly, the reason for the precise alloying emphasized in literature, may be explained by the heat effect and by the consequences experienced with cavitation; this makes it necessary at the same time also to consider the heat effect.

VI. Further statements and conclusions

Evaluating the results of the series of experiments and summarizing them with those already known, the following may be stated:

A) The macroscopic tests are not suitable for analyzing the mechanism of destruction. As for the starting of the destruction and clearing up its mechanism, the electron-photomicrograph gives a better explanation.

B) The *cavitation* attack results in a change of the local hardness of the material. The surface of the material in general, on the effect of a magnetostrictive destruction becomes more malleable but below the surface layer a hardening process may be observed, referring to the presence of HERTZ's stresses [18]. With a destruction by water jet impact a hardening is being formed on the surface and under the surface, too. These two kinds of behaviour may be explained by the different stresses.

C) The beginning of the destruction on the material surface after the incubation time has identical qualities both with the water jet impact and the magnetostrictive destruction. Also the origin of the micro-cracks is the same.

D) The water jet impact and magnetostrictive destruction differ from each other only in the order of magnitude. As against the idea accepted hitherto, with the water impact destruction the appearance of a cavitation phenomenon could be verified. Nevertheless, with the water jet impact, the more intense cold working increases the deformation.

E) With the water impact and magnetostrictive destruction, several phases of the destruction may be distinguished:

a) The surface cracks of the material without loss of weight;

b) formation of small, surface cavities;

c) destruction under the surface of the material;

d) total disintegration of the material surface.

On the whole, it may be stated that the magnetostrictive destruction is always started by a series of micro-cracks and cavities forming on the

surface, being established first of all by mechanical stresses and heat effect, further by the electrochemical phenomena connected with former. To the secondary importance of the electrochemical phenomena refers also the fact that the cathodic protection can influence the incubation time only.

The tests explain, why the relative resistances of the materials to the cavitation show the same order, both in the magnetostrictive and water impact tests. The work of the water impact test is greater by an order of magnitude than that of the magnetostrictive test, within a time unit it erodes a greater quantity of material, but this does not influence the relative resistance succession of the material.

Surveying in their correlation the factors influencing the destruction, we obtain a basis for selecting the metallic materials which resist to cavitation well. We expect these materials to meet the following requirements:

Fine, homogeneous grain texture;
thoughness;
high chemical resistance;
good heat-resistance (high strength also at high temperatures);
with alloyed materials neither solution, nor segregation should arise on heat effects.

It is worth of further reflections, how the heat effect is to be established. For this purpose, let us compare the metal surfaces eroded by magnetostriction with those processed with spark machining. In Fig. 18 the collodion impress of the surface of copper eroded by magnetostriction, in Fig. 19 the surface of stainless steel treated with spark machining, in Fig. 20 the impress of copper eroded by magnetostriction, finally in Fig. 21 the aluminium surface treated with spark machining, are shown. Comparing these, the configurations of the material destructions *are very similar*. This similarity is supported even more by comparing the electron microscopic records on the surfaces of gold slightly eroded by magnetostriction with those of stainless steel Cor 5 treated with spark machining (Figs. 22 and 23). At first sight the two metal surfaces destructed differently can hardly be distinguished, the characteristics of the initial destruction being so similar (circular starting of the cracks).

Beside the interesting analogies it remains an open question, what is the cause of the identical feature of the initial destruction?

1. Is it the concentrated mechanical impact of small water drops, which establish circular fatigue cracks due to repeated stresses?

2. Is it caused by the shrinkage originating from the heated elementary particles cooling down?

3. Or by both together?

4. Or by the local impact of the ionized steam (gas) particles onto the surface?

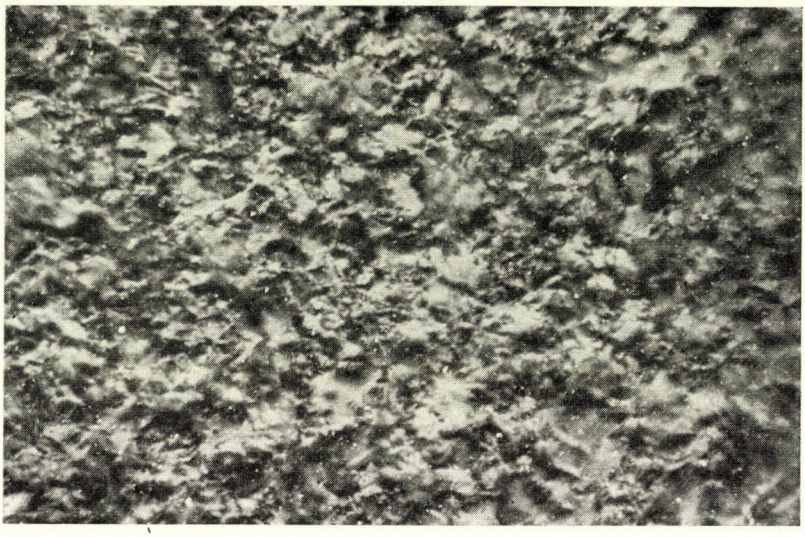

Fig. 18. Collodion impress of a surface eroded by magnetostriction (Cu) 460 ×

Fig. 19. Collodion impress of a surface processed by spark machining (Cor 5) 235 ×

Fig. 20. Collodion impress of a surface eroded by magnetostriction, showing hardness test impresses (Cu) 235 ×

Fig. 21. Collodion impress of a surface processed by spark machining (Al) 235 ×

Fig. 22. Surface eroded by magnetostriction (Gold) 16 600 ×

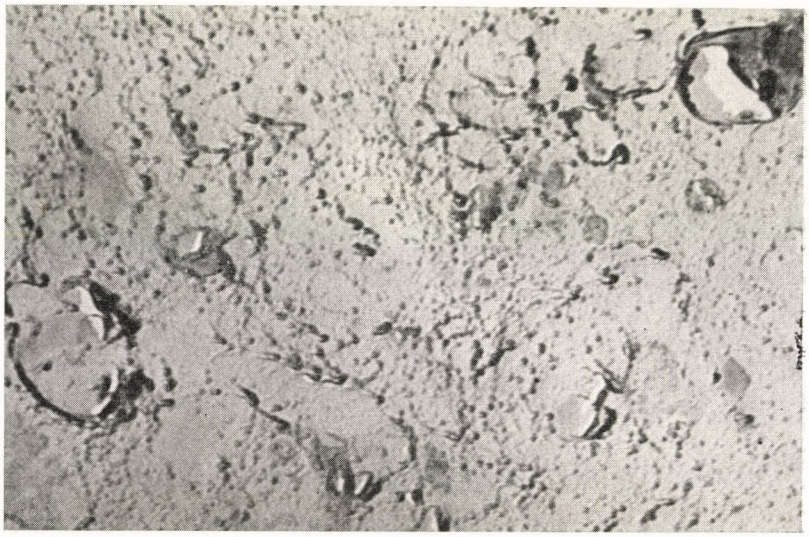

Fig. 23. Surface processed by spark machining (Cor 5) 21 400 ×

Comparing the initial destruction which was formed up till now with the initial destruction of spark machining, interesting conclusions may be drawn. About the phenomena of spark machining it is known that they are the electric discharges, sparks controlled periodically in petroleum (fluid) bath, that loosen, explode the elementary particles in places, where the process of heating and cooling changes within a short time. As for these, reference is made to LASARENKO's [19] tests.

It is an obvious idea, whether this is not the same phenomenon, which arises with cavitation and water impact, too?

According to our considerations this is possible. On KORNFELD's and other experts' observations, the surface of the bubble about to collapse on the metal surface is subjected to deformation oscillations, which bubble is then penetrated by the fluid jet from above it. When the fluid jet approaches the metal surface through the bubble, it becomes frictional in a high-pressure, high-temperature gas. When observing the propagation of the lightning strokes, LÉNÁRD [20] demonstrated that the surface of the rain drop frictioned in the gas becomes ionized and obtains an electric charge on the effect of the gas friction. Is this not partly possible also with the cavitation processes?

When the water drop charged electrically is approaching the metal surface through the bubble, it becomes electric charged, consequently, from the elementary part of the metal structure an electric arc is passing towards the fluid above it, similarly eroding the material to that of spark machining. This is shown by the circular traces and elementary broken out particles. It is assumed, that the traces with cracks to be seen on the records, are caused by *electric discharges* and also electric heat punctures both on the surfaces eroded by water impact, magnetostriction and by spark machining.

Many tests have proved that if an electric charge is imposed onto the metal surface (cathodic protection), the incubation time becomes longer, probably because an important part of the sparks cannot be established. Nevertheless, owing to the different charges of the fluid drop, one part of them is still formed and there is always one that begins to erode the material surface and once the destruction had been started, even the cathodic protection is not efficient enough against the further rapid destruction. Thus, it is obvious that the starting of the surface destruction can only be delayed by the cathodic protection, but cannot be hindered.

It was reported several times in the literature that cavitation is a phenomenon accompanied by pressure differential [13], thermic phenomenon [8], [14], luminous phenomenon [23], electric charge [19], [10], [22], [23], ionization [30], [12], and also noise [29] followed by a mechanical effect [24—28]. These have also been verified in detail by a great number of tests effected hitherto. If the incipience, the discharge of the atmospheric lightning is examined, entirely identical phenomena are met with. Assuming that the starting

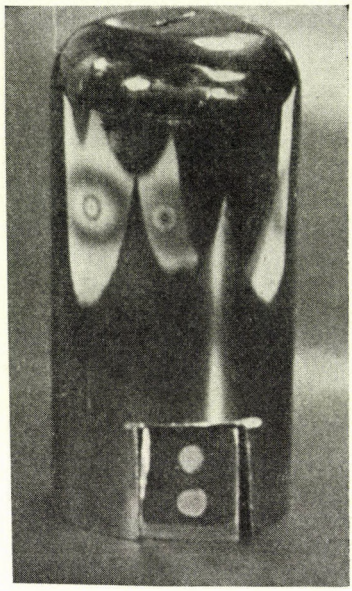

Fig. 24. Cold cathode of the electron microscope (V2) 0.75 ×

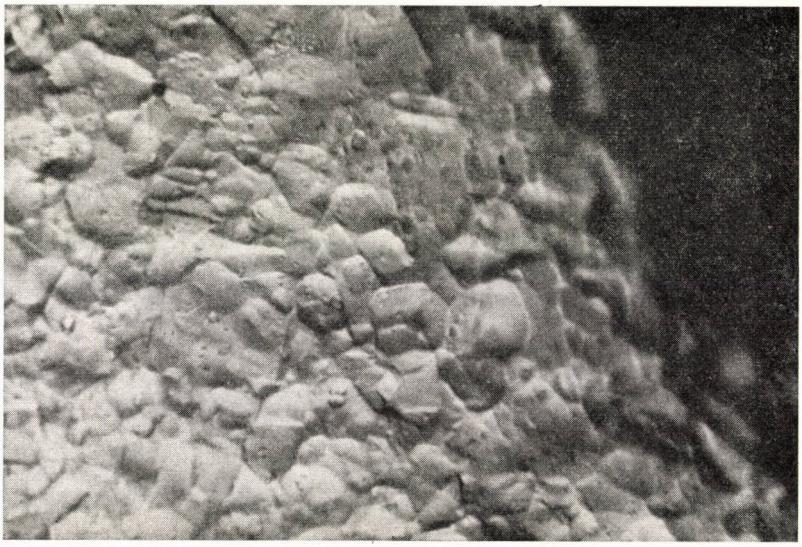

Fig. 25. Collodion impress of the cold cathode surface subjected to ion bombardment of the electron microscope 250 ×

Fig. 26. Crystallite periphery cracks on the cold cathode of the electron microscope 21 400 ×

Fig. 27. Surface processed by spark machining of the electron microscope cold cathode with circular cracks 21 400 ×

of the cavitation destruction is nothing but an electrical phenomenon of micro-thunder taking place in the fluid.

The results obtained complete our knowledges obtained up to now satisfactorily and also answer the question, why the elastic insulating materials (coatings) that cannot be treated with spark machining, show a good cavitation resistance (rubber, synthetic rubber, etc.). These cannot be attacked by cavitation, not even with an electric spark and the material is stressed only by the mechanical effect of cavitation; the above materials can avoid the latter elastically even reducing the mechanical effect significantly.

Finally it is worth comparing the destructions found in the foregoing and on the cold cathod of an electron microscope (Fig. 24, 0.75-times magnitude), from the bottom of which a specimen for spark machining was worked out. On the surface of the cold cathode one can recognize well, on the one hand, the concentric annealing colours caused by heat, and, on the other hand, in the middle of the annealing colours the electric heat punctured craters caused by ion bombardments.

Fig. 25 shows the collodion impress of the crater border. When comparing this record with the magnetostriction and water impact one, the deviation from the magnetostrictive destruction may be observed. Here the form of destruction is an oxidation metallic evaporation due to ion bombardment, (this being natural with vacuum tubes) and this is justified even more by traces due to oxidation at the crystallite peripheries, to be seen on the electron microscope record of Fig. 26.

For making a comparison between the same materials, checking up on the record of a specimen subjected to spark machining (Fig. 27), one may again observe the circular crack-traces.

Finally it may be mentioned that the tests and ideas discussed in the foregoing also support WEAWER's [16], COLOMBIER's and HOCHMANN's [17] statements, according to which even the steels type Nimonic 80 and austenite Cr. Ni show good heat resistance only in case of a precisely determined composition and at the same time features resisting cavitation.

REFERENCES

1. VASVÁRI, F.: New Data on the Theory of Cavitation Destruction of Metals. Thesis for obtaining the degree of Candidate of Techn. Sc. (in Hungarian). Budapest 1961.
2. VASVÁRI, F.: Investigation of the Initial Phase of Cavitation Damage. *Acta Techn. Hung.* **29** (1962), Fasc. 1—2.
3. VASVÁRI, F.: Beginnende Zerstörung von Metalloberflächen durch Wasserstrahlschlag. *Periodica Politechnica* (1962), No. 1.
4. REINER, M.: Stress due to Collapse of Vapour Bubbles in Liquid. *Engineering* **155** (1943), 454.
5. POULTER, T. C.: Mechanics of Cavitation Erosion. *Journ. of Appl. Mech.* **9** (1942), March 31—37.
6. PLESSET, M. S.—ELLIS, A. T.: On the Mechanism of Cavitation Damage. *Transactions ASME X.* **77** (1955), No. 7; 1055—1064.

7. NOVOTNY, H.: Werkstoffzerstörung durch Kavitation. VDI Verl., Berlin 1942, Bd. 12; 20.
8. ERDMANN, F.—JESNITZER: Werkstoffverhalten bei Kavitation. Journées de la Corrosion Dechema, Frankfurt 1954.
9. WHEELER, W. H.: Indentation of Metals by Cavitation. *Trans. ASME* (1960), March 184—194.
10. CREWDSON, E.: Impingement Attack in Turbines. *Water Power* **5** (1953), April 146—150.
11. RAYLEIGH, J. W.: On the Pressure Developed in a Liquid during the Collapse of a Spherical Cavity. *Philosophical Magazine*, Series 4 **34** (1917), 94—98.
12. HALLER, P. DE: Erosion und Kavitations-Erosion. Handbuch der Werkstoffkunde; Springer Verlag, Berlin 1939. Bd. II, S. 471—488.
13. KRENN, H.: Thermoelectric Corrosion. *Electr. Review* **145** (1949), September 545—548.
14. FÖTTINGER, H.: Untersuchungen über Kavitation und Korrosion bei Turbinen, Turbopumpen und Propellern. *Hydraulische Problemen*, Berlin 1926; 14—64.
15. AKIMOV, G. V.: Theory and Test Methods of Metal Corrosion. (in Hungarian). Nehézipari Kiadó, Budapest 1951; 223.
16. WEAVER, CW.: Intergranular Cavitation Structure and Creep of a Mimonic 80. a. Type Alloy. *The Journal of the Institute of Metals* (1960), March 296—300.
17. COLOMBIER, L.—HOCHMANN, I.: Aciers uraxydables utilisés turbines hydrauliques Auxen—Provence. Symposium de Nice 16—20 September, 1958.
18. BOSCH, M. ten: Berechnung der Maschinenelemente. Berlin 1953.
19. LASARENKO, B. R.: Problems regarding the electrical processing of materials (in Russian). Moscow 1960.
20. LÉNÁRD, P.: Über Wasserfallelektrizität und über die Oberflächenschaffenheit der Flüssigkeiten. *Ann. d. Phys.* (1913), 41: Note 2.
21. HARVEY, F. N.—MCELROY, W. D.—WHITELEY, A. H.: Cavity Formation in Water. *Journal of Appl. Physics* (1947), February.
22. NECHLEBA, M.: Das Problem der Kavitation. *Wissenschaftliche Zeitschrift der Techn. Hochschule Dresden* **3** (1953/54), Heft 4.
23. PETRACCHI, G.: Investigation of Cavitation Corrosion. *Engineers Digest* (1949), 314—316.
24. BOETSCHER, H. N.—BALTIMORE, M. D.: Failure of Metals due to Cavitation under Experimental Conditions. *Hydraulics*. I, 1958.
25. KERR, S.: Determination of the Relative Resistance to Cavitation Erosion by the Vibratory Method. *Trans. ASME* **59** (1937), 373—397.
26. LEITH, W. C.: Cavitation Damage of Metals. Doct. Diss. Me. Gill., Univ. Montreal 1960, March.
27. KORNFELD, M.: Elastizität und Festigkeit der Flüssigkeiten-Kavitations Erscheinungen. Verlag Technik, Berlin 1952; 80—108.
28. KERMABON, B.—WEIL-CONLY, P.: Étude de la dégradation d'un alliage soumis à la cavitation. *Water Power* **389** (1958), October; 377—387.
29. RATA, J. M.: The Acoustical Determination of the Threshold of Cavitation: Methods and Equipment Used (in French). Paper presented at the Société Hydrotechnique de France. Meeting June, 1962. Paris, France.
30. TAYLOR, L.: Cavitation Pitting by Instantaneous Chemical Action from Impacts. *ASME Paper A* **109** (1954), 11.

KAVITATION ALS ELEKTRISCHE ERSCHEINUNG

F. VASVÁRI

ZUSAMMENFASSUNG

Die Ergebnisse der Wiederholung und Weiterentwicklung der im Schrifttum mitgeteilten Untersuchungen der Werkstoffstruktur scheinen zu bestätigen, daß die vom Auftreffen eines Wasserstrahls, von der Kavitation und von der Funkenerosion hervorgerufenen anfänglichen Zerstörungen identisch sind. Diese Erfahrungen, im Verein mit den Theorien der Entstehung des Blitzes und der Funkenerosion, scheinen zu bestätigen, daß in der Hervorrufung der anfänglichen Zerstörungen, ebenso wie beim Aufprallen eines Wasserstrahls, bei der Kavitation die elektrischen Erscheinungen ebenfalls eine Rolle spielen.

LA CAVITATION COMME PHÉNOMÈNE ÉLECTRIQUE

F. VASVÁRI

RÉSUMÉ

Les résultats obtenus au cours de la répétition et du développement des essais de matériaux publiés semblent justifier l'identité des destructions initiales causées par l'impact du jet d'eau, la cavitation et l'électro-érosion. La confrontation de cette expérience avec les théories relatives au phénomène de l'éclair et à l'usinage par électro-érosion semble confirmer que, dans la production des destructions initiales, les phénomènes électriques jouent un rôle aussi bien dans l'impact des jets d'eau que dans la cavitation.

КАВИТАЦИЯ КАК ЭЛЕКТРИЧЕСКОЕ ЯВЛЕНИЕ

Ф. ВАШВАРИ

РЕЗЮМЕ

Результаты повторения и развития встречающихся в литературе исследований структуры материалов подтверждают идентичность начальных разрушений, вызванных ударом водяной струи, кавитацией и электроискровой обработкой. Сравнивая эти результаты с теорией образования молнии и теорией электроискровой обработки, как бы подтверждается, что в появлении начальных разрушений электрические явления играют роль также, как и при ударе водяной струи и при кавитации.

DIE BERECHNUNG DES VERFORMUNGS WIDERSTANDES PRISMATISCHER KÖRPER BEIM ZUSAMMENDRÜCKEN IHRER PARALLELEN FLÄCHEN

L. TÓTH

TECHNISCHE UNIVERSITÄT FÜR DIE SCHWERINDUSTRIE, MISKOLC

[Eingegangen am 19. März 1963]

Die Arbeit befaßt sich mit der annäherungsweisen Berechnung jener Kräfte, die zum plastischen Zusammendrücken des Materials zwischen parallelen Flächen nötig sind. Die annähernden Lösungen der Gleichungen werden behandelt. Die Wirkung der Oberflächenbeschaffenheit wird untersucht, und eine neue Versuchsmethode wird zur Bestimmung des Reibungsfaktors vorgeschlagen. Die Berechnung der Kräfte wird sowohl für ebene Verformung als auch für Quellungen an Körpern mit endlichen Abmessungen untersucht, und eine neue Annäherungsmethode wird vorgeschlagen.

1. Zeichenerklärung

h_0	mm	Abmessungen des gedrückten Körpers in Richtung der Kraftwirkung vor der plastischen Verformung,
h	mm	Abmessungen des gedrückten Körpers in Richtung der Kraftwirkung während der plastischen Verformung,
$2a$	mm	Abmessungen des gedrückten Körpers in Richtung der ebenen Verformung,
b	mm	Abmessungen des gedrückten Körpers senkrecht zur Richtung der ebenen Verformung,
c	mm	Grenze der Haftungszone,
d	mm	Grenze der „elastischen" Zone,
σ_1 σ_3 σ_x σ_y τ_{xy}	kg/mm²	Spannungen in den Punkten des gedrückten Körpers,
τ	kg/mm²	äußere Gleitspannung, die den gedrückten Flächen entlang auf den Körper wirkt,
p	kg/mm²	äußere Normalspannung, die den gedrückten Flächen entlang auf den Körper wirkt,
k_f	kg/mm²	Verformungsfestigkeit des Materials,
k_k	kg/mm²	Verformungswiderstand bei ebener Verformung,
k'_k	kg/mm²	Verformungswiderstand bei räumlicher Verformung,
μ		Der an der gedrückten Fläche bei relativer Verschiebung der Druckfläche und des Werkstückes auftretende Reibungsfaktor,
v_y	mm/sec	Geschwindigkeit des Druckwerkzeuges,
v_x	mm/sec	Geschwindigkeit in der x-Richtung eines beliebigen Punktes des gedrückten, Körpers, der sich unter dem Druckwerkzeug befindet,
δ	mm	durchschnittliche Stärke des Schmierfilms zu Beginn der plastischen Verformung,
δ_h	mm	durchschnittliche Stärke des Schmierfilms bei der Werkstückstärke h,
η	kg. sec/mm²	dynamischer Viskositätsfaktor des Schmiermittels,
λ		Faktor zur Bezeichung der Größe der an der Grenze der »elastischen« Zone auftretenden Gleitspannungen,
ξ		Formfaktor.

2. Einleitung

Bei einer großen Anzahl plastischer Verformungsvorgänge hat man es in der Praxis mit einem ebenen Verformungszustand zu tun. Bei den Preß- und Walzverfahren, bei denen die sich ändernde Hauptabmessung in der Verformungsrichtung im Verhältnis zu der Abmessung, die sich nur wenig ändert (Breite), sehr klein ist, tritt eine ebene Verformung auf. Auch bei anderen Walz- und Preßverfahren muß eine ebene Verformung angenommen werden, wo dies nur eine grobe Annäherung ist. Dies aus dem Grunde, weil sich für diese Fälle keine geeigneten Berechnungsmethoden ausgebildet haben.

Der einfachste praktische Fall besteht in der Zusammendrückung von Stücken großer Breite zwischen parallelen rauhen Flächen. Auf Grund von praktischen Daten und Versuchen kann festgestellt werden, daß die Größe und Verteilung der auf die Druckplatten wirkenden Kraft von den Ausgangsmaßen des Stückes, von der Qualität des Materials, von den Eigenschaften der Druckflächen, vom Ausmaß der Verformung, von der Geschwindigkeit der Formwandlung und von der Verformungstemperatur abhängt. Im Innern des Werkstückes ist der Spannungszustand und der Verformungszustand inhomogen.

Über die einen Einfluß auf die Größe und Verteilung der Druckkraft ausübenden Faktoren kann auf Grund von Versuchen folgendes festgestellt werden: Materialgüte, das Ausmaß der Verformung und die Verformungsgeschwindigkeit bestimmen bei gegebener Temperatur die Verformungsfestigkeit.

Die Materialgüte und die Eigenschaften der Druckflächen definieren einen Reibungsfaktor, wodurch eine äußere Gleitspannung an den Druckflächen bestimmt werden kann.

Geometrisch ähnliche Stücke mit anderen Abmessungen verhalten sich unter gleichen Umständen ähnlich.

Demgemäß können die im gedrückten Werkstück sich abspielenden Prozesse wie folgt erklärt werden:

Im Werkstück bildet sich ein inhomogener Spannungszustand aus, der von den Ausgangsabmessungen und von den Gleitspannungen an der Oberfläche abhängt. Man gewinnt diesen Spannungszustand durch partikulare Lösung der partiellen Differentialgleichungen, die aus den Gleichgewichtsgleichungen

$$\frac{\partial \sigma_x}{\partial x} + \frac{\partial \tau_{xy}}{\partial y} = 0\,, \qquad \frac{\partial \sigma_y}{\partial y} + \frac{\partial \tau_{xy}}{\partial x} = 0 \tag{1.1}$$

und den Plastizitätsbedingungen (nach Huber und Mieses)

$$(\sigma_x - \sigma_y)^2 + 4\,\tau_{xy} = \frac{4}{3}\,k_f^2 \tag{1.2}$$

gebildet werden, wenn man die an den Berührungsflächen auftretenden Gleitspannungen kennt.

Bild 1 veranschaulicht die Lösung der Differentialgleichungen (1.1) und (1.2) in dem im Bild gezeigten Fall [1]. Das Bild zeigt, daß im plastischen Körper auch elastische Zonen entstehen, die aber frei von Gleitlinien sind. Bild 2 zeigt diesbezügliche Versuchsergebnisse von MEYER und NEHL [2].

Die Verformungsfestigkeit von Metallen bildet eine monoton veränderliche Funktion des Verformungsausmaßes und der Verformungsgeschwindigkeit, was also bedeutet, daß Metalle bei der Verformung härter werden.

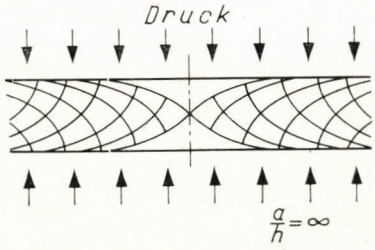

Bild 1

Wird das Maß der Höhenverringerung größer, dann verändert sich die Spannungsverteilung, u. zw. deshalb, weil durch die Inhomogenität der Spannung und der damit zusammenhängenden Verformung auch das Material seine Homogenität verliert. Das bedeutet, daß die Verformungsfestigkeit sich im Querschnitt von Punkt zu Punkt ändert. In dem nur elastisch verformten Teil wird sie ihren ursprünglichen Wert behalten, während sie im plastisch verformten Teil größer wird. Dementsprechend gehört zu den Gleichgewichtsgleichungen (1.1) die Plastizitätsbedingung (1.3)

$$(\sigma_x - \sigma_y)^2 + 4\,\tau_{xy}^2 = \frac{4}{3}\,(k_f(x, y))^2. \tag{1.3}$$

Für die angegebenen Differentialgleichungen sind bisher noch keine Lösungen gefunden worden, jedoch kann auf Grund von Versuchen festgestellt werden, daß sich eine solche Spannungsverteilung ausbildet, die eine Deformation der bisher nur wenig oder überhaupt nicht verformten Materialteile zur Folge hat.

Bild 3 zeigt eine versuchsmäßige Druckprobe. Bei den Versuchen wurde der in der Mitte entzweigeschnittene und an der geschnittenen Oberfläche mit einem Netz bezeichnete Prüfling so einer ebenen Verformung unterworfen, daß seine Maßänderung der Breite nach verhindert wurde. Das Bild zeigt, daß im Querschnitt zwei gesonderte Teile ausgebildet wurden. In dem im Bild mit II bezeichneten Teil war das Ausmaß der Verformung beinahe kon-

stant und stimmte mit dem Ausmaß der Verformung des Prüflings überein. In dem mit I bezeichneten Teil jedoch war das Ausmaß der Verformung kleiner. Man sieht außerdem, daß die Verformung an der Grenzlinie beider Zonen größer ist als die der Zone II.

3. Bestimmung der auf die Druckfläche wirkenden äußeren Gleitspannungen

KÖRBER und EICHINGER [3] haben festgestellt, daß das Material nur so weit auf der Druckfläche gleitet, bis die äußere Gleitspannung die kritische

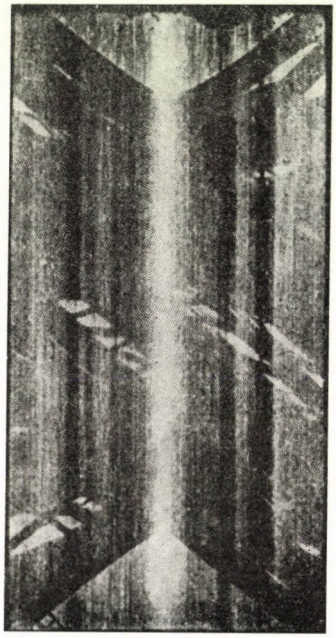

a)

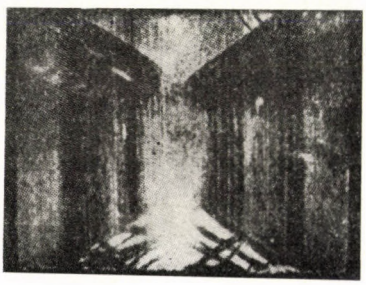

b)

Bild 2

Gleitspannung des Materials erreicht. Bei schlechten Oberflächenverhältnissen kann sich das Haften auch außerhalb der elastisch verformten Teile ausbilden [4]. Man kann also auf Grund von Bild 4 eine Gleitzone unterscheiden, in der das Material die Druckflächen entlang gleitet und eine Haftzone, in der sich das Material im Verhältnis zur Druckfläche nicht verschiebt.

In Übereinstimmung mit den Versuchsergebnissen müssen die Gleitspannungen in beiden Zonen gesondert bestimmt werden.

a) *Haftzone:*

Auf der Grenzfläche der ganzen Zone wirkt die konstante äußere Gleitspannung

$$\tau = \tau_{\max} = \frac{\psi k_f}{2}, \quad \text{wobei} \quad \psi = \frac{2}{\sqrt{3}}. \tag{2.1}$$

Eine größere Spannung kann nicht auftreten, weil die innere Materialverschiebung das verhindert.

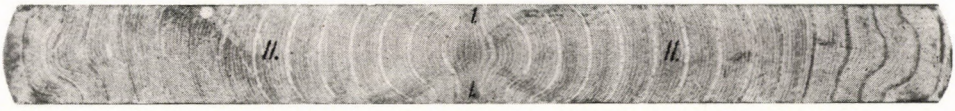

Bild 3

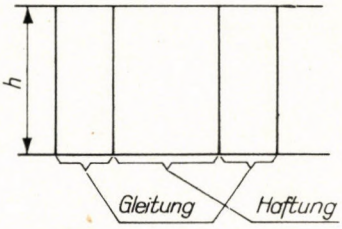

Bild 4

b) *Gleitspannung*:

Den Eigenschaften der Druckflächen entsprechend können zwei Fälle unterschieden werden.

Trockene Reibung

Auf diesen Fall kann das Coulomb'sche Reibungsgesetz als gültig vorausgesetzt werden.

$$\tau = \mu p. \tag{2.2}$$

Der trockene Reibungsfaktor hängt von der Oberflächenrauhheit der Druckplatten und des gedrückten Körpers ab, von der Oxydschicht an den berührenden Oberflächen bzw. von dem Adsorbtionsfilm, der Verformungsgeschwindigkeit, der Temperatur und dem Maß der Verformung. Zur Bestimmung des Reibungsfaktors können zwei grundlegend verschiedene Methoden angewendet werden. Bei der einen Methode wird der Verformungswiderstand gemessen und der Reibungsfaktor wird aus einem Ausdruck berechnet, der den Verformungswiderstand und den Reibungsfaktor enthält. Diese Methode hat den

Fehler, daß der Wert des Reibungsfaktors von dem zur Berechnung benutzten Ausdruck abhängt. Bei der anderen Methode wird der Prüfling gestaucht und gleichzeitig mit einer Dynamometervorrichtung in einer Richtung verschoben. Diese Methode mißt infolge der beim Stauchen auftretenden Formveränderung die Komponente der elementaren, in verschiedenen Richtungen wirkenden Reibungskräfte, die in die Verschiebungsrichtung fällt. Trotzdem steht diese Methode der Praxis näher, weil sie auf der Definition des Reibungsfaktors beruht. In Kenntnis der Mängel voriger Methoden soll eine Versuchsmethode vorgeschlagen werden, die voraussichtlich richtige Ergebnisse liefert und die von der Art des plastischen Verformungsvorganges unabhängig ist.

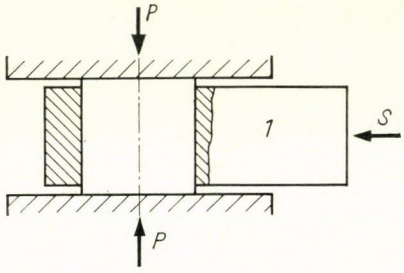

Bild 5

Bild 5 zeigt, daß der Prüfling in die Bohrung des mit 1 bezeichneten Stückes eingepaßt wird. Auf Grund der zur plastischen Verformung nötigen Kraft P tritt eine nahezu konstante Druckspannung auf. Die Oberflächenpunkte des Prüflings sind an ihrer Verschiebung behindert (die äußersten Punkte ausgenommen). Das mit 1 bezeichnete Stück wird mit einer Dynamometervorrichtung verschoben. Die zum Verschieben nötige Kraft S ist gleich der Summe der Reibungskräfte an der Oberfläche. Der Reibungsfaktor beträgt

$$\mu = \frac{S}{2P} \,. \tag{2.3}$$

Die Genauigkeit kann gesteigert werden, wenn der Spalt zwischen Einspannstück und Probefläche verringert und wenn der Durchmesser des Prüflings vergrößert wird.

Flüssigkeitsreibung

Soll während der plastischen Verformung an der Oberfläche eine Flüssigkeitsreibung auftreten, so muß zu Beginn der Verformung zwischen Druckfläche und Werkstück ein Schmiermittelfilm vorhanden sein, der die Belastung bis zum Beginn der plastischen Verformung trägt. Bei ebener Verformung

zwischen starren Parallelflächen beträgt die Belastung des Schmiermittelfilms [5]:

$$P = \frac{8\eta\, v_y\, a^3}{\delta^3}\,. \tag{2.4}$$

Die plastische Verformung beginnt dann, wenn die Belastung

$$P = 2a\,.1.k_k \tag{2.5}$$

beträgt. Aus den Gleichungen (2.4) und (2.5) ergibt sich für die mittlere Strecke des Schmiermittelfilms

$$\delta = \sqrt[3]{\frac{4\,\eta\, v_y \cdot a^2}{k_k}}\,. \tag{2.6}$$

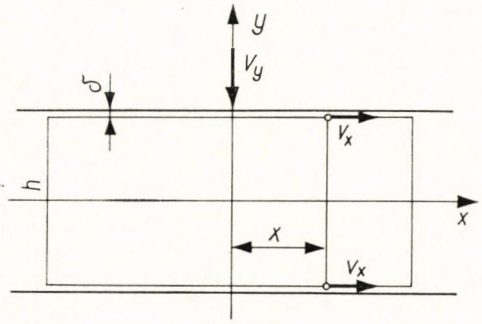

Bild 6

Ähnlich wie oben beträgt die nötige mittlere Stärke des Schmiermittelfilms bei endlichen Abmessungen des Werkstückes [5]:

$$\delta = \sqrt{\frac{10}{3} \cdot \frac{1}{1+\left(\frac{2\,a}{b}\right)^2} \cdot \frac{\eta v_y \cdot a^2}{k_k}}\,. \tag{2.7}$$

Der mit den Formeln (2.6) und (2.7) bestimmbare Schmiermittelfilm muß stärker sein als die Summe der Rauhheitswerte der Druckplatte des gedrückten Materials. Trifft dies nicht zu, dann tritt gemischte Reibung auf. Die Formeln ermöglichen auch die Bestimmung der Viskosität des für hydrodynamische Schmierung nötigen Schmiermittels.

Die Gleitspannung beträgt vom Beginn der plastischen Verformung bei kleinen Stärken, der Newton'schen Bezeichnung entsprechend

$$\tau = \eta\,\frac{\partial v_x}{\partial y} \cong \eta\,\frac{v_x}{\delta_h}\,. \tag{2.8}$$

Den Bedingungen der Gleichung (2.8) entsprechend verteilt sich die Geschwindigkeit in Richtung der y-Achse linear an Stelle der theoretischen parabolischen Verteilung. An Hand von Bild 6 kann die Geschwindigkeits-

verteilung in Richtung der x-Achse bestimmt werden. Aus der Konstanz des Rauminhaltes eines beliebigen Teiles des gedrückten Körpers bekommt man mit den Bezeichnungen des Bildes 6

$$v_x = x \frac{v_y}{h} . \tag{2.9}$$

Weil die anfängliche Schmiermittelmenge während des Pressens nur wenig verbraucht wird, verringert sich die mittlere Stärke des Schmiermittelfilmes durch die Vergrößerung von Δh. Auf Grund von Bild 7 kann man durch die Konstanz der Schmiermittelmenge folgende Gleichung aufstellen:

$$\delta_h = \delta \frac{h}{h_0} . \tag{2.10}$$

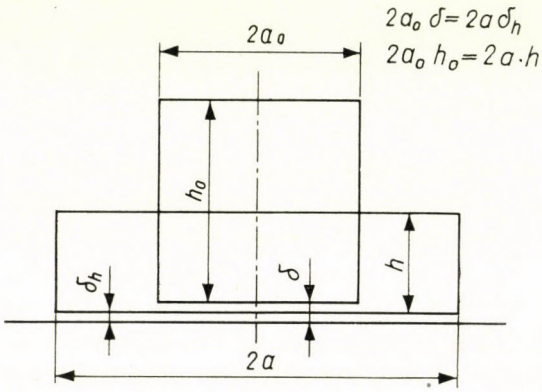

Bild 7

Auf Grund der Formeln (2.8), (2.9) und (2.10) beträgt die Gleitspannung au der Druckfläche des Materials, wenn noch zu Ende des Preßvorganges hydrodynamische Schmierung besteht:

$$\tau = \frac{\eta v_y h_0}{h^2 \delta} x . \tag{2.11}$$

4. Annähernde Bestimmung der auf die Druckfläche wirkenden Spannungsverteilung

Die Lösung der Gleichgewichtsgleichungen und der Plastizitätsbedingungen mit den im vorigen Abschnitt angegebenen Randbedingungen ist für die Praxis zu kompliziert. Um eine leichter zu behandelnde Formel zu gewinnen, sind entsprechende Vereinfachungen nötig. Eine bei den praktischen Berechnungen allgemein verbreitete Methode ist, daß man im Innern des gedrückten Stückes einen einachsigen Spannungszustand voraussetzt:

$$\tau_{xy} = 0 . \tag{3.1}$$

Damit können die Gleichgewichtsgleichungen und die Plastizitätsbedingungen in einfacher Form aufgeschrieben werden. Ihre Lösung führt zu einfachen Gleichungen, jedoch zeigen die Versuchs- und Meßergebnisse, daß diese Gleichungen in gewissen Fällen korrigiert werden müssen.

An Hand des Bildes 3 ist einzusehen, daß der Grund für solche Korrekturen in erster Linie aus der bedeutenden Abweichung der Spannungszustände in den Zonen I und II herrührt, weshalb in diesem Fall die Annahme eines einachsigen Spannungszustandes nur eine grobe Annäherung ist.

Dies erkannte zuerst UNSZKOV [4], indem er für die Zone I die Spannung besonders berechnete. Er rechnete auch in diesem Abschnitt mit der Annahme eines Spannungszustandes in einer Richtung, nahm aber an, daß die äußere Gleitspannung von der Grenze der Zone I bis zur Mitte des Stückes der Achse entlang linear bis auf Null abfiel. Mit dieser Annahme bekam er für die Druckverteilung Ergebnisse, die formell mit den Versuchsergebnissen übereinstimmten. Diese Methode wurde von GELEJI [1] weiterentwickelt, der in der ganzen Haftzone mit einer linearen, aber in der Mitte auf den Wert $\lambda \cdot \tau_{max}$ abfallenden Spannungsverteilung rechnet. Damit drückte er aus, daß diese Spannungsverteilung nur angenommen wurde, und es ist deshalb zweckmäßig, sie aus rechnungstechnischen Gründen in der einfachsten Form anzugeben.

Aus Bild 3 folgt, daß die Druckkraft nur für die Zone II berechnet wird, weil in diesem Teil ein Spannungszustand einheitlich angenommen werden kann, dessen Hauptrichtungen mit den Richtungen der Symmetrieachsen des Werkstückes zusammenfallen. Die auf die Grenzlinie der Zone II wirkende äußere Gleitspannung kann theoretisch begründet angegeben werden. Die Gleitspannung an der Grenzlinie der Zonen I und II ist die kritische Gleitspannung der dort befindlichen Materialteilchen. Die Härtung des Matetials ist der Grenzlinie entlang durch die größere Verformung, dem Maß der Höhenveränderung entsprechend größer als innerhalb der Zone II; demgemäß wird die an der Grenzlinie auftretende äußere Gleitspannung

$$\tau = \lambda \tau_{max}. \tag{3.2}$$

Die Berechnung wurde auf Grund von Bild 8 vorgenommen. Das beliebige Flächenelement in der Zone II beträgt $2ydx$. Das Gleichgewicht der in Richtung x auf das Flächenelement wirkenden Kräfte beträgt:

$$d\,(2y\,\sigma_3) = 2\,p \sin\varphi \frac{dx}{\cos\varphi} - 2\,\tau \cos\varphi \frac{dx}{\cos\varphi},$$

daraus:

$$\frac{d}{dx}(2 \cdot y \cdot \sigma_3) = 2\,p \tan\varphi - 2\,\tau. \tag{3.3}$$

In Richtung y:

$$\sigma_1\,dx = p \cos\varphi \frac{dx}{\cos\varphi} + \tau \sin\varphi \frac{dx}{\cos\varphi},$$

daraus:

$$p = \sigma_1 - \tau \tan \varphi . \tag{3.4}$$

Die Plastizitätsbedingung:

$$\sigma_1 - \sigma_3 = \psi k_f, \quad \text{wobei} \quad \psi = \frac{2}{\sqrt{3}} . \tag{3.5}$$

Berücksichtigt man aus den Formeln (3.3), (3.4) und (3.5), das ψk_f bei gegebener Höhenverminderung konstant ist und $dy/dx = \tan \varphi$:

$$\frac{d\sigma_1}{dx} = \psi k_f \frac{1}{y} \cdot \frac{dy}{dx} \cdot \frac{\tau}{y} \left[1 + \left(\frac{dy}{dx} \right)^2 \right] . \tag{3.6}$$

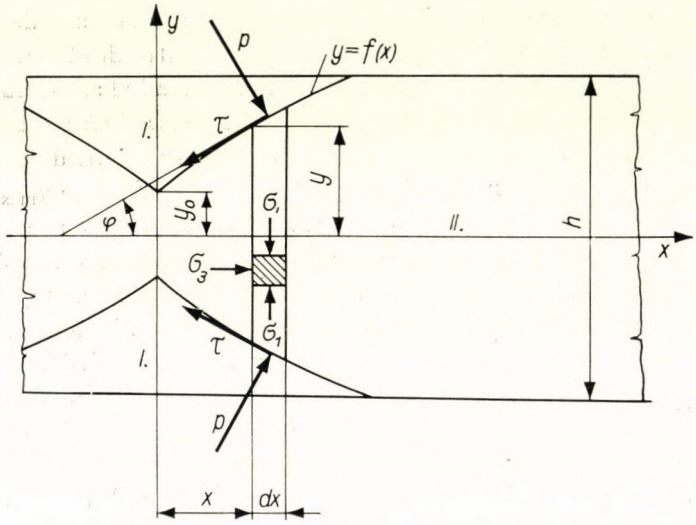

Bild 8

Die Differentialgleichung (3.6) ist bei den oben beschriebenen Bedingungen die Voraussetzung des plastischen Gleichgewichtes für eine beliebige äußere Gleitspannung mit beliebiger Grenzfläche, die an der Grenzfläche wirkt.

Auf Grund des im Abschnitt 2 Gesagten müssen die Fälle der Flüssigkeitsreibung und der trockenen Reibung gesondert behandelt werden.

Flüssigkeitsreibung

Weil $y = h/2$ ist, bekommt man aus der Differentialgleichung (3.6) mit Vernachlässigung der Stärke des Schmiermittelfilms neben der Höhe des Prüflings

$$\frac{d\sigma_1}{dx} = -\frac{2\tau}{h} . \tag{3.7}$$

Auf Grund der Gleichungen (3.7) und (2.11):

$$\frac{d\sigma_1}{dx} = -\frac{2\eta v_y h_0}{\delta h^3} x . \tag{3.8}$$

Werden die Veränderlichen getrennt und wird die Gleichung von x bis a integriert, wobei berücksichtigt wird, daß für $x = a$ $\sigma_1 = \psi k_f$ ist, so ist

$$\sigma_{1x} = \psi k_f + \frac{\eta v_y h_0}{\delta h^3} (a^2 - x^2) . \tag{3.9}$$

Trockenreibung

Bild 9 veranschaulicht den allgemeinsten Fall. Mit den Bezeichnungen des Bildes ist der Abschnitt II/a die gleitende Zone, der Abschnitt II/c ist die Haftungszone und Abschnitt II/d ist die elastische Zone die keine Formveränderung erleidet. Für alle drei Abschnitte muß die Spannungsverteilung besonders bestimmt werden, weil die Grenzflächen und die äußeren Gleitspannungen in allen drei Fällen verschieden sind.

Abschnitt II/a

Aus den Gleichungen (2.2) und (3.7) ist

$$\frac{d\sigma_1}{dx} = -\frac{2\mu}{h} \sigma_1 . \tag{3.10}$$

Nach der Trennung der Veränderlichen integriert man von x bis a und berücksichtigt, daß für $x = a$ $\sigma_1 = \psi k_f$ ist:

$$\sigma_{1x} = \psi k_f = \psi k_f \exp\left[\frac{2\mu}{h} (a - x)\right] . \tag{3.11}$$

Abschnitt II/c

Aus den Gleichungen (3.7) und (2.1):

$$\frac{d\sigma_1}{dx} = -\frac{\psi k_f}{h} . \tag{3.12}$$

Nach der Trennung der Veränderlichen wird die Gleichung von x bis c integriert und man berücksichtigt, daß σ_{1c} aus der Gleichung (3.12) berechnet werden kann:

$$\sigma_{1x} = \sigma_{1c} + \psi k_f \frac{c - x}{h} . \tag{3.13}$$

Abschnitt II/d

Die Lösung hängt von der Gleichung der Kurve $y = f(x)$ ab, die die elastische Zone begrenzt. Die Grenzkurve kann durch Versuche bzw. durch theoretische Berechnungen festgelegt werden; sie ist im allgemeinen eine Gerade und kann auch in abweichenden Fällen annäherungsweise als Gerade angenommen werden. Die Parameter der Geraden hängen wahrscheinlich von den geometrischen Abmessungen und von den äußeren Gleitspannungen des gedrückten Stückes ab. Die Grenzkurve kann allgemein durch folgende

Gleichung angegeben werden:

$$y = y_0 + x \tan \alpha. \tag{3.14}$$

Aus den Gleichungen (3.6) und (3.14):

$$\frac{d\sigma_1}{dx} = \psi k_f \frac{1}{y_0 + x \cdot \tan \alpha} \left[\tan \alpha - \frac{\lambda}{2} (1 + \tan^2 \alpha) \right]. \tag{3.15}$$

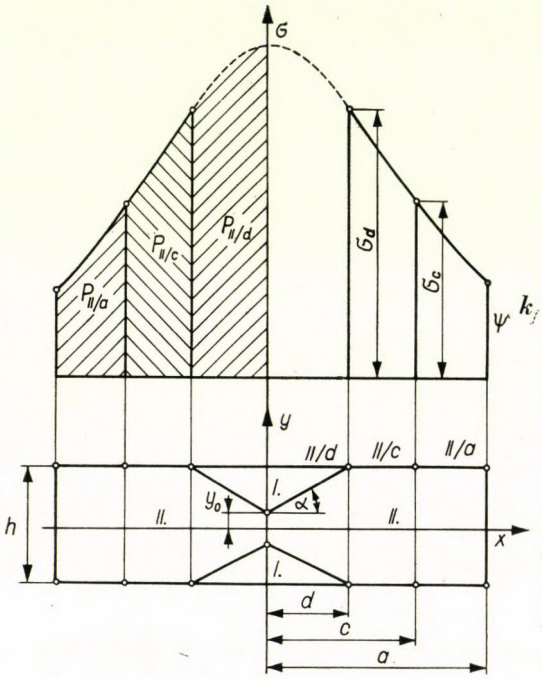

Bild 9

Nach der Trennung der Veränderlichen integriert man die Gleichung von x bis d und berücksichtigt, daß σ_{1d} aus der Gleichung (3.13) berechnet werden kann:

$$\sigma_{1x} = \sigma_{1d} + \psi k_f \left(1 - \lambda \frac{1 + \tan^2 \alpha}{2 \tan \alpha} \right) \ln \frac{2y}{h}. \tag{3.16}$$

5. Berechnung der auf die Druckfläche wirkenden Kraft

Es ist allgemein gebräuchlich, die Druckkraft aus dem Verformungswiderstand zu berechnen. Der Verformungswiderstand bedeutet eine durchschnittliche Spannung, mit der die auftretende Druckkraft berechnet werden kann:

$$P = 2a \cdot 1 \cdot k_k \tag{4.1}$$

Die Gesamtkraft ist auf Grund des vorigen Abschnittes bei trockener Reibung die Summe der drei Teilkräfte in den einzelnen Zonen. Abschnitt II/a: Unter Benutzung der Gleichung (3.11) bekommt man

$$P_{II/a} = \int_c^a \sigma_{1x}\, dx = \frac{h}{2\mu}\, \psi k_f \left[e^{\frac{2\mu}{h}(a-c)} - 1 \right]. \tag{4.2}$$

Abschnitt II/c: Mit Benutzung der Gleichung (3.11)

$$P_{II/c} = \int_d^a \sigma_{1x}\, dx = \left(\sigma_{1c} + c\, \frac{\psi k_f}{h} \right) (c - d) - \frac{\psi k_f}{h}\, \frac{c^2 - d^2}{2}\,. \tag{4.3}$$

Abschnitt II/d: Man berechnet durch Integrieren der Gleichung (3.16) die auf die Zone I wirkende Druckkraft, die aus Gleichgewichtsgründen der auf die Oberfläche wirkenden Druckkraft gleich ist:

$$P_{II/d} = \int_0^d \sigma_{1x}\, dx = \sigma_d \cdot d + \psi k_f \left(1 - \lambda\, \frac{1 + \tan^2 \alpha}{2 \tan \alpha} \right) \left[\frac{y_0}{\tan \alpha} \left(1 - \ln \frac{2 y_0}{h} \right) - \frac{h}{2 \tan \alpha} \right]. \tag{4.4}$$

Gleichung (4.4) ist bei $y_0 = 0$ nicht gültig. In diesem Fall wird die auf die Oberflächen wirkende Druckkraft mit Hilfe der Regel von L'Hospital bestimmt:

$$P_{II/d} = d \left[\sigma_d + \psi k_f \left(\lambda\, \frac{1 + \tan^2 \alpha}{2 \tan \alpha} - 1 \right) \right]. \tag{4.5}$$

Mit Hilfe der Gleichungen (4.2), (4.3) und (4.4) ist bei trockener Reibung ganz allgemein der Verformungswiderstand laut Gleichung (4.1):

$$k_k = \frac{1}{a} (P_{II/a} + P_{II/c} + P_{II/d})\,. \tag{4.6}$$

In den Gleichungen (4.2), (4.3) und (4.4) sind sowohl y_0 als auch $\tan \alpha$ unbekannt, ihre annäherungsweise Bestimmung kann mit Hilfe des Prinzips der minimalen Arbeit durchgeführt werden. Dieses Prinzip wird bei dem hier behandelten Verformungsfall annäherungsweise dann befreidigt, wenn sich die Grenze der elastischen Zone so ausbildet, daß die auftretenden Verformungskräfte die kleinsten sind [6, 7]. Für $a/h > 0{,}5$ kann man auf Grund von Versuchen voraussetzen, daß $y_0 = 0$ ist, womit die Bedingung für das kleinste Arbeitsminimum [6, 7] folgendermaßen lautet:

$$\frac{\partial P}{\partial (\tan \alpha)} = 0\,. \tag{4.7}$$

Der Einfachheit halber braucht man sich nur mit dem Fall zu beschäftigen, bei den sich auch die Haftzone ausbildet. In diesem Fall kann die Verformungskraft mit der Gleichung (4.6) bestimmt werden. Setzt man die Summe

der Gleichungen (4.2), (4.3), (4.4) und (4.5) in den Ausdruck (4.7) ein, so erhält man:

$$\frac{\partial}{\partial(\tan\alpha)}\left\{\sigma_{1c}\cdot c+\psi k_f\frac{(c-d)^2}{2h}+\psi k_f d\frac{c-d}{h}+\psi k_f d\left[\lambda\frac{1+\tan^2\alpha}{2\tan\alpha}-1\right]\right\}=0. \tag{4.8}$$

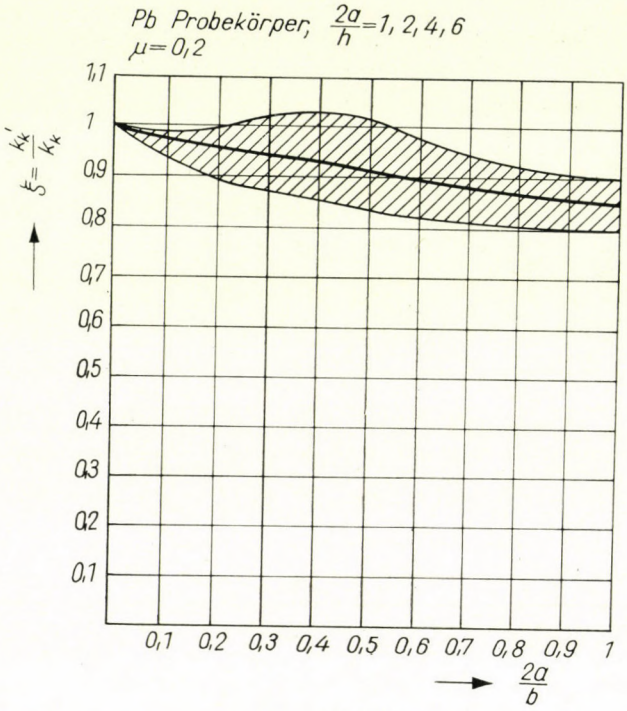

Bild 10

Setzt man nun in die Gleichung (4.8) für $d = h/(2\tan\alpha)$ ein und führt die partielle Differentiation durch, so bekommt man nach Kürzung für die Bedingung der minimalen Arbeit

$$\tan\alpha = \lambda - 0{,}5. \tag{4.9}$$

Gleichung (4.9) sagt aus, daß zu Beginn der plastischen Verformung ($\lambda = 1$) die elastische Zone von Geraden mit der Neigung $\alpha = 30°$ begrenzt wird. Dieser Wert wird durch die Versuche bestätigt, wie es Bild 3 zeigt.

Ist $\mu > 0{,}3$, so beeinflußt die Gleitzone in geringem Maß die auftretenden Kräfte, weshalb man annährungsweise der ganzen Druckfläche entlang mit Haften rechnen kann. Für den Verformungswiderstand bekommt man dann unter Benutzung der Gleichungen (4.3), (4.5), (4.6) und (4.9)

$$k_k = \psi k_f\left\{1+0{,}25\frac{a}{h}-\left[\frac{1}{2(\lambda-0{,}5)}+\frac{1}{8(\lambda-0{,}5)^2}-\frac{\lambda}{4}-\frac{\lambda}{4(\lambda-0{,}5)^2}\right]\frac{h}{a}\right\}. \tag{4.10}$$

Im Ausdruck (4.10) ändert sich λ als Funktion der spezifischen Verformung. Zu Beginn dieser Verformung ist $\lambda = 1$ und damit wird der Verformungswiderstand:

$$k_k = \psi k_f \left(1 + 0{,}25 \frac{a}{h} - 0{,}25 \frac{h}{a}\right). \tag{4.11}$$

Der Wert des mit der Formel (4.11) bestimmten Verformungswiderstandes zeigt gute Übereinstimmung mit den Versuchsergebnissen von O. Georg [8], deshalb ergibt die Rechnung mit den Gleichungen (4.10) und (4.11) im Falle $\mu > 0{,}3$ und $a/h > 1$ richtige Ergebnisse.

Beim Quellen prismatischer Körper mit endlichen Abmessungen ist die Annahme ebener Verformung nur eine grobe Annäherung. Berücksichtigt man die räumliche Verformung, so könnte man die Druckspannung durch Summieren der Spannungsvergrößerungen von Punkt zu Punkt bestimmen, wenn die Richtungen der Materialverschiebung bekannt sind. Es empfiehlt sich deshalb, bei der Berechnung vom ebenen Formveränderungszustand auszugehen. Auf Grund ähnlicher Berechnungen kann man folgendes voraussetzen:

$$k'_k = \xi\, k_k\,. \tag{4.7}$$

Der in der Gleichung (4.7) vorkommende Faktor ξ hängt von dem Verhältnis der Breite zur Länge des Werkstückes ab, wird aber auch in kleinerem Maße vom Reibungsfaktor und vom Ausmaß der Verformung beeinflußt.

Auf Grund von Untersuchungen von Prüflingen aus Blei wurde die im Bild 10 gezeigte Kurve konstruiert. Im Laufe der Untersuchungen wurde neben dem Verhältnis a/h auch das Verhältnis a/b geändert.

Im Abschnitt 4 wurde beschrieben, wie die beim plastischen Drücken prismatischer Körper auftretenden Kräfte berechnet werden können, während bei zylindrischen Körpern die beim Druck auftretenden Kräfte unter Verwendung der Gleichungen für ebene Verformung sinngemäß bestimmt werden können.

Das in dieser Arbeit vorgeschlagene Berechnungsverfahren muß noch ergänzt werden. Die konkrete Bestimmung des Oberflächenreibungsfaktors erfordert noch weitere Forschungsarbeit. Die Bestimmung der Grenzlinie des Teiles, dessen Verformung behindert ist sowie die Größe der an der Grenzlinie auftretenden Gleitspannungen und ihre Abhängigkeit vom Maß der Verformung erfordern weitere Forschungsarbeiten. Schließlich muß noch der Verformungswiderstand untersucht werden, der beim Quellen prismatischer Körper auftritt sowie sein Zusammenhang mit dem Verformungswiderstand bei ebener Verformung muß geklärt werden.

SCHRIFTTUM

1. GELEJI, A.: Bildsame Formung der Metalle in Rechnung und Versuch.
2. MEYER, H. und NEHL, F.: Die grundlegenden Vorgänge der bildsamen Verformung. *Stahl und Eisen* (1925), 1961—1962.
3. KÖRBER, F. und EICHINGER, A.: Die Grundlagen der bildsamen Verformung. *Mitteilungen des Kaiser Wilhelm Institutes* (1940), 57—80.
4. УНКСОВ: Новые исследование в области кузнечной технологии. Москва 1950.
5. CÉGI, J.: Siklóscsapágy kézikönyv (Gleitlager-Handbuch), Budapest 1953.
6. TÓTH L: A süllyesztékes kovácsolás esetén fellépő maximális erő meghatározása. (Bestimmung der beim Gesenkschmieden auftretenden Höchstkraft) *Acta Technica Hung.* 1965 (Erscheint demnächst).
7. JOHSON, W.; MELLOR, P. B.: Plasticity for Mechanical Engineers. D. von Norstrand Company L. T. D. 1962.
2. GEORG, O.: Der Arbeitsbedarf beim Stauchem dünner Ronden. *Schmidetechnische Mitteilungen* 1964, Heft 4.

CALCULATION OF THE DEFORMATION RESISTANCE OF PRISMATIC BODIES COMPRESSED BY PARALLEL PLATES

L. TÓTH

SUMMARY

The paper deals with the approximate calculation of the forces needed for the plastic compression of material by parallel plates. Cases of approximate solution for the equations, giving the exact solution, are discussed, as well as the influence of the qualities of the surfaces. For the determination of the coefficient of friction author suggests a new experimental method, and for the computation of the force he proposes a new approximate method for plane deformation, as well as for the swelling of bodies having finite dimensions.

LE CALCUL DE LA RÉSISTANCE A LA DÉFORMATION DES CORPS PRISMATIQUES COMPRIMÉS PAR PLAQUES PARALLÈLES

L. TÓTH

RÉSUMÉ

L'auteur étudie le calcul approché des forces nécessaires pour la compression plastique d'une matière se trouvant entre des plaques parallèles. Il traite des cas de solution approchée des équations donnant la solution exacte, ainsi que de l'influence des caractéristiques des surfaces. Pour la détermination du coefficient de friction, une nouvelle méthode expérimentale est proposée par l'auteur qui préconise, d'autre part, une nouvelle méthode approchée pour le calcul de la force, valable en cas de déformation plane aussi bien que pour le gonflement des corps finis.

РАСЧЕТ СОПРОТИВЛЕНИЯ ДЕФОРМАЦИИ ПРИ СЖАТИИ ПРИЗМАТИЧЕСКИХ ТЕЛ МЕЖДУ ПАРАЛЛЕЛЬНЫМИ ПЛОСКОСТЯМИ

Л. ТОТ

РЕЗЮМЕ

Работа занимается приближенным расчетом сил, необходимых для пластичного сжатия материала, размещенного между параллельными плоскостями. Рассматриваются случаи приближенных решений уравнений, служащих для точного решения. Исследуется действие свойств поверхности. Для определения коэффициента трения предлагается новый опытный метод. Для расчета силы как в случае плоской деформации, так и расковки тел с конечными размерами автор предлагает новый приближенный метод.

THE PROBLEM OF THE QUADRATIC WEIR

PROPORTIONAL FLOW MEASUREMENT WITHOUT DISTURBANCE OF THE WATERSURFACE

O. HASZPRA

RESEARCH INSTITUTE FOR WATER RESOURCES, BUDAPEST

[Manuscript received March 19, 1963]

A wide variety of methods has so far been developed for measuring flow volumes (i.e., for integrating the discharge passing per unit time over a given period). Highly attractive from among these because of its inherent simplicity is the *proportionate method of flow measurement* in a by-pass [1], which can be applied directly in clear water, while in polluted ones proper filtration must be resorted to, i.e., a suitable filter equipment must be used.

The prerequisite for the applicability of the proportionate measurement of flow is that the differential head across, and actuating, the meter should be in an approximately quadratic relationship with the discharge conveyed in the main branch. The flow passing through the by-pass is in this case over the entire discharge range, i.e., regardless of the magnitude of discharge, proportionate to the total flow. In other words, the total flow volume for a given period can be obtained from the flow volume passing through the by-pass during the same period, and recorded by the meter, simply by multiplying the latter value with a proportionality coefficient. Meters having the dial scaled to read the total flow volume directly are also conceivable.

Devices creating a differential head, which is proportionate to the square of the discharge, *in a closed pipeline*, or by means of a *closed section* installed in an open channel, are known in large numbers, in fact the number of possible alternatives is, in principle, infinitely large. Where it is essential not to disturb the free watersurface of an open channel by the installation of a closed section — e.g., because of the desire to ensure unobstructed passage for floating debris — the erection of a so-called *quadratic weir* may offer the necessary solution.

With the notations according to Fig. 1 the shape of the quadratic weir is governed by the integral equation:

$$Q = 2\mu \sqrt{2g} \int_0^h f(x) \sqrt{h - x}\, dx = B \sqrt{h} \tag{1}$$

wherein Q is the discharge, μ is the discharge coefficient, which is assumed to be constant, g is gravitational acceleration, $f(x)$ is the half-width of the

weir at height x above the lower edge of the weir, h is the weir head pertaining to the discharge Q and B is a proportionality coefficient.

The method of installation of the proportional meter is revealed by Fig. 1 as well as by Fig. 2, the latter illustrating the operating principle of the system more clearly. As is to be seen, the by-pass is branched off somewhere from below the prevailing headwater level, and the flow passing through it is

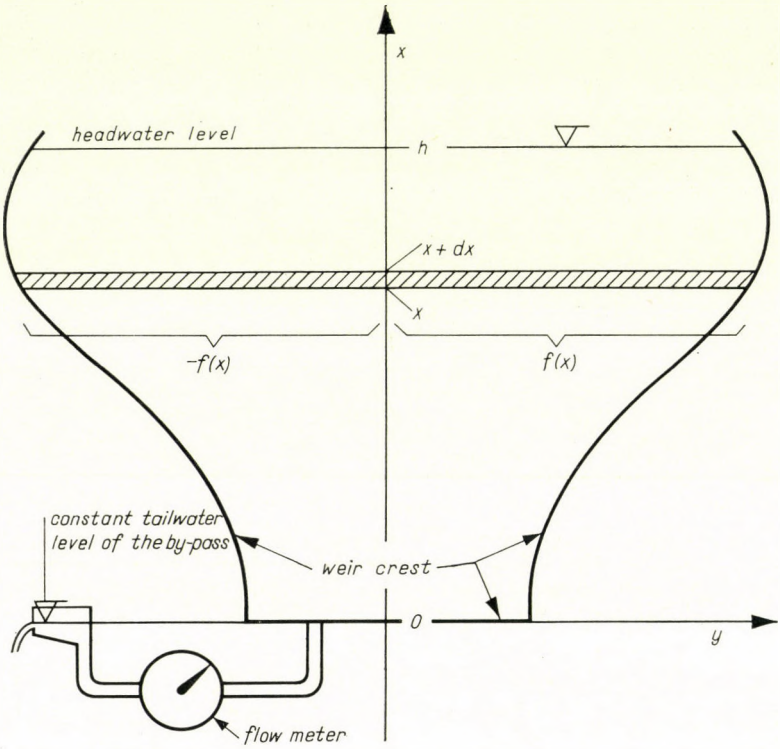

Fig. 1. Notations used in deriving the shape of the quadratic weir

returned into the main channel over a free discharge, with its watersurface flush with the lower edge of the weir. Consequently the differential head actuating the meter is the prevailing weir head, which, being in a quadratic relationship with the discharge, is suitable for operating the proportionate meter. As the resistance of the latter is also proportionate to the second power of the discharge passing through it, the ratio of the two discharges will remain constant.

A few solutions of the integral equation (1), among these two practically feasible solutions, could be derived earlier and mention has been made of these results in earlier publications [1, 2]. The general solution of the equation is due to Mr. E. Dux.

A modified version of the general solution is presented in the following, and the two practical solutions referred to above are derived therefrom.

The solution is preferably written in the following form:

$$f(x) = \frac{B\sqrt{h}}{2\mu\sqrt{2g}\sqrt{h-x}}\, g(x), \tag{2}$$

where besides the notations introduced previously, $g(x)$ is an arbitrary function, the definite integral of which in the $(0, h)$ interval is equal to unity, i.e.,

$$\int_0^h g(x)\,dx = 1. \tag{3}$$

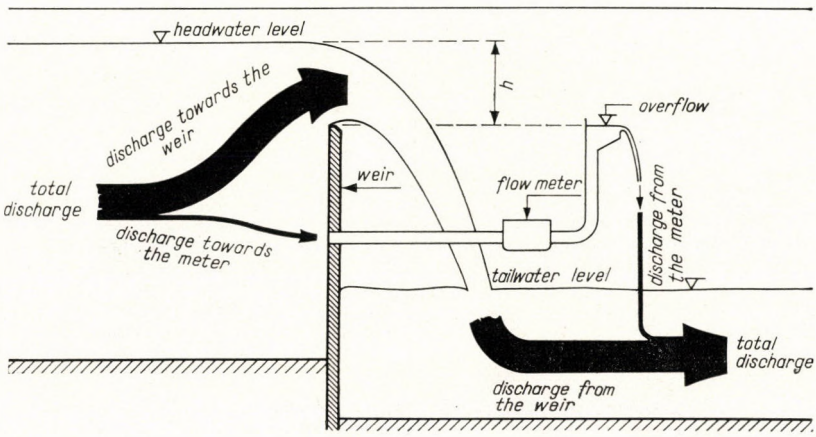

Fig. 2. Diagrammatical arrangement of the quadratic weir and the flow meter on the profile of the watercourse

In fact, on substituting Eq. (2) into Eq. (1) we obtain

$$2\mu\sqrt{2g}\int_0^h \frac{B\sqrt{h}}{2\mu\sqrt{2g}}\, g(x)\,dx = B\sqrt{h}\int_0^h g(x)\,dx. \tag{4}$$

With Eq. (3) this becomes

$$Q = B\sqrt{h}\int_0^h g(x)\,dx = B\sqrt{h}, \tag{5}$$

i.e., the specified right-hand side of Eq. (1) is actually obtained.

Inasmuch as there is an infinitely large number of $g(x)$ functions, the integral of which in the $(0, h)$ interval is unity, an infinitely large number of solutions can be obtained for Eq. (1).

In the following it is proposed to develop several functions and to examine the practical applicability of the solutions produced.

Case 1.

$$g(x) = \frac{1}{c} \quad \text{for } 0 \leq x \leq c, \tag{6}$$

$$g(x) = 0, \quad \text{for } c < x \leq h. \tag{7}$$

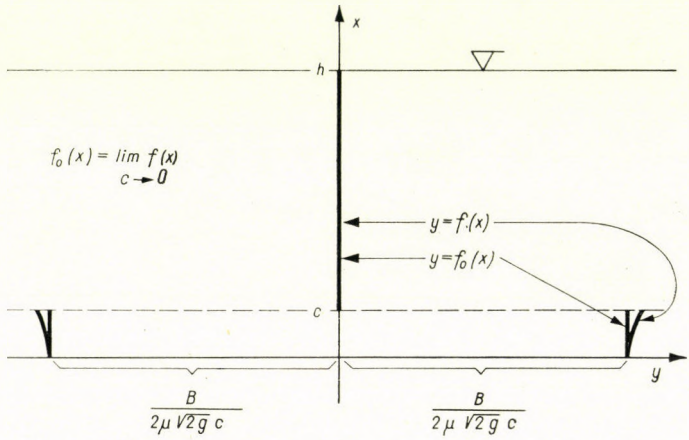

Fig. 3. One of the feasible shapes of the quadratic weir

On substitution into Eq. (3),

$$\int_0^h g(x)\,dx = \int_0^c \frac{1}{c}\,dx + \int_0^h 0\;dx = 1 + 0 = 1\,.$$

The equation of the weir crest is thus according to Eq. (2)

$$f(x) = \frac{B\sqrt{h}}{2\mu\sqrt{2g}\,c\sqrt{h-x}}\,, \quad \text{for } 0 \leq x \leq c\,, \tag{8}$$

respectively,

$$f(x) = 0, \qquad \text{for} \qquad c < x \leq h. \tag{9}$$

As is to be perceived from Eq. (8) this crest shape depends on the prevailing weir head h, and thus cannot be used in practice. Furthermore, the configuration obtained is an *orifice* rather than a weir.

The limit value of this solution may perhaps also prove interesting for practical purposes. Let the limit value $f(x)$ be denoted by $f_0(x)$, for $c \to 0$.

$$f_0(x) = \lim_{c \to 0} \frac{B\sqrt{h}}{2\mu\sqrt{2g}\, c\sqrt{h-x}} = \lim_{c \to 0} \frac{B}{2\mu\sqrt{2g}\, c}, \quad \text{for} \quad 0 \leq x \leq c; \tag{10}$$

$$f_0(x) = 0, \qquad \text{for} \qquad c < x \leq h. \tag{11}$$

The first term of $f_0(x)$ tends obviously toward infinity as c tends towards 0, but becomes independent of h. The "weir" is thus essentially an infinitely wide, infinitely low orifice, through which water flows under obeyance to the law relating to orifices, i.e., in a manner characterized by the expression $Q = B\sqrt{h}$.

This "weir" configuration is an interesting marginal condition of the familiar series of weir configurations (Fig. 4) described by the equation

$$Q = ah^n \tag{12}$$

and pertaining to different n values. Among these the parabolic weir obeying the equation $Q = ah^2$ reveals no particular features whatsoever and is sufficiently described by the name "parabolic". The term *quadratic* can thus justly be appropriated for weirs following the equation $Q = B\sqrt{h}$.

The "weir"-type derived can be realized in practice in the form of a long horizontal orifice, the height c of which is insignificant relative to the lowest weir head occurring.

Case 2.

$$g(x) = \frac{n+1}{h^{n+1}}(h-x)^n. \tag{13}$$

The expression itself represents an infinitely large number of solutions. The value of n is arbitrary, with the constraint that $n \neq -1$, in which case the function $g(x)$ and together with it its definite integral become zero. Indeed, for other n values, in keeping with Eq. (3)

$$\int_0^h g(x)\,dx = \int_0^h \frac{n+1}{h^{n+1}}(h-x)^n\,dx = \frac{n+1}{h^{n+1}} \left| \frac{(h-x)^{n+1}}{-(n+1)} \right|_0^h = \tag{14}$$

$$= \frac{n+1}{h^{n+1}} \cdot \frac{-h^{n+1}}{-(n+1)} = 1.$$

The shape of the weir crest is obtained by substitution into Eq. (2) as

$$f(x) = \frac{B\sqrt{h}}{2\mu\sqrt{2g}\sqrt{h-x}} \cdot \frac{n+1}{h^{n+1}}(h-x)^n = \\ = \frac{B(n+1)}{2\mu\sqrt{2g}} \cdot \frac{(h-x)^{n-1/2}}{h^{n+1/2}} . \tag{15}$$

For any given constant n value a different crest shape by this set of solutions is obtained for every h value. Thus any practical realization would

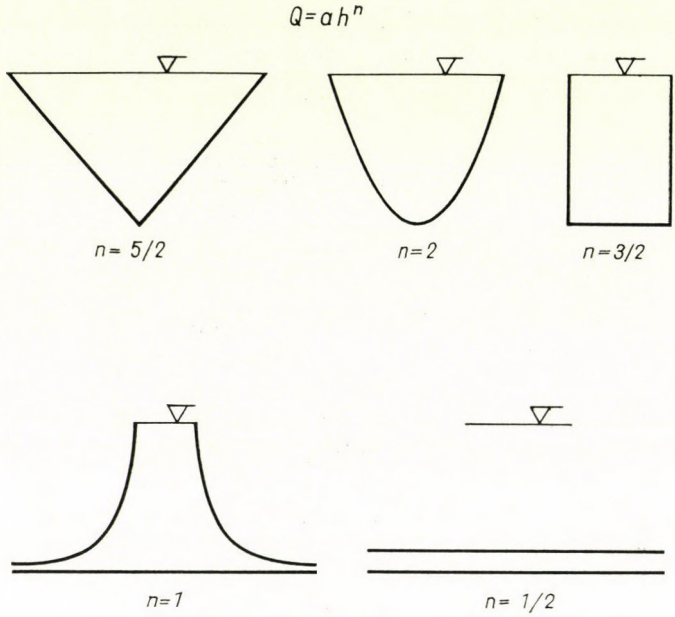

Fig. 4. Familiar weir shapes

be senseless, even almost impossible. The solution pertaining to

$$n = -\frac{1}{2}$$

is an exception to this:

$$f(x) = \frac{B/2}{2\mu\sqrt{2g}} \cdot \frac{(h-x)^{-1}}{h^0} = \frac{B}{4\mu\sqrt{2h}} \cdot \frac{1}{h-x} . \tag{16}$$

The weir crest specified by the equation is one having a constant shape, but of a position which changes with the weir head. Even this variation is

a very simple one, inasmuch as the horizontal asymptote of the hyperbola is always at the height h, i.e., it is bound to the headwater level and moves together with the watersurface. For this reason, with the y axis of the coordinate system coinciding with the headwater level, and with the x axis pointing downward, Eq. (16) assumes the following simplified form (Fig. 5):

$$f(x) = \frac{B}{4\mu\sqrt{2gx}}\,. \tag{17}$$

Attached to suitable floats this weir crest could be used in practical applications as well. A further problem is due to its infinite horizontal extension.

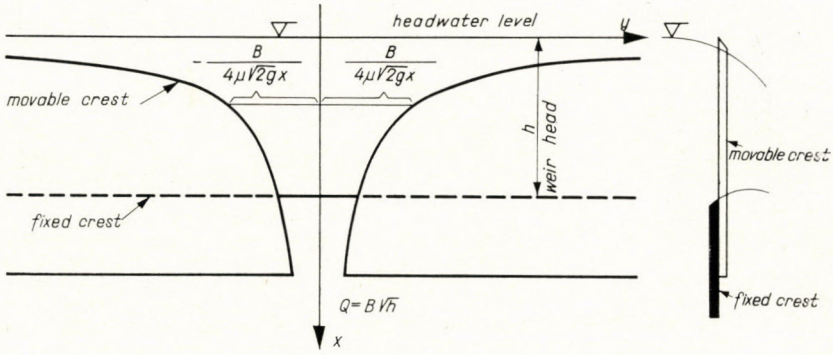

Fig. 5. Hyperbolical, movable quadratic weir

This difficulty can, however, be readily overcome by assigning a certain finite value, rather than zero, to the smallest discharge to be measured. The feasibility of this will be perceived if iti s remembered that the sensitivity of the meter applied is also limited. In fact, there is in practice a certain minimum differential head below which the meter remains inoperative, or fails to indicate the accurate value. This value, expressed as height of water column is of the order of 1—2 cm. The top 1—2 cm high section of the hyperbola may thus safely be replaced by a rectangular weir crest configuration, of which not only the height, but also the discharge is identical with the upper section of the hyperbola. Using the notations according to Fig. 6 the width b of the rectangular section can be calculated from the minimum weir head, which, in turn is determined by the sensitivity of the meter, or other considerations.

The discharge through the upper section of the hyperbolical weir crest is

$$Q_{\min} = B\sqrt{h_{\min}} \tag{18}$$

and must be equal to the discharge passing the rectangular section:

$$Q_{\min} = 2\,\mu\,\sqrt{2g}\,b \int_0^{h_{\min}} \sqrt{h_{\min} - x}\,dx = \frac{4}{3}\,\mu\,\sqrt{2g}\,b\,h_{\min}^{3/2}. \tag{19}$$

The width b of the rectangular section is obtained by combining Eqs. (18) and (19):

$$b = \frac{3\,B}{4\mu\,\sqrt{2g}\,h_{\min}}, \tag{20}$$

or, expressed in terms of $Q_{\min}$

$$b = \frac{3\,B^3}{4\mu\,\sqrt{2g}\,Q_{\min}^2}. \tag{21}$$

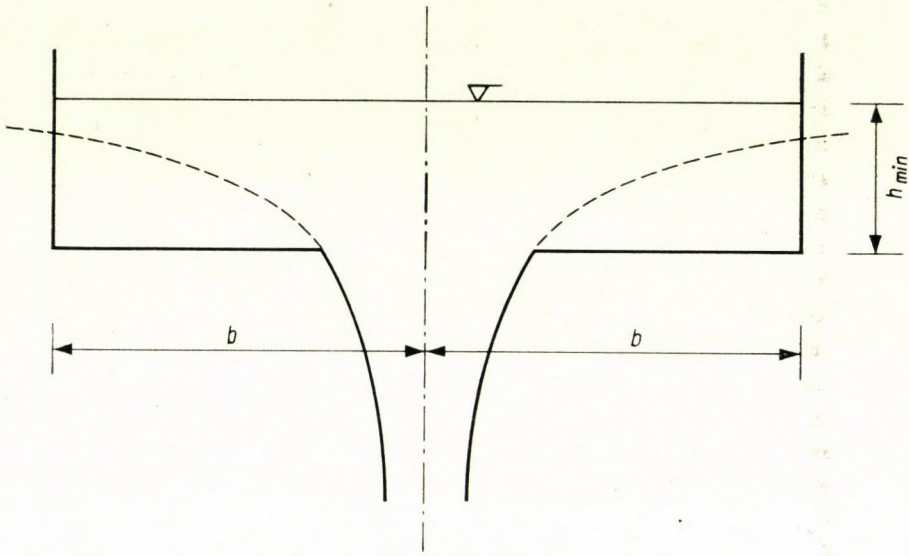

Fig. 6. Movable hyperbolical weir combined with a finite measuring range

The maximum horizontal dimension of the finite hyperbolical weir can be reduced further by realizing it with a cylindrical rather than a plane form. The circumference of the cylinder is, in principle, equal to $2b$. The overfall section is preferably composed of two, or more uniformly spaced hyperbolical slots, so as to make the resultant of the lateral thrust on the cylinder equal to zero in order to prevent the cylinder from jamming. A diagrammatical drawing of this solution in orthogonal axonometry, and with a watersurface idealized to a certain extent is given in Fig. 7. The weir shield is carried by floats, which have been omitted for the sake of clarity. Instead of a cylindrical surface prismatic surfaces composed of planes can, naturally, also be used.

3. The set of functions

$$g(x) = \frac{n+1}{h^{n+1}} \tag{22}$$

yields in a manner similar to the former, and with the condition $n \neq 1$, an infinite number of solutions. However, since the shape of the weir crest remains always a function of h, this solution is of no practical significance. Solutions of likewise purely mathematical character can be produced in unlimited quantity. Any function having a finite integral over any arbitrary

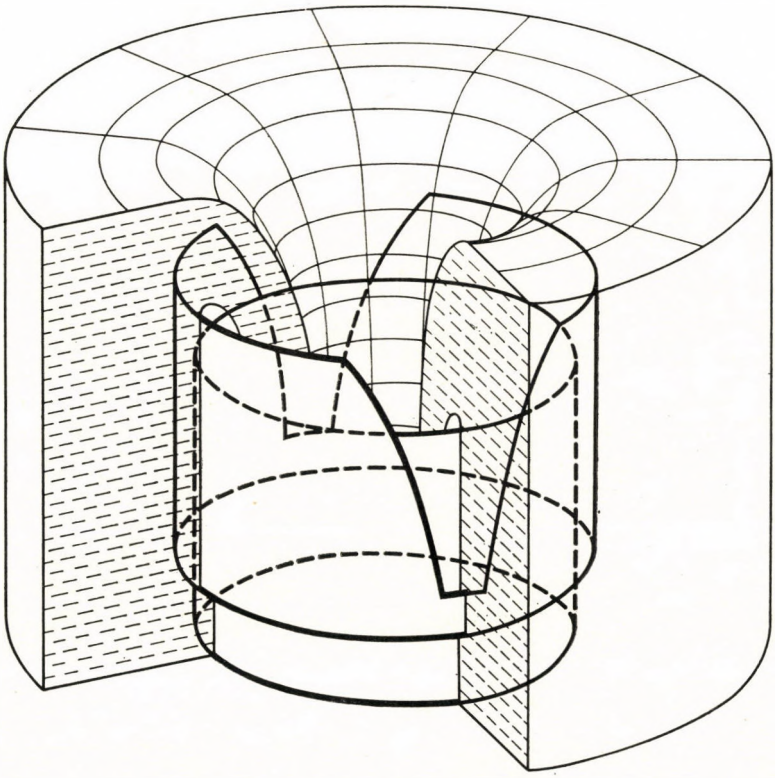

Fig. 7. Hyperbolical weir with a finite measuring range in cylindrical arrangement

section x_1, x_2 can be transformed by suitable distortions and translations along the two coordinate axes into a $g(x)$ function satisfying the condition formulated in Eq. (3). It should be pointed out by way of an example that the integral of the trigonometric function $y = \sin x$ over the section $(0, \pi/2)$ is equal to unity. The function

$$y = \frac{\pi}{2h} \sin \frac{\pi x}{2h}$$

may indeed be regarded as $g(x)$, because its definite integral between 0 and h is unity.

Example. Let us determine the dimensions of a quadratic weir having the following design criteria: $Q_{max} = 0{,}1$ m³/sec, $h_{max} = 1$ m, $\mu = 0{,}6$, $Q_{min} = 0{,}02$ m³/sec, and calculated therefrom $h_{min} = 0{,}04$ m.

Coefficient B from Eq. (1) is obtained as:

$$B = \frac{Q}{\sqrt{h}} = \frac{0{,}1}{1} = 0{,}1\,.$$

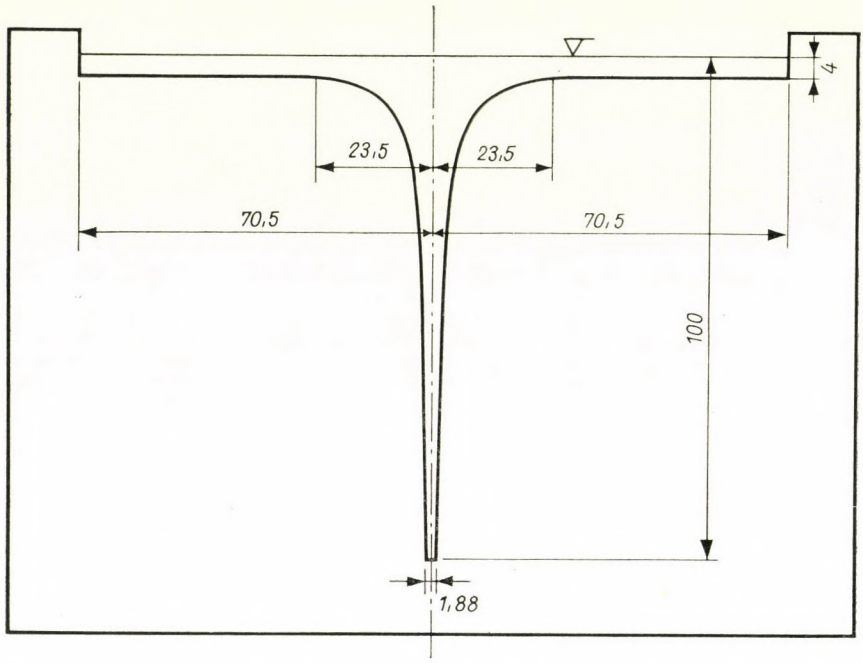

Fig. 8. Numerical example

The width b of the upper rectangular section is from Eq. (19)

$$b = \frac{3 \cdot 0{,}1}{4 \cdot 0{,}6 \cdot 4{,}43 \cdot 0{,}04} = 0{,}705\,\mathrm{m}\,,$$

The equation describing the shape of the hyperbolical section is according to Eq. (17)

$$f(x) = \frac{0{,}1}{4 \cdot 0{,}6 \cdot 4{,}43\,x} \cdot \frac{0{,}0094}{x}\,.$$

A drawing to scale of the weir is given in Fig. 8.

It may be found more practicable to realize the above weir in a cylindrical form similar to that shown in Fig. 7. The diameter of the cylinder is, provided that the overfalling nappe is not interrupted by ribs:

$$d = \frac{2 \cdot 0{,}705}{\pi} = 0{,}449\, m\,.$$

A general theoretical solution has been presented above for the shape of the quadratic weir, and two configurations of potential practical significance have also been developed.

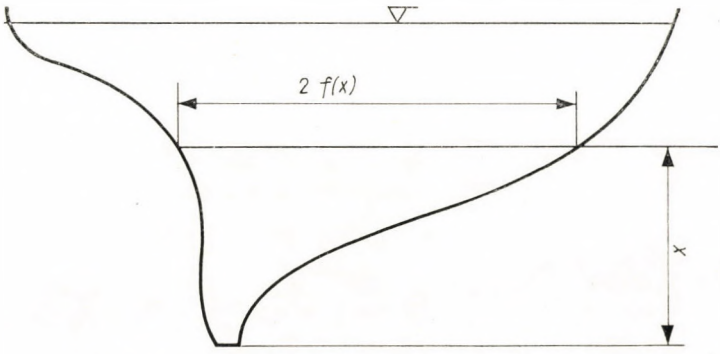

Fig. 9. Notations used for the asymmetrical weir

A symmetrical weir shape has been tacitly assumed in the derivation, but naturally, other arrangements may equally be adopted. In the simplified derivations commonly used in hydraulics the role played by the symmetry of the weir opening is neglected, the only terms entering into the calculations being the width of the opening above the lowest point of the crest, respectively below the headwater level. Within these limits the depth where width is measured is arbitrary. In the present case this is $2f(x)$. The derivations apply to asymmetrical weir openings as well, but then $f(x)$ must be defined and interpreted according to Fig. 9.

REFERENCES

1. Haszpra, O.: The Theory and Applications of Proportionate Flow Measurement (in Hungarian). *VízügyiKözlemények* (Hydraulic Review), No. 4, (1954).
2. Haszpra, O.: Scale Model Tests Serving the Development of Irrigation (in Hungarian). Paper presented at the Symposium on Model Tests in Water Resources Development, held by the Hungarian Academy of Sciences on the 24th October, 1962. *Az MTA Műszaki Tudományok Osztályának Közleményei* **33** (1964).

DAS PROBLEM DES QUADRATISCHEN ÜBERFALLS. WASSERMENGENMESSUNG OHNE UNTERBRECHUNG DER FREIEN OBERFLÄCHE

O. HASZPRA

ZUSAMMENFASSUNG

Die Arbeit beschäftigt sich mit der Berechnung einer Form des Überfalls, dessen Wasserschluckfähigkeit der Gleichung $Q = B\sqrt{h}$ genügt. Diese Form des Überfalls ermöglicht die Verwendung einer mit ihm parallelgeschalteten Nebenstrom-Wasseruhr, d. h. die einfache Summierung der über den Überfall strömenden Wassermenge während einer beliebigen Zeit.

LE PROBLÈME DU DÉVERSOIR QUADRATIQUE. MESURE DE DÉBIT PAR COURANT DÉRIVÉ, SANS RUPTURE DE LA SURFACE LIBRE

O. HASZPRA

RÉSUMÉ

L'auteur se propose la détermination d'une forme de déversoir dont la capacité satisfait à l'équation $Q = B\sqrt{h}$. Cette forme de déversoir permet l'application d'un débitmètre à dérivation monté parallèlement au déversoir, c'est-à-dire la totalisation simple du débit passant par ce dernier pendant une période donnée.

ПРОБЛЕМА КВАДРАТИЧНОГО ВОДОСЛИВА. ЗАМЕР КОЛИЧЕСТВА ВОДЫ ПОБОЧНОГО ПОТОКА БЕЗ НАРУШЕНИЯ СВОБОДНОЙ ПОВЕРХНОСТИ

О. ХАСПРА

РЕЗЮМЕ

Исследование занимается определением такой конфигурации водослива, водопропускная способность которого удовлетворяла бы уравнению $Q = B\sqrt{h}$. Такая конфигурация водослива позволяет применить водомер, установленный параллельно водосливу, то есть осуществить простое суммирование потока воды, протекающей по водосливу за любой промежуток времени. Конфигурация водослива по обозначениям рис. 1 и 2 определяется интегральным уравнением (1). Решение имеет вид (2), в котором содержится функция $f(x)$, которая должна удовлетворить условию (3). Таким образом, получается бесконечное множество решений.

STRUCTURAL ANALYSIS OF BUILDINGS WITH VERTICAL, THIN WALLED LOAD CARRYING ELEMENTS, AFFECTED BY HORIZONTAL FORCES

S. KALISZKY

CANDIDATE OF TECHNICAL SCIENCES
TECHNICAL UNIVERSITY OF BUILDING AND TRANSPORT ENGINEERING, BUDAPEST

[Manuscript received April 23, 1963]

The paper deals with the structural analysis of buildings the vertical load carrying elements of which are thin walled members. The horizontal arrangement, thickness and occasional joints of the vertical walls of the building in question, furthermore, the distribution of the acting horizontal forces are storeywise identical, but otherwise quite optional. It is assumed that the floors in their own plane constitute infinitely rigid disks, while perpendicularly to same they are perfectly flexible. Based on the above assumption and utilizing the equations of equilibrium, the distribution of external forces affecting the building, among the wall elements constituted by the vertical walls, can be determined. In the computation the effect exerted by the openings in the wall can also be taken approximately into consideration. After the distribution of the load with the aid of formulae (7), (9), (13) and (15), the individual wall elements can be regarded as being vertical cantilevers independent of each other, the dimensioning of which can be performed by using the methods of the elementary Theory of the Strength of Materials.

1. Introduction

When constructing living houses and public buildings, recently framed structures are ever more frequently replaced by thin walled load carrying elements simply called *walls* in the following. It is characteristic that these walls, in addition to the task of space bordering, completely fulfill that of load carrying too.

Related to the structural analysis of framed structures a great variety of generally valid, accurate or approximate calculative methods have been worked out, but no generally valid method can be found, with the aid of which the play of forces developing in an optionally arranged and loaded building, having load carrying walls, could be determined. The studies related to this subject published in the literature merely deal with that most simple case, when the vertical walls are situated in two, to each other perpendicular directions, and are not joined along their vertical edges. Each floor constitutes a rigid disk subjected to a horizontally acting load (wind pressure, horizontal mass power due to earthquake) [1, 3, 7, 8]. However, in designing practice such buildings might also be met with, where at least a part of the load carrying walls are skew to each other in the ground-plan. For the sake of increasing the horizontal stiffness of tower-like buildings, it might simulta-

neously occur that walls joining each other in the transversal direction should be stiffly connected with each other along their vertical edges. Owing to this the joined walls form irregularly shaped uninterrupted wall elements, the structural analysis of which cannot be performed by the methods used up till now.

In the following a new method of calculation will be dealt with. Provided certain simplifying assumptions are satisfied, the method in question is appropriate to make the structural analysis of buildings having load carrying walls even for the afore-mentioned, more general cases possible. The new method is based on the general principles applied by L. PALOTÁS in the calculation of water towers [10]. By using this method the distribution of the

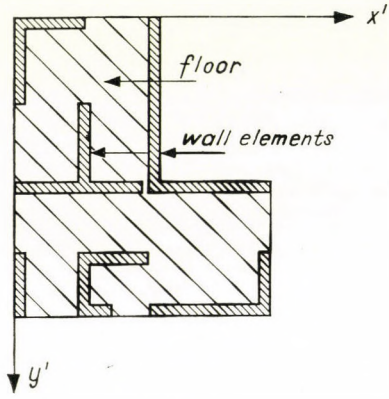

Fig. 1

horizontal load, acting on the building, among the individual vertical load carrying walls, can be determined. The paper does not deal with the dimensioning of the walls in question.

2. Assumptions and fundamental principles of the calculation

The load carrying structure of the living house or public building, which is the subject of the investigation, consists of horizontal floors and of vertical walls placed between them. The walls are formed in such a way that they are appropriate for load carrying (Fig. 1). Load carrying walls fixed to each other along their edges, so as to satisfy the requirements of the Theory of Strength of Materials, constitute one single *wall element*, however, if there is no joint which would satisfy the above condition, then each wall is to be regarded as a separate element.

The following calculations are based on the assumptions given hereunder:

a) The external load is horizontal and is transferred to the building in the plane of the floors. Although the load intensity might change in the vertical direction, at all floor levels it is horizontal and identically arranged.

b) The floors form in their own plane infinitely rigid disks, while perpendicularly to same they are perfectly flexible. This means that in the plane of the floors all wall elements are forced to a displacement and rotation of the same degree, while in the perpendicular direction they can deform independently of each other. Expressed in other words, the floors transfer only horizontal forces to the walls.

c) The horizontal arrangement, thickness and occasional joint of the wall elements are identical at all floor levels of the building, but otherwise quite optional. The co-working of walls and floors as well as that of walls and footings is, owing to the loading effect of vertical loads and due to joints between the joining walls, ensured, thus the walls standing above each other constitute vertical cantilevers.

d) In comparison to the bending stiffness of the single wall elements their torsional stiffness can be neglected.

If the individual wall elements form an open profile, then their torsional stiffness is in comparison to their bending stiffness really very low, therefore, the assumption under *d)* is perfectly justified. On the other hand, if the profile formed by the wall elements is a closed one, the neglect of the torsional stiffness influences the results to a greater degree.

According to the above assumptions the statical behaviour of the whole structure can be outlined as follows: The floors distribute the horizontal load among the cantilevers, formed by the wall elements, proportionately to their stiffness, while these cantilevers transfer the forces falling to their share to the footings by bending. The distribution of the load meets with increased difficulties, because owing to the general arrangement of the walls the direction of the external force, displacement of floors and forces falling to the share of the single wall elements are, in general, not parallel to each other, and in addition the floor also undergoes a rotation in its own plane. For these very reasons the computation conduces to more complicated results than those obtained in the case of the so far elaborated special problems.

3. The stiffness factors of the wall elements

The factors characterizing the stiffness of cantilevers constituted by the wall elements, first of all the *shear centre* (C) of the cross section of wall elements, the *main moments of inertia* (J_1, J_2) referring to the centre of gravity (S) and the *slope angle of the main direction of inertia*

(α) should be determined (Fig. 2). Knowing these quantities we suppose that a cross-section of the investigated cantilever, situated at the height h is displaced parallel to the main directions of inertia *1* and *2* by Δ_1 and Δ_2. To give rise to this displacement, in the centre of gravity of the cross section forces P_1 and P_2 must be set into action parallel to the main directions of inertia *1* and *2*. The magnitude of these forces determined on the basis of the elementary Theory of the Strength of Materials is equal to the values

$$P_1 = \frac{J_2}{L} \Delta_1 \quad \text{and} \quad P_2 = \frac{J_1}{L} \Delta_2 . \tag{1}$$

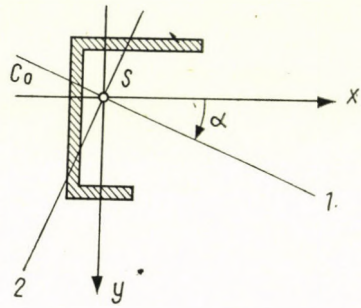

Fig. 2

The letter symbol L figuring in the above formula is obtained from the formula

$$L = \frac{sh^3}{3E}, \tag{2}$$

where

E is the modulus of elasticity of the material of the wall, and
s is a factor expressing the effect of door and window openings in the wall (see also paragraph 6).

In the following let us compute the magnitude of the external force to be set into action at the shear centre of the cross section in question, so as to give rise to a horizontal but otherwise optional x directed unit displacement. As the x axis generally does not coincide with any of the two main directions of inertia, the force sought for can be characterized by the components p_{xx} and p_{xy} which are parallel to the x and y axes and perpendicular to each other (Fig. 2). The aforementioned x-directed unit displacement can be divided into two components acting in the direction of the *1* and *2* axes, the magnitudes of which are $\cos \alpha$ and $\sin \alpha$, respectively. To bring these displacement components into existence — according to formulae (1) — the forces

$$Q_{x1} = \frac{J_2}{L} \cos \alpha \quad \text{and} \quad Q_{x2} = -\frac{J_1}{L} \sin \alpha \tag{3}$$

acting in the directions *1* and *2* are required. The quantitites p_{xx} and p_{xy} sought for are obtained as the sum of the x and y directed projections of forces determined from formulae (3), i.e.,:

$$\begin{aligned} p_{xx} &= Q_{x1} \cos \alpha - Q_{x2} \sin \alpha = \frac{1}{L} (J_1 \sin^2 \alpha + J_2 \cos^2 \alpha), \\ p_{xy} &= Q_{x1} \sin \alpha - Q_{x2} \cos \alpha = -\frac{\cos \alpha \cdot \sin \alpha}{L} (J_1 - J_2) \end{aligned} \tag{4}$$

The determination of forces p_{yy} and p_{yx} acting parallel to the y and x axes, which forces are required to cause an y directed unit displacement, has to be performed in a quite similar way and conduces to the following results:

$$\begin{aligned} p_{yy} &= \frac{1}{L} (J_1 \cos^2 \alpha + J_2 \sin^2 \alpha), \\ p_{yx} &= -\frac{\cos \alpha \cdot \sin \alpha}{L} (J_1 - J_2) = p_{xy} \cdot \end{aligned} \tag{5}$$

The above determined quantities p_{xx}, p_{yy} and $p_{xy} = p_{yx}$ in the following will be called the *stiffness factors of the wall element.*

4. The stiffness characteristics of a building having load carrying walls

Cutting through the building to be investigated in the immediate vicinity of one of the floors, the cross section of the building is obtained. This cross section is characterized by the composition of the cross sections of the detached wall elements. Though these elements do not change their mutual position in the plane of the cross section, perpendicularly to same they are able to deform independently of each other. In the cross section of the building such a point is also to be found which is characterized by the fact that if the resulting force of external forces affecting the floor runs through the point in question, then the cross section (i.e., the floor) merely displaces, but does not rotate. If the cross section (i.e., the floor) is subjected to a twisting moment, then the rotation occurs around this point. In the following the point in question is called the *shear centre of the cross section of the building* (i.e., that of the floor).

For the sake of determining the shear centre pertaining to the cross-section of the building a floor lying at the height h should be subjected to an x-directed horizontal force $R_x = 1$ Mp, put into action at the, for the time being, unknown shear centre of the cross section. Owing to the effect of this force the cross-section (floor) does not rotate, it merely undergoes a displacement of Δ_{xx} in the x direction, and in the y direction of Δ_{xy}. As according to a previous establishment the remaining floors do not influence this motion, therefore, utilizing the stiffness factors dealt with in the previous paragraph, the following projection equations related to the x and y directions can be set up:

$$\Delta_{xx} \sum_{i=1}^{n} p_{ixx} + \Delta_{xy} \sum_{i=1}^{n} p_{ixy} = 1,$$

$$\Delta_{xx} \sum_{i=1}^{n} p_{iyx} + \Delta_{xy} \sum_{i=1}^{n} p_{iyy} = 0.$$

In the above equation p_{ixx}, p_{iyy} and $p_{ixy} = p_{iyx}$ denote the stiffness factors of the i-th wall element, while the summation extends over all n wall elements.

Introducing the symbols

$$A = \sum_{i=1}^{n} p_{ixx}, \qquad B = \sum_{i=1}^{n} p_{iyy},$$
$$C = \sum_{i=1}^{n} p_{ixy}, \qquad D = AB - C^2, \tag{6}$$

from the above simultaneous equations for the displacement of the floor the following results are arrived at:

$$\Delta_{xx} = \frac{B}{D} \quad \text{and} \quad \Delta_{xy} = -\frac{C}{D}.$$

Knowing these the parts of force $R_x = 1$ Mp falling to the share of the i-th wall element and acting in the x and y directions can simply be computed:

$$r_{ixx} = \Delta_{xx} p_{ixx} + \Delta_{xy} p_{ixy} = \frac{1}{D}(Bp_{ixx} - Cp_{ixy}),$$
$$r_{ixy} = \Delta_{xx} p_{ixy} + \Delta_{xy} p_{iyy} = \frac{1}{D}(Bp_{ixy} - Cp_{iyy}). \tag{7}$$

These forces are in equilibrium with the external load, the sum of their moments referring to the centre of the system of coordinates is equal to the moment of the force $R_x = 1$ Mp related to the same point (Fig. 3):

$$\sum_{i=1}^{n} (x'_i r_{ixy} - y'_i r_{ixx}) = y'_c.$$

Substituting equations (7) into the above relation the result is

$$y'_c = \frac{B}{D}\left[\sum_{i=1}^{n} y'_i p_{ixx} - \sum_{i=1}^{n} x'_i p_{ixy}\right] + \frac{C}{D}\left[\sum_{i=1}^{n} x'_i p_{iyy} - \sum_{i=1}^{n} y'_i p_{ixy}\right]. \tag{8}$$

The so obtained distance y'_c equals the distance of force R_x from the axis x', thus, it is identical with the ordinate of the shear centre C of the cross-section

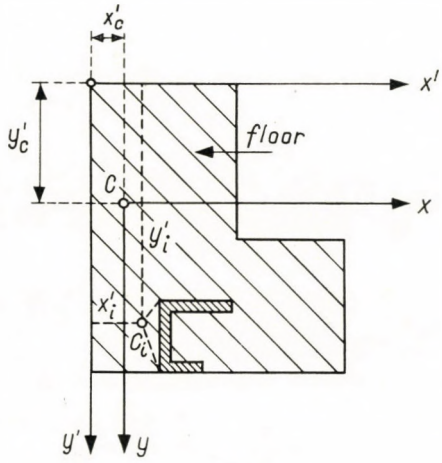

Fig. 3

of the building related to the system of coordinates (x', y'). In formula (8) x'_i and y'_i denote the coordinates of the shear centre C_i pertaining to the i-th wall element related to the system of coordinates (x', y') (Fig. 3).

Similarly the x and y directed portions of force $R_y = 1$ Mp falling to the share of the i-th wall element are obtained from formulae

$$\begin{aligned} r_{iyy} &= \frac{1}{D}(Ap_{iyy} - Cp_{ixy}), \\ r_{iyx} &= \frac{1}{D}(Ap_{ixy} - Cp_{ixx}), \end{aligned} \tag{9}$$

while the abscissa of the shear centre pertaining to the whole cross section of the building can be computed from formula

$$x'_C = \frac{A}{D}\left[\sum_{i=1}^{n} x'_i p_{iyy} - \sum_{i=1}^{n} y'_i p_{iyx}\right] + \frac{C}{D}\left[\sum_{i=1}^{n} y'_i p_{ixx} - \sum_{i=1}^{n} x'_i p_{iyx}\right]. \tag{10}$$

Finally, let us assume that the investigated floor is subjected to a twisting moment $M = 1$ mMp acting in its own plane. Owing to the effect of this moment the floor rotates around the shear centre by the angle φ. In this case the shear centre of the i-th wall element is displaced in the x direction by $-\varphi y_i$ and in the y direction by φx_i, consequently, in this shear centre the x and y directed forces $r_{i\varphi x}$ and $r_{i\varphi y}$ arise, the magnitude of which can be computed from formulae

$$r_{i\varphi x} = \varphi\,(x_i\,p_{ixy} - y_i\,p_{ixx})\,, \qquad r_{i\varphi y} = \varphi\,(x_i\,p_{iyy} - y_i\,p_{ixy})\,. \tag{11}$$

In these formulae $x_i = x'_i - x'_C$ and $y_i = y'_i - y'_C$ denote the coordinates of the shear centre pertaining to the i-th wall element relating to the system of co-ordinates the centre of which coincides with the shear centre of the floor (Fig. 3). The sum of moments of the above forces referring to the shear centre of the cross section is equal to the external twisting moment, thus

$$x_i\,r_{i\varphi y} - y_i\,r_{i\varphi x} = \varphi\left[\sum_{i=1}^{n} y_i^2\,p_{ixx} - 2\sum_{i=1}^{n} x_i\,y_i\,p_{ixy} + \sum_{i=1}^{n} x_i^2 p_{iyy}\right] = 1\,.$$

Introducing the notation

$$F = \sum_{i=1}^{n} y_i^2\,p_{ixx} - 2\sum_{i=1}^{n} x_i\,y_i\,p_{ixy} + \sum_{i=1}^{n} x_i^2\,p_{iyy}\,, \tag{12}$$

the magnitude of the rotation of the floor is $\varphi = 1/F$; and by utilizing formula (11) the x and y directed forces arising due to the action of a twisting moment $M = 1$ mMp, which affect the i-th wall element, can be computed from the following formulae:

$$\begin{aligned} r_{i\varphi x} &= \frac{1}{F}\,(x_i\,p_{ixy} - y_i\,p_{ixx})\,, \\ r_{i\varphi y} &= \frac{1}{F}\,(x_i\,p_{iyy} - y_i\,p_{ixy})\,. \end{aligned} \tag{13}$$

The values r_{ixx}, r_{iyx} and $r_{i\varphi x}$, furthermore r_{ixy}, r_{iyy} and $r_{i\varphi y}$ figuring in formulae (8), (9) and (13) determine the magnitudes of x and y directed forces, which arise owing to the effect of an x and y directed unit force acting at the shear centre of the cross section and a unit twisting moment. The above forces affect the single wall elements at the shear centres and are called the *force* and *moment distribution factors of the building*.

It follows from the meaning of the individual factors and conditions of equilibrium as well, that in the case of a proper calculation the distribution factors have to satisfy the following equations:

$$\sum_{i=1}^{n} r_{ixx} = \sum_{i=1}^{n} r_{iyy} = 1\,,$$
$$\sum_{i=1}^{n} r_{iyx} = \sum_{i=1}^{n} r_{ixy} = \sum_{i=1}^{n} r_{i\varphi x} = \sum_{i=1}^{n} r_{i\varphi y} = 0\,. \tag{14}$$

Analysing formulae (7), (9) and (13) it can be established that the force and moment distribution factors are independent of the height h at which the floor is situated.

5. The run of the calculation

The first step of calculation includes the determination of the geometrical and stiffness characteristics of the single wall elements and of the whole building utilizing the deduced formulae for this purpose. Thereafter the external load is to be distributed among the wall elements. According to our assumption, the arrangement of the external load is identical at all storey-levels. Simultaneously it has been established that the force and moment distribution factors of all floors coincide with each other. Therefore, a floorwise performed separate distribution of loads is unnecessary, and it is sufficient to carry out the calculation for the resulting force affecting the whole building as described hereunder.

First of all the resulting force of horizontal forces acting on the building is to be determined and reduced to the shear centre pertaining to the cross section of the building. Hereafter, this resulting force is divided into two components acting in the x and y directions. Now, the building is loaded by forces R_x and R_y acting at the shear centre, furthermore, by the twisting moment $M = Rt$ (Fig. 4). Knowing the force and moment distribution factors from forces R_x, R_y and moment M the x and y directed forces, falling to the share of the i-th wall element and acting at the shear centre of same, can be determined

$$P_{ix} = r_{ixx} R_x + r_{iyx} R_y + r_{i\varphi x} M\,,$$
$$P_{iy} = r_{ixy} R_x + r_{iyy} R_y + r_{i\varphi y} M\,. \tag{15}$$

Forces obtained from formulae (15) are the resultant forces of that part of the total load acting on the building, which falls to the share of the i-th wall element. However, the single wall elements actually bear the load distributed at the height of the floors. Knowing the resultant force and taking the distribution of external forces into consideration, forces affecting the single floors can be determined by a simple proportioning.

In the further computation the single wall elements can be treated as separated cantilevers, independent of the floors, which at the single floor

levels are affected by the previously determined horizontal forces. Taking in addition to these forces the vertical loads also into consideration, the walls can be dimensioned by methods which are usual for bent beams.

6. Remarks

When dealing with the calculation of the stiffness factors of wall elements, it has already been indicated that the effect of openings on the stiffness of wall elements is taken into consideration with the aid of the factor s figuring

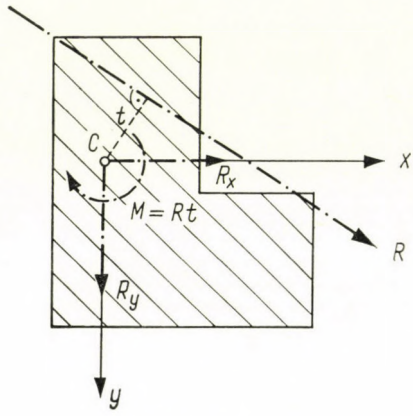

Fig. 4

in the constant L. Denoting the ratio of the width of the opening to the width of the wall by ε, then according to test results the factor s is to be determined as follows [9]:

$$\begin{aligned} &\text{for} \quad \varepsilon \leq 0.55\,, \qquad s = 3.46\,\varepsilon + 1\,, \\ &\text{for} \quad 0.55 \leq \varepsilon \leq 0{,}70\,, \quad s = \frac{1}{\sqrt[3]{(1-\varepsilon)^4}}\,. \end{aligned} \tag{16}$$

A wall element actually consists of several walls, each of these furnished, in general, with differently shaped and sized openings. In such a case the factor s characteristic for the whole wall element might approximately be taken as being identical with the average value of factors pertaining to the single walls constituting the element.

If the openings to be found in the wall are very large ($\varepsilon > 0.70$), or the structures in question are more special ones, then the effect of openings should be taken more accurately into consideration. One method which might be appropriate for this purpose is that the wall element clamped into the footing and weakened by openings is regarded as being a Vierendeel girder, and the

stiffness factors dealt with in paragraph 3 are determined accordingly to that assumption [4, 6, 7].

The method dealt with can be used only for the investigation of buildings, the walls of which and the loads acting on the building are identically arranged on all floors. In a more general case the investigation might be performed by applying the fundamental principles of the deformation method – which is well-known from the analysis of bar structures — or those of the moment distribution method. In this case all floors of the building are imagined as being fixed in the horizontal direction. Then the floors are gradually released and the force and moment distribution factors pertaining to the single floors are computed by using the previously deduced formulae. Thereafter, knowing the external loads, forces and twisting moments acting on the floors are determined, while their distribution is performed by displacing the floors one by one in the succession of storeys. The force and moment distribution has to be continued as long as the values of unbalanced forces and moments become on all floor levels so small as to be negligible.

7. Numerical example

The building shown in Fig. 5 is a ten-storeyed one having load carrying walls. The building is subjected to a horizontal wind load the intensity of which is $p = 0.105$ Mp/m². The horizontal arrangement of the load carrying walls can be seen in the section. The walls intersecting each other are stiffly joined to one another, this ensures their co-working so that they form a wall element. The thickness of these load carrying walls is 25 cm, the average values of factors s expressing the effect of openings related to the single wall elements are in turn $s_1 = 2.85$, $s_2 = 3.42$, $s_3 = 2.55$.

a) Moments of inertia pertaining to the single wall elements:

Wall element 1	$J_1 = 12.19$ m⁴,
	$J_2 = 2.37$ m⁴,
Wall element 2	$J_1 = 26.30$ m⁴,
	$J_2 = 8.40$ m⁴;
Wall element 3	$J_1 = 3.30$ m⁴,
	$J_2 \approx 0$.

b) When computing the stiffness factors the factor $h^3/3E$ is taken as being equal to the unit. Then according to formulae (4) and (5):

Wall element 1	$p_{1xx} = p_{1yy} = 2.55$,
($\alpha_0 = 45°$)	$p_{1xy} = -1.72$;
Wall element 2	$p_{2xx} = 2.45$,
($\alpha_0 = 0°$)	$p_{2yy} = 7.70$,
	$p_{2xy} = 0$;
Wall element 3	$p_{3xx} = 1.29$,
($\alpha_0 = 90°$)	$p_{3yy} = p_{3xy} = 0$.

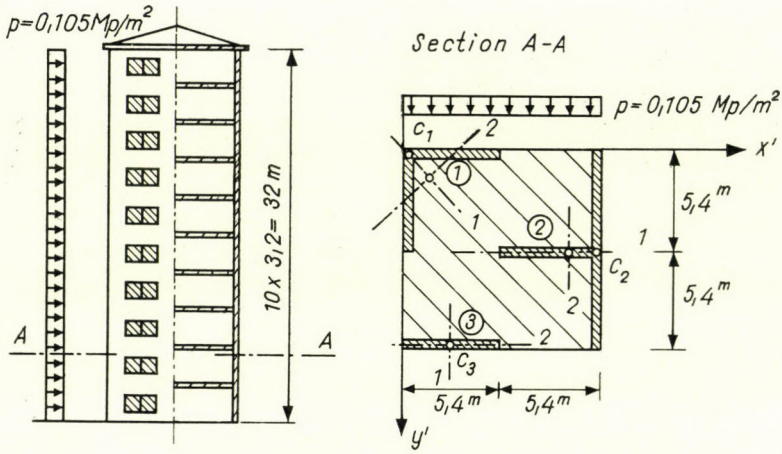

Fig. 5

c) Constants needed for the determination of the shear centre of the building, as well as for that of force and moment distribution factors were computed and the results are given in Tables I and II.

Table I

i	x_i'	y_i'	p_{ixx}	p_{iyy}	p_{ixy}	$y_i'p_{xx}$	$x_i'p_{iyy}$	$x_i'p_{ixy}$	$y_i'p_{ixy}$
1	0	0	2.55	2.55	—1.72	0	0	0	0
2	10.80	5.40	2.45	7.70	0	13.25	83.20	0	0
3	2.70	10.80	1.29	0	0	13.90	0	0	0
Σ	—	—	6.25	10.25	—1.72	27.15	83.20	0	0

Table II

	x_i	y_i	x_i^2	y_i^2	x_iy_i	$x_i^2p_{iyy}$	$y_i^2p_{ixx}$	$x_iy_ip_{ixy}$
1	—7.73	—2.19	59.80	4.80	16.90	153.0	12.3	—29.1
2	3.07	3.21	9.40	10.30	9.90	72.4	25.2	0
3	—5.03	8.61	25.30	74.00	43.30	0	32.7	0
Σ	—	—	—	—	—	225.4	70.2	—29.1

According to formulae (6):

$A = 6.29$, $B = 10.25$, $C = -1.72$, $D = 61.60$. The location of the shear centre computed from formulae (8) and (10)

$$x_C' = \frac{10.25}{61.60}(27.50 - 0) + \frac{(-1.72)}{61.60}(83.20 - 0) = 2.19 \text{ m},$$

$$y_C' = \frac{6.29}{61.60}(83.20 - 0) + \frac{(-1.72)}{61.60}(27.15 - 0) = 7.73 \text{ m}.$$

d) According to formula (12):

$F = 70.2 - 2\,(-\,29.1) + 225.4 = 353.8.$

The force and moment distribution factors were computed from formulae (7), (9) and (13), and the results are given in Table III.

Table III

i	r_{ixx}	r_{iyy}	r_{ixy}	r_{iyx}	$r_{i\varphi x}$	$r_{i\varphi y}$
1	0.377	0.224	−0.214	−0.104	0.0537	−0.0667
2	0.408	0.776	0.214	0.068	−0.0223	0.0667
3	0.215	0	0	0.036	−0.0314	0
Σ	1.000	1.000	0	0	0	0

e) Magnitude of the windload acting on the building:

$R = 10.8 \cdot 32.0 \cdot 0.105 = 36.3$ Mp.

$R_x = 0,\ R_y = 36.3$ Mp, $M = -\,2.33 \cdot 36.3 = -\,84.6$ Mp.

The force and moment distribution is performed by utilizing formula (15) as given below:

$$P_{1x} = -\,0.104 \cdot 36.3 + 0.0537\,(-84.6) = -\,8.31 \text{ Mp}$$
$$P_{2x} = +\,0.068 \cdot 36.3 - 0.0223\,(-84.6) = +\,4.35 \text{ Mp}$$
$$P_{3x} = +\,0.036 \cdot 36.3 - 0.0314\,(-84.6) = +\,3.96 \text{ Mp}$$
$$\Sigma P_{ix} = 0.00 \text{ Mp.}$$

$$P_{1y} = 0.224 \cdot 36.3 - 0.0667\,(-84.6) = 13.77 \text{ Mp}$$
$$P_{2y} = 0.776 \cdot 36.3 + 0.0667\,(-84.6) = 22.53 \text{ Mp}$$
$$P_{3y} = 0.00 \text{ Mp}$$
$$\Sigma P_{iy} = 36.30 \text{ Mp.}$$

The above results give the x and y directed components of the resultant load acting on the individual wall elements. These components are to be distributed in compliance with the distribution of the external load (in the present case a uniform one) into concentrated forces acting at the single floor levels. Knowing the latter forces the wall elements can be dimensioned.

REFERENCES

1. Beck, H.: Die Großtafelbauweise. Bemerkungen zur statischen Berechnung und konstruktiven Durchbildung. *Der Bauingenieur* 6 (1961), 382.
2. Born, J.: Faltwerke. Verlag Konrad Wittwer, Stuttgart 1954.
3. Csonka, P.: Szélerőkkel terhelt épületek födémeinek statikai viselkedése (The Statical Behaviour of Floors of Buildings Affected by Wind Forces; in Hungarian). *Magyar Építőipar* **9** (1962), 66—68.
4. Горнов, В. М.: Исследования прочности и жесткости индустриальных конструкций жилых зданий. Академия Архитектуры СССР. Москва 1954.
5. Kaliszky, S.: Vízszintes erőkkel terhelt teherhordó-falas épületek számítása (Calculation of Buildings with Load Bearing Walls Loaded by Horizontal Forces; in Hungarian). *Magyar Építőipar* **12** (1962), 541—548.
6. Klimov, B.: Előregyártott táblaelemekből épített épületek számítási elvei (The Principles of the Calculation of Buildings Built of Prefabricated Panels; in Hungarian.) *Építés- és Közlekedéstudományi Közlemények* **2** (1958), 171—180.

7. Lewicki, B.: Budynki Mieszkalne z Elementów Wielkowymiarowych (Living Houses Built of Large Panels; in Polish). Wydawnictwo "Arkady" Warszawa (1961).
8. Menyhárd, I.: Útmutató teherhordó nagypaneles rendszerű épületek statikai számításához. (Guide to the Structural Analysis of Buildings Built of Large Load-bearing Panels; in Hungarian.) *ÉTI Tudományos Közlemények* 15 (1960).
9 Поляков, С. Б.: Расчет стен каркасных зданий на горизонтальную нагрузку действующую в плоскосту стены. Стройтельная механика и расчет сооружений. № 2. 1961 г.
10. Palotás, L.: Keretek elmélete és számítása (Theory and Calculation of Frames; in Hungarian). Közlekedési Kiadó, Budapest 1951.

STATISCHE BERECHNUNG VON DURCH HORIZONTALKRÄFTE BELASTETEN GEBÄUDEN MIT TRAGWÄNDEN

S. KALISZKY

ZUSAMMENFASSUNG

Der Aufsatz befaßt sich mit der statischen Berechnung von Gebäuden, deren Wände tragfähig sind. Die grundrißliche Anordnung der vertikalen Wände, deren Wandstärke und fallweise Verbindung, ferner die Anordnung der horizontalen Lasten sind für alle Stockwerke bzw. Deckenniveaus die gleichen, im übrigen aber vollkommen beliebig. Die Voraussetzung, daß die Decken in ihrer eigenen Ebene vollkommen starre Scheiben bilden, während sie senkrecht zu ihr vollkommen biegsam sind, ermöglicht die Bestimmung der Verteilung der auf das Gebäude wirkenden Außenkräfte zwischen den durch die vertikalen Wände gebildeten Wandelementen mit Hilfe von Gleichgewichtsgleichungen. Bei der Berechnung kann die Wirkung der in den Wänden befindlichen Öffnungen ebenfalls annähernd berücksichtigt werden. Nach der mit Hilfe der Gleichungen (7), (9), (13) und (15) erfolgten Verteilung der Last können die einzelnen Wandelemente als voneinander unabhängige, vertikale Kragträger behandelt werden, wodurch ihre Bemessung nach den Regeln der elementaren Festigkeitslehre ermöglicht wird.

CALCUL STATIQUE DE BÂTIMENTS A MURS PORTEURS CHARGÉS PAR DES FORCES VERTICALES

S. KALISZKY

RÉSUMÉ

L'auteur se propose l'examen statique de bâtiments à murs porteurs, chez lesquels la disposition du plan, l'épaisseur et la jonction éventuelle des murs verticaux, ainsi que la disposition de la charge horizontale sont identiques pour chaque étage, mais peuvent être par ailleurs entièrement arbitraires. En supposant que les planchers forment un disque infiniment rigide dans leur plan propre et sont en revanche parfaitement flexibles en direction normale à ce plan, on peut déterminer, à l'aide d'équations d'équilibre, la répartition de la charge extérieure agissant sur le bâtiment entre les éléments de murs formés par les murs verticaux. Dans le calcul, on peut aussi tenir compte, d'une façon approchée, de l'influence des ouvertures des murs. Après la distribution de la charge à l'aide des formules (7), (9), (13) et (15), les éléments de murs peuvent être traités comme des consoles de plan vertical indépendantes les unes des autres, et leur dimensionnement peut s'effectuer selon la résistance des matériaux élémentaire.

СТАТИЧЕСКИЙ РАСЧЕТ ЗДАНИЙ С НЕСУЩИМИ СТЕНАМИ, ПОДВЕРЖЕННЫМИ ГОРИЗОНТАЛЬНЫМ НАГРУЗКАМ

Ш. КАЛИСКИ

РЕЗЮМЕ

В работе дается анализ таких зданий с несущими стенами, у которых план расположения вертикальных стен, далее их толщина и взаимосвязь, а также расположение горизонтальных нагрузок одинаковы по отметкам, а в остальном совершенно произвольны. Предполагая, что перекрытия в собственной плоскости образуют бесконечно жесткие пластины, а перпендикулярно к собственной плоскости совершенно гибки, при помощи уравнений равновесия можно определить, каким образом распределяется внешняя нагрузка по элементам стен, образованным вертикальными стенами. При расчете можно приближенно принять во внимание также влияние имеющихся в стенах отверстий (проемов). После распределения нагрузки при помощи формул (7), (9), (13) и (15), отдельные элементы можно рассматривать независимо друг от друга, как расположенные вертикально консоли. Их расчет можно производить на основе элементарной теории сопротивления материалов.

THE COMPUTATION OF THE FORCES OF THE COMMUTATOR RISER

I. HUSZÁR
CAND. OF TECHN. SC.

and

J. BODOR
GANZ ELECTRIC WORKS, BUDAPEST

[Manuscript received May 14, 1963]

The task of the commutator riser is to ensure a conductive connection between the commutator segments and the winding ends. From a mechanical point of view its load is determined by the assembly circumstances, by the power effects arising during rotation, finally by the forces arising from warming-up during operation. The first factor depends on production; the two latter can also be followed in a quantitative way. The power relations of the riser as of a structural element of indeterminate incorporation, arising during rotation and warming-up, are treated with approximate computation.

I. Introduction

The task of the commutator riser, as of a structural element, is to secure a proper conductive connection between the commutator segment and the winding ends (Fig. 1). At the same time, a mechanically safe shaping of the riser in respect to the operational safety of the electrical machine is absolutely necessary.

The commutator, the riser and the winding ends together form a statically indeterminate system. Therefore, the task of strength control is fairly complicated. This difficulty is increased by the complexity of operational load. On the one hand, certain power effects arise already during assembly, — on the other, certain stresses develop during rotation, finally in connection with warming-up during operation [1—3].

In the course of the assembly operations, the risers must be adjusted to a certain extent to the winding head, partly by permanent, partly by elastic deformation. This deformation becomes the source of an unawaited stress. A further residual stress is caused by the bandaging of the heads after their fixation in the riser. Although the assembly circumstances, resp. the stresses arising cannot be followed accurately with calculations, but a qualitative judgement of the stresses thus arising can be formed. The accuracy of manufacturing can accordingly be prescribed and the operational plans of assembly formulated. For the loads arising from rotation and warming-up, constituting a considerable part of the overall load, it is possible to develop an approximation procedure. The detailed calculations are presented here. There is applied the principle of the superposition. The loads are considered separately,

and the resulting stresses are obtained by the algebraic addition of the individual loads.

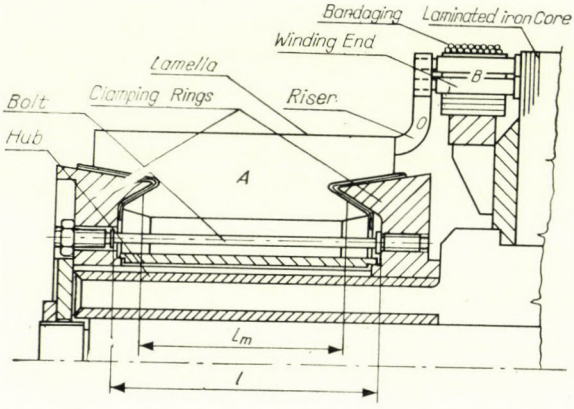

Fig. 1

II. Calculation of the loads resulting from rotation

The loads arising from rotation are radial. However, with regard to the statically indeterminate task the forces can be computed only with the aid of strength relations, namely, by means of a solution for clarifying the deformation of the system [4]. It is advisable to substitute the individual elements by springs. The approximate spring system is presented in Fig. 2. In drawing the system, the commutator hub on which the commutator is pressed, further the lamination are taken to be rigid. Only the commutator (A), the riser (O) and the winding head (B) are considered as elastic.

During rotation, the individual element would separately move by values $y_{A\omega}$, $y_{O\omega}$, $y_{B\omega}$. Since, however, they are connected, an inner force Q_ω arises between them, on the effect of which a deformation $\delta_A > 0$, $\delta_O > 0$, $\delta_B < 0$ will develop. From a force $Q_{\omega 1}$ affecting a single riser, the inner force acting in the system is defined by the relation

$$Q_\omega = K Q_{\omega 1},$$

where K is the number of riser (commutator segments). According to the figure, the following relation of the deformation may be written:

$$y_{A\omega} + y_{O\omega} + \delta_A + \delta_O = y_{B\omega} + \delta_B .$$

In greater detail, introducing the force and the spring constants,

$$y_{A\omega} + y_{O\omega} + Q_\omega c_A + Q_\omega c_O = y_{B\omega} + (-Q_\omega) c_B .$$

Hence, the force sought for is

$$Q_\omega = \frac{y_{B\omega} - y_{A\omega} - y_{O\omega}}{c_A + c_O + c_B} . \tag{1}$$

Let us take the individual quantities one by one included in the relation of Q_ω.

$y_{B\omega}$ is the radial displacement of the free-standing winding head during the rotation with an angular velocity ω. In approximation, the winding head

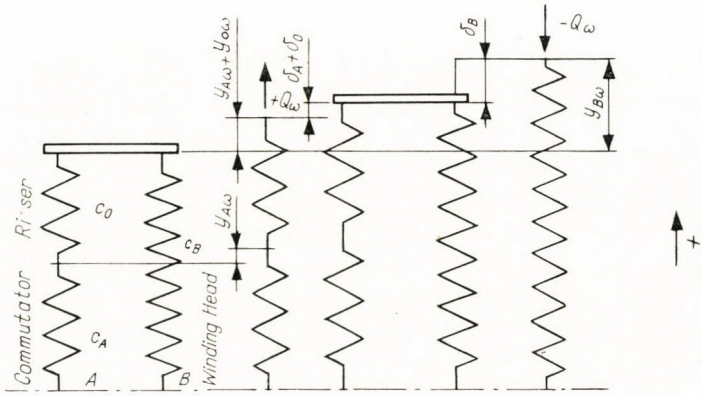

Fig. 2

is regarded as a rotating copper ring of specific weight γ_{Cu}. Thus, the specific elongation from the tangential stress arising in the head (Fig. 3) is

$$\varepsilon_t = \frac{\sigma_t}{E_{Cu}} = \frac{1}{E_{Cu}} \frac{\gamma_{Cu}}{g} r^2 \omega^2$$

where g is the gravitational acceleration, E_{Cu} is the elasticity coefficient of copper. The displacement sought for, in radial direction, is accordingly

$$y_{B\omega} = \varepsilon_t \, r_t = \frac{\gamma_{Cu}}{E_{Cu}\, g} r_t^3 \omega^2 .$$

$y_{A\omega}$ is the radial displacement of the commutator not connected to the winding head, in a spot a during rotation (Fig. 4).

The deformation consists of five parts:

$$y_{A\omega} = y_{A\omega}^{I} + y_{A\omega}^{II} + y_{A\omega}^{III} + y_{A\omega}^{IV} + y_{A\omega}^{V} .$$

$y^{\mathrm{I}}_{\mathrm{A}\omega}$ is the radial displacement of the gravity center of the clamping ring, which can be similarly calculated to $y_{\mathrm{B}\omega}$:

$$y^{\mathrm{I}}_{\mathrm{A}} = \frac{\gamma}{g \cdot E} r_g^3 \omega^2$$

where γ is the specific weight of steel, E is the elastic coefficient of steel, r is the gravity center radius of the clamping ring section.

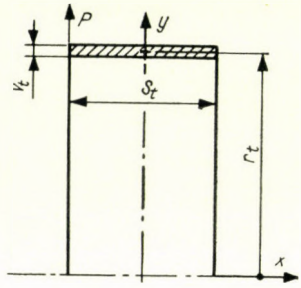

Fig. 3

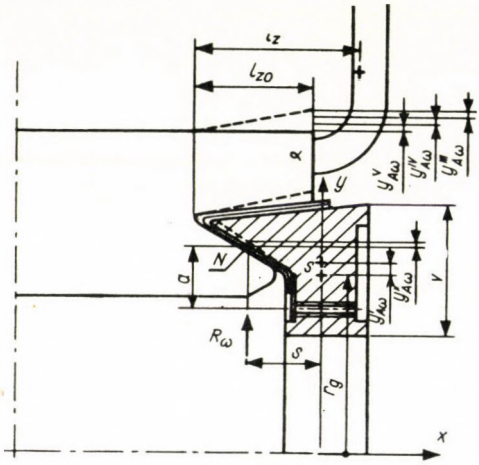

Fig. 4

$y^{\mathrm{II}}_{\mathrm{A}\omega}$ is the radial displacement arising in connection with the rotation of the commutator clamping ring, as an effect of the radial force R_ω appearing on the oblique surface and attacking arm s [5]:

$$y^{\mathrm{II}}_{\mathrm{A}\omega} = \frac{R_\omega s r_g v}{2 \pi I_y E} .$$

Here, I_y is the moment of inertia of the clamping ring calculated for the axis y; R_ω represents the resultant computable with the relation $R_\omega = K R_{\omega 1}$

from the force $R_{\omega 1}$ falling on a single segment, but only the force increase as related to the assembly.

$y_{A\omega}^{III}$ is the deformation of the segment-end under the effect of its own centrifugal force:

$$y_{A\omega}^{III} = \frac{p_\omega l_{z0}^4}{8 I_s E_{Cu}}$$

where p_ω is the rotational distributed load of the segment-end, l_{z0} is the length of the segment-end, I_s is the moment of inertia of the single segment-end taken for console.

$y_{A\omega}^{IV}$ is the deformation from the concentrated force corresponding to the centrifugal force C_{z1} of a single riser. Namely, by placing the centrifugal force affecting the riser into point a, the force C_{z1} can be substituted by a force equal to C_{z1} and by a moment $C_{z1}(l_z - l_{z0})$

$$y_{A\omega}^{IV} = \frac{C_{z1} l_{z0}^3}{3 I_s E_{Cu}} .$$

$y_{A\omega}^{V}$ is finally the deformation developing on the effect of the bending moment originating from the transposition of the centrifugal force C_{z1}.

$$y_{A\omega}^{V} = \frac{C_{z1}(l_z - l_{z0}) l_{z0}^2}{2 I_s E_{Cu}} .$$

$y_{O\omega}$ is the elongation of the riser on the effect of the centrifugal force. It consists of two parts, namely (Fig. 5):

$$y_{O\omega} = y_{O\omega}^{I} + y_{O\omega}^{II}.$$

$y_{O\omega}^{I}$ is the elongation of the vertical section. The stress arising in any spot x, in the radial direction, is

$$\sigma = \frac{C(x)}{ab} = \frac{1}{ab}\left(r - \frac{x}{2}\right)\omega^2 \frac{\gamma_{Cu}}{g}(abx),$$

consequently the unit elongation is

$$\varepsilon = \frac{\sigma}{E_{Cu}} = \frac{\gamma_{Cu}}{gE_{Cu}}\left(r - \frac{x}{2}\right)x\omega^2 .$$

The elongation of the vertical size of the riser, substituting the lower part by an approximation with the part indicated by a dotted line:

$$y_{I\omega}^{O} = \omega^2 \frac{\gamma_{Cu}}{gE_{Cu}} \int_0^h \left(r - \frac{x}{2}\right) x\, dx = \omega^2 \left(\frac{rh^2}{2} - \frac{h^3}{6}\right) \frac{\gamma_{Cu}}{gE_{Cu}} .$$

$y_{O\omega}^{II}$ is the displacement of the horizontal part on the effect of the centrifugal force C:

$$y_{O\omega}^{II} = \frac{C_{z1}\, r_0^3}{3\, I_z\, E_{Cu}},$$

again approximating the curved part by a straight section.

Here, I_z is the moment of inertia of the fixed cross section of the riser on the axis z.

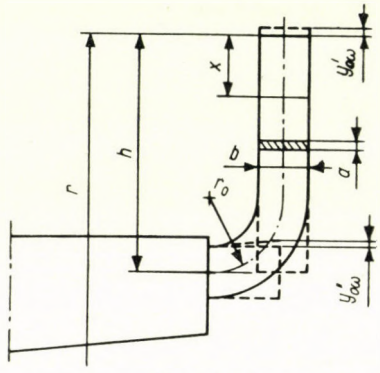

Fig 5.

c_A is the radial spring constant of the segment-end with the riser, that is, the deformation occurring in case of $Q_\omega = 1$ acting on the riser system on its right upper end and can be computed in a simple way from the relation $\delta_A = Q_\omega c_A$. In detail:

$$\delta_A = \frac{y_{A\omega}^{IV}}{C_{z1}} Q_{\omega 1} + \frac{y_{A\omega}^{V}}{C_{z1}} Q_{\omega 1} + \frac{y_{A\omega}^{II}}{R_\omega} Q_\omega =$$

$$= \frac{y_{A\omega}^{IV}}{C_{z1}} \frac{Q_\omega}{K} + \frac{y_{A\omega}^{V}}{C_{z1}} \frac{Q_\omega}{K} + \frac{y_{A\omega}^{II}}{R_\omega} Q_\omega .$$

Thus, finally,

$$c_A = \frac{y_{A\omega}^{II}}{R_\omega} + \frac{y_{A\omega}^{IV}}{K C_{z1}} + \frac{y_{A\omega}^{V}}{K C_{z1}} .$$

c_O is the spring constant of the riser-system in the radial direction to be computed from the spring constant c_1 of a single riser. By considering the vertical section of the riser as a drawn element, its horizontal section, on the other hand, as a bent element (Fig. 5):

$$c_1 = \frac{h}{ab \cdot E_{Cu}} + \frac{r_0^3}{3\, I_z\, E_{Cu}} .$$

The spring constant of the riser system, according to the parallel joint, is

$$c_O = \frac{c_1}{K} .$$

c_B is the spring constant of the winding end in the radial direction. The winding ends are approximately substituted by a solid ring of identical section. From this condition, the thickness v_t of the ring can be determined (Fig. 3). The spring constant is [6]

$$c_B = \frac{6}{2\pi r_t} \frac{m^2 - 1}{m^2 E_{Cu} v_t^3 \mu^3} \frac{\sinh 2\mu s_t - \sin 2\mu s_t}{\cosh 2\mu s_t + \cos 2\mu s_t - 2}$$

where.

$$\mu = \sqrt[3]{3 \frac{m^2 - 1}{m^2 v_t^2 r_t^2}}$$

Hereafter, the force Q_ω can be determined according to (1). Further, the load on a single riser, decisive from the point of view of sizing, is:

$$Q_{\omega 1} = \frac{Q_\omega}{K} .$$

III. Computation of loads originating from warming-up

On the effect of warming-up, radial and axial deformations develop. The forces arising from these will be discussed one by one.

1. In the radial direction

The spring system used for the computation is the same here as in the foregoing section, since the direction of the forces is the same in both cases (Fig. 6). According to the Fig. 6

$$Q_{\vartheta r} = \frac{y_{B\vartheta} - y_{A\vartheta} - y_{O\vartheta}}{c_A + c_O + c_B} . \tag{2}$$

Here, $y_{B\vartheta}, y_{A\vartheta}, y_{O\vartheta}$ is the displacement occurring on the effct of warming-up in the case when the individual parts are not impeded in their expansion. $Q_{\vartheta r}$ exactly signifies the force developing in the interconnected system. The spring constants are, of course, the same as in the case of rotation.

$y_{B\vartheta}$ is the expansion of the copper ring substituting the winding ends. Taking into consideration the steel-wire bandaging of the winding ends, the

radial expansion of the substitute copper ring is calculated, with the thermal expansion coefficient of steel (Fig. 3) α_{Fe}.

$$y_{B\vartheta} = \alpha_{Fe}\, r_t\, \vartheta_t$$

where ϑ_t is the difference of the working, resp. assembly temperatures of the winding end.

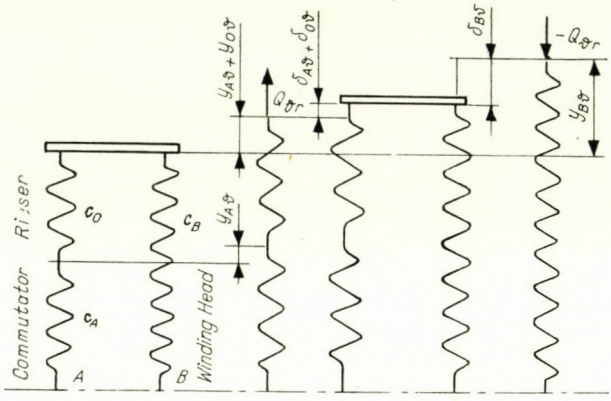

Fig. 6

$y_{A\vartheta}$ is the vertical displacement of the segment end with riser. One part is given by the radial expansion of the commutator on the effect of temperature increase ϑ_{Fe} (Fig. 4):

$$y^{I}_{A\vartheta} = \alpha_{Fe}\, r_g\, \vartheta_{Fe}.$$

The other part is obtained from the tipping of the ring because of the radial forces increasing on the effect of temperature:

$$y^{II}_{A\vartheta} = \frac{R_\vartheta\, s r_g\, v}{2\,\pi\, I_y\, E}$$

where $R_\vartheta = KR_{\vartheta 1}$ signifies the increase of the radial force as compared to the assembly, ϑ_{Fe} is the difference between the working, resp. assembly temperatures of the clamping ring. Finally,

$$y_{A\vartheta} = y^{I}_{A\vartheta} + y^{II}_{A\vartheta}.$$

$y_{O\vartheta}$ is the elongation of the riser because of temperature.

$$y_{O\vartheta} = \alpha_{Cu}\, h\, \vartheta_z$$

where h is the length of the riser, and ϑ_z is the increase of the temperature of the riser.

Substituting the computed y and c data in the formula of internal forces, the load of the riser, respectively, of a single riser is obtained:

$$Q_{\vartheta r1} = \frac{Q_{\vartheta r}}{K} .$$

2. In axial direction

The system formed by the commutator, the risers and the winding ends, can be substituted in the axial direction by the spring system delineated above (Fig. 7). Let us denote the free deformations caused by temperature in succession by $\eta_{A\vartheta}$, $\eta_{B\vartheta}$, $\eta_{O\vartheta}$. On account of the connection existing between the elements of the system, however, a force $Q_{\vartheta a}$ develops. The deformations appearing on its effect are, on the other hand, $\delta_{A\vartheta}$, $\delta_{B\vartheta}$, $\delta_{O\vartheta}$. According to the figure, it can be written that

$$l_A + l_B + l_O = l_A + \eta_{A\vartheta} + \delta_{A\vartheta} + l_B + \eta_{B\vartheta} + \delta_{B\vartheta} + l_O + \eta_{O\vartheta} + \delta_{O\vartheta} .$$

From this, on the basis of

$$\delta_\vartheta = (-Q_{\vartheta a})\, c_a < 0 ,$$

$$\eta_{A\vartheta} + \eta_{B\vartheta} + \eta_{O\vartheta} = -\delta_{A\vartheta} - \delta_{B\vartheta} - \delta_{O\vartheta} = Q_{\vartheta a}\, c_{Aa} + Q_{\vartheta a}\, c_{Ba} + Q_{\vartheta a}\, c_O .$$

Thus, the effect of the forces acting on the riser system is

$$Q_{\vartheta a} = \frac{\eta_{A\vartheta} + \eta_{B\vartheta} + \eta_{O\vartheta}}{c_{Aa} + c_{Ba} + c_{Oa}} .$$

The force acting upon a single riser is

$$Q_{\vartheta a1} = \frac{Q_{\vartheta a}}{K} .$$

One of the commutator clamping rings is supported, namely, on the commutator hub, i.e. it cannot move as compared to the axis. However, from the point of view of the forces of the above system, it is not indifferent, which of the rings is caught; therefore, the computation will be made for both cases.

a) *The commutator rests upon the clamping ring on the riser side.* $\eta_{A\vartheta}$, the displacement of the segment-end of the commutator on the effect of temperature change ϑ_{Cu} consists of two parts. One is the thermal expansion of the segment-end with riser:

$$\eta'_{A\vartheta} = \alpha_{Cu}\, l_{z0}\, \vartheta_{Cu} .$$

The other part is the displacement of the end of the commutator because of axial force increase $T_\vartheta = KT_{\vartheta 1}$ caused by the tipping of the clamping ring (Fig. 4):

$$\eta''_{A\vartheta} = \frac{T_\vartheta a r_g v}{2 \pi I_y E}.$$

Accordingly,

$$\eta_{A\vartheta} = \eta'_{A\vartheta} + \eta''_{A\vartheta}.$$

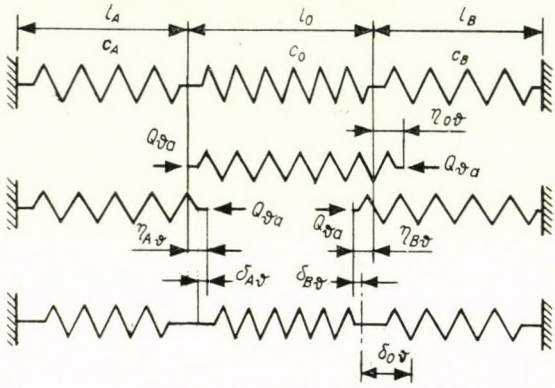

Fig. 7

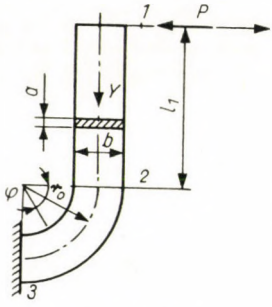

Fig. 8

The axial expansion of the copper ring substituting the winding ends (Fig. 3) is:

$$\eta_{B\vartheta} = \alpha_{Cu} s_t \vartheta_t.$$

The thermal expansion of the riser in the axial direction (Fig. 8) is:

$$\eta_{O\vartheta} = \alpha_{Cu} r_0 \vartheta_z.$$

b) *The commutator rests upon the outer clamping ring*. Now the displacement of the segment-end towards the winding heads will be larger than in

case *a)*, i.e. also the elongation λ_K of the whole commutator will be added. Thus,

$$\eta_{A\vartheta} = \eta'_{A\vartheta} + \eta''_{A\vartheta} + \lambda_K .$$

The commutator, however, may be considered as a spring system consisting of the sector crown, of clamping ring and of bolts. On the effect of temperature, one part of the expansion of the system can be approximated by the thermal elongation of the bolts:

$$\lambda'_K = \alpha_{Fe}\, l \vartheta_c ,$$

where ϑ_c is the difference of the working, resp. pre-working temperatures of the fixing bolts, l is the size visible in Fig. 1. The other part of the elongation is the stretching of the bolts caused by the arising internal forces. Namely the thermal expansion of copper is larger than that of iron; consequently the internal force T_ϑ originating from the various deformations causes a stretching of the bolts:

$$\lambda''_K = \frac{T_\vartheta\, l}{A_c E}$$

where A_c is the sum of the action areas of the bolts.

Thus

$$\lambda_K = \lambda'_K + \lambda''_K .$$

The spring constants in the cases *a)* and *b)* are identical. Their detailed calculation is presented in the following.

c_{Aa} is the axial spring constant of the circular ring formed by the end of the segment with riser, since only this takes part in the force play:

$$c_{Aa} = \frac{l_{z0}}{A E_{Cu}} ,$$

where l_{z0} is the length of the segment end with riser, A is the cross-section of the circular ring. In fact, in case *b)*, c_{A_a} slightly deviates from this, since now the deformation of the entire commutator system on account of the unit axial force, should be computed. Here, however, this is disregarded.

c_{1a} is the spring constant of a single riser in the axial direction, computable according to the princip of Castigliano. The displacement in the direction of P (Fig. 8) is:

$$f = \frac{\partial P}{\partial U} = \frac{1}{I_z E_{Cu}} \int_3^1 M \frac{\partial M}{\partial P}\, dl = P_{c1a} .$$

The determination of the moment on the individual sections:

1—2 section $\quad M_{12} = Py , \quad \frac{\partial M_{12}}{\partial P} = y , \quad dl = dy .$

2—3 section

$$M_{23} = P(l_1 + r_0 \sin\varphi),$$

$$\frac{\partial M_{23}}{\partial P} = l_1 + r_0 \sin\varphi,$$

$$dl = r_0\, d\varphi.$$

After integration, and substituting $P = 1$ kp for P, the spring constant of one riser is obtained:

$$c_{1a} = \frac{1}{I_z E_{\mathrm{Cu}}}\left[\frac{l_1^3}{3} + r_0\, l_1^2 \frac{\pi}{2} + 2\, l_1\, r_0^2 + \frac{r_0^2}{4}\pi\right].$$

The resulting spring constant of the riser system is then:

$$c_{\mathrm{O}a} = \frac{c_{1a}}{K}.$$

$c_{\mathrm{B}a}$ is the spring constant of the winding end in the axial direction (Fig. 3):

$$c_{\mathrm{B}a} = \frac{s_t}{2\, r_t\, \pi\, v_t\, E_{\mathrm{Cu}}}.$$

The above treated computation clears up the forces corresponding to the working conditions of the commutator riser, serving, in this way, for the basis of sizing. Since, however, the relations applied were derived with a certain degree of approximation, also the procedure itself furnishes an approximate result only. The correctness of the approximation can be checked by strength measurements.

REFERENCES

1. Liska J.: Villamosgépek, V. Szerkezettan (Electrical machines, V. Constructions theory). Tankönyvkiadó, Budapest 1954.
2. Arnold-la Cour: Die Gleichstrommaschine, II. Springer Verlag, Berlin 1927.
3. Hütte, IV. A., 28. Aufl. Berlin 1957.
4. Pattantyús: Gépész- és villamosmérnökök kézikönyve (Handbook for Mechanical Engineers and Electrical Engineers) Vol. 2. Műszaki Kiadó, Budapest 1961.
5. *Красовский, Б. Н.:* Вопросы прочности электрических машин. Академия Наук СССР, Москва 1951.
6. Huszár, I. — Bodor, J.: A kommutátorzászló erőjátékának számítása. *VI. Oszt. Közl.* **34** (1964).

BERECHNUNG DES KRÄFTESPIELS EINER KOMMUTATORFAHNE

I. HUSZÁR und J. BODOR

ZUSAMMENFASSUNG

Die Aufgabe der Kommutatorfahne ist die Sicherung einer Leitverbindung zwischen den Kommutatorlamellen und den Wicklungsenden. Vom mechanischen Standpunkt gesehen ist ihre Belastung durch die Montierungsverhältnisse, ferner durch die Rotations-Krafteffekte, endlich durch Kräfte, die in Zusammenhang mit der Aufwärmung während des Betriebes auftreten, bestimmt. Der erste Faktor ist von der Herstellung abhängig, die zwei letzteren können aber auch zahlenmäßig erfaßt werden. Die während der Rotation und der Erwärmung auftretenden Kräfteverhältnisse der Fahne eines Maschinenelementen von statisch unbestimmtem Einbau, sind durch Annäherungsrechnung geklärt.

CALCUL DU JEU DE FORCES DES TALONS DE COMMUTATEURS

I. HUSZÁR et J. BODOR

RÉSUMÉ

Le talon du commutateur sert à assurer la connexion conductive entre les lames du commutateur et les extrémités de l'enroulement. Au point de vue mécanique, sa charge est déterminée par les circonstances du montage, par le système des forces survenant au cours de la rotation, enfin par les forces produites par l'échauffement pendant la marche. Le premier de ces facteurs dépend du procédé de fabrication, les deux derniers peuvent être aussi suivis numériquement. Un calcul approché permet d'expliquer le jeu des forces du talon envisagé comme élément structurel encastré statiquement indéterminé, forces qui se produisent au cours de la rotation et de l'échauffement.

РАСЧЕТ РАБОТЫ КОЛЛЕКТОРНОГО ПЕТУШКА

И. ХУСАР И Я. БОДОР

РЕЗЮМЕ

Коллекторный петушок служит для того, чтобы создать электрическую связь между коллекторными пластинами и концами обмоток. С механической точки зрения действующую на коллекторный петушок нагрузку определяют условия сборки, силовые воздействия в процессе вращения и, наконец, силы, возникающие от нагрева, происходящего во время работы машины. Первый фактор зависит от производства, а последние два фактора можно выразить численно. Силовые условия петушка, являющегося статически неопределенным установочным конструкционным элементом, при вращении и нагреве выяснены приближенными расчетами.

ANALYSIS OF THE EFFECT EXERTED BY A VARIABLE HEAT–TRANSFER COEFFICIENT UPON THE HEATING PROCESS CARRIED OUT WITH A CYLINDRICAL BODY. PART I.

A. HOFFMANN

TECHNICAL UNIVERSITY BUDAPEST

[Manuscript received July 17, 1963]

The temperature distribution in a long cylindrical body is determined for the case of a stress-relieving anneal.The heat transfer coefficient α is considered as a function of temperature. Further, the influence of both radiation and convection are taken into account. The character of the boundary value proposition is inhomogeneous and non-linear. The solution is found by linearizing the curve section by section on the basis of a resulting formula which had already been developed and published by the author.

Introduction

Generally, the parameters of heat conduction are assumed — according to classical theoretic consideration — as constants; this proved to be an exaggerated idealisation of physical reality. From a more realistic viewpoint, these parameters vary — as is stated by concrete physical measurements — in dependence on the whole physical conditions and show, in many cases of practical experience, considerable variation. This again acts effectively on the temperature distribution in the heat conducting body.

In this paper, the following problem will be solved: how will the heat distribution in the body be influenced by the variation of the heat transfer coefficient α in the case when the body and furnace are heated simultaneously. This heating process is frequently practised in industry. E.g. this method is applied in order to avoid fissures probably caused by great inner stresses of thermic origin, when a rather voluminous cylinder of alloyed steel is heat-treated.

Practically, the heat-transfer coefficient is composed of two functions. One of them is the result of the heat radiation theorem, the second one results from the convectional heat transfer:

$$\alpha\ [\mathrm{k\ cal/m^2\ h\ ^\circ C}] = \alpha_s + \alpha_c.$$

The two members are functions of the temperature of both the surface and the surroundings (the furnace). i.e.

$$a_s(\vartheta_K, \vartheta_F) = \varepsilon C_s \frac{\left(\frac{\vartheta_K(t) + 273}{100}\right)^4 - \left(\frac{\vartheta_F + 273}{100}\right)^4}{\vartheta_K(t) - \vartheta_F}$$

where the radiation coefficient of an absolutely black body $C_s = 4.96$. ε is a constant depending on the heat radiation coefficient ε_1 of the heat delivering and ε_2 of the heat receiving surface respectively, and on the dimensions of both surfaces (F_1 and F_2). Practically, in our later calculations as $\varepsilon = 0.87$.

The heat convection coefficient α_c can be expressed by means of an exponential function:

$$Nu = C\, Gr^n$$

where G_r is the dimensionless Grashof number in explicit form:

$$Gr = \frac{gl^3 \Delta\vartheta \beta}{\nu^2}$$

where l is the characteristic dimension of heat flow (in this case the diameter of the cylinder), ν is the kinetic viscosity, $\beta = 1/T$ is the dilatation coefficient, $\Delta\vartheta$ is the heat difference between the body surface and the ambient gas.

In our special case, after due simplifications, we obtain the following formula:

$$\alpha_c = a(\Delta\vartheta)^{1/3} \qquad (\Delta\vartheta = \vartheta_K - \vartheta_F)$$

where $a \approx 1.7$

Contrary to what has been described in [5], for the heating process in our special case, both members of the heat-transfer coefficient are to be taken into account (cf. Table VI).

1. Solution of the differential equations by the linearization of the two members of the heat-transfer coefficient

In view of the relatively great length of the steel bar, as compared with its diameter, one can calculate by assuming a bar of infinite length. The differential equation is a dimensionless form and for a co-ordinate system pertaining to the cylinder goes as follows:

$$\frac{\partial^2 \vartheta}{\partial \varrho^2} + \frac{1}{\varrho} \frac{\partial \vartheta}{\partial \varrho} - A \frac{\partial \vartheta}{\partial t} \equiv \mathbf{D}\{\vartheta\} = 0, \qquad A = R^2 \frac{\gamma c}{\lambda}, \qquad 0 \leq \varrho \leq 1 \tag{1a}$$

The initial condition is

$$\vartheta(\varrho, 0) = f(\varrho) \tag{1b}$$

and the third boundary condition:

$$\left.\frac{\partial\vartheta}{\partial\varrho}\right|_F = R\frac{a}{\lambda}\left[\vartheta_K(t) - \vartheta_F\right]. \tag{1c}$$

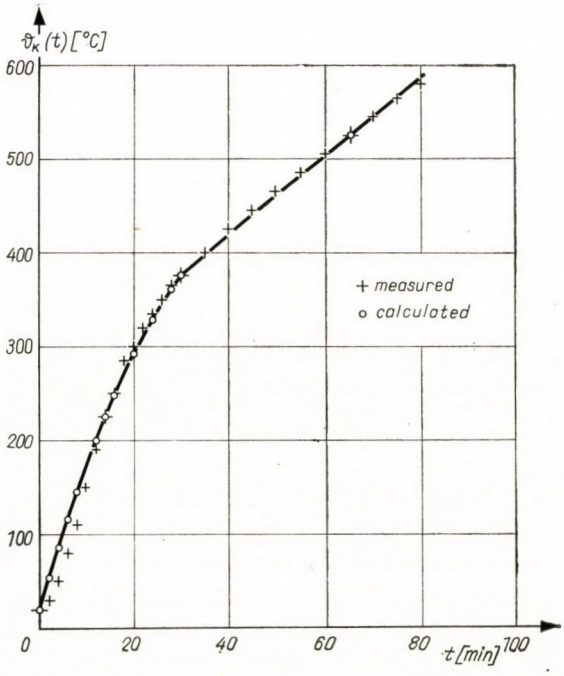

Fig. 1. Furnace-temperature as function of time

By putting the function:

$$a = a_s(\vartheta_K, \vartheta_F) + a_c(\vartheta_K, \vartheta_F),$$

we obtain

$$\left.\frac{\partial\vartheta}{\partial\varrho}\right|_F = \frac{R}{\lambda}\varepsilon c_s\left[\left(\frac{\vartheta_K(t)+273}{100}\right)^4 - \left(\frac{\vartheta_F+273}{100}\right)^4\right] + \frac{R}{\lambda}a\left[\vartheta_K(t) - \vartheta_F\right]^{4/3}.$$

Adopting the designations

$$\frac{R}{\lambda}\varepsilon c_s\left(\frac{\vartheta_K(t)+273}{100}\right)^4 = \vartheta_{K1}(t)$$

and

$$\frac{R}{\lambda}\varepsilon c_s\left(\frac{\vartheta_F+273}{100}\right)^4 = g_1(\vartheta_F),$$

the latter one shall be linearized within the determined interval. Thus,

$$g_1(\vartheta_F) \approx l_1(\vartheta_F) = c_1 \vartheta_F + c_0 .$$

The function

$$\frac{R}{\lambda} a \left[\vartheta_K(t) - \vartheta_F\right]^{4/3}$$

with two variables shall be designated as g_2 $(\vartheta_K, \vartheta_F)$, and now, by choosing an acceptable interval for the variables ϑ_K, ϑ_F, this function will be equalized by putting a plane

$$g_2(\vartheta_K, \vartheta_F) \approx l_2(\vartheta_K, \vartheta_F) = k_2 \vartheta_K + k_1 \vartheta_F + k_0 .$$

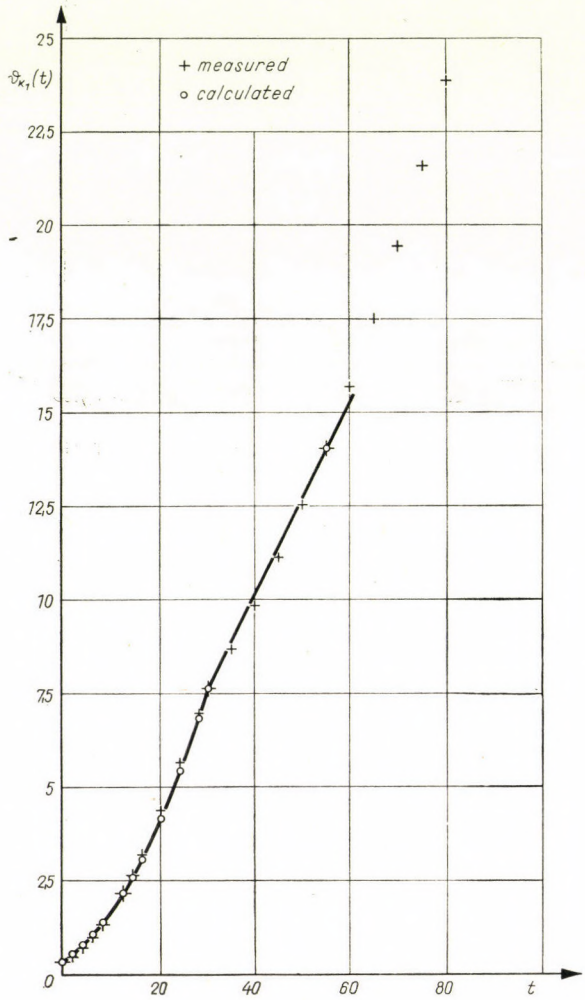

Fig. 2. The modified function furnace-temperature versus time

The suitableness of the equalization will be strengthened when the "zone of heating" of the plane $(\vartheta_K, \vartheta_F)$ is considered as the range of equalization.

On this basis, the boundary condition takes the form:

$$\left.\frac{\partial\vartheta}{\partial\varrho}\right|_F = \vartheta_{K1}(t) - c_1\,\vartheta_F - c_0 + k_2\,\vartheta_K(t) + k_1\,\vartheta_F + k_0 = \vartheta_{K2}(t) - \beta\vartheta_F$$

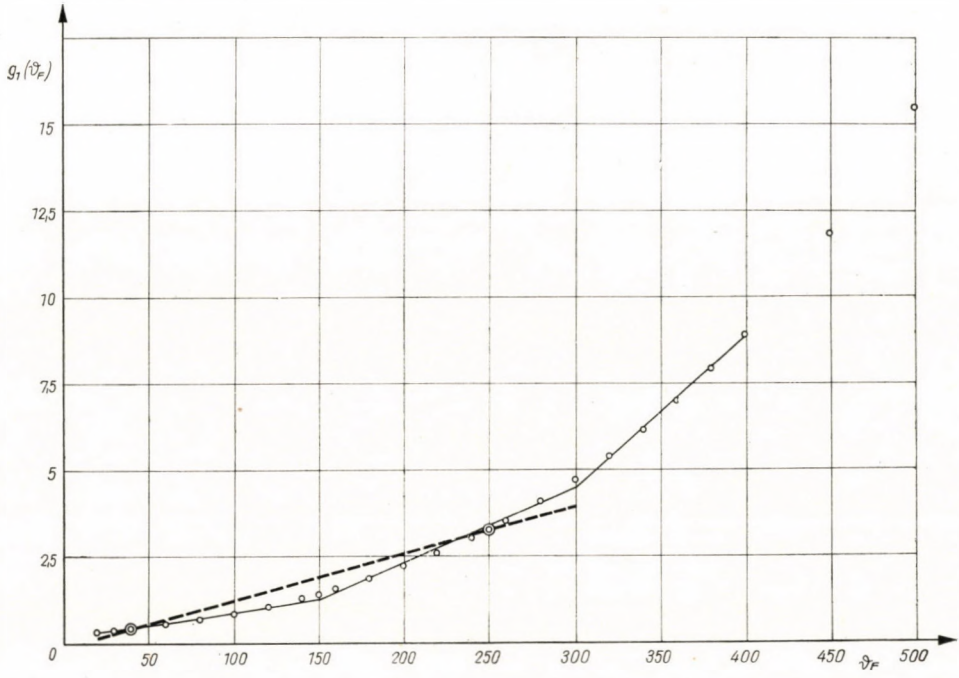

Fig. 3. Linearization of the auxlliary function $g_1(\vartheta_F)$

where

$$\vartheta_{K2}(t) = \vartheta_{K1}(t) + k_2\,\vartheta_K(t) - c_0 + k_0\,, \qquad \beta = c_1 - k_1\,,$$

and thus:

$$\left.\frac{\partial\vartheta}{\partial\varrho}\right|_F + \beta\vartheta_F \equiv \mathbf{L}\{\vartheta\}_F = \vartheta_{K2}(t). \tag{2}$$

In following the Duhamel theorem, as the solution for the differential equation will be chosen as follows:

$$\vartheta = \vartheta_1(\varrho, t) + \int_{\tau=0}^{t} \frac{d\varphi}{d\tau}\,\vartheta_2(\varrho, t-\tau)\,d\tau. \tag{3}$$

For the functions ϑ_1, ϑ_2 the following propositions will apply:

$$\begin{aligned} &\mathbf{D}\{\vartheta_1\} = 0\,, \qquad \vartheta_1(\varrho,0) = f(\varrho)\,, \qquad \mathbf{L}\{\vartheta_1\}_F = 0\,; \\ &\mathbf{D}\{\vartheta_2\} = 0\,, \qquad \vartheta_2(\varrho,0) = 0\,, \qquad \mathbf{L}\{\vartheta_2\}_F = 1\,. \end{aligned} \tag{4}$$

With these stipulations, the function $\vartheta(\varrho, t)$ as the solution for the differential equation will comply with both the original differential equation and the initial conditions. The function $\varphi(t)$ must now be determined so as to reach conformity with the boundary condition. Taking into account (2), (3) and (4), the following equation will result:

$$\begin{aligned} \mathbf{L}\{\vartheta\}_F &= \mathbf{L}\left\{\vartheta_1 + \int_{\tau=0}^{t} \frac{d\varphi}{d\tau}\,\vartheta_2(\varrho, t-\tau)\,d\tau\right\}_F = \mathbf{L}\{\vartheta_1\}_F + \\ &+ \mathbf{L}\left\{\int_{\tau=0}^{t} \frac{d\varphi}{d\tau}\,\vartheta_2(\varrho, t-\tau)\,d\tau\right\}_F = \mathbf{L}\left\{\int_{\tau=0}^{t} \frac{d\varphi}{d\tau}\,\vartheta_2(\varrho, t-\tau)d\tau\right\}_F = \\ &= \int_{\tau=0}^{t} \frac{d\varphi}{d\tau}\,\mathbf{L}\{\vartheta_2(\varrho, t-\tau)\}_F\,d\tau = \int_{\tau=0}^{t} \frac{d\varphi}{d\tau}\,d\tau = \vartheta_{K2}(t)\,. \end{aligned}$$

Assuming

$$\vartheta_{K2}(t) = \vartheta_{K2}(0) + \Delta(t),$$

the function $d\varphi/d\tau$ shall be determined as follows:

$$\frac{d\varphi}{d\tau} = \delta(\tau)\,\vartheta_{K2}(0) + \frac{d\Delta(\tau)}{d\tau}\,,$$

because

$$\int \frac{d\varphi}{d\tau}\,d\tau = \vartheta_{K2}(t)\,,$$

where $\delta(\tau)$ is the delta of Dirac. With all these assumptions, the solution (3) of the differential equation (1) will take the form:

$$\vartheta(\varrho, t) = \vartheta_1(\varrho, t) + \vartheta_{K2}(0)\,\vartheta_2(\varrho, t) + \int_{\tau=0}^{t} \frac{d\Delta(\tau)}{d\tau}\,\vartheta_2(\varrho, t-\tau)\,d\tau\,. \tag{5}$$

In (4) the function $\vartheta_1(\varrho, t)$ can be determined — by relying on the Bernoulli-Fourier method — as follows:

$$\vartheta_1(\varrho, t) = \sum_{n=1}^{\infty} a_n\,J_0(\nu_n\,\varrho)\,\exp\left(-\frac{\nu_n^2}{A}\,t\right)$$

where J_0 stands as the first kind of Bessel function of zero order. The eigenvalue series $\{\nu_n\}$ can be computed by applying the eigenvalue equation

$$\nu_n J_1(\nu_n) = \beta J_0(\nu_n) \qquad (n \geq 1) \tag{6}$$

obtained on the basis of the boundary condition (4). The coefficients a_n will be determined — by considering the orthogonal relations of the Bessel-functions — on the basis of the initial proposition (4).

In order to form the function $\vartheta_2(\varrho, t)$ we may make analogous steps as were made for ϑ_1. We then shall obtain the following equations:

$$\vartheta_1(\varrho, t) = 2 \sum_{n=1}^{\infty} \frac{\int_{\varrho=0}^{1} f(\varrho)\, \varrho\, J_0(\nu_n \varrho)\, d\varrho}{\left(1 + \frac{\beta^2}{\nu_n^2}\right) J_0^2(\nu_n)} J_0(\nu_n \varrho) \exp\left(-\frac{\nu_n^2}{A} t\right),$$

$$\vartheta_2(\varrho, t) = \frac{1}{\beta} - 2 \sum_{n=1}^{\infty} \frac{J_0(\nu_n \varrho)}{(\nu_n^2 + \beta^2)\, J_0(\nu_n)} \exp\left(-\frac{\nu_n^2}{A} t\right).$$

Consequently, by using the above functions, the solution for the differential equation (1) will be:

$$\begin{aligned} \vartheta(\varrho, t) = {} & \frac{1}{\beta} \vartheta_{K2}(t) + 2 \sum_{n=1}^{\infty} \frac{\int_{\varrho=0}^{1} f(\varrho)\, \varrho\, J_0(\nu_n \varrho)\, d\varrho}{\left(1 + \frac{\beta^2}{\nu_n^2}\right) J_0^2(\nu_n)} J_0(\nu_n \varrho) \exp\left(-\frac{\nu_n^2}{A} t\right) - \\ & - 2\, \vartheta_{K2}(0) \sum_{n=1}^{\infty} \frac{J_0(\nu_n \varrho)}{(\nu_n^2 + \beta^2)\, J_0(\nu_n)} \exp\left(-\frac{\nu_n^2}{A} t\right) - \\ & - 2 \sum_{n=1}^{\infty} \frac{J_0(\nu_n \varrho)}{(\nu_n^2 + \beta^2)\, J_0(\nu_n)} \int_{\tau=0}^{t} \frac{d\Delta(\tau)}{d\tau} \exp\left(-\frac{\nu_n^2}{A}(t - \tau)\right) d\tau. \end{aligned} \tag{7}$$

At the beginning of the process one may assume the heat distribution to be constant

$$f(\varrho) = \vartheta_a.$$

Consequently by considering the eigenvalue according to (6), the integral in the second member of (7) can be put as follows:

$$\int_{\varrho=0}^{1} \varrho\, J_0(\nu_n \varrho)\, d\varrho = \beta \frac{J_0(\nu_n)}{\nu_n^2}. \tag{8}$$

Finally, by using the above expressions, the solutions of (7) will be:

$$\begin{aligned} \vartheta(\varrho, t) = {} & \frac{1}{\beta} \vartheta_{K2}(t) - 2\, [\vartheta_{K2}(0) - \beta \vartheta_a] \sum_{n=1}^{\infty} \frac{J_0(\nu_n \varrho)}{(\nu_n^2 + \beta^2)\, J_0(\nu_n)} \exp\left(-\frac{\nu_n^2}{A} t\right) - \\ & - 2 \sum_{n=1}^{\infty} \frac{J_0(\nu_n \varrho)}{(\nu_n^2 + \beta^2)\, J_0(\nu_n)} \int_{\tau=0}^{t} \frac{d\Delta(\tau)}{d\tau} \exp\left(-\frac{\nu_n^2}{A}(t - \tau)\right) d\tau. \end{aligned} \tag{9}$$

Now the linearization (2) of the boundary condition as given under (1c), can be considered as valid (i.e. as a quite good approximation) only in a predetermined interval.

At the very moment, when the temperature ϑ exceeds this predetermined interval, the whole function of linearization has to be modified. In order to facilitate the calculation of $\vartheta_{k2}(t)$ this function will be approximated by means of a 2nd grade polynomial in every one of the sections. Thus, principally we will obtain two different series of sections with non-identic divisions. However it seems to be reasonable to make the limit points, originating from linearization (2), common for both sectioning steps. Thus a new function $\vartheta_{k2}^{(i)}(t)$ can always be inserted without further difficulties.

Now the boundary condition (2) can be determined in every one of the sections as follows:

$$\left.\frac{\partial\vartheta}{\partial\varrho}\right|_F + \beta_j\,\vartheta_F \equiv \mathbf{L}_j\{\vartheta\}_F = \vartheta_{K2}^{(i)}(t)\,; \qquad \begin{array}{l} j = 0, 1, 2, \ldots N\,, \\ i = 0, 1, 2, \ldots M\,. \end{array}$$

Here the variations of j and i are quite independent of each other, but only a coupling of both, with the above mentioned physical conditions, is valid. (For further details see [5]). For the sake of simplification, it is advisable to linearize along a larger section, while the functions $\vartheta_{k2}^{(i)}(t)$ may be formed for shorter sections without causing further difficulties in our calculation. Therefore:

$$\vartheta_{K2}(t) = \vartheta_{K2}^{(i)}(t) \approx a_{2i}\,t^2 + a_{1i}\,t + a_{0i}\,,$$

$$(t_{1i} \leqq t \leqq t_{1,i+1})\,, \qquad t_{10} = 0\,, \qquad i = 0, 1, 2, \ldots N\,,$$

and

$$\mathbf{L}\{\vartheta\}_F = \mathbf{L}_j\{\vartheta\}_F = \left.\frac{\partial\vartheta}{\partial\varrho}\right|_F + \beta_j\,\vartheta_F$$

$$(t_{2j} \leqq t \leqq t_{2,j+1})\,, \qquad t_{20} = 0\,, \qquad j = 0, 1, 2, \ldots M\,.$$

If every one of the dividing points t_{2j} coincides with one of the t_{2i}-s points (assumption that seems to be — from what has been said above — most useful) simply the symbol t_i can readily be substituted for t_{2i} and only the common dividing points should be always borne in mind.

The solution function $\vartheta(\varrho, t)$ when considered in every one of the sections, may be designated as $\vartheta^i(\varrho, t)$ and thus, the solution for the first section will be:

$$\vartheta^{(0)}(\varrho, t) = \frac{1}{\beta_0}\,\vartheta_{K2}^{(0)}(t) - 2\,[\vartheta_{K2}^{(0)}(0) - \beta_0\,\vartheta_a] \sum_{n=1}^{\infty} \frac{J_0(\nu_n\,\varrho)}{(\nu_n^2+\beta_0^2)\,J_0(\nu_n)} \exp\left(-\frac{\nu_n^2}{A}\,t\right) -$$

$$-\,2\,A \sum_{n=1}^{\infty} \frac{J_0(\nu_n\,\varrho)}{\nu_n^2(\nu_n^2+\beta_0^2)\,J_0(\nu_n)} \left[2a_{20}\,t + A_n^{(0)}\left(1 - \exp\left(-\frac{\nu_n^2}{A}\,t\right)\right)\right],$$

$$A_n^{(0)} = a_{10} - 2\,a_{20}\frac{A}{\nu_n^2}\,, \qquad (0 \leqq t \leqq t_1)\,.$$

The second section has to be determined by maintaining that $\mathbf{L}_0\{\vartheta\}$ is valid, but with $\vartheta_{k2}(t)$ already changing.

At the beginning when the temperature division is changing, i.e. the moment t_1

$$\vartheta^{(0)}(\varrho, t_1) = f_1(\varrho)\,.$$

By using this formula for (7) and considering (8), further on the basis of the orthogonality of Bessel functions, and applying the eigenvalue equation (6), we obtain:

$$\int_{\varrho=0}^{1} \varrho J_0^2(\nu_n\,\varrho)\,d\varrho = \frac{1}{2}\,J_0^2(\nu_n)\left[1 + \frac{\beta^2}{\nu_n^2}\right], \tag{10}$$

and the solution for the second section — $(t_1 \leqq t \leqq t_2)$ — will be:

$$\begin{aligned}
\vartheta^{(1)}(\varrho, t) = {} & \frac{1}{\beta_0}\,\vartheta_{K2}^{(1)}(t) - 2\,[\vartheta_{K2}^{(0)}(0) - \\
& - \beta_0\,\vartheta_a]\sum_{n=1}^{\infty}\frac{J_0(\nu_n\,\varrho)}{(\nu_n^2 + \beta_0^2)\,J_0(\nu_n)}\exp\left(-\frac{\nu_n^2}{A}\,t\right) - \\
& - 2\,A\sum_{n=1}^{\infty}\frac{J_0(\nu_n\,\varrho)}{\nu_n^2(\nu_n^2 + \beta_0^2)\,J_0(\nu_n)}\left\{\left[2\,a_{20}\,t_1 + \right.\right. \\
& \left. + A_n^{(0)}\left(1 - \exp\left(-\frac{\nu_n^2}{A}\,t_1\right)\right)\right]\exp\left(-\frac{\nu_n^2}{A}\,(t - t_1)\right) + \\
& \left. + 2\,a_{21}(t - t_1) + A_n^{(1)}\left[1 - \exp\left(-\frac{\nu_n^2}{A}\,(t - t_1)\right)\right]\right\},
\end{aligned}$$

$$A_n^{(1)} = 2\,a_{21}\,t_1 + a_{11} - 2\,a_{21}\frac{A}{\nu_n^2}\,; \qquad \vartheta_{K2}^{(0)}(t_1) = \vartheta_{K2}^{(1)}(t).$$

For the next section —, because of the changed linearization function in the boundary conditions (2), in the eigenvalue equation (6) the equality $\beta = \beta_1$ will hold true. From this a new series of values of $\{\nu_m\}$ will follow. As for the heat distribution at the beginning of the third section we may write:

$$\vartheta^{(1)}(\varrho, t_2) = f_2(\varrho)\,, \qquad (t_{21} = t_{12} = t_2)\,.$$

By substituting this into solution (7) and considering the equality in (8), and because of the diversity between the eigenvalueseries $\{\nu_n\}$ and $\{\nu_m\}$ the equality

$$\int_{\varrho=0}^{1} \varrho J_0(\nu_n\,\varrho) J_0(\nu_m\,\varrho)\,d\varrho = \frac{\beta_0 - \beta_1}{\nu_n^2 - \nu_m^2}\,J_0(\nu_n)\,J_0(\nu_m)$$

has to be applied instead of the orthogonality of Bessel-function. On this basis the solution in the third section will be:

$$\vartheta^{(2)}(\varrho, t) = \frac{1}{\beta_1} \vartheta_{K2}^{(2)}(t) + 2 \left[\frac{\beta_1}{\beta_0} \vartheta_{K2}^{(1)}(t_2) - \right.$$

$$\left. - \vartheta_{K2}^{(2)}(t_2) \right] \sum_{m=1}^{\infty} \frac{J_0(\nu_m \varrho)}{(\nu_m^2 + \beta_1^2) J_0(\nu_m)} \exp\left(- \frac{\nu_m^2}{A} (t - t_2) \right) -$$

$$- 4 \left[\vartheta_{K2}^{(0)}(0) - \beta_0 \vartheta_a \right] (\beta_0 - \beta_1) \cdot$$

$$\cdot \sum_{m=1}^{\infty} \sum_{n=1}^{\infty} \frac{J_0(\nu_m \varrho) \exp\left(- \frac{\nu_n^2}{A} t_2 - \frac{\nu_m^2}{A} (t - t_2) \right)}{\left(1 + \frac{\beta_1^2}{\nu_m^2} \right) (\nu_n^2 - \nu_m^2) (\nu_n^2 + \beta_0^2) J_0(\nu_m)} - 4 A (\beta_0 - \beta_1) \cdot$$

$$\cdot \sum_{m=1}^{\infty} \sum_{n=1}^{\infty} \frac{J_0(\nu_m \varrho) \exp\left(- \frac{\nu_m^2}{A} (t - t_2) \right)}{\left(1 + \frac{\beta_1^2}{\nu_m^2} \right) \nu_n^2 (\nu_n^2 - \nu_m^2) (\nu_n^2 + \beta_0^2) J_0(\nu_m)} \left\{ \left[2 a_{20} t_1 + \right. \right.$$

$$\left. + A_n^{(0)} \left(1 - \exp\left(- \frac{\nu_n^2}{A} t_1 \right) \right) \right] \exp\left(\frac{\nu_n^2}{A} (t_1 - t_2) \right) + 2 a_{21} (t_2 - t_1) +$$

$$\left. + A_n^{(1)} \left[1 - \exp\left(\frac{\nu_n^2}{A} (t_1 - t_2) \right) \right] \right\} - 2A \sum_{m=1}^{\infty} \frac{J_0(\nu_m \varrho)}{\nu_m^2 (\nu_m^2 + \beta_1^2) J_0(\nu_m)} \cdot$$

$$\cdot \left\{ 2 a_{22} (t - t_2) + A_m^{(0)} \left[1 - \exp\left(\frac{\nu_m^2}{A} (t_2 - t) \right) \right] \right\}.$$

2. Estimation of error

In elaborating the solution, the boundary condition (1) was linearized and thus equation (2) was obtained. The error of this calculation can be so estimated that the functions that should be linearized will be confined between 2 parallel straights or planes, respectively, and the new boundary condition will be considered as the basis of the calculation. Thus the upper and lower limits of the solution corresponding to the linearization are obtained, and the difference between these limits represents the maximum estimated error.

Therefore, the function $\vartheta_{K2}(t)$ on the right side of (2) will be substituted, for the upper limit, by $\vartheta_{K2}^{(\sigma)}(t)$ and, for the lower limit, by $\vartheta_{K2}^{(l)}(t)$.

Consequently, the estimated error as a function of place and time will be expressed as follows:

$$E(\varrho, t) = \vartheta^{(\sigma)} - \vartheta^{(l)} = \frac{1}{\beta}\left(\vartheta_{K2}^{(\sigma)} - \vartheta_{K2}^{(l)}\right) - 2\left[\vartheta_{K2}^{(\sigma)}(0) - \vartheta_{K2}^{(l)}(0) - \beta\vartheta_a\right] \cdot$$

$$\cdot \sum_{n=1}^{\infty} \frac{J_0(\nu_n \varrho)}{(\nu_n^2 + \beta^2) J_0(\nu_n)} \exp\left(-\frac{\nu_n^2}{A} t\right) - 2 \sum_{n=1}^{\infty} \frac{J_0(\nu_n \varrho)}{(\nu_n^2 + \beta^2) J_0(\nu_n)} \cdot$$

$$\cdot \int_{\tau=0}^{t} \frac{d}{d\tau}\left(\vartheta_{K2}^{(\sigma)} - \vartheta_{K2}^{(l)}\right) \exp\left(-\frac{\nu_n^2}{A}(t - \tau)\right) d\tau \,.$$

Because of the assumed parallelity this method is advantageous, as the eigenvalues (ν_n) remain the same; consequently, the error function can be obtained directly from the solution of the differential equation, resulting from the linearized boundary condition.

The estimation can be made more accurate when the division in sections is applied; besides, this method of estimation can easily be followed.

3. Application

Object of the present examination is the annealing heat treatment of a long steel bar having a diameter of 8 cm as described in [5]. Variations of the furnace temperature are shown in Table I. According to Fig. 1, the plotted points of measured values* form for the first 10 . . . 15 minutes — contrary to the calculated curve — a convex line, when seen from below. This seems to be probable, because, in a furnace heated by means of electric resistance, the heat which was developed during the first period of time, serves to heat the wires. In our case, this could be disregarded, since it does not bear upon the heat distribution in the material. Besides, one will not meet with any difficulty when taking it into account.

The approximating polynomials are for following:

$$\vartheta_K(t) \approx -0.176\, t^2 + 17.101\, t + 20 \qquad (0 \leqq t \leqq t_1)$$

$$\vartheta_K(t) \approx 4.286\, t + 246.429 \qquad (t_1 \leqq t \leqq t_2)$$

$$\vartheta_{K1}(t) \approx 0.005\, t^2 + 0.094\, t + 0.318 \qquad (0 \leqq t \leqq t_1)$$

$$\vartheta_{K1}(t) \approx 0.257\, t - 0.095 \qquad (t_1 \leqq t \leqq t_2)$$

$$l_1(\vartheta_F) = 0.0134\, \vartheta_F - 0.1222 \qquad (0 \leqq \vartheta_F \leqq 300)$$

$$l_2(\vartheta_K, \vartheta_F) = 0.0102\, \vartheta_K - 0.0108\, \vartheta_F + 0.0121 \qquad (0 \leqq \vartheta_F \leqq 300).$$

(For Tables I, II, III, IV and the Figures 1, 2 and 3;

$$g_2 = 0.017\,(\vartheta_K - \vartheta_F)^{4/3}; \qquad t = t\ [\text{min}].$$

With the polynomials as established above, the obtained constants are:

$$\beta_0 = 0.0242, \qquad t_1 = 30, \qquad t_2 = 60, \qquad R = 0.04\ [\text{m}].$$

* Measurements have been carried out in the Laboratory of the Department for Mechanical Technology of the Technical University Budapest.

Table I

Furnace temperature as function of time

t [min]	ϑ_{Km} [°C]	ϑ_K [°C]	ϑ_{K1}
0	20	20	0.312
2	30	53.5	0.490
4	50	85.6	0.714
6	80	116.3	0.991
8	110	145.6	1.325
12	190	200	2.160
14	225	225	2.654
16	250	248.7	3.197
20	300	291.8	4.391
24	335	329.3	5.679
28	365	361.2	6.981
30	375	375	7.609
35	400	396.4	8.664
40	425	417.8	9.827
45	445	439.3	11.108
50	465	460.7	12.505
55	485	482.1	14.029
60	505	503.6	15.696
65	525	525	17.499
70	545	546.4	19.453
75	565	568	21.587
80	580	589.3	23.858
85	595	610.7	26.316

Table II

The auxiliary functions g_1 and l_1 respectively, depending on the surface temperature

ϑ_F [°C]	$g_1(\vartheta_F)$	$l_1(\vartheta_F)$
20	0.318	0.146
30	0.364	0.280
40	0.414	0.414
60	0.531	0.682
80	0 670	0.950
100	0.835	1.218
120	1.029	1.486
140	1.255	1.755
150	1.382	1.889
160	1.517	2.023
180	1.817	2.291
200	2.160	2.559
220	2.549	2.827
240	2.989	3.095
250	3.229	3.229
260	3.483	3.363
280	4.036	3.631
300	4.652	3.899
320	5.336	4.167
340	6.093	4.435
360	6.928	4.704
380	7.846	4.972
400	8.852	5.240
450	11.791	5.910
500	15.407	6.580

Constants referring to the material:

$$\gamma = 7700\ [\mathrm{kg/m^3}], \qquad \lambda = 40\ [\mathrm{kcal/m\ h\ °C}], \qquad C = 0.115\ [\mathrm{kcal/kg\ °C}].$$

The variation of the heat transfer coefficient α during the heating process is relevant (Fig. 5, Table VI); therefore, results calculated with α = constant greatly differ from values obtained by more accurate calculations taking the variable α into account (Table VII, Fig. 6).

The heat distribution on the cylinder surface and along the center line is plotted in Fig. 4 in accordance with Table V.

An approximate estimation of the deviation between the two methods of calculation can easily be obtained by introducing a well defined average value of the temperature, on the basis of the following equation:

$$\int_{\varphi=0}^{2\pi} \int_{\varrho=0}^{1} \vartheta(\varrho, t)\, \varrho d\varrho d\varphi = \tilde{\vartheta}(t) \int_{\varphi=0}^{2\pi} \int_{\varrho=0}^{1} \varrho\, d\varrho\, d\varphi\,,$$

Table III

The auxiliary function g_2 depending on the temperature difference

$\vartheta_K - \vartheta_F$ [°C]	$g_2(\vartheta_K, \vartheta_F)$
20	0.0923
40	0.233
60	0.399
80	0.586
100	0.789
150	1.355
200	1.988
250	2.677
300	3.414
350	4.193
400	5.010
450	5.862
500	6.746

Table IV

The auxiliary functions g_2 and l_2 with two variables

ϑ_K [°C]	ϑ_F [°C]	$g_2(\vartheta_K, \vartheta_F)$	$l_2(\vartheta_K, \vartheta_F)$
200	50	1.355	1.509
200	100	0.789	0.970
200	200	0	0.109
300	100	1.988	1.988
300	150	1.355	1.449
300	200	0.789	0.910
300	300	0	0.169
400	100	3.414	3.006
400	200	1.988	1.928
400	300	0.789	0.849
400	400	0	−0.229
500	100	5.010	4.024
500	200	3.414	2.946
500	300	1.988	1.868
500	400	0.789	0.789
500	500	0	−0.289
600	100	6.746	5.042
600	200	5.010	3.964
600	300	3.414	2.886
600	400	1.988	1.807
600	500	0.789	0.729
600	600	0	0.349

and the defined average value of temperature is

$$\tilde{\vartheta}(t) = 2\int_{\varrho=0}^{1} \vartheta(\varrho, t)\, \varrho\, d\varrho.$$

Carrying out the integration on both sides of the differential equation relating to the cross-section of the cylinder (local average calculation according to ϱ)

$$\int_{\varphi=0}^{2\pi}\int_{\varrho=0}^{1}\left[\frac{\partial}{\partial\varrho}\left(\frac{\partial\vartheta}{\partial\varrho}\right)+\frac{1}{\varrho}\frac{\partial\vartheta}{\partial\varrho}\right]\varrho\, d\varrho\, d\varphi = A\frac{d}{dt}\int_{\varphi=0}^{2\pi}\int_{\varrho=0}^{1}\vartheta(\varrho,t)\,\varrho\, d\varrho\, d\varphi.$$

After integrating the left side, and by introducing the average temperature on the right side, we obtain:

$$\left.\frac{\partial\vartheta}{\partial\varrho}\right|_{\varrho=1} = \frac{A}{2}\,\frac{d\tilde{\vartheta}}{dt}\,.$$

By making use of the boundary condition (2), the equation is obtained:

$$\frac{d\tilde{\vartheta}}{dt} + \frac{2}{A}\beta\vartheta_F = \frac{2}{A}\vartheta_{K2}(t).$$

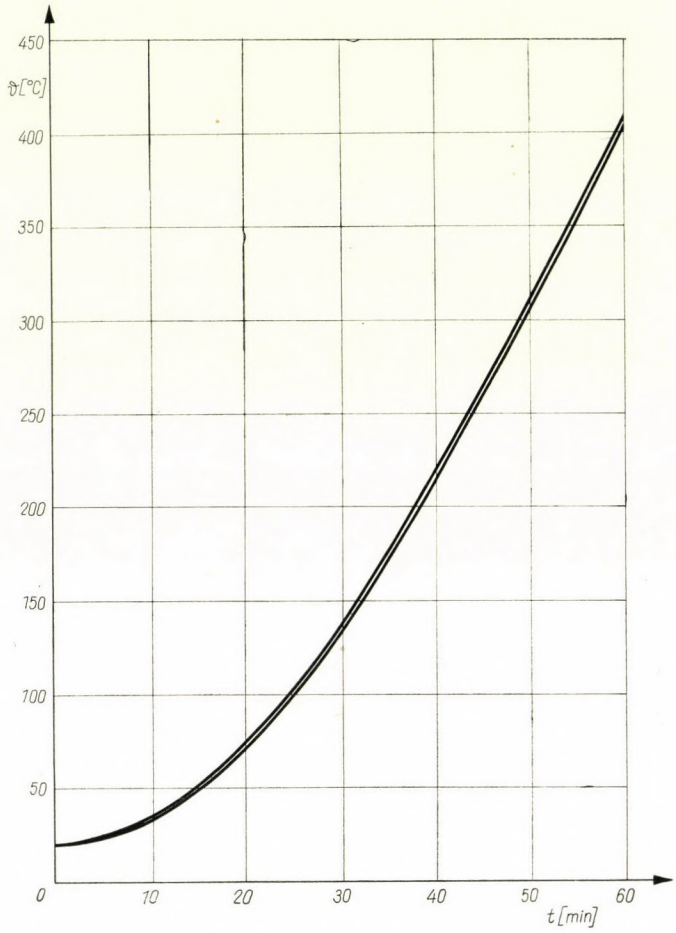

Fig. 4. Distribution of temperature on the sample surface and in the centre line

In substituting $\tilde{\vartheta}$ for ϑ_F, the approximating differential equation for $\tilde{\vartheta}$ runs as follows:

$$\frac{d\tilde{\vartheta}}{dt} + \frac{2}{A}\beta\tilde{\vartheta} = \frac{2}{A}\vartheta_{K2}(t).$$

For various values of the heat-transfer coefficient α, the numerical results of the solved differential equation are gathered together in Table VII and plotted in Fig. 6.

We made simplifications only to facilitate the computing process. Nevertheless, the deviations between the two calculating methods are obvious. The temperature distribution calculated with a variable α according to Fig. 6 assumes the same values as obtained with $\tilde{\alpha}$ only after a period of time of abt. 56 min, and in the continuation the first surpasses the second one. This is rather in conformity with the equalization of the effect of the heat-transfer coefficient α when considered differently.

Table V

Distribution of temperature in the body

t [min]	ϑ_0 [°C]	ϑ_F [°C]	ϑ [°C]
0	20	20	20
2	20.7	21	20.8
4	22.3	22.9	22.6
6	25	25.8	25.4
8	28.6	29.8	29.2
10	33.3	34.7	34.1
15	49.3	51.3	50.5
20	71.6	74.3	73.2
25	100.2	103.6	102.3
30	135.1	139.2	137.7
35	174.2	178.6	177.5
40	216.2	220.8	219.8
45	260.3	265.2	264.2
50	306.4	311.4	310.4
55	354.2	359.4	358.4
60	403.5	408.8	407.9

Table VI

Heat-transfer coefficient α as function of the furnace temperature and surface temperature

t [min]	ϑ_K [°C]	ϑ_F [°C]	α_c	α_s	α [kcal/m² h °C]
0	20	20	0	0	0
2	53.5	21	5.423	5.165	10.588
4	85.6	22.9	6.749	6.106	12.855
6	116.3	25.8	7.631	7.150	14.781
8	145.6	29.8	8.282	8.307	16.589
10	172.8	34.7	8.787	9.541	18.328
15	236.9	51.3	9.697	13.144	22.841
20	291.8	74.3	10.224	17.692	27.916
25	337.3	103.6	10.470	21.900	32.370
30	375	139.2	10.503	26.983	37.486
35	396.4	178.6	10.227	31.540	41.767
40	417.8	220.8	9.892	36.856	46.748
45	439.3	265.2	9.493	43.010	52.503
50	460.7	311.4	9.019	50.043	59.062
55	482.1	359.4	8.447	58.083	66.530
60	503.6	408.8	7.752	67.209	74.961

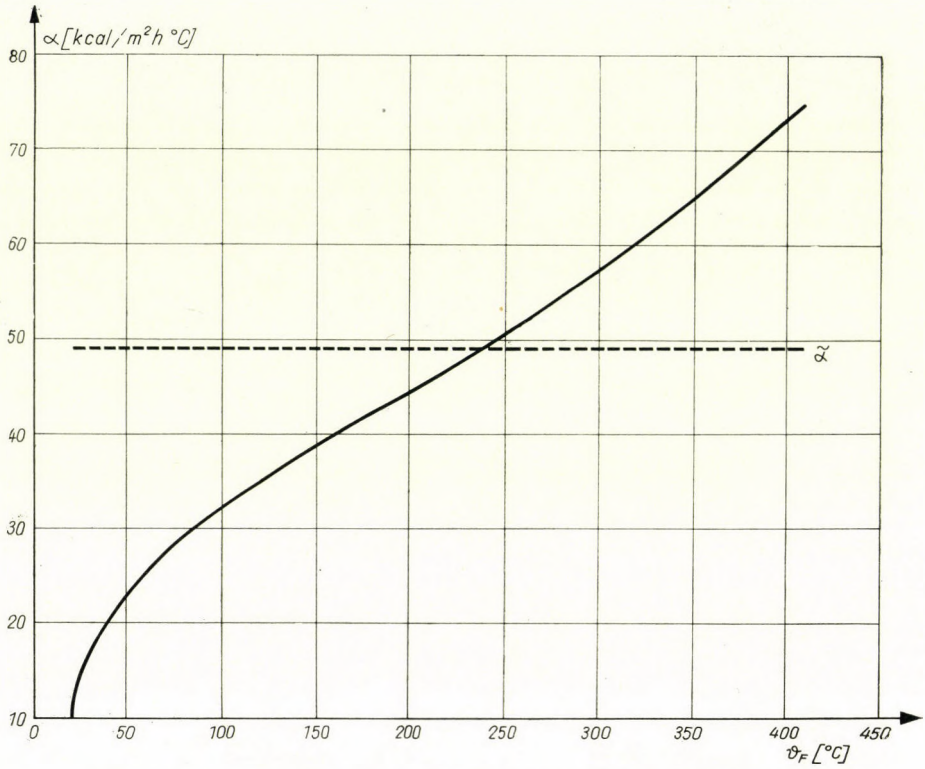

Fig. 5. The heat-transfer coefficient α as a function of surface temperature

Table VII

Approximate values of the average temperature as function of time, calculated with various values of α

t [min]	$\bar{\vartheta}_{\alpha=\alpha(\vartheta_K+\vartheta_F)}$ [°C]	$\bar{\vartheta}_{\tilde{\alpha}=49}$ [°C]	$\bar{\vartheta}_{\alpha=81}$ [°C]	t [min]	$\bar{\vartheta}_{\alpha=\alpha(\vartheta_K,\vartheta_F)}$ °C	$\bar{\vartheta}_{\tilde{\alpha}=49}$ °C	$\bar{\vartheta}_{\alpha=81}$ °C
0	20	20	20	25	102.3	161.1	210.5
1	20.3	20.4	20.6	30	137.7	201.5	257.3
2	20.8	21.5	22.4	35	177.5	239.4	298.2
4	22.6	25.7	29.2	40	219.8	274.0	332.9
6	25.4	32.4	39.4	45	264.2	305.8	363.5
8	29.2	41.1	52.4	50	310.4	335.5	391.1
10	34.1	51.5	67.6	55	358.4	363.5	416.8
15	50.5	83.5	112.1	60	407.9	390.2	441.1
20	73.2	121.0	161.1				

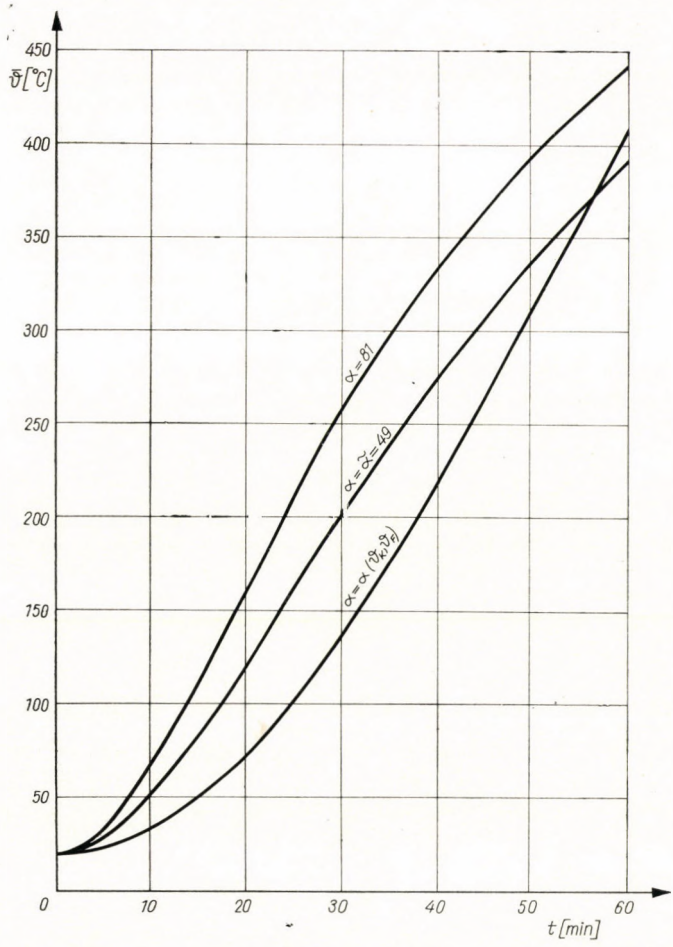

Fig. 6. Approximate course of the average temperature of the body

REFERENCES

1. KNESCHKE, A.: Über gesteuerte Abkühl- und Anwärmvorgänge bei festen Körpern. *Ing. Arch.* XXIV. B. (1956), 77—80.
2. JUNG, H.: Zur Theorie der gesteuerten Anheizvorgänge. *ZAMM* 38 (1958), 56—69.
3. BORBÉLY, S.: Nem linearis hővezetéssel kapcsolatos vizsgálatokról. (Some analyses relating to non-linear heat-conduction phenomena). *Proceedings of the Technical Scientific Section of the Hung. Academy of Sciences* Tom. XXIII. No. 3—4 (1959), 261—286.
4. BORBÉLY, S.: Hosszú hengeres testek hevítési folyamatainak műszaki matematikai meghatározásáról. (Study on the technical-mathematical determination of heating processes carried out with long cylindrical bodies. Techn). Univ. Budapest. *Annual* 1961. 7—24.
5. HOFFMANN, A.: Untersuchung des Heizvorganges an zylindrischen Körpern bei veränderlicher Ofentemperatur und veränderlichem Wärmeübergangskoeffizienten. *Acta Technica Hung.* XL (1962), 285—300.

ANALYSE DES EINFLUSSES EINES VERÄNDERLICHEN WÄRMEÜBERGANGS-KOEFFIZIENTEN AUF DEN ANWÄRMEVORGANG BEIM ERHITZEN EINES ZYLINDRISCHEN KÖRPERS

A. HOFFMANN

ZUSAMMENFASSUNG

Bestimmt wird die Temperaturverteilung in einem langen zylindrischen Körper für den Fall einer Glühentspannung. Der Wärmeübergangskoeffizient wird als Funktion der Zeit betrachtet, ferner wird dem Einfluß der Wärmestrahlung und auch dem der Konvektion Rechnung getragen. Die Randwertbedingung ist inhomogen und nicht-linear. Zur Lösung der Differentialgleichung wird eine vom Verfasser früher abgeleitete Formel herangezogen.

EXAMEN DE L'EFFET DU COEFFICIENT VARIABLE DE LA TRANSMISSION DE CHALEUR DANS LE CHAUFFAGE DES CORPS CYLINDRIQUES

A. HOFFMANN

RÉSUMÉ

L'étude détermine la répartition des températures de corps cylindriques longs, en cas de traitement thermique éliminant les tensions. L'auteur considère le coefficient de transmission de chaleur comme fonction de la température, et tient également compte des termes produits par le rayonnement et par la convection.

Le problème de la valeur au contour est inhomogène et non-linéaire. La linéarisation par étapes et l'application d'un résultat antérieur de l'auteur (5) permettent d'obtenir la solution.

ИССЛЕДОВАНИЕ ВЛИЯНИЯ ПЕРЕМЕННОГО КОЭФФИЦИЕНТА ТЕПЛОПЕРЕДАЧИ ПРИ НАГРЕВЕ ЦИЛИНДРИЧЕСКОГО ТЕЛА, I

А. ХОФФМАНН

РЕЗЮМЕ

В работе определяется распределение температур в длинном цилиндрическом теле при термообработке для снятия напряжений. Коэффициент теплопередачи α принимается за функцию температуры и учитывается как член, выражающий радиацию, так и член, выражающий конвекцию.

Задача определения крайних значений неоднородна и нелинейна. Решение отыскивается при помощи приведения к прямой отдельных участков и с применением ранее опубликованного результата автора (5).

HEAT TRANSFER BY LAMINAR FORCED CONVECTION IN MULTIPLY CONNECTED REGIONS

U. A. SASTRY

REGIONAL ENGINEERING COLLEGE WARANGAL (ANDHRA PRADESH), INDIA

[Manuscript received September 16, 1963]

In this paper the heat transfer by laminar forced convection in a pipe whose outer cross-section is a circle and inner section a square with rounded corners (with a coincident centre) was studied by using Schwarz—Neumann's Alternating Method [3]. Results for section bounded by concentric circles, confocal ellipses and eccentric circles can be deduced by mapping the cross-section on to the region bounded by concentric circles. To illustrate the method the heat transfer by laminar forced convection in a tube bounded by concentric circles has been treated.

I. Introduction

The heat transfer by laminar forced convection in tubes has been studied by a number of investigators. Using complex variable method L. N. TAO [1] has obtained the solution of the forced convection problems of fully developed laminar flow in tubes of equilateral triangular and elliptic sections with heat sources and linearly varying wall temperature. In another paper L. N. TAO [2] obtained the solution of the heat transfer by laminar forced convection in a duct of Pascal's limacon section by conformal mapping techniques.

II. Basic Equations

Consider a steady fully developed laminar flow with heat sources in a pipe of cross-section D bounded by a closed curve D_0. Let the axis of the pipe be in the Z-direction and the axial wall temperature gradient be constant. The momentum and energy equations of constant property non-dissipative fluid in cartesian coordinates (x, y, Z) are

$$\frac{\partial^2 u}{\partial x^2} + \frac{\partial^2 u}{\partial y^2} = C_1, \tag{1}$$

$$\frac{\partial^2 t^*}{\partial x^2} + \frac{\partial^2 t^*}{\partial y^2} = C_2 u - C_3. \tag{2}$$

The boundary conditions are

$$u = 0, \tag{3}$$

$$t^* = t_w^*. \tag{4}$$

on D_0, where

u local velocity,
t^* local temperature,
t_w^* wall temperature,
$\mu C_1 = \partial p/\partial Z$,
$k C_2 = \varrho c_p \partial t^*/\partial Z$,
$C_3 = Q/k$,
p pressure,
μ viscosity,
ϱ density,
c_p specific heat at constant pressure,
k thermal conductivity,
Q heat source intensity,
C_1, C_2 and C_3 are constant parameters.

Using complex variables $z = x + iy$, $\bar{z} = x - iy$, and new temperature variable $T = (t^* - t_w^*)$ the solutions of (1) and (2) can be deduced in the form [2]

$$u = C_1 z\bar{z}/4 + 4[X(z) + \bar{X}(\bar{z})]/C_2\,, \tag{5}$$

$$T = \frac{C(z\bar{z})^2}{64} - \frac{C_3}{4} z\bar{z} + 2\,\mathrm{Re}\,[\bar{z}\,\Phi(z) + Y(z)] \tag{6}$$

where

$C = C_1 C_2$,
$X(z) = \Phi'(z) = \dfrac{d\Phi}{dz}$,
$Y(z) = \psi(z) + \Phi_0(z)$,
Re = real part,
$\Phi(z)$, $\psi(z)$ and $\Phi_0(z)$ are holomorphic in the region D.

The average velocity u_m, the average temperature T_m and the mixed mean temperature T_M are given by

$$Au_m = \iint u\,dx\,dy\,, \tag{7}$$

$$AT_m = \iint T\,dx\,dy\,, \tag{8}$$

$$Au_m T_M = \iint uT\,dx\,dy\,. \tag{9}$$

The heat transfer rate q can be obtained from the heat balance equation

$$q = (\varrho c_p u_m - C_3)\,A\,. \tag{10}$$

The heat transfer coefficient h and the Nusselt number Nu are given by

$$h = -q/ST_M\,, \tag{11}$$

$$\mathrm{Nu} = hD_e/k\,. \tag{12}$$

where

S is the circumferential length,
D_e is the equivalent hydraulic diameter.

The area cross-section A is given by

$$2\,iA = \int \bar{z}\,dz\,. \tag{13}$$

III. Formulation of the problem for doubly connected regions

For the problem under study we have to determine the velocity and temperature fields subject to the conditions

$$u = 0, \text{ on the outer boundary;} \tag{14}$$

$$u = 0 \text{ on the inner boundary} \tag{15}$$

and

$$T = 0, \text{ on the outer boundary;} \tag{16}$$

$$T = T_0, \text{ on the inner boundary} \tag{17}$$

where u and T are given by (5) and (6).

IV. Cross-section bounded externally by a circle and internally by a square with rounded corners

1. Determination of the velocity field

Let us determine the velocity subject to the condition

$$u = 0, \text{ on the circle } S_2; \tag{18}$$

$$u = 0, \text{ on the square } S_1. \tag{19}$$

Assume the radius of the circle be β_2 and t be a variable point on S_1, S_2. Then on the circle S_2 we have $t\bar{t} = \beta_2^2$. Using the above boundary conditions in (5) we obtain

$$X(t) + \bar{X}(\bar{t}) = -C\beta_2^2/16, \quad \text{on} \quad S_2\,; \tag{20}$$

$$= -Ct\bar{t}/16\,, \quad \text{on} \quad S_1. \tag{21}$$

To determine the function X we use Schwarz—Neumann's Alternating Method. Now denote (20) and (21) by

$$L(X) = g. \tag{22}$$

a) *First approximation.* Let $X^{(1)}$ be the first approximation to X to be determined in the infinite region exterior to the square S_1 so that

$$L(X^{(1)})|_{S_1} = g|_{S_1}. \tag{23}$$

b) *Conformal Mapping.* The function

$$z = a(\zeta + m/\zeta^3) \tag{24}$$

$a > 0$, $|m| < 1/3$, $\zeta = \beta\sigma$, $\sigma = e^{i\theta}$ a point on the unit circle ($\beta = l$) conformally maps the region exterior to square S_1 on to the region exterior to the unit circle in the ζ-plane. Also we have

$$t = a(\sigma + m/\sigma^3). \tag{25}$$

Using (25), (21) in (23) we obtain

$$X_1^{(1)}(\sigma) + \overline{X_1^{(1)}(\sigma)} = -\frac{Ca^2}{16}(1 + m^2 + m\,\sigma^4 + m/\sigma^4)\,. \tag{26}$$

where $X^{(1)}(t) = X_1^{(1)}(\sigma)$. Multiplying the above equation by $d\sigma\,(2\pi i(\sigma - \zeta)$ where ζ is a point outside the unit circle and integrating we obtain

$$X_1^{(1)}(\zeta) = -\,Ca^2(1 + m^2)/32 - Ca^2\,m/16\,\zeta^4\,. \tag{27}$$

This equation is to be expressed in terms of z, using (24). For this we take

$$\left.\begin{aligned} \zeta &= dz + \sum_1^\infty c_n/z^n\,, & 1/\zeta &= \sum_1^\infty b_n/z^n \\ 1/\zeta^3 &= \sum_1^\infty E_n/z^n\,, & 1/\zeta^4 &= \sum_1^\infty H_{4n}/z^{4n} \end{aligned}\right\} \tag{28}$$

where

$$E_n = \sum_{\gamma=1}^{\infty} G_{n-r}\,b_r\,,\quad G_n = \sum_{\gamma=1}^{\infty} b_{n-r}\,b_r\,,\quad H_{4n} \sum_{\gamma=2}^{\infty} G_{4n-r}\,b_r^5. \tag{29}$$

Using (28) in (24) and comparing like powers of z we find

$$\left.\begin{aligned} &d = 1/a,\quad c_3 = -\,ma^3,\quad c_7 = -\,3\,m^2\,a^7,\quad c_{11} = -\,15\,m^3\,a^{11} \\ &c_{15} = -\,91\,m^4\,a^{15},\quad c_{19} = -\,712\,m^5\,a^{29},\ \ldots \text{ etc.} \\ &b_1 = a,\ b_5 = ma^5,\ b_9 = 4\,m^2\,a^9,\ b_{13} = 22\,m^3\,a^{13},\quad b_{17} = 140\,m^4\,a^{17},\ldots \\ &H_4 = a^4,\quad H_8 = 4\,ma^8,\quad H_{12} = 22\,m^2\,a^{12},\quad H_{16} = 140\,m^3\,a^{16},\ \ldots \text{ etc.} \end{aligned}\right\} \tag{30}$$

Now equation (27) can be put down in the form

$$X^{(1)}(z) = -\frac{Ca^2}{32}(1+m^2) - \frac{Ca^2}{16}\, m \sum_1^\infty H_{4n}/z^{4n}\,. \tag{31}$$

c) *Second approximation.* Let $X^{(2)}$ be the second approximation which is to be determined in the region interior to the circle S_2, so that

$$L(X^{(2)})|_{S_2} = g|_{S_2} - L(X^{(1)})|_{S_2}\,. \tag{32}$$

Using (31) in (32) we obtain

$$\begin{aligned} X^{(2)}(t) + \overline{X^{(2)}(t)} = &- C\,\beta_2^2/16 + Ca^2(1+m^2)/16 + \\ &+ \frac{Ca^2}{16}\, m \sum_1^\infty H_{4n}\,(1/t^{4n} + t^{4n}/\beta_2^{8n})\,. \end{aligned} \tag{33}$$

Multiplying this equation by $\mathrm{d}t/2\pi i(t-z)$ where z is a point inside the circle S_2, we obtain after integration

$$X^{(2)}(z) = -\frac{C\beta_2^2}{32} + \frac{Ca^2}{32}(1+m^2) + \frac{Ca^2}{16}\, m \sum_1^\infty H_{4n}\, z^{4n}/\beta_2^{8n}\,. \tag{34}$$

For the first two approximations we get

$$X(z) = -\frac{C\beta^2}{32} + \frac{Ca^2}{16}\, m \sum_1^\infty H_{4n}\,(z^{4n}/\beta_2^{8n} - 1/z^{4n})\,. \tag{35}$$

The velocity and the average temperature are given by

$$u = C_1\,(z\bar{z} - \beta_2^2) - \frac{C_1\, a^2}{2}\, m\, Re \sum_1^\infty H_{4n}\,(1/z^{4n} - z^{4n}/\beta_2^{8n})\,, \tag{36}$$

$$\begin{aligned} Au_m = -\frac{\pi C_1}{8}\Bigg[&\beta_2^4 + a^4\,(1 - 4\,m^2 - 3\,m^4) - 2\,a^2\,\beta_2^2(1 - 3\,m^2) - \\ &- 4\,m^2\,a^4 + 4\,a^2\,m \sum_1^\infty \frac{H_{4n}\, m^n\, a^{4n+2}}{(4n+1)\,\beta_2^{8n}} \left\{\binom{4n+1}{n} - 3\,m^2 \binom{4n+1}{n+1}\right\}\Bigg]. \end{aligned} \tag{37}$$

2. *Determination of the temperature field*

Let us determine the temperature field subject to the condition

$$T = 0, \text{ on the circle } S_2; \tag{38}$$

$$T = T_0. \text{ on the square } S_1. \tag{39}$$

Using the above relations in (6) we find

$$\bar{t}\,\Phi(t) + t\,\overline{\Phi(t)} + Y(t) + \overline{Y(t)} = C_3\,\beta_2^2/4 - C\beta_2^4/64 \cdot \text{on } S_2\,; \tag{40}$$

$$= T_0 + C_3\,t\bar{t}/4 - C(t\bar{t})^2/64 \cdot \text{on } S_1. \tag{41}$$

For convenience the above equations will be denoted by

$$L(\Phi,\, Y) = g_0. \tag{42}$$

a) *First approximation* Let $\Phi^{(1)}$, $Y^{(1)}$ be the first approximation to be determined in the region exterior to S_1 so that

$$L(\Phi^{(1)},\, Y^{(1)})|_{S_1} = g_0|_{S_1}. \tag{43}$$

Since $d\Phi/dz = X(z)$, we obtain from (31)

$$\Phi^{(1)} = -\frac{Ca^2}{32}(1 + m^2)\,z + \frac{Ca^2}{16}\,m \sum_1^\infty H_{4n}/(4\,n - 1)\,z^{4n-1}. \tag{44}$$

From (41), (43) and (44) we get

$$\begin{aligned} Y_1(\sigma) + \overline{Y_1(\sigma)} &= T_0 + C_3\,a^2\,(1 + m^2)/4 + Ca^4(3 + 2\,m^2 + 3\,m^4)/64 + \\ &+ \left\{C_3\,a^2\,m/4 + Ca^3\,m\,(1 + m^2)/32\right\}\left(\sigma^4 + \frac{1}{\sigma^4}\right) + \frac{Ca^4}{64}\,m^2\left(\sigma^8 + \frac{1}{\sigma^8}\right) - \\ &- \frac{Ca^2}{16}\,m \sum_{n=1}^\infty H_{4n}\,(4n - 1)^{-1}\,a^{2-4n}\left\{(1 + m^2) + m/\sigma^4 + m\,\sigma^4\right\} \times \\ &\times \left\{\sum_{\gamma=0}^\infty \binom{-4\,n}{\gamma} m^r/\sigma^{4(n+r)} + \sum_{\gamma=0}^\infty \binom{-4\,n}{\gamma} m^r\,\sigma^{4(n+r)}\right\}. \end{aligned} \tag{45}$$

Multiplying the above equation by $d\sigma/2\pi i(\sigma - \zeta)$ where z is a point outside the unit circle and integrating we easily obtain

$$\begin{aligned} Y_1(\zeta) &= T_0/2 + C_3\,a^2\,(1 + m^2)/8 + Ca^4(9 - 2m^2 + 9\,m^4)/384 + \\ &+ \left\{C_3\,a^2\,m/4 + Ca^4\,m(1 + m^2)/32\right\}/\zeta^4 + Ca^4\,m^2/64\,\zeta^8 - \\ &- \frac{Ca^2\,m}{16}\left[\sum_{n=1}^\infty \frac{H_{4n}\,(1 + m^2)}{(4\,n - 1)\,a^{4n-2}} \sum_{\gamma=0}^\infty \binom{-4\,n}{\gamma} m^r/\zeta^{4(n+r)} + \right. \\ &+ \sum_{n=1}^\infty \frac{H_{4n}\,m}{(4\,n - 1)\,a^{4n-2}} \sum_{\gamma=0}^\infty \binom{-4\,n}{\gamma} m^r/\zeta^{4(n+r+1)} + \\ &+ \left. \sum_{n=2}^\infty \frac{H_{4n}\,m}{(4\,n - 1)\,a^{4n-2}} \sum_{\gamma=0}^\infty \binom{-4\,n}{\gamma} m^r/\tau^{4(n+r-1)}\right]. \end{aligned} \tag{46}$$

b) *Second approximation.* Let $\Phi^{(2)}$, $Y^{(2)}$ be the second approximation to be determined so that

$$L(\Phi^{(2)}, Y^{(2)})|_{S_2} = g_0|_{S_2} - L(\Phi^{(1)}, Y^{(1)})|_{S_2}. \tag{47}$$

Since $d\Phi/dz = X(z)$ we obtain from (34)

$$\Phi^{(2)} = \frac{C}{32}\,[a^2(1+m^2) - \beta_2^2]\,z + \frac{Ca^2}{16}\,m \sum_1^\infty H_{4n}\, z^{4n+1}/(4\,n+1)\,\beta_2^{8n}. \tag{48}$$

Using (48), (46), (44), (42), (40) in (47) and then multiplying the resulting equation by $dt/2\pi i(t-z)$ where z is a point inside the circle S_2 we obtain integration

$$\begin{aligned}
Y^{(2)}(z) = {} & 3\,C\,\beta_2^4/128 + C_3\,\beta_2^2/8 - Ca^2(1+m^2)\,\beta_2^2/16 - \\
& - [T_0/2 + C_3\,a^2(1+m^2)/8 + Ca^4(9 - 2\,m^2 + 9\,m^4)/384] - \\
& - \frac{Ca^2\,m}{2} \sum_1^\infty H_{4n}\, z^{4n}\,(4\,n^2 - 1)^{-1}\,\beta_2^{2-8n} - C\,a^4\,m^2\,Z_1^2/64 - \\
& - \{C_3\,a^2\,m/4 + Ca^4\,m(1+m^2)/32\}\,Z_1 + \\
& + \frac{Ca^2\,m}{16}\left[\sum_{n=1}^\infty \frac{H_{4n}(1+m^2)}{(4\,n-1)\,a^{4n-2}} \sum_{\gamma=0}^\infty \binom{-4\,n}{\gamma} m^r\,Z_1^{n+r} + \right. \\
& + \sum_{n=1}^\infty \frac{H_{4n}\,m}{(4\,n-1)\,a^{4n-2}} \sum_{\gamma=0}^\infty \binom{-4\,n}{\gamma} m^r\,Z_1^{n+r+1} + \\
& \left. + \sum_{n=2}^\infty \frac{H_{4n}\,m}{(4\,n-1)\,a^{4n-2}} \sum_{\gamma=0}^\infty \binom{-4\,n}{\gamma} m^r\,Z_1^{n+r-1}\right]
\end{aligned} \tag{49}$$

where

$$Z_1 = \sum_1^\infty \frac{H_{4n}\,Z^{4n}}{\beta_2^{8n}}.$$

Using $\Phi = \Phi^{(1)} + \Phi^{(2)}$, $Y = Y^{(1)} + Y^{(2)}$ in (6) we obtain the temperature field for the first two approximations. Then the average temperature can be calculated from formula (8). The area of the doubly connected cross-section is given by

$$A = \pi[\beta_2^2 - a^2\,(1 - 3\,m^2)]. \tag{50}$$

3. *Numerical Example*

For convenience let us take $m = -1/6$ in the transformation formula (24). The size of the square depends on a. The area of the doubly connected region is given by

$$A = \pi\,(\beta_2^2 - 11\,a^2/12). \tag{51}$$

Substituting the above value of m in the equation (37) we find after simplification

a) for $n = 1$

$$Au_m = -\frac{\pi C}{8}\,[\beta_2^4 + a^4\,(335/432 - 11\,b_0^2/6 + 5\;b_0^8/54)] \tag{52}$$

b) for $n = 2$ we find

$$Au_m = -\frac{\pi C_1}{8}\left[\beta_2^4 + a^4\left(335/432 - 11\,b_0^2/6 + 5\;b_0^8/54 + \frac{29\,b_0^{11}}{729}\right)\right] \tag{53}$$

c) for $n = 3$ we obtain $+\,2299$

$$\begin{aligned} Au_m = -\frac{\pi C_1}{8}\,[\beta_2^4 + a^4\,(335/432 - 11\,b_0^2/6 + \\ + 5\,b_0^8/54 + 29\,b_0^{16}/729 + 2299\,b_0^{24}/69984)] \end{aligned} \tag{54}$$

where A is given by (51) and $b_0^2 = (a^2/\beta_2^2)$.

For $m = -1/6$ and $n = 1$ the average temperature is given by

$$\begin{aligned} (AT_m\,\pi) = \frac{C}{192}(\beta_2^6 - 14075\,a^6/15552) - \frac{C_3}{8}\,(\beta_2^4 - 383\,a^4/432) - \\ - \frac{C}{32}\left\{\beta_2^6 - \frac{383}{432}\,\beta_2^2\,a^4 + \frac{a^6}{3}\left(\frac{553}{9720}\,b_0^8 + \frac{11}{324}\right)\right\} + \\ + \left\{\frac{3\,C}{64}\,\beta_2^2 + \frac{C_3}{4} - \frac{Ca^2}{8}\,(1 + m^2)\right\}\beta_2^4 - \\ - Ca^6\left[\frac{39}{62208} + \frac{273}{373248}\,b_0^8 - \frac{493\,b_0^{16}}{3359232}\right]. \end{aligned} \tag{55}$$

In deducing this formula Z_1, Z_1^2 has been retained in the formula (49). Results for $n = 2$, 3 are highly complicated. If we take $m = 1/6$ the square will be rotated through an angle of $\pi/4$.

V. Cross-section bounded by concentric circles

1. *Determination of the velocity field*

Using the condition

$$u = 0, \text{ on the outer circle } L_2; \tag{56}$$

$$u = 0, \text{ on the inner circle } L_1 \tag{57}$$

in the formula (5) we get

$$X(z) + \overline{X(z)} = -\,Cz\bar{z}/16 \cdot \text{on } L_2\,; \tag{58}$$

$$= -\,Cz\bar{z}/16 \cdot \text{on } L_1\,. \tag{59}$$

a) *Conformal transformation.* The function $z = \zeta$ (60)

$\zeta = \beta\sigma$, $\sigma = e^{i\theta}$ conformally maps the section of the pipe on to the ring $\beta_1 < |\zeta| < \beta_2$ in the ζ-plane. β_1, β_2 are the radii of the concentric circles L_1', L_2^1 corresponding to the concentric circles L_1, L_2 in the z-plane. Using (60) in (58) and (59) we obtain

$$X_1(\zeta) + \overline{X_1(\zeta)} = -C\beta_2^2/16, \text{ on } L_2'; \tag{61}$$

$$= -C\beta_1^2/16, \text{ on } L_1', \tag{62}$$

where $X(z) = X_1(\zeta)$. To determine $X_1(\zeta)$ we take in general

$$X_1(\zeta) = B \ln \zeta + \sum_{-\infty}^{\infty} B_n \zeta^n. \tag{63}$$

Substituting (63) in (61), (62) and comparing the like powers of σ on either side of the equations we can determine the constants B and B_n. In this simple problem we find

$$X_1(\zeta) = B \ln \zeta + B_0, \tag{64}$$

where

$$B_0 = C(\beta_2^2 \ln \beta_1 - \beta_1^2 \ln \beta_2)/32 \ln (\beta_2/\beta_1); \tag{65}$$

$$B = -C(\beta_2^2 - \beta_1^2)/32 \ln (\beta_2/\beta_1). \tag{66}$$

Using (64) to (66) in (5) we obtain after simplification

$$u = -\frac{C_1}{4}\left[(\beta_2^2 - \beta^2) + \frac{(\beta_2^2 - \beta_1^2)\ln(\beta/\beta_2)}{\ln(\beta_2/\beta_1)}\right]. \tag{67}$$

From (67) and (7) we find

$$Au_m = -\frac{\pi C_1}{8}\left[(\beta_2^4 - \beta_1^4) - \frac{(\beta_2^2 - \beta_1^2)^2}{\ln \beta_2/\beta_1}\right]. \tag{68}$$

These are well known results.

2. *Determination of the temperature field*

Using the boundary conditions

$$T = 0, \text{ on } L_2; \tag{69}$$

$$T = T_0, \text{ on } L_4, \tag{70}$$

in (6) we find

$$2\,\mathrm{Re}\,[\bar{z}\,\Phi(z) + Y(z)] = \frac{C_3}{4}\,z\bar{z} - \frac{C}{64}\,(z\bar{z})^2\,,\ \text{on circle } L_2\,; \tag{71}$$

$$= T_0 + \frac{C_3}{4}\,z\bar{z} - \frac{C}{64}\,(z\bar{z})^2 \text{ on the inner circle } L_1. \tag{72}$$

Since $d\Phi/dz = X(z) = \mathrm{X}_1\,(\zeta)$ we obtain from (64)

$$\Phi(z) = B\,\zeta(\ln\beta - 1) + B_0\,\zeta\,. \tag{73}$$

The constant of integration was chosen in such a way that the function $\Phi(z)$ is single valued in the doubly connected region.

Using (73) and (60) in (71), (72) we find

$$Y_1(\zeta) + \overline{Y_1(\zeta)} = \frac{C\beta_2^4}{64} - \frac{C_3}{4}\,\beta_2^2 - 2\,\beta_2^2(B_0 - B + B\ln\beta_1) \text{ on } L_2' \tag{74}$$

$$= T_0 + \frac{C\beta_1^4}{64} - \frac{C_3}{4}\,\beta_1^2 - 2\,\beta_1^2\,(B_0 - B + B\ln\beta_1) \qquad \text{on } L_1' \tag{75}$$

where $Y(z) = Y_1(\zeta)$. To find the value of $Y_1(\zeta)$ we take

$$Y_1(\zeta) = E\ln\zeta + \sum_{-\infty}^{\infty} E_n\,\zeta^n. \tag{76}$$

Substituting (76) in (74), (75) and comparing like powers of σ on either side we can determine the constants E and E_n. In this problem we find

$$Y_1(\zeta) = E\ln\zeta + E_0. \tag{77}$$

where

$$2E_0\ln\beta_1/\beta_2 = f_0(\beta_2)\ln\beta_1 - [f_0(\beta_1) + T_0]\ln\beta_2, \tag{78}$$

$$2E\ln\beta_2/\beta_1 = f_0(\beta_2) - [f_0(\beta_1) + T_0], \tag{79}$$

$$f_0(\beta) = \frac{C\beta^4}{64} - \frac{C_3}{4}\,\beta^2 - 2\,\beta^2(B_0 - B + B\ln\beta)\,. \tag{80}$$

Substituting (77), (73) and (60) into (6) we obtain the temperature field in the form

$$T = \frac{C\beta^4}{64} - \frac{C_3}{4}\,\beta^2 + 2\,[E_0 + E\ln\beta + \beta^2(B_0 - B + B\ln\beta)]. \tag{81}$$

$(\beta_1 \leqslant \beta \leqslant \beta_2)$. Using (81) in the formula for the average temperature (8) we obtain after simplification

$$(AT_m/\pi) = C(\beta_2^6 - \beta_1^6)/192 + (B_0 - C_3/8)(\beta_2^4 - \beta_1^4) + \\ + 2E_0(\beta_2^2 - \beta_1^2) + 2E\left[(\beta_2^2 \ln \beta_2 - \beta_1^2 \ln \beta_1) - \frac{(\beta_2^2 - \beta_1^2)}{2}\right] + \\ + B\left[(\beta_2^4 \ln \beta_2 - \beta_1^4 \ln \beta_1) - 5(\beta_2^4 - \beta_1^4)/4\right]. \tag{82}$$

In this example

$$A = \pi(\beta_2^2 - \beta_1^2). \tag{83}$$

We can easily calculate the T_m, h and q using the formulae (9), (11) and (10).

ACKNOWLEDGEMENT

I wish to thank the referee of my paper for his valuable comments and suggestions.

REFERENCES

1. TAO, L. N.: On Some Forced Convection Problems. *Trans. ASME* **83** (1961), 467—472.
2. TAO, L. N.: Heat Transfer of Laminar Forced Convection in Indented Pipes. LAY, J. E.—MALVERN, L. E.: Developments in Mechanics. Vol. 1. Proceedings of the seventh Mid-western Conference, September 6—8, 1961 at Michigan State University, East Lansing, Michigan, 510—525.
3. SOKOLNIKOFF, I. S.: Mathematical Theory of Elasticity. Mc Graw-Hill Book Company 1956. 2nd ed., 318—326.

WÄRMEÜBERTRAGUNG BEI ERZWUNGENER LAMINARER KONVEKTION IN MEHRFACH ZUSAMMENHÄNGENDEN BEREICHEN

U. A. SASTRY

ZUSAMMENFASSUNG

Es wird mit Hilfe der Alterationsmethode von SCHWARZ—NEUMANN die Wärmeübertragung durch erzwungene laminare Konvektion in einem Rohr behandelt, wobei der Außenquerschnitt des Rohres ein Kreis und Innenquerschnitt ein Quadrat mit abgerundeten Ecken (mit gemeinsamem Mittelpunkt) ist [3]. Ergebnisse für von konzentrischen Kreisen, konfokalen Ellipsen und exzentrischen Kreisen begrenzte Querschnitte können durch Abbildung des Querschnitts auf den von konzentrischen Kreisen begrenzten Bereich abgeleitet werden. Um die Methode zu illustrieren, wurde die Wärmeübertragung durch erzwungene laminare Konvektion in einem von konzentrischen Kreisen begrenzten Rohr behandelt.

TRANSMISSION DE LA CHALEUR PAR CONVECTION LAMINAIRE FORCÉE DANS DES DOMAINES MULTIPLEMENT CONNECTÉS

U. A. SASTRY

RÉSUMÉ

L'auteur utilisant la méthode alternante de Schwarz—Neumann [3], traite de la transmission de la chaleur dans un tube dont la section extérieure est circulaire et la section intérieure présente un carré aux angles arrondis (avec centres coïncidants). Pour les sections limitées par des cercles concentriques, des ellipses confocales et des cercles excentriques, les résultats peuvent être déduits par représentation de la section sur le domaine limité par des cercles concentriques. Pour illustrer la méthode, la transmission de la chaleur par convection laminaire forcée a été étudiée pour un tube limité par des cercles concentriques.

ПЕРЕДАЧА ТЕПЛА ПРИ ЛАМИНАРНОМ ПРИНУДИТЕЛЬНОМ ДВИЖЕНИИ ПОТОКА В МНОГОКРАТНО ЗАВИСЯЩИХ ОБЛАСТЯХ

У. А. ШАСТРИ

РЕЗЮМЕ

В работе при помощи альтернирующего метода *Шварца* и *Неймана* [3] теплопередача рассматривается в такой трубе, наружное сечение которого представляет собою круг, а внутреннее округленный на углах квадрат (с совпадающими центрами). Результаты, относящиеся к концентрическим кругам, конфокальным эллипсам и эксцентрическим кругам, можно вывести путем проекции на область сечения, ограниченную концентрическими кругами. В целях демонстрации метода автором выведена теплопередача при ламинарном принудительном движении потока для случая трубы, ограниченной концентрическими кругами.

AUSBILDUNG ACHSENSYMMETRISCHER BELASTUNG IN DER UMGEBUNG VON STRECKEN MIT RUNDPROFIL

J. HORVÁTH

FORSCHUNGSINSTITUT FÜR BERGBAU, BUDAPEST

[Eingegangen am 5. November 1963]

Die Abhandlung befaßt sich mit den Spannungen der ungestützten runden Strecken. Der Verfasser hat die Gesteinskennzeichen der Nebengesteine vom Mecseker Lias-Bergbau durch Versuche bestimmt. Es kann festgestellt werden, daß die Mehrzahl der Nebengesteine ein elastisches Bereich besitzt. Hier ist die Poissonziffer konstant. Wenn die Gesteine weiter belastet werden, so strebt die Poissonziffer nach 0,5. Nach dem Beweis der Versuche haben die Nebengesteine allgemein ein elastisches und plastisches Bereich.* Der Verfasser hat das Plastizitätsgesetz im Falle runder ungestützter Strecken abgeleitet. Es wurden mit Hilfe des Plastizitätsgesetzes die kritische Teufe, die Abmessung des plastischen Bereichs und die elastischen und plastischen Spannungen festgestellt. Die Resultate wurden an einem Zahlenbeispiel dargestellt.

Formelzeichen

H	Teufe;
b	Radius der ungestützten Strecke;
γ	Raumgewicht;
ν	Poissonziffer;
E	Young-Modul;
$r,\ \varphi$	Polarkoordinaten;
$\sigma_r, \sigma_\varphi, \sigma_z\ \tau_{r\varphi}$	Spannungen in Zylinderkoordinaten;
$\sigma_{rk}, \sigma_{\varphi k}, \sigma_{zk}$	Spannungen im plastischen Bereich;
$\sigma_r'\ \sigma_\varphi', \sigma_z'$	Spannungen im elastischen Bereich nach der Ausbildung des plastischen Bereichs;
$s_r, s_\varphi, s_x, s_y, s_z, s_k$	Spannungsdeviator-Komponenten;
$\varepsilon_x, \varepsilon_y, \varepsilon_z$	Formänderungs-Komponenten;
$\gamma_{xy}\ \gamma_{yz}, \gamma_{zx}\ e_r, e_\varphi$	Formänderungsdeviator-Komponenten;
y_z	Zweite Invariante des Spannungsdeviators;
σ_F	Fließspannung;
$k^2 = \sigma_F^2/3$	Zweite Invariante des Deviators des einachsigen Spannungszustandes;
ϱ	Radius des plastischen Bereichs.

I. Elastische Spannungen in der Umgebung runder Strecken

Es soll in der Teufe ein ausgedehntes Streckennetz zum Abbau des Mineralschatzes aufgefahren werden.

Man nimmt an, daß der Halbraum isotrop und elastisch ist. Vorausgesetzt, daß vor dem Auffahren der Strecken die senkrechten Spannungen

* Darum kann man sie als Konstruktionsmaterialien behandeln.

$H\gamma$ und die waagerechten Spannungen $\nu/1 - \nu \cdot H\gamma$ sind, [3] ist der Mittelpunkt der kreisrunden Strecke von der Erdoberfläche in der Teufe H (Bild 1).

Das Verhältnis des Streckenradius b zur Teufe H ist $b/H = 0{,}01 \div 0{,}001$, darum können wir die Änderung von $H\gamma$, bei unseren Untersuchungen, in der Umgebung von der Strecke vernachlässigen. Die Spannungskonzentration erweckt ebene Formänderungen nach dem Auffahren der Strecken. Die Spannungskomponenten sind in der Umgebung der nicht unterstützten kreisrunden Strecken — nach KIRSCH — die folgenden [2]

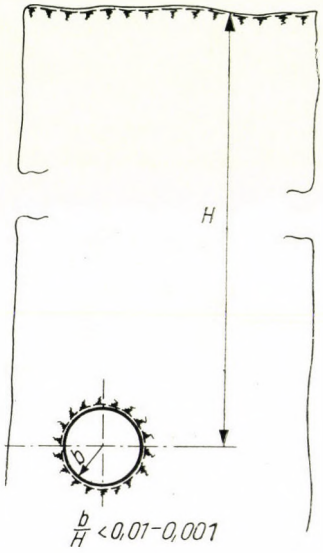

Bild 1. Aufgefahrene Strecke in bergbaulicher Teufe

$$\sigma_r = -\frac{H\gamma}{2}\left[\frac{1}{1-\nu}\left(1-\frac{b^2}{r^2}\right)+\frac{1-2\nu}{1-\nu}\left(1-4\frac{b^2}{r^2}+3\frac{b^4}{r^4}\right)\cos 2\varphi\right],$$

$$\sigma_\varphi = -\frac{H\gamma}{2}\left[\frac{1}{1-\nu}\left(1+\frac{b^2}{r^2}\right)-\frac{1-2\nu}{1-\nu}\left(1+3\frac{b^4}{r^4}\right)\cos 2\varphi\right],$$

$$\tau_{r\varphi} = -\frac{H\gamma}{2}\,\frac{1-2\nu}{1-\nu}\left(-1-2\frac{b^2}{r^2}+3\frac{b^4}{r^4}\right)\sin 2\varphi. \tag{1}$$

In der Fachliteratur sind die Zusammenhänge der Spannungszustände im Halbraum in der Teufe H, in der Umgebung der Strecke bekannt [7]. Wenn wir diese Zusammenhänge $b/H = 0{,}01 \div 0{,}001$ vereinfachen und die durch die Teufenänderung verursachten Spannungsänderungen in der Um-

gebung der Strecke unbeachtet lassen, erhalten wir die einfacheren Gleichungen (1).

Die störende Wirkung der Spannungskonzentration verschwindet im elastischen Bereich bei: $b/r = 1/8$ (Bild 2).

Die Größe der Spannungskomponenten hängt vom Radius der Strecke, von der Entfernung und Lage des Streckenmittelpunktes, von der Teufe, vom Raumgewicht und von der Poissonziffer ab.

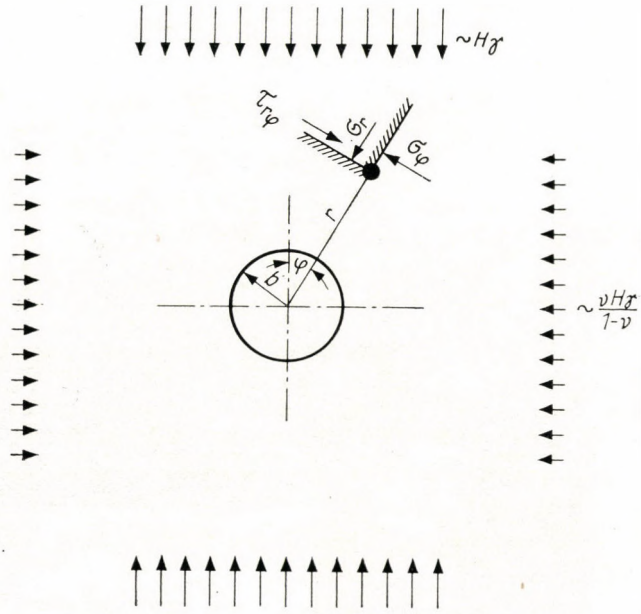

Bild 2. Spannungen in der Umgebung einer Strecke

Die Spannungskomponenten können teils aus geodetischen, teils aus Gesteinskennzeichen berechnet werden.

In Kentnis der genannten Daten sind die Formänderungen und die Verschiebungen bestimmbar.

Die Gültigkeit der Gleichungen (1) wurden bei Metallen durch Messungen festgestellt, aber im Falle der Gesteine kennen wir solche Messungen nicht.

II. Die Bestimmung der Gesteinskennzeichen

Die Gesteinskennzeichen werden mit Labormessungen bestimmt. Die Bestimmung des Raumgewichts wird einfach und pünktlich mit Gewichstmessungen durchgeführt.

Die Bestimmung der Poissonziffer wird mit einachsigen Druckversuchen durchgeführt, wo man auch die Formänderungen messen muß. Die Poissonziffer

$$\nu = \frac{\varepsilon_k}{\varepsilon_h} \tag{2}$$

ist das Verhältnis der Kreuzdehnung zu der Längszusammendrückung. Dieses Verhältnis ist bei elastischen und isotropen Gesteinen konstant. Die andere wichtige Gesteinskennzahl ist der Young-Modul. Er ist ein Proportionalitätsfaktor bei der Spannung und Formänderung:

$$E = \frac{\sigma}{\varepsilon_h}. \tag{3}$$

Die Versuche wurden an solchen Gesteinszylindern durchgeführt, bei denen das Verhältnis des Durchmessers zur Höhe 1 : 1,5 war. Die Messungen

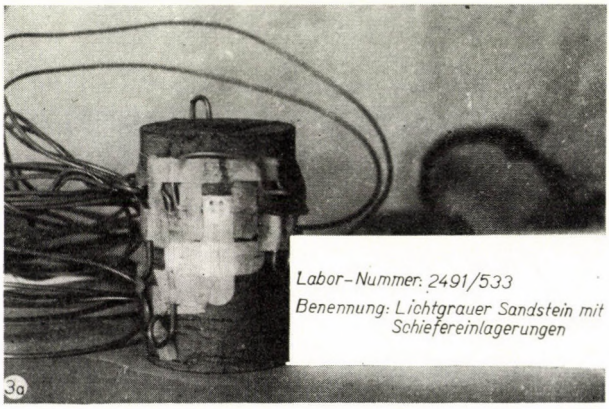

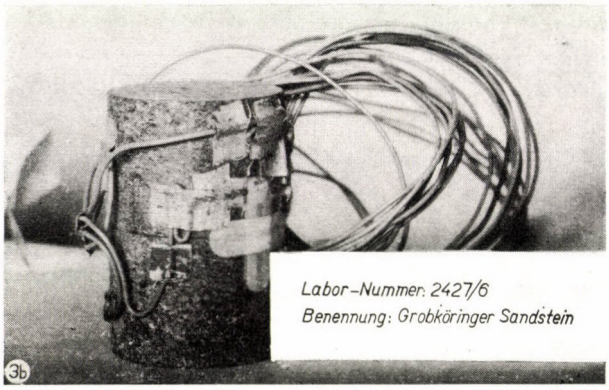

Bild 3a-3b. Mit Dehnungsmeßstreifen verschene und mit einachsigen Versuchen untersuchte Gesteinsprobekörper (Bild 3c-3d siehe auf Seite 197)

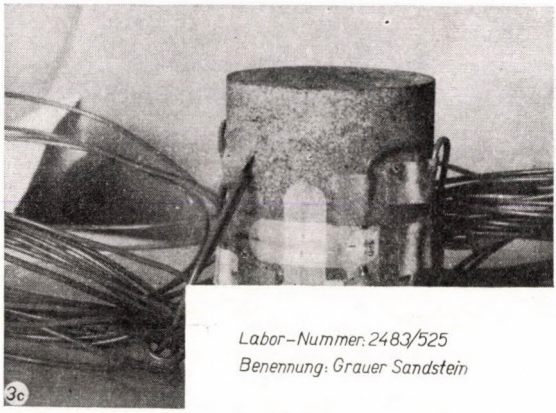

Bild 3c-3d Mit Dehnungsmeßstreifen versehene und mit einachsigen Versuchen untersuchte Gesteinsprobekörper (Bild 3a-3b siehe auf Seite 196)

der Formänderungen erfolgten mit Meßuhren von 1—10 μ Ablesegenauigkeit. Die festgestellten Gesteinskennzahlen waren nicht genau.

Wir fingen an, seit dem Jahre 1959, in der Abteilung für Gebirgsmechanik des Forschungsinstituts für Bergbau in Budapest Dehnungsmeßstreifen zu benützen. Die auf den Probekörpern geklebten Meßstreifen erleiden dieselben Formänderungen wie die Probekörper. Dabei verändert sich ihre elektrische Leitfähigkeit. Die Formänderung ist durch die Widerstandsänderung zu messen,

$$\varepsilon = \frac{\Delta L}{L} = \frac{1}{k} \frac{\Delta R}{R} . \tag{4}$$

Es werden auf den Probekörper in der Symmetrieebene in der Richtung des Druckes und senkrecht darauf zwei, zusammen vier Dehnungsmeßstreifen aufgeklebt (Bild 3a—d). Die symmetrisch aufgeklebten Dehnungsmeßstreifen

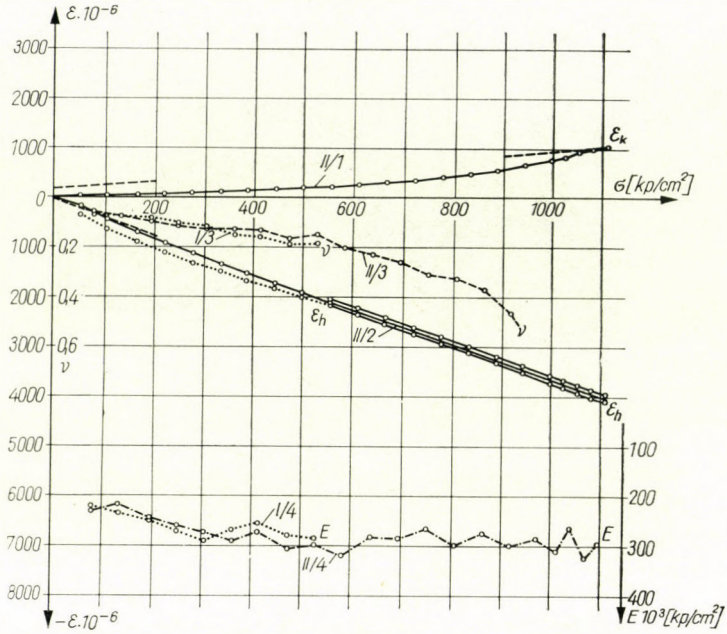

Bild 4. Diagramm eines Versuchs von Sandstein mit Schiefereinlagerungen (Siehe auch Tafel II)

Formelzeichen der Bilder 4—9: I erster Versuch; *II* zweiter Versuch; *1* Formänderungsdiagramm senkrecht zur Druckrichtung; *2* Formänderungsdiagramm parallel zur Druckrichtung; *3* Diagramme der Poissonziffer; *4* Diagramme des Young-Moduls.

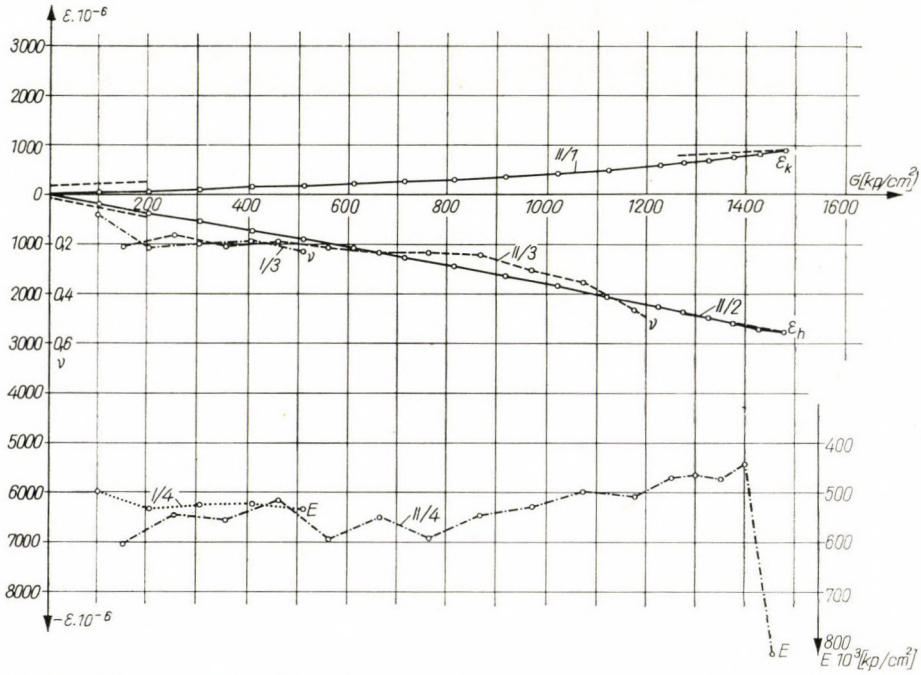

Bild 5. Diagramm eines Versuchs von grobkörnigem Sandstein (Siehe auch Tafel II)

Tafel I

Nr.	
Labor-Nummer	2488/530
Benennung	Sandstein mit Schiefereinlagerungen
Fundort	Komló—Zobák
Mächtigkeit der Schicht	
Lage zur Kohlenschicht	
Richtung des Druckes zur Schichtung	
Form und Abmessung des Probekörpers	Zylinder $d = 47{,}95$ mm $h = 72{,}05$ mm $F = 18{,}0$ cm²
Poissonziffer	
Young-Modul	
Fließspannung	
Druckfestigkeit	
Tabellen-Nummer	
Bemerkungen	

Tafel II

Nr.	
Labor-Nummer	2427/6
Benennung	Grobkörniger Sandstein
Fundort	Komló—Zobák Querschlag am II. Horizont
Mächtigkeit der Schicht	
Lage zur Kohlenschicht	
Richtung des Druckes zur Schichtung	
Form und Abmessung des Probekörpers	Zylinder $d = 50$ mm $h = 74{,}3$ mm $F = 19{,}62$ cm²
Poissonziffer	
Young-Modul	
Fließspannung	
Druckfestigkeit	
Tabellen-Nummer	
Bemerkungen	

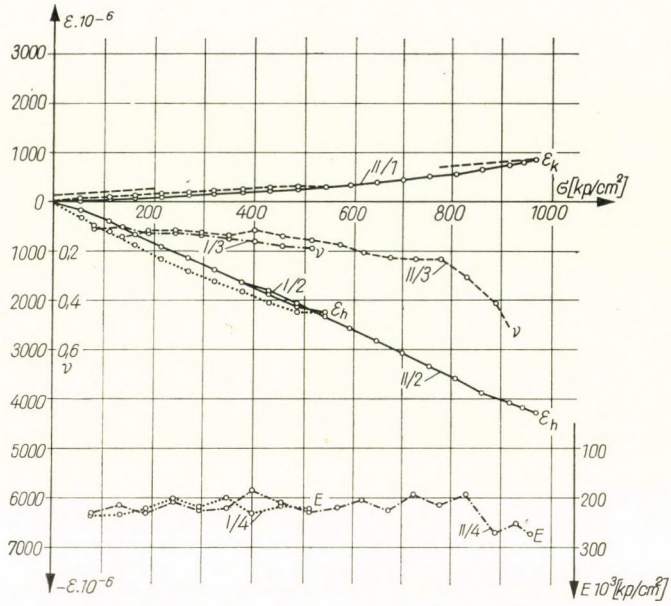

Bild 6. Diagramm eines Versuchs von einer Andesit-Intrusion (Siehe auch Tafel III)

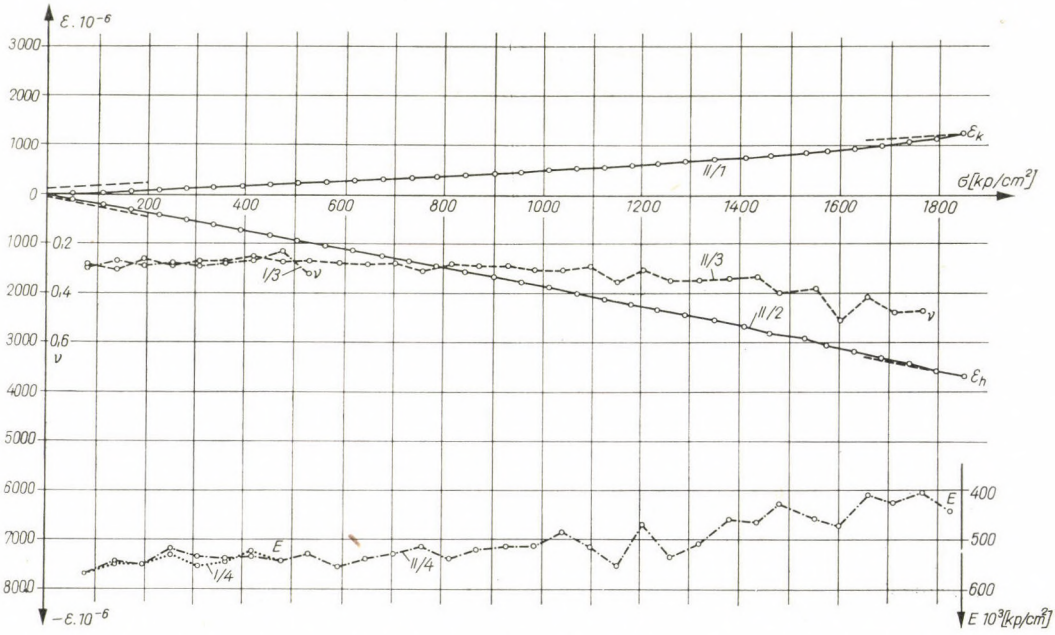

Bild 7. Diagramm eines Versuchs von einer Trachidolerit-Intrusion (Siehe auch Tafel IV)

Tafel III

Nr.	
Labor-Nummer	2479/521-II.
Benennung	Andesit Intrusion
Fundort	Komló—Zobák
Mächtigkeit der Schicht	
Lage zur Kohlenschicht	
Richtung des Druckes zur Schichtung	
Form und Abmessung des Probekörpers	Zylinder $d = 48{,}75$ mm $h = 71{,}43$ mm $F = 18{,}6$ cm²
Poissonziffer	
Young-Modul	
F ließspan nung	
Druckfestigkeit	
TabellenNummer	
Bemerkungen	

Tafel IV

Nr.	
Labor-Nummer	2498/241
Benennung	Trachidolerit Intrusion
Fundort	Komló—Zobák
Mächtigkeit der Schicht	
Lage zur Kohlenschicht	
Richtung des Druckes zur Schichtung	
Form und Abmessung des Probekörpers	Zylinder $d = 47{,}56$ mm $h = 70{,}98$ mm $F = 17{,}8$ cm²
Poissonziffer	
Young-Modul	
Fließ-spannung	
Druckfestigkeit	
TabellenNummer	
Bemerkungen	

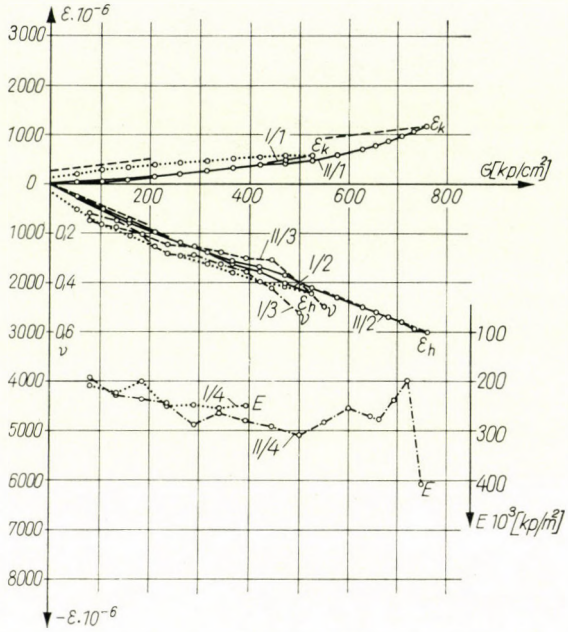

Bild 8. Diagramm eines Versuchs von einer Sandsteinschicht (Siehe auch Tafel V)

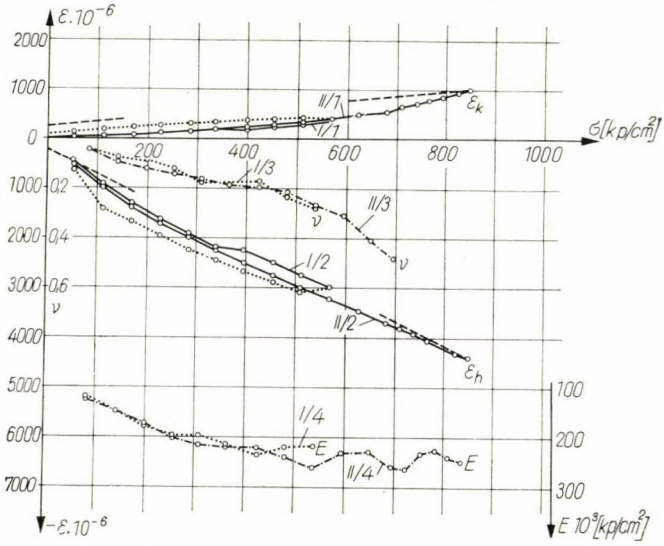

Bild 9. Diagramm eines Versuchs von lichtgrauen Sandstein mit Schiefereinlagerungen (Siehe auch Tafel VI)

Tafel V

Nr.	
Labor-Nummer	2483/525
Benennung	Sandsteinschicht
Fundort	Komló—Zobák
Mächtigkeit der Schicht	
Lage zur Kohlenschicht	
Richtung des Druckes zur Schichtung	
Form und Abmessung des Probekörpers	Zylinder $d = 49{,}3$ mm $h = 74{,}09$ mm $F = 19{,}1$ cm²
Poissonziffer	
Young-Modul	
Fließspannung	
Druckfestigkeit	
Tabellen-Nummer	
Bemerkungen	

Tafel VI

Nr.	
Labor-Nummer	2491/533-I.
Benennung	Lichtgrauer Sandstein mit Schiefereinlagerungen
Fundort	Komló—Zobák
Mächtigkeit der Schicht	
Lage zur Kohlenschicht	
Richtung des Druckes zur Schichtung	
Form und Abmessung des Probekörpers	Zylinder $d = 47$ mm $h = 71{,}025$ mm $F = 17{,}6$ cm²
Poissonziffer	
Young Modul	
Fließspannung	
Druckfestigkeit	
Tabellen-Nummer	
Bemerkungen	

erleichtern in der Prüfmaschiene durch Hin- und Herschieben, daß der symmetrische Spannungszustand hergestellt werde.

Die Messung erfolgt in kleinen Laststufen nach einem vorgeschriebenen Meßplan. Bei jeder Belastungsstufe werden die Formänderungen abgelesen, und die Gesteinskennzahlen berechnet. Bei den Diagrammen werden die elastischen Kennzahlen in der Mitte der Stufen dargestellt.

Die Veränderung der Formänderungen und der Gesteinskennzahlen kann von Anfang bis zum Bruch in Abhängigkeit von der Spannung beobachtet werden.

Die im Bilde 3a—d gezeigten Probezylinder sind aus den Nebengesteinen des ungarischen Mecseker-Liasbergbaus. Die Resultate der Versuche zeigen die Diagramme von den Bildern 4—9 und den Tafeln I-VI.

Aus den Ergebnissen der Versuche können wir feststellen:

a) Ein Teil der untersuchten Gesteine besitzt ein elastisches Bereich, wo die Poissonziffer konstant ist;

b) die Poissonziffer strebt nach 0,5,

c) der Young-Modul bleibt im elastischen Bereich konstant.

Wir können aus den Versuchen die allgemeine Tatsache feststellen, daß bei den Gesteinen ein elastisches und plastisches Bereich zu unterscheiden ist.

III. Fließgrenze in der Umgebung der kreisförmig aufgefahrenen Strecke

Man benützt keinen Ausbau in solchen Strecken, wo die Nebengesteine nach der Auffahrung elastisch geblieben sind. Wenn die Nebengesteine plastisch geworden sind, dann muß man einen kostspieligen Ausbau einbauen.

Nach der *Huber—Mises—Hencky* Theorie kann man die Fließgrenze in der Umgebung der Strecke den aus Spannungskomponenten der Gleichung (1) berechnen, wenn wir die zweite Invariante des Deviator-Tensors bilden [5, 6].

$$J_2 = \frac{1}{2}(s_r^2 + s_r s_\varphi + s_\varphi^2) + \tau_{r\varphi}^2 = \text{konst.} \tag{5}$$

Man kann an — aus Nebengesteinen hergestellten — Probezylindern mit einachsigen Versuchen die zweite Invariante des Deviators ausmessen. Die zwei Invarianten sind einander gleich. Aus einachsigen Versuchen ist die Fließspannung bekannt:

$$J_2 = \frac{\sigma_F^2}{3}\,. \tag{6}$$

Die zweite Invariante ist der Verzerrungsteil der Formänderungsarbeit. Man kann die Poissonziffer gleich 0,5 in der Nähe des plastischen Bereichs in

der elastischen Zone annehmen [4, 5]. Nach Gleichung (5) kann man mit diesem Wert die zweite Invariante berechnen:

$$J_2 = H^2 \gamma^2 \frac{b^4}{r^4} . \tag{7}$$

Die hergestellten zwei Invarianten sind einander gleich. Man kann auf Grund einachsiger Druckversuche mit Gesteinsprobekörpern die zweite Invariante des Deviators des Spannungszustandes angeben, weil dort $\nu \to 0{,}5$.

Es gilt bei der Fließgrenze:

$$H^2 \gamma^2 \frac{b^4}{r^4} = \frac{\sigma_F^2}{3} . \tag{8}$$

Wenn wir die übliche Benennung: $\sigma_F/\sqrt{3} = k$ benützen, können wir Gleichung (8) in folgender Form schreiben:

$$\frac{H\gamma}{k} = \frac{r^2}{b^2} . \tag{9}$$

Wenn am Mantel der Strecke das Fließen auftritt, dann ist $r = b$ und darum ist

$$\frac{H\gamma}{k} = 1 . \tag{10}$$

Die Teufe, bei der das Fließen am Mantel der ungestützten Strecke auftritt nennen wir kritische Teufe:

$$H_{\text{krit}} = \frac{k}{\gamma} . \tag{11}$$

Das Gestein bleibt elastisch, wenn die Strecke über der kritischen Teufe aufgefahren wird. In diesem Falle wird — theoretisch — auf den Ausbau kein Druck ausgeübt.

Die unter der kritischen Teufe aufgefahrene Strecke wird von einem kreisförmigen plastischen Mantel mit Radius ϱ umgeben.

In diesem Falle lautet das plastische Gesetz:

$$\frac{H\gamma}{k} = \frac{\varrho^2}{b'^2} . \tag{12}$$

Die Strecke wird durch die plastische Zone vom elastischen Bereich getrennt.

Darum müssen wir zur Berechnung der elastischen Spannungen den fiktiven Wert von Radius b' benützen.

In solchen Strecken wird der Ausbau durch die plastische Zone belastet.

IV. Die Spannungen des plastischen Bereichs

Das plastische Bereich soll man als nicht zusammendrückbar annehmen:

$$e_r + e_\varphi = 0 \tag{13}$$

und

$$e_z = c\left[\sigma_z - \frac{1}{2}(\sigma_r + \sigma_\varphi)\right], \tag{14}$$

das heißt

$$\sigma_z = \frac{1}{2}(\sigma_r + \sigma_\varphi)\,. \tag{15}$$

Man kann das Kriterium der Unzusammendrückbarkeit auf einen Teil des elastischen Bereichs ausdehnen.

Im plastischen Bereich ist die Gleichgewichtsgleichung auch gültig:

$$\frac{\partial \sigma_r}{\partial r} + \frac{\sigma_r - \sigma_\varphi}{r} = 0\,. \tag{16}$$

In der plastischen Zone bis zum Rande des elastischen Bereichs gilt das Plastizitätsgesetz:

$$\sigma_r - \sigma_\varphi = 2\,k\,. \tag{17}$$

Weil im plastischen Bereich

$$\frac{\partial \sigma_r}{\partial r} = \frac{2\,k}{r}\,, \tag{18}$$

so sind die plastischen Spannungen in einem gegebenen Zeitpunkt;

$$\begin{aligned} \sigma_{r_k} &= -\,2\,k \ln \frac{r}{b}\,, \\ \sigma_{\varphi_k} &= -\,2\,k \ln \frac{r}{b} - 2\,k\,, \\ \sigma_{z_k} &= -\,2\,k \ln \frac{r}{b} - k\,. \end{aligned} \tag{19}$$

V. Der Radius des plastischen Bereichs

Man kann den Radius des plastischen Bereichs aus der Bedingung berechnen, daß an der Grenze der plastischen Zone die Spannungen der nach unserer Annahme axialsymmetrischen plastischen und elastischen Bereiche in Gleichgewicht sind.

Die Spannungen des elastischen Bereichs sind nach der Ausbildung der plastischen Zone die folgenden:

$$\begin{aligned} \sigma'_r &= -H\gamma\left(1-\frac{b'^2}{r^2}\right), \\ \sigma'_\varphi &= -H\gamma\left(1+\frac{b'^2}{r^2}\right), \\ \sigma'_z &= -H\gamma. \end{aligned} \tag{20}$$

An der Grenze des plastischen und elastischen Bereichs, bei $r = \varrho$, sind die mittleren Hauptspannungen der beiden Zonen einander gleich:

$$s_k = H\gamma. \tag{21}$$

Der Absolutwert der Deviatorkomponenten von Radial- und Ringspannungen im plastischen Bereich sind miteinander identisch und besitzen den Wert k:

$$|s_r| = |s_\varphi| = k, \tag{22}$$

aber

$$s_z = 0.$$

Darum kann die Gleichgewichtsgleichung (16) in folgender Form geschrieben werden:

$$\frac{\partial\sigma_r}{\partial r} = \frac{\partial s}{\partial r} = \frac{2\,k}{r}. \tag{23}$$

Daraus folgt für den Wert s_k der Zusammenhang:

$$s_k = 2k \ln r + f(\varrho). \tag{24}$$

An der Grenze des plastischen Bereichs ist

$$s_k = H\gamma = 2k \ln \varrho + f(\varrho), \tag{25}$$

und so ergibt sich

$$f(\varrho) = H\gamma - 2k \ln \varrho. \tag{26}$$

Darum

$$s_k = H\gamma + 2\,k \ln \frac{r}{\varrho}\,. \tag{27}$$

In der plastischen Zone und am Rande desselben gilt:

$$s_{rk} = s - k, \tag{28}$$

und so ist

$$\sigma_{r_k} = H\gamma + 2\,k \ln \frac{r}{\varrho} - k\,. \tag{29}$$

Am Mantel der Strecke bei $r = b$ ist: $\sigma_{rk} = 0$. Mit der Benützung der obigen Grenzbedingung kann man den Radius der plastischen Zone berechnen:

$$\varrho = b e^{\frac{1}{2}\left(\frac{H\gamma}{k} - 1\right)}. \tag{30}$$

VI. Die elastischen Spannungen

Aus dem vorausgesetzten Gleichgewicht am Rande des elastischen-plastischen Bereichs muß man entlang ϱ die Identität der Radialspannungen annehmen:

$$2\,k \ln \frac{\varrho}{b} = H\gamma \left(1 - \frac{b'^2}{\varrho^2}\right). \tag{31}$$

Wenn wir für ϱ an beiden Seiten der obigen Gleichung die Gleichung (30) einsetzen, erhalten wir:

$$b'^2 = \frac{b^2 e^{\frac{H\gamma}{k} - 1}}{H\gamma}\, k. \tag{32}$$

So sind die elastischen Spannungen nach der Ausbildung des plastischen Bereichs:

$$\begin{aligned} \sigma'_r &= -H\gamma \left(1 - \frac{b^2 e^{\frac{H\gamma}{k} - 1}}{r^2 H\gamma}\, k\right), \\ \sigma'_\varphi &= -H\gamma \left(1 + \frac{b^2 e^{\left(\frac{H\gamma}{k} - 1\right)}}{r^2 H\gamma}\, k\right), \\ \sigma'_z &= -H\gamma\,. \end{aligned} \tag{33}$$

Die momentanen Werte der Spannungen können mit Hilfe obiger Zusammenhänge unter Benützung folgender Daten veranschaulicht werden (Bild 10):

$$H = 100\,000 \text{ cm},$$

$$\gamma = 0{,}0025 \text{ kp/cm}^3,$$

$$b = 200 \text{ cm},$$

$$\sigma_F = 100 \text{ kp/cm}^2.$$

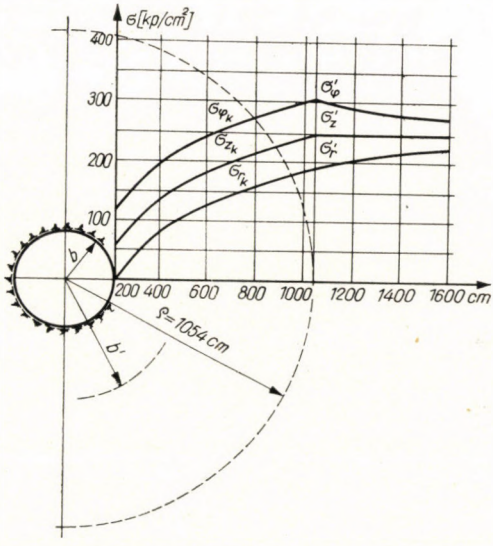

Bild 10. Elastische und plastische Spannungen in der Umgebung einer kreisrunden Strecke

Die angedeuteten Arbeitshypothesen und Meßverfahren geben eine Möglichkeit zur Dimensionierung von starren kreisrunden Mauerungen und starren Stahlringen in Abhängigkeit von der Teufe und den Gesteinskennzahlen.

SCHRIFTTUM

1. Horváth, J.: Die Bestimmung der Gesteinskennzeichen mit einachsigem Druckversuch und die Verwendung der Ergebnisse im Bergbau. *Mitteilungen des ungarischen Forschungsinstitutes für Bergbau* (1963), H. VIII. 1.
2. Kirsch: Die Theorie der Elastizität und Bedürfnisse der Festigkeitslehre. *V. D. I.* (1898).
3. Kühn: Betrachtungen über die Gebirgsdruckfragen. *Glückauf* 1931.
4. Nádai, A.: Theory of Flow and Fracture of Solids. New York 1951.
5. Prager—Hodge: Theory of Perfectly Plastic Solids. New York 1951.
6. Reuss, E.: Die Methoden der Plastizitätstheorie. Budapest 1962.
7. *Сабин:* Концентрация напряжений около отверстий. Ленинград 1951.

THE DEVELOPMENT OF CENTRALLY SYMMETRIC LOADS AROUND MINE ENTRIES OF CIRCULAR CROSS SECTION

J. HORVÁTH

SUMMARY

The paper deals with the state of stress arising around mine entries of circular cross-section. The mineralogical characteristics of the accompanying rocks of the Lias mines in the *Mecsek* were investigated in the laboratory. A great part of the rocks has an elastic range where Poisson's ratio is constant. While increasing the load, Poisson's ratio tends towards 0.5. According to the experiments, the minerals have generally an elastic and a plastic range, therefore they can be dealt with like structural materials. Author has deduced the law of plasticity for unsupported circular mine workings. Using the law of plasticity, the critical depth, the dimensions of the plastic range developing around the entry and the elastic and plastic stresses were determined. The results of the experimental and theoretical investigations are shown by an example.

LA FORMATION D'ÉTATS DE CONTRAINTES SYMÉTRIQUES PAR RAPPORT A L'AXE AUTOUR DE GALERIES DE MINE DE SECTION CIRCULAIRE

J. HORVÁTH

RÉSUMÉ

L'étude traite de l'état de contraintes se produisant autour des galeries de mine de section circulaire. L'auteur a déterminé, par des essais de laboratoire, les caractéristiques des roches encaissantes liassiques de l'exploitation minière de Mecsek. Il constate qu'une grande partie des roches a un domaines élastique où le nombre Poisson est constant. Si la charge augmente, le nombre Poisson converge vers 0,5. D'après les données expérimentales, les roches ont en général un domaine élastique et plastique, et peuvent donc être envisagées comme des matériaux de construction. La loi de plasticité est déduite pour des galeries de section circulaire non supportées. En utilisant la loi de plasticité, l'auteur détermine la profondeur critique, les dimensions de la zone plastique se produisant autour de la galerie et les contraintes élastiques et plastiques. Les résultats des recherches expérimentales et théoriques sont illustrés par un exemple terminant l'étude.

ВОЗНИКНОВЕНИЕ ОСЕСИММЕТРИЧНЫХ НАГРУЗОК ВОКРУГ ГОРНЫХ ВЫРАБОТОК КРУГЛОГО СЕЧЕНИЯ

Й. ХОРВАТ

РЕЗЮМЕ

В работе рассматривается напряженное состояние, возникающее вокруг горных выработок круглого сечения. Автор путем лабораторных опытов определил характеристики горных пород, сопровождающих лиасовые выработки Мечека. Можно установить, что большинство пород имеет эластичную зону; в этой зоне число Пуассона постоянно. С ростом нагрузки число Пуассона стремится к 0,5. По опытным данным горные породы вообще имеют эластичные и пластичные зоны, то есть могут рассматриваться как конструкционные материалы. Автор вывел закон пластичности для некрепленных выработок круглого сечения. Используя закон пластичности, определяются критическая глубина, размеры образующегося вокруг выработки пластичного пояса, а также пластичные и эластичные напряжения. Результаты опытов и теоретических исследований продемонстрированы на примерах.

DIE STANDZEITSFRAGEN DER SCHLEIFSCHEIBEN*

A. HORNUNG

DOKTOR DER TECHNISCHEN WISSENSCHAFTEN

[Eingegangen am 16. Dezember 1963]

Die Bestimmung der Standzeit der Schleifscheiben ist in der Fachliteratur sehr wenig aufgeklärt. Der meistens angegebene Gütegrad oder die Wirtschaftlichkeit der Schleifscheiben geben sehr wenig Aufklärung über die Standzeit. Außerdem hängt der Gütegrad und auch die Standzeit sehr stark von der chemischen Zusammensetzung des zu bearbeitenden Stahlmaterials oder mit anderen Worten von der Schleifbarkeit des Materials ab. Nach den Versuchen des Verfassers gibt es eine Möglichkeit für die Bestimmung der Standzeit durch eine Verhältniszahl ε, welche das abschleifbare Materialvolumen durch die Wirkflächen-Einheit der Schleifscheibe angibt. Diese Verhältniszahl ist unabhängig von dem verbrauchten Schleifscheibenvolumen durch Selbstschärfung und durch Abrichten, aber sie hängt von den Parametern der Schleifbarkeit und auch von den Eigenschaften der Schleifscheiben ab. Im weiteren gibt der Aufsatz eine Berechnungsmethode für die Ausnutzung der Antriebsleitung der Schleifmaschine an, durch welche die Hauptzeit der Arbeitstücke bestimmbar ist. Durch die angegebenen Versuchswerte der Verhältniszahl ε kann man die Standzeit der Schleifscheibe berechnen.

I. Einleitung

Bei der Schleifarbeit ist am wenigsten die Standzeit oder die Standhaltigkeit der Schleifscheiben aufgeklärt. Die Fachliteratur gibt größtenteils den Gütegrad oder die Wirtschaftlichkeit der Schleifscheiben an, das bedeutet, daß man mit abgenutztem Kubikinhalt der Schleifscheiben mal Kubikinhalt Metall abarbeiten kann. Die Tafel I veranschaulicht eine solche Zusammenstellung über verschiedene Werkzeugstähle.**

Diese Zusammenstellung gibt die sogenannte Schleifbarkeit der verschiedenen Werkzeugstähle in Verhältnis, welche folgendermaßen bestimmt wurde: Auf einer Flächenschleifmaschine mit alternierend bewegtem Arbeitstisch wurden die Probestücke aufgespannt. Die Schleifspindel war horizontal, mit einer Schleifscheibe von $200 \times 13 \times 32$ mm Edelkorund, Korngröße 46, Härte I, Struktur 8, keramische Bindung; Umfangsgeschwindigkeit 30,5 m/sec; Vorschub pro Tischhub 1,27 mm; Zustellung 0,025 mm; Tafelgeschwindigkeit 18,3 m/min; Kühlung: Ölemulsion. Unter diesen Bedingungen wurden die

* Vortrag auf der Schleifmittelkonferenz in Prag, 16. Oktober 1963.

** CLIFTON, C.—NICKERSON: How to Select Wheels for Grinding Tool Steels. *American Machinist* (1955), May 9.

Tafel I

Schleifbarkeit von Werkzeugstählen

Stahlbeschreibung	Analyse (Angaben in Prozent)					Härte (HRC)	Schleifbarkeit
Reiner Kohlenstoffstahl	C 1,0	Si 0,3	Mn 0,3			63	über 40
Niedrig legierter, verzugsarmer Ölhärter	C 0,9 Cr 0,85	Si 0,25 Mo 0,5	Mn 1,6 Ni 1,5	V 0,25		58	über 40
Chrom-Nickel-Stahl	C 0,75 Cr 0,85	Si 0,25 Mo 0,5	Mn 0,7 Ni 1,5			61	über 40
Verzugsarme Stähle Lufthärter						59	über 40
Niedrig legierter Stahl						59	über 40
Gesenkstahl						59	über 40
Stahl für Schlagwerkzeuge	C 0,5 Mo 0,4	Si 1,0 V 0,25	Mn 0,4			60	über 40
Warmarbeitsstahl für Matrizen und Gesenke	C 0,35 Cr 5,0	Si 1,0 Mo 1,5	Mn 0,3 V 0,4			50	über 40
Verzugsarmer mittellegierter Lufthärter	C 1,0 Cr 5,25	Si 0,25 Mo 1,1	Mn 0,6 V 0,4			60	20
Warmarbeitsstahl	C 0,32 Cr 3,25	Si 0,2 V 0,4	Mn 0,3 W 9,0			53	20
Gesenk- und Schnittstähle Hochchromlegierter Ölhärter	C 2,15 Cr 12,0	Si 0,35 Mo 0,8	Mn 0,35 Ni 0,5	V 0,8	W 0,75	62—64	3,5
Hochchromlegierter Lufthärter	C 1,5 Cr 12,0	Si 0,4 Mo 0,9	Mn 0,4 V 0,8	Co 3,5		59	3,5
Hochvanadiumlegierter Stahl	C 3,0	Cr 1,0	Mo 1,0	V 12,0		61	0,4
Graphitischer Stahl, Ölhärter	C 1,45	Si 1,0	Mn 0,75	Mo 0,25		63	über 40
Schnellstähle auf Wolframbasis	W 18	Cr 4	V 1			64	6 ÷ 12
	W 18	Cr 4	V 2			63	4
	W 18	Cr 4	V 2	Co 12		63	3
	W 18	Cr 4	V 3			62	1,1
	W 18	Cr 4	V 4			64	0,4
	W 14	Cr 4	V 2			63	6
	W 10	Cr 4,5	V 2,5—3			63	2 ÷ 3
	W 14	Cr 4	V 3			63	0,6
	W 13	Cr 5	V 5	Co 5		67	0,8
Schnellstähle auf Molibdänbasis	W 2	Mo 8	Cr 4	V 1		64	7
		Mo 8	Cr 4	V 2		64	3,5
	W 6	Mo 5	Cr 4	V 1	Co 1	64	7
	W 6	Mo 5	Cr 4	V 2		64	4
	W 6	Mo 6	Cr 4	V 2,5		65	1,0
	W 6	Mo 6	Cr 4	V 3		64	1,0
	W 6	Mo 5	Cr 5	V 4		65	0,7
	W 6	Mo 4	Cr 4	V 5	Co 5	65	0,8
	W 6	Mo 3	Cr 5	V 5	Co 5	66	0,6

Probestücke solange geschliffen, bis es überhaupt geht, abgesehen davon, ob die Scheibe brennt oder Schleifrisse hervorruft, oder die Oberfläche ganz rauh wird.

Aus dem obigen folgt, daß die Schleifbarkeit gleich der Verhältniszahl des abgearbeiteten Metallvolumens zu dem Scheibenverschleiß ist. Diese Schleifbarkeit kann man nicht ohne weiteres für die Bestimmung der Schleifscheibenstandzeit benutzen, mit Hilfe der Schleifbarkeit kann man aber die Standzeit von einer Stahlsorte unter bekannten Schleifbedingungen auf eine andere Stahlsorte umrechnen.

Zum Beispiel nehmen wir an, daß man eine Oberfläche irgendeines Arbeitsstückes von gehärtetem Werkzeugstahl mit Zustellung von 0,025 mm so abschleifen kann, daß das Volumenverhältnis der Schleifscheibe zu dem Stahl 1 : 20 ist. Wenn man noch weiter schleift, dann fängt die Oberflächengüte an, so minderwertig zu sein, daß das Werkstück unbrauchbar wird. (In dem verbrauchten Scheibenvolumen ist durch das feine Abrichten das abgearbeitete Scheibenvolumen auch eingerechnet.)

Die Zeit, die für das Abschleifen des Stahlvolumens notwendig ist, kann man aus der Zustellung, dem Scheibenvorschub, der Werkstückgeschwindigkeit und von den Abmessungen des Werkstückes und der Scheibe ermitteln. Die durch diesen Weg bestimmte Zeit wird die Standzeit der Schleifscheibe unter den vorigen Schleifbedingungen sein.

Wenn man ein Werkstück aus gehärtetem normalem Schnellstahl unter den vorigen Schleifbedingungen schleifen will, so wird die Standzeit annähernd aus der Tafel I ermittelt und ist 1/4.

Aus Tafel I ist ersichtlich, daß die niedriglegierten Stähle sehr gut und manche hochlegierte Stähle sehr schlecht schleifbar sind. Von dem Ersten kann man mit einem Kubikinhalt der Schleifscheibe über 40 Kubikinhalt der gehärteten Stähle abarbeiten, aber von dem Zweiten kann man nicht einmal einen Kubikinhalt der Stähle abschleifen.

Wenn wir annehmen, daß wir von der abarbeitenden Umfläche der Schleifscheibe eine Dicke von 0,05 mm durch Selbstschärfung und durch Abrichten abtrennen, das bedeutet, daß wir eine $40 \cdot 0{,}05 = 2$ mm Dicke von den gut schleifbaren Stählen abarbeiten können, wenn die Umflächen der Schleifscheibe und des zu bearbeitenden Werkstückes gleich sind.

In der Praxis verlangt man durch Schleifen genaue Maße und annehmbare Oberflächengüte ohne Schleifrisse und ohne Brennen. Diese können wir nur durch entsprechendes Abrichten der Scheibe erzielen. In diesem Fall können wir nicht die in Tafel I angegebene Schleifbarkeit als Gütegrad erreichen, weil da man außer der Selbstschärfung oder außer dem Scheibenverschleiß auch mit dem durch Abrichten abgetrennten Scheibenvolumen rechnen muß. Dieses kann sehr verschieden sein und dadurch können wir für die Schleifscheibenstandzeit sehr abweichende Daten bekommen.

Aus dem vorausgehenden ist es klar, daß die richtige Schleifscheibenstandzeit aus der folgenden Verhältniszahl bestimmbar ist: ε Kubikinhalt Metall kann man mit einer arbeitenden Umflächen-Einheit der Scheibe abschleifen:

$$\varepsilon = \frac{V_w}{A_s} \, [\mathrm{mm}^3/\mathrm{mm}^2] \, ,$$

wo V_w abgeschliffenes Metallvolumen des Werkstückes während der Standzeit;
A_s die arbeitende Umfläche der Schleifscheibe bedeutet.

Die Dimension dieser Verhältniszahl ist $\mathrm{mm}^3/\mathrm{mm}^2$, aber die Standzeit soll Minute oder Sekunde sein. Selbstverständlich muß man durch diese Verhältniszahl auch die Minuten ausrechnen, ebenso wie es im vorerwähnten Beispiel geschehen ist.

Die Verhältniszahl ε ist unabhängig von dem verbrauchten Schleifscheibenvolumen durch Selbstschärfung und durch Abrichten. Diese Verhältniszahl ist auch charakteristisch für die Parameter der Schleifarbeit und auch für die Eigenschaften der Schleifscheiben und zwar: Schleifkornart, Korngröße, Bindung, Härte, Struktur (Porosität) und nicht minder für die Qualität der Schleifscheiben. Diese letzte Bemerkung ist nicht überflüssig, weil Schleifscheiben mit denselben Eigenschaftsangaben aber von verschiedenen Fabrikaten ganz verschiedene Leistungen ergeben.

II. Die Bestimmung erzielbarer Leistungen beim Schleifen

Beim Schleifen soll man eine Methode finden, durch die man die Hauptzeit oder Maschinenzeit der Schleifarbeit eines Werkstückes bestimmen kann. In den folgenden Zeilen wird eine solche Methode vorgeführt. Wenn die Hauptzeit eines Werkstückes bestimmt wurde, so ist es sehr einfach, die Verhältniszahl ε aus den Abmessungen des Werkstückes und der Schleifscheibe zu ermitteln. Wenn man diese Verhältniszahl aus vorigen Versuchen kennt, dann ist sehr einfach zu bestimmen, bei wievieltem Arbeitstück ε erreicht wird. So bekommt man die Standzeit der Schleifscheibe in Minuten.

Bei einer Schleifarbeit kennen wir das abzuarbeitende Metalvolumen. Dieses wollen wir in zwei Teile aufteilen, und zwar Schruppvolumen und Schlichtvolumen. Das Erste hängt hauptsächlich von der Antriebsleistung der Schleifmaschine, von den Eigenschaften und Qualität der Schleifscheiben und nicht zuletzt von der Art des Abrichtens ab.

Beim Schlichtschleifen soll man hauptsächlich auf Maßgenauigkeit und auf die Oberflächengüte achten, da die Antriebsleistung der Schleifmaschine nicht maßgebend ist.

Für Bestimmung des in einer Minute abschleifbaren Metallvolumens nehmen wir die Grundgleichung der Spanung:

$$P = \frac{kV}{4500} \text{ PS}$$

oder

$$P = \frac{kV}{6120} \text{ kW},$$

woraus

$$V = \frac{4500\,P}{k} \text{ cm}^3/\text{min},$$

wo P die netto Spanungsleistung an dem Schleifscheibenumfang in PS oder kW ist
k ist der spezifische Schnittwiderstand oder die spezifische Schnittkraft in kp/mm² und
V ist das in einer Minute mit P abschleifbare Metallvolumen in cm³.

V kann man bestimmen bei Längs-Rundschleifen (Rundschleifen mit Seitenvorschub):

$$V = v_w\, as \text{ cm}^3/\text{min},$$

v_w ist die Werkstückgeschwindigkeit in m/min;
a ist die Zustellung in mm pro Längshub;
s ist der Seitenvorschub der Schleifscheibe in mm/Werkstückumdrehung.

V ist beim Einstechrundschleifen

$$V = v_w\, ab \text{ cm}^3/\text{min},$$

hier ist a die Zustellung in mm/Werkstückumdrehung;
b die Schleifbreite in mm.

Flächenschleifen mit am Umfang angreifender Schleifscheiben und auch Innenrundschleifen ist ebenso wie der Längs-Rundschleifen.

Flächenschleifen mit stirnseitig angreifender Topfscheibe oder Segmenten:

$$V = v_w\, ab \text{ cm}^3/\text{min}.$$

In der Rechnung muß man in Kauf nehmen, daß das wirklich abgearbeitete Metallvolumen immer kleiner ist als die durch obigen Formeln ausgerechneten Werte. Nähmlich die abgeschliffene Metalldicke ist immer weniger als die Zustellung. Die Ursache liegt in der Elastizität der Schleifmaschine und in der Werkstückeinspannung sowie im Schleifkornverschleiß. Aus diesem Grunde muß man V in den obigen Formeln mit dem Faktor ϑ multiplizieren. Die Werte von ϑ liegen zwischen 0,70—0,90, welche Werte von der Starrheit der Maschine und der Werkstückeinspannung sowie auch von den Eigenschaften und von der Qualität der Schleifscheiben abhängen.

Die Bestimmung der Werte von k sind nur durch Versuche möglich, weil die Schleifarbeit sehr verwickelt ist. Die Werte von k werden kleiner, wenn die mittlere Spandicke größer wird, also größere Zustellung, größere Korngröße, größere Werkstückgeschwindigkeit und kleinere Scheibenumfangsgeschwindigkeit geben kleinere Werte von k und umgekehrt. Außerdem können wir nur mit dem mittleren Werte von k rechnen, weil wir sofort nach dem Abrichten, wenn die Scheibe noch griffig ist, niedrigere Werte bemerken können. Aber wenn die Scheibe gegen Ende der Standzeit schon abgestumpft ist, werden höhere Werte gemessen.

Nach den Versuchen des Verfassers sind die Werte von k für Schleifscheiben von mittlerer Qualität und für Korngröße von 46 bei verschiedenen Schleifarten in der Tafel II angegeben.

Die Eigenschaften der Schleifscheibe wählen wir für die durchzuführende Schleifarbeit nach den Erfahrungstabellen und auch die Werkstückgeschwindigkeit und den Seitenvorschub. Aus der reinen Spanungsleistung P, bei Berücksichtigung des Wirkungsgrades des Antriebes der Schleifspindel berechnen wir die Zustellung aus

$$a = \frac{4500\,P}{k v_w s}\ \text{mm},$$

wo P in PS angegeben ist.

Tafel II

Die Werte der mittleren spezifischen Schnittwiderstände k_m bei verschiedenen Schleifarten, Korngröße 46, Struktur 5

Schleifart		Werkstückmaterial	Zustellung a [mm]	k_m [kp/mm²]
Längs-Rundschleifen		Gehärteter Stahl Ungehärteter Stahl Gußeisen	0,015 ÷ 0,02	4 500 4 000 4 000
Einstech-Rundschleifen		Gehärteter Stahl Ungehärtet Stahl Gußeisen	0,015 ÷ 0,02 [mm/Umdrehung]	3 600 3 000 3 000
Flächenschleifen		Gehärteterer Stahl Ungehärteterer Stahl Gußeisen	0,015 ÷ 0,02	5 000 4 000 4 000
Innen-schleifen	$D = 10 \div 15$ mm	Gehärteter Stahl Ungehärteter Stahl Gußeisen	0,002 ÷ 0,003	15 000
	$D = 15 \div 25$ mm		0,002 ÷ 0,003	12 000
	$D = 25 \div 50$ mm		0,003 ÷ 0,005	10 000
	$D = 50 \div 100$ mm		0,005 ÷ 0,01	8 000
	$D = 100 \div 250$ mm		0,005 ÷ 0,01	7 000
	$D > 250$ mm		0,01 ÷ 0,015	6 000
Spitzenloses Schleifen		Gehärteter Stahl Ungehärteter Stahl Gußeisen	0,015 ÷ 0,025	4 050 3 600 3 600

In der Bestimmung der Maschinenzeit bei der Schleifarbeit soll man den Faktor ϑ auch berücksichtigen. Wenn die Materialzugaben für Schruppschleifen h mm ist, so bekommen wir beim Längs-Rundschleifen die Hubzahl i oder beim Einstechschleifen die Werkstückumdrehungszahl:

$$i = \frac{h}{a\vartheta} .$$

Beim Schlichtschleifen nimmt man manche Hübe oder Umdrehungen mit feiner Zustellung, um das genaue Maß zu bekommen und einige Hübe oder Umdrehungen ohne Zustellung, um bessere Oberflächengüte zu erzielen (also ausfunkeln).

Die Hauptzeit des Schlichtschleifens kann man ähnlich wie beim Schruppschleifen bestimmen.

III. Die Bestimmung der Standzeit der Schleifscheiben

In obenangeführter Weise kann man die Maschinen- oder Hauptzeit für Schrupp- und Schlichtschleifen bestimmen. Aber in der Gesamtzeit der Schleifarbeit nehmen die Abrichtzeiten einen bedeutenden Anteil der Nebenzeiten in Anspruch. Man muß nähmlich die Schleifscheiben bei sehr schlecht schleifbaren Stählen so oft abrichten, daß die Abrichtzeiten die Hauptzeiten annähern, wie es aus der Tafel I ersichtlich ist. Die Schleifbarkeit ist die Eigenschaft der zu schleifenden Materialien. Darum ist es wichtig, die Standzeit der Schleifscheiben zu bestimmen.

Die Standzeit der Schleifscheiben hängt von sehr vielen Variablen ab und davon, ob die Eigenschaften der Schleifscheibe, hauptsächlich die Härte, ferner die Werkstückgeschwindigkeit entsprechend für die Schleifarbeit gewählt wurden.

In dem Beurteilen der Schleifscheibenstandzeit ist es wichtig, die Merkmale des Endes der Standzeit beim Schleifen zu erkennen.

In der Werkstattpraxis sind die üblichen Merkmale beim Schleifen von Stählen: Die Werkstückoberfläche wird vieleckig, und man höhrt ein Murmeln; die Scheibe brennt. Diese Erscheinungen kommen beim Schleifen von Gußeisen auch vor. Das Vieleckigwerden hängt mit der Vergrößerung der Schwingungsamplituden auch zusammen, wie es durch die Versuche von VUOSO in Prag ausgewertet wurde.

Der Verfasser hat auch Versuche durchgeführt, welche die Erscheinungen des Standzeitendes bei verschiedenen Scheibeneigenschaften in Funktion der Veränderung der Spanungsleistungen anzeigen.

Bild 1 veranschaulicht die Veränderung der Spanungsleistung beim Längs-Rundschleifen in Funktion der Hubzahl, wenn die Härte der Schleif-

scheibe, die Werkstückgeschwindigkeit und der Seitenvorschub entsprechend für die Schleifarbeit gewählt wurden. Man sieht, daß die Spanungsleistung am Anfang, wenn die Scheibe noch griffig ist, niedrig ist. Später, wenn die Schleifkörner abgestumpft sind, ist die Spanungsleistung höher. Am Ende, wenn die abgestumpften Schleifkörner von der Bindung sich auslösen und das Werkstück vieleckig wird, also die Standzeit beendet ist, vermindert sich die Spanungsleistung. In Bild 1 ist der mittlere Wert der Spanungsleistung

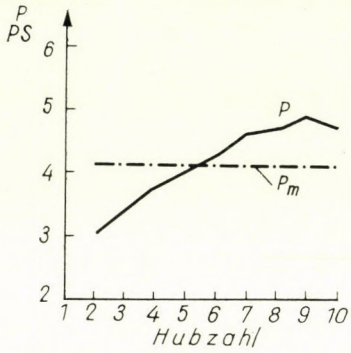

Bild 1. Die Veränderung der Spanungsleistung beim Längs-Rundschleifen in Funktion der Hubzahl, wenn die Härte der Schleifscheibe richtig gewählt wurde. Die Schleifbedingungen-Schleifscheibenumfangsgeschwindigkeit $v_S = 30{,}5$ m/sec; Werkstückumdrehungszahr $n_w = 43$/min; Zustellung a = 0,02 mm pro Hub; Seitenvorschub $s = 20$ mm/Werkstückumdrer hung; Werkstücklänge $L \approx 800$ mm; Werkstückdurchmesser $d \approx 100$ mm; Werkstückmaterial: gehärteter Kugellagerstahl

auch eingezeichnet, aus welchem der mittlere spezifische Schnittwiderstand berechnet wurde. Sonst folgen die Werte des momentanen spezifischen Schnittwiderstandes den Werten der Spanungsleistungen. Es soll bemerkt werden, daß der Faktor ϑ am Ende der Standzeit sich auch vermindert.

Die Standzeit war bei diesem Versuche 10 Minuten, welche aus den Angaben des Versuches mit 860 mm Gesamtvorschub pro Hub bestimmbar ist.

Bild 2 zeigt die Veränderung der Spanungsleistung in Funktion der Hubzahlen, wie in Bild 1, aber die Härte der Schleifscheibe ist nicht entsprechend hoch, also die Scheibe ist zu weich. Die Spanungsleistung fängt an, sich rasch zu vermindern, die Standzeit ist beträchtlich kürzer als im Bild 1. Der Faktor ϑ vermindert sich viel rascher als bei entsprechender Härte der Scheibe.

Die Standzeit war nur 5 Minuten, also rund die Hälfte des vorigen Versuches. Aber bei noch weicheren Schleifscheiben kann die Standzeit sich um 5—10% herabsinken, wie andere Versuche es bewiesen haben.

Bild 3 veranschaulicht die Veränderung der Spanungsleistung wie in Bild 1, aber bei einer zu harten Schleifscheibe. Die Spanungsleistung zeigt eine steigende Tendenz und am Ende der Standzeit, wenn die Scheibe schon

brennt, zeigt dieselbe eine rapide Steigung. Auch der Faktor ϑ vermindert sich sehr stark in diesem Fall.

Die Standzeit war bei diesem Versuche 7 Minuten, also 70% des ersten Versuches.

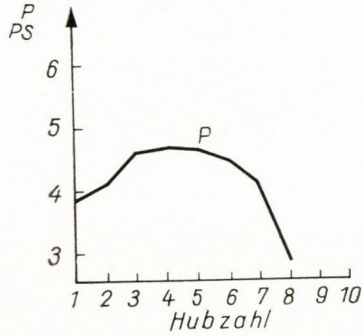

Bild 2. Die Veränderung der Spanungsleistung in Funktion der Hubzah bei zu hart gewählter Schleifscheibe. Die Schleifbedingungen sind wie bei Bild 1

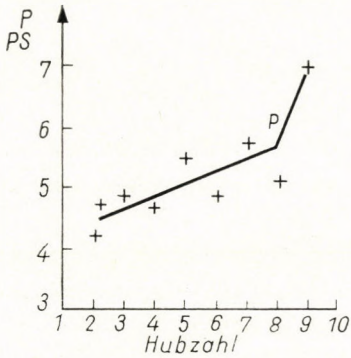

Bild 3. Die Veränderung der Spanungsleistung in Funktion der Hubzahl bei zu weich gewählter Schleifscheibe. Schleifbedingungen sind wie bei Bild 1

Aus dem obenangeführten folgt, daß die Vorbedingungen der richtigen Standzeit die Wahl der entsprechenden Eigenschaften der Schleifscheibe sowie die richtige Wahl der Parameter des Schleifens für die Schleifarbeit sind.

Außerdem beeinflußt auch die Art des Abrichtens die Schleifscheibenstandzeit. Die griffig abgerichtete Schleifscheibe gibt eine längere Standzeit, aber sie erzeugt eine etwas rauhere Oberflächengüte.

Das Abrichten der griffigen Schleifscheibe erfolgt mit scharfem Diamant und die Steigung des durch Abrichten erzeugten Gewindes an der Schleifscheibenumfläche ist 0,10—0,25 mm, abhängig von der Schleifkorngröße. Das Abrichten mit einem abgestumpften Diamant und mit kleinerer Gewindesteigung gibt eine weniger griffige Schleifscheibe, welche niedrigere Standzeit aber bessere Oberflächengüte erzielt.

Die mit stark abgestumpftem Diamant abgerichtete Schleifscheibe gibt eine stark verminderte Standzeit und gute Oberflächengüte, aber fängt an ziemlich rasch zu brennen.

Dr. Ing. STADE gibt in seinem Buch: »Technologie des Schleifens« (Hanser Verlag, München 1962) Angaben für Schleifscheibenstandzeit, welche sehr wertvoll sind, besonders für Gewindeschleifen. Er rechnet mit einer mm Schleifscheibenbreite abarbeitbarem Schleifvolumen. Dies ist richtig, wenn man mit Schleifscheiben gleichen Durchmessers arbeitet, wie es im Gewindeschleifen größtenteils der Fall ist. Aber wenn man mit einer Verhältniszahl arbeiten will, welche für Schleifscheiben mit sehr verschiedenen Durchmessern gültig ist, ist es richtiger, die Schleifscheibenstandzeit auf das mit einer arbeitenden Schleifscheibenumfläche-Einheit abschleifbare Metallvolumen zu beziehen.

STADE gibt in seinem Buche Beispiele für Einstechschleifen für Motorkurberlwellenzapfen an, da man eine Verhältniszahl von 0,6 mm^3/mm^2 bei Schruppschleifen berechnen kann. Die näheren Angaben für die Oberflächengüte fehlen, so daß diese mit Versuchsergebnissen des Verfassers von einer Verhältniszahl 0,9 mm^3/mm^2 bei Schlichtschleifen im großen und ganzen gut übereinstimmen. Nähmlich beim Schruppschleifen sind die Schleifkörner mehr beansprucht und es gibt eine niedrigere Verhältniszahl ε. Diese bezieht sich auf eine Schleifscheibe: Edelkorund, Korngröße 60/70, Härte L, gekühlt mit Ölemulsion, die geschliffene Kurbelzapfen wurden gehärtet. Bei Versuchen des Verfassers hat die Schleifscheibe die folgenden Eigenschaften: Edelkorund, Korngröße 46/60, Härte M, gekühlt mit einer Sodalösung. Die geschliffene Kurbelzapfen wurden auch gehärtet.

Bei den Versuchen des Verfassers war die Qualität der Schleifscheibe eine mittlere, aber es stehen Angaben zur Verfügung, daß man mit Schleifscheiben von sehr guter Qualität ungefähr die doppelte Verhältniszahl $\varepsilon = 1{,}8$ mm^3/mm^2 erreichen konnte. Dies kann von der besseren Schleiffähigkeit der Schleifscheibe von besserer Qualität stammen. Die Schleiffähigkeit ist die Eigenschaft der Schleifscheibe.

Zur Vollständigkeit fehlen noch weitere Versuchsdaten für Flächen- und Innenrundschleifen mit Schleifscheiben von verschiedenen Eigenschaften und Schleifarbeit von verschiedenen Metallsorten.

Um für die Praxis brauchbare Versuchsangaben zu geben, muß man bei den Versuchen die Art und Weise des Abrichtens sehr genau feststellen.

THE PROBLEM OF THE DETERMINATION OF THE TOOL LIFE OF GRINDING WHEELS

A. HORNUNG

SUMMARY

Few data can be found in the literature on the tool life of grinding wheels. Mostly such data on their grinding ratio are published which give very little information on the tool life of the tool. Moreover, the grinding ratio as well as the endurance of the tool depend

to a high degree on the chemical composition of the steel material or, in other words, on the grindability of the material.

According to the author's experiments, the ratio ε indicating the volume of material that can be ground off the wheel per unit working surface, permits to state the tool life of the grinding wheel. This ratio is independent of the self-sharpening of the wheel and of the volume loss caused by its dressing, but it does depend on the parameters of the grinding work and on the data characterizing the quality of the wheel.

Furthermore, the paper presents a method for calculating the utilization of the driving power of the grinding machine as well as experimental data of the ratio ε, by the aid of which the machining time of the workpiece and the tool life of the wheel can be calculated.

LES PROBLÈMES DE LA DÉTERMINATION DE LA DURÉE DES MEULES

A. HORNUNG

RÉSUMÉ

Les données relatives à la détermination de la durée des meules sont peu nombreuses dans la littérature. La plupart du temps, c'est le rendement de la rectification qui est communiqué, mais cette donnée n'offre que très peu d'informations sur la durée des meules. En outre le rendement et aussi la durée dépendent fortement de la composition chimique de l'acier à usiner, ou en d'autres mots, de son usinabilité à la meule.

Suivant les essais de l'auteur, la durée de la meule peut être définie par le rapport ε, qui indique le volume de matière pouvant être enlevé par unité de surface active de la meule. Ce rapport est indépendant de la perte de volume due à l'auto-affutage et au dressage de la meule, mais dépend des paramètres du travail de meulage et des caractéristiques qualitatives de la meule.

L'auteur présente aussi une méthode de calcul pour l'utilisation de la puissance de la rectifieuse, ainsi que des données expérimentales relatives au rapport ε, à l'aide desquelle-on peut déterminer les temps d'usinage principaux des pièces et la durée de la meule.

ВОПРОСЫ ОПРЕДЕЛЕНИЯ СРОКА СЛУЖБЫ ШЛИФОВАЛЬНОГО КРУГА

А. ХОРНУНГ

РЕЗЮМЕ

В технической литературе имеется очень мало данных относительно методики опres деления срока службы шлифовальных кругов. В большинстве случаев указывают степень добротности или экономичность шлифовального круга, которые однако в отношении срока службы дают очень мало сведений. Кроме того, как степень добротности, так и срок службы очень сильно зависят от химического состава обрабатываемого стального материала, или же, другими словами, от шлифуемости материала. На основе проведенных автором опытов в отношении определения срока службы шлифовального круга открывается возможность при использовании показателя ε, который показывает объем материала, могущий быть обработанным единицей действующей поверхности шлифовального круга. Этот показатель независим от потерь объема шлифовального круга, образующихся при самозаточке и правке, но зависит от параметров шлифовальной работы и качественных характеристик шлифовального круга. В дальнейшем в работе показан новый метод расчета использования приводной мощности шлифовального станка и приведены экспериментальные данные значений показателя ε, при помощи которых можно рассчитать основное машинное время обрабатываемых заготовок и срок службы шлифовального круга.

PROBLEMS OF DEAERATION IN HEAT EXCHANGERS CONSISTING OF STEAM-HEATED PARALLEL TUBES

L. FORGÓ

CAND. OF TECHN. SC.
INSTITUTE FOR ENERGETICS, BUDAPEST

[Manuscript received May 5, 1964]

The output of heat exchangers in operation, consisting of steam-heated parallel tubes dimensioned and built according to modern technical literature, frequently fall short of the rated thermal output. The reason for it lies in difficulties of deaeration, due to non-uniform thermal load on the heat transfer surface or to non-uniform flow resistance on the steam side. Such heat exchangers operate either without steam loss but at lower thermal output, or at their rated output, yet with steam loss. Loss in efficiency is higher if the heat transfer surface is built up of finned tubes and lower if it is built up of plain ones. Further factors increasing loss are the relatively short and wide tubes, the horizontal arrangement of the tubes and the low flow velocity of the external medium. The paper recommends methods for the calculation of the drop in output and for its partial or complete elimination.

Symbols

$$A = \frac{\varrho}{2}\left(\frac{1}{\alpha} - 1\right)^2 \text{ [kg s}^2/\text{m}^4\text{]} ;$$

$$A_1 = 1 + \frac{E}{b} \cdot \frac{1}{w_1 \vartheta_{11} \Phi_1} ;$$

$$A_2 = 1 + \frac{E}{b} \cdot \frac{1}{w_1 \vartheta_{11} \Phi_2} ;$$

$$A_3 = 1 + \frac{E}{b} \cdot \frac{1}{w_1 \vartheta_{11} \Phi_3} ;$$

$$B = 0.115 \frac{\varrho}{2} L d^{-5/4} \nu^{1/4} \text{ [kg s}^{1,75}/\text{m}^{3,75}\text{]};$$

$$B_1 = \frac{1}{A_2}\left(A_1 - \frac{E}{b} \cdot \frac{1}{w_1 \vartheta_{11}}\right);$$

$$B_2 = \frac{1}{A_3}\left(A_2 - \frac{E}{b} \cdot \frac{1}{w_1 \vartheta_{11}}\right.;$$

$$B_3 = \frac{1}{A_3}\left(A_3 - \frac{E}{b} \cdot \frac{1}{w_1 \vartheta_{11}}\right);$$

$C = Lg\,(\varrho_g - \varrho) \cos \delta$ [kg/m²];
$D = Lg\,\varrho_g \cos \delta$ [kg/m²];
$E = 2826\, d^2 z\, \varrho\, g\, r$ [kcal/m];
F external heat transfer surface, [m²];
F_1 the external heat transfer area of the first tube row, [m²];
F_b internal heat transfer surface, [m²];
L length of the tubes, [m];

$$N = \frac{2\,A + 0.875\,B}{A + 0.5\,B} \text{ exponent;}$$

Pr = Prandtl number;

Re = Reynolds number;

$$b = \frac{0.5}{\left(\dfrac{v_{1n}^2\,A + v_{1n}^{1.75}\,B + 0{,}5\,C}{A + 0.5\,B}\right)^{1/N} - v_{1n}} \text{ [s/m];}$$

d inside diameter of the tubes, [m];
e basis of the natural logarithm;
f approach steam cross-section, [m²];
f_1 tube cross-section, [m²];
g gravitation constant, [m/s²];
k over-all coefficient of heat transfer, [kcal/m²h °C];
k_1 the over-all coefficient of heat transfer of the first tube row, [kcal/m²h°C];
l_1 the active tract of the first tube row, [m];
n the number of rows in the direction of the flow of the external medium;
p pressure drop, [kg/m²];
p_0 pressure in the manifold, [kg/m²];
p_g pressure in the condensate-collecting main, [kg/m²];
q thermal output of the heat exchanger, [kcal/h];

$$q = \frac{E}{b}\left(\frac{1}{A_1 - B_1\,B_2\,B_3^{n-3}}\right)\cdot\left(1 + B_1 + B_1\,B_2\,\frac{1 - B_3^{n-2}}{1 - B_3}\right), \qquad n \geqq 3;$$

$$q = \frac{E}{b}\left(\frac{1}{A_1 - B_1}\right)\cdot(1 + B_1), \qquad n = 2;$$

q_1 thermal output of the first tube row, [kcal/h];
q_{max} maximum thermal output of the heat exchanger, [kcal/h];
r evaporation heat of steam, [kcal/kg];
t temperature, [°C];
t_0 temperature of heating steam, [°C];
t_1 inlet temperature of external medium, [°C];
v_1 inlet velocity of steam in the tube, [m/s];

$$v_{1n} = \frac{1}{b\cdot\left(\dfrac{A_1}{B_1} - 1\right)}, \quad n = 2 \text{ [m/s];}$$

$$v_{1n} = \frac{1}{b\cdot\left(\dfrac{A_1}{B_1\,B_2\,B_3^{n-3}} - 1\right)}, \quad n \geqq 3 \text{ [m/s];}$$

v_2 outlet velocity of steam from the tube, [m/s];
w_1 the water equivalent of the external heat-carrying medium, [kcal/(h °C)];
z number of the tubes normal to the flow of the external medium;
α f_1'/f contraction factor;
α_1 surface coefficient of the heat transfer of the first tube row, [kcal/(m² h °C)]
ϱ density of the heat-carrying medium, [kg s²/m⁴];
ϱ_g density of non-condensing gases, [kg s²/m⁴];

$\Phi_1 = 1 - e^{-k_1F_1/w_1}$
$\Phi_2 = 1 - e^{-k_2F_2/w_1}$
$\Phi_3 = 1 - e^{-k_3F_3/w_1}$
$\varepsilon_1 = 1 - \Phi_1$;
ν = kinematic viscosity of steam, [m²/s];
$\omega = E/w_1\,\vartheta_{11}$ [h/m].

I. Introduction

It frequently happens in practice that the actual heat output of steam-heated heat exchangers falls short of the value determined in the designer's preliminary calculations. Among such cases only those are of interest in which the heat output below the rated value cannot be traced to some error in the calculation or to some fault in construction.

In this paper we intend to throw light upon certain phenomena that occur in heat exchangers consisting of steam-heated parallel tubes which may cause low actual heat outputs of heat exchangers, designed and built according to the latest principles published in modern technical literature.

II. Deaeration of heat exchangers

It is a known fact that one of the basic criteria of the appropriate functioning of vapour-heated heat exchangers (not only water vapour) is their perfect "deaeration" viz. the removal of all kinds of non-condensing gases from the steam-filled space. Deaeration is essential not only when the equipment is started up but also during its operation, since the heating steam always contains a certain amount of impurities in the form of non-condensing gases, on the one hand, and air may penetrate through leaky spots into the steam-heated space in equipments operating under vacuum, on the other. If the steam pressure is above the atmospheric, such gases can easily be removed by blowing them out into the atmosphere, but with steam pressures below atmospheric, vacuum pumps are required. In each case, however, the removed non-condensing gases will sweep steam — in a quantity according to their momentary partial pressure — with them into the atmosphere. To prevent the loss of considerable quantities of steam, simultaneously with the removal of condensate and non-condensing gases, various devices, more or less suitable for the purpose, have been applied in technical practice (automatic steam traps). Having no intention to go into particulars about these devices, we shall assume that the heat exchangers to be dealt with are equipped with perfect steam traps or with vacuum pumps, which let pass the condensate and the non-condensing gases accumulated in the heat exchangers, but preclude the escape of steam. Accordingly, the possibilities of removing non-condensing gases from steam-heated heat exchangers will be investigated on the assumption of such "ideal" steam traps.

What is meant under "ideal" steam traps is illustrated in Fig. 1 which shows a conventional radiator into the upper horizontal manifold of which steam (for the sake of simplicity water vapour) is introduced at the point marked by an arrow. From this manifold vertical tubes branch off to lead

into a lower horizontal condensate-collecting main. To the lower main of the radiator a ballsloat trap of conventional type is connected, which carries away the condensate in the direction of the arrow marked K in the drawing. If this device operates perfectly, the float-actuated cock will pass only fluid, and, to dispose of the non-condensing gases which accumulate inside the radiator, another mechanism is required — likewise shown in the drawing — which extracts the gases at the point marked G. This latter is provided with a thermostat which, according to its setting, keeps the outlet valve closed until the temperature in the exhaust tube attains the saturation temperature

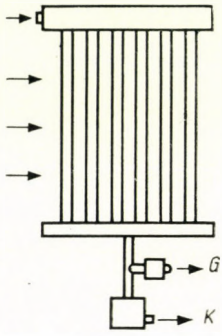

Fig. 1

that corresponds to steam pressure. Should, however, non-condensing gases cause the temperature to drop, the sensor will open the valve and keep it open until the gases escape and the temperature resumes the value of saturated steam. Consequently, the quantity of steam escaping from the heat exchanger with the non-condensing gases, depending on its partial pressure, will be very small and the heat exchanger operate practically without losses.

If adequate undercooling is applied ahead of the vacuum pump, non-condensing gases can be completely extracted also from heat exchangers heated with vacuum steam.

III. Difficulties in deaeration due to non-uniform thermal load on the heat transfer surface

1. Operation of steam-heated heat exchangers

Let us now look into the operation of a steam-heated heat exchanger equipped with the above-determined "ideal steam trap". Let us assume, for example, a heat exchanger of conventional design — as the one shown in Fig. 2 — consisting of a manifold above, a collecting main below, and vertically

arranged smooth or finned radiator tubes in between. Steam at a pressure above the atmospheric flows inside the manifold, collecting main and tubes, while air streams at the outside, in the direction marked in the drawing by arrows. For the problem in hand the number of tube rows in the heat exchanger parallel to the sheet of the paper are entirely indifferent, so, for simplicity's sake, we may as well assume that the whole set consists of the four tubes as shown in Fig. 2.

As a further simplification let us assume also that both the upper and the lower headers have very large cross-sections, consequently the velocity

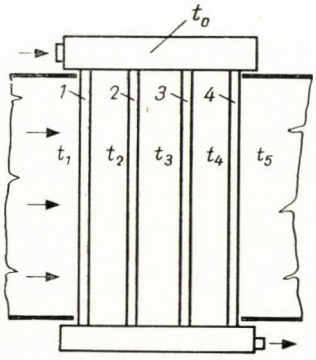

Fig. 2

of steam and condensate flow is very low, resulting in a negligible pressure drop in the mains.

Let us examine now whether under such simplifying conditions the heat exchanger shown in Fig. 2 still yields perfect operation. (Perfect operation means that each vertical tube is filled with steam in its full length and that on the arrow-marked part of the collecting main only condensate and the appropriately undercooled non-condensing gases can escape but no steam at saturation temperature.)

When introducing steam — more or less contaminated by gases (CO_2, O_2, N_2) — into the upper manifold of the heat exchanger according to Fig. 2 at the point marked, and removing the residual gases after the condensation of steam, via the lower collecting main, steam will fill the entire interior space of the tube system and air flowing normal to the tubes will be heated up from t_1 to t_5. Under such conditions of heat transfer it is obvious that the thermal output of the first tube — being in contact with the coldest air — will be the highest (more steam will condense in it that in the others) and that the heat output of tube *4* will be the lowest. Having assumed very large manifold and collector cross-sections in which pressures are practically identical, the pressure drop between the two ends of each tube will also be identical. The question

will naturally arise, how different steam quantities can flow in the individual tubes, with identical pressure drop; the answer is given in Fig. 3.

As Fig. 3 indicates, a flow pattern corresponding to the above conditions will evolve if the first tube, which consumes the largest quantity of steam, is fed from below, through the intermediary of the bottom collecting main with some additional steam passing through the rearmost tube of the row. Consequently, more steam flows through the rearmost tube than it can condense, and the balance is distributed among the three tubes ahead of it. The

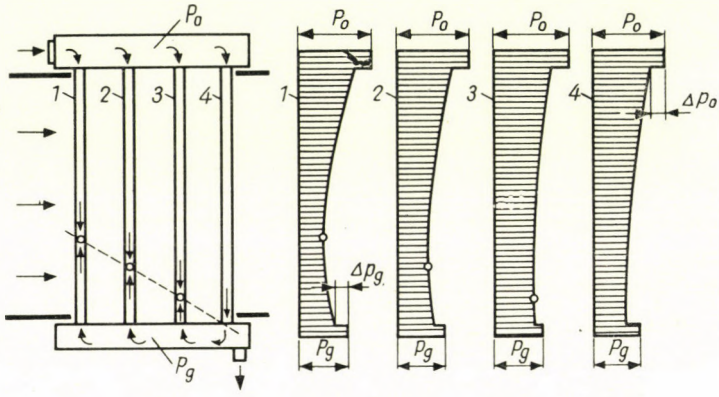

Fig. 3

first gets the most, the succeeding ones gradually less. The spot in tubes *1* to *3*, where the steam flows coming from above and from below meet, is indicated in the drawing. The pressure conditions resulting from such a flow pattern are shown in the right-hand side of Fig. 3 (not true to scale). In this part of the drawing each tube is represented by a vertical line. Starting from these lines, the local steam pressure prevailing inside the tubes has been plotted horizontally. Since according to our assumption no pressure gradients exist in the manifold, the absolute pressure p_0 in each tube at the branching point is identical. The situation is similar at the lower collecting main with respect to the pressure p_g. The pressure drop $p_0 - p_g$ along the last tube occurs in such a way that more steam flows through it than is condensed. The pressure drop Δp_0 marked at the last tube is brought about by the acceleration of the steam flow on its entry into the vertical tube.

Such pressure gradients manifest themselves also in the rest of the tubes. The same happens in the lower collector main with the sole difference that the pressure drop Δp_g marked at the first tube becomes considerably lower in tubes *2* and *3* (because of the decreasing quantity of steam coming from below). At this point of the last tube the pressure increases and slows down the velocity of steam at the entry from the tube to the collecting main. A strik-

ing thing in the figure is that, according to the pattern of pressure distribution, a lower pressure prevails at the points marked by rings on the first three tubes than in the collecting main. Although the physical possibility thereof exists, even a short consideration will show that such flow pattern and pressure distribution cannot be steady. Steam flowing in a heat exchanger practically always contains non-condensing gases swept along by still uncondensed steam. These gases, with the flow conditions indicated in the drawing, will ultimately collect at the points marked with rings, to which steam arrives from two

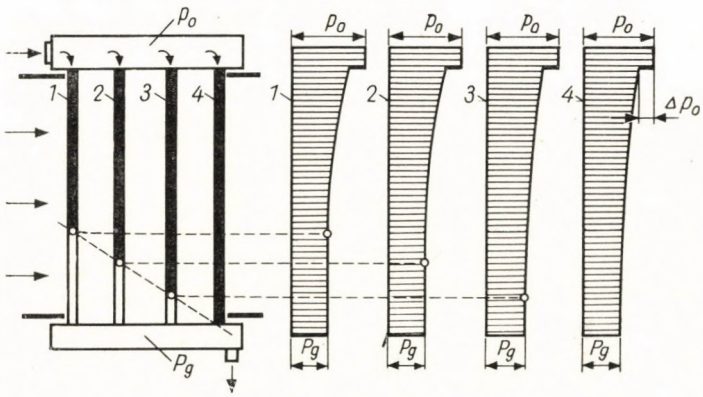

Fig. 4

opposite directions. Non-condensing gases, accumulating at these points in increasing quantities, cannot leave until they completely fill out these spaces beneath the critical points. Accordingly, the flow pattern of Fig. 3 is not steady and, soon after the heat exchanger has been put into service, is followed by another, this time steady, flow pattern which is shown in Fig. 4.

According to Fig 4, which is similar to Fig. 3 both in structure and denotations, the flow pattern evolves in a way that pressure in the top manifold is p_0, in the bottom collector p_g throughout. Under the pressure difference $p_0 - p_g$, approximately the same quantity of steam will enter into each tube. Because of the flow of cold air outside the tubes, a highest rate of condensation will take place in the first tube, this one will have the shortest steam-heated (active) tract — as indicated in the drawing by a strong black line. In the steady state the tube section beneath this active part is filled out by non-condensing gases. The steam-heated tracts of the rest of the tubes will be gradually longer, the rate of increase corresponding to the rate of the warming up of the air, until the rearmost tube is completely filled with steam. The pressure difference $p_0 - p_g$ occurs when the last tube is filled with steam, but no steam flows in the collector main since a perfect steam trap will not

let steam pass into the atmosphere. Should steam from the rearmost tube (the fourth in the drawing) flow into the collector, the only free path for its flow would be to the tubes ahead, which would ultimately result in the above-outlined unsteady state. Steady state cannot set in until the tubes beneath the steam-heated tube tracts are filled with non-condensing gases and the steam flow along them discontinues. This precludes pressure drop from occurring in these tube tracts. The flow pattern (in the right-hand side of the drawing) proves that in the tube tracts filled by non-condensing gases (apart from some static differential pressures and the pressure gradients due to the extremely low flow rate of non-condensing gases) the pressure is constant. Since obviously no steam is condensed in these tracts, they do not take part in the heat exchange. Accordingly, the heat output of the heat exchanger is lower than would be with all tubes completely filled with steam.

It clearly follows that heat exchangers, built of parallel tubes but yielding different heat outputs, can be operated according to two methods. Either with practically no steam loss but then the tubes are partially filled with non-condensing gases (Fig. 4), and consequently the heat output is lower, or by letting a certain quantity of steam escape from the collecting main into the atmosphere which, by increasing the pressure difference between the manifold and the collector, causes all tubes to be filled completely with steam. In the latter case — although at the cost of steam loss — no drop in efficiency will occur.

The above considerations contain some implicit simplifications. It is assumed, for instance, that there is a sharp limit between the tube tracts filled up by steam and or by non-condensing gases; or that the axial metallic heat conductance of the tubes is negligible, etc. Since, however, such simplifications do not interfere with the principal concept, there is no need for their closer treatment.

2. *Criteria for perfect heat exchanger operation*

Heat exchangers according to Fig. 2 operate faultlessly i.e. their tubes are hot throughout when the heat output of all tubes is identical. In the case according to Fig. 2 the precondition for it is to keep the heat transfer coefficient of the first tube row at the lowest value, as low in fact as is necessary to counterbalance the effect of the lowest temperature of the external medium. Simultaneously, in the other tube rows the heat transfer coefficient must increase at the rate as the temperature difference decreases with the warming up of the external medium. The criteria of such heat exchange can readily be derived mathematically. The author shall refrain from giving the sequence of calculations and will bring here only its end result. Accordingly the heat output of the individual tubes (tubes rows) is identical if, for any m^{th} tube

row of a heat exchanger comprising n rows of tubes, the following formula can be written:

$$\Phi_m = \frac{1}{\frac{1}{\Phi_{m-1}} - 1} \tag{1}$$

taking at the same time into consideration that $\Phi_n \leq 1$.*

If factor Φ for the first tube row is known, the above formula will help to determine the Φ_2, Φ_3, . . . Φ_n factors of the other tube rows, at which the heat output of each row is identical. It is however unlikely that the variations of the Φ factors of the succeeding tube rows of a heat exchanger will actually conform to the law contained in equation (1). It is just as unlikely that heat exchangers built up according to the same principles, will operate with tubes warm throughout (unless they operate with a steam loss).

If the Φ factors of the second and subsequent tube rows are less than ɛdrived with equation (1), the heat output of the first tube row is the highest Φed its active tract the shortest, viz. its cold portion the longest. Should the tinfactor of the rows behind the first one exceed the values according to equaton (1), the heat output of the first tube row will be the lowest and therefore ha t is warm along its whole length. It may occur that the value of Φ in one f) the tube rows is higher, in another one lower than calculable from equation otl But the rule that the tube row having the lowest heat output is warm (hroughout and the others have shorter or longer cold tracts depending on their outputs, remains valid. In heat exchangers made up of finned tubes, the longest cold tracts are found in the first tube row and the ones behind it show gradually shorter cold sections, while the rearmost row is hot all along. On the other hand, in heat exchangers having a small number of plain tubes, the opposite may occur.

3. *Basic principles for the calculation of the heat output of steam-heated parallel-connected heat transfer surfaces*

With the assumption of certain simplifications, the phenomena dealt with in the previous chapter can be readily followed by calculations. Their aim will obviously be to determine the effective heat outputs, without steam losses, of heat exchangers built up of parallelly connected heat transfer surfaces according to Fig. 1. Such calculations must proceed from the data and be performed with the methodology found in latest technical literature. The information available in the literature enables us to compute the heat output of a given heat exchanger (already existing or in the design stage) but on the

* This Φ factor is identical with the one introduced by BOSNJAKOVIĆ and given in paragraph 4 of Section III — in equations (2) and (3).

proviso that the heat transfer surface is hot throughout. However, it will be clear of what has been stated above that such calculations yield higher values for the heat output than can actually be obtained without steam loss.

Calculations by necessity start on the assumption that the heat output of the tubes of heat exchangers would depend exclusively on thermodynamical conditions provided all tubes were hot from beginning to end. This state, however, cannot be maintained indefinitely and is always followed by the state of equilibrium shown in Fig. 4.

To resolve the problem, obviously two systems of equations are required. One to embody the thermodynamical criteria, considering of course that the actually steam-heated tracts of the individual tubes vary in length; the other to determine the pressure drop inside the tubes between their two ends, according to the flow conditions, considering the length of the active tube tracts. The problem can be considered as solved if the two equations systems help to determine the steam-heated (active) portions of the tubes in a way that yields identical pressure differences on the steam side between the ends of each tube — under the given thermodynamical conditions. In possession of the active tube lengths, the actual heat exchanger output can also be derived.

4. *Determination of the output of heat exchangers built up of steam-heated parallel tubes with heat transfer surfaces hot throughout*

In this chapter we shall present a method for the calculation of the heat output of a conventional heat exchanger according to Fig. 2 on the basis of data found in the literature, the only deviation in the sequence of calculations being that the conditions met in practice have been taken into consideration insofar as the over-all heat transfer coefficient to the first two tube rows has been substituted by values deviating from those of the following rows.

It is generally known that the operational conditions of heat exchangers can be characterized by the dimensionless factor introduced by Bosnjaković [1] which has gone down in the literature as Φ. This coefficient which is the sole function of kF/w_1 and w_1/w_2 denotes the ratio of the temperature variations of the heat-carrying medium of lower water equivalent to the difference in the inlet temperatures of the two media taking part in the heat exchange. The properties of this coefficient being dealt with in the quoted literature in detail, we shall abstain from its accurate explanation and confine ourselves to writing down the equations that will be needed in our further calculations. Since this paper treats steam-heated heat exchangers only, the heat carrier of the higher water equivalent will at all times be steam, at $w_2 = \infty$ water equivalent. The medium of lower water equivalent flows perpendicular to the tubes. For such conditions, using the designations of Fig. 2, the following can

be written according to BOSNJAKOVIĆ for heat exchangers consisting of n tube rows:

$$\Phi = \frac{t_{n+1} - t_1}{t_0 - t_1} = \frac{t_{n+1} - t_1}{\vartheta}, \tag{2}$$

$$\Phi = 1 - e^{-kF/w_1}, \tag{3}$$

$$q = w_1 \Phi \vartheta. \tag{4}$$

With these three equations, along the usual methods, the main parameters of a steam-heated heat exchanger, viz. its heat output and the exit temperature of the external heat-carrying medium (mostly air) can be determined without any difficulty. To do so, the over-all heat transfer coefficient of the heat exchanger in the function of flow velocity, its heat transfer surface and all other factors affecting heat exchange, must be known. In possession of these factors, the equations (2)—(4) can be readily calculated. In equation (3) k denotes the average over-all heat transfer coefficient of the heat exchanger, which at the same time applies to each tube separately, and F denotes the complete heat transfer surface. It is obvious that this equation disregards the fact that the over-all heat transfer coefficient of the first two tube rows differs from that of the third and the subsequent ones. Since, however, its consideration will be required in our later calculations, equation (3) shall be thrown into the following form:

$$\Phi = 1 - e^{-\frac{1}{w_1}[k_1F_1 + k_2F_2 + (n-2)k_3F_3]} \tag{5}$$

whereby we shall have three different heat transfer coefficients and three different heat transfer surfaces. In practice, if a bank of tubes arranged in line are concerned with an identical number of tubes in each row, $F_1 = F_2 = F_3$ etc. In a bank of staggered tubes, according to the varying number of tubes in each row, the heat transfer surfaces in the odd and even rows will vary; hence only $F_1 = F_3 = F_5 \ldots$ and $F_2 = F_4 = F_6 \ldots$.

If in the calculation of the heat output of the heat exchangers we wish to consider the heat transfer coefficient of the first two rows — which differ from the rest — then we shall have to substitute the Φ value from equation (5) into equation (4). In this manner we shall arrive at the maximum heat output that the heat exchanger would yield with tubes hot throughout. Since we shall need this equation later on, we may write that:

$$q_{\max.} = w_1 \vartheta_1 \left(1 - e^{-\frac{1}{w_1}[k_1F_1 + k_2F_2 + (n-2)k_3F_3]}\right). \tag{6}$$

Equation (6) determines the heat output that can be calculated, from the literature, this output, however, cannot be attained without steam loss in practice, as borne out by experience. Neither can it be achieved in theory — as will be shown in the following.

5. *Determination of heat exchanger output with steam-heated parallel tubes having cold tracts*

If the first tube row is hot throughout, calculations are relatively simple because the quantity of steam condensing in the first row and the corresponding pressure difference between the two ends of the tubes can be readily derived from the known rules of thermodynamics. This pressure difference being iden-

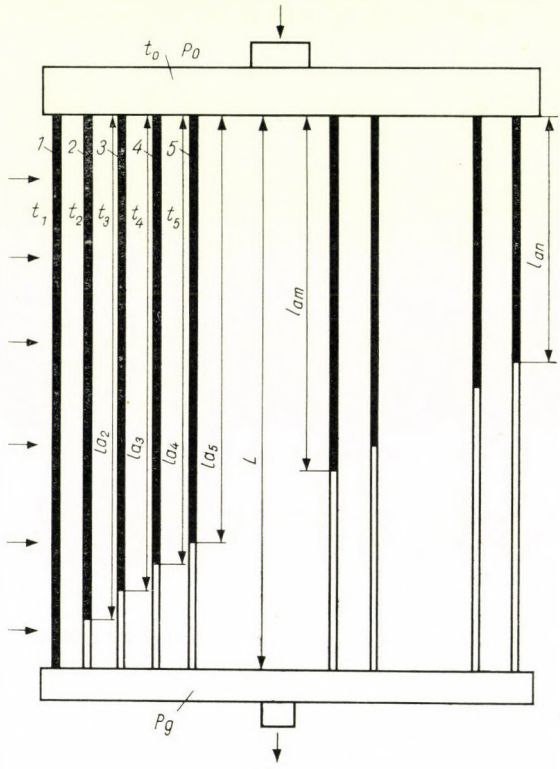

Fig. 5

tical for each tube row, steam quantities and heat outputs can be determined for the individual tube rows. Such cases — as has been said before — are relatively rarely met in practice.

Fig. 5 shows a heat exchanger with the lowest heat output in its first tube row, viz. the tubes hot all along in that row. The active tracts of the tubes in the rest of the rows are gradually decreasing. (The active tube tracts are indicated in the drawing by strong black lines while the portions filled out with non-condensing gases have a white zone between two thin lines). In the first tube row the external medium, being in contact with tubes that

are hot throughout, warm up evenly. Accordingly, the dimensionless factor Φ mentioned in item 4 of Section III as per equation (3) and (4), can be written without any difficulty for the first tube row:

$$\Phi = \frac{t_2 - t_1}{t_0 - t_1} = \frac{\Delta t_1}{\vartheta_1} = 1 - e^{-k_1 F_1/w_1} . \tag{7}$$

The warming up of the external medium in the first tube row is expressed by:

$$\Delta t_1 = t_2 - t_1 = \vartheta_1 \Phi_1 \tag{8}$$

with the heat output of the first row amounting to:

$$q_1 = w_1 \Delta t_1 = w_1 \vartheta_1 \Phi_1 . \tag{9}$$

On similar principles, the following generic formula may be written for the mth row of a heat exchanger having n rows:

$$q_m = w_1 \frac{l_{am}}{L} \vartheta_1 (1 - \Phi_1)(1 - \Phi_2)(1 - \Phi_3)^{m-3} \cdot \Phi_3 . \tag{10}$$

This equation ha sonly two unknown quantities, q_m and l_{am}. Since according to equation (9) q_1 is readily calculable, the $p_0 - p_g$ pressure difference which applies to each tube row, can also be determined (according to the next chapter). Now only those l_{am} values must be determined for the individual tube rows for which the corresponding q_m values result in the same $p_0 - p_g$ pressure difference.

The calculation procedure will be substantially more complicated if the heat output is lowest in the last tube row (as per Fig. 6) which is hot all over. Its heat output will be seriously affected by the cold tracts of varying lengths in the rows ahead. Nor can the heat output of this last row be determined without knowing these lengths. A solution to the problem is presented by the fact that the two systems of equations combining the flow dynamics of the condensing steam and the thermodynamics of the external medium yield the same number of equations as the number of the unknown quantities.

Assuming that $\Phi_1 \neq \Phi_2 \neq \Phi_3$, and simultaneously $\Phi_3 = \Phi_4 = \ldots = \Phi_n$, and using the denotations of Fig. 6, the equations expressing the thermodynamical conditions of the external medium can be written down. In this case, the heat outputs of the individual tube rows are expressed by the following

equations:

$$q_1 = w_1 \Delta t_{11} \frac{l_1}{L} = w_1 \vartheta_{11} \Phi_1 \frac{l_1}{L}, \tag{11}$$

$$q_2 = w_1 \left(\Delta t_{12} \frac{l_1}{L} + \Delta t_{22} \frac{l_2}{L} \right) = w_1 \vartheta_{11} \Phi_2 \left(\varepsilon_1 \frac{l_1}{L} + \frac{l_2}{L} \right), \tag{12}$$

$$\begin{aligned} q_3 &= w_1 \left(\Delta t_{13} \frac{l_1}{L} + \Delta t_{23} \frac{l_2}{L} + \Delta t_{33} \frac{l_3}{L} \right) = \\ &= w_1 \vartheta_{11} \Phi_3 \left(\varepsilon_1 \varepsilon_2 \frac{l_1}{L} + \varepsilon_2 \frac{l_2}{L} + \frac{l_3}{L} \right), \end{aligned} \tag{13}$$

$$\begin{aligned} q_n = w_1 \vartheta_{11} \Phi_3 \Big(& \varepsilon_1 \varepsilon_2 \varepsilon_3^{n-3} \frac{l_1}{L} + \varepsilon_2 \varepsilon_3^{n-3} \frac{l_2}{L} + \\ & + \varepsilon_3^{n-3} \frac{l_3}{L} + \varepsilon_3^{n-4} \frac{l_4}{L} + \varepsilon_3^{n-5} \frac{l_5}{L} + \ldots + \frac{l_n}{L} \Big). \end{aligned} \tag{14}$$

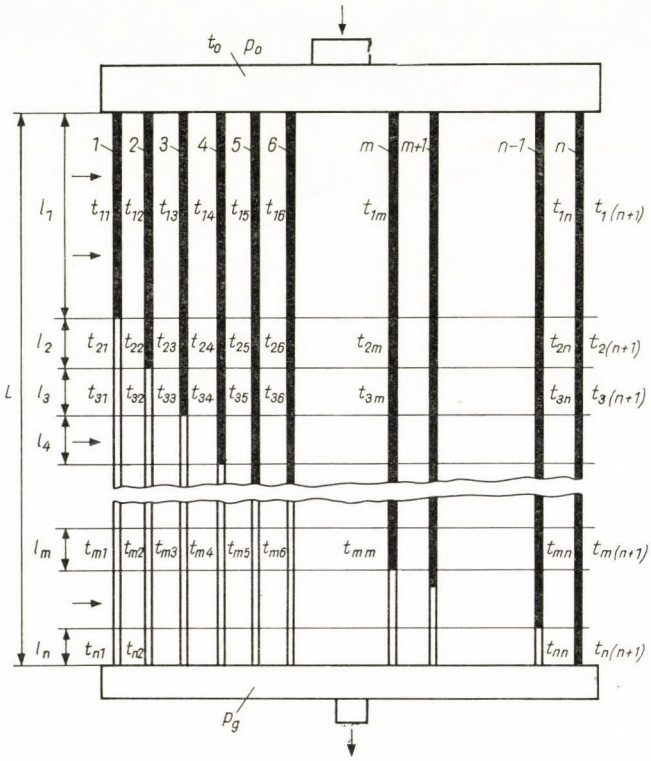

Fig. 6

Thus, for a heat exchanger consisting of n rows of tubes, there are n equations which comprise n tracts of unknown lengths

$$\frac{l_1}{L} \cdots \frac{l_n}{L},$$

and n unknown heat outputs $q_1 \ldots q_n$. From the equations expressing the flow dynamics of condensing steam, other n equations can be derived, according to the next section.

6. Steam flow criteria in steam-heated parallel heat exchanger tubes

The flow pattern evolving in a vertical tube is shown in Fig. 7. The figure shows only one tube of the bank and a portion of the tube plates on top and bottom. Steam enters the tube from the top manifold (of very large cross-section). The tubes of the bank are fixed into the end plates according to a certain spacing. The approach cross-section available for each tube has, according to this spacing, been marked f. Since the tubes are generally positioned in the tube plates with sharp angles, the entering steam flow will contract to the cross-section f_1' [2]. However, passing length l_0, the whole cross-section will be filled out once more. As a consequence, from value v_1' at the narrowest spot flow velocity, will drop to v_1 whereupon the pressure pattern shown in the drawing will develop and pressure p_1 set in behind tract l_0. Losses from the pressure drop $p_0 - p_1$ will arise only with the slowing down of the velocity of v'_1 to v_1 (in the drawing $p_1^* - p_1$) while the rest of the pressure drop is utilised to produce the kinetic energy of steam. A further pressure drop will be caused by friction between the flowing steam and the tube wall and or the condensate trickling down on it. Pressure loss by friction is shown by the dotted line between $p_1 - p_a^*$. Since steam condensing during its flow in the tube loses velocity, the pressure drop due to friction will be highest at the entry and gradually decrease in the direction of flow. According to our earlier assumptions, the velocity of steam flow at the end of the active tube tract l_a is 0. Simultaneously with the pressure drop due to friction, a pressure rise takes place, according to Bernouilli's theorem, as a consequence of decreasing steam velocity [3]. This is shown by the dotted line connecting points p_1 and p_2. The value of this pressure rise at the end of the active tract l_a (with flow velocity 0) amounts to $p_a' - p_a^*$, indicated in the drawing. This value is equal to the velocity pressure that corresponds to the velocity of v_1 and thus equal to the pressure that had been utilised at the entry of the tube, to produce the velocity v_1 without losses. Should vertical tubes be concerned, the flow pattern would be affected also by gravitation, since both the steam column in the tube and the one consisting of non-condensing gases underneath it

create a static pressure increasing downward. This is shown in the drawing by the pressure gradient $p_a - p'_a$ at the lowest part of the active tube tract, and by the gradient $p_g - p_a$ at the bottom end of the tube. The development of the effective pressure in vertical tubes under such conditions is indicated by a full line, between the points p_1 and p_a. Pressure, if vertical tubes are concerned, will continue to rise according to the static pressure of the non-condensing gases, until it reaches p_g, while with tubes in horizontal arrange-

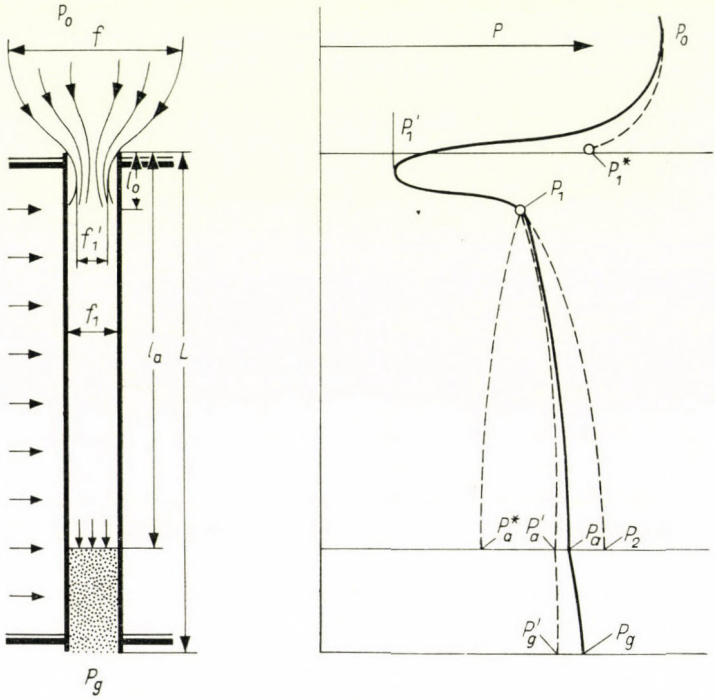

Fig. 7

ment, neither the increase $p_a - p'_a$, nor the increase $p_g - p_a$ will take place; the pressure pattern will be according to the dotted line p_1, p'_a, p'_g. Summing up, it may be stated that pressure conditions in vertical tubes develop according to the p_0, p'_1, p_1, p_a, p'_g pattern and in horizontal tubes according to the p_0, p'_1, p_1, p'_a, p'_g pattern. The $p_0 - p_g$ and $p_0 - p'_g$ pressure differences between the manifold and the collector main are consequently dependent on the position of the tubes. There is no difficulty whatever in determining the pressure conditions in tubes placed at any optional slope either.

In the framework of this paper we have to abstain from going into details on the above problems and rather confine our treatment to the simplifying assumptions made in the calculations.

We assume that steam having covered a very short path after its entry into the tube, will evenly fill out the full tube cross-section. In what follows, it will consequently be assumed that the initial tube tract seen in the drawing is $l_0 \simeq 0$;

we assume that saturated steam is applied to feed the heat exchanger, whose density does not vary during flow and partial condensation;

we assume that the quantity of steam flowing into the tubes is proportional to velocity v_1. This velocity gradually slows down along the active tract l_a and obtains 0 value at its terminal point. This assumption is at the same time a simplification of the phenomenon actually taking place.

According to the above, the pressure difference between manifold and collecting main can be expressed by the following equation:

$$p_0 - p_g = v_1^2 \frac{\varrho}{2} \left(\frac{1}{\alpha} - 1 \right)^2 + \frac{l_a}{L} \left[v_1^{7/4} \cdot 0{,}115 \frac{\varrho}{2} L d^{-5/4} \nu^{1/4} + \right. \\ \left. + L \cdot g \cdot \cos\delta \, (\varrho_g - \varrho) \right] - L \cdot g \cdot \varrho_g \cos\delta \,, \tag{15}$$

which is of general validity for tubes positioned at an angle of δ in relation to the vertical. With vertical tubes $\cos\delta = 1$, while with horizontal tubes $\cos\delta = 0$. Beside the geometric dimensions of the heat exchanger and the known factors depending on the physical properties of non-condensing gases, this equation contains the inlet steam velocity v_1 and the relative active tube tract l_a/L only. While the pressure difference $p_0 - p_g$ applies to all tubes, the value of v_1 and l_a/L varies with each tube row. The quantity of steam entering the individual tube rows is determined by v_1. The equations clearly reveal that, provided $p_0 - p_g =$ constant, the active tube length l_a/L will be smaller with the tube rows in which v_1 and with it the heat output of the row are higher. This tends to show that some rows, with smaller active tube tracts, yield higher heat outputs than others with longer active portions.

In the case of Fig. 5 in which the heat output of the first row is the lowest, this row being hot throughout, equation (15) can be written without any difficulty on the basis of available thermodynamical data. Should, however, the last tube row yield the lowest output, equation (15) cannot be determined without further calculations.

To render this equation suitable for further calculations, some transformations are required. These shall be carried out on the following considerations:

a) the pressure difference $p_0 - p_g$ given in equation (15) is identical for all tubes;

b) the equation can consequently be written in the following form:

$$\frac{l_a}{L} = f\,[v_1]_{p_0 - p_g = \text{const.}}$$

c) this equation interests us only within a limited range since it never occurs in practice that the active tube tract is less than half of the entire tube length and it is, of course, never longer than the full tube length. Therefore the equation should be used between the following limits only:

$$1 > \frac{l_a}{L} > 0.5\,;$$

d) in this rather restricted range the curves representing the function may be substituted by straight lines.

Neither can we deal with further problems of detail and with mathematical deductions. We shall confine ourselves to equations figuring in our subsequent calculations. The equation for the straight lines that stand for the curves of equation (15) is as follows

$$v_1 = v_{1n} + \frac{1}{b}\left(1 - \frac{l_a}{L}\right). \tag{16}$$

In it

$$b = \frac{0{,}5}{\left(\dfrac{v_{1n}^2\,A + v_{1n}^{7/4}\,B + C/2}{A + B/2}\right)^{1/N} - v_{1n}}\,. \tag{17}$$

If the velocity of steam entering the rearmost tube row v_{1n} were known, then relying on equations (16) and (17) we could write down the equation of the straight line which at given A, B and C constants could stand for the function $l_a/L = f(v_1)$ with fair approximation.

The steam velocities v_1 and v_{1n} in equation (16) are naturally determinant for the heat output of any one of the tube rows to which the equation is referred, the heat output of the mth row being:

$$q_m = v_{1m}\,\frac{d^2\,\pi}{4}\,3600\,z\,\varrho\,g\,r = v_{1m}\,E. \tag{18}$$

7. *The resolution of the system of equations determining heat exchange and flow conditions*

Since the number of thermodynamic equations contained in item 5 of Section III and the flow dynamics equations given in item 6 of the same Section, are sufficient to determine the unknown tube lengths l_a/L and the

similarly unknown heat outputs q_m, the actual heat output of the heat exchangers can be calculated at any time.

This calculation procedure is relatively simple in the case of Fig. 5, with the tubes of the first row hot throughout. In such instances the heat output of the first row can be expressed without any difficulty, since

$$q_1 = w_1 \vartheta_1 \Phi_1,$$

whence

$$w_{11} = \frac{q_1}{E}.$$

Knowing v_{11}, equation (17) can also be written in a simple manner as $l_a/L = 1$. Thereby the constant pressure difference $p_0 - p_g$, identical for each tube row, has been determined. Now equation (17) may be written once more, with the value $p_0 - p_g$ known now in its left-hand side and the substitution of the values e.g. of the mth tube row, the steam velocity v_{1m} and the active tube tract l_{am}/L in its right-hand side. Substituting the same values into equation (10) as well, the two unknown quantities can be derived from the two equations. If they are known, the heat output of the heat exchanger will be:

$$q = \sum_{m=1}^{m=n} q_m. \tag{19}$$

This same calculation for the case according to Fig. 6 is substantially more complicated. The system of equations being non-linear, their solution too has to be adapted to the special conditions and even so, they will yield but an implicit equation. For lack of available space, only the principal stages of the calculation procedure can be mentioned.

After the introduction of approximating methods and the condensation of the known factors into suitable symbols, we may write down the heat output of the individual tube rows of a heat exchanger having n rows, as referred to the output of the rearmost row, in the following form:

$$q_1 = \frac{1}{A_1}\left(q_n + \frac{E}{b}\right), \tag{20}$$

$$q_2 = B_1 q_1, \tag{21}$$

$$q_3 = B_2 q_2 = B_1 B_2 q_1, \tag{22}$$

$$q_4 = B_3 q_3 = B_1 B_2 B_3 \cdot q_1, \tag{23}$$

$$\vdots$$

$$q_n = B_3 q_{n-1} = B_1 B_2 B_3^{n-3} \cdot q_1 \tag{24}$$

where $n \geq 3$.

The heat output of the last row at the same time, is

$$q_n = \frac{E}{b\left(\frac{A_1}{B_1 \cdot B_2 \cdot B_3^{n-3}} - 1\right)}, \qquad \text{for } n \geqq 3; \tag{25}$$

i.e.

$$q_n = \frac{E}{b\left(\frac{A_1}{B_1} - 1\right)}, \qquad \text{for } n = 2.$$

The equation determining the active tube tracts is derived in a similar manner. Written in its generic form for the mth tube row, it becomes:

$$\frac{l_m}{L} = \frac{l_1}{w_1 \vartheta_{11} \Phi_3} (q_m - \varepsilon_3 \cdot q_{m-1}). \tag{26}$$

Should the heat exchanger consist of two rows only, then:

$$\frac{l_2}{L} = \frac{q_2}{w_1 \vartheta_{11} \Phi_2} - \frac{\varepsilon_1 \left(q_n + \frac{E}{b}\right)}{w_1 \vartheta_{11} \Phi_1 + \frac{E}{b}} = \frac{q_2}{w_1 \vartheta_{11} \Phi_2} - \frac{\varepsilon_1 q_1}{w_1 \vartheta_{11} \Phi_1}, \tag{27}$$

while the total heat output (of all tube rows) of the heat exchanger is given as

$$q = \frac{1}{A_1}\left(q_n + \frac{E}{b}\right)\left(1 + B_1 + B_1 B_2 \frac{1 - B_3^{n-2}}{1 - B_3}\right), \qquad n \geqq 3; \tag{28}$$

i.e.:

$$q = \frac{E}{b}\left(\frac{1 + B_1}{A_1 + B_1}\right), \qquad n = 2.$$

The above equations determine the heat output of the individual rows and the lengths of their active tracts, exclusively on the ground of the geometric dimensions of the heat exchanger, the position of the tubes and the thermodynamical parameters of operation.

Equation (25) cannot be resolved without iteration or graphic methods.

Now, dividing the actual heat output calculated according to equation (28) with the heat output according to equation (6), the deficiency in heat exchanger output can be determined, viz.:

$$\psi = \frac{q}{q_{\max}}. \tag{29}$$

8. The temperature field developing behind the heat exchanger

With tubes hot throughout and with uniform velocity of the external medium over the cross-section, the temperature across the full outlet cross-section will also be uniform (provided it had been so at the entry). The situation will change, however, if the tubes are not hot throughout their length. In such cases the temperature field will develop according to Fig. 8, i.e. according to the dotted line in it — provided the heat exchanger is operated with a sufficient steam loss. Since the temperature field can be readily calculated from the above, we shall not go into its particulars.

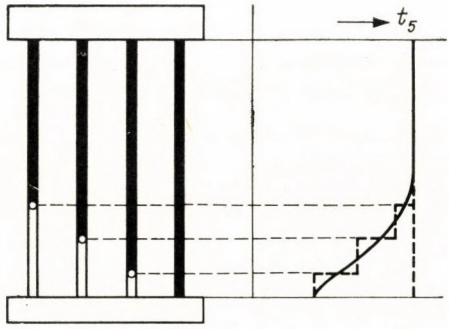

Fig. 8

9. The determination of the minimum steam loss in order to attain maximum heat output

As will be apparent from the above steam-heated heat exchangers can be operated with their heat transfer surfaces hot throughout. In this case the heat exchanger will yield the output that is calculable from the literature, indicated in item 4 of Section III. This way of operation, however, calls for more steam to be passed across the heat exchanger than it is capable of condensing under the given thermodynamical conditions. The question arises, how much additional steam such an operation will require for the heat exchanger that does not take part in the actual heat exchange and thus figures as a loss.

The minimum excess steam that has to be passed through the heat exchanger to ensure maximum heat output is determined by the proviso that even the tube row having the highest heat output must be hot throughout, but in such a way that the steam quantity entering this row must be actually condensed in it. This is the quantity which in the case in hand determines the pressure difference $p_0 - p_g$ between steam manifold and condensate collecting main. This difference is equal for each tube row and, excepting the one having

a maximum heat output, will cause more steam to flow along the rest of the tubes than they are capable of condensing. The surplus so arising will pass along the tubes without condensation and escape through the deaerator valve.

Omitting the actual calculation procedure we only wish to mention at this point that the minimum steam loss required for maximum heat output may amount to 40 to 50 per cent of the quantity of useful steam.

IV. Difficulties in deaeration due to flow resistance in the heat exchanger manifold

In the previous chapter we have endeavoured to throw light upon the phenomena called forth by the deaeration of the steam side of heat exchangers. They are caused by the fact that the heat transfer surfaces connected parallel on the steam side seldom operate under equal thermal load. This non-uniformity of thermal load causes various sorts of flow resistances to arise on the steam side, resulting in a deficiency in output. Flow resistances on the steam side of heat exchangers may, however, be due not only to non-uniform thermal loads but also to the fact that flow resistances in the manifold or the tubes are not equal for all tubes. Such effects may bring about the phenomena outlined before. Therefore, in what follows, we shall treat cases in which the assumption that the steam manifold and collector have very wide cross-sections does not apply and, on the contrary, their cross-sections are relatively narrow and cause a deficiency of heat output.

In dealing with these problems we shall have to explain first what is meant by "relatively narrow" steam manifold. Since steam during its path across the distributing chambers condenses to a negligible extent only, we may safely make use of the theoretical and experimental data known from the literature for non-condensing gases [3]. The authors of the publication referred to investigated the distribution of flow in a flat manifold and determined the flow conditions without condensation, in a system of tubes equivalent in ist principles to our Fig. 2. They used air flow in the experiments. They found that the volume of air flowing along parallel tubes strongly varies with the position the tubes occupy within the system. The rate of variations depends on the cross-section of the manifold and the collector chambers in relation to the cross-section of the parallel tubes. In the experiments the role of the manifold, parallel tubes and collector main in the entire system was examined separately. For our own investigations the study of the manifolds with the ports formed in them for the parallel tubes is of particular inte rest. In our heat exchanger, namely, the steam condenses in the parallel tubes, the flow conditions thus differing from those in air flow, and what flows in the collector main is only condensate which does not fill the entire cross-section. It is therefore obvious

that from among the experiments with air, only the ones concerning the manifold are important for us.

In the course of investigations of the manifold, the authors established the volumes of air escaping through the openings to the atmosphere and found that they varied according to the position of the openings. The cross-section of the manifold in relation to the openings was varied during the experiments. Without going into details, let us briefly summarise the most important findings:

a) Theoretical calculations and practical experiments have shown that under adequate conditions a fluid stream can be divided into partial streams at relatively slight losses. The arrangement of the flow sections according to the actual practice should be understood under adequate conditions.

b) Exit velocity through the openings of the manifold may, from the practical angle, be considered adequately uniform, if the flow cross-section of the manifold is at least twice the total cross-section of the openings.

From the above two main findings of the experimental results we may draw the conclusion that in the deaeration problem in question, the appropriate distribution of steam between the individual tubes, by providing a sufficiently large manifold, can be solved to satisfaction. Since increased flow cross-section will cause but an insignificant rise in the price of the manifold and since the latter's absolute value amounts to only a small fraction of the total cost of the heat transfer surface, it always pays to dimension it abundantly.

Since the assumption which we have stressed on several occasions before — a manifold of large cross-section — can in most cases be put into practice, the deductions of the previous sections can be considered as generally valid. The only exceptions are cases in which, for some constructional reasons, the manifold cannot be dimensioned large enough. Should this happen, the influence of the manifold may be assessed on the basis of the afore-mentioned publication [3] and the value so assessed, considered in the calculations.

V. The numerical values of deficiency in heat output

There are no data in the literature relying on which the phenomena treated in the above could be followed up numerically. Although significant drops in efficiency are rather frequent, people are liable to ascribe them to errors in calculations or faults in construction. By all means, without information on the reasons of the described phenomena, such errors may seem random and they result in wider safety margins in the designers' calculations.

The applicability of the above calculation method was proved in a vacuum-steam-operated large heat exchanger in which the loss in output was determined by measurements. Their results approximated ± 5 per cent of the

measured values. Owing to its considerable length, the sequence of calculations cannot be given here.

To help establish the degree of drop in output met with in practice, to show in what way this phenomenon manifests itself in heat exchangers with tubes of different numbers and lengths — in vertical and horizontal arrangement — we have compiled Tables I. and II. The data refer to a heat exchanger of a more or less conventional type, having tubes with round fins, in which the number of tube rows and the length and position of the tubes are varied. The characteristic dimensions of the tubes are shown in the Table II. In the calculations it is assumed that heating is carried out by saturated water vapour of 1.1 ata pressure whilst air, in varying quantity, at 30° C temperature and 760 mm mercury pressure, is flown normal to the tubes. The variable air quantity is denoted by Re, variations are within wide limits. A mean rate of air flow referred to the narrowest cross-section between the fins is associated, to each Re number. The mean flow rates associated to the Re numbers are the following:

Table I

Mean rates of flow

Re	W [m/s]
$4 \cdot 10^3$	2.74
$1 \cdot 10^4$	6.85
$4 \cdot 10^4$	27.40

The flow rate pertaining to the highest Re number is far in excess of the rates applied in practice, but the calculations clearly show the effect of air velocity on the drop in efficiency.

The calculation results have been compiled in Table III which in thirty-six variations shows the value ψ of drop in efficiency in a heat exchanger built up of finned tubes according to Table II. As seen from Table III, the degree of drop in efficiency strongly varies. This explains why similar phenomena could not be dealt with systematically so far and why they had been attributed to faulty design or faulty execution. Particularly interesting from this respect is the heat exchanger consisting of 0.4 m long tubes. With tubes vertically arranged, this set is very efficient, since its ψ value is merely some per cent below 1. This finds its reason in the fact that the internal flow resistance of a heat exchanger composed of tubes of relatively wide cross-section and small length is low, so that the gravity of the steam column in the tubes, as a factor that stimulates flow, has considerable influence; what is more, this influence acts on each tube row to an equal extent. The same heat exchanger with horizontally arranged tubes would show a substantially higher drop

Table II

The characteristics of the AR-7 heat exchanger

Arrangement of tubes	In line
Shape of fins	Circular
Fin material	Steel
Tube pitch normal to flow, mm	54.5
Tube pitch in flow direction, mm	54.5
Number of tubes normal to flow	7
Number of tubes in flow direction	1, 2, 3, 4
Height of air duct (tube length), mm	401
Width of air duct, mm	381
Tube position	Vertical
Inside dia. of tubes, mm	24
Outside dia. of tubes, mm	28
Diameter of fins, mm	48
Fin spacing, mm	2
Fin thickness, mm	1.5
Fin pitch, mm	3.5
Surface of 1 m finned tube, sq. m.	0.797
Narrowest cross-section of the tube bank, sq. m.	0.05
Frontal area of tube bank, sq. m.	0,153
Heat transfer surface of one tube row, sq. m.	2.24

Table III

The effect of air velocity on efficiency drop

Length of tubes, L [m]	Position of tubes	No. of tube rows, n	ψ when Re		
			$4 \cdot 10^3$	$1 \cdot 10^4$	$4 \cdot 10^4$
0.4	Vertical	2	0.965	0.965	0.980
		3	0.948	0.958	0.922
		4	0.955	0.948	0.929
	Horizontal	2	0.825	0.965	0.930
		3	0.695	0.757	0.837
		4	0.740	0.765	0.843
2.0	Vertical	2	0.883	0.922	0.966
		3	0.880	0.860	0.886
		4	0.865	0.895	0.964
	Horizontal	2	0.865	0.895	0.964
		3	0.727	0.795	0.870
		4	0.759	0.815	0.875

in efficiency, since with such arrangement the influence of gravity is absent. The situation is similar in a heat exchanger built up of 2 m long tubes, with the only difference that, owing to the higher flow resistance of the longer tubes, the same phenomena manifest themselves with different numerical values. The extent of efficiency drop, as shown in the table, may be as high as round 30 per cent.

It should be noted also that, to operate the heat exchanger having three rows of horizontally arranged 0.4 m tubes without loss in efficiency, 1,412 times as much steam must be passed across it than it can condense — i.e. 41.2 per cent of the useful steam is wasted. The values in Table III refer only to the case in hand, because heat exchangers with different dimensions and operational conditions yield different results.

VI. Methods to prevent loss in efficiency

In this section we shall deal with methods that may help to prevent the above-described loss in efficiency — partly or wholly — without loss of steam.

a) Providing each tube row of the heat exchanger, — each having a different output — with separate steam traps and deaerators, drop in effi-

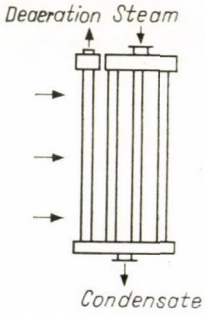

Fig. 9

ciency will at once be abolished. This solution, however, cannot be resorted to because it renders the equipment complicated and costly.

b) Drop in efficiency can be prevented by creating in each tube a pressure drop, which would arise in the tube having highest thermal output, were it hot throughout. This, in other words, means that with the exception of the one yielding the highest thermal output, appropriate orifices should be inserted into each tube of each row, at the point of the steam inlet.

The orifices should be dimensioned on the basis of what has been said above. This solution, of course, is fully efficient under certain circumstances only, and under varying operational conditions it would bring partial result.

c) Since, at the cost of steam loss, heat exchangers can be operated at maximum thermal output, ways and means must be found to utilize this waste steam. One idea to this end is the connection shown in Fig. 9 applied in a heat exchanger which otherwise is of the conventional building. Witb such connection, however, care must be taken that the velocity of steam flowing upwards in the first tube row should not be too high and eventually hamper the downward flow of the condensate. In certain cases it is expeditive to let waste steam condense in the rearmost tube row.

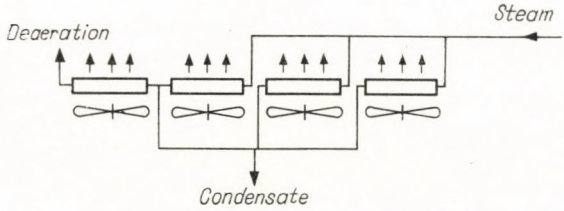

Fig. 10

Should several heat exchangers be connected parallel, the solution presented in Fig. 10 shall apply, which is the same as Fig. 9, the latter referring to one single heat exchanger.

d) In possession of the above-described basic principles and calculation methods, there will be further facilities to eliminate drop in efficiency, as for instance the development of different fins for each tube row, the application of different tube diameters, etc., which however are outside the scope of the present paper.

REFERENCES

1. Bosnjaković—Vilicić—Slipcević: Einheitliche Berechnung von Rekuperatoren. *VDI Forschungsheft* **432**, 1—6.
2. Eck, B.: Technische Strömungslehre, 4 Auflage; 94 and 230.
3. Reichardt, R.—Tollmien, W.: Die Verteilung der Durchflussmenge in einem ebenen Verzweigungssystem. *Mitteilungen aus dem Max Planck Institut für Strömungsforschung*, Göttingen (1952), 13.

PROBLEME DER ENTLÜFTUNG VON WÄRMEAUSTAUSCHERN AUS DAMPFGEHEIZTEN PARALLEL GESCHALTETEN RÖHREN

L. FORGÓ

ZUSAMMENFASSUNG

Wärmeaustauscher aus parallelgeschalteten Rohren, welche nach der modernen Literatur richtig dimensioniert und ausgeführt wurden, arbeiten oft mit einer wesentlich geringeren Wärmeleistung als projektiert worden war. Der Grund hiefür ist, daß die Wärmebelastungen oder die dampfseitigen Strömungswiderstände der einzelnen Teile der wärmeübertragenden Oberfläche nicht gleich sind, und deswegen Schwierigkeiten bei der Entlüftung entstehen. Infolgedessen arbeiten solche Wärmeaustauscher entweder ohne Dampfverlust, aber mit verminderter Wärmeleistung, oder aber mit der projektierten Wärmeleistung und mit Dampfverlust. Das Ausmaß der Leistungsverminderung ist größer, wenn die wärmeübertragende Oberfläche gerippt ist und kleiner, wenn sie aus glatten Rohren besteht. Das Ausmaß der Leistungsverminderung wird noch vergrößert, wenn der Wärmeaustauscher aus verhältnismäßig kurzen und weiten Rohren besteht, wenn die Rohre waagerecht angeordnet sind, und wenn die Strömungsgeschwindigkeit des äußeren Mediums gering ist. Mit den in der Arbeit veröffentlichten Methoden kann die Leistungsverringerung berechnet, bzw. teilweise oder zur Gänze beseitigt werden.

PROBLÈMES DE DÉSAÉRATION DES ÉCHANGEURS A RANGÉES DE TUBES PARALLÈLES, CHAUFFÉS A LA VAPEUR

L. FORGÓ

RÉSUMÉ

Des échangeurs composés de rangées de tubes parallèles et chauffés à la vapeur, dont le calcul et l'exécution peuvent d'ailleurs être conformes aux prescriptions les plus modernes, ont souvent un rendement notablement inférieur à celui projeté par l'ingénieur. La cause en est que la charge spécifique ou la chute de pression côté vapeur n'étant pas identique en chaque point de la surface d'échange, des difficultés de désaération se produisent. De tels échangeurs pourront fonctionner sans perte de vapeur mais auront alors un rendement réduit, ou travailleront avec le rendement prévu, mais avec une certaine déperdition de vapeur. La diminution du rendement sera plus grande si la surface d'échange est à ailettes, et moins grande si elle est formée de tuyaux lisses. Elle augmente également en cas de tuyaux relativement courts et larges, d'une disposition horizontale de ces tuyaux ou de la faible vitesse du gaz ou liquide au contact des surfaces extérieures. Les méthodes présentées permettent de calculer le degré de diminution du rendement, resp. d'éliminer en partie ou entièrement cette dernière.

ПРОБЛЕМЫ ОБЕЗВОЗДУШИВАНИЯ ТЕПЛООБМЕННИКОВ, СОБРАННЫХ ИЗ ПАРАЛЛЕЛЬНО СОЕДИНЕННЫХ И ОТАПЛИВАЕМЫХ ПАРОМ ТРУБ

Л. ФОРГО

РЕЗЮМЕ

Теплообменники, собранные из параллельно соединенных и отапливаемых паром труб, при условии правильного их расчета и изготовления на основе данных современной технической литературы, часто работают со значительно меньшей теплопроизводительностью чем запроектированная. Причина сказанного заключается в том, что тепловая нагрузка или сопротивление течению со стороны пара некоторых частей теплопередающей поверхности является не идентичной и из-за этого возникают затруднения по обезвоздушиванию. Вследствие упомянутого выше такие теплообменники работают или без потерь пара, но с пониженной тепловой производительностью, или же с проектной тепловой производительностью, но с потерей пара. Степень снижения производительности выше в том случае, если теплопередающая поверхность сделана из ребристых труб, и меньше, если она изготовлена из гладких труб. Повышается степень понижения теплопроизводительности, если теплообменник собран из относительно большого диаметра труб малой длины, далее, если трубы размещаются горизонтально и если скорость движения потока внешней среды является низкой. При помощи методов, сообщенных в работе, можно высчитать степень снижения тепловой производительности, далее устранить его полностью или частично.

RECENT DEVELOPMENTS OF LINE PROFILE ANALYSIS USED IN X-RAY METALLOGRAPHY*

I. S. SZÁNTÓ
CAND. OF TECHN. SC.
RESEARCH INSTITUTE FOR TECHNICAL PHYSICS OF THE HUNGARIAN ACADEMY OF SCIENCES, BUDAPEST

[Manuscript received December 11, 1964]

The paper reviews and comments on A. J. C. WILSON's recently published theoretical evaluation technique, designed to be applied on the variance method. The author points out the way how to improve the method. The numerical course of solution is illustrated by a metallographic example based on observed data. The scheme of program for electronic computer also published in the paper, gives the possibility to determine the curves of variance characteristic by means of successive approximation. Finally, in connection with the discussion of the results, the separation problem of particle size and lattice distortion effects is dealt with. Comparison is made with other methods and the magnitude of the range of measured parameters is limited within which reliable evaluation of the detected X-ray evidences may be expected.

I. Introduction. Review of literature. Problem setting

The problem of deducing reliable data for the strain condition of meta samples and for the size of crystallites and subgrains from the broadening or from the profile change of X-ray diffraction lines has for a long time been discussed by the research workers of solid structure but has so far not been solved satisfactorily. The difficulties arise from the fact that the effects of grain size and lattice distortion are superimposed in the X-ray evidences. Since the fourties numerous efforts have been devoted to the separation of these two effects. For the description of the various methods, based upon different assumptions and for their criticism, we refer to one of our earlier publications [1].

Different opinions have been voiced to answer the question: which parameter of the X-ray lines should be accepted as the best means for measuring the above mentioned quantities. Chronologically the first answer, a comparatively simple one was given by SCHERRER [2], who preferred to take into account the half-peak width. The integral breadth, introduced by JONES [3], is a widely used parameter and has firm foundations also from the physical point of view. In his criticism of the suitability of these two widely used X-ray evidences, TOURNARIE [4] points out, that they rely only on a few

* A lecture given at the 2nd Hungarian X-Ray Diffraction Conference, Balatonszéplak, 11. June 1964, with additions.

points of the diffraction line profile, instead of yielding information based on the complete series of detected points. Therefore he recommends to use the variance of the line profile as parameter because it fulfills these requirements and, in addition, may be correlated with the crystallite size. A somewhat similar measure for the characterization of the profile has been introduced by SZÁNTÓ [5]; the inflexion breadth is essentially analogous, it resembles the distribution concept of mathematical statistics and is correlated with the lattice distortion spectrum, defining the stress condition of the sample. This has laid the foundation for one of the deformation indices [6].

The synthesis of the variance concept is WILSON's [7, 8, 9] merit; he has developed a method for the determination of average particle size and for that of the lattice strain from a given $I(2\Theta)$ intensity distribution, by means of separating the superimposed effects.

It is worth noting that we had the opportunity to attend the Laue Memorial Congress in Munich , in Summer 1962, where WILSON gave a lecture describing for the first time the principal features of the variance method.* He emphasized that, in contrast to all other characterizations of line profile, only the variance involves the advantage that it can be corrected additively (with simple subtraction) for both geometrical and spectral aberrations. It is generally known that in all evaluating procedures used so far the most serious difficulties originate from the operations necessary to eliminate the different aberrations. Thus, Wilson's method seemed immediately more practicable than the unfolding procedure of WARREN and AVERBACH [10—12], which had been developed for similar purposes, but required much more complicated data-handling.

This background prompted the idea that, in order to solve some problems of physical metallurgy, the very accurate $I(2\Theta)$ intensity distributions, detected with the aid of our precision diffractometer, should be interpreted by the new method mentioned above. First we merely wanted to reproduce this modern method of evaluation, so very closely related to our topics. In the course of our work, however, it became clear that some details of the evaluating techniques were open to criticism. As an almost regular consequence, the method could be improved. The aim of the present paper is to compare the modified version of the variance method with the original one, and to illustrate the new ideas by practical examples.

* The title of this lecture, given on 30. July 1962, in Munich, at the Symp. Recent Adv. in the Exp. and Theor. Methods of Cryst. Structure Res. was as follows: "General theory of the use of line profile variance as a measure of particle size, domain size and strain."

II. Basic concepts

In the region adjacent to a certain maximum position, the distribution density of intensity, recorded by an X-ray diffractometer, may be regarded as a mass distribution along a given range of angles. The zero-order momentum of this mass distribution equals the surface area under the curve. Its center of gravity, or *centroid*, is derived as the mean of the first statical momentum referred to the origin. The second-order or inertia momentum of the distribution yields the mean-square deviation from the centroid, i.e. the *variance*. It is worth to note that MITRA [13] recently used even the fourth moment of diffraction profiles in order to determine the gradient of distortion-changes; unfortunately, however, his theoretically based paper fails to produce convincing experimental data.

The shift of the centroid implies the displacement of the $I(2\Theta)$ intensity distribution (line profile). The problem of precision lattice parameter measurement might be approached in a rational way by such procedure [14]. The variance, on the other hand, should be applied in cases when the information might rather be obtained from line-broadening.

For the sake of definiteness the following rule can be given to determine the W variance of an $I(2\Theta)$ line profile, detected in the $\Theta_a \leq 2\Theta \leq \Theta_z$ angular range: first the T_B background scattering must be subtracted from the profile area T_L and in this way the $T_L(2\Theta)$ curve derived; then the variance is defined as the J_C second order moment of the T_L surface lying under the T_L curve, provided the area T_L is unity. Meanwhile, the momentum must be referred to the ordinate running through the centroid or, what comes to the same, through the Θ_C abscissa of the center of gravity. The stated relations are illustrated in *Fig. 1* and can be expressed in a formula:

$$W = \frac{\int_{\Theta_a}^{\Theta_z} (\Theta - \Theta_C)^2 \cdot I_L(2\Theta) \cdot d(2\Theta)}{\int_{\Theta_a}^{\Theta_z} I_L(2\Theta) \cdot d(2\Theta)} \equiv \frac{J_C}{T_L} \tag{1}$$

where

$$I_L = I_T - I_B. \tag{2}$$

LANGFORD and WILSON's [15] paper contains a somewhat different formulation. They derive the variance as the difference of two squared arms of momentum:

$$W = K_L^2 - l^2. \tag{3}$$

K_L is the arm belonging to the second order momentum of the surface under the $I_L(2\Theta)$ curve, referred to the axis of the centroid, while l is the first order momentum between the center of gravity and the origin. K_L may be calculated

according to Eqs. (13) and (14) of Ref. [15] and l according to Eq. (27) of PIKE and WILSON's original paper [16].

The variance, defined in this manner, is composed of a constant and a variable part:

$$W = W_0 + k \cdot n \cdot \Delta(2\Theta). \tag{4}$$

In order to determine the W_0 and k parameters, a whole series of W values,

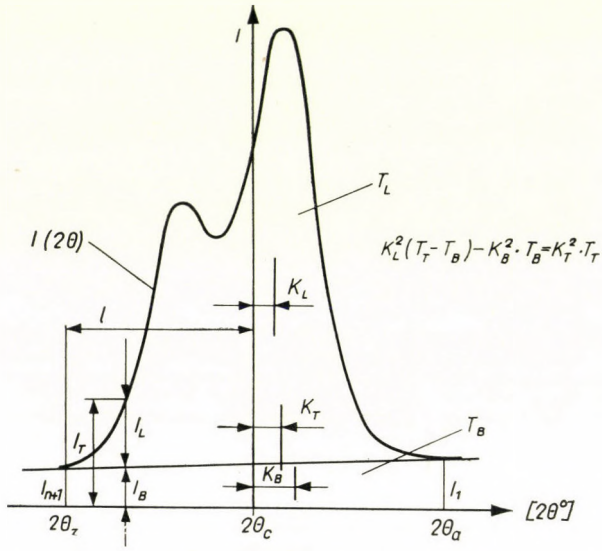

Fig. 1

i.e. a W *characteristic* is needed. The W_0 intercept of a characteristic may in principle, be either positive or negative. This depends upon the magnitude of instrumental aberrations, as well as upon the X-ray intensity emitted in the primary beam of radiation, but first of all upon the specific value of the ε elastic lattice distortion. The other parameter of a particular W characteristic is the tangent of its slope: k. This indicates, besides the effect of the emission-profile shape, the size of the coherent particles, occurring in the tested specimen. This correlation is, however, not so straightforward as the exclusive influence of ε on the magnitude of the W_0 intercept. We shall elucidate this rather complicated compound relation in a later section on the practical application of the method.

The W curves are obtained during the symmetrical shortening of the (Θ_a, Θ_z) interval of the line profile. Finally, the $n \cdot \Delta(2\Theta)$ range of integration is reduced to the vertical, passing through the centroid. In each step of constriction the W values must be determined and the gained data plotted *vs.* the interval width. This procedure results graphically in the variance-range

characteristic belonging to the profile concerned. The scheme of operations is shown in Fig. 2.

In this manner one can obtain several W curves which have a more or less similar appearance (Fig. 3). Each of them belongs to a selected background level B. The way of selecting this background value will be discussed below. For the determination of W_0 and k we shall take into account the physically true curve, which exhibits quasi-linear behaviour in the longest section of the given 2Θ range, i.e. the slope of which is approximately constant.

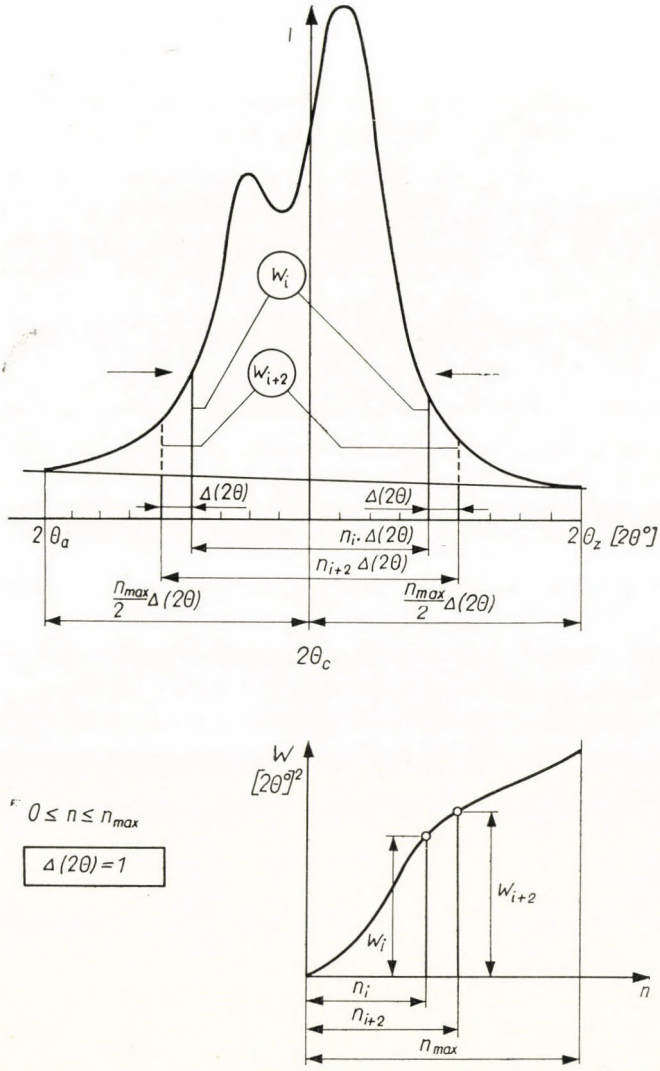

Fig. 2

Thus, one can conclude that the second term of Eq. (4) varies proportionally with the length of integration interval. Where the change is nearest to linear, the gradient k will be the real indicator of p, the average size of particles, i.e. domains. Besides, still another condition must be fulfilled: the interval of integration must be wide enough, namely in case of Cu$K\alpha$ radiation, its length must be at least ten times that of the interspacing of the peaks $K\alpha_1 - K\alpha_2$ separated.

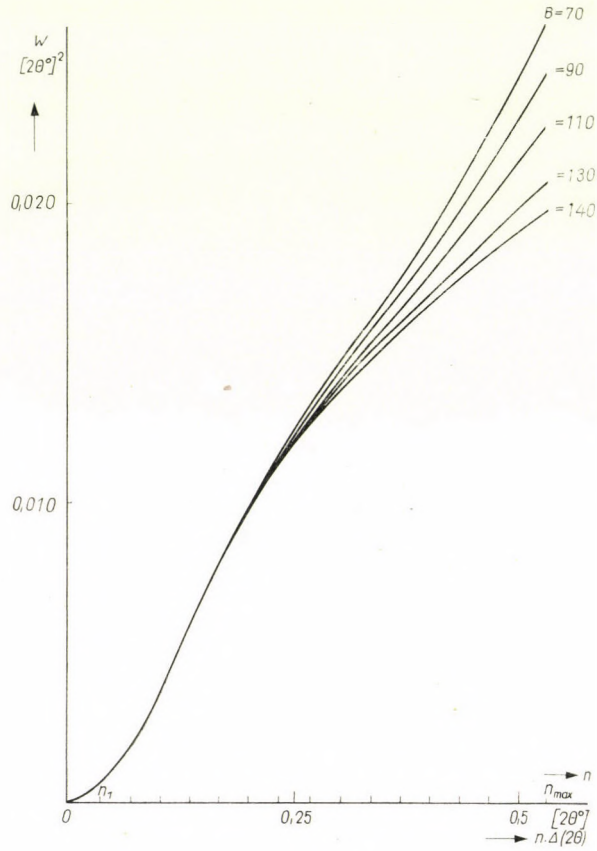

Fig. 3

III. Technics of evaluation

It seems superfluous to describe here the physical bases and theoretical considerations regarding the application of the variance method. A monograph recently published by WILSON [17] contains ample material and gives detailed derivations for those interested in this topic. The practical accomplishment

of the evaluation is, however, worthy of detailed examination, and our comments refer also to this problem.

The interpretation of the observed $I(2\Theta)$ distribution is introduced by subjective operations both in the variance calculation and in the case of other methods:

1. The registered line profile has to be confined by horizontal and vertical limits, then the part so conserved for the work of evaluation must be divided into intervals, sections.

a) First the Θ_a and Θ_z limits are admitted along the horizontal axis of the diagram. These must be introduced in principle at those sites where the distribution curve contacts the background at both sides of the peak. The assignment of these points is rendered more intricate by the fact that in the corresponding region the spread of intensity readings is relatively large. It is recommended in the literature [14] to "truncate" the profile by cutting away these limiting sections. In our opinion it is not wise to disregard these parts of the distribution, because they contribute considerably to the total information. It is well known that the use of these two tails has an advantage also for the sake of correct estimation of the background level. In the course of our experimental practice we have obtained satisfactory results by smoothing the recorded curves in the critical range with the aid of least squares.

The (Θ_a, Θ_z) angular range is divided into n sections of $\Delta(2\Theta)$ width, where n is a positive integer. According to the required accuracy, the value of n varies usually between 30 and 120. The higher the n, the finer details of the profile can be taken into account during evaluation. Thus

$$n = \frac{2(\Theta_z - \Theta_a)}{\Delta(2\Theta)} \tag{5}$$

where

Θ_a the beginning of the angular range,
I_1 the intensity in this point,
Θ_z the end point of the range,
I_{n+1} the corresponding intensity.

b) The vertical partition of the profile means the marking out of the background level — in first approximation only in a subjective manner — which results in the T_L and T_B areas, to be seen in Fig. 1.

The total surface area under the curve may be written as:

$$T_T = T_L + T_B. \tag{6}$$

It is a logical consequence that the total intensity, belonging to a certain abscissa of the profile, may be similarly divided into two parts. This can be taken from Eq. (2) which is formulated in conformity with Fig. 1.

Thus, in a particular intermediate angular position Θ_i,

$$I_{\mathrm{Ti}} = I_{\mathrm{Li}} + I_{\mathrm{Bi}}. \tag{7}$$

In the case of a correct assignment of the limiting points of the angular range

$$I_1 = (I_B)_1 \qquad I_{n+1} = (I_B)_{n+1} \qquad \text{and} \qquad (I_L)_1 = (I_L)_{n+1} = 0 \tag{8}$$

whence the mean background

$$B = \frac{1}{2}\left[(I_B)_1 + (I_B)_{n+1}\right] \tag{9}$$

and the area under the background level

$$T_B = Bn \cdot \Delta(2\Theta). \tag{10}$$

Having finished the discussion of steps I. *a)* and *b)* of the procedure, we believe it necessary to point out one important advantage of the method already at this stage. The arbitrary horizontal and vertical partitions mentioned above may be corrected in the later course of the calculation by means of objective operations. Consequently, the final result does not depend on the circumstance whether the initial divisions were chosen in a convenient way or not.

2. The position of the centroid has to be determined within the given range of the line profile. This affords a criterion for the correctness of the horizontal division. The (Θ_a, Θ_z) angular range is chosen appropriately if the angle co-ordinate of its center approximately matches the calculated abscissa of the center of gravity. It can be prescribed that:

$$\left| \frac{n}{2} \cdot \Delta(2\Theta) - l \right| \leq \frac{1}{4} \cdot \Delta(2\Theta). \tag{11}$$

If this condition is not met, the Θ_a and Θ_z limits must be modified by convenient shifts, accomplished by the aid of successive approximation. The variation can be carried out best on electronic computer machines, just as the determination of the centroid is also the most economic in this way. The computer tests automatically the (11) criterion and distinguishes between two kinds of deviations. If the difference is a multiple of $\Delta(2\Theta)$, it extrapolates the $\mathrm{I}(2\Theta)$ curve in the right direction, simultaneously increasing the value of n. If, however, the difference is a fraction of $\Delta(2\Theta)$, the machine modifies the I_{Ti} data to I'_{Ti} by interpolation.

3. Now within the correct $(\Theta_a. \Theta_z)$ limits, the second moment of the surface area under the profile should be calculated, and W determined from

this moment in the way described in connection with relation (3). The procedure is carried out continuously; meanwhile n is diminished successively to $(n-2)$, $(n-4)$, etc. In this way a certain $W(n)$ characteristic is obtained to which an arbitrarily admitted B level belongs. Afterwards the calculation of the characteristic is repeated several times for B values decreasing stepwise.

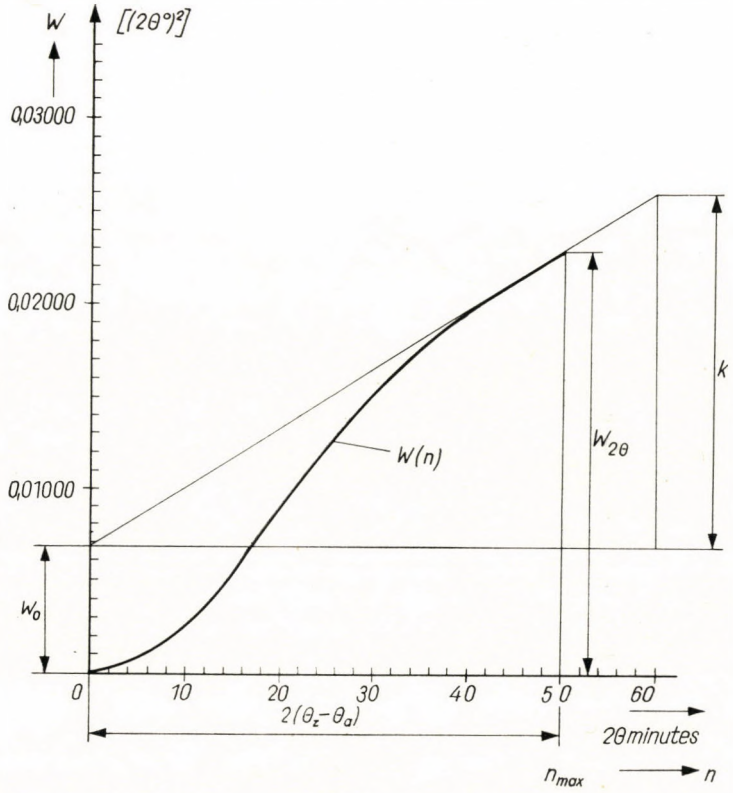

Fig. 4

It must be noted that the ΔB error, which arises from the incorrect ratio of the areas T_L and T_B, is eliminated during this series of operations. The real B value which is physically correct, is set free from the additional "background noise" due to the atmospheric radioactive contaminations. The search after this value is facilitated by the fact, that the W characteristics may be *concave* when looked upon from below (if the chosen B level is higher than it ought to be), or *convex* when looked upon from below (if the chosen B value involved in the calculations, is lower than it ought to be) (Fig. 3). As already mentioned above, the correct B value corresponds to the W characteristic which has a section closest to linear in the typical range between 0,5 to 0,95 · $n_{\max}$. According to physical interpretation: in the array of curves

the distinguished W characteristic, belonging to the appropriate level of background scattering, will be the one which is quasi-linear in the very angular range where the profile vanishes into the background level, in accordance with the local regularity of intensity decrease.

4. Fig. 4 shows a distinguished W characteristic. The W_0 intercept can be obtained by means of extrapolating this characteristic; the k coefficient of proportionality, from the slope of its linear section; $W_{2\Theta}$ (the quantity characterizing the grain size) is ordered to the end point of the investigated range and can be calculated with the aid of relation (4). Being aware of the numerical values of the geometrical and spectral aberrations concerned, the corrections corresponding to ΔW_0 and Δk are carried out. Thus we obtain quantitative data referring to the physical parameters of the investigated specimen (specific lattice distortions, density of dislocations, particle size). That is the solution of the problem.

IV. Critical remarks

The above-described method seems to be quite correct. Nevertheless, when the practical calculations are performed, some sources of error emerge, which deserve criticism. Namely:

a) The weighting system of intensity data is impractical. The I_T values must be multiplied by the longest $n \cdot \Delta(2\Theta)$ arms in the region of background level where the measurement is the most uncertain. This method introduces the square of the intensity measurement's error into the variance calculation (from one side) and so this gains predominance.

b) The l and K_L values, measured from the Θ_a or Θ_z limiting angular positions, are commensurable; moreover, they are equal not only in order of magnitude, but are also identical up to 1—2 decimals. After the subtraction, required by Eq. (3), the possible error of the third and fourth decimals appears in the result in an enlarged form.

c) While calculating the W characteristic, the Θ'_z limiting value — which is the basis of reference — moves away owing to the symmetric stepwise restriction of the angular range. Therefore different $n \cdot \Delta(2\Theta)$ arms have to be appointed repeatedly to unchanged I_{Ti} values and this impedes the repeated use of the subresults, and so the computer program is rendered more complicated.

V. Improvements of the method

The listed sources of errors have been eliminated as follows. The centroid position should be referred to an axis of gravity admitted according to preliminary estimation of the Θ_c angle and not to the axis of the Θ'_z limiting value. Between $-n/2$ and $+n/2$ we form the $I_{Ti}\,(n_i/2) \cdot \Delta(2\Theta)$ products (the

sign must be respected, too), then these products are reduced and divided by ΣI_{Ti}. This operation provides a distance

$$|l| = |< \Theta - \Theta_C >| \tag{12}$$

which may be interpreted like the one occurring in Eq. (1).

If $|l|$ turns out to be approximately zero, or does not exceed $\Delta(2\Theta)/4$, then the assignment of Θ_c is correct. If, however, the criterion is not fulfilled, the postulated position of the centroid must be shifted in the appropriate direction by twice the distance of the deviation, and then the calculation is repeated. Experience shows that a third trial is usually not needed. The result provided by the second modification will approach zero up to a 10^{-3} difference maximum.

After the determination of the centroid within the prescribed degree of accuracy, the second moment of the $\Delta(2\Theta)$ sections is calculated about the ordinate passing through the center of gravity from both sides. Since in this case $l \simeq 0$, Eq. (3) will be simplified to

$$W \simeq K_L^2 . \tag{13}$$

The transfer of the axis, to be found in LANGFORD and WILSON's paper [15], and consequently the application of STEINER's theorem become unnecessary. The subtraction of quantities of the same order of magnitude, a possible source of errors, is also eliminated.

As the moment of the bands (intensity groups) is calculated for the real mean, the multiplication by arms represents a natural weighting system both in the cases of first and second moments, and therefore the errors of measurement are equalized when taking the average. It is to be noted that the distances of the arms, corresponding to each I_{Ti} intensity, remain unchanged; thus, the subproducts, once available, may be used again in the repeated operations following the restriction of the range. As an advantage, the computer program becomes more simple.

A further refinement of the procedure can be achieved, if the second moment is calculated about the proper axis of gravity of each $\Delta(2\Theta)$ section, and the additional terms derived in this way, are summarized too. According to the symbols of Fig. 5, the second moment of a section will be

$$J_i = I_{Ti}\left(\frac{n_i}{2}\right)^2 + \frac{I_{Ti}\cdot 1^3}{12} = \frac{I_{Ti}}{4}\left(n_i^2 + \frac{1}{3}\right) \tag{14}$$

provided the value of $\Delta(2\Theta)$ is taken for unity. This is a practical and usual convention in calculation techniques.

Taking into account the above-mentioned facts, the investigated angular range may be divided into wider $\Delta(2\Theta)$ sections, and thus the evaluation is abbreviated without rendering the variance method less accurate on account of the coarser divisions.

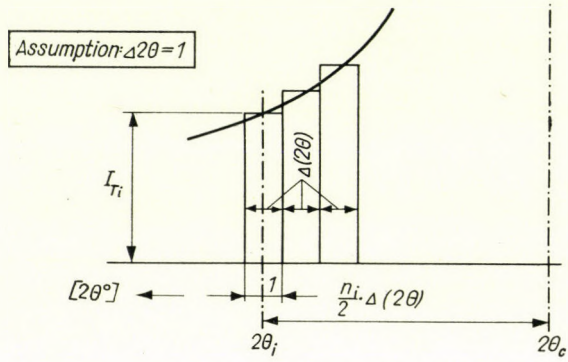

Fig. 5

Considering all these modifications, the basic formulae, used by us in order to determine the centroid and variance, can be given without any detailed reference to their derivation, as follows:

$$l = \left\{ \frac{M_T}{T_T} + \frac{r}{1-r} \cdot \left[\frac{M_T}{T_T} - \frac{\delta}{B} \cdot \frac{(n+1)}{12\,n} \right] \right\} \cdot \Delta(2\Theta) \approx 0\,, \tag{15}$$

$$W \cong K_L^2 = \left\{ \frac{\Psi}{T_T} + \frac{1}{12} + \frac{r}{1-r} \left[\frac{\Psi}{T_T} - \frac{n\,(n+2)}{12} \right] \right\} \cdot [\Delta(2\Theta)]^2\,, \tag{16}$$

fi $n = n_{\max}$ and $|l| \leqq 0{,}25 \cdot \Delta(2\Theta)$.

The symbols occurring in these equations and those not yet used in the present paper are:

$$M_T = \sum_{i=-n/2}^{n/2} I_{Ti} \cdot i\,, \tag{17}$$

$$I_T = I_{T1} + I_{T2} + I_{T3} + \ldots + (I_T)_{n+1}\,, \tag{18}$$

$$I_B = (n+1) \cdot B\,, \tag{19}$$

$$r = \frac{I_B}{I_T}\,, \tag{20}$$

$$\delta = (I_B)_{n+1} - (I_B)_1\,, \tag{21}$$

$$\Psi = \sum_{i=-n/2}^{n/2} I_{Ti} \cdot i^2\,. \tag{22}$$

It is noteworthy, that the basic equations (15) and (16) are shorter, each by one term, than the original ones published in [15]. Our calculations, performed on the $M-3$ electronic digital computer for the sake of control, exhibited, however, up to four decimals no difference in any case between the results obtained by the two different formulae and by the same array of observed data.

VI. Application

Finally we demonstrate the application of the advanced method by an example taken from our laboratory practice. Fig. 6 shows the (200) line profile of a drawn W-wire taken from the ADG diffractogram as registered on a Hilger apparatus. The operational conditions were: 47 kV, 3 mA; slit dimensions: 0,3; 0,8; 0,2 mm; speed of registration = 1/32 (2 $\Theta°$ per min.); time constant: $\tau = 16$ sec. Amplification: x 5; mean value of 2 Θ range = 58,473°; Cu$K\alpha$ radiation) ($\lambda = 1{,}54$ Å).

The line profile was divided horizontally into sections $\Delta(2\,\Theta) = 1$ minute (arc) wide, and the corresponding pairs of (I_{Ti}, 2 Θ_i) values ($n = 50$) were fed onto the punched input tape of the M-3 computer. The machine transferred these, in turn, to its memory unit. The program, containing the commands necessary to accomplish the prescribed operations is

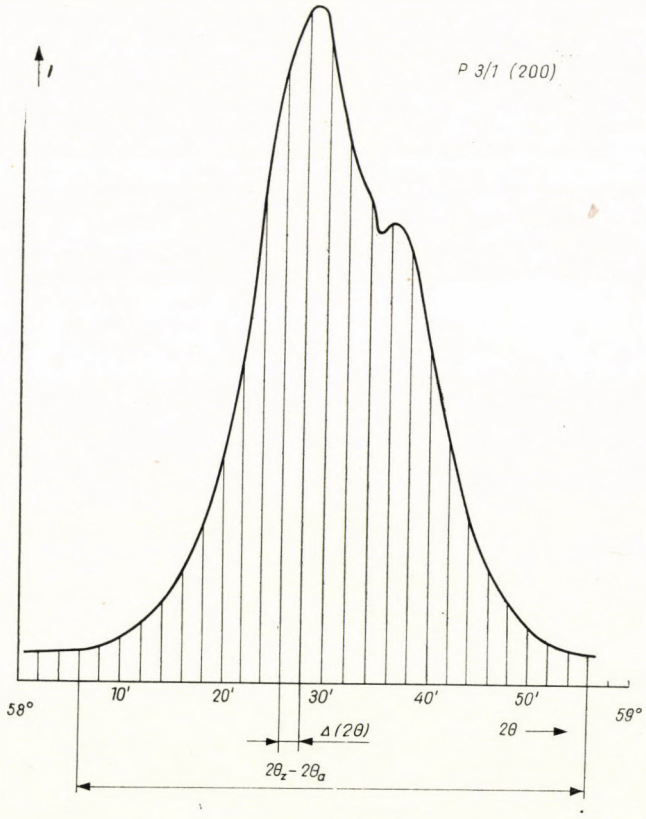

Fig. 6

stored in the same memory. The program is similarly coded to the input data. Without describing in detail the orders translated into "machine language", we want to show the theoretical scheme of the program of operations (Fig. 7).

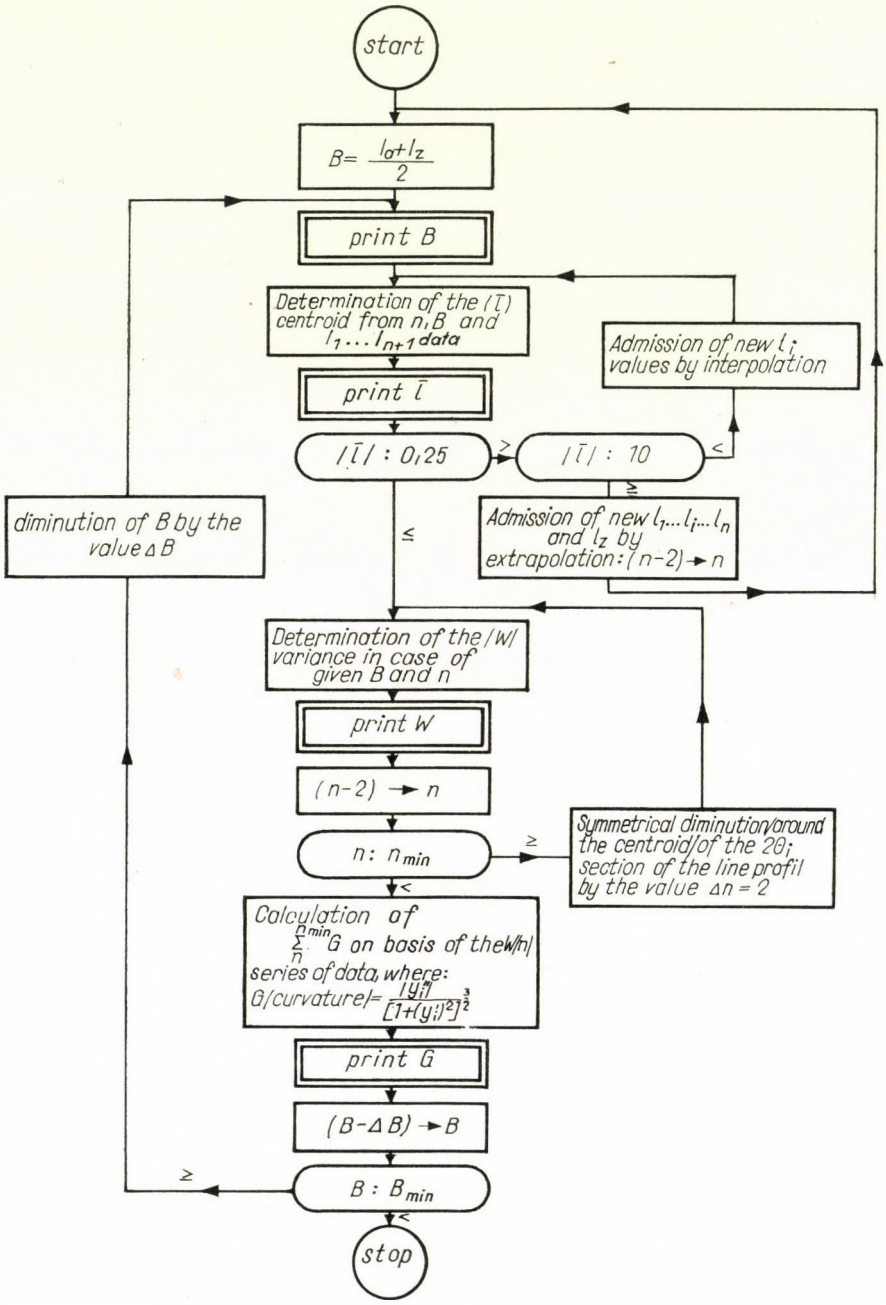

Fig. 7

It is to mentioned that, beside the described operations, the computer program includes also an additional one. The calculation of ΣG_i involves the point-by-point investigation of the curvature of the variance characteristics and the summarization of the findings. The quasi-linear characteristic, corresponding to the optimal B value, is selected best by the computer, which indicates, in an objective manner, the W characteristic having an inflexion in the investigated range. For this sake the ΔB steps must be chosen adequately. The change in the curvature direction of the characteristics is displayed by the derivated function in the form of a steep fall. Starting from the curve with a parameter B_{max}, the first derived curve exhibiting steep changes yields, in most cases, more accurate information than can be gained from a graphical plot of reasonable dimensions. On the other hand, it is not worth to perform the extrapolation by the machine, because after the selection of the distinguished W characteristic, it can be accomplished graphically with sufficient precision. Fig. 8 shows some data

P - 3/1 - /200/

B_1 =	+3 +1344999		B_2 =	+3 +1244999	
ℓ =	-0 -2520095		ℓ =	-0 -2427341	
ℓ' =	-4 +1076422				
W_{50} =	-1 +1570728	n = 50	W_{50} =	-1 +1739238	n = 50
	-1 +1570729			-1 +1715100	
	-1 +1570450			-1 +1693865	
	-1 +1565140			-1 +1669723	
	-1 +1554100			-1 +1640577	
	-1 +1535580			-1 +1607094	
	-1 +1506336			-1 +1564630	
	-1 +1466643			-1 +1513456	
	-1 +1413874			-1 +1456034	
	-1 +1362409			-1 +1390965	
	-1 +1296781			-1 +1317792	
	-1 +1223293			-1 +1238823	
	-1 +1142022			-1 +1152356	
	-1 +1053421			-1 +1059925	
	-1 +0956836			-1 +0959996	
	-1 +0854861			-1 +0854543	
	-2 +7491720			-2 +7476538	
	-2 +6377069			-2 +6355814	
	-2 +5257148			-2 +5236010	
	-2 +4144605			-2 +4114157	
	-2 +3102082			-2 +3079813	
W_8 =	-2 +2178364		W_8 =	-2 +2163733	
ΣG_1 =	-2 +4048240		ΣG_2 =	-2 +3394803	

Fig. 8

on a strip, printed automatically by the computer according to the program. Finally Fig. 9 shows how an array of variance characteristics can be produced with the help of these data. After selecting the curve which belongs to the background B true, one can determine the parameters of the straight line corresponding to Eq. (4) (Fig. 10).

In our case the result was: $W = 10{,}45 \cdot 10^{-3}\,[(2\Theta°)^2]$; $k = 8{,}0 \cdot 10^{-3}[2\Theta°]$. After the simple subtraction of the correction terms $\Delta W_0 = 2{,}5 \cdot 10^{-3}$ and $\Delta k = 5{,}5 \cdot 10^{-3}$ (these constants are typical for the given experimental layout), we obtain the form of the variance function, characteristic of the given line profile:

$W_{2\Theta} = [7{,}95 + 2{,}5\ n\,\Delta(2\Theta)]$ in $[(2\Theta°)^2]$ dimension. For the entire width of range: $2\Theta_z - 2\Theta_a = 50$ minute (arc) $\cong 0{,}835\ (2\Theta)°$. This yields the value

$$W'_{2\Theta} = 10{,}04 \cdot 10^{-3}\,[(2\Theta°)^2]$$

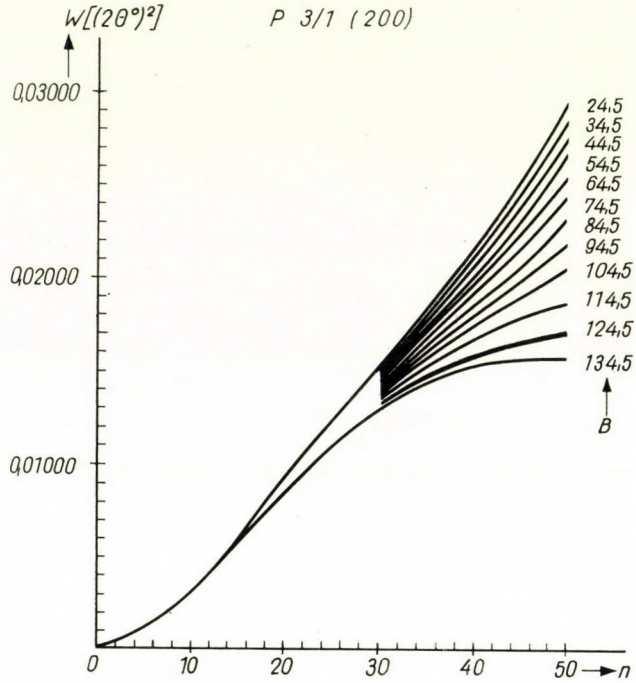

Fig. 9

which must be converted into radian units in order to be able to finish the operations.

In the last stage of the calculations the formulae given by TOURNARIE [4] and WILSON [9], are used. Accordingly, the average linear dimensions of the coherent lattice domains (particles) occurring in the wire may be determined by solving the following relation for p:

$$W_{2\Theta} = \frac{\lambda K (2\Theta_z - 2\,\Theta_a)}{2\,\pi^2\,p\cos\Theta} - \frac{\lambda^2 L}{4\,\pi^2\,p^2\cos^2\Theta} \tag{23}$$

where K and L are dimensionless, and their role is to account for the dependence of true and apparent particle size upon the crystal's shape and upon the particular (hkl) family of reflecting lattice planes. The numerical values of K and L may be found in Table 2 of Ref. [7], as well as in Table No. 19.2 of the monograph [17].

In our example we have investigated the (200) reflexion of a cubic crystal. For these

$$K = 1 \quad \text{and} \quad L = 0.$$

The mean square strain, characteristic of the magnitude of lattice distortions, may be calculated from

$$\varepsilon = \frac{1}{2} \cdot \sqrt{(W_0)_{2\Theta}} \cot \Theta \cdot 10^2 \quad [\%] \tag{24}$$

where $(W_0)_{2\Theta} = 7{,}95 \cdot 10^{-3}$ $[(2\,\Theta°)^2]$ is substituted in our case.
Using the given observed data we obtain as the result of calculations
$p \cong 450$ Å for the linear dimension of particles and
$\langle\varepsilon\rangle = 0{,}139\%$ elastic lattice strain.

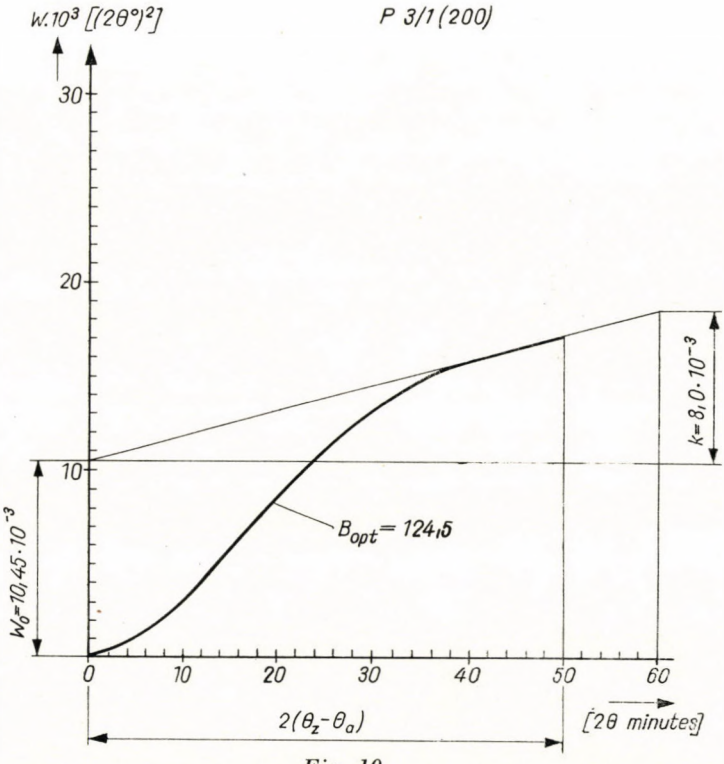

Fig. 10

Discussion

As the result of several series of experiments it has been established that the above-described method of evaluation generally yields a higher degree of relative accuracy than do the classical methods of line profile analysis mentioned in the introduction. Compared to the convolution method, the present technique of calculation has the advantage of being more straightforward, furthermore, the handling of its additive corrections seems to be easier. Its drawback is that in the technically important 0,1 $\mu \div 10$ μ range of particle sizes it is not sensitive for the increase of grains. Just as in any other measuring method of line broadening, this zone is a "no man's land" from the point of view of grain size determination. Thus, in this respect it is neither superior, nor inferior to other evidences. An important argument speaks, however, in favour of the variance method. By using a single line profile, one can

separate the effects of lattice distortion and particle size. And this can be done with more reliability than the results obtained e. g. by the HALL [18] procedure, although the latter requires the evaluation of the data of at least three, or rather five, reflexions.

The author wishes to express his thanks to Mr. L. VARGA, who has contributed to the advancement of the variance method with numerous valuable comments and by solving several details of the problem. Thanks are due to Mr. B. UHRIN, Fellow of the Computer Centre of the Hungarian Academy of Sciences, who prepared the computer programs and directed the actual calculations with great competence.

REFERENCES

1. SZÁNTÓ I.: *Mérés és Automatika* (Budapest) **7** (1960), 66.
2. SCHERRER, P.: *Nachr. Ges. Wiss.* (Göttingen) (1918), 98.
3. JONES, F. W.: *Proc. Roy. Soc. A.* **166** (1938), 16.
4. TOURNARIE, M.: *C. R. Acad. Sci.* (Paris) **242** (1956), 2016; 2161.
5. SZÁNTÓ, I. S.: *Periodica Polytechnica* (Budapest) **2** (1958), M/4. 275.
6. SZÁNTÓ, I. S.: *Acta Techn. Hung.* **32** (1961), 65.
7. WILSON, A. J. C.: *Proc. Phys. Soc.* (London) **80** (1962), 286.
8. WILSON, A. J. C.: *Nature*, **193** (1962), 568.
9. WILSON, A. J. C.: *Proc. Phys. Soc.* (London) **81** (1963), 41.
10. AVERBACH, B. L.—WARREN, B. E.: *J. Appl. Phys.* **20** (1949), 885.
11. WARREN, B. E.—AVERBACH, B. L.: *J. Appl. Phys.* **21** (1950), 595.
12. WARREN, B. E.—AVERBACH, B. L.: *J. Appl. Phys.* **23** (1952), 497.
13. MITRA, G. B.: *Brit. J. Appl. Phys.* **15** (1964), 917.
14. TAYLOR, J.—MACK, M.—PARRISH, W.: *Acta Cryst.* **17** (1964), 1229.
15. LANGFORD, J. I.—WILSON, A. J. C.: Crystallography and Crystal Perfection (ed. G. M. Ramachandran) Academic Press, London 1963, 207.
16. PIKE, E. R.—WILSON, A. J. C.: *Brit. J. Appl. Phys.* **10** (1959), 57.
17. WILSON, A. J. C.: Mathematical Theory of X-ray Powder Diffractometry. Centrex Publ. Eindhoven 1963.
18. HALL, W. H.: *J. Inst. Metals* **75** (1950) 1127.

ÜBER EINE NEUE METHODE DER LINIENPROFILANALYSE IN DER RÖNTGEN-METALLOGRAPHIE

I. S. SZÁNTÓ

ZUSAMMENFASSUNG

In dem vorliegenden Aufsatz wird die Rechentechnik der von A. J. C. WILSON theoretisch entwickelten und in letzter Zeit mitgeteilten Methode der Varianz-Bewertung beschrieben und einer Kritik unterzogen. Der Autor weist darauf hin, wie die Methode weiter entwickelt werden kann. Unter Heranziehung von experimentellen Daten wird der numerische Gang der Lösung an einem metallographischen Beispiel illustriert. Auch das Blockschema der Programmierung der elektronischen Rechenmaschine wird mitgeteilt, mit dessen Hilfe die charakteristischen Kurven der Varianz durch eine Reihe von Approximationsoperationen sukzessiv bestimmt werden können. Zuletzt wird als Diskussion der Ergebnisse das Problem der Trennung der Effekte von Gitterverformung und Korngröße behandelt, wobei die Methode mit anderen Verfahren verglichen und die Größenordnung des Bereiches der zu messenden Parameter bestimmt wird, innerhalb dessen die detektierten Röntgen-Evidenzen zuverlässig ausgewertet werden können.

UNE NOUVELLE MÉTHODE D'ANALYSE RADIOGRAPHIQUE DE LA DISTRIBUTION DE L'INTENSITÉ DIFFRACTÉ EN MÉTALLURGIE

I. S. SZÁNTÓ

RÉSUMÉ

L'auteur expose et discute la technique de calcul de la méthode d'évaluation de la variance, publiée dernièrement par A. J. C. WILSON, qui en a aussi élaboré la théorie. L'auteur explique le développement possible de la procédure. Par un exemple métallographique utilisant des résultats d'essais, l'auteur illustre la marche du calcul. Il communique également le schéma synoptique du calculateur programme, dont l'application permet de déterminer les courbes de la variance par une suite d'opérations correspondant à des approximations successives. En discutant ensuite les résultats, l'auteur examine le problème de la séparation des effets de la distorsion de réseau et des mesures des particules en comparaison des autres méthodes. Il indique enfin l'ordre de grandeur du domaine des paramètres à mesurer, à l'intérieur duquel les signes radiographiques détectés peuvent être interprêtes correctement.

О НОВОМ МЕТОДЕ АНАЛИЗА ПРОФИЛЕЙ ЛИНИЙ В РЕНТГЕНОВСКОМ МЕТАЛЛОВЕДЕНИИ

И. С. САНТО

РЕЗЮМЕ

В работе изложена и подвергнута критике техника расчета теоретически разработанного и недавно опубликованного *А. Дж. С. Вильсоном* метода оценки расхождения (варианции). Автор предлагает методы, с помощью которых способы расчета могут получить дальнейшее развитие. На конкретном металлографическом примере, основанном на данных эксперимента, иллюстрируется нумерический ход решения. Публикуется групповая схема программы для электронной вычислительной машины. С помощью схемы характеристические кривые могут быть определены операционным рядом последующего приближения. Наконец, автор, оценивая свои результаты, обсуждает проблематику разделения эффектов деформации решетки и величины частиц. Сравнивает свой метод с другими и указывает пределы порядка величин измеряемых параметров, в рамках которых зарегистрированные рентгеновские сигналы могут быть надежно оценены.

INDEX

Batta, I.: Calculation of Water Hammer Phenomena by Automatic Sequence Controlled Digital Computers, I. — Wasserstoßberechnung mit Hilfe einer programmgesteuerten, digitalen Rechenmaschine, I. — Calcul du coup de bélier par calculatrice électronique digitale à programme, I. — *Батта, И.:* Расчет водяного удара при помощи цифровой электронной вычислительной маш иныпрограмм- ного управления. I. 3

Stvrteczky, F.—Szabó, Á.: The Influence of the Blade-Breadth on the Characteristics of Centrifugal Pumps with Open Type Impellers — Einfluß der Schaufelbreite auf die Gestaltung der Charakteristik-Kurven von Zentrifugalpumpen mit offenem Laufrad — L'influence de la largeur d'aube sur les caractéristiques des pompes centrifuges à roue ouverte — *Штвртецки, Ф.—Сабо, А.:* Влияние ширины рабочего колеса центробежных насосов с полуоткрытой лопастной решеткой на вид кривых 31

Tóth, L.—Vincze, E.: Solution of Kármán's Differential Equation for Rolling with the Aid of Infinite Power Series — Die Lösung der Kármánschen Differentialgleichung des Walzvorganges durch unendliche Potenzreihen — Résolution, par séries de puissances infinies, de l'équation différentielle de Kármán se rapportant au processus de laminage — *Тот, Л.—Винце, Е.:* Решение дифференциального уравнения прокатки по Карману с помощью бесконечных экспоненциальных рядов 45

Bujdosó, E.—Czoboly, E.—Magyary, F.: The Determination of the Distribution Coefficient of Zinc with Radioisotope Zn^{65} by the Zone Melting of Aluminium — Bestimmung des Verteilungskoeffizienten von Zink mittels des Radioisotops Zn^{65} beim Zonenschmelzen des Aluminiums — Détermination du coefficient de distribution du zinc avec isotope Zn^{65}, au raffinement par zone fondue de l'aluminium — *Буйдошо, Э.—Цоболь, Э.—Мадяри, Ф.:* Определенние коэффициента распределения цинка при помощи изотопа Zn^{65} в процессе зонной плавки алюминия 63

Vasvári, F.: The Phenomena Arising with the Cavitation Processes — Kavitation als elektrische Erscheinung — La cavitation comme phénomène électrique — *Вашвари, Ф.:* Кавитация как электрического явление 81

Tóth, L.: Die Berechnung des Verformungswiderstandes prismatischer Körper beim Zusammendrücken ihrer parallelen Flächen — Calculation of the Deformation Resistance of Prismatic Bodies Compressed by Parallel Plates — Le calcul de la résistance à la déformation des corps prismatiques comprimés par plaques parallèles — *Тот, Л.:* Расчет сопротивления деформации при сжатии призматических тел между параллельными плоскостями 105

Haszpra, O.: The Problem of the Quadratic Weir. Proportional Flow Measurement without the Disturbance of the Free Watersurface — Das Problem des quadratischen Überfalls. Wassermengenmessung ohne Unterbrechung der freien Oberfläche — Le problème du déversoir quadratique. Mesure de débit par courant dérivé, sans rupture de la surface libre — *Хаспра, О.:* Проблема квадратичного водослива. Замер количества воды побочного потока без нарушения свободной поверхности 121

Kaliszky, S.: Structural Analysis of Buildings with Vertical, Thin Walled Load Carrying Elements, Affected by Horizontal Forces — Statische Berechnung von durch Horizontalkräfte belasteten Gebäuden mit Tragwänden — Calcul statique de bâtiments à murs porteurs chargés par des forces verticales — *Калиски, Ш.:* Статический расчет зданий с несущими стенами, подверженными горизонтальным нагрузкам 133

Huszár, I.—Bodor, J.: The Computation of the Forces of the Commutator Riser — Berechnung des Kräftespiels einer Kommutatorfahne — Calcul du jeu de forces des talons de commutateurs — *Хусар, И.—Бодор, Я.:* Расчет работы коллекторного петушка 149

Hoffmann, A.: Analysis of the Effect Exerted by a Variable Heat-Transfer Coefficient upon the Heating Process Carried out with a Cylindrical Body. I. — Analyse des Einflußes eines veränderlichen Wärmeübergangskoeffizienten auf den Anwärmevorgang beim Erhitzen eines zylindrischen Körpers — Examen de l'effet du coefficient variable de la transmission de chaleur dans le chauffage des corps cylindriques — *Хоффманн, А.:* Исследование влияния переменного коэффициента теплопередачи при нагреве цилиндрического тела, I. 163

Sastry, U. A.: Heat Transfer by Laminar Forced Convection in Multiply Connected Regions — Wärmeübertragung bei erzwungener laminarer Konvektion in mehrfach zusammenhängenden Bereichen — Transmission de la chaleur par convection laminaire forcée dans des domaines multiplement connectés — *Шастри, У. А.:* Передача тепла при ламинарном принудительном движении потока в многократно зависяших областях 181

Horváth, J.: Ausbildung achsensymmetrischer Belastung in der Umgebung von Strecken mit Rundprofil — The Development of Centrally Symmetric Loads Around Mine Entries of Circular Cross Section — La formation d'états de contraintes symétriques par rapport à l'axe autour de galeries de mine de section circulaire — *Хорват, Й.:* Возникновение осесимметричных нагрузок вокруг горных выработок круглого сечения 193

Hornung, A.: Die Standzeitsfragen der Schleifscheiben — The Problem of the Determination of the tool life of Grinding Wheels — Les problèmes de la détermination de la durée des meules —*Хорнунг, А.:* Вопросы определения срока службы шлифовального круга 211

Forgó, L.: Problems of Deaeration in Heat Exchangers Consisting of Steam-Heated Parallel Tubes — Probleme der Entlüftung von Wärmeaustauschern aus dampfgeheizten parallel geschalteten Röhren — Problèmes de désaération des échangeurs à rangées de tubes parallèles, chauffés à la vapeur — *Форго, Л.:* Проблемы обезвоздушивания теплообменников, собранных из параллельно соединенных и отапливаемых паром труб 223

Szántó, I. S.: Recent Developments of Line Profile Analysis Used in X-Ray Metallography — Über eine neue Methode der Linienprofilanalyse in der Röntgen-Metallographie — Une nouvelle méthode d'analyse radiographique de la distribution de l'intensité diffractée en métallurgie — *Санто, И. С.:* О новом методе анализа профилей линий в рентгеновском металловедении 251

VDI-VERLAG STELLT AUS

Bücher und Schriften
VDI-Richtlinien-VDI-Handbücher
Schriftenreihen-Zeitschriften

Unsere Fachgebiete:

Werkstoffe
Maschinenbau
Wärme und Kraft
Kerntechnik
Heizungs- und Lüftungstechnik
Kältetechnik
Bauingenieurwesen
Leichtbau
Feinmechanik
Verkehrstechnik
Staubtechnik
Reinhaltung der Luft
Verfahrenstechnik
Betriebstechnik
Materialfluß
Betriebswissenschaft
Patentwesen
Fachsprache
Technikgeschichte
Mensch und Technik
Schrifttumsnachweise
Literaturberichte

Wir stellen unsere Veröffentlichungen vom 27. 9. bis 2. 10. 1965 in der

AKADÉMIAI KÖNYVESBOLT
VÁCI UTCA 22 BUDAPEST-V

aus und bitten um Ihren Besuch.

VDI-VERLAG GMBH
VERLAG DES VEREINS DEUTSCHER INGENIEURE
4 DÜSSELDORF 10 · POSTFACH 10 250

Printed in Hungary

A kiadásért felel az Akadémiai Kiadó igazgatója. Műszaki szerkesztő: Farkas Sándor
A kézirat a nyomdába érkezett: 1965. IV. 12. — Terjedelem: 24 (A/5) ív. 152 ábra

65.60638 Akadémiai Nyomda, Budapest — Felelős vezető: Bernát György

The Acta Technica publish papers on technical subjects in English, German, French and Russian.

The Acta Technica appear in parts of varying size, making up volumes.

Manuscripts should be addressed to

Acta Technica
Nádor u. 7.
Budapest V.
Hungary

Correspondence with the editors and publishers should be sent to the same address.

The rate of subscription to the Acta Technica is 110 forints a volume. Orders may be placed with "Kultúra" Foreign Trade Company for Books and Newspapers (Budapest I., Fő utca 32. Account No. 43-790-057-181) or with representatives abroad.

Les Acta Technica paraissent en français, allemand, anglais et russe et publient des travaux du domaine des sciences techniques.

Les Acta Technica sont publiés sous forme de fascicules qui seront réunis en volumes.

On est prié d'envoyer les manuscrits destinés à la rédaction à l'adresse suivante:

Acta Technica
Nádor u. 7.
Budapest V.
Hongrie

Toute correspondance doit être envoyée à cette même adresse.

Le prix de l'abonnement est de 110 forints par volume.

On peut s'abonner à l'Entreprise pour le Commerce Extérieur de Livres et Journaux «Kultúra» (Budapest I., Fő utca 32. Compte courant No. 43-790-057-181) ou à l'étranger chez tous les représentants ou dépositaires.

«Acta Technica» публикуют трактаты из области технических наук на русском, немецком, английском и французском языках.

«Acta Technica» выходят отдельными выпусками разного объема. Несколько выпусков составляют один том.

Предназначенные для публикации рукописи следует направлять по адресу:

Acta Technica
Nádor u. 7.
Budapest V.
Венгрия

По этому же адресу направлять всякую корреспонденцию для редакции и администрации.

Подписная цена «Acta Technica» — 110 форинтов за том. Заказы принимает предприятие по внешней торговле книг и газет «Kultúra» (Budapest I., Fő utca 32. Текущий счет № 43-790-057-181) или его заграничные представительства и уполномоченные.

68,— Ft

Index: 26.025

ACTA TECHNICA

ACADEMIAE SCIENTIARUM HUNGARICAE

ADIUVANTIBUS
L. GILLEMOT, GY. HEVESI, K. P. KOVÁCS,
K. SZÉCHY, G. TARJÁN

REDIGIT
A. GELEJI

TOMUS 51 FASCICULI 3—4

AKADÉMIAI KIADÓ, BUDAPEST
1965

ACTA TECHNICA

A MAGYAR TUDOMÁNYOS AKADÉMIA MŰSZAKI TUDOMÁNYOK OSZTÁLYÁNAK KÖZLEMÉNYEI

SZERKESZTŐSÉG ÉS KIADÓHIVATAL: BUDAPEST V., ALKOTMÁNY U. 21.

Az Acta Technica német, angol, francia és orosz nyelven közöl értekezéseket a műszaki tudományok köréből.

Az Acta Technica változó terjedelmű füzetekben jelenik meg, több füzet alkot egy kötetet.

A közlésre szánt kéziratok a következő címre küldendők:

Acta Technica
Budapest V., Nádor u. 7.

Ugyanerre a címre küldendő minden szerkesztőségi és kiadóhivatali levelezés.

Az Acta Technica előfizetési ára kötetenként belföldre 80 forint, külföldre 110 forint. Megrendelhető a belföld számára az „Akadémiai Kiadó"-nál (Budapest V., Alkotmány utca 21. Bankszámla 05-915-111-46), a külföld számára pedig a „Kultúra" Könyv- és Hírlap Külkereskedelmi Vállalatnál (Budapest I., Fő utca 32. Bankszámla: 43-790-057-181) vagy annak külföldi képviseleteinél és bizományosainál.

Die Acta Technica veröffentlichen Abhandlungen aus dem Bereiche der technischen Wissenschaften in deutscher, französischer, englischer oder russischer Sprache.

Die Acta Technica erscheinen in Heften wechselnden Umfanges. Mehrere Hefte bilden einen Band.

Die zur Veröffentlichung bestimmten Manuskripte sind an folgende Adresse zu senden

Acta Technica
Nádor u. 7.
Budapest V.
Ungarn

An die gleiche Anschrift ist auch jede für die Schriftleitung und den Verlag bestimmte Korrespondenz zu richten.

Abonnementspreis pro Band: 110 Forint. Bestellbar bei dem Buch- und Zeitungs-Außenhandels-Unternehmen »Kultúra« (Budapest I., Fő utca 32. Bankkonto Nr. 43-790-057-181) oder bei seinen Auslandsvertretungen und Kommissionären.

IMRE RÁZSÓ

1904—1964

Imre Rázsó wurde am 14. Oktober 1904 in Kassa geboren. Das Diplom eines Maschineningenieurs erwarb er 1927 an der Technischen Hochschule Budapest und das Diplom der Landwirtschaftlichen Akademie an der Landwirtschafts-Akademie Magyaróvár, im Jahre 1931.

Im Jahre 1929 begann er seine Tätigkeit als Assistent am Lehrstuhl für Maschinenkunde der Landwirtschafts-Akademie Magyaróvár; später beteiligte er sich auch an den Arbeiten der dortselbst befindlichen Forschungsstelle für landwirtschaftliche Maschinen. Von seinen dort durchgeführten Untersuchungen seien die Forschungsarbeiten über Biogas-Anlagen, ferner über Kornverluste beim Dreschen hervorgehoben.

1946 wurde er Leiter des Lehrstuhls für Landwirtschaftliche Maschinenbaukunde an der neu organisierten Universität für Agrarwissenschaft und seit 1949 war er Professor des Lehrstuhls für Landwirtschaftliche Maschinenbaukunde an der Technischen Universität Budapest.

Imre Rázsó spielte auf dem Gebiet des landwirtschaftlichen Maschinenwesens eine hervorragende Rolle. Mit seinem Namen sind Untersuchungen verknüpft, die sich auf die Stabilitätsverhältnisse von Traktoren, Abrollverhältnisse von Rädern, auf die eingehende Wirkungsgradforschung des Traktorenzuges beziehen. Auf Grund von eingehenden theoretischen Studien wurden von ihm der Aufbau und die Bemessungsgrundsätze von Grabenziehmaschinen zum Ausheben von tiefen und steilwandigen Gräben entwickelt. Eine erhebliche Arbeit leistete er auch bei der Schaffung eines ungarischen Mähdreschers und bei der Ausarbeitung eines geeigneten Systems zur Ernteeinbringung. In der letzen Zeit beschäftigten ihn Probleme der Mechanisierung der Bearbeitung von sandigen Böden, und seine Direktiven grundsätzlicher Art konnten auch hier aktiv mitwirken.

An dem wissenschaftlichen Leben in Ungarn und im Ausland nahm er regen Anteil. Seit 1949 war er korrespondierendes Mitglied der Ungarischen Akademie der Wissenschaften. Für seine im Wissenschaftlichen Verein für Maschinenbau entfaltete Aktivität wurde er mit der goldenen *Bánki Donát Medaille* ausgezeichnet.

Die ungarischen Ingenieure bewahren Imre Rázsó, dem Gelehrten und Menschen ein ehrendes Andenken.

Gy. Sitkei

FERENC RATKOVSZKY

1900—1965

Der Akademiker und Kossuthpreisträger Ferenc RATKOVSZKY verstarb am 9. März 1965. Er war eine der hervorragendsten Persönlichkeiten der ungarischen Starkstromtechnik und galt als Pionier der modernen Starkstromtechnik. Sein Tod bedeutet einen schweren Verlust für diesen Wissenschaftszweig.

Ferenc RATKOVSZKY wurde am 18. Mai 1900 in Sopron geboren. Er absolvierte seine Studien an der Technischen Hochschule in Budapest. Einige Monate vor seiner Diplomprüfung, trat er in den Dienst der *Ganz Elektrizitäts A.G.* ein. Seine Tätigkeit begann im Prüfraum der Fabrik; bald wurde er hier stellvertretender Leiter und gleichzeitig unmittelbarer Mitarbeiter von Otto Titus BLÁTHY. Im Jahr 1924 wurde er zum Oberingenieur ernannt, und i. J. 1925 wurde ihm die Leitung des Büros für die Berechnung und Konstruktion von Transformatoren übertragen.

Im Jahr 1929 ist er bereits der stellvertretende Direktor der Fabrik, i. J. 1935 wurde er ihr Direktor und erhielt den Auftrag zur Leitung sämtlicher Abteilungen für Berechnung, Entwurf, Versuch und technisch-kaufmännische Fragen. Im Jahr 1939 wurde er zum geschäftsführenden Direktor ernannt.

Die Fabrik Ganz hat von 1927 an etwa 50 Patente von RATKOVSZKY angemeldet bzw. verwirklicht. Die von ihm entworfenen Transformatoren waren sowohl hinsichtlich der Leistung (i. J. 1927 von 42 MVA, i. J. 1928 von 110 kV Einheiten) als auch hinsichtlich des geringen Gewichtes von führendem Weltniveau. Er trug auch zur Modernisierung von Hochspannungseinrichtungen bei. Er bestimmte die technische Entwicklung der ganzen Starkstromindustrie und nahm aktiv an den Arbeiten der Elektrifizierung des Landes teil. Insbesondere auf dem Gebiet der Spannungsregler entwickelte er neue Konstruktionen. Entsprechend den zur Verfügung stehenden Schalteinrichtungen löste er die Regelungsschaltung auf der Seite mit der geringeren Spannung. Sein Verteilungs-Netzspannungsregler, sein selbsttätiger Verbraucher-Spannungsregler, insbesondere die dazugehörende Automatik hat auch im Ausland große Anerkennung gefunden. Zu den von ihm erzielten

bedeutenden Ergebnissen kann auch gezählt werden, daß er im Weltmaßstab als erster das System der Kandó'schen Elektrolokomotive im Rahmen der in Ungarn eingeführten Eisenbahnelektrifizierung mit 50-Frequenz weiterentwickelt hat. Das von ihm entworfene Fahrzeug vom Frequenzwandler-System, das sich für beliebige Leistung und Geschwindigkeit eignet, und dessen Geschwindigkeit stetig geregelt werden kann, wurde auch bei den Französischen Staatsbahnen verwendet.

An der Technischen Hochschule in Budapest, im Jahr 1932, und später an der Technischen und Wirtschaftswissenschaftlichen Universität, i. J. 1939, erlangte er die Würde eines Privatdozenten. Die Ungarische Akademie der Wissenschaften zeichnete ihn i. J. 1939 mit dem Berzeviczypreis aus.

Auf Ersuchen der Hauptstadt verzichtete er auf die in der Ganz-Fabrik bekleidete Stellung und übernahm die Leitung der Elektrizitätswerke der Hauptstadt Budapest. Nach der Befreiung nahm er seine Arbeit mit erneuten Kräften auf. Unter Beibehaltung der Leitung der Elektrizitätswerke folgte er einer Aufforderung der Regierung und nahm als technischer Leiter an den Elektrifizierungsarbeiten des Landes, in den Jahre 1948—1960, teil. Außerdem war er als technischer Ratgeber der *Ganz Elektrowerke* leitend beteiligt an den wichtigsten Entwurfsarbeiten. Anhand seiner Vorschläge sind zahlreiche neue bzw. wirtschaftlichere Lösungen entstanden. Einer der wichtigsten Vorschläge betraf die Erhöhung der Spannung des Landesnetzes von 100 kV auf 120 kV. Diese Maßnahme ergab in 10 Jahren eine Einsparung von 200 Millionen Forint, und erleichterte wesentlich die Übertragung der erforderlichen großen Energiemengen. Die nach seinen Patenten ausgeführten Hochspannungstransformatoren und Regelungseinrichtungen von großer Leistung bedeuteten gleichfalls erhebliche Ersparnisse. In Anerkennung seiner hervorragenden wissenschaftlichen Verdienste im Zusammenhang mit der Erhöhung des Spannungspegels im Grundnetz und mit der Gestaltung von großen Transformatoren, ferner unter Berücksichtigung seiner vielseitigen schöpferischen Tätigkeit, zeichnete ihn die Regierung 1952 mit dem Kossuthpreis aus. Die Ungarische Akademie der Wissenschaften ernannte ihn i. J. 1951 zum korrespondierenden Mitglied, und i. J. 1954 wurde er zum ordentlichen Mitglied gewählt.

Die wissenschaftlichen Beiträge von Ferenc RATKOVSZKY geben nur unvollständige Auskunft über seine Tätigkeit. Sowohl seine theoretischen als auch seine konstruktiven und wirtschaftlichen Berechnungen konzentrierte er immer auf die Lösung der tatsächlich auftretenden wichtigsten Aufgaben. Er war bemüht, unsere Starkstromindustrie ständig zu entwickeln und ihr ein zeitgemäßes Niveau zu sichern.

RATKOVSZKY besaß zwei Patente, die nicht nur konstruktiv, sondern auch theoretisch, im Weltmaßstab, vollkommen Neues brachten: den i. J. 1935 konstruierten automatischen, dezentralisierten Spannungsregler von

kleiner Leistung, und die i. J. 1937 herausgebrachte Lokomotive mit Frequenzwandler. Der letzteren folgte die erste praktisch anwendbare 50 Hz Kandó'sche Lokomotive. Die Ausbildung der neuzeitlichen Typen von Hochspannungs- und Hochleistungstransformatoren nach seinen eigenen Patenten bedeuten ebenfalls ein Beispiel seiner hervorragenden wissenschaftlichen und technischen Leistungen.

Er befaßte sich mit vielen Fragen der elektrischen Energiewirtschaft. Mit seinen schöpferischen Vorschlägen trug er in erheblichem Maß zur Entwicklung des elektrischen Energiesystems bei. Im Rahmen seiner außerordentlich vielseitigen Tätigkeit kamen neben den technischen Kenntnissen und der geeigneten Qualifikation auch seine wirtschaftlichen Fähigkeiten zur Geltung. Zwischen den weitverzweigten Aufgaben konnte er sich immer auf das Wesentliche konzentrieren.

Wenn wir seine Lebensarbeit überblicken, so können wir feststellen, daß die ungarische Elektroindustrie, die ungarische Energiewirtschaft in seiner Person einen ihrer hervorragendsten Persönlichkeiten verloren hat. Seine schöpferische, an Erfolgen reiche Tätigkeit steht als Musterbeispiel vor uns. Wir werden ihm ein pietätvolles Gedenken bewahren.

K. Szendy

FERENC RATKOVSZKYS FACHLITERARISCHE ARBEITEN

1. Die Erwärmung der elektrischen Maschinen (Villamos gépek melegedése). *Elektrotechnika* (1923), 15. April.
2. Die Erwärmung elektrischer Maschinen. *ETZ* (1925), 22. Mai.
3. Die Harmonischen des Magnetisierstromes (A mágnesező áram harmonikusai). *Elektrotechnika* (1925), 25. Februar.
4. Schutzeinrichtungen für Transformatoren (Transzformátor védőberendezések). *Elektrotechnika* (1928), 15. Februar.
5. Schutzeinrichtungen für Transformatoren. *Elektrotechnik und Maschinenbau* (1928), Heft 27.
6. Transformatoren (Transzformátorok). *Elektrotechnika* (1929), 15. November.
7. Selbsttätiger Spannungsregler (Önműködő feszültségszabályozó). *Elektrotechnika* (1935).
8. Ein neuer Spannungsregler. *Elektrotechnik und Maschinenbau* (1935), Heft 31.
9. Le réglage décentralisé de la tension et son importance économique. Haager Konferenz der *UNIPEDE*, 10—20 Juni 1936 (III—C—11).
10. Die wirtschaftliche Bedeutung der Spannungsregelung der Beleuchtung (A világítási feszültség szabályozásának gazdasági jelentősége). *Községfejlesztés* (1936), 31. Januar.
11. Spezielle Probleme der Hochleistungs- und Hochspannungstransformatoren (Nagyteljesítményű és nagyfeszültségű transzformátorok különleges problémái). Mérnöki Továbbképző Intézet, Bd. VI. (1942), Heft 4.
12. Technische Beschreibung der elektrischen Lokomotive System Ganz—Kandó—Ratkovszky, Reihe MÁV V-44 (A MÁV V-44 sorozatú Ganz—Kandó—Ratkovszky rendszerű villamos mozdony műszaki leírása). Katalog der Fa. Ganz &. Co. 1943.
13. Das Mátravidéker Kraftwerk auf dem Wege zur Verwirklichung (A mátravidéki erőmű a megvalósulás útján). *Magyar Energiagazdaság* **1** (1948), No. 1.
14. Elektrifizierung von Vollbahnen mit 50 Hz und das Periodenwandlersystem (Nagyvasutak 50 periódusú villamosítása és a periódusváltós rendszer). *Mitt. d. Tech. Abt. d. Ung. Akad. d. Wiss.* **8** (1952), Nr. 2.

15. Elektrifizierung von Vollbahnen mit 50-Hz-Einphasenstrom und das Periodenumformersystem. *Acta Techn. Hung.* **4** (1952), 1—4.
16. 50-Cycle Main-Line Electrification and the Frequency-Changer System. *Hungarian Heavy Industries* (1953), 12.
17. Fehlerstatistik von Transformatoren der Elektrizitätswerke der Hauptstadt Budapest (Budapest Főváros Elektromos Művei transzformátorainak hibastatisztikája). *Villamosság* (1959), Mai.
18. Weiterentwicklung der 50-Perioden-Eisenbahnelektrifizierung im In- und Ausland (Az 50-periódusú vasútvillamosítás továbbfejlődése hazánkban és külföldön). Akademische Antrittslesung. *Mitt. d. Techn. Abt. d. Ung. Akad. d. Wiss.* **33** (1964), 1—4.

MASS SPECTROMETRIC STUDIES OF ADDITIVE MATERIALS EVAPORATING FROM TUNGSTEN PRODUCED BY POWDER METALLURGICAL TREATMENT

P. ROBOZ
RESEARCH INSTITUTE FOR TECHNICAL PHYSICS OF THE HUNGARIAN ACADEMY OF SCIENCES, BUDAPEST

A. KOVÁCH
INSTITUTE OF NUCLEAR RESEARCH OF THE HUNGARIAN ACADEMY OF SCIENCES, DEBRECEN

[Manuscript received December 3, 1962]

The reason of arcing, observed when heating tungsten wires in noble gases at near atmospheric pressure, can be assumedly the space charge destroying effect of materials evaporating from the filament itself. In order to verify this assumption, comparative measurements were carried out with a mass spectrometer on the additive material emission of two different tungsten types used by the vacuum industry, and that of a tungsten wire produced by a modified technology. The most important part of additive emission was found to be that of sodium and potassium. The time and temperature dependence of atomic and ionic emission of Na and K was investigated for all three tungsten types. Tungsten produced by the modified technology emits much less sodium and potassium as compared with the emission of tungsten types used until now, so a decrease in the probability of arcing can be expected by using this tungsten as filament e.g. in incandescent lamps.

I. Introduction

Arcing is a phenomenon often observed in the functioning of tungsten wires produced by powder metallurgical treatment and heated in noble gases at near atmospheric pressure. This effect is more marked in the case of an instantaneous increase of the filament voltage. T. Z. SZELÉNYI has been investigating this arcing effect caused by the alteration of heating voltage [1, 2]. The conclusion was drawn that the cause of arcing might be the cease of the limiting effect of space charge existing in the environment of a heated tungsten wire [3]. The primary reason which is destroying this limiting space charge was unknown.

E. WINTER proposed to explain the cease of the limiting effect of space charge and thus the arcing in noble gases at elevated pressure by the space charge destroying effect of contaminants evaporating from the heated filament, especially if the evaporation occurs in an ionic form. Based on this idea the primary reason of arcing could be the presence of additive materials introduced into the tungsten wire but appropriately unremoved therefrom.

The production technology of tungsten wires used at present by the vacuum industry and consisting of great tungsten crystals was elaborated in the Research Laboratory of the Tungsram Corporation [5, 6]. In the course of producing tungsten rods used in wire-drawing, additive materials as NaCl, KCl, SiO_2, Al_2O_3, Fe_2O_3 are intermixed to the tungsten trioxide powder used

as a starting substance in well defined proportions. Metallic tungsten is produced from this base material by reduction in the hydrogen flow. Rods are pressed from the reduced tungsten powder and sintered in the hydrogen flow, whilst the greatest part of the additive materials leave the tungsten rod, the numerical concentration of the residual impurities usually being in the order of 10^{-5}. The temperature of recrystallization and the crystal sizes depend on the additive materials introduced into the basic substance. According to the references quoted, three different additive materials are necessary and sufficient to allow for the development of great-crystalline structure. After sintering only a small part of the residual additive materials is built into the tungsten lattice, the greater proportion being placed as intercrystalline centres.

Three types of tungsten were compared in course of our measurements, differing from each other in quality and quantity of additives, as well as in length and temperature of the sintering process. Tungsten No. 1 was produced by adding Na, K and Si, tungsten No. 2 by the addition of Na, K, Si, Al and Fe in appropriate amounts. Tungsten No. 3 is similar, in respect to its composition, to tungsten No. 2, but differs in the production treatment. The recrystallization of tungsten No. 1 occurs at about 2000 °C, while that of tungsten No. 2 and No. 3 follows this at about 2300÷2400 °C. In order to develop tungsten No. 3, T. Millner and J. Neugebauer introduced a modified sintering technology to achieve a more perfect elimination of additive materials. The description of the production technology of the different tungsten types can be found in the references already cited [5, 6] and in patent descriptions referring to this subject [7—9].

As tungsten No. 3 presumably involves less amounts of impurities as compared either to tungsten No. 2 or No. 1, it is highly probable that the emission of positive ions from a wire made of tungsten No. 3 would be less as compared to that of wires No. 1 and No. 2, and consequently the probability of arcing could be reduced by using wires made of tungsten No. 3 as filaments.

To verify this assumption, we had to examine the emission of impurities from heated tungsten wires, with particular attention paid to ionic emission. These measurements could be made more practical by using a mass spectrometer, as our aim was not to determine impurities quantitatively, but only to compare the emission properties of various tungsten types.

II. Experimental Methods

Conical coils of 4 mm base diameter and of 5 mm height were made of tungsten wires 0,2 mm diameter, heated to 700 °C during coiling. To assure regular pitch and constant space between the turns, the wires were provided

with a molybdenum armour. To ensure a permanent shape the coils were heated for 5 minutes at 1000 °C in a hydrogen furnace, followed by dissolving the molybdenum armour in an acid mixture of one part nitric acid in three parts sulphuric acid. Finally the coils were electrically polished.

Our measurements were made at the Institute of Nuclear Research of the Hungarian Academy of Sciences with an *MI 1305* type mass spectrometer. Considering our intention to examine the emission of ions as well as that of neutral atoms, the crucible source of the mass spectrometer was adapted to our purposes. The furnace and its heating coil having been removed the sample coils were mounted onto the place of the heating coil. The schematic drawing of the ion source and the placing of the samples are shown in Fig. 1.

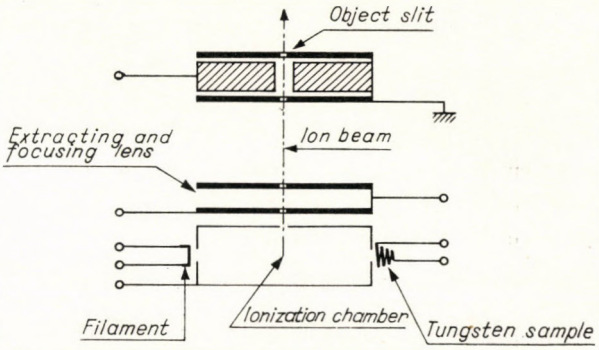

Fig. 1. Schematic view of the ion source indicating the placing of the samples

The current-temperature characteristics of the tungsten wires were measured with an optical pyrometer in high vacuum. The calibrating curves were found to be linear in the temperature range of 800—1800 °C, but gave appropriate accuracy at higher temperatures, too. A stabilized current supply was not available, and fluctuations in the coil temperature took place occasionally. According to this and to the inaccuracy of the pyrometer itself, temperature data are given throughout this paper with an inaccuracy of ± 25 °C.

Prior to the measurements the vacuum system was heated for several hours under high vacuum, the probe coils were outgassed by heating to 1000 °C. As a result of this treatment the vacuum in the analyzing system of the mass spectrometer never exceeded a value of $4 \cdot 10^{-7}$ mmHg. Measurements were made only by raising coil temperatures, the resolving power of the mass spectrometer being about $250 \div 300$.

III. Experimental Results

1. *Mass spectrum of evaporating materials from heated tungsten*

The mass spectrum of evaporating materials from each tungsten sample was taken at different but constant temperature values in the mass range of 16÷62. The record of one spectrum needed about 35 minutes, and during this time the shape of the spectrum did not essentially alter, except at the higher temperatures, where some peaks (Na, K) showed a noticeable decrease with time.

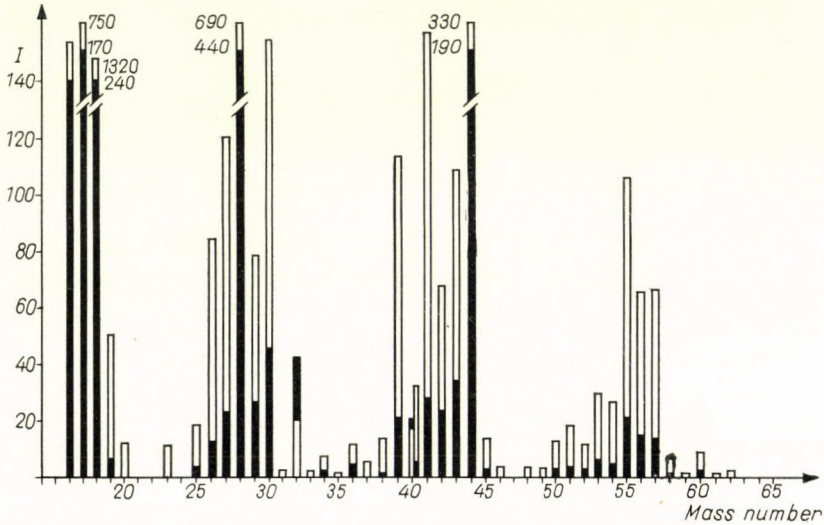

Fig. 2. Mass spectrum of residual gases and of materials evaporating from tungsten No. 2 at 1800 °C the residual pressure in the mass spectrometer being $2{,}5 \cdot 10^{-7}$ mmHg. Background spectrum is shown by full lines

The mass spectrum taken with tungsten No. 2 at 1800 °C is shown on the diagram of Fig. 2, the pressure in the analyzer system having been about $2{,}5 \cdot 10^{-7}$ mmHg. The peak intensities are given in millivolts measured at the output of the D. C. measuring amplifier, as they are given everywhere in this paper. One millivolt measured at the output of the amplifier corresponds to about $2 \cdot 10^{-15}$ A ion current. On Fig. 3 one can see the mass spectrum taken with tungsten No. 3 heated to 1800 °C at a background pressure of $2{,}7 \cdot 10^{-7}$ mmHg. In both cases the heights of background peaks — measured with cold probes — are indicated by full lines.

The shapes of spectra shown in Fig. 2 and Fig. 3 are very similar and the greater part of the peaks is due to hydrocarbons. The differences in background peak heights correspond to the difference in residual pressure in the

vacuum system. It is interesting, however, to note that at mass numbers 23 (Na) and 39 (K) there is a remarkable difference in peak heights, indicating that tungsten No. 3 emits less sodium and potassium as compared with tungsten No. 2.

The spectrum taken with tungsten No. 1 is similar to the spectra shown on Figs. 2 and 3, it is however to be noted that the intensities of peaks due to impurities are the highest in the case of tungsten No. 1.

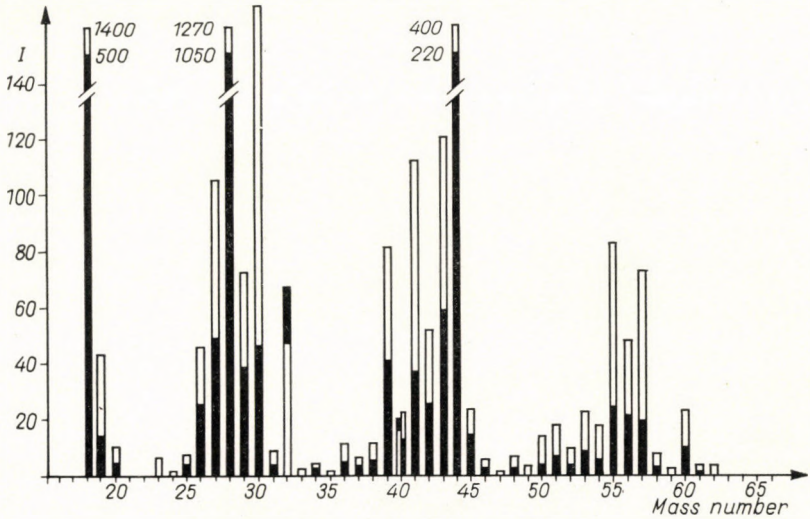

Fig. 3. Mass spectrum of residual gases and of materials evaporating from tungsten No. 3 at 1800 °C the residual pressure in the mass spectrometer being $2{,}7 \cdot 10^{-7}$ mmHg. Background spectrum is shown by full lines

2. *Time dependence of sodium and potassium emission*

In order to examine the emission of sodium and potassium, the changes in the peak intensities of mass numbers 23 and 39 with time were investigated. It is obvious, that besides potassium and sodium the presence and emission of silicon, aluminium and iron would be expected, too. It can be inferred, however, from Figs. 2 and 3 that the emission of these metals (especially that of iron) must be very low. On the other hand, the relatively poor resolving power of our mass spectrometer did not allow us to resolve an eventual Si^{28} peak from the background peaks due to N_2^+, CO^+ and $C_2H_4^+$ ions, similarly, to separate Al^{27} and Si^{29} peaks from hydrocarbons occurring at the same mass numbers. The time dependence of peak intensities was therefore measured only at mass numbers 23 and 39, attributed to sodium and potassium, respectively. There is no hydrocarbon background at mass number 23 at all, $C_3H_3^+$ ions are present at mass number 39, but do not essentially influence the accuracy of our measurements.

The samples were heated for 15 minutes at 1500 °C so as to be well outgassed, following this the temperature was raised to 1800 °C, and peaks due to potassium and sodium were recorded at each 10 minutes. The evaluation was made more difficult by the fact, that at mass number 39 a double peak appeared, the partial peak with a slightly greater apparent mass being smaller in intensity. The reason for the development of this double peak is, that the ion source discriminates directly emitted ions from the probe and ions generated by electron impact in the ion source. Potassium ions emitted thermally

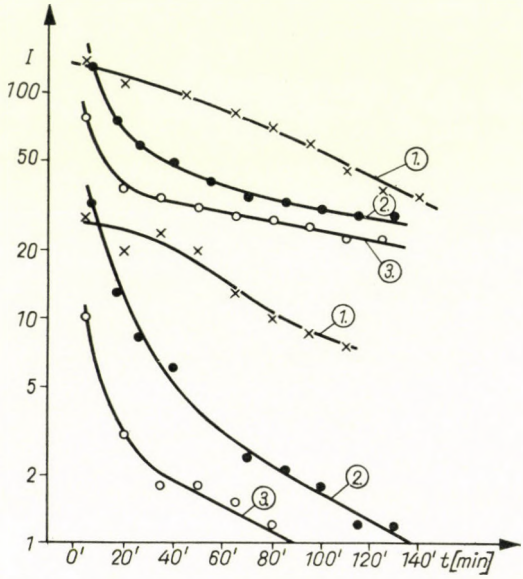

Fig. 4. Time dependence of potassium emission at a constant temperature of 1800 °C in the case of the three tungsten types investigated

from the probe obtain an additional energy by crossing a part of the electron accelerating region, and thus enter the analyzing magnetic field with a slightly greater average energy as compared with the energy of potassium ions generated by electron impact, and emitted originally in an atomic form. Thus, the partial peak with a slightly higher apparent mass is due to potassium ions emitted from the probe. The luminosity of the ion source, of course, is not the same for both groups of ions, so one cannot conclude from the peak intensity ratio as to the emission ratio of ions and neutral atoms.

On Fig. 4 is shown the time dependence of emission at mass number 39 (K^{39}) for the three tungsten types. Similarly, one can see on Fig. 5 the time dependence of sodium emission, measured at mass number 23. There are two groups of curves on Fig. 4, one group with the higher intensity values refers to K^{39} emission in atomic form (including $C_3H_3^+$ background), the

other with smaller intensity values describes ionic emission of potassium. From curves given in Figs. 4 and 5 one can conclude that at the given temperature the potassium and sodium emission of wires made of tungsten No. 3 is less by about one order of magnitude as compared to that of wire No. 1 within a broad time interval, tungsten No. 2 having a medium emissivity between the other two types.

It is worth noting, that the changes with time are very similar for tungsten No. 2 and No. 3 — especially in the case of potassium emission.

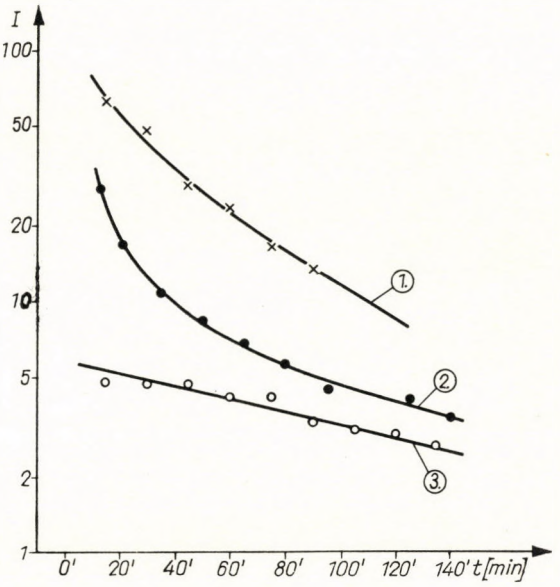

Fig. 5. Time dependence of sodium emission at a constant temperature of 1800 °C in the case of the three tungsten types investigated

This is, as was to be expected, because of the similarity in the production technologies of these two types.

3. *Thermal ion emission*

As it was assumed, the limiting effect against arcing and attributed to the space charge surrounding the heated tungsten filament might be destroyed by ions emitted by the filament itself. According to this, the primary aim of these measurements was to compare the sodium and potassium ion emission of various types of tungstens.

The heating power of the filament supplying the ionizing electrons for the ion source as well as the electron beam accelerating voltage were switched off. In this way the conditions of electron impact ionization were eliminated

and it was guaranteed that ions emitted from the tungsten probe would reach the ion collector only. Under these circumstances peaks appeared only at mass numbers 23 (Na) and 39 (K). A little peak was observed at mass number 41 representing the K^{41} isotope, with a relative peak intensity corresponding to the ratio of potassium isotope abundances.

The change of K^{39} ion peak intensity is shown on Fig. 6, measured with all three tungsten types at 1800 °C and subsequently for tungsten No. 1 and

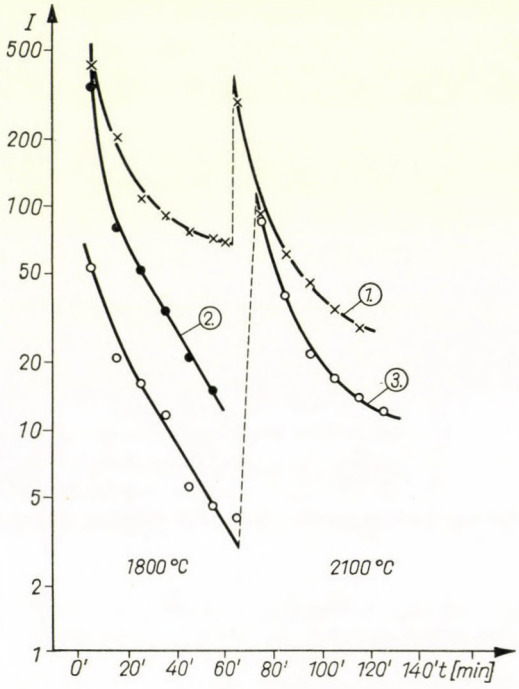

Fig. 6. Time dependence of potassium ion emission at 1800 °C and 2100 °C temperatures

No. 3 at 2100 °C. On Fig. 7 one can see the change with time in the intensity of sodium ion current under the same conditions. Except for the initial portions of the curves, the change of emission current with time is nearly exponential.

The curves characterizing the various tungsten types support our previous statement that tungsten No. 3 emits far less additives than either tungsten No. 1 or No. 2. The ratios of ion emission values are about $I_1 : I_2 : I_3 = 9 : 3 : 1$ where I_1, I_2 and I_3 indicate the measured emission current for the individual tungsten types.

It is to be mentioned, that the ion emission current sometimes increased unsystematically, while the average intensity continued to decrease, unaffected by the current pulses noticed occasionally and lasting only for a very

short time with varying intensities. This phenomenon is due to the fact, that the filament does not emit the ions continuously, but sometimes the material of an intercrystalline centre suddenly bursts out of the surface of the wire, resulting in an instant increase in the ion current intensity. The phenomenon of ion bursts is well known [10] and — according to our opinion — it is of great importance in explaining the arcing phenomenon.

The quantitative study of these ion bursts was not rendered possible

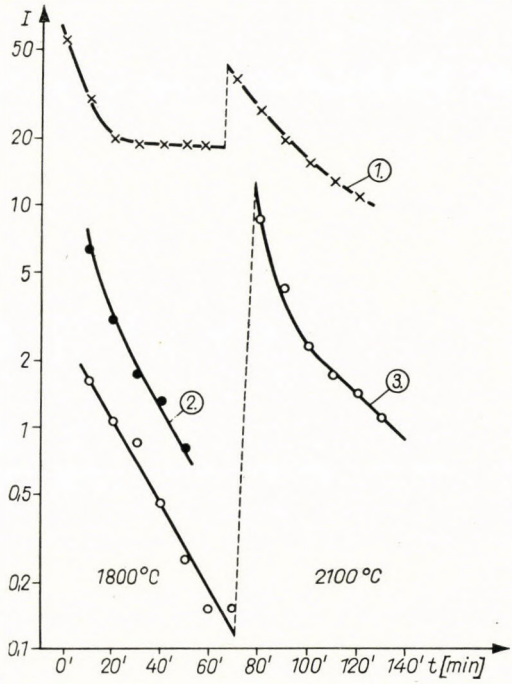

Fig. 7. Time dependence of sodium thermal ion emission at 1800 °C and 2100 °C temperatures

because of the great time constant of the D. C. amplifier. As a qualitative observation it can be mentioned, that the least ion bursts were noticed in the case of tungsten No. 3 and those with the smallest amplitudes.

4. *Temperature dependence of emission*

According to theoretical considerations as well as to our preliminary investigations one could expect a strong dependence of additive emission on temperature, in so far as at higher temperatures higher emission values might be expected; so it was found necessary and advisable to study the temperature dependence of additive emissivity as well.

The temperature was varied in the range of 1000÷2200 °C. Fig. 8 and Fig. 9 show the temperature dependence of potassium resp. sodium emission. As a conclusion one can state, that the least amount of ions is emitted in the whole temperature range investigated from tungsten No. 3, with the ratio of ion emissivity of the individual tungsten types increasing with temperature. At 2000 °C the ion emissivity of tungsten No. 3 is by near one order of magnitude less than that of tungsten No. 1, No. 2 having an intermediate value.

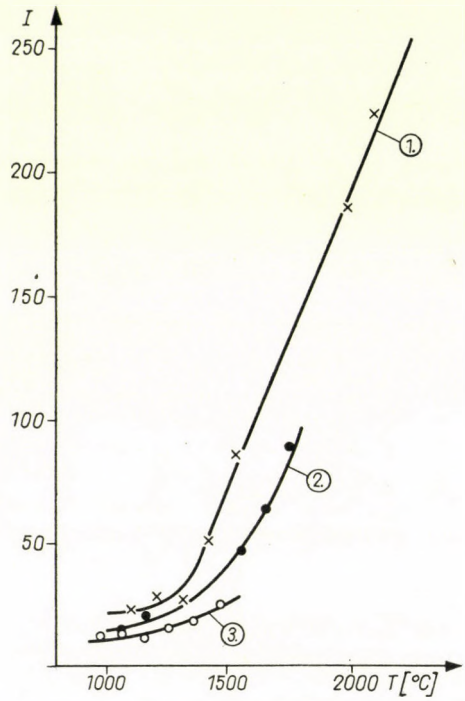

Fig. 8. Temperature dependence of potassium emission in case of the three tungsten types investigated

It is to be mentioned that a rather great scatter was noticed in results obtained in parallel runs in the course of these measurements. The curves of Figs. 8 and 9 correspond to the average behaviour of the individual types, but the data obtained did not allow us to evaluate exactly the bond energies of the tungsten-additive material systems.

In these measurements as well as in measurements reported in the previous chapters at least three parallel runs were made, with results not differing from each other by more than 20%. The differences observed between the various tungsten types in their additive emissivities seem thus to be significant.

IV. Conclusions

A general conclusion can be drawn from the measurements reported here, that tungsten No. 3, made with a modified technology emits much less additive materials in the temperature range investigated (1000 ÷ 2200 °C) than tungsten No. 1 and No. 2, generally used in vacuum industry. At lower temperatures the emission of tungsten No. 3 proved to be less by one order of magnitude as compared to that of tungsten No. 1, the emissivity of tungsten No. 2 being an intermediate value. At elevated temperatures the difference

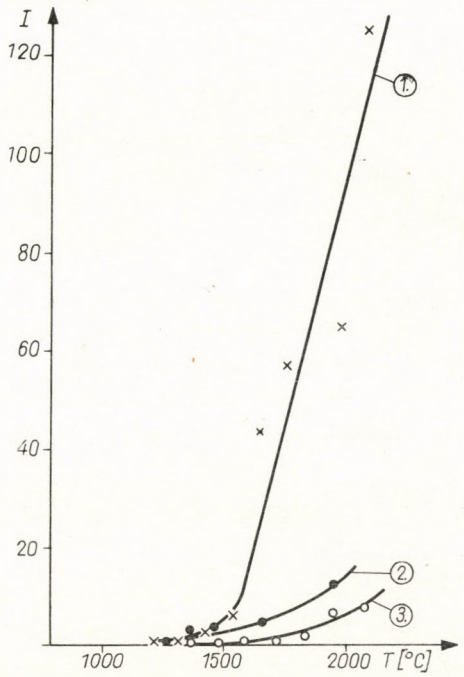

Fig. 9. Temperature dependence of sodium emission in case of the three tungsten type investigated

in additive material emission between tungsten No. 1 and No. 3 is somewhat less than one order of magnitude.

The measurements of time dependence lead to the conclusion that — except for the initial period of heating — the emission decreases exponentially. At elevated temperatures this exponential decrease follows only after a somewhat longer time and the half period of the exponential decrease is essentially longer as compared to that measured at lower temperatures. This might indicate that the role of diffusion cannot be neglected even in the temperature range investigated.

It is to be noted that as opposed to our expectations, a lengthy preheating of wires in high vacuum does not improve the emission relations. Preheating for 100 hours at 1850 °C causes an essential decrease in ion intensity only in the initial period of heating at higher temperatures as compared with wires not treated by preheating. The difference in ion emission intensity between preheated and not preheated wires decreases gradually with time and after some hours the emissivity of preheated and untreated wires will be essentially the same.

The conclusion can be drawn on the basis of the investigations reported here, that so far as the evaporation of residual additive materials have an effect on arcing to be observed in noble gases of near atmospheric pressures, the probability of arcing would decrease by applying tungsten No. 3 as filament instead of tungsten No. 1 and No. 2 used so far. Of course, this could be proved only by experiments carried out under appropriate conditions.

* * *

Authors wish to express their thanks to dr. E. WINTER for proposing the idea of the experiments and for paying constant attention to their work, as well as to Prof. dr. A. SZALAY rendering possible to carry out the measurements reported here in the institute under his direction.

Thanks are due to dr. MILLNER who kindly provided us with samples of tungsten No. 3 made with the modified technology elaborated by him and his co-workers.

REFERENCES

1. SZELÉNYI, T.: *Acta Techn. Hung.* **34** (1961), 453.
2. SZELÉNYI, T.: *Acta Techn. Hung.* **34** (1961), 457.
3. CLAPP, R. H.: *Illumin. Engng.* **6** (1950), 357.
4. VÁCZ, I.: *MTA Műsz. Tud. Oszt. Közl.* **25** (1960), 222.
5. MILLNER, T.: *MTA Műsz. Tud. Oszt. Közl.* **21** (1957), 243.
6. MILLNER, T.: *MTA Műsz. Tud. Oszt. Közl.* **27** (1960), 111.
7. MILLNER, T.—TURY, P.: Hung. Pat. 106268 (1933) and USP 2012825 (1935).
8. MILLNER, T.—NEUGEBAUER, J.: Hung. Pat. 143027 (1954) and USP 2948609 (1955).
9. MILLNER, T.—NEUGEBAUER, J.: Hung. Pat. 143595 (1954) and USP 2806774 (1955).
10. MINTURN, R. E. et al.: *J. Appl. Phys.* **31** (1960), 876.

MASSENSPEKTROMETRISCHE UNTERSUCHUNG VON AUS PULVERMETALLURGISCH HERGESTELLTEM WOLFRAM—VERDAMPFENDEN ZUSÄTZEN

P. ROBOZ—A. KOVÁCH

ZUSAMMENFASSUNG

Beim Glühen von Wolframspiralen in edelgashaltiger Atmosphäre unter annähernd atmosphärischem Druck kann eine der Ursachen der von thermischen Elektronen bewirkten Lichtbogenbildung die raumladungverringernde Wirkung der aus dem Glühfaden verdampfenden Stoffe sein. Um diese Frage zu klären, haben die Verfasser unter Verwendung des Massenspektrometers vergleichende Untersuchungen über die Emission der Zusätze von zwei in der

Vakuumindustrie gebräuchlichen Wolframwerkstoffen, sowie einem mittels einer modifizierten Technologie hergestellten Wolfram angestellt. Sie stellten fest, daß in der Emission der Zusätze die bedeutendste Rolle die Emission des Kaliums und des Natriums spielt, und zwar hauptsächlich in der Form von Ionenemission. Die Zeit- und Temperaturabhängigkeit der atomaren und der ionischen Emission des Kaliums und des Natriums wurden für alle drei Wolframsorten untersucht. Das nach der modifizierten Technologie hergestellte Wolfram emittiert wesentlich weniger Kalium- und Natriumionen bzw. Atome als die bisher verwendeten Wolframsorten, weswegen zu erwarten ist, daß durch seine Verwendung die Wahrscheinlichkeit der Lichtbogenbildung, z. B. in Glühlampen, verringert werden kann.

EXAMEN PAR LE SPECTROMÈTRE DE MASSE DES ADDITIFS S'ÉVAPORANT DU TUNGSTÈNE PRODUIT PAR LA MÉTALLURGIE DES POUDRES

P. ROBOZ—A. KOVÁCH

RÉSUMÉ

Au chauffage des spirales de tungstène sous une pression à peu près atmosphérique, dans un espace contenant des gaz rares, des arcs se forment sous l'action des électrons thermiques. L'une des causes de ce phénomène peut être la détérioration des charges spatiales par les matières s'évaporant du filament. Pour élucider la question, les auteurs ont fait des recherches comparatives à l'aide d'un spectromètre de masse, sur l'émission des additifs de deux sortes différentes de tungstènes utilisés dans l'industrie du vide, et sur un tungstène produit par une technologie modifiée. Dans l'émission des additifs, le rôle prépondérant est joué par l'émission du potassium et du sodium, surtout par sa forme ionique. Pour les trois sortes de tungstènes, les auteurs ont examiné les émissions atomique et ionique du potassium et du sodium en fonction du temps et de la température. Le tungstène produit par la méthode modifiée émettant beaucoup moins d'ions et d'atomes de potassium et de sodium que les tungstènes généralement utilisés, on peut s'attendre à voir diminuer par son emploi la probabilité de la formation d'arcs, par exemple dans les lampes à incandescence.

МАСС-СПЕКТРОСКОПИЧЕСКИЙ АНАЛИЗ ДОБАВОК, ИСПАРЯЮЩИХСЯ ИЗ МЕТАЛЛОКЕРАМИЧЕСКОГО ВОЛЬФРАМА

П. РОБОЗ—А. КОВАЧ

РЕЗЮМЕ

Одной из причин образования дуги, наблюдаемой при накале вольфрамовых спиралей в атмосфере, содержащей нейтральный газ при давлении близком к нормальному атмосферному, может быть эффект ухудшения заряда пространства веществами, испаряющимися из нити накала. Для выяснения этого, используя масс-спектроскоп, проводились сравнительные исследования двух различных вольфрамовых материалов, применяемых в вакуумной технике, а также анализ эмиссии добавок вольфрама, полученного по измененной технологии. Установлено, что в отношении эмиссии добавок наибольшую роль играет эмиссия натрия и калия, в основном ее ионная форма. Исследовались атомная и ионная эмиссии натрия и калия в функции времени и температуры для всех трех исследованных видов вольфрама. Вольфрам, полученный по измененной технологии, эмиттирует значительно меньшее количество натрия и калия, чем использованные до сих пор виды вольфрама, поэтому можно ожидать, что с использованием этого модифицированного вида вольфрама можно будет уменьшить вероятность образования дуги, например, в лампах накаливания.

STATIONARY TEMPERATURE DISTRIBUTION IN THERMOMETER PROTECTING TUBES

A. HAAS

CENTRAL MEASUREMENT RESEARCH LABORATORY, BUDAPEST

[Manuscript received April 29, 1963]

Sheated thermometers are the most important sensors of industrial thermometry. Heat equilibrium equations for thermometer protecting tubes are very important from the point of view of analysis of errors caused by disturbing parameters. The article contrasts the equations of CLOSTERHALFEN with the more precise equations deduced by the author, reflecting the actual relations and parameters more adequately. The comparison is also backed by measurements which justify the theoretical presumptions. The new equations are free from any arbitrary assumptions and are valid for plane or slightly curved walls of finite heat resistance and also the cooling effect of the outside parts of the protecting tube are taken into account.

I. Introduction

The temperature control is one of the largest and most important territory in automation, forming, according to foreign statistics, nearly 50% of the whole automation. Therefore, the unsolved problems of this nowadays less favoured area, which is regarded by mistake as closed, should not be overlooked.

The sensors of continuous temperature measurement and control based on various principles, have almost in every case to be placed into protecting tubes, that the pressure, the corroding or soiling effects of the medium to be measured should not affect the steadiness and stability of the sensor and the probe. Hence, the sensor does not in fact measure the temperature of the medium to be measured but that of the protecting tube. In case of unsuitable mounting or in unfavourable circumstances the temperature of the protecting tube and that of the sensor may differ even by 20÷30 per cent from the medium to be measured. Perhaps this problem could still be tackled by appropriate calibration, but because of the variations of the ambient parameters, the repeatability accuracy of the probe may deteriorate to such an extent that the temperature of the controlled medium could not be kept between prescribed error limits. Therefore it is important that the influence of the numerous parameters determining the heat equilibrium of the protecting tube should be numerically known, so that temperature controlling and measuring systems of prescribed error and repeatability accuracy might be designed, mounted and calibrated.

Several researchers have already investigated the heat equlibrium of thermometer protecting tubes using simplified models [1—7]. Yet these models

incorporate such simplifications which do not allow the exact and for every disturbing parameters extending treatment of protecting tubes.

As a consequence of this as the measurements carried out by the author also testified, the known equations for protecting tubes are inadequate if the cooling effects of the outer parts of the protecting tube which influence the temperature of the sensor can not be neglected. Therefore, it is necessary to deduce such equations, which implicate the actual ambient circumstances, too.

II. Heat-equilibrium of a Protecting Tube not Protruding beyond the Space of Measurement

The simplified theory of thermometer protecting tubes for technical purposes was developed after the first attempts of REIHER and CLEVE [1] by TEWES [2, 4] and CLOSTERHALFEN [3].

In the literature for the approximate treatment of the protecting tube it is not emphasized that in order to be able to proceed from the equation of convection, incorporating velocity and friction terms to the simplified equation, the following conditions should be observed [8].

a) The velocity of the medium along the thermometer and in the space of measurement must be practically constant with a known mean value;

b) the temperature of the medium along the thermometer and in the space of measurement must be practically constant with a known mean value. Fig. 1 shows the protecting tube model of CLOSTERHALFEN.

If the wall-thickness related to the l_1 length of the protecting tube is thin, then the temperature distribution in the cross-sectional area of the tube may be regarded as uniform, hence only the one dimensional axial temperature distribution remains to be analysed.

The stationary heat equilibrium of an infinitesimal protecting tube volume of dx height and t temperature is determined by the total of the heat, flowing in and out of the volume:

The volume obtains by conduction

$$q = -\lambda f \, dt/dx \tag{1}$$

heat, where λ is the thermal conductivity and f the cross-sectional area of the tube. The volume loses by conduction:

$$q + dq = -\lambda f (dt/dx) - \lambda f \frac{d}{dx} (dt/dx) \, dx \tag{2}$$

heat.

From the medium to be measured to the volume flows

$$dq_1 = \alpha_t (d \, \pi \, dx) (t_m - t) \tag{3}$$

heat, where α_t is the coefficient of convection, and t_m is the temperature to be measured.

To the wall of t_w temperature

$$dq_2 = c'' (d\pi \, dx) (T^4 - T_w^4) \, 10^{-8} \tag{4}$$

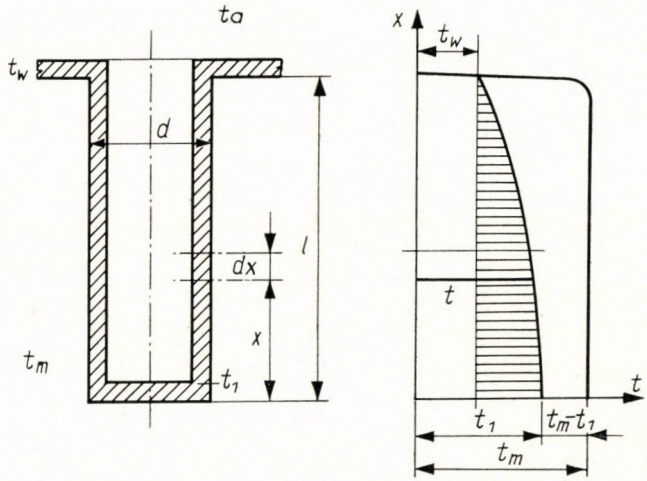

Fig. 1

t_m temperature of the space to be measured;
t_w wall temperature;
t_a ambient temperature;
t_1 tip temperature of the protecting tube.

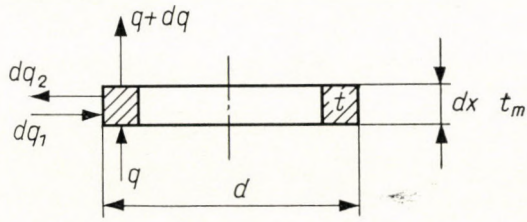

Fig. 2

heat is transferred from the surface of the infinitesimal volume element, where c'' is the mutual heat radiation coefficient. As is known

$$1/c'' = 1/c + F/F_w \, (1/C_w - 1/C_s) \tag{5}$$

where c and F are the heat radiation coefficient and surface of the tube respectively. The F_w and C_w are respectively the surface and heat radiation coefficient of the surrounding walls and C_s is the heat radiation coefficient of the blackbody.

In view of the $F/F_w \ll 1$ condition which is generally satisfied, therefore, the

$$C'' \simeq C \tag{6}$$

approximation is justified.

For properly mounted protecting tubes, if

$$T > T_w \text{ and } T > 273^\circ \text{ C}$$
$$|T - T_w| < T \tag{7}$$

unequality holds, that is Equ. (4) can be linearised

$$\mathrm{d}\, q_2 = \alpha_s\, (d\, \pi\, \mathrm{d}x)\, (t - t_w) \tag{8}$$

where the coefficient of heat radiation is

$$\alpha_s = c \cdot 10^{-8} \frac{T^4 - T_w^4}{t - t_w} \simeq 4 \cdot 10^{-8} \cdot C T_b^3 \tag{9}$$

and the mean temperature of the tube is

$$T_b = \frac{1}{l} \int_0^l T(x)\, \mathrm{d}x\,. \tag{10}$$

The heat equilibrium of the infinitesimal protecting tube volume is

$$q + \mathrm{d}q_1 = q + \mathrm{d}q + \mathrm{d}q_2\,. \tag{11}$$

Substituting Equs. (1), (2), (3) and (8) in Equ. (11) and with

$$\vartheta = (\alpha_s + \alpha_t)\, t - (\alpha_s\, t_w + \alpha_t\, t_m) \tag{12}$$

and

$$m^2 = \pi\, \mathrm{d}(\alpha_s + \alpha_t)/\lambda\, f \tag{13}$$

designations

$$(\mathrm{d}^2\, \vartheta/\mathrm{d}x^2) - m^2 \vartheta = 0 \tag{14}$$

equation is obtained. The well known solution of this equation yields, with

$$\left.\begin{array}{l} x = 0 \\ \mathrm{d}\vartheta/\mathrm{d}x = 0 \end{array}\right\} \quad \text{and} \quad \left.\begin{array}{l} x = l \\ t = t_w \end{array}\right\}$$

boundary conditions, as discussed in details by author [3], the temperature distribution of the protecting tube:

$$\frac{(\alpha_s + \alpha_t)\, t - (\alpha_s\, t_w + \alpha_t\, t_m)}{(\alpha_s + \alpha_t)\, t_w - (\alpha_s\, t_w + \alpha_t\, t_m)} = \frac{\cosh mx}{\cosh ml}\,. \tag{15}$$

From Equ. (15) with $(t)_{x=0} = t_1$ the tip temperature of the protecting tube is expressed by the Closterhalfen superposition principle

$$(t_m - t_1)/(t_m - t_w) = \varphi_1 - \varphi_1\varphi_2 + \varphi_2 = \varphi \tag{16}$$

where

$$\varphi_1 = 1/\cosh(ml)$$

and

$$\varphi_2 = \alpha_s/(\alpha_s + \alpha_t)\,. \tag{17}$$

If t_w wall temperature is known, Equ. (16) yields the relation between t_1 the temperature of the protecting tube tip and t_m the temperature to be measured.

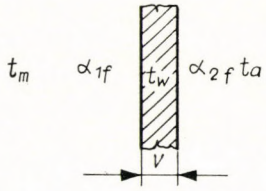

Fig. 3

As the measurement of t_w wall temperature is cumbersome, therefore it is more convenient to specify the wall temperature as a function of t_m and t_a temperatures, where t_a stands for the ambient temperature.

In case of plane or slightly curved metal walls if the conductive heat resistance of the wall can be omitted beside the inner and outer surface heat transfer resistance, the wall temperature t_w may be written as

$$t_w = (\alpha_{1f}\, t_m + \alpha_{2f}\, t_a)/(\alpha_{1f} + \alpha_{2f})\,. \tag{18}$$

The condition for the use of Equ. (18) may be expressed for plane or slightly curved walls, as

$$\alpha_{1f} \ll \lambda_f/V \quad \text{or} \quad \alpha_{2f} \ll \lambda_f/V\,,$$

where α_{1f} and α_{2f} are the inner and outside wall surface heat transfer coefficients of the wall of λ_f thermal conductivity and V thickness.

By Equ. (18) the Equ. (16) may be rewritten as

$$(t_m - t_1)/(t_m - t_a) = \alpha_{2f}\,\varphi/(\alpha_{1f} + \alpha_{2f}) \tag{19}$$

where the temperature of the protecting tube-tip is expressed by the t_m and t_a temperatures, which can be well measured.

III. The Criticism of the Tewes-Closterhalfen Model

The author carried out measurements on protecting tubes with geometries resembling that of the Closterhalfen model, and the measurements showed an agreement with the calculations within a $2 \div 4\%$ margin. Yet with protecting tubes differing from the model having protruding exterior parts with a cooling effect, no such agreement could even be found.

The temperature of the sensor within the tip of the tube and the temperature at the tip of the tube were generally different. Only in that special case when the heat coupling between sensor and tip was close enough did this difference become negligible. Though by the repetition of the Closterhalfen method the temperature of the sensor was computable in each case. In this second computation the mean value of the temperature distribution of the protecting tube along the sensor did it figure as t_{m1}.

The known literature on this subject did not reveal this circumstance.

On ground of the above mentioned experiences, the following criticisms against the Tewes-Closterhalfen model are justified.

a) The actual temperature of the emplacement wall is not uniform but has a radial distribution since the heat resistance of the wall is not zero but a finite quantity;

b) the temperature distribution of the protecting tube is not independent of the temperature-conditions of the sections protruding beyond the wall of emplacement.

Therefore the Tewes-Closterhalfen method cannot be applied for such protecting tubes which have appreciable protruding parts outside of the measurement space. Thus, in the practice the Closterhalfen method does not give satisfactory results for most of the protecting tubes. The present paper therefore uses another model which approaches more closely the real boundary conditions of protecting tubes.

IV. Heat Equilibrium of Protruding Protecting Tubes with outside Heat-transfer

Some authors [6, 7] discussed the heat equilibrium of protruding protecting tubes with special assumptions for the sake of simplified mathematical treatment. Namely they assume that the radial heat resistance of the wall of emplacement is either zero or infinitely great. The emergence of such border cases are in practice generally seldom and only approximate and the real heat-couplings between protecting tube and the distant parts of the wall are maintained by heat resistances having finite values. The geometric model of the protruding protecting tube is shown in Fig. 4.

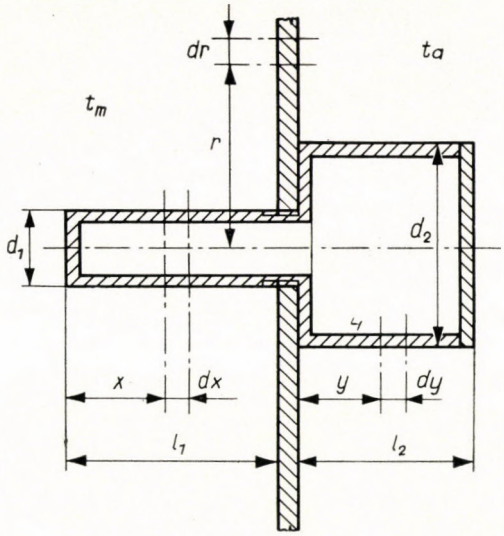

Fig. 4

1. *Temperature distribution in the wall of emplacement*

The wall in the new model is assumed to be plane and extending to the infinite. This assumption is only an approximation for extended plane or slightly curved wall surfaces. The measured and computed temperature distributions in metal walls are in good agreement in the vicinity of the protecting tube. For cases where the above conditions are not fulfilled separate treatment is required. The searched for wall temperature distribution should have t_0 value at the stem of the tube and the value t_w, defined in Equ. (18) if $r \to \infty$. By investigating the heat balance of an infinitesimal ring volume of dr thickness cut out of the wall the $t = f(r)$ temperature distribution is obtained [10].

The ring receives dQ_1 heat from the space to be measured and transfers dQ_2 heat to the surroundings. The ring obtains by radial conductance Q_r heat and loses $Q_r + dQ_r$ heat. From these the expression of heat balance is

$$Q_r + dQ_1 = Q_r + dQ_r + dQ_2 \,. \tag{20}$$

Writing each term in explicit form:

$$Q_r = -\lambda_f \, 2 \, \pi \, r \, v \, (dt/dr) \,, \tag{21}$$

$$Q_r + dQ_r = -\lambda_f \, 2 \, \pi r v (dt/dr) - \lambda_f (2 \, \pi v) \, (dt/dr) + r(d^2t/dr^2) \, dr; \tag{22}$$

$$dQ_1 = \alpha_{1f}(2 \, \pi r \, dr) \, (t_m - t) \,, \tag{23}$$

$$dQ_2 = \alpha_{2f}(2 \, \pi r \, dr) \, (t - t_a) \,. \tag{24}$$

Substituting these into Equ. (20) and introducing the

$$\vartheta = (\alpha_{1f} + \alpha_{2f})t - (\alpha_{1f}\, t_m + \alpha_{2f}\, t_a) \tag{25}$$

and

$$m_f^2 = (\alpha_{1f} + \alpha_{2f})/\lambda_f\, v \tag{26}$$

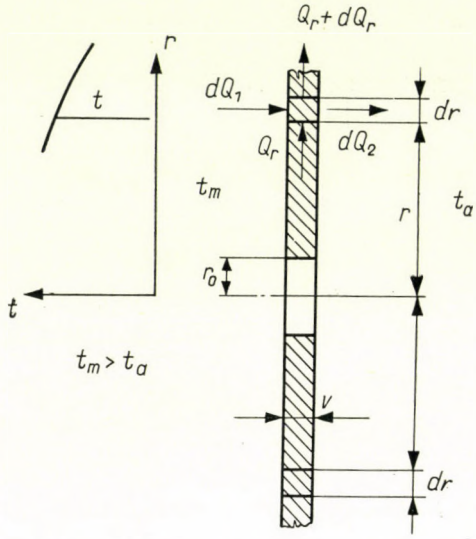

Fig. 5

designations, the differential equation of Bessel is obtained:

$$(d^2\vartheta/dr^2) + 1/r(d\vartheta/dr) - m_f^2\vartheta = 0\,. \tag{27}$$

The general solution of Equ. (27) is

$$\vartheta = c_1\, J_0\,(m_f\, r) + c_2 K_0(m_f\, r) \tag{28}$$

where $J_0\,(m_f, r)$ is the Bessel function of zero order of the first kind and $K_0(m_f, r)$ is the modified Bessel function of zero order of the second kind. The c_1 and c_2 constants of integrations may be determined by the boundary conditions. For

$$\left.\begin{matrix} r \to \infty \\ t \to t_w \end{matrix}\right\} \text{is} \lim_{\to\infty} J_0\,(m_f, r) \to \infty \tag{29}$$

and

$$\text{is} \lim_{r\to\infty} K_0\,(m_f, r) \to 0\,, \tag{30}$$

therefore

$$c_1 = 0\,.$$

The second boundary condition is

$$\left.\begin{array}{l} r = r_0 \\ t = t_0 \end{array}\right\} \vartheta = \vartheta_0$$

which gives

$$c_2 = \vartheta_0 / K_0 (m_f r_0). \tag{31}$$

The sought for temperature distribution is

$$\vartheta = \vartheta_0 \, K_0(m_f \, r)/K_0(m_f \, r_0). \tag{32}$$

By Equ. (25) and Equ. (32):

$$\frac{(\alpha_{1f} + \alpha_{2f}) \, t - (\alpha_{1f} \, t_m + \alpha_{2f} \, t_a)}{(\alpha_{1f} + \alpha_{2f}) \, t_0 - (\alpha_{1f} \, t_m + \alpha_{2f} \, t_a)} = \frac{K_0 \, (m_f \, r)}{K_0 \, (m_f \, r_0)} \, . \tag{33}$$

It is easy to show on ground of Equs. (18) and (30) that Equ. (33) satisfies the first boundary condition that is

$$t_\infty = t_w \, . \tag{34}$$

At r_0, q_{0f} heat flows radially into the wall

$$q_{0f} = -\lambda (2 \, \pi \, r_0 v) \, (dt/dr)_{r=r_0}. \tag{35}$$

From Equ. (32)

$$d\vartheta/dr = \left[(\vartheta_0/K_0) \, (m_f \, r_0)\right] \, [dK_0(m_f \, r)/dr]. \tag{36}$$

By the known

$$\frac{d}{dr} \, K_0 \, (m_f \, r) = - \, m_f K_1 \, (m_f \, r) \tag{37}$$

relation, where $K_1(m_f r)$ is a modified Bessel function of first order of the second kind, and from Equs. (25), (35) and (37)

$$q_{0f} = \lambda_f \, (2 \, \pi r_0 \, v) \, m_f \, \frac{K_1 \, (m_f \, r_0)}{K_0 \, (m_f \, r_0)} \, \frac{(\alpha_{1f} + \alpha_{2f}) \, t_0 - (\alpha_{1f} \, t_m + \alpha_{2f} \, t_a)}{\alpha_{1f} + \alpha_{2f}} \, . \tag{38}$$

As is to be seen from (38) the sign q_{0f} depends on the inequality

$$t_0 \gtrless t_w \, .$$

2. *Temperature distribution of the protecting tube section in the space of measurement*

The model of the protecting tube section in the space of measurement is shown by Fig. 6.

The deduction of heat equilibrium of the protecting tube does not differ up to a point from that of CLOSTERHALFEN. According to our supposition the extension of the wall of emplacement is large compared to the tube diameter,

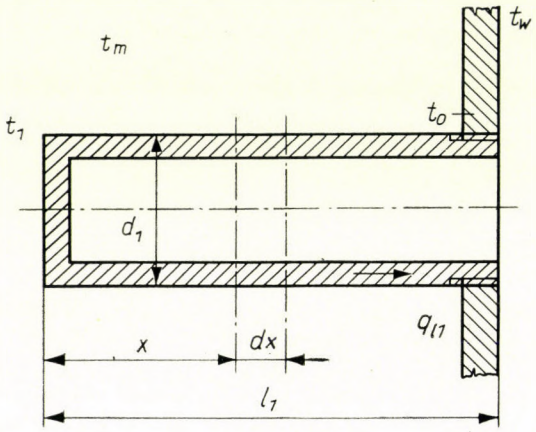

Fig. 6

and therefore, parts of the wall surfaces with temperatures differing from t_w which take only a negligible part in the heat exchange. Thus the heat radiated to the wall may be approximated as mentioned earlier by Equ. (8).

The temperature distribution of the tube is in form the same as in the equ. deduced from Equ. (14) that is

$$\vartheta = \vartheta_1 \cosh (m_1 x) .$$

On the other hand, the stem temperature of the protecting tube is now t_0 instead of t_w:

$$\vartheta_0 = \vartheta_1 \cosh (m_1 l_1) . \tag{39}$$

By Equ. (39) the sought for distribution in contrast to that of Tewes-Closterhalfen is

$$\vartheta = \vartheta_0 \cosh (m_1 x)/\cosh (m_1 l_1) \tag{40}$$

or expressed by t

$$\frac{(\alpha_{S1} + \alpha_{l1})\, t - (\alpha_{s1}\, t_w + \alpha_{t1}\, t_m)}{(\alpha_{S1} + \alpha_{t1})\, t_0 - (\alpha_{s1}\, t_w + \alpha_{t1}\, t_m)} = \frac{\cosh (m_1 x)}{\cosh (m_1 l_1)} \tag{41}$$

where t_0 is the, for the time being, unknown temperature of the stem of the tube.

The axial heatflow at the stem is

$$q_{l1} = -\lambda_1 f_1 (dt/dx)_{x=l_1}$$
$$= \lambda_1 f_1 m_1 \, th\,(m_1 l_1) \frac{(\alpha_{s1} t_w + \alpha_{t1} t_m) - (\alpha_{s1} + \alpha_{t1}) t_0}{\alpha_{s1} + \alpha_{t1}} . \tag{42}$$

3. *The temperature distribution in the head of the protecting tube*

Most frequently the shape of the head is cylindrical or tubelike. The discussed model of the head is shown in Fig. 7. The heat increment of the

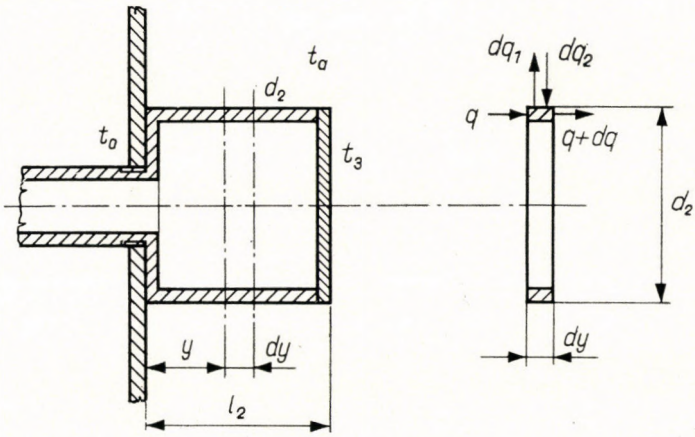

Fig. 7

infinitesimal ring of dy height from the received q and the delivered $q + dq$ conductive heat is

$$dq = -\lambda_2 f_2 (d^2t/dy^2)\, dy . \tag{43}$$

By surface heat transfer the ring loses to the surroundings

$$dq_1 = (\alpha_{t2} + \alpha_{s2}) d_2 \, \pi (t - t_a)\, dy \tag{44}$$

heat.

The heat obtained by radiation from the wall of the emplacement

$$dq_2 = \alpha'_{s2}\, d_2 (t_w - t) dy \tag{45}$$

may be omitted because of the order of the $(t_w - t)\alpha'_{s2}$, term compared to $(\alpha_{t2} + \alpha_{s2})\,(t - t_k)$.

The heat equilibrium becomes:

$$dq_1 + dq \simeq 0 \tag{46}$$

By collating Equs (43), (44), (45), (46) and introducing the following substitutions

$$\vartheta = t - t_a \tag{47}$$

and

$$m_2^2 = d_2\, \pi/\lambda_2 f_2\, [\alpha_{t2} + \alpha_{s2}] \tag{48}$$

the

$$(d^2\vartheta/dy^2) - m_2^2\,\vartheta = 0 \tag{49}$$

differential equation is obtained.

Taking also in account the

$$q_3 = (\alpha_3 d_2^2\, \pi/4)\,(t_3 - t_a) \tag{50}$$

heat lost by the end face of the head and by Equ. (49) with the boundary conditions

$$\left.\begin{matrix} y = 0 \\ \vartheta = \vartheta_0 \end{matrix}\right\} \quad \text{and} \quad \left.\begin{matrix} y = l_2 \\ q_3 = -\lambda_2 f_2 (dt/dy) \end{matrix}\right\}$$

the temperature distribution of the head is

$$t - t_a = (t_0 - t_a)\, \frac{\cosh\,[m_2\,(y - l_2)] - \dfrac{\alpha_3\, d_2^2\, \pi/4}{\lambda_2 f_2\, m^2} \sinh\,[m_2\,(y - l_2)]}{\cosh\,[m_2\, l_2] + \dfrac{\alpha_3\, d_2^2\, \pi/4}{\lambda_2 f_2\, m_2} \sinh\,[m_2\, l_2]}\,. \tag{51}$$

The heat entering the head at the bottom is

$$q_{02} = -\,\lambda_2 f_2\,(dt/dy)_{y=0} = \lambda_2 f_2\, m_2\,(t_0 - t_a)\, \frac{1 + \dfrac{\lambda_2 f_2\, m_2}{\alpha_3\, d_2^2\, \pi/4} \tanh\,(m_2\, l_2)}{\tanh\,(m_2\, l_2) + \dfrac{\lambda_2 f_2\, m_2}{\alpha_3\, d_2^2\, \pi/4}}\,. \tag{52}$$

4. *The heat balance of the stem of the protecting tube*

In the deduced formulas the t_0 temperature of the protecting tube stem was not known and the former equations gave no possibility for its determination.

Therefore, a further equation is required for the determination of t_0.

Such an equation is obtained from the heat balance of the protecting tube stem.

Towards the stem of the tube q_{l_1} heat flows. This heat is divided and q_{0f} heat flows towards the wall and q_{02} towards the head.

As has already been stressed the sign of q_{0f} that is the direction of the flow depends on the $t_0 \gtrless t_w$ inequality. Presuming that $t_0 > t_w$ the heat equilibrium is expressed by the

$$q_{l1} = q_{0f} + q_{02} \tag{53}$$

equation.

By substituting into Equ. (53) the values of (38), (42), (52) t_0 the stem temperature becomes

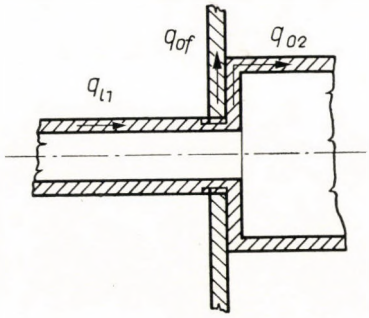

Fig. 8

$$t_0 = \frac{A}{B} \tag{54}$$

where

$$A = \lambda_1 f_1 m_1 \cdot \tanh(m_1 l_1) \frac{\alpha_{s1} t_w + \alpha_{l1} t_n}{\alpha_{s1} + \alpha_{l1}} +$$

$$+ \lambda_f 2 \pi r_0 v m_f \frac{K_1(m_f r_0)}{K_0(m_f r_0)} \cdot \frac{\alpha_{1f} t_m + \alpha_{2f} t_a}{\alpha_{1f} + \alpha_{2f}} +$$

$$+ \lambda_2 f_2 m_2 \left[\frac{1 + \frac{\lambda_2 f_2 m_2}{\alpha_3 d_2^2 \pi/4} \tanh(m_2 l_2)}{\tanh(m_2 l_2) + \frac{\lambda_2 f_2 m_2}{\alpha_2 d_2^2 \pi/4}} \right] t_a;$$

$$B = \lambda_1 f_1 m_1 \cdot \tanh(m_1 l_1) + \lambda_f 2 \pi v_0 v m_f \frac{K_1(m_f v_0)}{K_0(m_f v_0)} +$$

$$+ \lambda_2 f_2 m_2 \left[\frac{1 + \frac{\lambda_2 f_2 m_2}{\alpha_3 d_2^2 \pi/4} \tanh(m_2 l_2)}{\tanh(m_2 l_2) + \frac{\lambda_2 m_2 f_2}{\alpha_3 d_2^2 \pi/4}} \right].$$

By Equ. (54) the implicit formulas for wall protecting tube section and head temperatures are numerically calculable from Equs. (33), (41), (51) respectively.

The formula resembling Equ. (16) for t_1 temperature of the protecting tube tip is

$$(t_m - t_1)/(t_m - t_0) = \varphi_1 - \varphi_1\varphi_2 + \varphi_2 = \varphi \,. \tag{55}$$

From Equ. (55) by using Equs. (54) and (18) t_1 may be numerically determined.

In contrast to the equation of Closterhalfen, by Equ. (54) all geometrical and heat kinetical parameters, influencing the temperature distribution of the protecting tube were taken in account.

Hence the influence of each disturbing parameter causing temperature deviations in t_1 may be analysed. For instance, the influence of t_a the ambient temperature is calculable:

with $$dt_1 = \varphi \; dt_0 \quad \text{is}$$

$$\Delta t_1 = \varphi \frac{\partial t_0}{\partial t_a} \Delta t_a .$$

Similar analysis is feasible for the study of heat-insulation effects on t_1 or for the change of any heat conductance.

V. Collation of Computed and Measured Temperature Distributions

The exactness of the distributions computed by the deduced formulas mainly depend on the exactness of the applied constants.

The coefficients of heat conduction and surface heat transfer are given by tables and nomograms. Hence, it is obvious that it would be in vain to expect accuracies in the 1% margin. It seems, collating measurement and computation results, that the errors fall into the 5% margin.

For instance Fig. 9 shows the simplified scheme of an examined protecting tube and the results found. The material of the tube was MSZ Cr Mo 2.

At the tip and stem and at exterior end of the head of the tube dia. 0.4 mm Fe—Co thermocouples were pressed in to small bores.

The junctions of these thermocouples do not exactly attain the temperatures of the bores, but as a consequence of their heat transfer with the surroundings they are on a higher or lower value.

If the actual measured value for the tip of the tube is $t_1 = 85°$ C then the deviation from the true value may be approximated by the

$$\Delta t = (t_m - t_1) \frac{\sqrt{\dfrac{0{,}02\,\lambda_1\,\pi^2}{8\,\lambda^2}}}{1 + \sqrt{\dfrac{0{,}02\,\lambda_1\,\pi^2}{8\,\lambda^2}}} \tag{57}$$

expression, where λ_1 is the thermal conductivity of the thermocouple and λ that of the tube. With $\lambda_1 = 30$ kcal/m, h, °C and $\lambda = 45$ kcal/m, h, °C at $t_m = 125$ °C Equ. (57) yields $\Delta t = \simeq 0.77$ °C. At the outer extremity of the head the deviation, of the actually measured 60° C, from the value is again $\Delta t \simeq 0.77°$ C.

Regarding the expected 5% error margin and the order of the above found deviations the actually measured values can be accepted without any correction.

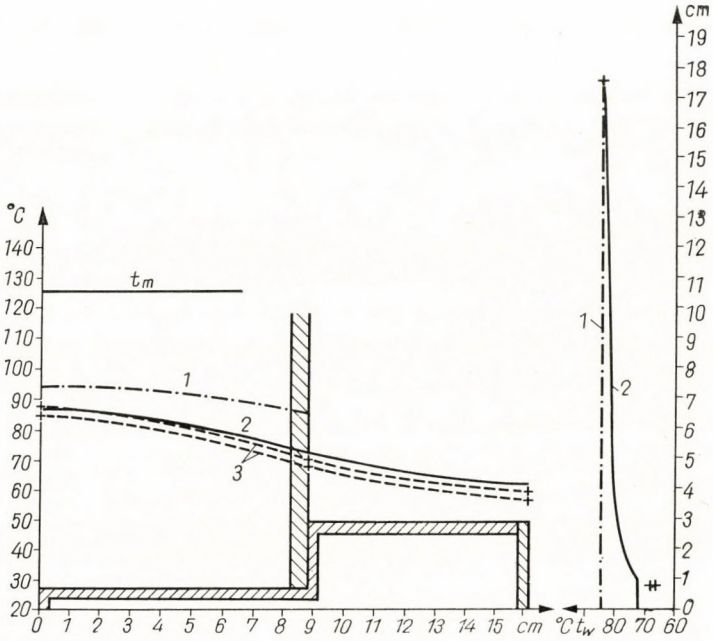

Fig. 9

t_m temperature to be measured;
1 computed according to CLOSTERHALFEN;
2 computed according to the author;
3 corrected by measurements;
+ points measured;
$t_a = 20$ °C.

The examined protecting tubes fitted with the thermocouples were mounted in an ultrathermostat through a wall made of a steel plate of 5 mm thickness. In the plate a properly fitted Fe—Co thermocouple measured t_w. Into the space of measurement an unarmed Fe—Co thermocouple and a mercury in glass control thermometer, graded into tenth of °C, were fitted.

The thermo e. m. f.-es were recorded on a six coloured registrating instrument. Taking also cold point temperatures into account, simultaneous t_1, t_0, t_3, t_w, t_m and t_a temperature sets were obtained.

The measured points and the distributions calculated according to the author's method versus the Closterhalfen method and distributions, corrected by measurements, are shown in Fig. 9.

The temperature of the tip computed according to CLOSTERHALFEN deviated by +7.7°C from the 85.5°C mean value of the measured tip temperatures. The alternative method of the author resulted only in +0.7° deviation, which is better by one order.

The constant t_w wall temperature distribution of CLOSTERHALFEN is also contrasted in Fig. 9 with that of the author.

The deviation shown at the outer extremity of the head originates certainly from its idealized geometry. Although this deviation is a bit smaller than 6°C, the effect of this remains insignificant on the temperature of the sensor and on the sectional temperature distribution influencing the temperature of sensor.

VI. Summary and Conclusions

The author deduced a new formula of increased accuracy relating to thermometer protecting tubes protruding from the space of measurement.

The present article did not aime either at a detailed discussion of all the measurements carried out or for enumeration of the methods for the improvement of accuracies when measuring with tubed thermometers.

Using the equations presented, the design of such methods becomes more reliable compared to the use of other known methods.

By eliminating the defficiencies of the older methods the effects of all disturbing parameters acting on the protecting tube were incorporated in the deduced relations.

As our measurements were carried out in ambient air of $\simeq$ 20 °C at rest, it is justified to expect that the temperature values computed by the Closterhalfen method would still considerably deviate from measured ones, at less favourable ambient conditions.

The comparison of measured and computed temperatures justifies the new formulas.

REFERENCES

1. REIHER, H.—CLEVE, K.: Temperaturmessfehler in Gasen und überhitzten Dämpfen. *Technische Mechanik* (1925), 49.
2. TEWES, W.: Temperaturmessfehler in strömenden Gasen durch Wärmeableitung und Wärmeabstrahlung von der Messtelle. *Arch. Wärmewirtschaft* **19** (1938), 189.
3. CLOSTERHALFEN, A.: Messfehler bei Thermometereinbauten. *Forsch. Ingenieurwesen* **9** (1938), 279.
4. TEWES, W.: Temperaturmessfehler in strömenden Gasen und Dämpfen. *Z. f. techn. Physik* (1941), 160—167.
5. FISCHER, J.: Temperaturfühler und Strahlungsempfänger. *Z. f. techn. Physik* (1941), 316—323.
6. KNOBLAUCH, O.—HENCKY, K.: Anleitung zu genauen technischen Temperaturmessungen. München—Berlin 1926; Nachdruck 1941.
7. MILLAR, N. P.: Heat-Flow Effects in a Resistance Type Thermometer. *Transactions Electrical Engineering* **64** (1945), 678—685.
8. LANDAU, L. D.—LIFSCHITZ, E. M.: Fluid Mechanics. Pergamon Press, London 1959.
9. HAAS, A.: Sugárzásnélküli felületi hőmérsékletmérés hőáramlástani alapelvei (Thermokinetic Principles of Non-Radiant Surface Temperature Measurement). *Mérés és Automatika* (1960), 331—337.
10. MIHEJEV, M. A.: A hőátadás gyakorlati számításának alapjai (The Principles of Practical Heattransfer calculations). Tankönyvkiadó, Budapest 1956.

DIE STATIONÄRE TEMPERATURVERTEILUNG IN SCHUTZROHREN VON THERMOMETERN

A. HAAS

ZUSAMMENFASSUNG

Die in Schutzrohren untergebrachten Thermometer sind die wichtigsten Fühler der industriellen Temperaturmessung. Die Gleichungen des Wärmegleichgewichts von Schutzrohren sind für die Analyse der Meßgenauigkeit und des Einflusses des Störparameter sehr wichtig. In der Arbeit werden die von CLOSTERHALFEN abgeleiteten Gleichungen den vom Verfasser ausgearbeiteten genaueren Gleichgewichts-Gleichungen gegenübergestellt, die die wirklichen Verhältnisse und Parameter besser wiedergeben. Daß die Gegenüberstellung berechtigt ist, wird auch durch Messungen nachgewiesen. Die neuen Gleichungen sind frei von jeder willkürlichen, auf die Wurzel des Thermometers bezüglichen Annahme und sind auch für eine ebene oder wenig gekrümmte Wand mit größerem Wärmewiderstand als Null gültig. Sie berücksichtigen auch die vom Schutzrohrkopf verursachte Abkühlung.

LA DISTRIBUTION STATIONNAIRE DES TEMPÉRATURES DANS LES GAINES PROTECTRICES DES THERMOMÈTRES

A. HAAS

RÉSUMÉ

Les thermomètres à gaîne protectrice sont les plus importants récepteurs utilisés dans la mesure industrielle de la température. Les équations d'équilibre de la température sont très importantes pour l'analyse de la précision des mesures et de l'influence des paramètres perturbateurs. Dans l'étude, l'auteur oppose les équations déduites par CLOSTERHALFEN aux équations d'équilibre déduites par lui-même, plus précises et représentant mieux les conditions et les paramètres réels. Des mesures prouvent qu'il est justifié d'opposer les deux méthodes. Les nouvelles équations, valables aussi pour des parois planes ou peu courbées, à résistance thermique finie différente de zéro, n'impliquent pas de suppositions arbitraires quant à la base du thermomètre. Elles tiennent compte aussi du refroidissement causé par la tête de raccordement.

РАСПРЕДЕЛЕНИЕ УСТАНОВИВШЕЙСЯ ТЕМПЕРАТУРЫ ЗАЩИТНЫХ ТРУБОК ТЕРМОМЕТРОВ

А. ХААС

РЕЗЮМЕ

Термометры с защитными трубками являются важнейшими средствами при измерении температуры в промышленности. Уравнения терморавновесия защитных трубок с точки зрения анализа точности измерения и воздействия мешающих параметров играют очень важную роль. В статье приводятся и сравниваются выведенные Клостергальфеном и выведенные автором уравнения равновесия. Последние являются более точными и лучше отражают действительные условия и параметры. Справедливость сравнения подтверждается также измерениями. Новые уравнения (независимо от всякого рода предположений самовольного характера, касающихся основы термометра) действительны для плоских стен или стен небольшой кривизны с бесконечным или выше нуля термосопротивлением и, кроме того, учитывают охлаждение от головки защитной трубки.

BERECHNUNG DER VOM SCHWINDEN DES BETONS HERRÜHRENDEN KRÄFTE IN STAHLBETONELEMENTEN

GY. BALÁZS

KANDIDAT DER TECHNISCHEN WISSENSCHAFTEN,
TECHNISCHE UNIVERSITÄT FÜR BAU- UND VERKEHRSWESEN, BUDAPEST

[Eingegangen am 22. Mai, 1963]

Die wichtige Rolle, welche dem Schwinden im Kräftespiel des Betons und der Spannbetonkonstruktionen zukommt sowie die schwinderhöhende Wirkung des Chlorkalziums ließen es angebracht erscheinen aufzuzeigen, in welchem Maße die inneren Kräfte durch die Annahme, daß die Schwind- und Kriechkurven nicht affin sind, Änderungen erfahren. Es hat sich gezeigt, daß das gehemmte Schwinden seinen Höchstwert nicht zu dem Zeitpunkt $t = \infty$ erreicht, vielmehr kann dieser in Abhängigkeit von dem unterschiedlichen zeitlichen Verlauf des Schwindens bzw. Kriechens, den Materialien und Abmessungen des Trägers, der Außermittigkeit der Bewehrung, dem Endwert des Kriechfaktors und dem Bewehrungsprozentsatz beträchtlich schneller eintreten. Aus diesem Grund ist es zweckmässiger, bei der Berechnung des Spannungszustandes, in dem sich der vorgespannte Träger während des Transports befindet, den vollen Wert des Schwindens zu berücksichtigen. Im Fall von aus Fertigteilen zusammengebauten, nachträglich gespannten Trägern, wenn das Spannen nicht unmittelbar nach der Fabrikation vorgenommen wurde, braucht ein Teil des Schwindens nicht berücksichtigt zu werden.

I. Einleitung

Schwinden und Kriechen lösen im Beton — wenn sie unbehindert vor sich gehen können, und die Betonstärke im Vergleich mit den anderen Abmessungen geringfügig ist — keine Spannungen aus. Wenn man aber durch Einlegung der Bewehrung die spontane Formänderung des Betons behindert, wird in demselben eine Anfangsspannung entstehen, welche von der Druckspannung, wie sie in der Bewehrung auftritt, ausgeglichen wird. (Dadurch ensteht eine gehemmte Formänderung im Beton.)

Bedingt durch das Schwinden werden im Betonträger bereits im unbelasteten Zustand sowohl Beton- als auch Bewehrungsspannungen im Wege ineinandergreifender rheologischer Prozesse aufgebaut.

Die genaue Berechnung wird selbst in den einfachsten Fällen sehr durch den Umstand erschwert, daß man eine Vielzahl von Variablen zu berücksichtigen hat. Man pflegt daher, wenn es sich um die Berechnung der inneren Kräfte von Stahlbetonkonstruktionen und Verbundträgern handelt, die zeitbedingte Veränderung des Kriechens der Bewehrung und die des Betonelastizitätsmoduls meistens unberücksichtigt zu lassen. Darüber hinaus wird auch angenommen, daß der zeitliche Verlauf vom Schwinden und Kriechen des Betons affin sei. Diese Vernachlässigungen wurden von DISCHINGER eingeführt [1, 2], und die Berechnung wurde auch seither nur durch Mitberück-

sichtigung der zeitlichen Änderung des Betonelastizitätsmoduls verfeinert. Bei der Dischinger'schen Berechnungsmethode trat die vom Schwinden herrührende Höchstspannung im Zeitpunkt $t = \infty$ ein.

Die an der Universität zu Illinois [3] an bewehrten Betonträgern vorgenommenen Schwindmessungen haben die Aufmerksamkeit auf den Umstand gelenkt, daß die Höchtswerte an Schwindspannungen nicht bei $t = \infty$ auftreten. Ähnliche Resultate gingen auch aus den am Lehrstuhl für Baustoffe der Technischen Universität für Bau- und Verkehrswesen, Budapest durchgeführten Versuchen hervor [4]. Die Ursache hierfür liegt darin, daß die Kurven des Schwindens und die des Kriechens nicht affin sind.

Die das Schwinden erhöhende Wirkung des Chlorkalziums und die wichtige Rolle, welche das Schwinden im Kräftespiel der Beton- und Spannbeton- sowie Verbundskonstruktionen spielt, dürften eine genaue Untersuchung dieses Phänomens rechtfertigen, es ist also aufzuzeigen, welche Änderungen in den inneren Kräften die Annahme mit sich bringt, daß die Schwind- und Kriechkurven als nicht-affin angesehen werden.

Im folgenden soll das innere Kräftespiel eines asymmetrisch bewehrten Stahlbetonfertigteils, unter Einwirkung des Betonschwindens, als äußere Bewegung untersucht werden. Auf die Prüfung der komplexeren Fälle (die der Verbundskonstruktionen) wird hier nicht eingegangen, da eine detaillierte Behandlung dieser Fragen allzu weit führen würde.

Angesichts der äußerst verwickelten Problematik vermag auch die vorliegende Abhandlung keine endgültige Lösung zu geben, jedoch dürfte sie dazu beitragen, daß die unter Wirkung des Schwindens stattfindende Kräfteumlagerung wirklichkeitsgetreuer berechnet werden kann.

II. Bezeichnungen

E_{b0} [kp/cm²]	Elastizitätsmodul des Betons mit dem Anfangswert Null bei beendigter Dampfbehandlung
E_{bt} [kp/cm²]	Elastizitätsmodul des Betons in einem Zeitpunkt t nach der Dampfbehandlung
E_v [kp/cm²]	Elastizitätsmodul der Stahleinlage
n_1	E_v/E_{b0}
ε_t [‰]	Schwinden des ungehemmten (nicht bewehrten) Betons in einem Zeitpunkt t nach Beginn des Schwindens
ε_n [‰]	Schwinden des ungehemmten Betons im Zeitpunkt $t = \infty$
φ_t	plastische Formänderung : elastische Formänderung = Kriechbeiwert des Betons in einem Zeitpunkt t nach Beginn des Schwindens
φ_n	Kriechbeiwert des Betons im Zeitpunkt $t = \infty$
F_v [cm²]	Querschnittsfläche der Stahleinlagen
F_b [cm²]	Querschnittsfläche des Betons
μ	$100\ F_v/F_b$ Bewehrungsprozentsatz
I_b [cm⁴]	das auf seine eigene Schwerpunktachse bezogene Trägheitsmoment des Betonquerschnittes
I_v [cm⁴]	das auf seine eigene Schwerpunktachse bezogene Trägheitsmoment des Stahlquerschnittes

III. Die der Berechnung zugrundegelegten Annahmen

a) Beton und Stahl sind homogen und isotrop.

b) Nach der Untersuchungen von WHITNEY hat das Hooksche Gesetz auch für die langsame Formänderung Gültigkeit.

c) Die Querschnitte bleiben auch nach der Formänderung Ebenen, es wurde also der Gültigkeitsbereich der Benoulli—Navierschen Hypothese erweitert.

d) Der Elastizitätsmodul des Betons ist zeitunabhängig gleichbleibend. $E_{bt} = E_{t0}$

e) Das Kriechen der Stahleinlage wird wegen seines geringfügigen Wertes vernachlässigt.

f) An der Berührungsfläche der Stahleinlage und des Betons geht keine relative Verschiebung vor sich, das Zusammenwirken ist also einwandfrei, die Verbindung starr.

g) Die spezifische Verformung, wie sie durch das Schwinden des Betons bedingt ist, läßt sich durch die Formel

$$\varepsilon_t = \varepsilon_n(1 - e^{-\beta t}) \tag{1}$$

beschreiben.

h) Das Kriechen des Betons ist sowohl für Zug als auch für Druck gleich, und die zeitliche Veränderung des Kriechbeiwerts läßt sich durch die Formel

$$\varphi_t = \varphi_n(1 - e^{-\alpha t}) \tag{2}$$

kennzeichnen.

i) Der Beton ist rißfrei, es kann also der volle Betonquerschnitt als wirksam angesehen werden.

j) Die Biegesteifigkeit der Stahleinlagen kann im Vergleich mit der des Betons vernachlässigt werden.

IV. Die Bedingung der Formänderung und die Differentialgleichung der inneren Kräfte

Im Zeitpunkt t nach Beendigung der Betonierung wirken auf den Beton des Fertigteils als Folge des Schwindens und Kriechens die Zugkraft N_{bt} und das Biegemoment M_{bt}, diese werden durch die Druckkraft N_{vt} und das Biegemoment M_{vt}, die in der Stahleinlage auftreten, ausgeglichen (Bild 1).

Die Änderung der inneren Kräfte läßt sich mit Hilfe der Gleichungen ermitteln, die das Gleichgewicht und die Verformung beschreiben. Die Bedingung der Verformung besagt, daß die Verformung der Stahleinlage und die des Betons auf die Berührungsfläche gleich sind, und zwischen ihnen keine relative

Verschiebung stattfindet; das heißt:

$$\frac{d\varepsilon_{vt}}{dt} = \frac{d\varepsilon_{bt}}{dt}, \tag{3}$$

wo

$$\frac{d\varepsilon_{bt}}{dt} = \frac{\sigma_{bt}}{E_{b0}} \frac{d\varphi_t}{dt} + \frac{1}{E_{b0}} \frac{d\sigma_{bt}}{dt} - \frac{d\varepsilon_t}{dt} \tag{4}$$

und

$$\frac{d\varepsilon_{vt}}{dt} = \frac{1}{E_v} \frac{d\sigma_{vt}}{dt} \tag{5}$$

ist.

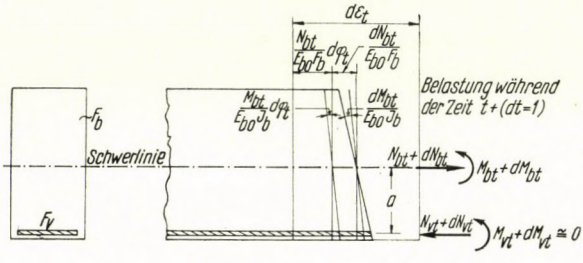

Bild 1

Das erste Glied der rechten Seite der Gleichung (4) drückt die plastische Dehnung aus, die unter Einwirkung der Zugkraft N_{bt} und des Biegemoments M_{bt} vor sich geht, während das zweite Glied die in der Schwerlinie der Stahleinlagen eintretende elastische Dehnung beschreibt, welche als Folge der Zugkraft dN_{bt} und des Biegemoment dM_{bt}, wie sie während der von der Zeit t an berechneten Zeitspanne dt zustandekommen entsteht, während das dritte Glied das in der Zeit dt vor sich gehende ungehemmte Betonschwinden bedeutet. Die rechte Seite der Gleichung (5) drückt die Zusammendrückung aus, wie sie aus der Kräftezunahme dN_{vt} der Stahleinlage während der Zeit dt resultiert.

Soll der Wert der inneren Kräfte in die Gleichung (3) eingesetzt und die Verformung auf die Zeitdifferenz $dt = 1$ bezogen werden, dann erhält man die folgende Gleichung:

$$-\frac{dM_{vt}\,a}{E_v I_v} - \frac{dN_{vt}}{E_v F_v} = \left(\frac{N_{bt}}{E_{b0} \cdot F_b} + \frac{M_{bt}\,a}{E_{b0} I_b}\right) d\varphi_t + \\ + \left(\frac{dN_{bt}}{F_b} + \frac{dM_{bt}\,a}{I_b}\right) \frac{1}{E_{b0}} - d\varepsilon_t\,. \tag{6}$$

Die Zahl der Unbekannten wird abnehmen, wenn die Gleichgewichtsbedingungen

$$N_{bt} = N_{vt} \tag{7}$$

und

$$M_{bt} + M_{vt} = aN_{bt} \tag{8}$$

berücksichtigt werden.

Für schlaffbewehrte Stahlbetonkonstruktionen kann die unter *j)* angeführte Annahme als erfüllt angesehen werden. Es ist also

$$M_{vt} = 0\,.$$

In diesem Fall ist

$$M_{bt} = aN_{bt} \tag{8a}$$

Werden in der Gleichung (6) die Substitutionen, wie sie die Gleichungen (7) und (8a) ermöglichen, vorgenommen und die Bezeichnungen

$$K_b = E_{b0}\,F_b\,,$$

$$K_v = E_v\,F_v\,,$$

$$S_b = E_{b0}\,I_b\,,$$

$$A = 1 + \frac{K_b}{K_v} + a^2\,\frac{K_b}{S_b}\,, \tag{9}$$

$$B = 1 + a^2\,\frac{K_b}{S_b} \tag{10}$$

eingeführt, erhält man nach Umgruppierung die folgende Differenetialgleichung:

$$A\,dN_{bt} + B\,N_{bt}\,d\varphi_t = K_b\,d\varepsilon_t\,. \tag{11}$$

Berücksichtigt man noch daß

$$d\varphi_t = \varphi_n\,\alpha e^{-\alpha t}\,dt$$

und

$$d\varepsilon_t = \varepsilon_n\,\beta e^{-\beta t}\,dt$$

so erhält man nach Multiplizierung mit $1/(Adt)$, ferner durch Einsetzung der Werte

$$Q = \frac{B}{A}\,\varphi_n \tag{12}$$

und

$$K = K_b\,\frac{\varepsilon_n}{\varphi_n}\,\frac{\beta}{B} \tag{13}$$

die Differentialgleichung in einer zur Lösung geeigneten Form:

$$\frac{dN_{bt}}{dt} + Qa N_{bt}\,e^{-\alpha t} = KQe^{-\beta t}\,. \tag{14}$$

V. Lösung der Differentialgleichung

Die zu lösende Differentialgleichung stellt eine inhomogene Differentialgleichung erster Ordnung dar.

Die Lösung des homogenen Teiles ist wie folgt:

$$N_{bt} = C(t)\, e^{Qe^{-\alpha t}}. \tag{15}$$

Zur allgemeinen Lösung der Differentialgleichung gelangt man durch Variation der Konstanten. Wird nun die unter (15) angeführte Funktion deriviert und in die Gleichung (14) eingesetzt, erhält die geordnete Gleichung nach Durchführung der Vereinfachungen die folgende Form:

$$\frac{dC(t)}{dt} = e^{-Qe^{-\alpha t}} \cdot K\, Q\, e^{-\beta t}. \tag{16}$$

Zur Erleichterung der Integration sollen in der rechten Seite der Gleichung folgende Substitutionen vorgenommen werden:

$$v = Q\, e^{-\alpha t}. \tag{17}$$

$$n = \frac{\beta}{\alpha} - 1. \tag{18}$$

Hier stellt n eine positive ganze Zahl dar. Dadurch wird die Funktion (16) die folgende Form erhalten:

$$\frac{dC(v)}{dv} = -\frac{K}{\alpha Q^n}\, v^n\, e^{-v}. \tag{19}$$

Die Funktion $C(t)$ hat die Form:

$$C(t) = \frac{K}{\alpha Q^n}\left[\sum_{k=1}^{n} \frac{n!}{(n-k+1)!}(Q - e^{-\alpha t})^{(n-k+1)} + n\,!\right] e^{-Qe^{-\alpha t}} + C_1$$

und durch Einsetzen wird die Gleichung (15)

$$N_{bt} = e^{-Qe^{-\alpha t}}\left\{\frac{K}{\alpha Q^n}\left[\sum_{k+1}^{n} \frac{n!}{(n-k+1)!}\,(Qe^{-\alpha t})^{(n-k+1)} + n!\right]\cdot e^{-Qe^{-\alpha t}} + C_1\right\}. \tag{20}$$

Die Integrationskonstante C_1 kann man auf Grund der Ausgangsbedingungen $t = 0$, $N_{bt} = 0$ erhalten. Folglich

$$0 = e^{Q}\left\{\frac{K}{\alpha Q^n}\left[\sum_{k=1}^{n} \frac{n!}{(n-k+1)!}\, Q^{(n-k+1)} + n!\right] e^{-Q} + C_1\right\}.$$

Aus dieser Bedingungsgleichung läßt sich

$$C_1 = \frac{K}{\alpha Q^n} e^{-Q} \left(\sum_{k-1}^{n} \frac{n!}{(n-k+1)!} Q^{(n-k+1)} + n! \right)$$

ausdrücken und schließlich

$$N_{bt} = \frac{K}{\alpha Q^n} \left\{ \left[\sum_{k-1}^{n} \frac{n!}{(n-k+1)!} (Qe^{-\alpha t})^{(n-k+1)} + n! \right] - \right.$$
$$\left. - e^{-Q(1-e^{-\alpha t})} \left[\sum_{k-1}^{n} \frac{n!}{(n-k+1)!} Q^{(n-k+1)} + n! \right] \right\}. \tag{21}$$

Im Falle einer symmetrisch bewehrten Betonstütze sind

$$A = 1 + \frac{K_b}{K_v} = \frac{1 + \mu n_1}{n_1},$$

$$B = 1,$$

$$Q = \varphi_n \frac{B}{A} = \varphi_n \frac{\mu n_1}{1 + \mu n_1},$$

$$K = E_b F_b \frac{\varepsilon_n}{\varphi_n},$$

$$N_{bt} = E_b F_b \frac{\varepsilon_n}{\varphi_n} (n+1) \frac{1}{Q_n} \left\{ \left[\sum_{k=1}^{n} \frac{n!}{(n-k+1)!} (Qe^{-\alpha t})^{(n-k+1)} + n! \right] - \right.$$
$$\left. - e^{-Q(1-e^{-\alpha t})} \left[\sum_{k=1}^{n} \frac{n!}{(n-k+1)!} Q^{(n-k+1)} + n! \right] \right\}. \tag{21a}$$

Wenn es sich um eine asymmetrisch bewehrte Betonstütze handelt, wird die Gleichung (21) unter der Annahme, daß zwischen der Kurve des Schwindens und der des Kriechens eine Affinität besteht ($\alpha = \beta$, das heißt $n = 0$) die folgende Form annehmen:

$$N_{bt} = \frac{K}{\alpha} \left[1 - e^{-Q(1-e^{-\alpha t})} \right]. \tag{21b}$$

Dies ist aber die Form der Funktion N_{bt}, wie sie aus dem Fachschrifttum bekannt ist [1], [2], [5]. Wird darüber hinaus noch angenommen, daß die Bewehrung eine symmetrische ist, erhält man den Zusammenhang:

$$N_{bt} = E_b F_b \frac{\varepsilon_n}{\varphi_n} \left[1 - e^{\frac{\mu n_1}{1+\mu n_1} \varphi_n (1-e^{-\alpha t})} \right]. \tag{21c}$$

VI. Untersuchung der Funktion. Form der Kurve für das gehemmte Schwinden bzw. zeitliche Änderung der vom Schwinden herrührenden inneren Kräfte

Schwinden und Kriechen einer Betonstütze sind unzertrennbare und gleichzeitig vor sich gehende Prozesse, die aufeinander einwirken und sich gegenseitig beträchtlich beeinflussen. Die im Beton befindliche Stahleinlage widersetzt sich dem Schwindvorgang, wodurch in der Stahleinlage eine Druckkraft auftritt, die vorerst ständig größer wird. Zur gleichen Zeit tritt im Beton eine Zugkraft auf, die hinsichtlich ihrer Größe mit der in der Stahleinlage auftretenden Druckkraft übereinstimmt. Die im Beton entstehende Zugkraft wechselnder Größe ist mit einer Dauerlast gleichbedeutend.

Unter der Wirkung der Dauerlast tritt im Beton Kriechen auf. Diese führt zu einer Verformung, welche der durch das Schwinden ausgelösten entgegengesetzt ist. Unter der Wirkung dieses Kriechens nimmt das gehemmte Schwinden ab. Infolge der entgegengesetzten Wirkungen erreicht das gehemmte Schwinden einen Höchstwert, welcher zunächst rapider, später langsamer abnimmt, um sich einer Asymptote zu nähern. Die Schwindkurve erreicht ihr Maximum, wenn die Geschwindigkeit der durch das Schwinden bedingten Kontraktion der der Ausdehnung, die vom Kriechen herrührt, gleich wird. Dies hängt von den Materialkonstanten und vor allem von der Stärke der Bewehrung ab und tritt bei einem größeren Bewehrungsprozentsatz schneller als bei einem kleineren ein.

Der Extremwert der Verformungskurve kann mit Hilfe der Gleichung

$$\sum_{k=1}^{n} \frac{1}{(n-k)!} (Qe^{-at})^{(n-k)} - \left| \sum_{k=1}^{n} \frac{1}{(n-k+1)!} Q^{(n-k+1)} + 1 \right| \cdot e^{-Q(1-e^{-at})} = 0 \tag{23}$$

erhalten werden.

Wie aus dieser Gleichung hervorgeht, hängt die Stelle des Maximums von der Zahl n ab, die besagt, inwieweit sich der zeitliche Ablauf des Schwindens von dem des Kriechens unterscheidet, aber auch der Beiwert Q spielt dabei mit, letzterer trägt der Biegesteifigkeit des Trägers, dem Bewehrungsprozentsatz, der Verhältniszahl der Elastizitätsmoduln, dem Endwert des Kriechfaktors und der Außermittigkeit der Bewehrung Rechnung.

Die Gleichung (23) läßt sich jedoch in expliziter Form nach t nicht lösen. Zur Erleichterung der Berechnung ist die Funktion $a\,t - Q$ rechts im Bild 2 angegeben; dieser können die Stellen der Maxima für die Fälle, wo n den Wert von ganzen Zahlen hat, entnommen werden. An der Abbildung läßt sich der Wert von $a\,t$ ablesen, zu dem der Höchstwert an Kraft gehört.

Bild 2 ist für die Bestimmung der Stelle des maximalen Schwindens, und zwar sowohl für Stahlbetonfertigteile mit symmetrischer als auch für solche mit asymmetrischer Bewehrung, geeignet; man braucht nur den Wert von Q mit Hilfe der entsprechenden Formel zu berechnen.

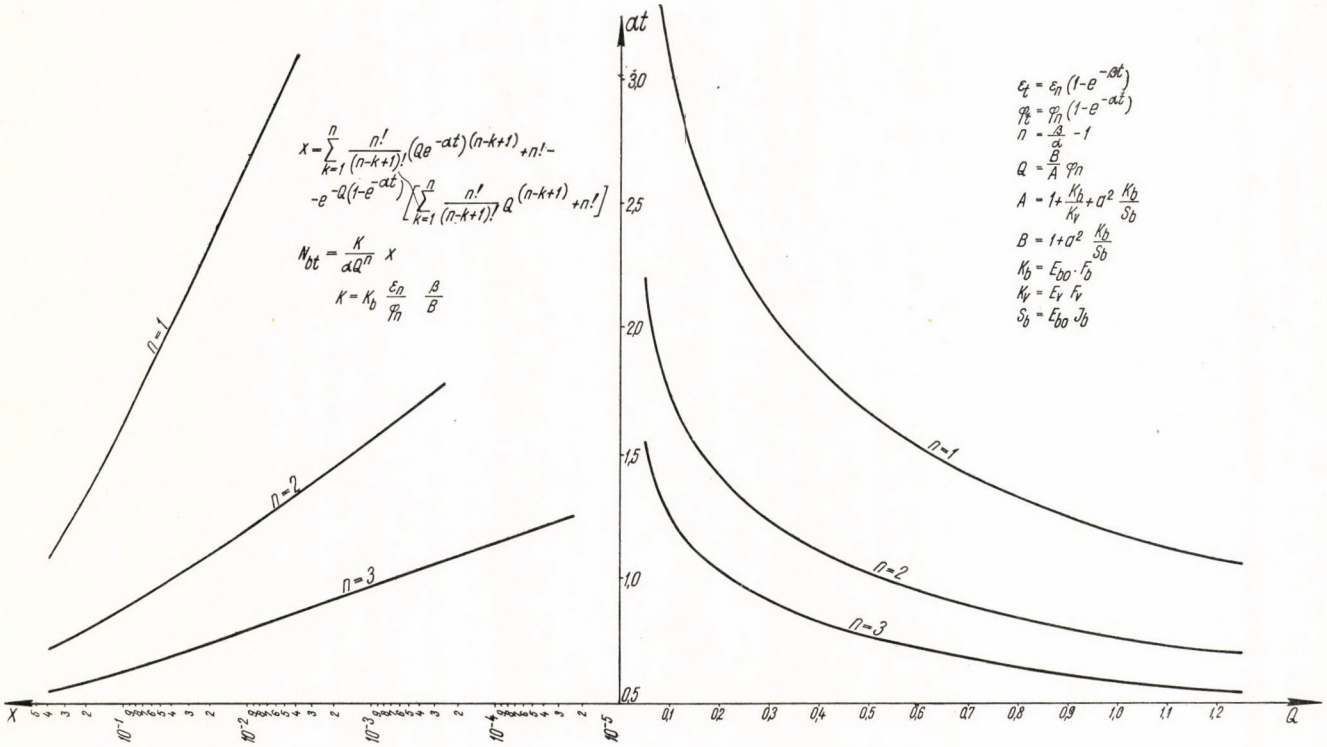

Bild 2. Kurven zur Bestimmung der Höchstwerte der vom Schwinden herrührenden inneren Kräfte und des Zeitpunktes ihres Auftretens

Nach Ermittlung der Stelle des Höchstwertes gilt es nun die Maxima der inneren Kräfte zu bestimmen. Zu diesem Zweck soll unsere Gleichung in der folgenden Form aufgeschrieben werden:

$$N_{bt} = \frac{K}{\alpha Q^n} X, \tag{24}$$

wo

$$X = \sum_{k=1}^{n} \frac{n!}{(n-k+1)!} (Qe^{-\alpha t})^{(n-k+1)} + n! -$$

$$- e^{-Q(1-e^{-\alpha t})} \left[\sum_{k=1}^{n} \frac{n!}{(n-k+1)!} Q^{(n-k+1)} + n! \right]. \tag{25}$$

Nun werden für die verschiedenen Werte von n die von X bestimmt, welche zu den verschiedenen Werten von $\alpha\, t$ gehören, die die Stellen der Maxima anzeigen. Die X-Werte sind links im Bild 2 angegeben.

Im einzelnen wird die Berechnung folgendermaßen vorgenommen:

a) In Kenntnis des Querschnitts — bzw. Materialkennzahlen und der Funktionen, welche den Prozeß des Schwindens und Kriechens beschreiben, werden die Zustandsgrößen n bzw. Q und $K/(\alpha Q^n)$ ermittelt.

b) Dem Bild 2 entnimmt man die zu den berechneten Werten n und Q gehörenden Größen $\alpha(t)$, und nun wird mit diesen in Kenntnis von α der Zeitpunkt t bestimmt, der die Stelle, wo das Maximum ist, anzeigt.

c) Dem Bild 2 werden von links die X-Werte, die zu den Werten von n und $\alpha\, t$ gehören, entnommen.

d) Mit Hilfe der Formel (23) wird der Wert von $N_{b\,\max}$ berechnet.

Es ist zu bemerken, daß während Bild 2 eine genaue Ermittlung des Aufbaues der vom Schwinden herrührenden maximalen inneren Kraft ermöglicht, erhält man für die Größe der inneren Kraft nur einen annähernden Wert. Da das Maximum der durch das Schwinden bedingten inneren Kräfte vom Endwert nur unwesentlich abweicht, kann man die Größe der inneren Kraft ohne Bedenken mit Hilfe der einfacheren Dischingerschen Formel ermitteln, während der Zeitpunkt des Auftretens der Höchstkraft mit Hilfe des Bildes 2 bestimmt wird.

VII. Die Rechnung der Spannungen

Die Spannungen sind aus den Gleichungen

$$\sigma_b = \frac{N_{bt}}{F_b} \pm \frac{M_{bt}}{I_b} y$$

und

$$\sigma_v = \frac{N_{vt}}{F_v}$$

zu berechnen.

VIII. Zahlenbeispiel

a) Querschnitts- und Material-Kennzahlen und andere Ausgangsdaten

Es seien nun beispielsweise die innere Kräfte berechnet, die im mittleren Abschnitt eines gespannten Betonträgers als Folge des Schwindens des Betons auftreten. Bild 3 zeigt den untersuchten Querschnitt des Trägers. In diesem Abschnitt laufen die Achsen der Kabel der statischen Achsen des Trägers parallel. Der Kabelkanal wurde nach dem Anspannen injektiert.

Betongüte: B 400; $E_{b0} = 365\,000$ kp/cm²; $F_b = 4488$ cm²; $I_b = 737\,000$ cm⁴.

Stahlgüte: KB 150 (⌀ 5 mm). In den unten befindlichen Kabelkanälen sind 18, in denen in der oberen Platte des Kastenquerschnitts 6 Kabel untergebracht.

$E_v = 2\,100\,000$ kp/cm², $F_v = 30{,}6$ cm², $a = 46{,}7$ cm, $\varepsilon_n = 0{,}25^0/_{00}$, $\varphi_n = 2$, $\alpha = 0{,}006$.

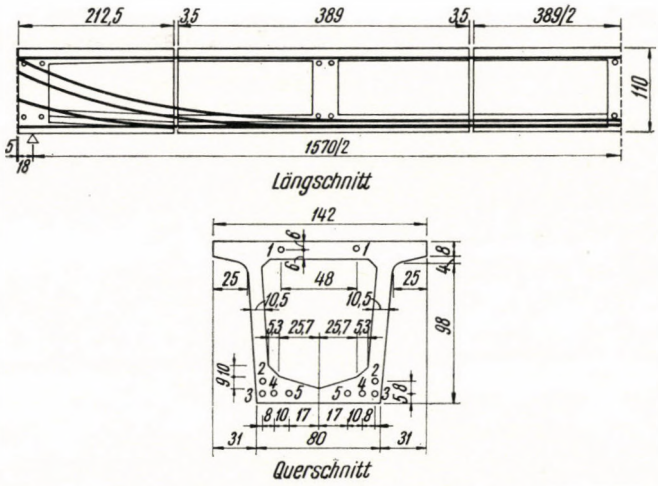

Bild 3. Der untersuchte Spannbetonträger

b) Berechnung der, vom Betonschwinden verursachten Spannkraftverlust

Laut der Gleichung (9) ist

$$A = 169{,}8217 \cdot 10^{-10}\ 1/\text{kp}.$$

Laut der Gleichung (10) ist

$$B = 14{,}2117 \cdot 10^{-10}\ 1/\text{kp}.$$

Laut der Gleichung (12) ist

$$Q = 0{,}167.$$

Unter Heranziehung dieser Hilfsgrößen wurden die inneren Kräfte in Abhängigkeit von der Zeit, die seit der Spannung verstrichen ist, für die Fälle, daß $n = 1, 2, 3$ bzw. 4 ist, berechnet; die erhaltenen Funktionen sind im Bild 4 zusammengefaßt. Diese Kraft tritt in den Spannkabeln des Spannbetonträgers als Spannkraftverlust in Erscheinung.

Aus Bild 4 geht klar hervor, daß, wenn der angenommene zeitliche Verlauf des Kriechens und Schwindens an den wirklichen Prozeß nahe herankommt, der Höchstwert der inneren Kräfte von dem Schwinden her zwar keine nennenswerte Änderung erfährt, jedoch wird diese innerhalb einer ganz kurzen Frist das Maximum erreicht haben. Diese Berechnung ist also geeignet, den zeitlichen Verlauf der durch das Schwinden bedingten inneren Kräfte wahrheitsgetreuer zu erfassen.

Man sieht auch, daß falls n gleich 2 bzw. 3 gewählt wird — Annahmen die

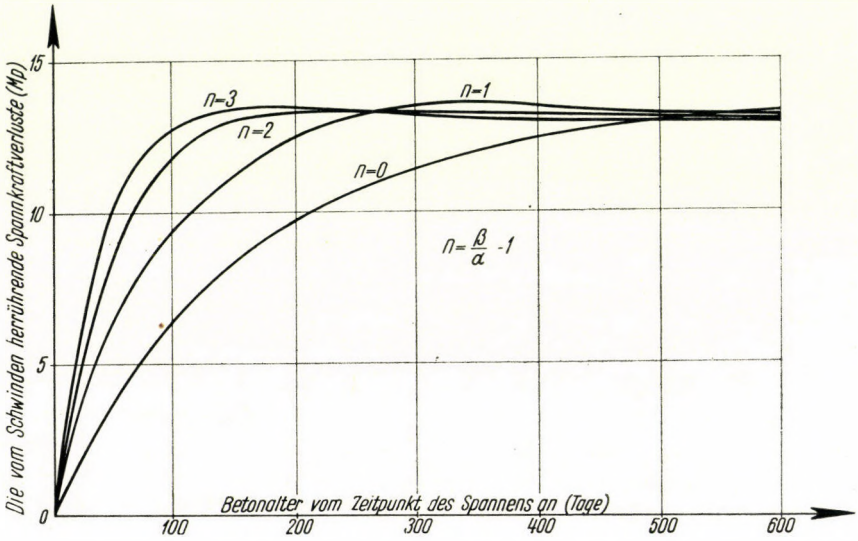

Bild 4. Die vom Schwinden herrührenden Spannkraftverluste bei verschiedenen Werten von n

den tatsächlichen Verhältnissen ziemlich gut entsprechen — die Kurven nahe einander verlaufen.

Bei der Untersuchung des Spannungszustandes während des Transports wird das Schwinden gewohnheitsgemäß mit halbem Wert in die Berechnung des Kräftespiels des vorgespannten Trägers eingestellt. Die hier angeführte Rechnung legt die Folgerung nahe, daß es auch bei dieser Untersuchung richtiger ist, das Schwinden mit vollem Wert zu berücksichtigen.

Bei einem aus Fertigteilen zusammengebauten gespannten Träger wirken sich die in die Elemente eingelegten schlaffen Stahleinlagen dahingehend aus, daß der Höchstwert an Kriechmaß schneller erreicht ist; unterläßt man es also, das Spannen unmittelbar nach der Fertigung vorzunehmen, kann bei der Berechnung das Schwinden größtenteils oder zur Gänze unberücksichtigt bleiben.

Handelt es sich um eine Spannbetonkonstruktion, wo durch nachträgliches Spannen der Kabel eine Möglichkeit zur Regulierung der Kabelverluste

gegeben ist, können auf Grund der hier angeführten Berechnungsmethoden die auf das Schwinden zurückführenden Kabelkräfteverluste binnen einer kurzen Frist praktisch entfallen.

IX. Versuche an mittig bewehrten Betonprismen

Um die Berechnungsmethode zu überprüfen, wurden an mittig bewehrten Betonprismen mit den Abmessungen 10 cm × 10 cm × 50 cm Schwindmessungen durchgeführt. Die Stoffe des Betons waren wie folgt: 600 p. c. von Tatabánya (~ *Z 275*) 450 kg/m³, Wasserzementfaktor: 0,4, das Feinheitsmodul der Zuschlagstoffe von etwa 5, Chlorkalzium 0 bzw. 2%. In die Achsenlinie der Prismen wurden Stahleinlagen mit unterschiedlichen Durchmessern

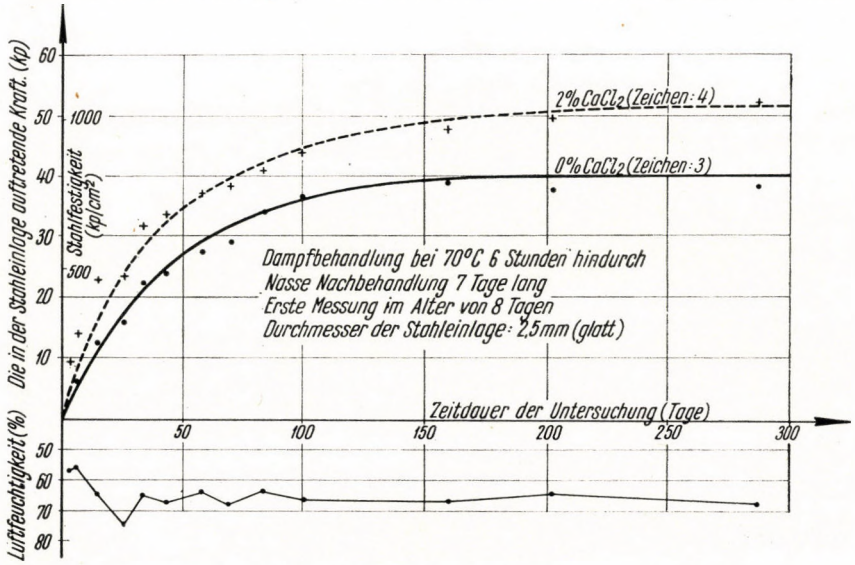

Bild 5. Kräfte aus dem Schwinden in den Stahleinlagen mittig bewehrter Betonprismen

Tafel I

Der Berechnung der den vom Betonschwinden herrührenden inneren Kräften zugrundegelegten Abmessungen bzw. Materialkennzahlen

Zeichen des Versuchs	Durchmesser der Stahleinlage mm	Querschnittsfläche der Stahleinlage F_v/cm²	E_{bo} Mp/cm²	E_v Mp/cm²	ε_n 0/00	β	φ_n
3	2,5	0,0491	300	1900	0,44	0,024	2,5
4	2,5	0,0491	340	1900	0,55	0,030	3,0
29	15,95	2,00	300	2100	0,44	0,024	2,5
30	15,95	2,00	340	2100	0,55	0,030	3,0
35	14,15	1,58	300	2100	0,44	0,024	2,5
36	14,15	1,58	340	2100	0,55	0,030	3,0
	$F_b = 100$ cm²						

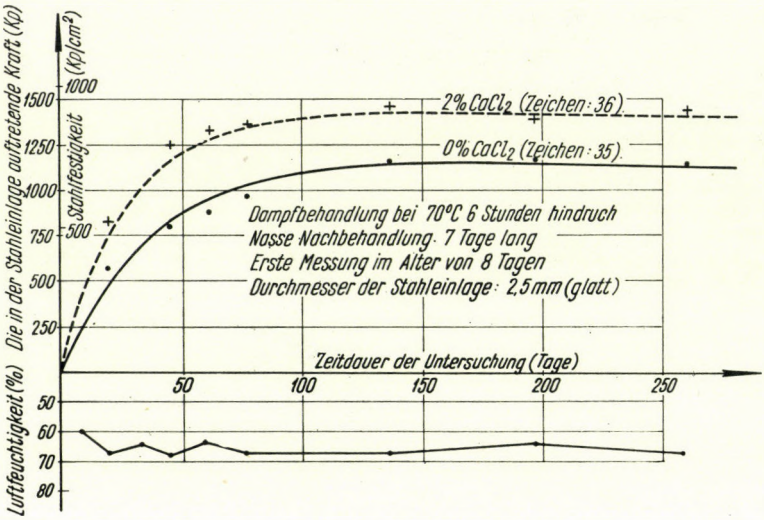

Bild 6. Kräfte aus dem Schwinden in den Stahleinlagen mittig bewehrter Betonprismen

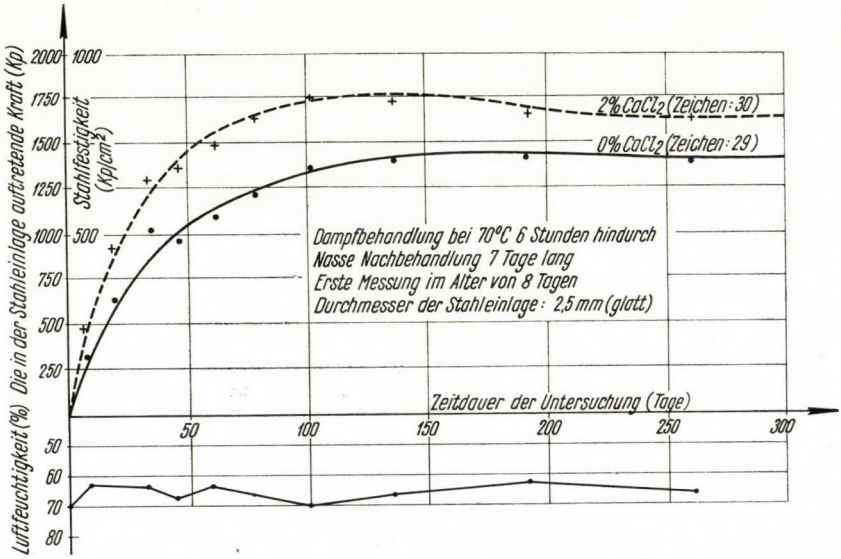

Bild 7. Kräfte aus dem Schwinden in den Stahleinlagen mittig bewehrter Betonprismen

und Oberflächenausbildung eingelegt. Für Vergleichszwecke wurden zur gleichen Zeit auch unbewehrte Betonprismen angefertigt. Der Beton wurde bei einer Temperatur von 70 °C einer 6stündigen Dampfbehandlung unterzogen, darauffolgend langsam abgekühlt und etwa für 7 Tage mit einem nassen Tuch abgedeckt. Von diesem Zeitpunkt an wurden die Prismen in einer Klimatisierungskammer, wo die umgebende Luft einen Feuchtigkeitsgehalt von etwa 60 bis 70% aufweist, bei Temperaturen zwischen 16 und 20 °C gelagert.

Die Stahleinlagen der bewehrten Prismen und die Formänderung des Betons der Prismen ohne Bewehrung wurden mittels einer Amsler'schen Schwindmeßvorrichtung bestimmt. Die Kräfte bzw. Spannungen, wie sie aus den im Laufe des Versuchs gemessen Schwind-

werten berechnet wurden, sind in den Bildern 5 bis 7 zusammengefaßt. In denselben sind auch die unter Verwendung der Formel (21a) berechneten Kraft- bzw. Spannungsfunktionen eingezeichnet. Die der Berechnung zugrundegelegten Materialkennzahlen sind in der Tafel 1 zu finden. Die Werte β und ε_n, welche das ungehemmte Schwinden betreffen, wurden auf Grund von den unbewehrten Prismen ermittelten Schwindmeßwerten berechnet. Die Größen $n = \beta/\alpha - 1$ wurden in allen Fällen zu 2 angesetzt. Der Wert von φ_n wurde gleichzeitig durch Messungen der langsamen Formänderung, wie sie Betonprismen gleichen Materials aufweisen, bzw. auf Grund früher durchgeführter Versuche schätzungsweise ermittelt.

Die Versuche haben gezeigt, daß die Berechnungsmethode richtig war.

X. Bemerkungen zu den der Berechnung zugrundegelegten Annahmen

Die angewandte Berechnungsannahmen unterscheiden sich von denjenigen Dischingers nur darin, daß die Schwind- und Kriechkurven als nichtaffin angesehen wurden. Hiedurch haben die Berechnungsannahmen eine Verfeinerung erfahren. Trotzdem erscheint es angebracht, in Kürze zu untersuchen, wann und in welchem Maße dies zutrifft.

a) Obzwar die homogene und isotrope Beschaffenheit des Betons nicht einwandfrei feststeht, müssen wir sie hier voraussetzen. Nach Whitney hat das Hooksche Gesetz bei erhärteten Betonen in bezug auf das Kriechen Gültigkeit, mag es sich nun um eine, die vom Zug oder um eine solche, die vom Druck herrührt, handeln. Als Betone dieser Art sind die sich immer mehr durchsetzenden künstlich erhärteten Betone anzusehen; diese haben bereits bei Beginn des Aufbaus der durch das Schwinden bedingten Spannungen ihren Endfestigkeitswert so gut wie erreicht. Bei diesen ist die Annäherung $E_{b0} = E_{bt}$ als sehr gut anzusprechen, insbesondere da die Kriechkurve üblicherweise an Betonen aufgenommen zu werden pflegt, deren Elastizitätsfaktoren in der Zwischenzeit Änderungen erfahren. In solchen Fällen trägt die Kriechfunktion dem Ansteigen des Elastizitätsfaktors während der Zeit der Belastung bereits Rechnung.

Schlechter ist es hingegen um die auf natürlichem Weg erhärteten Betonarten bestellt, da man ihre Kriechfunktionen nur in groben Zügen zu veranschlagen vermag; hier sollte man die Zusammenhänge unter einer langsam vom Nullwert aus ansteigenden Belastung an einem Beton aufnehmen, dessen Festigkeitswert in der Zwischenzeit ebenfalls von Null ausgehend ansteigt.

Unter den Bedingungen, wie sie die Dischinger'sche Formel stellt, wurde die Berechnung auch mit einem veränderlichen Elastizitätsfaktor vorgenommen; diese führte zu dem Ergebnis, daß die Berücksichtigung der Veränderlichkeit des Elastizitätsfaktors keinen wesentlichen Einfluß auf die inneren Kräfte ausübt. Dies dürfte ohne weiteres einleuchten, da in der Anfangsperiode die Betonfestigkeit sprunghaft ansteigt, wobei eine noch rapidere Erhöhung des Wertes des Elastizitätsfaktors vor sich geht.

b) Der zeitliche Verlauf sowohl des Schwindens, wie auch des Kriechens hängt von vielen Faktoren ab. Die wichtigsten unter ihnen stellen der Feuch-

tigkeitsgehalt der umgebenden Luft und die Abmessungen des untersuchten Betonkörpers dar. Die Auswirkungen dieser Faktoren im einzelnen werden im Fachschrifttum nicht behandelt.

Aus unseren Versuchen ging hervor, daß in einer Kammer, wo der Feuchtigkeitsgehalt der Luft gleichbleibend ist, das Schwinden nach vier Monaten bereits abgeklungen war, während nach in- [6], [7] und ausländischen [8], [9] Versuchen sogar nach Verstreichen eines Jahres ein beträchtliches Ansteigen des Kriechens beobachtet werden konnte. Nach Roš geht diese erst innerhalb zehn Jahren, nach SALIGER in zwei Jahren zu Ende.

Bei Betonarten mit $CaCl_2$-Zusatz wurden Kriechmessungen nur bei geringzahligen Exemplaren durchgeführt. Es ist aber anzunehmen, daß — ähnlich wie dies beim Schwinden der Fall ist — das Chlorkalzium keinen wesentlichen Einfluß auf den zeitlichen Verlauf des Kriechprozesses ausübt. In Anlehnung an die Versuche, die am Lehrstuhl für Baustoffe der Technischen Universität für Bau- und Verkehrswesen, Budapest, durchgeführt wurden, kann ausgesagt werden, daß sich die Zahl n — gleichgültig, wie die Lagerungsumstände, die Betonzusammensetzung und die Abmessungen beschaffen waren, — zu 2 bis 3 ergab. Der Unterschied zwischen den zwei Werten hat — wie aus dem Beispiel hervorging — keinen wesentlichen Einfluß auf die Herausbildung der inneren Kräfte ausgeübt.

c) Der zeitliche Verlauf des Kriechens und Schwindens in Stahlbetonfertigteilen, die auf der Baustelle eingebaut werden, läßt sich im Fall, daß der Feuchtigkeitsgehalt der Luft starken Schwankungen unterliegt, nicht immer mit einer exponentiellen Funktion beschreiben. Man vermag jedoch der Funktion N_{bt} auch in diesem Fall Hinweise über die Tendenz des Aufbaues der inneren Kräfte zu entnehmen.

SCHRIFTTUM

1. DISCHINGER, F.: Untersuchungen über die Knicksicherheit, die elastische Verformung und das Kriechen des Betons bei Bogenbrücken. *Bauingenieur* (1937), 487—508.
2. DISCHINGER, F.: Elastische und plastische Verformungen der Eisenbetontragwerke und insbesondere der Bogenbrücken. *Bauingenieur* (1939), 54—63.
3. SARTORIUS—THALBORN, H.: Schwinden und Kriechen des Betons. *Beton und Eisen.* (1938), 219—224.)
4. BALÁZS GY.—KILIÁN J.: A vasbeton zsugorodás okozta feszültségei. (Durch das Schwinden des Betons verursachte Spannungen). ÉKME *Tudományos Közleményei* (1958), IV. 5., 3—19.
5. SCHLEICHER, R.: Taschenbuch für Bauingenieure. (Springer-Verlag, 1955.)
6. BALÁZS GY.—KILIÁN J.: Das Kriechen und die Verdichtung hochwertiger Betone: Kriechfeste Betone. *Acta Techn. Hung.* **17** (1957), 113—142.
7. BALÁZS GY.—KILIÁN J.: Zúzott adalékanyagú betonok zsugorodása és lassú alakváltozása. (Schwinden und Kriechen von Betonen mit Splittzusatzstoffen.) *Mélyépítéstudományi Szemle* (1959), 423—431.
8. LEONHARDT, F.: Spannbeton für die Praxis. Berlin 1955.
9. L'HERMITE, M. R.: Que savons-nous de la déformation plastique et du fluage du béton? *Annales de l'Institut Technique du batiment et des travaux publics* **10** (1957), 777—810.

ANALYSIS OF FORCES DUE TO SHRINKAGE

GY. BALÁZS

SUMMARY

The important role played by concrete shrinkage in the cowork played between concrete and prestressed concrete structures and the increasing effect that calcium chloride exerts on shrinkage justify the showing to what degree the internal forces are changed if it is assumed that the curves for shrinkage and creep are not affine. In this case the hindered shrinkage is not to reach its maximum at $t = \infty$, but this will happen much earlier depending on the fact, to what extent the temporal process of shrinkage and that of the creep differ from one another, depending on the materials and dimensions of the beam, on the excentricity of the reinforcement and on its percentage. Therefore it seems desirable that shrinkage be considered in its full value when the stress state as is prevailing during transportation is to be calculated. In case of posttensioned structures built up from prefabricated elements — assuming that posttensioning does not follow immediately after prefabrication — the bulk of shrinkage need not to be taken into account.

CALCUL DES CONTRAINTES INTÉRIEURES DUES AU RETRAIT DU BÉTON

GY. BALÁZS

RÉSUMÉ

Le retrait joue un rôle important dans le jeu de forces des constructions en béton et béton précontraint, et l'emploi de chlorure de calcium influence à son tour le retrait. Pour ces raisons, l'auteur a cru nécessaire d'examiner en quelle mesure les contraintes intérieures se modifient si l'on suppose que les courbes de retrait, resp. de fluage ne sont pas affines. La résolution des équations différentielles établies par l'auteur permet de constater que ce n'est pas au temps $t = \infty$, mais bien avant que le retrait retardé arrive à sa valeur maximum. Cette différence de temps dépend de l'écart entre la vitesse des deux processus de retrait et de fluage, du matériau et des dimensions de la poutre, enfin du pourcentage d'acier et de l'excentricité de l'armature.

Sur la base de ces observations, il paraît recommandable de tenir compte de la valeur totale du retrait lors du dimensionnement des éléments préfabriqués ou le calcul de l'état de transport et de montage. En cas de constructions postcontraintes faites d'éléments préfabriqués, une grande partie du retrait peut déjà être négligée, à condition que la postcontrainte ne s'effectue pas directement après la préfabrication des éléments.

РАСЧЕТ ВНУТРЕННИХ СИЛ БЕТОНА, ВОЗНИКАЮЩИХ ОТ ЕГО УСАДКИ

Д. БАЛАЖ

РЕЗЮМЕ

Усадка играет важную роль в работе бетона и напряженных бетонных конструкций, а применение хлорида кальция воздействует на усадку бетона; эти причины заставили автора изучить проблему, что в какой мере изменяются внутренние силы в том случае, если предположить, что кривые усадки и деформации являются не аффинными. На основе решения выведенных дифференциальных уравнений можно установить, что тормозимая усадка достигает наибольшей своей величины не за время $t = \infty$, а значительно раньше. Это опережение зависит от того, что в какой мере отличаются друг от друга протекание во времени процессы усадки и деформации, далее от материала балки и размеров последней, а также от процента армирования и эксцентричности его.

На основе проведенного изучения вопроса можно сделать вывод, что желательно учитывать усадку полной ее величиной — при расчете сборных элементов, далее при расчете состояния поставки — сборки. В случае сборных элементов с последующим напряжением, — предполагая, что последующее напряжение производится не непосредственно после изготовления сборных элементов, — большую часть усадки уже не следует учитывать.

DIE WIRKUNG DES SCHMIERENS BEIM STAUCHEN VON METALLEN

L. TÓTH

TECHNISCHE UNIVERSITÄT DER SCHWERINDUSTRIE, MISKOLC

[Eingegangen am 14. Juni, 1963]

Es wird in dieser Arbeit das Stauchen zwischen parallelen Flächen von Körpern behandelt, deren Stirnfläche geschmiert ist. Zur Erklärung der Entstehung eines Diabolo-Körpers wird die Deformation der Stirnfläche als Ursache angegeben. Es werden numerische Zusammenhänge zwischen Druckverteilung an der Stirnfläche, der wirkenden Druckkraft und der Abweichung des Verformungswiderstandes von der Verformungsfestigkeit bekanntgegeben. Die Angaben betreffs Wirkung des Ausmaßes der Verformung entsprechen den praktischen Beobachtungen. Diesbezüglich wird festgestellt, daß sowohl die monoaxiale Deformation als auch der monoaxiale Spannungszustand jeweils nur von einem einzigen Verformungsgrad bedingt wird. Es wird noch ein Rechnungsgang zur annähernden Bestimmung dieser Verformungsmaßwerte angegeben.

I. Einleitung

Beim bildsamen Formen von Metallen ist das Schmieren eines der wichtigsten Aufgaben. Mit dem Schmieren bezweckt man die Herabsetzung der Reibung an der Berührungsfläche zwischen Werkzeug und Werkstück. Dieses Verfahren ist geeignet, zweierlei Vorteile zu bieten; einerseits wird der Leistungsbedarf herabgesetzt, da durch Verminderung der Reibungskräfte auch die Formungskraft kleiner wird, anderseits weist das Endprodukt eine erhöhte Homogenität auf, da infolge herabgesetzter Reibungskräfte sich auch der Spannungszustand gleichmäßiger gestaltet, also die Formveränderung bringt eine Mäßigung der Inhomogenität mit sich.

Aus diesem Fragenkomplex wollen wir als grundlegendes Beispiel und einfachen Fall das Stauchen zwischen parallelen, ebenen Flächen behandeln. Dies spielt in der Praxis beim Pressen und in vielen Schmiedeoperationen eine bedeutende Rolle.

Um die mathematische Behandlung einfacher zu gestalten, sollen folgende Bedingungen und Vereinfachungen vorausgesetzt werden:

a) das dem Stauchen unterworfene Material ist homogen, mit bekannten Festigkeitseigenschaften;

b) beim bildsamen Formen kann ein Deformationszustand in der Ebene verwirklicht werden;

c) die Druckfläche des Werkzeuges ist eine Ebene mit nur elastischen Deformationen, deren Wirkung im folgenden vernachlässigt werden soll;

d) die Verformungsgeschwindigkeit bleibt konstant;

e) die Bewegung des Schmierstoffes ist laminar;

f) die Geschwindigkeit des Schmierstoffes in rechtwinkeliger Richtung zur Druckfläche kann gegenüber der Geschwindigkeit parallel zurselben vernachläßigt werden;

g) die Viskosität des Schmierstoffes beträgt einen konstanten Wert, welcher der Mitteltemperatur und dem Mitteldruck, die an der Druckfläche auftreten, entspricht.

Die theoretischen Bedingungen mit womöglich kleinstem Fehler können natürlich nur im Laufe eines im Laboratorium ausgeführten Stauchversuches

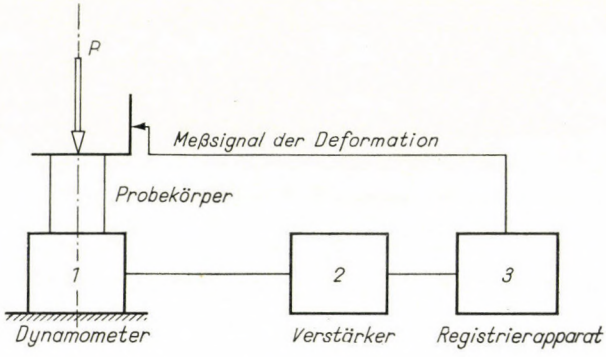

Bild 1

verwirklicht werden. Die Bedeutung einer versuchsweise ausgeführten Stauchoperation ist nicht zu unterschätzen, da sie als eine der wichtigsten technologischen Proben gilt. Der Stauchversuch soll sehr genau sein, und unsere Untersuchungen sollen gerade für diesen Fall durchgeführt werden. Man kann in allen anderen Fällen die derart erhaltenen Resultate durch entsprechende Vereinfachungen bzw. durch Beachtung der geänderten Umstände richtig anwenden.

Zur Bestimmung des zur Durchführung jedweder plastischen Formungsoperation benötigten Kraftbedarfes ist die Verformungsfestigkeit des zu bearbeitenden Metalles die richtige Grundlage. Deshalb ist die möglichst genaue Bestimmung der Verformungsfestigkeit als Funktion der beeinflussenden Faktoren unentbehrlich. Im Bild 1 ist das prinzipielle Schema der Meßvorrichtung dargestellt. Die zum Stauchen des zwischen parallelen Flächen einge-

klemmten Probekörpers notwendige Kraft wird vom Dynamometer (1) in ein elektrisches Signal transformiert, durch den Verstärker (2) verstärkt und in dem Registrierapparat (3) vermerkt. Von demselben wird auch das die Deformation des Probekörpers anzeigende Signal aufgenommen. Bei einer bestimmten Temperatur und gegebener Verformungsgeschwindigkeit kann man auf Grund des registrierten Diagramms die zum Zusammendrücken des Probekörpers effektiv benötigte Spannung (den Verformungswiderstand) als Funktion des Verformungsgrades errechnen.

Es soll der in der eben geschilderten Weise gemessene Verformungswiderstand als der annähernde Wert der Verformungsfestigkeit des Metalles angenommen, also vorderhand die Wirkung der Reibung an den Druckflächen vernachlässigt werden. Aus diesen Erörterungen folgt natürlicherweise das Bestreben die Bedingungen der Verformungswiderstandmessung derart zu gestalten, daß die Abweichung zwischen dem Meßwert und dem wirklichen Verformungsfestigkeitswert möglichst klein gehalten werden soll. Eine immerhin auftretende Abweichung muß dennoch in Betracht gezogen werden. Dieses Prinzip führte zu dem Schmieren der Druckflächen, um einen monoaxialen Spannungszustand zu erreichen.

Im Stauchvorgang lassen sich zwei voneinander unterscheidbare Zeitabschnitte feststellen; in dem ersten wird der Schmierstoff herausgedrängt, bzw. ein tragfähiger Schmierfilm wird gebildet; im zweiten erfolgt die bildsame Deformation des Probekörpers.

II. Bildung des Schmierfilms

Um die mathematische Behandlung einfacher zu gestalten, wird noch vorausgesetzt, daß die Dicke des Schmierfilms gegenüber dem Flächenhalbmesser vernachlässigbar ist. Bild 2 zeigt den Planschnitt des Schmierfilms. Laut dieser Zeichnung gilt für das Gleichgewicht eines Raumelementes $2r\,\pi \cdot dr \cdot dy$:

$$2r\,\pi \cdot dr \cdot d\,\tau - 2r\,\pi \cdot dy \cdot dp = 0, \tag{1}$$

wonach

$$\frac{\partial p}{\partial r} = \frac{\partial \tau}{\partial y} \tag{2}$$

ist.

Für die als Folge der Verschiebung der Flüssigkeitspartikel entstehende Scheerspannung gilt nach Newton's Theorie:

$$\tau = \eta \frac{\partial v_r}{\partial y}\,. \tag{3}$$

Aus den Gleichungen (2) und (3) ergibt sich die Differentialgleichung der Druckverteilung:

$$\frac{\partial p}{\partial r} = \eta \frac{d^2 v_r}{dy^2} . \tag{4}$$

Mit Hilfe der Gleichung (4) ist es möglich, die Verteilung des Geschwindigkeit v_r entlang y an einer beliebigen Stelle r zu bestimmen. Auf Grund der Präliminarien ist $\partial p/\partial r$ für einen gegebenen Wert von r konstant. Mit dieser

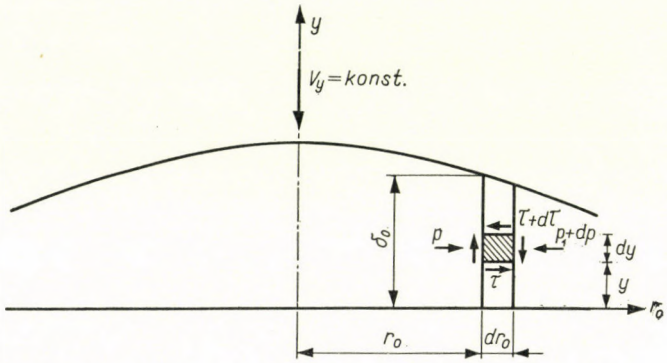

Bild 2

Annahme erhält man nach zweifacher Integration der Gleichung (4) als Geschwindigkeitsfunktion:

$$v_r = \frac{1}{\eta} \frac{\partial p}{\partial r} \frac{y^2}{2} + C_1 y + C_2 . \tag{5}$$

Die Bestimmung der Integrationskonstanten erfolgt auf Grund der Grenzflächen. Unter Berücksichtigung der Bedingung der Adhäsion des Schmierstoffes und gemäß Bild 2 ergeben sich folgende Grenzwertepaare:

$$\text{bei } y = 0, \text{ ist } v_r = 0;$$
$$\text{bei } y = \delta, \text{ ist } v_r = 0 .$$

Daher ergibt sich aus der Gleichung (5):

$$v_r = \frac{1}{2\eta} \cdot \frac{\partial p}{\partial r} y^2 - \frac{1}{2\eta} \frac{\partial p}{\partial r} \delta y . \tag{6}$$

Man erhält die Differentialgleichung der Strömung auf Grund der Kontinuitätsbedingung. Die an einer Zylinderfläche vom beliebigen Halbmesser

r und Höhe δ herausströmende Schmierstoffmenge ist gleich der Menge, die infolge der sich einander nähernden Druckplatten herausgedrückt wird:

$$v_y \cdot r^2 \pi = 2\, r\, \pi \int_{y=0}^{\delta} v_r\, dy. \tag{7}$$

Nach Einsetzen der Werte aus Gleichung (6) und nach erfolgter Integration der Gleichung (7) ergibt sich:

$$\frac{dp}{dr} = -\frac{6\, \eta\, r\, v_y}{\delta^3}. \tag{8}$$

Mit Rücksicht darauf, daß bei $r_0 = a_0$ der Druck $p = 0$ ist, erhält man für die Druckfunktion:

$$p = \frac{3\, \eta\, v_y}{\delta_0^3} (a_0^2 - r_0^2), \tag{9}$$

(wo a den größten Halbmesser des Probestärkes bedeutet).

Der maximale Druck ergibt sich bei $r_0 = 0$; p steigt, wenn die Entfernung δ_0 zwischen den Druckflächen abnimmt. In dem Moment, wo das Druckmaximum den der Fließgrenze des Materials gleichen Wert erreicht, nimmt die Schmierschichtstärke nicht mehr ab, und es beginnt die Deformation des Probekörpers. Daher entsteht an der Druckfläche ein Schmierfilm, bei welchem an jedem Punkt der Fläche der Druck p den Wert k_f erreicht. Die Schmierfilmstärke δ_0 ergibt sich aus Gleichung (8) für den Fall $p = k_f$:

$$\delta_0 = \sqrt[3]{\frac{3 \cdot \eta\, v_y}{k_f} (a_0^2 - r_0^2)}. \tag{10}$$

Nach Umstellung erhält man

$$\delta_0 = \delta_{00} \sqrt[3]{1 - \left(\frac{r_0}{a_0}\right)^2}, \tag{11}$$

wobei

$$\delta_{00} = \sqrt[3]{\frac{3\, \eta v_y\, a_0^2}{k_f}} \tag{12}$$

die Schmierfilmstärke bei $r = 0$ bedeutet.

Mit Rücksicht auf die durch die mechanische Bearbeitung auf der Druckplatte und an den Probestücken verursachten mikrogeometrischen

Unebenheiten, kann der Zustand $\delta_0 = 0$ niemals eintreten (d. h. das restlose Herausdrängen des Schmierstoffes). Wie dies aus der Zeichnung im Bild 3 ersichtlich ist, kann an den Stellen in engster Randnähe am Probestück der zur bildsamen Verformung notwendige Druck im Schmierfilm nicht mehr auftreten, da der Zustand einer mechanischen Berührung zwischen Druckplatte und Probestück bereits erreicht ist, noch bevor dieser Druckwert entstehen könnte. Es sollen die Oberflächenrauheits-Kennwerte mit h'_q und h''_q bezeichnet werden, die also die Ölmenge bestimmen, welche zwischen den Unebenheiten

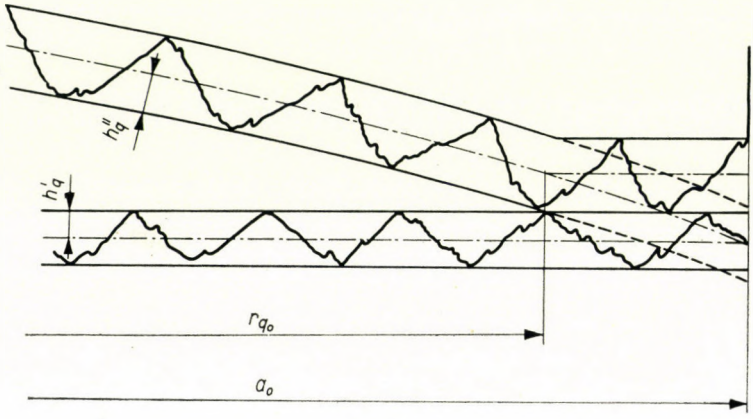

Bild 3

Platz finden kann, und damit erhält man aus den Gleichungen (11) und (12): $\delta_0 = h'_q + h''_q$

$$r_{q0} = a_0 \sqrt{1 - \left(\frac{h'_q + h''_q}{\delta_{00}}\right)^3} \,. \tag{13}$$

Mit diesem Wert r_{q0} wird die Fläche in zwei Teile geteilt, uzw: der Flächenteil $0 \leqslant r \leqslant r_{q0}$ ist das Gebiet der Flüssigkeitsschmierung und der Flächenteil $r_{q0} \leqslant r \leqslant a_0$ ist das Gebiet der gemischten Reibung.

III. Bildsame Formänderung des Probestückes

Zur mathematischen Darstellung der bildsamen Deformation sollen Druckkraftwerte bzw. die an der Druckfläche entstehenden Druckverteilung — allenfalls als Funktion des Deformationsgrades — herangezogen werden. Vor allem ist es also notwendig, die Differentialgleichung der Druckverteilung aufzustellen.

Aus allem, was im ersten Kapitel gesagt wurde, geht es klar hervor, daß dem eigentlichen Stauchvorgang zwischen parallelen Ebenen ein solches

Probestück unterworfen ist, dessen Oberfläche mit den Gleichungen (11) und (12) bestimmt wird. Diese Feststellung stimmt mit den wirklichen Umständen unmittelbar überein, da die gedrückte Stirnfläche eine meßbare Deformation erleidet, und die Übereinstimmung ist dadurch erwiesen, daß die mögliche Entstehung der Diabolo-Gestalt mit Hilfe einer richtigen Schmierung anders nicht zu erklären wäre.

Bild 4 zeigt — etwas verzerrt — den Planschnitt des zylindrischen Probestückes. Das Raumelement ist von den zwei Zylinderflächen mit dem

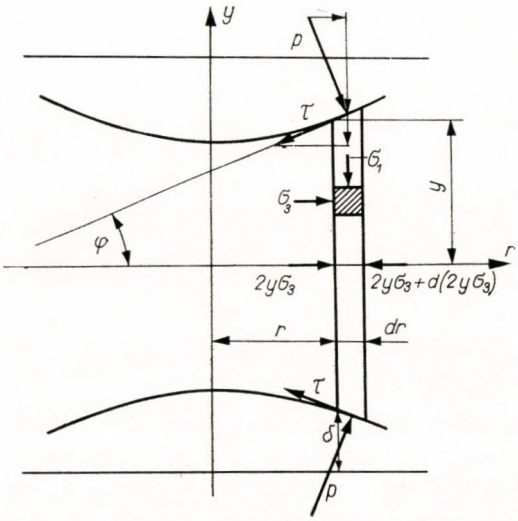

Bild 4

Umfang $2r\pi$ bzw. $2(r+dr)\pi$ und den zwei Stirnflächen begrenzt. Das Gleichgewicht der auf das Raumelement in Richtung r wirkenden Kräfte läßt sich wie folgt anschreiben:

$$d\,(2\,y\sigma_3)\,2\,r\pi = (2\,p\sin\varphi - 2\,\tau\cos\varphi)\,2\,r\pi\,\frac{dr}{\cos\varphi} \tag{14}$$

und daher

$$\frac{d}{dr}\,(y\sigma_3) = p\cdot\tan\varphi - \tau\,. \tag{15}$$

Die Gleichgewichtsbedingung in Richtung y:

$$\sigma_1\,2\,r\pi\cdot dr = (p\cdot\cos\varphi + \tau\cdot\sin\varphi)\,2\,r\pi\cdot\frac{dr}{\cos\varphi} \tag{16}$$

und daher

$$p = \sigma_1 - \tau\cdot\tan\varphi\,. \tag{17}$$

Es gilt als Bedingung der Bildsamkeit nach HUBER—MISES:

$$\sigma_1 - \sigma_3 = \psi k_f; \quad \psi = 1{,}15\,. \tag{18}$$

Mit $\tan\varphi = dy/dr$ und aus den Gleichungen (15), (17), (18) ergibt sich:

$$\frac{d\sigma_1}{dr} = \psi k_f \frac{1}{y}\frac{dy}{dr} - \frac{\tau}{y}\left[1 + \left(\frac{dy}{dr}\right)^2\right]. \tag{19}$$

Mit Rücksicht auf die Zweiteilung der Stirnfläche in Flächenteile mit verschiedenen Reibungsumständen muß man für jeden Flächenteil eine eigene Lösung der Differentialgleichung (19) finden.

1. Flächenabschnitt der Flüssigkeitsreibung

Um die Differentialgleichung (19) zu lösen, muß man die Funktionen y und δ kennen. Gemäß Bild 4 und aus den Gleichungen (11) und (12) ergibt sich:

$$y = \frac{h}{2} - \delta\,. \tag{20}$$

Für τ ist die Gleichung (3) maßgebend.

Mit dem fortschreitenden Preßvorgang ändern sich die Werte δ und τ; demnach ist $y = f_1(r, \varepsilon)$; und $\tau = f_2(r; \varepsilon)$ [wo ε, laut Gl. (26), die relative Formänderung bedeutet]. Zur Entwicklung dieser Funktionen muß vorausgesetzt werden, daß während des Stauchens die Schmierstoffmenge zwischen Druckplatte und Probestück konstant bleibt, daß also eine Abnahme der Schmierfilmstärke nur einem Anwachsen der Stirnfläche zugeschrieben werden kann. Im Sinne dieser Voraussetzung wird also die während des Stauchens verdrängte Schmierstoffmenge und auch die Wirkung eines Ansteigens der Verformungsfestigkeit vernachlässigt. Dies wird anscheinend auch durch die praktischen Erfahrungen [3] gerechtfertigt.

Die äußere Schubspannung kann aus Gleichung (3) bestimmt werden, die hier vorkommende Größe kann aus Gleichung (5) errechnet werden. Die Integrationskonstanten ergeben sich wiederum aus den Adhäsionsbedingungen des Schmierstoffes; bei $y = 0$ ist $v_r = 0$, und bei $y = \delta$ ist $v_r = v_{rd}$. Demgemäß ist

$$v_r = \frac{1}{2\eta}\frac{dp}{dr}y^2 + \left(\frac{v_{rd}}{\delta} - \frac{1}{2\eta}\frac{dp}{dr}\delta\right)y\,. \tag{21}$$

Der Satz über die Beständigkeit des Rauminhaltes des Probestückes bestimmt zugleich die Geschwindigkeit v_{rd} der Oberfläche in Richtung r,

d. h.

$$r^2\pi h = r_0^2\pi h = \text{konst}\,. \tag{22}$$

Differenzieren wir nach h:

$$\frac{dr}{dh} = -\frac{r}{2h}; \tag{23}$$

wegen

$$\frac{dr}{dh} = \frac{dr}{dt} \cdot \frac{dt}{dh} = v_{rd} \frac{1}{v_y}$$

ist

$$v_{rd} = -v_y \frac{r}{2h}. \tag{24}$$

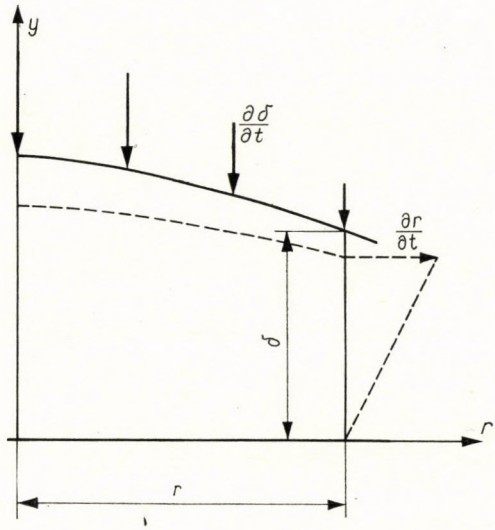

Bild 5

Es folgt für die äußere Schubspannung aus den Gleichungen (3), (21) und (24) nach durchgeführter Differentiation und Einsetzung:

$$\tau = \frac{dp}{dr} \frac{\delta}{2} - \frac{\eta}{\delta} \frac{r}{2h}. \tag{25}$$

Zur Bestimmung der Funktion $\delta = f_2(x, \varepsilon)$ stützen wir uns auf Bild 5.

Der Index 0, wie bisher verwendet, weist auf den Fall $h = h_0$ hin. Im folgenden soll auch das Maß der Formänderung in Betracht gezogen werden. Diese beträgt:

$$\varepsilon = \frac{h_0 - h}{h_0}, \tag{26}$$

und daher:

$$h = h_0 (1 - \varepsilon) . \tag{27}$$

Aus den Gleichungen (22) und (27) erhält man:

$$r = r_0 \frac{1}{\sqrt{1 - \varepsilon}} . \tag{28}$$

Da nun $\partial\delta/\partial t$ nicht konstant ist, lautet die Kontinuitätsgleichung wie folgt:

$$-\int_0^r 2\, r\pi \frac{\partial\delta}{\partial t}\, dr = 2\, r\pi \frac{dr}{dt}\, \delta \frac{1}{2} . \tag{29}$$

Weiter ist:

$$\begin{aligned} \frac{d\delta}{dt} &= \frac{d\delta}{dh} \cdot \frac{dh}{dt} = \frac{d\delta}{dh} \cdot v_y , \\ \frac{dr}{dt} &= \frac{dr}{dh} \cdot \frac{dh}{dt} = \frac{dr}{dh} \cdot v_y . \end{aligned} \tag{30}$$

Aus Gleichungen (29) und (30) ergibt sich:

$$-\int_0^r r \frac{d\delta}{dh}\, dr = r \frac{dr}{dh} \cdot \frac{\delta}{2} . \tag{31}$$

Es wird die Gleichung (31) nach der oberen Integrationsgrenze differenziert, und man erhält mit Hilfe der Gleichung (23) in geordneter Form:

$$\frac{d\delta}{dh} = \frac{1}{4\, h} \left(2\, \delta + r \frac{d\delta}{dr} \right) . \tag{32}$$

Bei Berücksichtigung der Gleichung:

$$\frac{d\delta}{dh} = \frac{d\delta}{dr} \frac{dr}{dh}$$

und mit Hilfe der Gleichungen (32) und (23) ergibt sich:

$$\frac{d\delta}{dr} = -\frac{2}{3} \frac{\delta}{r} . \tag{33}$$

Nach Trennung der Veränderlichen und erfolgter Integration der Gleichung (33) von r_0 bis r, bzw. δ_0 bis δ erhält man:

$$\delta = \delta_0 \left(\frac{r_0}{r} \right)^{\frac{2}{3}} . \tag{34}$$

Man erhält für die Schmierfilmstärke aus den Gleichungen (11), (12), (15) und (34):

$$\delta = \delta_{00} \sqrt[3]{\left[1 - \left(\frac{r}{a}\right)^2\right](1-\varepsilon)}. \tag{35}$$

Die Differentiation der Gleichung (19) erfolgt mit Hilfe der Gleichungen (25) und (35); vorerst erhält man aus Gleichungen (19) und (25):

$$\frac{d\sigma_1}{dr} = \psi k_f \frac{1}{y}\left\{\frac{dy}{dr}\right\} - \left\{\left[\frac{dp}{dr}\,\frac{\delta}{2} - \frac{\eta r v_y}{2\,h\delta}\right]\left[1 - \left(\frac{dy}{dr}\right)^2\right]\right\}\frac{1}{y}\,. \tag{36}$$

Mit Rücksicht darauf, daß φ klein ist, kann man als Annäherung: $d\sigma_1/dr \sim$ $\sim dp/dr$ und $1 + (dy/dr)^2 \sim 1$ voraussetzen; hiedurch ergibt sich aus Gleichung (36):

$$\frac{d\sigma_1}{dr} = \psi k_f \frac{1}{y}\left[\frac{dy}{dr}\right] - \left[\frac{1}{y}\cdot\frac{d\sigma_1}{dr}\cdot\frac{\delta}{2}\right] + \left[\frac{\eta}{\delta}\cdot\frac{r}{2h}\cdot\frac{1}{y}\,v_y\right]. \tag{37}$$

Da δ neben $h/2$ vernachlässigbar ist, ergibt sich aus Gleichungen (20) und (37):

$$\frac{d\sigma_1}{dr}\left(1 + \frac{\delta}{2y}\right) = -\psi k_f \frac{2}{h}\frac{d\delta}{dr} + \frac{\eta r}{\delta h^2}\,v_y. \tag{38}$$

Mit $1 + \delta/2h \sim 1$ erhalten wir aus Gleichung (38):

$$\frac{d\sigma_1}{dr} = -\psi k_f \frac{2}{h}\frac{d\delta}{dr} + \frac{\eta r}{\delta h^2}\,v_y. \tag{39}$$

Durch Integration der Gleichung (39) von r_0 bis r_q ergibt sich:

$$\sigma_q - \sigma = -\psi k_f \frac{2\,(\delta_q - \delta)}{h} + \int_r^{r_q} \frac{\eta r}{\delta h^2}\,v_y\,dr\,. \tag{40}$$

Für die Spannungsverteilung erhält man aus Gleichung (40) mit Hilfe der Gleichungen (25), (27) und (35)

$$\begin{aligned}\sigma' = \sigma_q - \psi k_f \Bigg[& 2\,\frac{\delta_{00}}{h_0}\cdot\frac{1}{(1-\varepsilon)^{\frac{2}{3}}}\,(X - X_q) - \\ & - \frac{1}{4}\,\frac{\delta_{00}}{h_0}\Big)^2 \cdot \frac{1}{(1-\varepsilon)^{\frac{1}{3}}}\,(X^2 - X_q^2)\Bigg].\end{aligned} \tag{41}$$

Es ist zu bemerken, daß hier

$$X = \sqrt[3]{1 - \left(\frac{r}{a}\right)^2} \quad \text{und} \quad X_q = \sqrt[3]{1 - \left(\frac{r_q}{a}\right)^2} \tag{41a}$$

ist.

Die Funktionen X und X^2 sind aus dem Bilde 6 zu entnehmen.

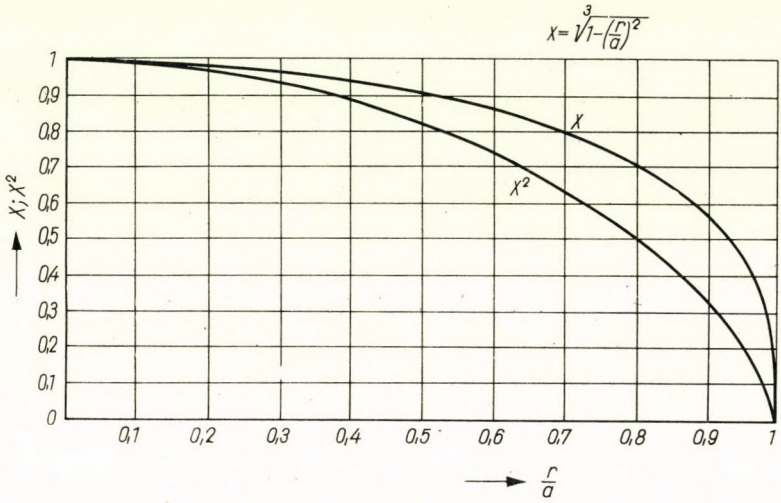

Bild 6

2. *Abschnitt der gemischten Reibung*

Mit Rücksicht darauf, daß im Bereiche $r_q \leqslant r \leqslant a$ die metallische Berührung eintritt, ist

$$y = \frac{h}{2}\,. \tag{42}$$

Bei Annahme der Coulombschen Reibungssatzes

$$\text{ist } \tau = \mu\sigma\,, \tag{43}$$

wobei noch zu bemerken ist, daß der Reibungskoeffizient auch von v_r abhängt. Aus den Gleichungen (19), (42) und (43) ergibt sich:

$$\frac{d\sigma_1}{dr} = -\frac{2\,\mu}{h}\,\sigma_1\,. \tag{44}$$

Nach Trennung der Veränderlichen und durch Integration der Gleichung (44) von r bis a erhält man für die Druckverteilung:

$$\sigma'' = \psi k_f \, e^{\frac{2\mu}{h}(a-r)}. \tag{45}$$

Also ist die Druckverteilung auf die einzelnen Flächengebiete

für $0 < r < r_q$ nach Gl. (41);

für $r_q < r < a$ nach Gl. (45)

zu bestimmen, wobei gemäß (13) und (15)

$$r_q = a \sqrt{1 - \left(\frac{h'_q + h''_q}{\delta_{00}}\right)^3}. \tag{46}$$

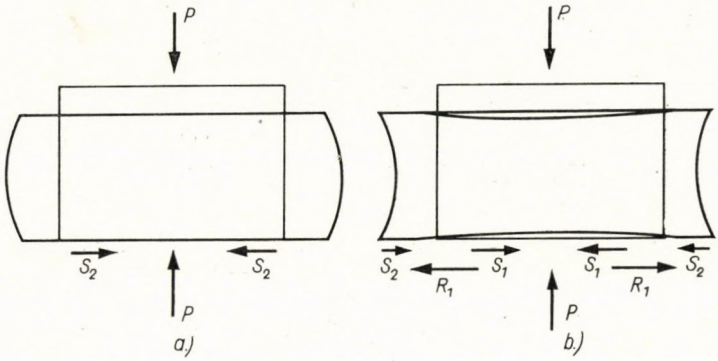

Bild 7

IV. Praktische Anwendung der Druckverteilung

Die oben abgeleitete Berechnungsmethode der Druckverteilung ist geeignet, andere, mit dem Druckversuch verknüpfte Fragen zu lösen bzw. klären. Vor allem sind wir in der Lage, die Ursache der Entstehung der Diabolo-Gestalt anzugeben. Wie dies aus dem Bilde 7 ersichtlich ist, wird unter dem Einfluß einer einzigen Reibungskraft S_2, welche gegen den Mittelpunkt des Körpers gerichtet ist, durch Stauchen nur ein faßförmig deformierter Probekörper entstehen. In der Zeichnung auf Bild 7b ist ein Fall zu sehen, wo sich an der Oberfläche ein tragfähiger Schmierfilm gebildet hat. Unter solchen Umständen wirkt auf die Stirnfläche eine der Bewegungsrichtung entgegen-

setzte und zum Körpermittelpunkt gerichtete Kraft, hervorgerufen durch die Ölreibung S_1, und die gemischte Reibung S_2. Vom Mittelpunkt nach außen gerichtet wirkt infolge der Oberflächenkrümmung, in Übereinstimmung mit der Bewegungsrichtung, die Kraft R_1. Ist nun die Resultante der drei Kräfte nach dem Mittelpunkt gerichtet, so entsteht ein faßförmiger Körper; ist die Resultante gleich Null, so behält der Körper seine gerade Gestalt; wirkt die Resultante nach außen, so erhält der Körper die Diabolo-Gestalt. Der gesamte Verlauf ist selbstredend ziemlich kompliziert, da während des Stauchvorganges die Richtung der Resultante sich ändern kann.

Ferner kann man nun mit Hilfe der Druckverteilung die Werte der wirkenden Druckkraft, die relative Abweichung während der Messung der Verformungsfestigkeit und die Bedingungen des monoaxialen Spannungszustandes bestimmen.

1. Die wirkende Druckkraft

Man erhält die Druckkraft durch Integration der die Druckkraft bestimmenden Gleichungen;

$$P = \int_0^{r_q} 2\, r\pi\sigma'\, dr + \int_{r_q}^{a} 2\, r\pi\sigma''\, dr. \tag{47}$$

Das erste Integral-Glied läßt sich mit Hilfe der Gleichung (41) ausdrücken:

$$\int_0^{r_q} 2r\,\pi\sigma'\, dr = r_q^2\,\pi\,(\sigma_q + A_1) - a^2\,\pi\psi k_f \left[4\,\frac{\delta_{00}}{h_0}\,\frac{1}{(1-\varepsilon)^{\frac{2}{3}}}\, C_1 + \right. \\ \left. + \frac{1}{2}\left(\frac{\delta_{00}}{h_0}\right)^2 \frac{1}{(1-\varepsilon)^{\frac{1}{3}}}\, C_2 \right], \tag{48}$$

$$\sigma_q = \psi k_f\, e^{\frac{2\,\mu}{h}(a - r_q)}, \tag{48a}$$

$$A_1 = \psi k_f \left[2\,\frac{\delta_{00}}{h_0}\,\frac{1}{(1-\varepsilon)^{\frac{2}{3}}}\, X_q - \frac{1}{4}\left(\frac{\delta_{00}}{h_0}\right)^2 \frac{1}{(1-\varepsilon)^{\frac{1}{3}}}\, X_q^2 \right]; \tag{48b}$$

$$C_1 = \int_0^{r_q/a} \frac{r}{a} \sqrt[3]{1 - \left(\frac{r}{a}\right)^2}\, d\left(\frac{r}{a}\right), \tag{48c}$$

$$C_2 = \int_0^{r_q/a} \frac{r}{a} \left(\sqrt[3]{1 - \left(\frac{r}{a}\right)^2} \right)^2 d\left(\frac{r}{a}\right). \tag{48d}$$

Die obigen Werte C_1 und C_2 ergeben sich also durch Integration. Im Bilde 8 findet man diese Werte als Funktion des Quotienten $(h'_q + h''_q)/\delta_{00}$. Auf

Grund von (45) läßt sich das zweite Integral-Glied in Gleichung (47) ausdrücken:

$$\int_{r_q}^{a} 2\, r\pi\sigma'\, dr = \psi k_f\, a^2 \pi \frac{h^2}{\mu^2 a^2} \left[\left(\frac{\mu r_q}{h} + \frac{1}{2} \right) e^{2\frac{\mu a}{h}\left(1 - \frac{r_q}{a}\right)} - \left(\frac{\mu a}{h} + \frac{1}{2} \right) \right]. \quad (49)$$

Also ergibt sich die totale Druckkraft als die Summe der Teilkräfte gemäß

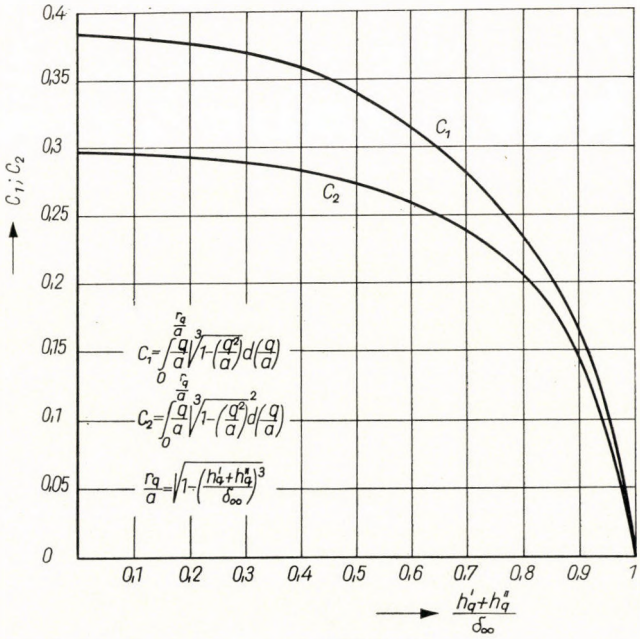

Bild 8

(48) und (49). Auch läßt sich die totale Druckkraft mit Hilfe des Umformwiderstandes k_K ausdrücken:

$$P = a^2 \pi k_K, \quad (50)$$

wobei sich der Verformungswiderstand aus den Gleichungen (48), (49) und (50) mit Hilfe von (27) und (28) folgenderweise anschreiben läßt:

$$\begin{aligned} k_K = {} & \left(\frac{r_q}{a}\right)^2 (\sigma_q + A_1) - \psi k_f \left[4 \frac{\delta_{00}}{h_0} \frac{1}{(1-\varepsilon)^{\frac{2}{3}}} C_1 + \right. \\ & \left. + \frac{1}{2} \left(\frac{\delta_{00}}{h_0}\right)^2 \frac{1}{(1-\varepsilon)^{\frac{1}{3}}} C_2 \right] + \psi k_f \left(\frac{h_0}{\mu a_0}\right)^2 (1-\varepsilon)^3 \times \\ & \times \left[\left(\frac{\mu a_0}{h_0} \frac{r_q}{a} \frac{1}{(1-\varepsilon)^{\frac{3}{2}}} + \frac{1}{2} \right) e^{2\frac{\mu a_0}{h_0} \frac{1}{(1-\varepsilon)^{3/2}} \left(1 - \frac{r_q}{a}\right)} - \right. \\ & \left. - \left(\frac{\mu a_0}{h_0} \frac{1}{(1-\varepsilon)^{\frac{3}{2}}} + \frac{1}{2} \right) \right]. \end{aligned} \quad (51)$$

Nun ist der Ausdruck $\delta_{00}/h_0 \leqslant 10^{-1}$, und folglich kann dessen Quadrat unbeachtet bleiben, und so erhält man aus den Gleichungen (48b) und (51) nach entsprechenden Umordnen:

$$k_K = \psi k_f \left\{ 2 \frac{\delta_{00}}{h_0} \frac{1}{(1+\varepsilon)^{2/3}} \left[X_q \left(\frac{r_q}{a} \right)^2 - 2 C_1 \right] + \right.$$

$$+ \left(\frac{r_q}{a} \right)^2 e^{\frac{2\mu a_0}{h_0} \frac{1}{(1-\varepsilon)^{3/2}} \left(1 - \frac{r_q}{a}\right)} + \frac{h_0}{\mu a_0} (1-\varepsilon)^3 \left[\left(\frac{\mu a_0}{h_0} \frac{r_q}{a} \frac{1}{(1-\varepsilon)^{3/2}} + \frac{1}{2} \right) \cdot \right.$$

$$\left. \left. \cdot e^{\frac{2\mu a_0}{h_0} \frac{1}{(1-\varepsilon)^{3/2}} \left(1 - \frac{r_q}{a}\right)} - \left(\frac{\mu a_0}{h_0} \frac{1}{(1-\varepsilon)^{3/2}} + \frac{1}{2} \right) \right] \right\}. \tag{52}$$

Die Summe aus dem zweiten und dritten Gliede der Gleichung (52) ist gleich der Höhe eines zylindrischen Körpers, dessen Volumen dem Volumen des im Bilde 9 dargestellten räumlichen Spannungsgebildes entspricht. In Wirklichkeit ist der Reibungskoeffizient als Funktion von r unbekannt, dessen Wert nur nach gewissen Vereinfachungen geschätzt werden kann. Setzt man also an Stelle der Gleichung (48a) die entsprechende Taylorsche Reihe, und zieht man davon nur die ersten zwei Glieder in Rechnung, so erhält man für die Spannungsverteilung zwischen $r_q \leqslant r \leqslant a$ einen annäherungsweisen Ausdruck. In dieser Weise erhält man für den Verformungswiderstand (mit Hilfe der laut Bild 9 giltigen mittleren Höhe):

$$k_K = \psi k_f \left\{ 1 - 2 \frac{\delta_{00}}{h_0} \frac{1}{(1-\varepsilon)^{2/3}} \underbrace{\left[2 C_1 - X_q \left(\frac{r_q}{a} \right)^2 \right]}_{C_3} + \right.$$

$$\left. + \frac{1}{2} \frac{\mu a_0}{h_0} \frac{1}{(1+\varepsilon)^{3/2}} \underbrace{\left(1 + \frac{r_q}{a} \right) \left[1 - \left(\frac{r_q}{a} \right)^2 \right]}_{C_4} \right\}, \tag{53}$$

wobei für C_3 und C_4 die Funktionswerte aus Bild 10 entnommen werden können.

2. Die relative Abweichung des Verformungswiderstandes k_K von der Verformungsfestigkeit k_f

Die relative Abweichung ist:

$$\nu = \frac{k_k - k_f}{k_f} = \frac{k_k}{k_f} - 1. \tag{54}$$

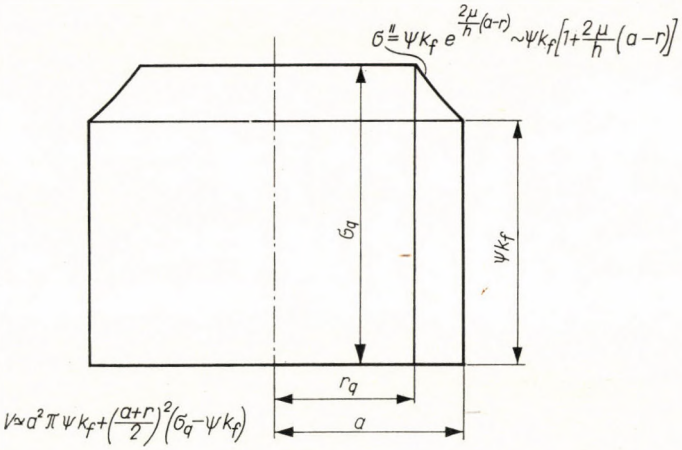

Bild 9

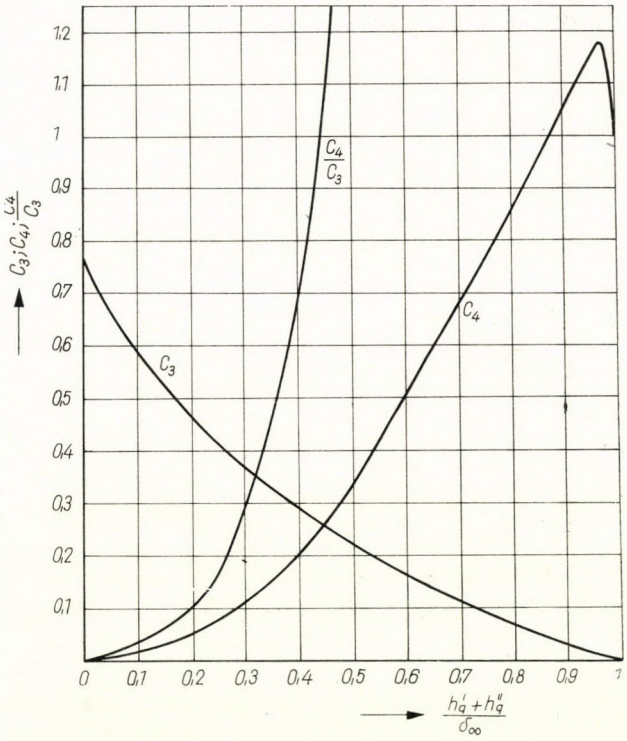

Bild 10

Mit Hilfe der Gleichung (53) erhält man aus (54):

$$\nu = -2\frac{\delta_{00}}{h_0}\frac{1}{(1-\varepsilon)^{2/3}}C_3 + \frac{1}{2}\frac{\mu a_0}{h_0}\frac{1}{(1-\varepsilon)^{3/2}}C_4 . \tag{55}$$

3. *Grundbedingung des monoaxialen Spannungszustandes*

Wie dies aus dem Sinn der Gleichung (55) hervorgeht, ist die relative Abweichung eine Funktion des Maßes der Deformation. Wenn man also die unter gleichen Umständen durchgeführten Stauchproben in Betracht zieht, so muß man sich darüber klar sein, daß sich die monoaxiale Spannung nur bei einem bestimmten Maß der Verformung einstellt. Da aber die relative Abweichung solange einen negativen Wert annimmt, bis schließlich der durch Gleichung (47) bestimmte Verformungsgrad erreicht wird, so muß der Preßkörper bei der der monoaxialen Spannung entsprechenden (prozentualen) Deformation immer in eine Diabolo-Gestalt umgeformt werden. Dies entspricht vollauf den experimentellen Erfahrungen.

Mit $\nu = 0$ ergibt sich aus Gleichung (55):

$$\delta_{00} = \frac{1}{4}\mu a_0 \frac{C_4}{C_3} C_5 , \tag{56}$$

wo

$$C_5 = \frac{1}{(1-\varepsilon)^{5/6}}$$

ist.

Wenn nun der Deformationsgrad gesteigert wird, erhält die relative Abweichung einen positiven Wert, der Probekörper beginnt die Diabolo-Form zu verlieren und allmählich in eine faßähnliche Gestalt zu übergehen.

Die Grundbedingung dafür, daß der Probekörper bei einem gewissen Deformationsgrad die gerade Gestalt beibehalten soll, läßt sich annäherungsweise folgenderweise bestimmen: $\nu_{(\varepsilon=0)} = \nu_{(\varepsilon)}$.

Aus Gleichung (55) wird der Probekörper bei einem gewissen $\varepsilon\%$ seine gerade Gestalt behalten, falls:

$$\delta_{00} = \frac{1}{4}\mu a_0 \frac{C_4}{C_3} C_6$$

ist, wo

$$C_6 = \frac{1 + \dfrac{1}{(1-\varepsilon)^{2/2}}}{1 + \dfrac{1}{(1-\varepsilon)^{2/3}}} \tag{57}$$

ist.

Die Größe C_4/C_3 ist aus dem Bilde 10 als Funktion von $(h'_q + h''_q)/\delta_{00}$ zu entnehmen; die Größen C_5 und C_6 lassen sich aus Bild 11 als Funktionen von $\varepsilon\%$ bestimmen. Bei Benützung des Diagrammes im Bilde 10 muß man in Betracht ziehen, daß an der Stelle, wo $(h'_q + h''_q)$ den Wert Null annimmt, der Rechnungsgang der Funktion C_4/C_3 einer Berichtigung (Korrektion) unter-

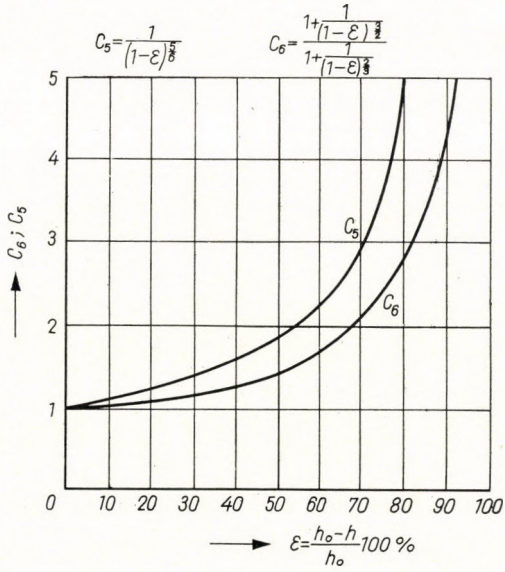

Bild 11

zogen werden muß, da man in diesem Falle in Gleichung (48) das Glied mit der Funktion C_2 nicht mehr vernachlässigen kann.

So geht es aus den Gleichungen (56) und (57) klar hervor, daß bei einem gegebenen Verformungsgrad der monoaxiale Spannungszustand und die gerade Gestalt des Probekörpers niemals gleichzeitig vorkommen können.

SCHRIFTTUM

1. Geleji, A.: Bildsame Formung der Metalle in Rechnung und Versuch. Berlin 1960.
2. Fuller, D.: Theory and Practice of Lubrication for Engineers. New-York—London 1956.
3. Jaoul, B.—Séjournet, J.: Lubrification de la déformation à chaud des métaux. *Métaux, Corrosion, Industries* (1959), 221—235.

THE INFLUENCE OF LUBRICANTS ON THE DEFORMATION OF A COMPRESSION TEST PIECE

L. TÓTH

SUMMARY

The problem of deformation of a compression test piece is discussed on the basis of lubricated parallel faces. The phenomenon of a test piece when its originally cylindrical shape is changed into a convex one (forming two inverted tapers like a "diabolo") is ascribed to plastic deformation of the faces under pressure. Author gives a system of formulae relating to the interdependence between the pressure distribution on the face, the effective compressive force and the deviation observed between shaping strength and shaping resistance. The influence of the shaping grade is given in accordance with practical observations. In this connection it is stated that monoaxial deformation as well as monoaxial stress condition is bound to only a special grade of shaping. Formulae are found in order to determine the approximative value of the deformation grades in question.

L'INFLUENCE DE LA LUBRIFICATION DANS LE GONFLEMENT DES MÉTAUX

L. TÓTH

RÉSUMÉ

L'auteur traite du gonflement par plaques parallèles des corps lubrifiés sur leur surface frontale. La formation d'éprouvettes en forme de deux cônes superposés par leur sommet est expliquée par la déformation de la surface frontale du matériau comprimé. Pour la distribution des pressions agissant sur la surface frontale, la force de pression effective et l'écart existant entre la résistance à la déformation et la tension de déformation, des relations numériques sont présentées par l'auteur. L'influence du degré de déformation est donnée en accord avec les données pratiques. A ce propos, l'auteur constate que la déformation monoaxiale aussi bien que l'état de contraintes monoaxial ne se produisent qu'à des degrés de déformation déterminés. La détermination approchée de ceux-ci peut se faire par les relations présentées en fin de l'étude.

ВЛИЯНИЕ СМАЗКИ ПРИ ВЫСАДКЕ МЕТАЛЛОВ

Л. ТОТ

РЕЗЮМЕ

Работа занимается вопросом высадки смазанных на лобовых поверхностях тел между параллельными плоскостями. Деформацией лобовой поверхности сжимаемого материала объясняется образование образцов в форме сдвоенного гиперболоида. Даются числовые зависимости распределения давления, действующего на лобовую поверхность, возникающего усилия сжатия и масштаба отклонения сопротивления деформации от прочности по отношению к деформации. Влияние степени деформации даются в согласии с практическими данными. В связи с этим устанавливается что как одноосная деформация, так и одноосное напряженное состояние возникают только при одной определенной степени деформации. В работе приведены зависимости для приближенного определения этих степеней деформации.

MOMENT CALCULATION OF CONTINUOUS REINFORCED CONCRETE BEAMS ON THREE SUPPORTS BY INTRODUCING ECONOMICAL CONDITION

Z. VISY
MINISTRY OF HOUSING AND PUBLIC CONSTRUCTION,
OFFICE FOR THE COORDINATION OF THE RESEARCHES

[Manuscript received September 2, 1963]

Developing J. PELIKÁN's method of moment distribution [1—4] the method described in the present paper extends the possibility of the application of the same over the field of continuous reinforced concrete beams on three supports, too. The precise solution of the problem is obtained by solving the system of nonlinear equations with four unknowns given under (2), (3), (4) and (5) or (8). From the view-point of practice the solution of the system of linear equations consisting of equations (21), (22), (23) and (24) or (25) also gives a satisfactorily approximate result. The as final result obtained extreme moment diagram makes the determination of the most economic reinforcement of the investigated reinforced concrete beams possible.

I. Introduction

For the calculation of continuous reinforced concrete beams subjected to a constant load J. PELIKÁN [1—4] introduced the condition

$$\int \frac{|M|}{h}\, ds = \text{Min.} \tag{1}$$

where M denotes the bending moment affecting the beam, h the depth of the cross-section of the beam, while ds the line element of the beam axis. Subsequently, for the investigation of details and general relations of the group of problems in question, in Hungary researches on a wider range were commenced. On the result of same a number of scientific publications issued during recent years are reported [5—9].

The investigation of cantilever beams on two supports and hinged continuous beams, furthermore, of arches subjected to a constant and occasional load, performed on the base of similar principles was also dealt with by A. GUERRIN in 1950 [10], where he also reported on interesting economic comparisons. Within the scope of this paper the author compared actually carried out bridge structures (1), with customary structures built for similar purposes, and established significant savings to the benefit of the former ones.

There is a fundamental difference between PELIKÁN's and GUERRIN's train of thoughts, namely :

a) PELIKÁN in addition to conditions of equilibrium introduces, instead of conditions of elasticity the condition of economy (1), and dealing with the problem in generality takes the loads and the reinforced concrete structure as a given whole excepting reinforcement.

b) GUERRIN on the other hand, upholding conditions of equilibrium and elasticity only deals with such individual cases for which the change of loads or occasionally of certain further important parameters of the beam (supports, location of hinges etc.), accidentally by changing both, a solution *also* satisfying condition (1) might be arrived at.

Based on PELIKÁN's sequence of thoughts and taking conditions introduced by him into consideration, the present paper gives the solution of continuous reinforced concrete beams on three supports, loaded by constant and occasional loads. For the beams in question the possibility of a partial load within the single spans can be disregarded. Consequently, the determination of the maximum moment diagram merely requires to subject the single spans, either only to the *constant*, or only to the *total* (constant and occasional) load.

The generalization of the method in question makes the solution of beams deviating from the introduced type of beam and loading on the base of a similar train of thought possible, too.

II. Determination of the Problem, Initial Conditions and Notations

The set task should be the determination of the moment diagram of the continuous reinforced concrete beam on three supports shown in Fig. 1a. The moment diagram sought for is presented in Fig. 1b.

In respect to the investigated reinforced concrete beam the following are assumed:

a) The outermost supports of same do not hinder the free rotation of the beam ends.

b) Furthermore, the beam has a rectangular cross section the width of which is constant along its whole length, while its depth (h) is constant within the single spans.

c) Finally, the constant loads (g) and occasional loads (p) extend over the whole length of the beam and have within the single spans the same intensity (g_1, g_2, p_1, p_2).

In connection with the maximum moment diagram to be produced stipulations given hereunder are to be satisfied:

a) Regarding the diagram as a whole it should satisfy the economic condition (1) along the whole length of the beam, i. e., the area of the diagram reduced by the value h should be minimal.

b) Furthermore, excepting the case of a partial load within the single spans, among the innumerable moment diagrams separately belonging to all possible loading cases, and separately satisfying conditions of equilibrium along the whole length of the beam, for each loading case at least one moment diagram should remain inside the area of the diagram of maximum moments in question.

For that particular joint of beam and loading data, in the case of which the enveloping curves of the diagram of the maximum moment (curves *I* and *II* in Fig 1b) do not intersect the closing line of the moment diagram or inter-

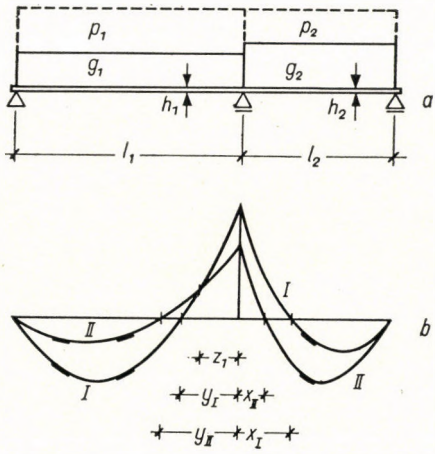

Fig. 1

sect each other below same, the method to be dealt with is, in its present form not utilizable.

In conformity with J. PELIKÁN's quoted paper [3], in the following investigations notations shown in Fig. 1 are to be used.

III. Precise Solution of the Problem

To obtain an accurate solution of the problem according to conditions specified in the previous paragraph, it is sufficient to take loading cases *I* and *II* — shown in Figs. 2a and 2b — into consideration. Namely, if moment distributions complying with these two loading cases separately satisfy the conditions of equilibrium along the whole length of the beam, then to any other load acting on the investigated continuous beam on three supports, at least one moment distribution can be attached which satisfies the conditions of equilibrium and remains inside the enveloping curves of the diagram of the maximal moment established on the base of moment distributions pertaining

to load cases *I* and *II*. In the case in question the above statement can also be proved by observation. Namely, the point of intersection of curves *I* and *II* lying in the vicinity of the intermediate support and above same, falls either above the left-hand or the right-hand span, or into the vertical running through the intermediate support. Owing to this, the curve pertaining to the total load can be drawn — in the extreme case — either on the left-hand or the right-hand side, and may be on both sides within the area of the diagram of maximum

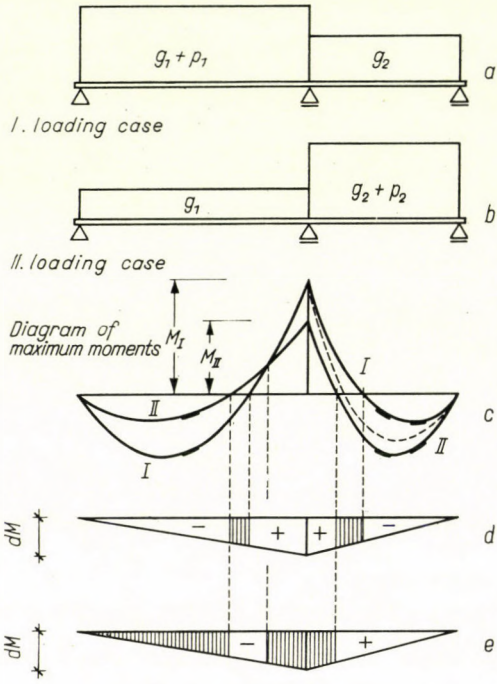

Fig. 2

moments. In Fig. 2c this curve is denoted by a dotted line. According to the above interpretation the enveloping curves belonging to the total load are in the left-hand span curve *I*, while in the right-hand span the parabola drawn with a dotted line. The joint of these two curves satisfies the conditions of equilibrium along the whole length of the beam.

In the investigations to come the distances between the zero-points of moments and the intermediate support belonging to both loading cases, i. e., distances x_I, x_{II}, y_I and y_{II} (see Fig. 1) are regarded as unknown. With the aid of these distances the so-called *load equations* (L_I and L_{II}) can be separately set up for both loading cases. These equations express the equality of support-moments set up as functions of the position of zero points situated on the left-

hand and right-hand side of the intermediate support. Accordingly, the load function L_I pertaining to the loading case I is:

$$L_I \equiv \frac{g_1 + p_1}{2} l_1 y_I = \frac{g_2}{2} l_2 x_I , \tag{2}$$

while the equation pertaining to the loading case II is

$$L_{II} \equiv \frac{g_1}{2} l_1 y_{II} = \frac{g_2 + p_2}{2} l_2 x_{II} . \tag{3}$$

In the following the satisfaction of condition (1) should be ensured with reference to the entire maximum moment diagram. Thus, in conformity with the closing line as well as with each other the two curves should be placed in such a way that the area enveloped by these curves reduced by the beam depth (h) should be the smallest.

If the maximum moment diagram satisfies the above conditions, then both, the displacement of the closing line by any infinitely small value dM and the displacement of the support moments by any infinitely small value dM in relation to each other increases and diminishes the area of the reduced moment diagram to the same degree, i. e., the amount of the so produced increments and diminutions coincides with each other. These conditions can also be set up in the form of equations. As these relations are independent of the load acting on the beam and express certain formal demands, they can expediently be called *form equations* (F_z and F_M).

Shifting the closing line at the place of the intermediate support downwards by dM, the area of the maximum moment diagram decreases by the negative area portions and increases by positive ones as is indicated in Fig. 2d. The magnitude of these area portions can be expressed by using notations to be found in Fig. 1, and can be reduced in the case of the left-hand span by h_1, while for the right-hand span by h_2. Taking the so reduced minute area portions into consideration, form equation F_z can be set up as follows:

$$F_z \equiv \left[\frac{dM}{h_1} + \frac{dM\,(l_1 - y_I)}{l_1\, h_1} \right] \frac{y_I}{2} - \frac{dM\,(l_1 - y_{II})^2}{2\, l_1\, h_1} + \\ + \left[\frac{dM}{h_2} + \frac{dM\,(l_2 - x_{II})}{l_2\, h_2} \right] \frac{x_{II}}{2} - \frac{dM\,(l_2 - x_I)^2}{2\, l_2\, h_2} = 0 . \tag{4}$$

On the other hand, altering the *position* of the two moment diagrams pertaining to the two loading cases and related to each other, e.g., by lessening the value of the support moment M_{II} by the value dM, then taking Fig. 2c and the interpretation given in connection with the setting up of form equation

F_z into consideration, the form equation F_M^* will take the following form:

$$F_M^* \equiv \frac{dM(l_2 - x_{II})^2}{2\,l_2\,h_2} - \left[\frac{dM(l_1 - y_{II})}{l_1\,h_1} + \frac{dM(l_1 - z_1)}{l_1\,h_1}\right]\frac{y_{II} - z_1}{2} = 0\,. \tag{5}$$

In the above equation

$$z_1 = \frac{g_1}{p_1}(y_I - y_{II}) + y_I\,. \tag{6}$$

The two *load equations* (L_I and L_{II}) set up under (2) and (3) as well as the two *form equations* (F_z and F_M^*) set up under (4) and (5) are necessary and exactly sufficient to make the solution of the problem in question possible, if the point of intersection of parabolas I and II is situated either according to Fig. 2, i.e., above the left-hand span or above the intermediate support. Expressed in other words the solution of the system of equations in question is right if the value z_1 computed from relation (6) satisfies the condition

$$z_1 \geqq 0\,. \tag{7}$$

If this condition is not fulfilled the point of intersection in question is situated above the right-hand span. In compliance with this fact equation (5) figuring in the system of equations, has to be replaced by the equation given hereunder, which expresses the actual situation:

$$F_M^{**} \equiv \frac{dM(l_1 - y_I)^2}{2\,l_1\,h_1} - \left[\frac{dM(l_2 - x_I)}{l_2\,h_2} + \frac{dM(l_2 - z_2)}{l_2\,h_2}\right]\frac{x_I - z_2}{2} = 0\,. \tag{8}$$

In the above equation

$$z_2 = \frac{g_2}{p_2}(x_{II} - x_I) + x_{II}\,. \tag{9}$$

Thus, the condition making the utilization of the form equation F_M^{**} set up under (8) possible is that the distance z_2 computed from relation (9) should satisfy the relation

$$z_2 \geqq 0\,. \tag{10}$$

Summing up the previous deductions, the accurate solution of the set problem is supplied by the following systems of nonlinear equations with four variables: for $z_1 \geqq 0$ by simultaneous equations L_I, L_{II}, F_z, F_M^*, while for $z_2 \geqq 0$ by simultaneous equations L_I, L_{II}, F_z, F_M^{**}.

Knowing the distances of the moment zero points from the intermediate support obtained as final result, the support moments M_I and M_{II}

sought for are obtained from the following equations:

$$M_I = -\frac{g_1 + p_1}{2} l_1 \cdot y_I = -\frac{g_2}{2} l_2 \cdot x_I . \tag{11}$$

$$M_{II} = -\frac{g_1}{2} l_1 \cdot y_{II} = -\frac{g_2 + p_2}{2} l_2 \cdot x_{II} . \tag{12}$$

Particular case

In the special case if

$$l_1 = l_2 = l, \quad h_1 = h_2 = h,$$

$$g_1 = g_2 = g, \quad p_1 = p_2 = p,$$

the accurate solution of the problem in question is given by the simple relations given hereunder:

$$y_I = x_{II} = \frac{k + 1 - \sqrt{2k}}{k^2 + 1} \cdot l , \tag{13}$$

$$y_{II} = x_I = k \cdot y_I = k \cdot x_{II} . \tag{14}$$

In the above relations

$$k = \frac{g + p}{g} . \tag{15}$$

IV. Approximate Solution of the Problem

As regards complications connected with the solution of nonlinear equations the application of the previously described accurate method generally meets with difficulties. Therefore, it is expedient to introduce an approximate method. This method based on the linearization of the load and form equation makes possible the optionally accurate solution of the problem by using either traditional methods or an electronic computer for this purpose.

For the sake of this purpose let us replace the unknowns (x_i, y_i) by their approximate values $(\bar{x}_i, \bar{y}_i)$, and the deviations of these approximate values from the accurate ones $(\Delta x_i, \Delta y_i)$, and disregard the products and squares of these deviations as small quantities of the second order. Accordingly, utilizing the relations

$$x_i = \bar{x}_i + \Delta x_i \quad \text{and} \quad y_i = \bar{y}_i + \Delta y_i ,$$

furthermore,

$$x_i^2 \cong \bar{x}_i^2 + 2\,\bar{x}_i\,\Delta x_i \quad \text{and} \quad y_i^2 \cong \bar{y}_i^2 + 2\,\bar{y}_i \cdot \Delta y_i\,,$$

finally

$$x_i\,y_i \cong \bar{x}_i\,\bar{y}_i + \bar{x}_i\,\Delta y_i + \bar{y}_i\,\Delta x_i$$

the linearized load equations ($\bar{L}$) and form equations ($\bar{F}$) can be written as follows:

$$\bar{L}_I \equiv g_2 \cdot l_2 \cdot \Delta x_I - (g_1 + p_1)\,l_1 \cdot \Delta y_I = (g_1 + p_1)\,l_1 \cdot \bar{y}_I - g_2 \cdot l_2 \cdot \bar{x}_I\,, \tag{16}$$

$$\bar{L}_{II} \equiv g_1 \cdot l_1 \cdot \Delta y_{II} - (g_2 + p_2)\,l_2 \cdot \Delta x_{II} = (g_2 + p_2)\,l_2 \cdot \bar{x}_{II} - g_1 \cdot l_1 \cdot \bar{y}_{II}\,, \tag{17}$$

$$\begin{aligned}\bar{F}_z \equiv{}& 2\,l_1\,h_1\,[(l_2 - \bar{x}_I)\,\Delta x_I + (l_2 - \bar{x}_{II})\,\Delta x_{II}] + \\ &+ 2\,l_2\,h_2\,[(l_1 - \bar{y}_I)\,\Delta y_I + (l_1 - \bar{y}_{II})\,\Delta y_{II}] = \\ ={}& l_1 \cdot h_1\,[(l_2 - \bar{x}_I)^2 - (2\,l_2 - \bar{x}_{II})\,\bar{x}_{II}] + l_2\,h_2\,[(l_1 - \bar{y}_I)^2 - (2\,l_1 - \bar{y}_{II})\,\bar{y}_{II}],\end{aligned} \tag{18}$$

$$\begin{aligned}\bar{F}_M^* \equiv{}& \frac{2\,l_1\,h_1\,(l_2 - \bar{x}_{II})}{1 + c_1}\,\Delta x_{II} - 2\,l_2\,h_2\,\{[l_1 - c_1\,(\bar{y}_I - \bar{y}_{II}) - \bar{y}_I]\,\Delta y_I - \\ &- [l_1 - c_1\,(\bar{y}_I - \bar{y}_{II}) - \bar{y}_{II}]\,\Delta y_{II}\} = \frac{l_1\,h_1\,(l_2 - \bar{x}_{II})^2}{1 + c_1} - \\ &- l_2\,h_2\,[c_1(\bar{y}_I - \bar{y}_{II})^2 + \bar{y}_I^2 - \bar{y}_{II}^2 - 2\,l_1\,(\bar{y}_I - \bar{y}_{II})]\,,\end{aligned} \tag{19}$$

$$\begin{aligned}\bar{F}_M^{**} \equiv{}& \frac{2\,l_2\,h_2\,(l_1 - \bar{y}_I)}{1 + c_2}\,\Delta y_I - 2\,l_1\,h_1\,\{[l_2 - c_2\,(\bar{x}_{II} - \bar{x}_I) - \bar{x}_{II}]\,\Delta x_{II} - \\ &- [l_2 - c_2\,(\bar{x}_{II} - \bar{x}_I) - \bar{x}_I]\,\Delta x_I\} = \frac{l_2\,h_2\,(l_1 - \bar{y}_I)^2}{1 + c_2} - \\ &- l_1\,h_1\,[c_2\,(\bar{x}_{II} - \bar{x}_I)^2 + \bar{x}_{II}^2 - \bar{x}_I^2 - 2\,l_2\,(\bar{x}_{II} - \bar{x}_I)]\,.\end{aligned} \tag{20}$$

In the above equations

$$c_1 = \frac{g_1}{p_1} \quad \text{and} \quad c_2 = \frac{g_2}{p_2}\,.$$

The conditions referring to the possibility of utilizing form equations $\bar{F}_M^*$ and $\bar{F}_M^{**}$ coincide with those given in the description of the accurate method.

In the first step it is expedient to assume the approximate value of the distances between the zero points and the intermediate support as in both spans being equal to those distances which in the case of a beam firmly clamped at the intermediate support would satisfy the initial conditions set up in respect to the diagram of maximum moments. As owing to the above assumption the equilibrium of support moments related to the whole beam

is not a demand any longer, and as in this case condition (1) can be satisfied independently of the load intensity [1—4], the advantage also arises that two by two of the assumed approximate values being identical, the system of equations in question can be set up in an exceedingly simple form.

Introducing on the basis of the above explanations the approximate values

$$\bar{x}_{I1} = \bar{x}_{II1} = \frac{2-\sqrt{2}}{2} l_2$$

and

$$\bar{y}_{I1} = \bar{y}_{II1} = \frac{2-\sqrt{2}}{2} l_1$$

equations (16), (17), (18), (19) and (20) take the following form:

$$\bar{L}_{I1} \equiv g_2 l_2 \cdot \Delta x_I - (g_1 + p_1) l_1 \cdot \Delta y_I =$$

$$= \frac{2-\sqrt{2}}{2} [(g_1 + p_1) l_1^2 - g_2 l_2^2] , \tag{21}$$

$$\bar{L}_{II1} \equiv g_1 l_1 \Delta y_{II} - (g_2 + p_2) l_2 \Delta x_{II} =$$

$$= \frac{2-\sqrt{2}}{2} [(g_2 + p_2) l_2^2 - g_1 l_1^2] \tag{22}$$

$$\bar{F}_{z1} \equiv h_1 (\Delta x_I + \Delta x_{II}) + h_2 (\Delta y_I + \Delta y_{II}) = 0 , \tag{23}$$

$$\bar{F}^*_{M1} \equiv h_1 \Delta x_{II} - h_2 (1 + c_1)(\Delta y_I - \Delta y_{II}) = \frac{l_2 h_1}{2\sqrt{2}} , \tag{24}$$

$$\bar{F}^{**}_{M1} \equiv h_2 \Delta y_I - h_1 (1 + c_2) (\Delta x_{II} - \Delta x_I) = \frac{l_1 h_2}{2\sqrt{2}} . \tag{25}$$

Merely the solution of the above system of equations gives, regarded from the view point of practice, in general, a sufficiently accurate result. The so obtained values Δx_I, Δx_{II}, Δy_I and Δy_{II} have to be algebraically added to the assumed approximate values $\bar{x}_I, \bar{x}_{II}, \bar{y}_I, \bar{y}_{II}$ and then the support moments are to be computed from relations (11) and (12), taking the rectified values $x_I = x_I + \Delta x_I$ etc. into consideration.

Of course, there is no obstacle in taking the zero point distances obtained in the above described way as first approximation again as approximate values, and to solve again and again the system of linear equations consisting of equations (16), (17), (18) and (19) or (20). By so doing the accuracy of the computation can be increased to the desired degree.

V. Comments on the Practical Application

In the previous discussions the possibility referring to the selection of the proper equation between equation F_M^* and F_M^{**} was not dealt with yet. This is important because a badly chosen selection might make a repetition of the whole computation necessary. To eliminate this danger it is expedient to try — before the beginning of the computation — to draw the diagram of reduced moments in such a way that the total area of this diagram should be seemingly minimal. On the basis of such a diagram an equation close to the right one can be introduced already at the beginning. In such a case, but even if the aforementioned preparations were neglected, the computation should be directed so that first the values y_I and y_{II} (if using equation F_M^*) or the values x_I and x_{II} (if using equation F_M^{**}) are determined. Namely, knowing these values the sign of z_1 or z_2 can be settled, thus, the necessity of an occasional "reversion" might become perceptible in due time.

When applying the method dealt with in practice, the principle to be kept in mind is that the diagram of maximum moments being the base of dimensioning in the vicinity of the positive maximum moment should not conduce to the development of primary plastic zones.

VI. Numerical Example

The task should be the determination of the diagram of maximum moments of the continuous reinforced concrete beam on three supports shown in Fig. 3a, by using the approximate method dealt with for this purpose.

The data referring to the beam and load acting on same can be substituted into relations (21), (22), (23) and (25) because owing to the reduced moment diagram outlined on the base of previous trials, the intersection of parabolas I and II above the right-hand span became probable. Accordingly:

$$\overline{L}_{I1} \equiv 1 \cdot 4 \cdot \Delta x_I - (2+2)4 \cdot \Delta y_I = \frac{2-\sqrt{2}}{2}\,[(2+2)4^2 - 1 \cdot 4^2]\,,$$

$$\overline{L}_{II1} \equiv 2 \cdot 4 \cdot \Delta y_{II} - (1+1)4 \cdot \Delta x_{II} = \frac{2-\sqrt{2}}{2}\,[(1+1)4^2 - 2 \cdot 4^2]\,,$$

$$\overline{F}_{z1} \equiv 2\,(\Delta x_I + \Delta x_{II}) + 1\,(\Delta y_I + \Delta y_{II}) = 0\,,$$

$$\overline{F}_{M1}^{*,*} \equiv 1 \cdot \Delta y_I - 2\,(1+1)\,(\Delta x_{II} - \Delta x_I) = \frac{4 \cdot 1}{2 \cdot \sqrt{2}}\,.$$

Solving the above system of equations:

$$\Delta x_I \cong 0.478 \text{ m}\,, \qquad \Delta y_I \cong -0.760 \text{ m}\,,$$

$$\Delta x_{II} \cong -0.066 \text{ m}\,, \quad \Delta y_{II} \cong -0.066 \text{ m}\,.$$

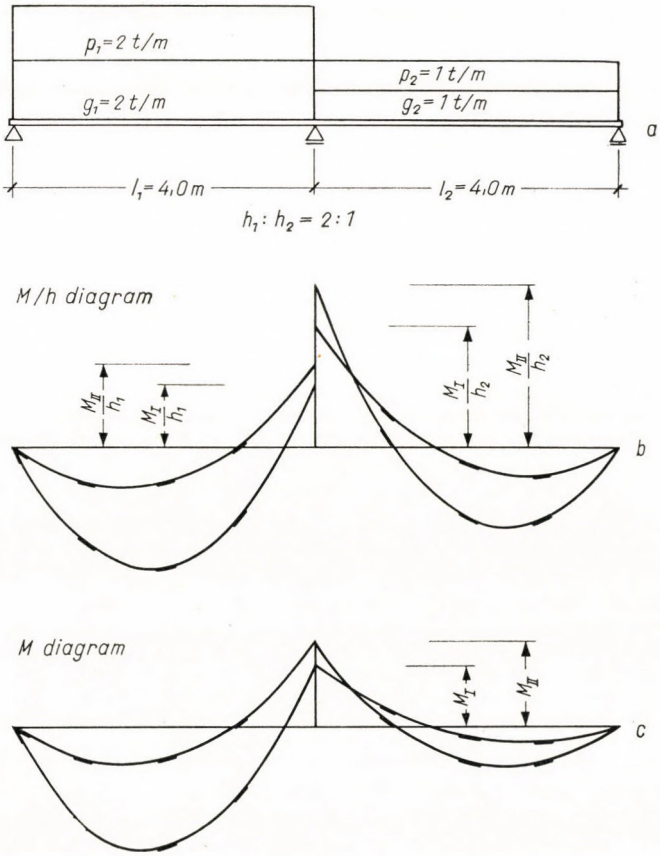

Fig. 3

Algebraically summing up the above values and the approximate values in the system of equations taken into consideration:

$$x_I \cong \frac{2-\sqrt{2}}{2}\,4 + 0.478 = 1.650 \text{ m},$$

$$x_{II} \cong \frac{2-\sqrt{2}}{2}\,4 - 0.066 = 1.106 \text{ m},$$

$$y_I \cong \frac{2-\sqrt{2}}{2}\,4 - 0.760 = 0.412 \text{ m},$$

$$y_{II} \cong \frac{2-\sqrt{2}}{2}\,4 - 0.066 = 1.106 \text{ m}.$$

Checking the sign of z_2 by usign the above values:

$$z_2 = \frac{1}{1}(1.106 - 1.650) + 1.106 = +0.562 \text{ m},$$

thus, our assumption proved to be right.

Knowing the zero point distances the values of support moment computed from relations (11) and (12) are in the first approximation:

$$\overline{M}_I = -\frac{2+2}{2} 4 \cdot 0.412 = -\frac{1}{2} 4 \cdot 1.650 \cong 3.300 \text{ tm},$$

$$\overline{M}_{II} = -\frac{2}{2} 4 \cdot 1.106 = -\frac{1+1}{2} 4 \cdot 1.106 \cong -4.424 \text{ tm}.$$

The diagram of maximum moments of the investigated beam is shown in Fig. 3c.

REFERENCES

1. PELIKÁN, J.: Többtámaszú, nyílásonként egyenletesen megoszló teherrel terhelt vasbetontartók plasztikus nyomatékszámítása (Plastic Calculation of Moments of Continuous Reinforced Concrete Beams Loaded Span by Span with Uniformly Distributed Loads). *Az Építőipari és Közlekedési Műszaki Egyetem Tudományos Ülésszakának Előadásai* (1955), 345—350.
2. PELIKÁN, J.: The Plastic Calculation of Moments on Continuous Reinforced Concrete Beams, *Acta Techn. Hung.* **15** (1956), 373—380.
3. PELIKÁN, J.: Theory of Highly Economical Reinforced Concrete Beams. *Acta Techn. Hung.* **17** (1957), 39—56.
4. PELIKÁN, J.: A többtámaszú vasbetontartók új elmélete (The New Theory of Continuous Reinforced Concrete Beams). *Építés- és Közlekedéstudományi Közlemények* **1** (1957), 275—284.
5. VISY, Z.: Fokozatosan közelítő eljárás többtámaszú vasbetontartók nyomatékszámítására (Gradually Approaching Method for the Calculation of Continuous Reinforced Concrete Beams). *Építés és Közlekedéstudományi Közlemények* **1** (1957), 285—293.
6. VISY, Z.: Iterative Method for the Calculation of Moments on Highly Economical Reinforced Concrete Beams). *Acta Techn. Hung.* **22** (1958), 12—26.
7. PEREDY, J.: Über eine neue Minimumaufgabe der technischen Festigkeitslehre. *Acta Techn. Hung.* **24** (1959), 329—346.
8. PEREDY, J.: Die Planung wirtschaftlicher Tragwerke. *Acta Techn. Hung.* **29** (1960), 251—273.
9. PEREDY, J.: Wirtschaftliche, statisch unbestimmte Konstruktionen. *Acta Techn. Hung.* **31** (1960), 285—309.
10. GUERRIN, A.: Utilization de la notion de "surface minimum de la courbe enveloppe des moments fléchissants" à la recherche des structure economique. *Travaux* (1950), Novembre, 739—761.

DIE BERECHNUNG DER MOMENTE VON STAHLBETON-DURCHLAUFTRÄGERN AUF DREI STÜTZEN UNTER DER EINFÜHRUNG DER WIRTSCHAFTLICHKEITSBEDINGUNG

Z. VISY

ZUSAMMENFASSUNG

Die im Aufsatz behandelte Methode bedeutet eine Weiterentwicklung des PELIKÁN-schen Momentenberechnungsverfahrens, wodurch dessen Anwendungsmöglichkeit auch auf das Gebiet der durch ständige und veränderliche Belastungen beanspruchten Stahlbeton-Durchlaufträger auf drei Stützen ausgebreitet wird. Die genaue Lösung des Problems liefert das nichtlineare Gleichungssystem mit vier Unbekannten das aus den Gleichungen (2), (3),(4) und (5) oder (8) besteht. Eine vom Gesichtspunkte der Praxis aus betrachtet befriedigende Annäherung liefert auch die Lösung des aus den Gleichungen (21), (22), (23) und (24) oder (25) bestehenden linearen Gleichungssystems. Das als Endergebnis erhaltene Diagram der Maximalmomente ermöglicht die Bestimmung des wirtschaftlichsten Stahlbedarfes der untersuchten Stahlbetonträger.

CALCUL DES MOMENTS DES POUTRES A TROIS APPUIS AVEC INTRODUCTION DE LA CONDITION D'ÉCONOMIE

Z. VISY

RÉSUMÉ

La méthode décrite développant le procédé de calcul des moments de *J. Pelikán* (1—4), en élargit le domaine d'application aux poutres en béton armé à trois appuis soumises à des charges réparties permanentes et accidentelles. La solution exacte du problème est donnée par le système d'équations non linéaires à quatre inconnues (2), (3), (4) et (5) ou (8). Une approximation pratiquement satisfaisante est fournie également par la solution du système d'équations linéaires formé des équations (21), (22), (23) et (24) ou (25). Le diagramme des moments extrêmes obtenu comme résultat définitif permet un maximum d'économie dans l'utilisation de l'acier pour les poutres en béton armé examinées par l'auteur.

РАСЧЕТ МОМЕНТА ТРЕХОПОРНЫХ ЖЕЛЕЗОБЕТОННЫХ БАЛОК, НАГРУЖЕННЫХ ПОСТОЯННОЙ И ВРЕМЕННОЙ НАГРУЗКАМИ, С ВВЕДЕНИЕМ УСЛОВИЯ ЭКОНОМИЧНОСТИ

З. ВИШИ

РЕЗЮМЕ

Излагаемый в работе метод усовершенствует метод Й. Пеликан, касающийся расчета момента (1—4), расширяет его применимость к трехопорным железобетонным балкам, нагруженным постоянными и временными распределяющимися нагрузками. Точное решение задачи дают системы нелинейных уравнений с четырьмя неизвестными, приведенные в (2), (3), (4) и (5) или же (8). Удовлетворительное с точки зрения практики приближение дает решение системы линейных уравнений, состоящих из уравнений, обозначенных через (21), (22), (23) и (24) или (25). Полученная в результате крайняя эпюра моментов позволяет осуществить наиболее экономичное использование арматуры железобетонных балок.

UNTERSUCHUNG DES MASSSTABEFFEKTES DER KAVITATIONSEROSION*

J. VARGA GY. SEBESTYÉN
TECHNISCHE UNIVERSITÄT BUDAPEST

K. K. SCHALNEW B. A. TSCHERNAWSKIJ
INSTITUT FÜR MECHANIK DER AKADEMIE DER WISSENSCHAFTEN DER UDSSR, MOSKAU

[Eingegangen am 23. November, 1963]

Die vorliegende Studie gibt außer der Darstellung der bisherigen Ergebnisse eine Übersicht über die Fragen der Methodik, auf deren Grund die Untersuchung des Maßstabeffektes der Kavitationserosion im Rahmen eines gemeinsamen Forschungsprogramms im Mechanischen Institut der Akademie der Wissenschaften der Sowjetunion und von der Strömungstechnischen Arbeitsgemeinschaft der Ungarischen Akademie der Wissenschaften am Lehrstuhl für Wasserkraftmaschinen der Technischen Universität Budapest, durchgeführt wird. Es wird eine kritische Beleuchtung der prinzipiellen Grundlagen der auf den energetischen Parameter des Maßstabeffektes fußenden Methoden der Forschungsarbeiten im Laboratorium gegeben. Die Studie beschreibt die Versuchseinrichtungen und erläutert die Bedingungen, mit deren Hilfe die Bestimmung des energetischen Parameters und der Kriterien der Ähnlichkeit erfolgt. Es werden die möglichen Fehler der Meßwerte und der Fehlereinfluß im Hinblick auf die Endergebnisse der Versuche analysiert. Es wird gezeigt, daß die Ergebnisse der an der Technischen Universität Budapest durchgeführten Versuche die früher gewonnenen Versuchsergebnisse bestätigen, und damit die Gültigkeit des Zusammenhanges der Maßstabeffekt-Beschreibung auch für einen breiteren Bereich aufzeigen.

I. Einführung

Während des Betriebs von Wasserkraftmaschinen und hydraulischen Einrichtungen kann oft ein Zustand eintreten, bei dem sie eine längere oder kürzere Zeit in einem Kavitationszustand im Betrieb gehalten werden müssen, oder bei dem in der Maschine lokale Kavitation auftritt. Sofern man diesen Umstand bei der Auswahl des Konstruktionsmaterials nicht genügend berücksichtigt, so können schwere Beschädigungen auftreten, die auch die Zerstörung der ganzen Maschine verursachen können. Infolge dieser Erkenntnis wurden viele theoretische und versuchsmäßige Forschungsarbeiten zur Klärung der Erscheinungen der Kavitationserosion durchgeführt, um die Faktoren, die für die Intensität der Zerstörung bestimmend sind, kennenzulernen. Wesentlich weniger Aufmerksamkeit wurde jedoch der Klärung des Maßstabeffektes der Kavitationserosion geschenkt. Ohne ihre Kenntnis können jedoch die Forschungsergebnisse bei der Konstruktion von Maschinen nur in beschränktem Maß nutzbar gemacht werden.

* Der Inhalt obigen Aufsatzes ist zum Teil in der unter [29] des Schrifttums registrierten Arbeit in russischer Sprache erschienen.

In den folgenden Ausführungen werden jene Erfahrungen zusammengefaßt, die während der Versuche gewonnen wurden, deren Zweck die Beobachtung des Erosionseinflusses von Kavitationszonen hinter Kreiszylindern war. Die Versuche wurden unter Berücksichtigung des hydromechanischen Modellgesetzes durchgeführt, mit dem Zweck, den Maßstabeffekt der Kavitationserosion auf Grund von Versuchen zu klären, die mit Modellen von verschiedenen geometrischen Abmessungen unternommen wurden.

II. Die Forschungsmethode

1. *Intensität der Erosion*

Zur Untersuchung der Widerstandsfähigkeit von Werkstoffen gegen die Kavitationserosion werden verschiedene Methoden verwendet [1].

Im Flüssigkeitsstrom durchgeführte Versuche; bei diesen wird der aus dem zu untersuchenden Material angefertigte Probekörper dem Kavitationseinfluß ausgesetzt; die Kavitation bildet sich hinter den in den Flüssigkeitsstrom eingetauchten Körpern.

Vibrations- und Schallmethoden. Diese betreffen magnetostriktiven Schwingungen ausgesetzte Probekörper oder mit Schall- und Ultraschallwellen bestrahlte Probekörper.

Drehscheiben-Methode. Der Probekörper wird aus dem zu untersuchenden Stoff angefertigt, und auf der Oberfläche einer Scheibe, die in Flüssigkeit rotiert, befestigt. Auf der Scheibenoberfläche wird ein hervorspringender Teil angebracht, oder eine Vertiefung erzeugt; dahinter entsteht eine Kavitation, und ihrer Wirkung setzt man den Probekörper aus.

Flüssigkeitsstrahl-Schlagmethode. Auf einer Drehscheibe sind Probekörper befestigt; diese werden periodisch dem Schlag eines mit großer Geschwindigkeit auftreffenden freien Strahles ausgesetzt. Es ist anzunehmen, daß der in dieser Weise verursachte Zerstörungsvorgang mit dem Zerstörungsvorgang übereinstimmt, der durch Kavitation erzeugt wird [2]. Da diese Annahme nicht als eine allgemein anerkannte angesehen werden kann, erschien es zweckmäßig, Versuche zu bevorzugen, die im Flüssigkeitsstrom von unmittelbarer Wirkung ausgeführt werden.

Bei der Wahl der Untersuchungsmethoden scheint die Bestrebung gerechtfertigt zu sein, das den praktischen Verhältnissen am besten angenäherte Verfahren zu verwenden, und zwar ein Verfahren, bei dem der Kavitationsangriff, der durch Wirbelbildung in der Ablösungszone entsteht, untersucht werden kann [3]. Die dieser Forderung entsprechende und den natürlichen Verhältnissen am besten nahekommende Methode besteht darin, daß die Wirkung der Kavitation untersucht wird, die hinter den Körpern entsteht, die durch einen Flüssigkeitsstrom umströmt werden. Der Angriff der Werkstoffe durch Kavitationserosion erfordert eine gewisse Energiemenge; daher ist es zweckmäßig, bei Untersuchungen im Flüssigkeitsstrom Verhältnisse zu schaffen, bei denen zwischen der Intensität der Erosion und dem Widerstand des in Flüssigkeit getauchten Körpers, bzw. der zur Überwindung des Körperwiderstandes aufgewendeten Energie, die einfachsten Beziehungen bestehen. Daher wurde als erste Annäherung ein Kreiszylinder-Modell gewählt, und dieses Modell wurde in den Meßkanal des hydrodynamischen Kanals eingesetzt (Bild 1 und 2). Diese Wahl ist auch aus dem Grund vorteilhaft, weil die Strömung als eine zweidimensionale betrachtet werden kann, und weil die Strömung um einen Kreiszylinder bisher eingehender untersucht wurde als bei allen anderen Modellen [4—6].

Es gibt Parameter, die die Intensität der Erosion anzeigen und die mit den hydrodynamischen Parametern der Strömung in keiner Beziehung stehen [7]. Die Erosionsintensität kann nämlich auf Grund nachfolgender Kennzeichen gemessen werden:

a) Tiefe und Ausbreitung der Erosionshohlräume [8, 9];

b) Gewichtsverlust der Etalons nach einer bestimmten Zeitdauer [10, 11];

c) Raumverlust, bezogen auf die Einheit von Fläche und Zeit [1];

d) dasselbe wie vorher, jedoch in Gewicht ausgedrückt [12];

e) Anzahl der auf der Flächeneinheit während der Zeiteinheit entstandenen Erosions-Hohlräume [13];

f) Raumverlust des Etalons, bezogen auf die kennzeichnenden Abmessungen des Körpers [14];

g) Verminderung der Strahlungsintensität von Isotopen, aufgebracht auf die Oberfläche des Probekörpers, die dem Angriff ausgesetzt ist [15];

h) Zeit, die erforderlich ist, um einen gegebenen und visuell verfolgbaren Zerstörungszustand zu erreichen [16].

Die Mehrzahl der aufgeführten Parameter kann man durch Messungen, die an den Etalons vor und nach den Versuchen durchgeführt werden, bestimmen. Die Bedingungen und Zweckmäßigkeitsgründe beeinflussen im allgemeinen die Wahl der Parameter. So z. B. wurden

Bild 1. Aufnahme einer hinter einem Kreiszylinder erzeugten Kavitationszone; das Bild wurde aufgenommen im Kavitationskanal des Lehrstuhls für Wasserkraftmaschinen an der Technischen Universität Budapest

$\varkappa = 0{,}85$; $Re = 6{,}6 \cdot 10^5$; $A = 198\text{x}200$ mm^2; $d = 48$ mm; Belichtungszeit: $t = 5 \cdot 10^{-5}$ s

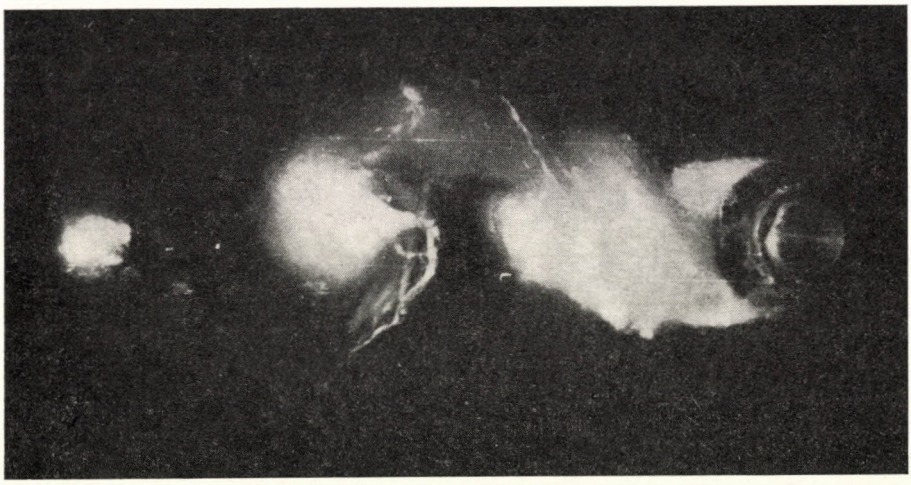

Bild 2. Bild einer hinter einem Kreiszylinder erzeugten Kavitationszone, aufgenommen im Kavitationskanal des Lehrstuhls für Wasserkraftmaschinen an der Technischen Universität Budapest

$\varkappa = 1{,}23$; $Re = 6{,}35 \cdot 10^5$; $A = 198\text{x}200$ mm^2; $d = 48$ mm; Belichtungszeit: $t = 2 \cdot 10^{-6}$ s

die Versuche mittels Isotope für die Kavitationsuntersuchungen an Francis-Turbinen angewandt. Außer den obengenannten hat RATA [17] die Änderung des ohmischen Widerstandes von Etalons infolge von Erosion gemessen und verband diese Änderung mit dem Raumverlust. GOVINDA RAO [18] schlug für die Kennzeichnung der Kavitationserosion dimensionslose Parameter vor. Dieser Parameter ist im wesentlichen eine Verhältniszahl, die das Verhältnis zwischen der zur Zerstörung eines bestimmten Werkstoffvolumens erforderlichen Energie und der Energie der zusammenbrechenden Blasen ausdrückt. Die Berechnung der Energie von zusammenbrechenden Blasen kann unter Verwendung der Theorie von RAYLEIGH [19] nur bei gewissen Voraussetzungen — z. B. die Blasen müssen von einer homogenen Flüssigkeit umgeben sein, ferner muß eine isothermische Kompression vorausgesetzt werden — durchgeführt werden und daher ist sie unsicher. Bei den Versuchen von GOVINDA RAO, die als Grundlage für die Bestimmung des Parameters dienten, bestand die Kavitationszone aus einer Vielzahl von Blasen, und in dieser Weise ist eine homogene Flüssigkeitsumgebung der Blasen nicht gesichert. Der Govinda Rao'sche Parameter für die Kavitationserosion ist von einer spezifischen Eigenschaft, er hängt nämlich vom Maß der Kavitationsentwicklung und von der Zeitdauer der Kavitationswirkung ab.

2. *Der energetische Parameter*

Unter dem energetischen Parameter der Erosion [7] versteht man die Verhältniszahl von dem erodierten Volumen und von einem bestimmten Teil des Kavitationswiderstandes des Modells. Die Maßeinheit des energetischen Parameters besteht aus dem reziproken Wert der Bruchenergie des Werkstoffes von einem Einheitsvolumen. Dieser Parameter — im Gegensatz zu allen in den vorhergehenden Ausführungen aufgeführten Parametern — hängt nicht von einem gegebenen Kavitationszustand ab, und im Fall eines gegebenen Werkstoffes weder von der Strömungsgeschwindigkeit, noch von den Modellabmessungen, und auch nicht von den Reynolds'schen und Weber'schen Ähnlichkeitskriterien. Der reziproke Wert des energetischen Parameters ergibt den wirklichen Kavitationswiderstand des Werkstoffes, der einer Kavitationserosion unterworfen ist, im Gegensatz zu den anderen Parametern, mit deren Hilfe lediglich der relative Erosionswiderstand des Stoffes bestimmt werden kann, mit anderen Worten, man kann nur den Widerstand des einen Stoffes mit dem des anderen vergleichen.

Im Einklang mit Versuchen, die über die Brucharbeit bezogen auf das Einheitsvolumen von Metallen durchgeführt wurden — derartige Versuche haben GILLEMOT und SINAY unternommen [20] — wonach die Brucharbeit unabhängig ist von der Art der mechanischen Kräfte, die den Bruch verursachen und sie ist auch praktisch unabhängig davon, wieviel aufeinander folgende Beanspruchungen die Brucharbeit ergeben, außerdem ist sie für jeden Stoff von konstantem Wert — ermöglicht der energetische Parameter ein gegenseitiges Verhältnis zwischen der Brucharbeit, die aus Kavitations-Kräftewirkungen stammt und der aus mechanischen Kraftwirkungen sich ergebenden Brucharbeit. Bei Metallen, die selbst im Kavitationszustand keine Neigung zur chemischen Korrosion aufweisen, wird die Brucharbeit aus Kavitationsbeanspruchungen herrührend höchstwahrscheinlich identisch sein mit der Brucharbeit, die sich aus den mechanischen Kräften ergibt. Sofern an der Zerstörung von Metallen im Verlauf der Kavitation auch Korrosions-

wirkungen beteiligt sind, muß die mit Hilfe des energetischen Parameters bestimmte Brucharbeit noch um diese Wirkungen erhöht werden, und in dieser Weise erhält man das neue Kennzeichen der physikalisch-mechanischen Eigenschaften von Metallen: den Kavitationswiderstand.

Im Sinne der Definition von SCHALNEW [7] kann der energetische Parameter durch folgende Beziehung ausgedrückt werden:

$$\Delta V_0 = \frac{\Delta V\, 10^7}{36\, \Delta C_x\, h d q_\infty\, v_\infty\, \gamma}\, [\mu^3\, kp^{-1}\, m^{-1}]\,;$$

$$\Delta V = \frac{\Delta G}{\gamma_s\, \tau}\, [\mathrm{mm}^3\, h^{-1}]\,; \qquad q_\infty = \frac{v_\infty^2}{2\, g}\, [\mathrm{m}]\,; \tag{1}$$

$$\Delta C_x = C_{xc} - C_x + |\Delta C_x'|\,.$$

In den Gleichungen bedeuten: ΔV das Volumen der erodierten Stoffmenge; ΔG Gewichtsverlust des der Kavitation ausgesetzten Etalons während der Zeitdauer τ; γ_s spezifisches Gewicht des Etalon-Stoffes; d Durchmesser des Zylinders; h Höhe des Zylinders; v_∞ Strömungsgeschwindigkeit im durch den Zylinder verengten Querschnitt; γ spezifisches Gewicht der Flüssigkeit; C_x Widerstand des Zylinders ohne Kavitation; C_{xc} Widerstand des Zylinders im Kavitationsfall; $\Delta C_x'$ ein gewisser Anteil des Kavitationswiderstandes, den man durch die Beziehung $C_{xc} - C_x = f(W)$, d. h. durch das Extrapolieren der *Weber*'schen Zahl bis zum Wert $W = 0$ erhält. Die *Weber*'sche Zahl lautet: $W = \varrho v^2_\infty d/\sigma$ wobei ϱ die Flüssigkeitsdichte, σ die Oberflächenspannung bedeuten.

3. *Der Maßstabeffekt*

Der energetische Parameter ermöglicht die Bestimmung des Maßstabeffektes, d. h. auf Grund des Modellversuches kann man den Volumenverlust des Materials, der am Werkstück mit den wirklichen Abmessungen auftritt, feststellen. Sofern die Kavitationsverhältnisse geometrisch ähnlich und auch die Flüssigkeiten identisch sind, dann erhält man beim Vergleich des Ausdrucks, bezogen auf das Modell und auf die wirklichen Abmessungen (1), folgende Beziehung:

$$\Delta V_n = \Delta V_m\, L^\alpha\, V^\beta, \tag{2}$$

wobei L ein auf die linearen Abmessungen des Modells und auf die Kavitation bezogener Maßstabwert ist, und V einen Maßstabwert, bezogen auf die Strömungsgeschwindigkeit, bedeutet.

Die Beziehung (2) gibt die Bedingungen an, die bei der Durchführung von Modellversuchen über Kavitationserosion berücksichtigt werden müssen. Bei den der Gleichung (1) entsprechend durchgeführten Versuchen ergaben sich die Exponentwerte $\alpha = 3$ und $\beta = 5$.

Diese Werte wurden auch durch die Versuche anderer Autoren bestätigt. KNAPP [13] führte Versuche aus an achsensymmetrischen Modellen und an Turbinen wirklicher Abmessung [21], wobei er die Intensität der Kavitationserosion auf Grund der Zahl der entstandenen Hohlräume abschätzte, und wobei der Wert von β 4 ÷ 6 betrug. Auf Grund ihrer Versuche, die von KERR und ROSENBERG unter Anwendung von Isotopen im Maßstab 1 : 1 durchgeführt wurden, nehmen sie an [15], daß der wahrscheinlichste Wert $\beta = 5$ sei. RATA stellte bei seinen

Tafel I

v, m/s	ΔV_6, mm³/h	ΔV_{12}, mm³/h	ΔV_{24}, mm³/h	ΔV_{48}, mm³/h	$\frac{\Delta V_{12}}{\Delta V_6}$	α
14	0,18	1,74	—	73,4	9,7	3,28
17	0,76	4,50	48,2	—	6,0	2,58
20	1,78	15,42	101	—	8,5	3,09
23	2,56	19,2	—	—	7,4	2,89
					$\alpha_{\text{mittl.}}$	2,96

Versuchen [17], die mit voneinander nicht allzu sehr abweichenden Geschwindigkeiten durchgeführt wurden, Exponentenwerte für $\beta = 4 \div 8$ fest. GOVINDA RAO [18] fand bei seinen mit Zylindern angestellten Versuchen die Werte $\beta = 5{,}3 \div 8$, und bei den Versuchen mit rechteckigen Prismen $\beta = 4 \div 8$ Exponentwerte.

Der auf Grund unserer Versuche festgestellte Einfluß der Modellabmessungen wurde in der Tafel 1 dargestellt. In dieser Tafel sind folgende Werte angegeben: das Volumen der erodierten Stoffmenge bei vier Zylindern von verschiedenen Abmessungen, und die hieraus gebildeten zehn Verhältniszahlen bei vier verschiedenen Geschwindigkeitswerten. Aus diesen Daten kann der Erfahrungswert von α bestimmt werden. Die mittleren Werte der Volumenverhältnisse ergeben einen Wert von $\alpha = 2{,}95$, der dem theoretischen Wert von $\alpha = 3$ nahesteht.

Mit der in dieser Weise durchgeführten Untersuchung des Einflusses der Abmessungen haben sich andere noch nicht beschäftigt. KNAPP [13] bestreitet den Einfluß der Abmessungen auf die Intensität der Erosion. Die Streuung der Ergebnisse weist vor allem darauf hin, daß man sehr sorgfältig die Bestimmung von allen jenen Werten an der Versuchsanlage vornehmen muß, die kennzeichnend für die Intensität der Erosion sind.

III. Versuchseinrichtungen

1. *Die Wasserkanäle*

Die Versuche über die Kavitationserosion werden in den mit GT—3 und GT—2 bezeichneten Wasserkanälen des Mechanischen Instituts (IM) der Wissenschaftlichen Akademie der Sowjetunion und in den Wasserkanälen der Akademie der Wissenschaften in Ungarn, die sich am Lehrstuhl für Wasserkraftmaschinen der Technischen Universität Budapest befinden [22], ausgeführt. Alle die hier aufgeführten Kanäle haben einen geschlossenen Wasserkreislauf, und die Wasserzirkulation erfolgt durch Pumpenbetrieb. Die Regelung der Strömungsgeschwindigkeit wird auf dem Wege der Regelung des elektrischen Antriebs durchgeführt. Der Druck kann unabhängig von der

$\frac{\Delta V_{24}}{\Delta V_6}$	a	$\frac{\Delta V_{24}}{\Delta V_{12}}$	a	$\frac{\Delta V_{48}}{\Delta V_6}$	a	$\frac{\Delta V_{48}}{\Delta V_{12}}$	a
—	—	—	—	408	2,89	42,3	2,70
63,5	2,99	10,7	3,42	—	—	—	—
57	2,92	6,6	2,72	—	—	—	—
—	—	—	—	—	—	—	—
	2,96		3,07		2,89		2,70

$\sum a_{\text{mittl.}} = 2{,}95$

Geschwindigkeit geregelt werden. Im Kanal der Technischen Universität Budapest beträgt die höchste erreichbare Geschwindigkeit innerhalb der Meßstrecke von der Größe 200×48 mm² den Wert von 18 m/s. In den Kanälen des IM kann die Geschwindigkeit in den Meßkanälen von verschiedenen Abmessungen in den Grenzen von 0—25 m/s verändert werden. Den Querschnitt des Meßkanals vom Kanal der Technischen Universität Budapest zeigt das Bild 3.

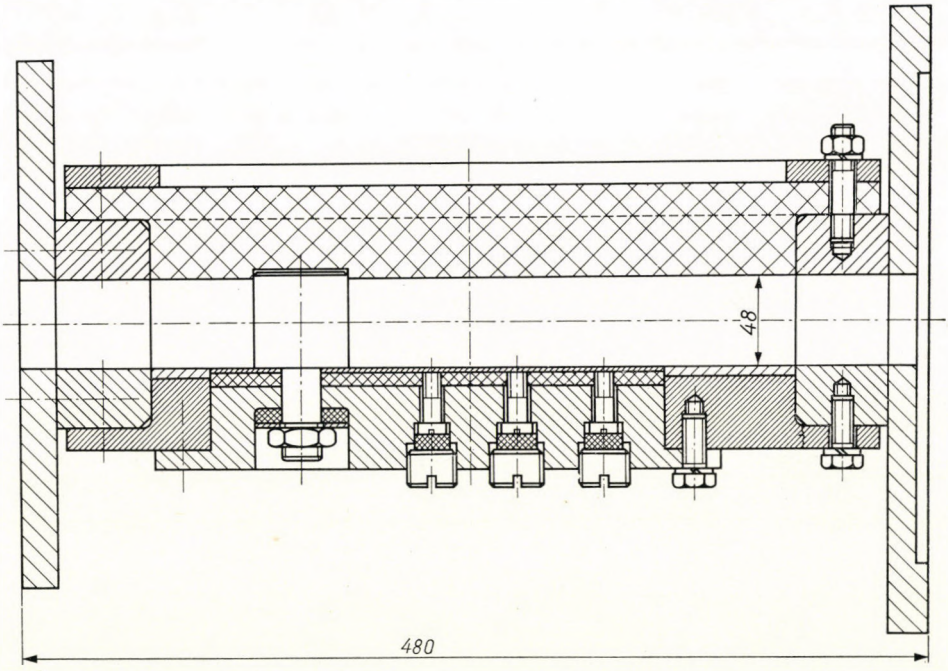

Bild 3. Der Meßkanal mit eingebrachtem Etalon im Kavitationskanal des Lehrstuhls für Wasserkraftmaschinen an der Technischen Universität Budapest. Die Querschnittsmaße der Meßstrecke sind: $A = 48 \times 200$ mm²; Durchmesser des Kreiszylinders: $d = 48$ mm

2. *Der Konfusor*

Der Konfusor ist zwischen dem Druckbehälter und der Meßstrecke untergebracht. Den in den Kanal eingebauten Konfusor hat man sehr große Forderungen zu stellen, da der Charakter der Strömung in dem Meßkanal von ihm bestimmt wird. Der Konfusor muß daher so ausgebildet werden, daß er im vollen Querschnitt des Meßkanals die größtmöglichste Gleichmäßigkeit sichere, d. h. die Geschwindigkeitsänderungen in Längs- und Querrichtung minimal seien. Dieser Umstand kann durch die entsprechende Ausführung des Strömung-

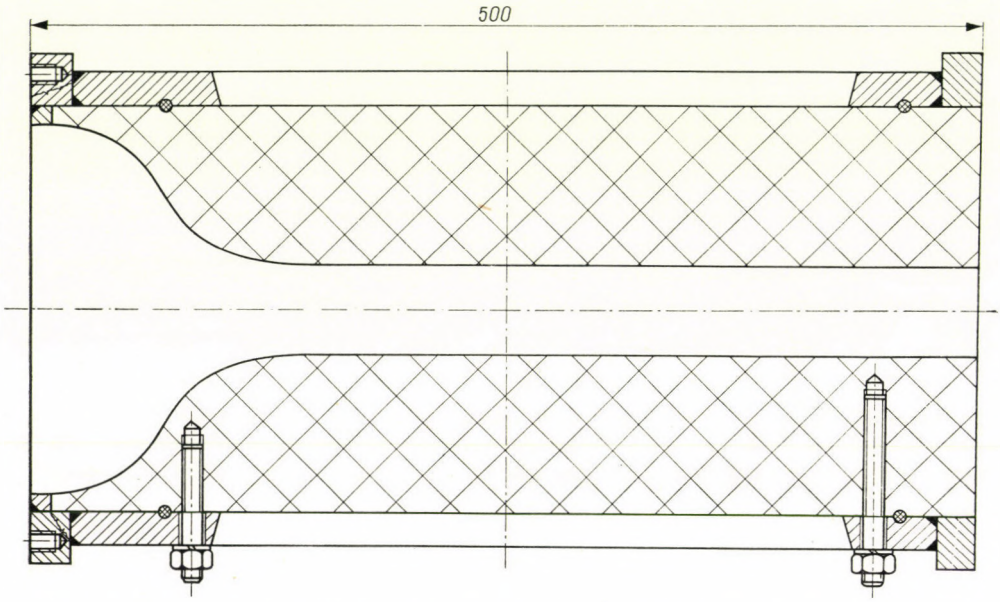

Bild 4. Konfusor vor dem Meßkanal im Kavitationskanal des Lehrstuhls für Wasserkraftmaschinen der Technischen Universität Budapest. Abmessungen des Austrittsquerschnitts: $A = 48 \times 200$ mm²

querschnittes erreicht werden. Das Verengungsverhältnis vom Ein- und Austrittquerschnitt des Konfusors wurde auf Grund der einschlägigen Untersuchungen von PRANDTL [23] festgestellt. Das Längsprofil des Konfusors besteht aus zwei Kurven. Die auf der Eintrittsseite befindliche Kurve sichert einen entsprechenden Anschluß für die austrittsseitige Kurve des Konfusors, deren Profil nach WITOSZYNSKI [24] berechnet wurde (Bild 4).

Um die Entstehung einer Wirbelzone zu vermeiden, haben wir die Länge des zweiten Teiles vom Konfusor, der sich in der Meßstrecke befindet, im Wert von $l = 3\,d$ ausgeführt. Den Konfusor verwenden wir — nach der Eichung — zur Messung der durch die Meßstrecke strömenden Flüssigkeitsmenge bzw. der Geschwindigkeit.

3. *Meßkanal*

Bei den erwähnten drei Wasserkanälen wurden zur Durchführung der Versuche über Kavitationserosion Meßstrecken mit vier verschiedenen Querschnitten verwendet. Die Querschnittsabmessungen der Meßstrecken betragen:

a) In den Kanälen des Mechanischen Instituts: 6×25; 12×50; 24×100 mm^2;

b) Im Kanal der Technischen Universität Budapest: 48×200 mm^2.

Die weiteren Ausführungen geben über den Meßkanal mit dem Querschnitt 48×200 mm^2, die in den Kavitationskanal des Lehrstuhls für Wasserkraftmaschinen an der BME eingebaut ist, Auskunft. Das Gerüst des Meßkanals wird von zwei Stahlrahmen gleicher Abmessung gebildet; diese Rahmen werden durch an Ecken angebrachten vier Einsatzstücken voneinander in einer Entfernung von 48 mm gehalten. Der Profilquerschnitt, begrenzt durch die Einsatzstücke und die Rahmenkanten, beträgt 48×200 mm^2. Die beiden Enden des Meßkanals sind mittels Flanschverbindungen an einen Teil, der auch den Konfusor enthält, bzw. an den Diffusor angeschlossen. Die Stahlrahmen lassen Öffnungen frei, in denen entsprechende Schließstücke angebracht werden können. Zwecks visueller Beobachtung und zum Fotografieren sind drei Seiten mittels Plexiglas, und die vierte Fläche mit einer, eine weitere Öffnung enthaltenden Vollscheibe abgeschlossen. In die Öffnung der letztgenannten Vollscheibe kann der für die Untersuchungen angefertigte Etalon samt Etalonhalter eingeführt werden. In dieser Weise kann das Ein- und Ausmontieren der Etalons einfach durchgeführt werden.

Der für die Durchführung der Messungen verwendete Etalon besteht aus zwei Teilen, aus der sog. Tragscheibe und aus der gewalzten Bleiplatte, die der Erosion ausgesetzt wird. Die Bleiplatte wurde mit Hilfe eines Metallklebers auf der Grundplatte, die aus einer Aluminiumlegierung besteht, befestigt. In dieser Grundplatte befinden sich Bohrungen, um sie am Etalonhalter befestigen zu können.

Der Kreiszylinder wurde aus Bronze mit großer Maßgenauigkeit angefertigt, und die Oberfläche sehr sorgfältig bearbeitet. Das eine Ende des Kreiszylinders ist, wie aus dem Bild ersichtlich, im Etalonhalter befestigt, das andere Ende dagegen ragt in die für diesen Zweck angefertigte Bohrung des auf der gegenüberliegenden Seite vorhandenen Plexifensters hinein.

4. *Die Gestaltung des Diffusors*

Die Gestaltung des Diffusors wurde mit großer Sorgfalt vorgenommen, mit Rücksicht darauf, daß vom Standpunkt der Kavitation der Diffusor der empfindlichste Punkt des Wasserkanals ist, wobei er gleichzeitig die Qualität des Kanals bestimmt. Von diesen Überlegungen ausgehend haben wir den Öffnungswinkel des Diffusors mit 7° gewählt, also kleiner als er bei Windkanälen empfohlen wird. Um den Diffusor leicht herstellen zu können, besteht er aus mehreren Teilen, mit Rücksicht darauf, daß ein Übergang vom Vierkantprofil in ein Kreisprofil stattfinden muß.

IV. Bestimmung der grundlegenden Werte

1. *Bestimmung der Geschwindigkeit im Meßquerschnitt*

Die mittlere Geschwindigkeit der Strömung bestimmt man im allgemeinen im Querschnitt vor dem Modell auf Grund der durchgeströmten Wassermenge, die in verschiedener Weise (mittels Meßflansches, mit Venturimesser) gemessen werden kann. Die Geschwindigkeit kann man auch mit Hilfe des Druckwertes bestimmen, den man in einer Bohrung erhält, die in der Strömungsachse am Zylinder ausgeführt ist. Im Wasserkanal kann die Bestimmung der Geschwindigkeit auf Grund folgender Überlegungen vorgenommen werden. Bezeichne man mit p_1 den am Eintritt des Konfusors herrschenden Druck,

p_2 den am Austritt des Konfusors meßbaren Druck,

p_3 den Druck am Eintritt der Meßstrecke,

p_4 den an der Wand der Meßstrecke in einem der Mittellinie des Zylinders entsprechenden Punkt meßbaren Druck, wenn der Zylinder nicht in den Meßkanal eingesetzt ist.

Bezeichnet man den Druck, der am vorderen Punkt der Mittellinie des in die Strömung eingesetzten Zylinders meßbar ist, mit p_c, dann muß man die Beziehungen

$$p_3 - p_4 = f(p_1 - p_2)$$

oder

$$p_3 - p_4 = f(p_1 - p_3)$$

$$(p_3 - p_c) - (p_3 - p_4) = q = f(p_1 - p_3)$$

experimentell ermitteln, wobei $q = v_0^2/2g$ ist, und dann mit Hilfe eines graphischen Verfahrens

$$v_0 = f(p_1 - p_3)\,, \quad v_0 = \sqrt{2gq}$$

[25] bestimmen.

Bei Berücksichtigung der Querschnittsverengung, verursacht durch den Zylinder, ergibt sich

$$v_\infty = v\,\frac{b}{b-d}\,,$$

wobei b die Breite der Meßstrecke bedeutet. Bei der Auswertung der Versuchsergebnisse verwenden wir folgende Geschwindigkeiten: v ist die Mittelgeschwindigkeit vor dem Modell; v_∞ die unter Berücksichtigung der Querschnittsverengung der Strömung erhaltene mittlere Geschwindigkeit; v_0 die in der Mittellinie der Strömung vorhandene Geschwindigkeit; $v_{\infty 0}$ die in der Mittellinie der Strömung, unter Berücksichtigung der Kanalverengung, sich ergebende Geschwindigkeit. Die genaue Bestimmung der Geschwindigkeitswerte bedeutet eine sehr wichtige Aufgabe, denn das Volumen der erodierten Stoffmenge hängt von der Potenz $\beta = 5$ ab.

2. *Die Druckbestimmung im Meßquerschnitt*

Der Druck im Meßquerschnitt p_4 kann nicht unmittelbar bestimmt werden. Im Verlauf der Versuche wird mittels Messung der Druck p_3 vor dem Modell bestimmt. Unter Verwendung der Beziehung

$$p_3 - p_4 = f(p_1 - p_3)\,,$$

die wir bereits vorher in der Meßstrecke, im Falle der Strömung ohne eingesetzten Zylinder, gefunden haben, ergibt sich der genannte Druck aus der Gleichung $p_4 = p_3 - (p_3 - p_4)$ und damit wurde die Druckverminderung zwischen den Punkten 3—4 der Meßstrecke berücksichtigt.

3. *Bestimmung der Kavitationszahl ($\varkappa$)*

Die Ermittlung der Kavitationszahl ist für Bestimmung von ΔC_x erforderlich. Diesen Wert kann man mit oder ohne Berücksichtigung der Verengung bestimmen. Im ersten Fall ist

$$\varkappa = \frac{p_\infty - p_d}{\gamma q_n}\,,$$

wobei $p_\infty = p_4$, q_n die Geschwindigkeitshöhe bedeutet, die nach der oben angeführten Methode (s. IV. 1) gefunden wurde. p_d ist der Druck des Wasserdampfes bei der gegebenen Temperatur, und γ das spezifische Gewicht des Wassers.

4. *Länge der Kavitationszone*

Die Länge der Kavitationszone mißt man mittels der Entfernung, die von der Mittellinie des Zylinders bis zum Ende des zusammenhängenden Teils reicht, und die mit l_c bezeichnet wird. In dimensionsloser Form ausgedrückt ergibt $\lambda = l_c/d$ die sog. relative Zonenlänge, wobei d den Zylinderdurchmesser bedeutet.

5. *Die Bestimmung von* ΔC_x

Für die Bestimmung von ΔC_x verwendet man die Beziehungen $C_x(Re, \varkappa)$ und $\lambda(\varkappa)$. Darüber findet man mehr in [4] und [7] (Bild 5 und 6). Es ist wünschenswert, die dort angegebenen Daten sowohl aus dem Bereich der großen als auch der kleinen *Reynolds*'schen Zahlen zu erweitern, damit wir für die Werte von C_x möglichst zuverlässige Zahlen erhalten. Die

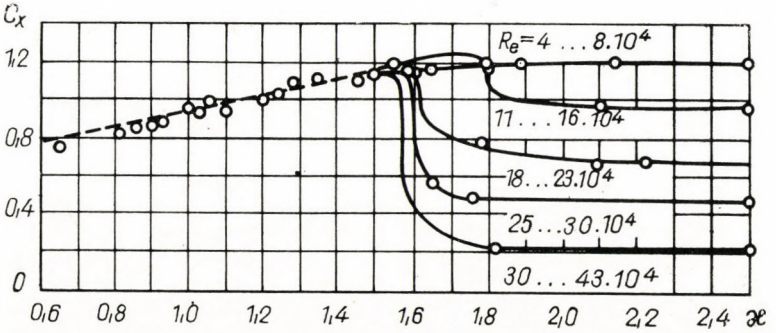

Bild 5. Einfluß der Reynoldschen Zahl und der Kavitationszahl auf den Zylinderwiderstandszahl

$Re = 4 \div 8 \cdot 10^4$, $d = 5{,}10$ mm; $Re = 11 \div 16 \cdot 10^4$, $d = 20$ mm; $Re = 18 \div 23 \cdot 10^4$, $d = 30$ mm; $Re = 25 \div 30 \cdot 10^4$, $d = 40$ mm; $Re = 30 \div 43 \cdot 10^4$, $d = 50$ mm.

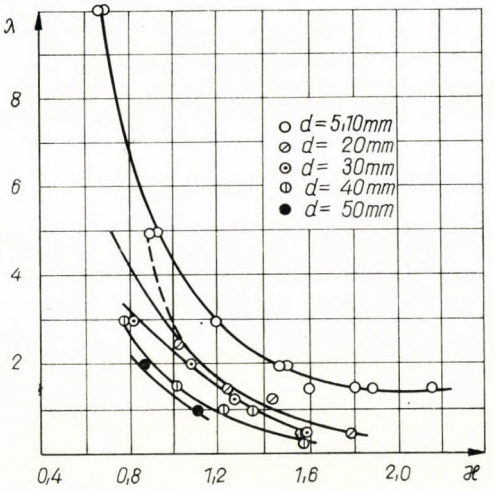

Bild 6. Einfluß der Kavitationszahl und des Zylinderdurchmessers auf die Länge der Kavitationszone

einfachste, und gleichzeitig auch die genaueste Methode für die Bestimmung von C_x besteht in der Ermittlung der Druckverteilung im Mittelquerschnitt des Modells. Bei Bestimmungen, die in anderer Weise vorgenommen werden, wie z. B. bei der unmittelbaren Kraftmessung, führen die in der Einrichtung notwendigerweise vorhandenen Spalte zur Verzerrung der Strömung.

Die Funktionen $C_x = C_x(W)$ und $C_{xc} = C_{xc}(W)$ (Bild 7) können auf Grund der Beziehungen $C_x(Re, \varkappa)$ und $\lambda(\varkappa)$ dargestellt werden. Im Sinne der Beziehung (1) muß man zwecks Bestimmung des Wertes von ΔC_x auch das Glied $\Delta C_x'$ bestimmen, das identisch ist mit dem absoluten Wert einer Größe, die dadurch gewonnen wird, daß man als Funktion von W die Differenzen $C_{xc}(W) - C_x(W)$ bildet, und daraus durch Interpolation die Gerade erhält, die dann durch Extrapolation bis $W = 0$ im negativen Bereich der Ordinate C_x die genannte Größe abschneidet.

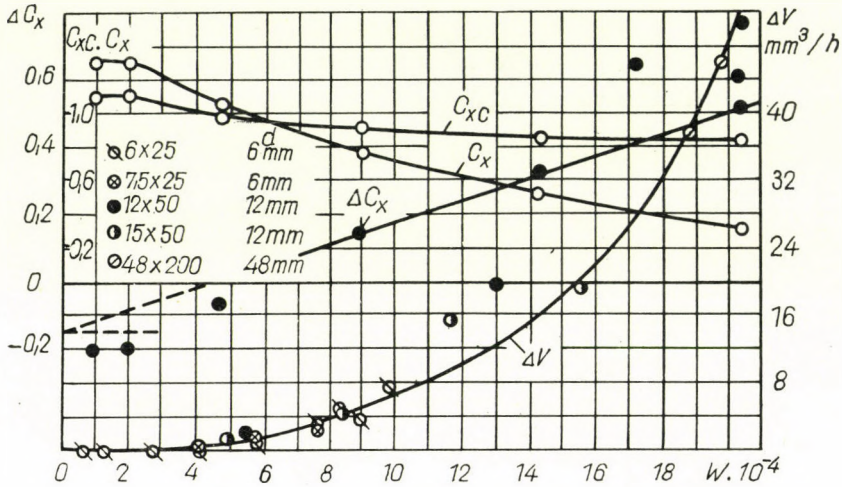

Bild 7. Die Werte von C_x, C_{xc}, ΔC_x und ΔV in Abhängigkeit von der Weberschen Zahl (W)

6. *Die Bestimmung von ΔV*

Das Volumen des erodierten Materials kann man aus dem Gewichtsverlust ΔG, ferner aus der Zeitdauer τ des Versuches ermitteln, d. h.

$$\Delta V = \frac{\Delta G}{\gamma_s \tau} \; [\mathrm{mm}^3 \; \mathrm{h}^{-1}] \, ,$$

wobei γ_s das spezifische Gewicht des Etalonmaterials bedeutet. Zwecks Vermeidung von Irrtümern ist es wünschenswert, die Beziehung $\Delta V = f(W)$ bereits vorher, auf Grund von Versuchen zu bestimmen, unter Gewinnung einer entsprechenden Anzahl von Werten für ΔV. Aus den Mittelwerten der gewonnenen ΔV Werte kann die Beziehung $\Delta V = f(W)$ konstruiert werden (s. Bild 7).

7. *Die Bestimmung von ΔG*

Die im Verlauf der Versuche am Etalon entstehende Gewichtsverminderung kann durch — mit entsprechender Genauigkeit durchgeführten — Wägung vor und nach dem Versuch bestimmt werden. Die Genauigkeit der Wägung hängt vom Wert ΔG ab. Die annehmbare Genauigkeit der Wägung kann — im Vergleich zur Bestimmungsgenauigkeit von anderen Werten — eine Toleranz von $\pm 1\%$ aufweisen, wir konnten jedoch im Verlauf der Versuche, insbesondere bei Etalons großer Abmessung, die Bestimmung mit einer wesentlich größerer Genauigkeit vornehmen ($\pm 0{,}1\%$).

8. *Die Bestimmung von τ*

Die Versuchsdauer wird von dem Versuchszweck und von den Faktoren bestimmt, die die Genauigkeit der Versuchsergebnisse beeinflussen (s. Kapitel V). Sofern man Versuche ausführt, bei denen, bei konstanten Werten von d und λ, die Geschwindigkeit verändert wird, dann wird die Zeitdauer der Versuche von der Zeit bestimmt, die zum Erreichen des gleichen Gewichtsverlustes erforderlich ist. In dem Fall jedoch, wenn auch die Abmessungen des Modells verändert werden, wird die Zeitdauer der Versuche von der Beziehung $\Delta G_n/\Delta G_m \cong L^3$ bestimmt.

9. *Die Wassertemperatur*

Die Wassertemperatur wird mit einem Quecksilberthermometer gemessen, das sich in einer mit Öl gefüllten Bohrung des Konfusorflansches befindet.

10. *Weitere Werte*

Der barometrische Druck wird mittels eines Quecksilberbarometers gemessen. Diejenigen Werte, die zur Berechnung der Beziehungen (1) und (2) erforderlich sind, wie z. B. das spezifische Gewicht des Wassers γ, das spezifische Gewicht des Etalonmaterials γ_s, der Druck des Wasserdampfes p_d, die Oberflächenspannung σ, die kinematische Viskosität des Wassers ν, werden aus Tabellen, die die entsprechenden physikalischen Konstanten enthalten, entnommen.

V. Faktoren, die die Genauigkeit der Ergebnisse beeinflussen

1. *Einfluß des Luftgehaltes*

Mit magnetostriktiven Einrichtungen wurden Kavitationsversuche mit verschiedenen Wassersorten durchgeführt (Novotny [26]); die Ergebnisse zeigen, daß der Luftgehalt des Wassers einen erheblichen Einfluß auf die Intensität der Erosion ausübt. In destilliertem Wasser ist der Erosionsverlust um etwa 80% größer als im Leitungswasser. Die im Leitungswasser sich ergebenden Erosionsverluste vermindern sich etwa um 30%, wenn im Wasser Luft durchgelassen wird. Aus diesen Erfahrungen folgt, daß man die Untersuchungen über Kavitationserosion mit einem Wasser von unverändertem Luftgehalt durchführen muß. Daher ist die Konstruktion der für die Versuche verwendeten Wasserkanäle so ausgeführt, daß im Druckbehälter die Wasseroberfläche in keine unmittelbare Berührung mit der Luft kommt, und das Wiederauffüllen des Kanals mit Wasser erfolgte immer mit einem Wasser von konstanten Eigenschaften.

2. *Einfluß der Temperatur*

Im Verlauf unserer Versuche [3], als wir die Abmessung und den Zustand der Kavitationszone, ferner die Strömungsgeschwindigkeit auf konstanten Werten hielten, konnten wir feststellen, daß bei der Schwankung der Wassertemperatur zwischen den Grenzen von $10 \div 26$ °C die Intensität der Erosion sich um $0 \div 7\%$ verminderte (Bild 8). In Fällen, bei denen wir die Schwankungen der Wassertemperatur auf Werte zwischen $1 \div 8$ °C beschränkten, war der Einfluß der Temperaturerhöhung vollkommen belanglos. Im Verlauf unserer Versuche haben wir Temperaturschwankungen von ± 5 °C zugelassen.

3. *Einfluß des Kavitationszustandes*

Nach unseren Untersuchungen [3] zeigt sich das Maximum der Erosionsintensität im Falle der Kavitation hinter einem Kreiszylinder bei einem Wert von $\lambda = 3$ der Zonenlänge der Kavitation (Bild 9). Die Erosionsintensität verminderte sich etwa um 25% bei Änderung der Werte von $\lambda = 3$ bis zu $\lambda = 2$, und bei Änderung des λ-Wertes bis zu $\lambda = 4$ mindestens um 16%. Diesen Umstand berücksichtigend kann bei der Bestimmung von ΔG ein maximaler Fehler von $\delta_G = \pm 5\%$ auftreten.

4. *Einfluß der Abmessungsverhältnisse des Modells*

Bei unseren Versuchsbedingungen ist der Einfluß des Größenverhältnisses von l/d im wesentlichen identisch mit dem Einfluß der Breite des Meßkanalquerschnittes. Aus unserer Forschungsarbeit geht hervor [1], daß die Intensität der Erosion ihren maximalen Wert bei einem Größenverhältnis von $l/d = 1$ erreicht (Bild 10). Die Intensität der Erosion vermindert

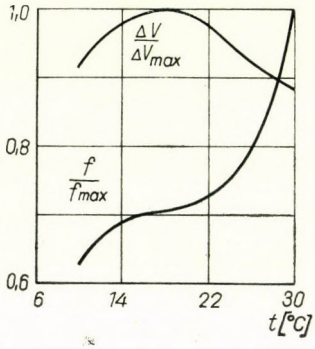

Bild 8. Die ausgeglichenen Funktionen des relativen Volumens der Erosion [$\Delta V/\Delta V_{max}$] bzw. der relativen Oberfläche der Erosion [f/fmax] und der Wassertemperatur (t °C)

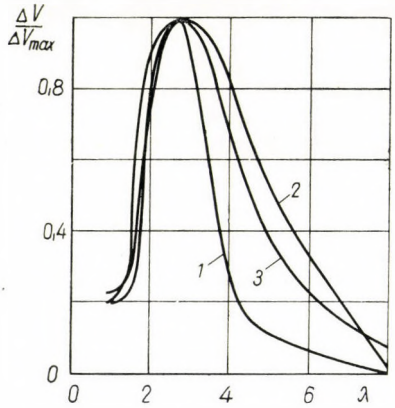

Bild 9. Die ausgeglichene Funktion des relativen Volumens der Erosion [$\Delta V/\Delta V_{max}$] und der relativen Länge der Kavitationszone (λ)

1. Bei der Geschwindigkeit $v_0 = 14$ m/s,
2. bei der Geschwindigkeit $v_0 = 17$ m/s,
3. bei der Geschwindigkeit $v_0 = 20$ m/s.

sich plötzlich mit der Erhöhung der Proportion von l/d. Bei der Vergrößerung des Verhältnisses von l/d um 10% vermindert sich die Intensität der Erosion gleichfalls um 10%; erhöht man dagegen den Wert der Verhältniszahl von l/d um 30%, so geht die Intensität auf ein Drittel oder ein Viertel ihres Wertes zurück. Im Verlauf unserer Versuche konnten wir die Verhältniszahl l/d mit einer Genauigkeit von $\pm 1\%$ einhalten, und in dieser Weise entstand bei der Bestimmung von ΔV höchstens ein Fehler, der geringer als 1% war.

5. *Einfluß der Zeitdauer des Versuches*

Wenn man die Beziehung $\Delta G(\tau)$ für verschiedene Metalle bestimmt, so kann man feststellen, daß bei den elastischen Metallen in der Anfangsperiode des Angriffs eine sog. Inkubationsperiode zu beobachten ist, und während dieser Periode findet lediglich eine Deformation der Oberflächenschicht ohne Gewichtsverminderung (Kaltverfestigung) statt. Eine derartige Gewichtsverminderungskurve zeigt das Bild 11. Bei den verwendeten Bleietalons wächst der Wert ΔG als Funktion der Zeit bis zu einem gewissen Grad ungefähr linear. In diesem Zeitabschnitt bilden sich auf der Materialoberfläche ausgeprägte erodierte Oberflächen, im allgemeinen in Form von kreisrunden Vertiefungen. Da angenommen werden kann, daß in der Umgebung der Vertiefungen, die durch Kavitationsangriff aufgetreten sind, weitere örtliche

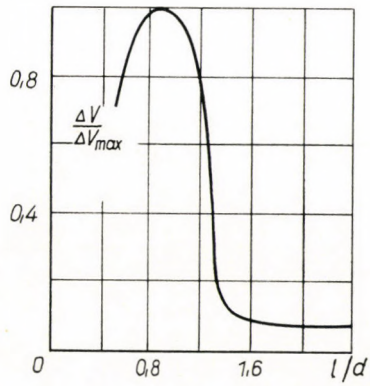

Bild 10. Die ausgeglichene Funktion des relativen Volumens der Erosion $[\Delta V/\Delta V_{max}]$ und der relativen Abmessungen des Modells $[l/d]$

Kavitation sich meldet, erscheint es erforderlich, im Interesse der Vergleichbarkeit der Versuchsergebnisse, aus der Zeitdauer der Versuche den Zeitabschnitt herauszugreifen, während dem sich nur noch die Wirkung der Kavitationserosion, verursacht durch das ursprüngliche Strömungsbild, zeigt.

6. *Einfluß der Oberflächengüte der Etalons*

Einfluß der Oberflächengüte der Etalons wurde bereits im Verlauf der früher durchgeführten Versuche geklärt [7]; bei diesen Versuchen wurden Vergleichsuntersuchungen mit Etalons von verschiedener Oberflächenrauhigkeit durchgeführt. Nach den so gewonnenen Erfahrungen muß man im Interesse der Vergleichbarkeit der Versuchsergebnisse diese Versuche immer mit Etalons von der gleichen Oberflächengüte durchführen.

7. *Einfluß des Versuchsbereiches*

Wie bereits vorher erwähnt, wurde von verschiedenen Forschern der Exponentenwert des Maßstabfaktors im Bereich von $\beta = 4 \div 8$ ermittelt. Die Daten der ausgedehnten Versuche von Govinda Rao [27] verwendend, kann man zu dem Ergebnis gelangen, daß sowohl im Fall des in die Strömung eingesetzten Zylinders als auch bei den im Venturirohr ausgeführten Versuchen sich ein Exponentenwert von $\beta = 5$ ergibt, wenn man die extrem kleinen Geschwindigkeitswerte vernachlässigt. Einige Versuche wurden lediglich bei drei Geschwindigkeiten ausgeführt — was offensichtlich zu wenig ist — unter Berücksichtigung des Umstandes, daß die Beziehung $\Delta V(v)$ graphisch bestimmt wurde. Der aus den *Rata*schen Versuchen sich ergebende sehr breite Bereich $\beta = 4 \div 8$ des Exponenten kann gleichfalls mit den zufälligen Fehlern erklärt werden, denn bei diesen Versuchen lagen die Geschwindigkeiten den Werten $v = 30 \div 40$ m/s nahe.

8. *Der größte mögliche Fehler bei der Bestimmung von ΔV_0 und ΔV_n*

Eine annähernde Berechnung verwendend [28] kann man bei der Bestimmung von ΔV_0 für den dabei sich ergebenden größten möglichen Fehler folgenden Ausdruck anschreiben:

$$\delta_0 = \delta_G + \delta_\tau + \delta_{Cx} + \delta_h + \delta_d + 3\delta_v + \delta_g + \delta_\gamma ;$$

für ΔV_n

$$\delta_n = \delta_m + 3\delta_L + 5\delta_V = \delta_m + 3 \cdot 2\delta_l + 5 \cdot 2\,\delta_{v_0} .$$

Die Indizes bezeichnen die maximal möglichen Fehler der in Frage stehenden Werte. Bei der Bestimmung von δ_G darf man nicht nur aus der Genauigkeit der Etalonwägung ausgehen,

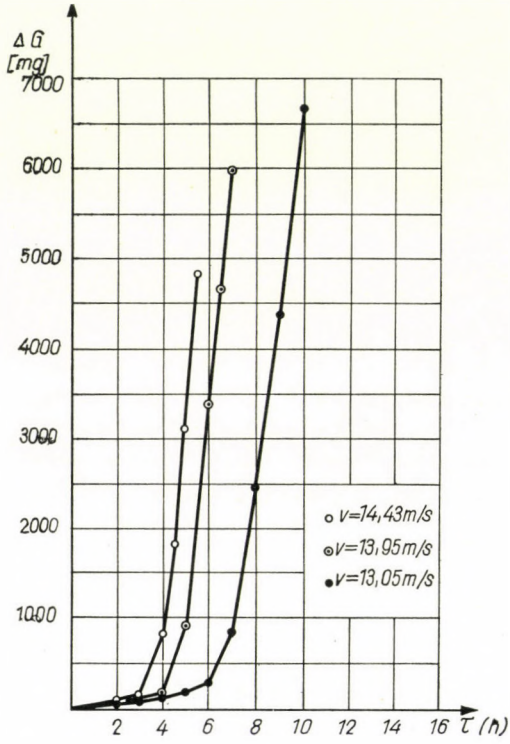

Bild 11. Die Versuchsfunktionen des erosiven Gewichtsverlustes ΔG und der Zeitdauer der Erosionsuntersuchung (τ)

sondern auch davon, wieweit λ, l/d und andere, oben genannte Faktoren einen konstanten Wert beibehielten. Auf Grund dieser Überlegungen kann man folgendes errechnen:

$$\delta_0 = 0{,}05 + 0{,}01 + 0{,}05 + 0{,}005 + 0{,}005 + 3 \cdot 0{,}02 + 0 + 0 = 0{,}18 \cong \pm 18\%$$

und

$$\delta_n = 0{,}06 + 3 \cdot 2 \cdot 0{,}005 + 5 \cdot 2 \cdot 0{,}02 = 0{,}29 \approx \pm 30\% .$$

Bei diesen relativ hohen Werten der möglichen Fehler wird die in dem Bild $\Delta V_0(W)$ dargestellte Streuung der Versuchswerte von ΔV_0 verständlich [7]. Besonders groß kann der Fehler bei der Bestimmung der Erosionsintensität werden, wenn die Versuche an wirklichen Maschinen ausgeführt werden.

VI. Folgerungen

Bei der Untersuchung des Maßstabeffektes der Kavitationserosion hat man besondere Aufmerksamkeit zu richten auf:

a) die Genauigkeit der Bestimmung des Kavitationswiderstandes und der Strömungsgeschwindigkeit, ferner auf die Ermittlung des Volumenverlustes durch die Erosion;

b) das Einhalten der Identität des Kavitationszustandes und der Abmessungsverhältnisse der verwendeten Versuchsmodelle;

c) die richtige Festlegung der Versuchsdauer. Für Verminderung der Fehlergrößen sind die Versuche in einem breiten Geschwindigkeitsbereich bei einer großen Zahl an Variationen vorzunehmen.

Die Ergebnisse der an der Technischen Universität Budapest durchgeführten Versuche bestätigen die früher gewonnenen Versuchsergebnisse, sie bestätigen ferner die Gültigkeit der für den Maßstabeffekt angegebenen Beziehung für einen noch breiteren Bereich.

SCHRIFTTUM

1. *Шальнев, К. К.:* Гидромеханические аспекты кавитационной эрозии. *Изв. АН СССР. Отд. техн. н.* (1958), № 1.
2. Vasvári, F.: Beginnende Zerstörung von Metalloberflächen durch Wasserschlag. *Periodica Polytechnica* **6** (1962), No. 1.
3. *Шальнев, К. К.:* Условия интенсивности кавитационной эрозии. *Изв. АН СССР. Отд. техн. н.* (1956), № 1.
4. *Константинов В. А.:* Влияние числа Рейнольдса на отрывное обтекание. *Изв. АН СССР, Отд. техн. н.* (1946), № 10.
5. Martyrer, E.: Kraftmessungen an Widerstandskörpern und Flügelprofilen im Wasserstrom bei Kavitation (G. Kempf und E. Foerster: Hydromechanische Probleme des Schiffsantriebs), Hamburg 1932.
6. Silbermann, E.: Experimental studies of supercavitating flow about simple two-dimensional bodies in a jet. *Journal of Fluid Mechanics*, **5** (1959), 337—354.
7. *Шальнев, К. К.:* Энергетический параметр и масштабный эффект кавитационной эрозии. *Изв. АН СССР Отд. техн. н.* (1961), № 5.
8. Plesset, M. S.; Ellis, A. T.: On the Mechanism of Cavitation Damage. *Trans. ASME* **77** (1955), No. 7.
9. Parsons, C. A.; Cook, S. S.: Investigations into the causes of corrosion or erosion of propellers. *Engineering* **107** (1919).
10. Kerr, S. L.: Determination of the Relative Resistance to Cavitation Erosion by the Vibratory Method. *Trans. ASME* **59** (1937), No. 5.
11. Mousson, J. M.: Pitting Resistance of Metals under Cavitation. *Trans. ASME* **59** (1937), No. 5.
12. *Гавранек, В. В.:* Изучение кавитационной эрозии металлических материалов на магнитострикционном вибраторе. *ХПИ им. В. И. Ленина* **9** (1957), № 1.
13. Knapp, R. T.: Recent Investigation of the Mechanics of Cavitation Damage. *Trans. ASME* **77** (1955), No. 7.
14. Noskievic, J.: Beitrag zur Ähnlichkeit bei Kavitation. *Bergakademie* **8** (1956), No. 2.
15. Kerr, S. K.; Rosenberg, K.: An index of Cavitation Erosion by Means of Radioisotops. *Trans. ASME* **80** (1958), No. 6.
16. Schröter, H.: Korrosion durch Kavitation in einem Diffusor. *Z. VDI* **76** (1932), No. 21.
17. Rata, J. M.: Érosion de cavitation. Mesure de l'érosion par jauges résistantes, Symposium Recherche sur les Turbines Hydrauliques de Nice, 16—20 sept. 1960.
18. Govinda Rao, N. S.; Thiruvengadam, A.: Prediction of Cavitation Damage. *J. Hydraul. Div. Proc. Amer. Soc. Civil Engrs.* **87** (1961), No. Hy. 5.

19. RAYLEIGH: On the Pressure Developed in a Liquid During the Collapse of a Spherical Cavity. *Phil. Mag.* Ser. 4. **34** (1917).
20. GILLEMOT—L.;SINAY, F.: Die Brucharbeit als Werkstoffkenngröße. *Acta Techn. Hung.* **22** (1958), No. 1—2.
21. KNAPP, R. T.: Accelerated Field Tests of Cavitation Intensity. *Trans. ASME* **80** (1958), No. 1.
22. FÁY, CS.: A Vízgépek Tanszékének kavitációs csatornája (Der Kavitationskanal des Lehrstuhls für Wasserkraftmaschinen). *MTA Műsz. Tud. Oszt. Közl.* **22** (1958), No. 1—3.
23. PRANDTL, L.: Herstellung einwandfreier Luftströme. Handbuch der Experimentalphysik, 1932; Bd. 4, Teil 2.
24. WITOSZYNSKI, E.: Über Strahlerweiterung und Strahlablenkung. Vorträge aus dem Gebiete der Hydro- und Aerodynamik, Berlin 1924.
25. *Шальнев, К. К.:* Кавитация неровностей поверхности треугольного профиля. *ПМТФ* (1962), № 6.
26. NOVOTNY, H.: Werkstoffzerstörung durch Kavitation. VDI-Verlag, Berlin 1942.
27. GOVINDA RAO, N. S.: Cavitation — its Inception and Damage. *Irrigat. and Power* **18** (1961), No. 1.
28. *Франк, М. П.:* Элементарные приближенные вычисления. Москва 1932.
29. *Варга, И. И.—Чернявский, Б. А.—Шальнев, К. К.:* О методе исследования масштабного эффекта кавитационной эрозии. *Ж. Прикл. Мех и Техн. Физ. АН СССР Москва* (1963), № 3, 122—129.

INVESTIGATION OF THE INFLUENCE OF THE SCALE EFFECT ON THE EROSION BY CAVITATION

J. VARGA, GY. SEBESTYÉN, K. K. SHALNYEV and B. A. TSHERNIAVSKY

SUMMARY

The paper presents results achieved up to date and surveys the methodologic problems which are the bases of research on the scale effect of cavitation erosion within the common research program of the Mechanical Institute of the Soviet Academy of Sciences and the Fluid Mechanical Working Group of the Hungarian Academy of Sciences at the Department of Hydraulic Machines, Budapest Technical University. The theoretical bases of the laboratory research methods for investigating the scale effect, based on an energetic parameter, are critically dealt with. The authors describe the experimental gear and the conditions with the aid of which the energetic parameter and the similarity criterion of the erosion are determined. The possible errors of the measured values and the influence of the errors on the final experimental results are analyzed. It is shown that the results of the experiments carried out at the Budapest Technical University confirm the earlier experiments, and thus the validity of the relation describing the scale effect is proved for a still larger range.

EXAMEN DE L'EFFET D'ÉCHELLE DE L'ÉROSION DE CAVITATION

J. VARGA, GY. SEBESTYÉN, K. K. SHALNYEV et B. A. TSHERNIAVSKY

RÉSUMÉ

Un aperçu des résultats déjà atteints accompagne l'exposé des méthodes qui servent de base à l'étude de l'effet d'échelle de l'érosion de cavitation. Cette étude se fait dans le cadre d'un programme commun de recherces entreprises par l'Institut de Mécanique de l'Académie des Sciences de l'URSS et une équipe de spécialistes de l'Académie des Sciences de Hongrie, dont les recherches sur l'écoulement se poursuivent à la Chaire des Machines Hydrauliques de l'Université Technique de Budapest. L'étude envisage d'un point de vue critique les principes des recherches de laboratoire sur l'effet d'échelle, basées sur le para ètre énergétique. Les auteurs font aussi connaître l'installation et les conditions dans lesquelles sont déterminés les

critères de similitude du paramètre énergétique et de l'érosion. Les erreurs possibles des valeurs mesurées et leur influence sur les résultats définitifs des essais sont analysés. Les auteurs montrent enfin que les résultats des essais faits à l'Université Technique de Budapest confirment ceux des essais antérieurs. Le domaine de la validité de la relation exprimant l'effet d'échelle se trouve ainsi considérablement élargi.

ИССЛЕДОВАНИЕ ВОЗДЕЙСТВИЯ НА МАСШТАБ КАВИТАЦИОННОЙ ЭРОЗИИ

Й. ВАРГА,—Д. ШЕБЕШТЬЕН и К. К. ШАЛЬНЕВ — Б. А ЧЕРНЯВСКИЙ

РЕЗЮМЕ

В работе, наряду с показом достигнутых до сих пор результатов, дается обзор тех методических вопросов, на основе которых исследование воздействия на масштаб кавитационной эрозии проводится в рамках совместной программы исследований в Механическом институте Академии наук СССР и на Кафедре гидромашин Будапештского политехнического института. В критическом освещении излагаются теоретические основы лабораторных исследовательских методов, основанных на энергетическом параметре воздействия масштаба. Описываются опытное устройство и те условия, при помощи которых производится определение энергетического параметра и критерия подобия эрозии. Дается анализ возможных ошибок измеренных данных и воздействия ошибок на опытные результаты. Показано, что результаты опытов, проведенных в Будапештском политехническом институте, подтверждают предыдущие опытные данные и этим действительность зависимости, описывающей воздействие масштаба, подтверждается для еще большей области.

THREE-DIMENSIONAL PHOTOELASTIC INVESTIGATION OF A TWISTED BAR

I. HUSZÁR
CANDIDATE OF TECHNICAL SCIENCES

and

L. CSIZMADIA

[Manuscript received September 3, 1963]

As a first application of three-dimensional photoelasticity in Hungary, the stresses, resp. stress-concentration factors of a twisted prismatic, resp. of a grooved circular section bar were measured. The characteristics of the resins Polikon ES (manufactured in Hungary) and Araldit D, further the modelling, the freezing-in of stresses and the evaluation are discussed in detail.

I. Introduction

Among the methods of the experimental stress analysis, increasingly more ground is gained by photoelasticity. In Hungary, however, this method was applied uptill now only for the case of plane stress condition [1].

In a general case, for the determination of the stress condition, the computation of six stress components for each point is understood. In those cases, however, where the principal stress directions are known or certain elements of the stress tensor are zero, the evaluation of the measurements becomes simpler. Such a case is, for example, the torsion of a prismatic bar of constant cross-section, characterised by the tensor

$$F = \begin{vmatrix} 0 & 0 & \tau_{xz} \\ 0 & 0 & \tau_{yx} \\ \tau_{zx} & \tau_{xy} & 0 \end{vmatrix}.$$

For the time being, as a more modest aim the investigations of torsion was set by the authors.

In case of a three-dimensional model, the principal directions and the stresses themselves vary from point to point. Therefore, the pattern obtained from the entire three-dimensional model cannot be evaluated. In this case the model must be reduced to such slices for which, with a good approximation, along the thickness of the slice, $\sigma_1' - \sigma_2' = \text{const}$ and also the principal directions are constant. Here, σ_1' and σ_2' are the socalled secondary principal stresses, to be explained in more detail later. By this the three-dimensional investigation is reduced to a plane one.

The photoelasticity in a three-dimensional case consists of the following steps:

a) A model of the machine part has to be made.

b) Loading the model according to the original load, a permanent deformation has to be produced; the stresses are, so to say, frozen into the model.

c) The model has to be cut into thin slices.

d) The slices are to be photographed.

e) By evaluating the photographs, the stress condition at the points of the model can be determined.

II. Material and Preparation of the Model

With regard to a proper shaping of the model, the most appropriate raw material is casting resin, since it can be moulded and also glued into any wanted form.

The requirements for the material of the model are:

1. Slow hardening after moulding, with only a slight shrinkage;
2. proper hardness and strength at room temperature;
3. machinability at room temperature;
4. thermoplasticity;
5. transparency;
6. sufficient optical sensitivity;
7. elasticity.

The experiments were made with two kinds of materials: Hungarian made Polikon ES and Swiss made Araldit D synthetic resins. According to the experiments, both resins meet the requirements described under 1—7 well. For comparison, the following can be said:

The optical sensitivity of the Araldit used is higher, i.e. a much higher maximal fringe value belongs to the same deformation. The shrinkage of Araldit is less, this is a great advantage in the casting of more complicated forms. The advantage of Polikon is on the other hand, that it can be used for stress tests immediately after moulding, while Araldit must first be heat-treated. Araldit softens at a temperature somewhat lower than Polikon does, therefore, the temperature of freezing-in may be lower. As to machinability — when comparing the two materials — it must be stated that Araldit is more durable. This is also proved by the tensile tests made on these materials (Figs. 1 and 2).

In the technology of model processing, three different methods can be followed:

a) Ready moulding;

b) machining after moulding;

c) gluing after moulding.

The first one is worth applying if the model consists of simple geometric forms. With smaller, more complicated forms, the second, — with larger, featured geometrical shaping, the third procedure is advisable.

The casting of the synthetic resin is the first operation. The casting is made in a cold state, after having mixed the appropriate components well. The perfect mixing of the components is very important. Inhomogeneities as

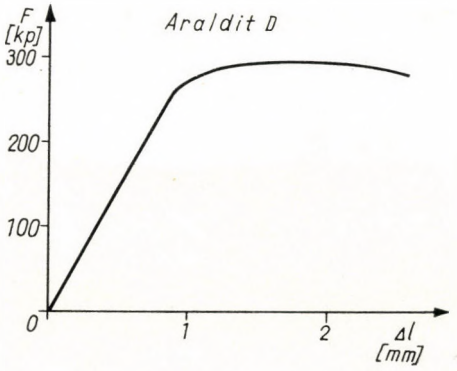

Fig. 1

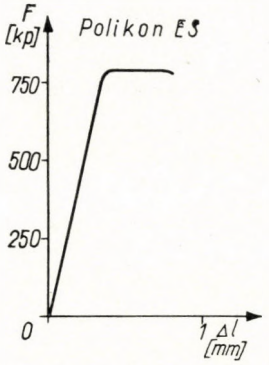

Fig. 2

well as improper proportions of the components cause an uneven hardening of the model. This, on the other hand, produces permanent stresses, falsifying the measurements (Fig. 3).

Considering that these synthetic resins are good adhesives when in a liquid state, the mould before casting has to be smeared with silicon grease on the surfaces contacting with the model. If this is omitted, the model will become stuck. Attention must also be paid to the slow pouring in of the synthetic resin. If the casting is made quickly, smaller or larger air bubbles will be confined in the casting, causing the model to lose its homogeneity.

An experiment was made, in order to prevent the confinement of air bubbles, by casting in a vacuum furnace. This led to much better results, since an appropriate degree of vacuum (660 Hg mm) sucks out the air bubbles from the material.

After 24 hours drying the model can be taken out of the mould. At this time, the Polikon casting can be taken as ready, its strength at a temperature of 20 °C, attaining the degree sufficient for the machinability of the model, whereas the Araldit model can easily be shaped, in this state, even by hand. In order to stop this procedure the model must be heat-treated. It rapidly heats up to 90 °C, then is cooled — after having been kept at this temperature for 4 hours — at a rate of 5 °C/hour. In this way, a well machinable material

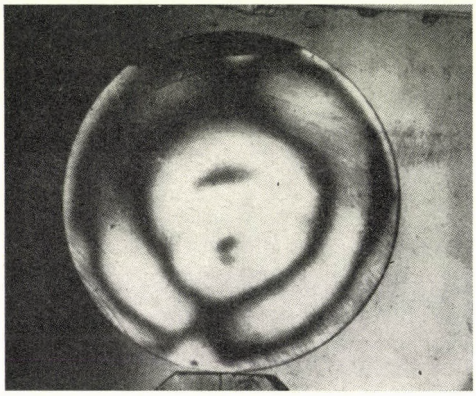

Fig. 3

of a strength similar to that of Polikon is obtained, but much more durable than Polikon.

If the model is cast and heat-treated, the above mentioned can immediately be followed by the freezing in of the stresses. In most cases, however, casting is followed by machining. When applying any kind of machining, this must be done with utmost care. One must be careful not to allow too large power effects arise further that the model should not become heated. These would lead, namely, to a permanent deformation of the model: that is, stresses disturbing from the point of view of analysis would freeze in.

In both synthetic resins, model parts can be attached to each other with their own material. The most advisable is to glue before the casting pieces are fully dry; glued in this state, namely, the spot of gluing will be nearly equivalent to the remaining sections of the model in respect to both strength and optics. However, in this procedure, attention must be paid to the even distribution of the liquid resin used for gluing, on the surfaces glued. The so obtained connection will not alter the stress conditions.

III. Freezing in of the Stresses

As the next step, the model is loaded. The loaded model will be warmed up, then the deformed model will be again cooled. Thus, latter will harden in this shape deformed at a higher temperature.

After several trials, heat-treatments carried out according to the following description proved to be satisfying.

With Polikon, the model under load is warmed up at a rate of 10 °C/hour to 130 °C; then, after having kept it heated for half an hour, cooled to 70 °C at a rate of 5 °C/hour finally, it is left in the furnace to finish cooling.

With Araldit, it is sufficient to reach 100 °C at the same rate and to let cool from this temperature — after having kept the model heated for half an hour — similarly to Polikon, at a rate of 5 °C/hour.

Attention must be paid especially two things when freezing in the stresses. One is a proper selection of load extent, the other is slow cooling. A cooling made without proper care may easily lead, on account of uneven shrinking, to a cracking of the model.

IV. Slicing of the Model

The stress conditions of the model, which was made birefractively in the way described, cannot be evaluated, since the stress condition and thus also the optical factors proportional to it vary from point to point along the thickness of the model. For this very reason, the model is cut into slices limited by parallel planes. In the slices obtained, the evaluation can be made as if one were confronted by a plane stress condition. At a given point of the structure, the stress condition cannot be determined by evaluating the plane stress condition of a single slice passing through this point. Therefore, slices must be cut out in several directions, or the problem approached by some other method.

In case of a three-dimensional stress distribution, the stress condition and the principal directions also vary along the thickness of the slice, the analysis furnishing therefore an average value for the stresses. Therefore it is advisable to choose the thickness of the slices to be as small as possible. Accordingly, the decrease of the thickness increases the accuracy of the analysis. On the other hand again, it makes the experiment more difficult, since the order of the isochromatics will decrease with the decrease of the thickness of the slice. Consequently, if the thickness is chosen too small, only a restricted number of measuring points will stand at one's disposal from the loose net of isochromatics along each section; that is, the decrease of slice thickness is at the expense of accuracy. According to experiences, the optimal slice thickness may vary between 3 and 6 mm.

The slicing must be done very carefully, in order to prevent residual stresses, it is evident the latter will falsify the measurements. It is advisable to make the slicing on a milling machine with a slitting saw. No permanent stresses caused by machining were observed in a model sliced in the described way.

V. Photographic Recording of the Isochromatics and Isoclinics

In the slices, isochromatic and isoclinic lines can be observed. By setting $\lambda/4$ plates also between the polarizers the isochromatics can be examined separately too. For their recording, photography is the most suitable. It is worth constructing a device for the fitting of the slices, revolving around the vertical axis and adjustable to calibrated accuracy. Later it will be seen that this is needed, because it is advisable, in certain cases to make records of the slices at several different illumination angles.

VI. Evaluation of the Measurements

The aim of the evaluation is to determine the stress condition at every point of the model.

Let us investigate the stress condition frozen-in under the effect of a force system at any point P of the model. If a slice is to be cut out of the model across point P and parallel to a plane xy (Fig. 4) and this slice is transilluminated by polarized light ($\vec{k}'$) passing in the plane xz, with the normal $\vec{k}$ at an angle ψ, then the fringe value of the isochromatics is obtained for the point in question. This order of the fringes naturally is related, even in this case, to the stress condition of point P. More strictly taken, however, it is related to the so-called secondary stresses. The notion of secondary stress is explained by the following. Let us draw a very small cubic element at a point P in the system $\xi\,\eta\,\zeta$ of coordinates (Fig. 5). Here the stress condition can be characterised by the stress vectors $\vec{\varrho}_\xi$, $\vec{\varrho}_\eta$, $\vec{\varrho}_\zeta$, respectively by the tensor

$$F = \begin{bmatrix} \sigma_\xi & \tau_{\xi\eta} & \tau_{\xi\zeta} \\ \tau_{\eta\xi} & \sigma_\eta & \tau_{\eta\zeta} \\ \tau_{\zeta\xi} & \tau_{\zeta\eta} & \sigma_\zeta \end{bmatrix}.$$

Under secondary stresses, the components of the stress vectors $\vec{\varrho}_\xi$ and $\vec{\varrho}_\eta$ falling into the plane perpendicular to the direction of the light

$$\vec{\varrho}'_\xi = \sigma_\xi \vec{i}' + \tau_{\xi\eta} \vec{j},$$

and

$$\vec{\varrho}'_\eta = \tau_{\eta\xi} \vec{i}' + \sigma_\eta \vec{j}$$

are understood.

For their determination, let us produce F as the sum of two tensors:

$$F = F' + F^* = \begin{bmatrix} \sigma_\xi & \tau_{\xi\eta} & 0 \\ \tau_{\eta\xi} & \sigma_\eta & 0 \\ 0 & 0 & 0 \end{bmatrix} + \begin{bmatrix} 0 & 0 & \tau_{\xi\zeta} \\ 0 & 0 & \tau\eta \\ \tau_{\zeta\xi} & \tau_{\zeta\eta} & \sigma_\zeta \end{bmatrix}.$$

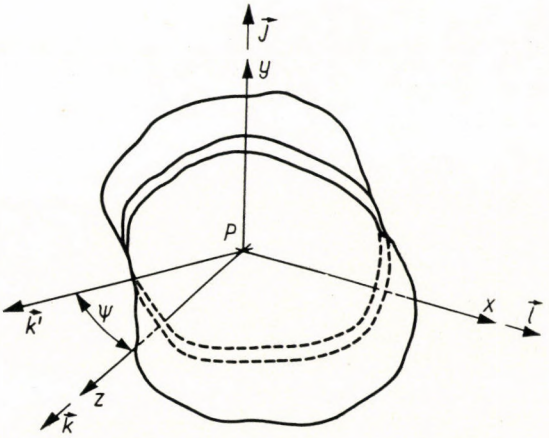

Fig. 4

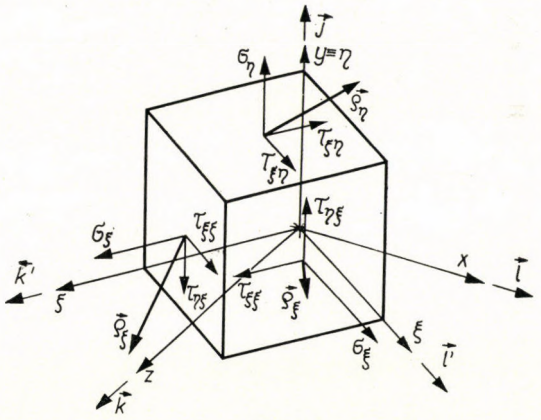

Fig. 5

From this expansion, one can at once see that the tensor describing the secondary stresses will be F'.

The order of the isochromatics measured in point P is proportional to the difference of the secondary principal stresses calculable from tensor F' interpreted in this way [2].

$$m' = Kd'(\sigma_1' - \sigma_2'),$$

where K is the optical constant, d' — the path of the light in the slice.

Omitting the detailed calculations:

$$\sigma_1' - \sigma_2' = \sqrt{(\sigma_y - \sigma_x \cos^2\psi - 2\,\tau_{xz} \sin\psi \cos\psi - \sigma_z \sin^2\psi)^2 + 4\,(\tau_{yx} \cos\psi + \tau_{zy} \sin\psi)^2}\,.$$

VII. Solution of Torsional Problems

As an example, let us investigate the measuring of the distribution of stresses arising during the torsion of a prismatic bar. Let us cut a slice out of the

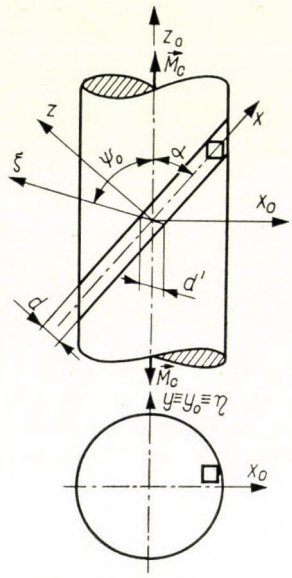

Fig. 6

model at an angle α to the axis, according to Fig. 6; then, transilluminating the slice thus obtained, similarly at an angle ψ measured from the axis of the bar, with the light passing in the plane $x_0 z_0$, let us apply the above stated.

Taking an elementary prism of the twisted bar (Fig. 7), the stress tensor belonging to the system $x_0 y_0 z_0$ of coordinates can be written in the form

$$F_0 = \begin{array}{c} \begin{array}{ccc} \vec{\varrho}_{x0} & \vec{\varrho}_{y0} & \vec{\varrho}_{z0} \end{array} \\ \begin{bmatrix} 0 & 0 & \tau_{xz} \\ 0 & 0 & \tau_{yz} \\ \tau_{zx} & \tau_{zy} & 0 \end{bmatrix} \end{array}.$$

Let us determine then the tensor of the secondary stresses F' belonging to the system $\xi\eta\zeta$ of coordinates bound to the direction of illumination (ξ lies

in the plane $x_0 z_0$, $\eta \equiv y_0$). The normal stress belonging to $\vec{e}_\xi$ lying in the plane perpendicular to the direction of the light is:

$$\sigma_\xi = \vec{e}_\xi F \vec{e}_\xi = [\cos\psi_0;\ 0;\ \sin\psi_0] \begin{bmatrix} 0 & 0 & \tau_{xz} \\ 0 & 0 & \tau_{yz} \\ \tau_{zx} & \tau_{zy} & 0 \end{bmatrix} \begin{bmatrix} \cos\psi_0 \\ 0 \\ \sin\psi_0 \end{bmatrix} = \tau_{zx} \sin 2\psi_0 ,$$

and the shear stress is:

$$\tau_{\xi\eta} = \vec{e}_\eta F \vec{e}_\xi = [0;\ 1;\ 0] \begin{bmatrix} 0 & 0 & \tau_{xz} \\ 0 & 0 & \tau_{yz} \\ \tau_{zx} & \tau_{zy} & 0 \end{bmatrix} \begin{bmatrix} \cos\psi_0 \\ 0 \\ \sin\psi_0 \end{bmatrix} = \tau_{zy} \sin\psi_0 ,$$

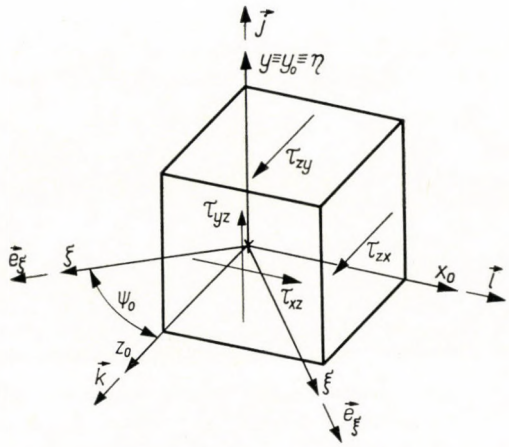

Fig. 7

finally the normal stress belonging to $\vec{e}_\eta$ is:

$$\sigma_\eta = 0 .$$

According to these, tensor F' is:

$$F' = \begin{bmatrix} \tau_{zx} \sin 2\psi_0 & \tau_{yz} \sin\psi_0 \\ \tau_{yz} \sin\psi_0 & 0 \end{bmatrix}.$$

Drawing Mohr's circle diagram the differences of the secondary principal stresses are easily obtained according to Fig. 8:

$$\sigma_1' - \sigma_2' = \overline{20\Xi} = 2\sqrt{(\sigma_\xi/2)^2 + \tau_{\xi\eta}^2} .$$

Substituting the values of σ_ξ and $\tau_{\xi\eta}$, after reduction:

$$\sigma_1' - \sigma_2' = 2 \sin\psi_0 \sqrt{\tau_{zx}^2 \cos^2\psi_0 + \tau_{zy}^2} .$$

The thickness of the model in the direction of the light is easily calculable from the geometrical conditions according to Fig. 9:

$$d' = \frac{d}{\sin(\alpha + \psi_0)} .$$

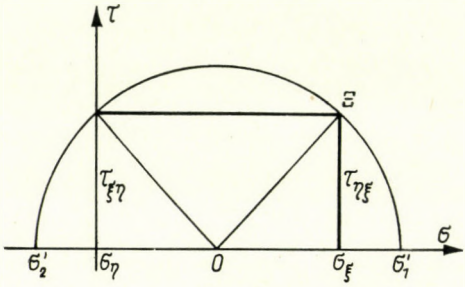

Fig. 8

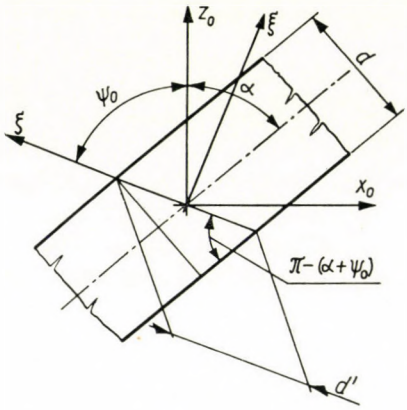

Fig. 9

According to this, finally:

$$m' = 2\,Kd\,\frac{\sin\psi_0}{\sin(\alpha + \psi_0)}\sqrt{\tau_{zx}^2\cos^2\psi_0 + \tau_{zy}^2}.$$

It is advisable to investigate the stress distribution along an — arbitrarily chosen — axis y. By considering that, along the y-axis, $\tau_{zy} = 0$, the above expression becomes simpler:

$$m' = Kd\,\frac{\sin 2\,\psi_0}{\sin(\alpha+\psi_0)}\,\tau_{zx}.$$

This is the relation on the basis of which it is possible to compute the stresses from the pattern obtained in the photoelastic investigation, with the

aid of the individual m' fringe value of the isochromatics. Let us examine this more detailed.

The measuring points can be densified — similarly to plane investigations — by photographs made in parallel and cross setting of the polarizers. In this way, namely, besides the order: 1, 2, 3, . . ., also the isochromatics of orders 0,5; 1,5; 2,5; . . . are obtained. There is another method with which one can increase the measuring accuracy, i.e. to densify the measuring points. Its essence is, that by changing the transillumination angle also the obtained fringe patterns will change according to the above explained relation.

Choosing a point on the y-axis, let us examine, how the value of the order m' will change with the variation of angle ψ_0. If $\psi_0 = \alpha$,

$$m'_\alpha = Kd\,\tau_{zx}\,.$$

Applying this notation, on the other hand, in case of an arbitrary angle ψ_0:

$$m' = m'_\alpha\,\varkappa\,,$$

if the factor

$$\varkappa = \frac{\sin 2\,\psi_0}{\sin(\alpha + \psi_0)}$$

is introduced. If, for example, the pattern illuminated at an angle $\psi_0 = \alpha$ is taken as a basis, and every wanted order to be given is the same, the isochromatics of the integers $m = 0, 1, 2, 3, \ldots$ will align on the pattern obtained in this way. The orders of the fringes appearing in case of a record illuminated at any other angle $\psi_0 = \alpha$ can be converted to the former by multiplying their fringe values taken for integers 0, 1, 2, 3, by $1/\varkappa$.

Choosing in this way, for example, the value $\alpha = 30°$ and making the records with exposures at $\psi_0 = 30°, 45°, 60°$ (with parallel and cross-setting polarizers), the isochromatics of the orders 0; 0,48; 0,5; 0,575; 0,96; 1; 1,15; 1,44; 1,5; 1,725; 2; . . . will stand at disposal.

This was the way the isochromatics were recorded having a prismatical bar of circular cross section (Fig. 10), then the diagram of the values m' drawn along the y-axis (Fig. 11). It is clearly visible that the measuring points lie, with a very slight dispersion, on a straight line. In this case, however, also the stress $\tau_{zx} = \tau(\varrho)$ proportional to the above relation is linear. In case of a circular cross section, however, the distribution of the τ stresses is exactly the same, i.e. the measured values agree well with the calculated ones. This can be set down as a control for the measurement. There is no objection, of course, to draw, instead of the m' diagram, the curve of the τ stresses. Namely, in the knowledge of α, ψ_0, d, only the material constant K has to be determined; this, however, can be easily done with the aid of a simply bent or drawn specimen.

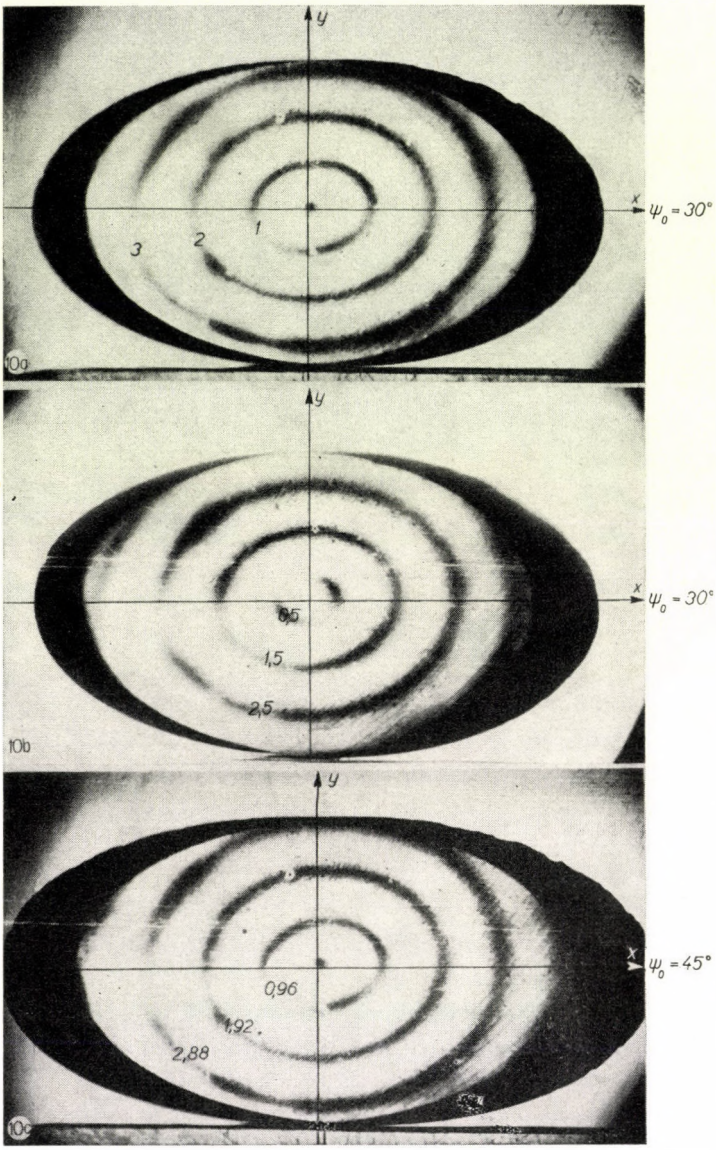

Fig. 10

Besides, the results can be directly utilized in the course of the three-dimensional photoelasticity, precisely for the determination of the material constant.

In this case, namely, the value τ_{max} on the boundary can be computed in an exact way. With the method discussed previously, on the other hand, the value of m'_{max} in the boundary point corresponding to τ_{max} in case of $\psi_0 = a$

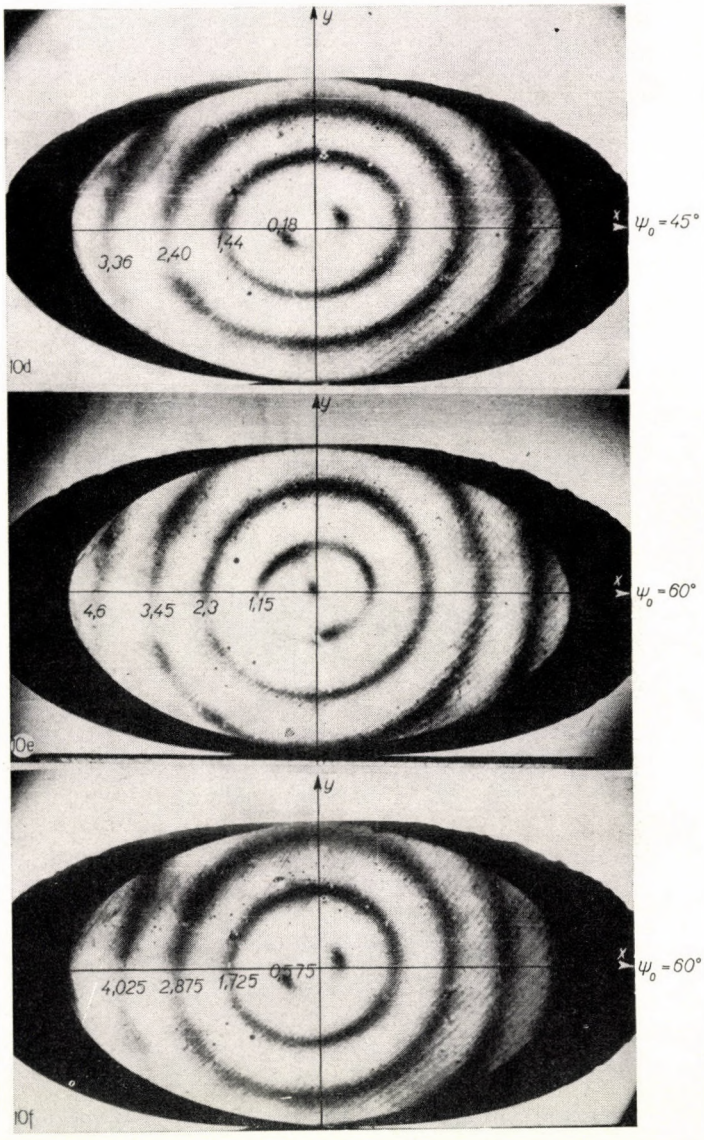

Fig. 10 (continued from page 392)

stands at our disposal. With these,

$$\tau_{\max} = \frac{M_c}{K_p} = \frac{m'_{\max}}{K_d} .$$

After reduction:

$$K = \frac{m'_{\max} K_p}{M_c d} .$$

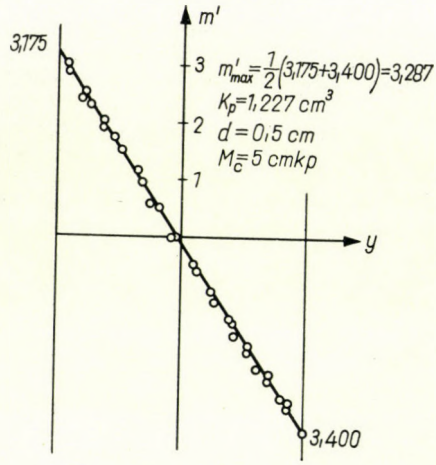

Fig. 11

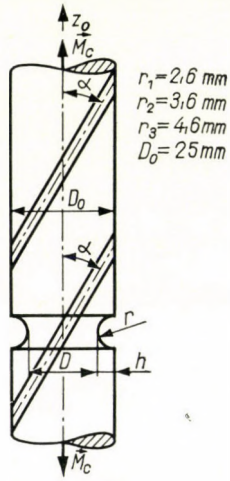

Fig. 12

Having carried out the calculations, the value $K = 1{,}61$ cm/kp was obtained for the optical constant of Araldit according to the diagram presented.

VIII. The Stress Concentration Factor of a Grooved Twisted Bar

Next, applying the previously described method, the determination of the maximum stress in the case of torsion of grooved bars was set as our task. In the evaluation, based on a literary example [2], no consideration is given to the fact that the procedure quoted is, on account of the groove, not strictly valid. First the semicircular groove was investigated. Three stress concentrations of three different radiuses r were determined, assuming that they were produced at the boundary points of the smallest diameter cross section. (A posi-

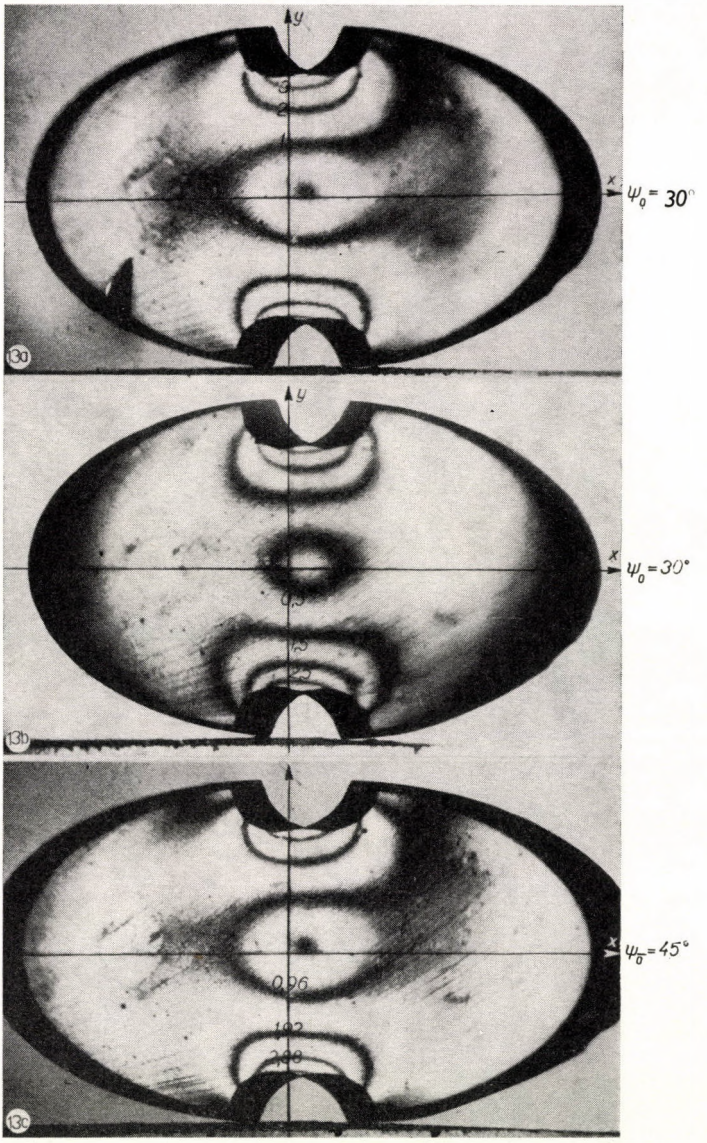

Fig. 13

tive statement as to this would require further investigations, since it is possible that the critical points of the twisted bar are not in the places mentioned.)

Knowing the sizes of the so interpreted maximum stresses, the values of the form factors a_k can be determined.

Two slices were cut out of the frozen-in model at an angle $\alpha = 30°$. One was cut in such a way that the incision was in the center of the slice, the

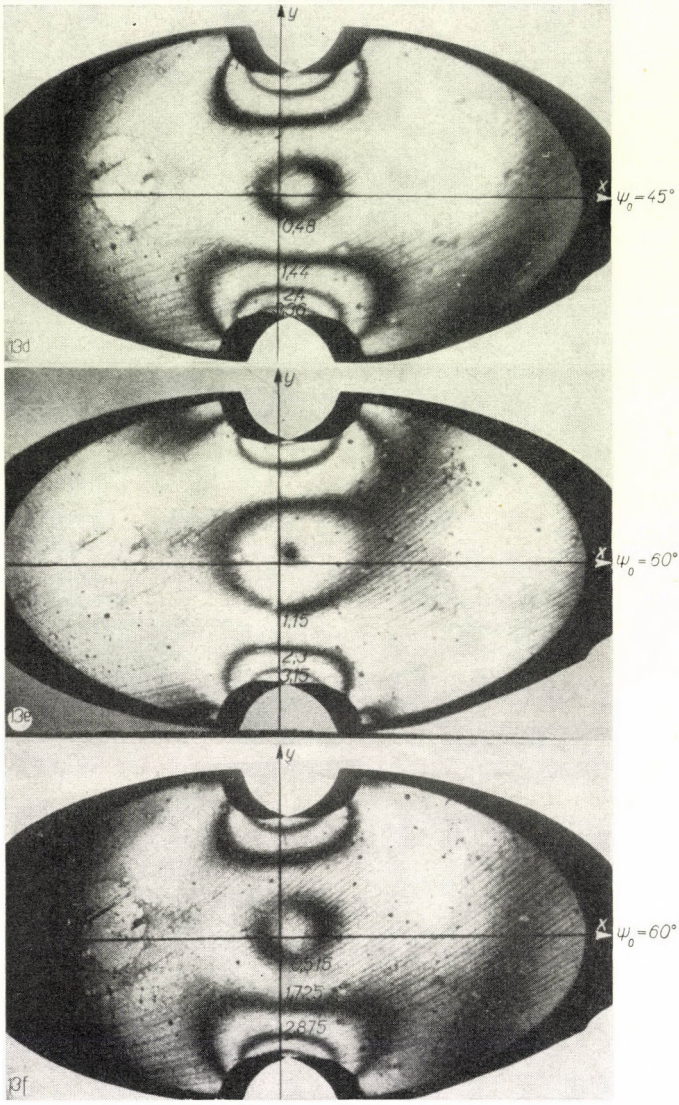

Fig. 13 (continued from page 395)

other one was taken from the undisturbed part of the bar (Fig. 12). Records were taken of both slices at angles of $\psi_0 = 30°$, $45°$ and $60°$ — at parallel and cross settings. According to the isochromatic patterns (in case of $r = 3{,}6$ mm and $r = 4{,}6$ mm, all records are shown by Figs. 13 and 14), the $m'(y)$ curves along the y-axis were drawn (Figs. 15, 16 and 17) according to the method presented above. Here, $m'(y)$ is proportional to the function $\tau(y)$ representing the stress distribution. From the diagrams, the $m'_{\max}$ values referring to the

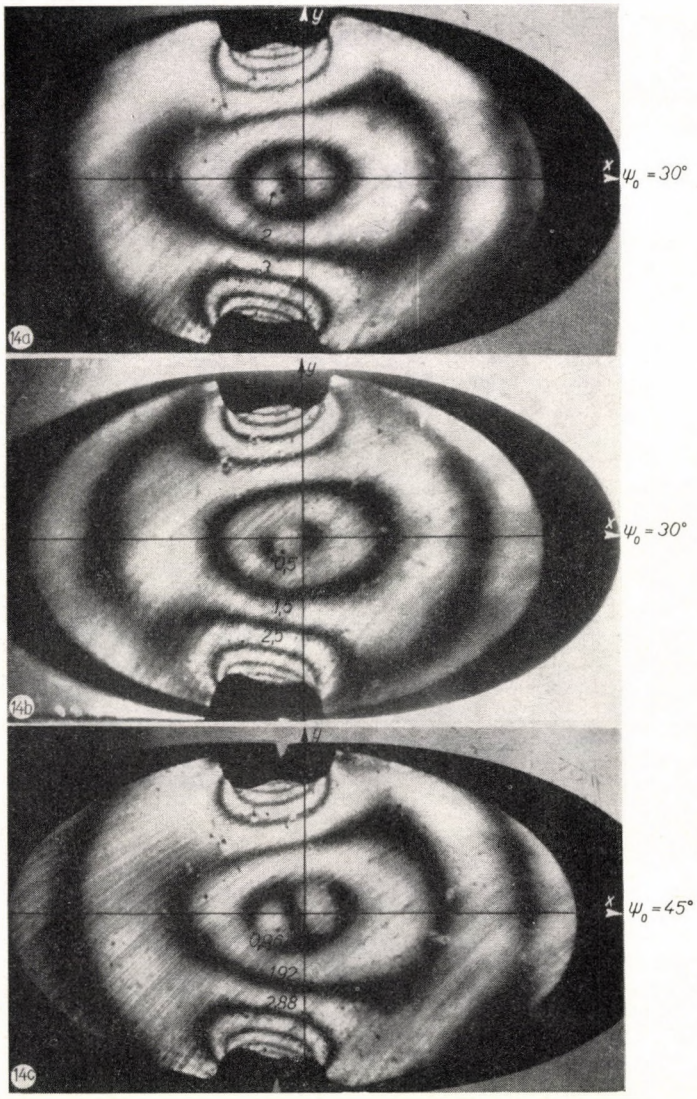

Fig. 14

incision and m_0' referring to the undisturbed section can be read, and, with their aid, the stress concentration factor α_k directly determined.

The average shear stress, namely, according to a simple calculation is:

$$\tau_k = \frac{M_c}{D^3 \pi/16} .$$

The maximal shear stress, on the other hand, on the basis of the measure-

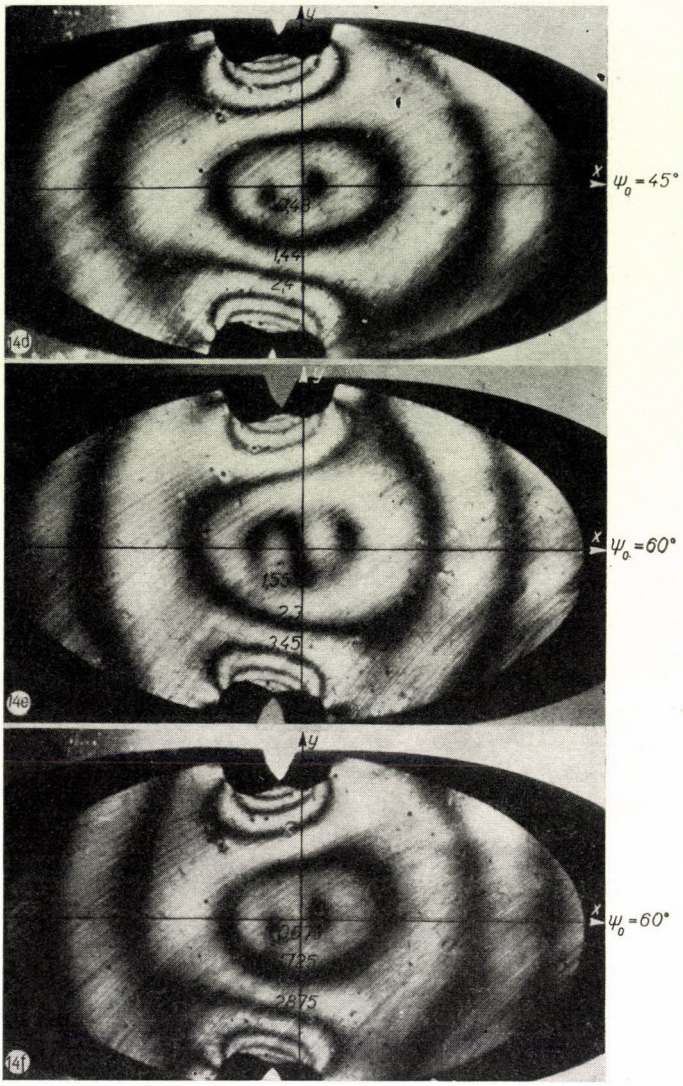

Fig. 14 (continued from page 328)

ment, is:

$$\tau_{\max} = \frac{m'_{\max}}{Kd} .$$

At the same time, on the undisturbed part,

$$\tau_0 = \frac{m'_0}{Kd} = \frac{M_c}{D_0^3 \pi/16} ,$$

hence

$$\frac{1}{Kd} = \frac{M_c}{m'_t D_0^3 \pi/16} .$$

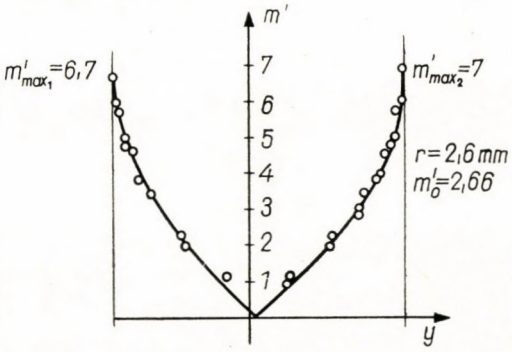

Fig. 15

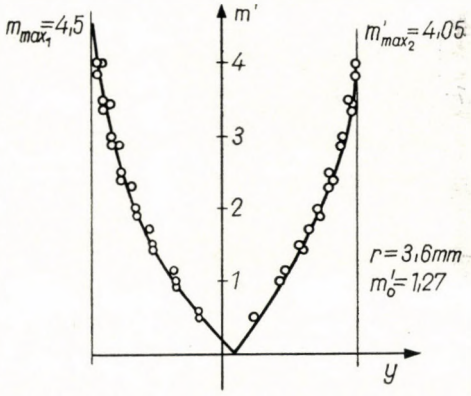

Fig. 16

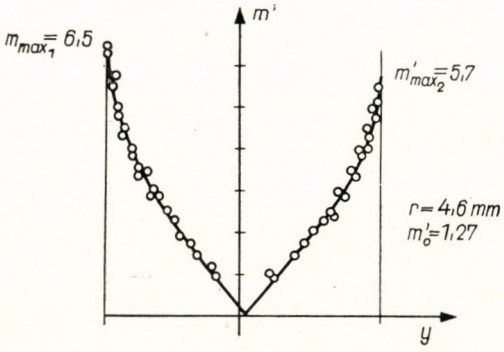

Fig. 17

Let us interpret the form factor in this way:

$$\alpha_k = \frac{\tau_{\max}}{\tau_k} .$$

According to the above stated, then:

$$\alpha_k = \frac{m'_{\max}}{m'_0} \frac{D^3}{D_0^3} ,$$

using the relations obtained for $\tau_{\max}$ and τ_k, further for $1/Kd$. In this way was the value of α_k for three different r values, keeping the ratio $h/r = 1$, determined and drawn as diagram in the function of r/D. The results were compared to the similarly defined α_k diagram of PETERSON, published in his publications listed in the literature [3] and based on the computations of NEUBER [4] (Fig. 18). At the place of the maximum stress of the groove the transmitted light beam passes on account of the obliquely cut model, places of different stress states.

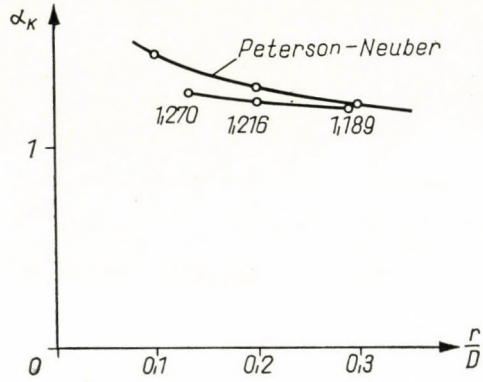

Fig. 18

Therefore, the order of the isochromatics presenting itself there gives a kind of average of the stress conditions lying in the path of the light, anyway lower than the one corresponding to the maximum stress value. Thus, α_k values lower than the actual ones are furnished by the measurement. Comparing this to values obtained in other ways (see Fig. 18), the deviation is less than 10%.

Let it be finally remarked that it would be more sensible to interprete the form factor according to

$$\alpha_k = \frac{\sigma_{r\,\max}}{\sigma_{rk}} ,$$

where $\sigma_{r\,\max}$ is the reduced maximal stress, σ_{rk} — the reduced average stress. This kind of computation would be justified, because an impeded torsion is produced at the incision, consequently also normal stresses arise beside shear stresses.

REFERENCES

1. HUSZÁR, I.: 25 Years of Photoelasticity in Hungary. *Acta Techn. Hung.* **31** (1960).
2. FROCHT, M. M.: Photoelasticity II. Wiley, New York 1948.
3. PETERSON, R. E.: Stress Concentration Design Factors. Wiley, New York 1953.
4. NEUBER, H.: Kerbspannungslehre. Springer, Berlin 1958.

RÄUMLICHE PHOTOELASTISCHE UNTERSUCHUNG EINES VERDREHTEN STABES

I. HUSZÁR—L. CSIZMADIA

ZUSAMMENFASSUNG

Als eine erstmalige Anwendung der räumlichen Spannungsoptik in Ungarn wurden die Spannungen bzw. Formfaktoren eines verdrehten prismatischen bzw. eingekerbten Stabes mit Kreisquerschnitt von den Verfassern ausgemessen. Im Aufsatz werden die Eigenschaften der Gießharze Polikon ES (hergestellt in Ungarn) und Araldit D, die Anfertigung des Modells, das Einfrieren des Spannungen und die Auswertung ausführlich behandelt.

PHOTOÉLASTICIMÉTRIE TRIDIMENSIONNELLE D'UNE BARRE TORDUE

I. HUSZÁR—L. CSIZMADIA

RÉSUMÉ

Une première application de la photoélasticimétrie tridimensionnelle en Hongrie a été faite par les auteurs ayant mesuré les tensions, resp. les facteurs de forme d'une barre tordue prismatique ou de section circulaire incisée. Dans l'article, les propriétés des résines synthétiques Polikon ES (faites en Hongrie) et Araldit *D*, ainsi que la production du modèle, l'enraidissement des tensions et l'évaluation sont discutés en détail.

ИЗУЧЕНИЕ КРУЧЕННОЙ ШТАНГИ ПРОСТРАНСТВЕННЫМ ОПТИЧЕСКИМ ПУТЕМ

И. ХУСАР—Л. ЧИЗМАДИА

РЕЗЮМЕ

Метод пространственного оптического изучения напряжения был использован в Венгрии впервые для определения напряжений и коэффициентов формы крученной штанги с призматическим или надрезанным круговым сечением. В настоящей работе подробно описаны свойства типов литейной смолы венгерской Поликон ES и Аралдит D, способы изготовления моделей, замораживание и дается оценка.

IMPEDANCES SEEN BY DISTANCE RELAYS IN A GENERAL CASE

P. O. GESZTI
DOCTOR OF TECHN. SC.

GY. PÓKA
TECHNICAL UNIVERSITY, BUDAPEST

[Manuscript received January 24, 1964]

The measuring of a distance protection is distorted by several factors. It is possible that the operation of protection is not selective or the protection does not work at all because of these distortions. The authors try to specify the general equation of distance relay and the deviation from the precise measuring, respectively, taking all distortion factors into account. The relation of universal validity is applied to a typical protection and in two cases of typical faults. After that they demonstrate with some examples the practical application of the method in some special cases.

I. Introduction

The distance protections applied in high-voltage systems may form a selective protection excellent in principle, even on double circuit lines fed from two sides and forming part of an interconnected system. Their impedance measuring, due to the suitable development, is independent of the magnitude of current and sort of fault and it is proportional to the distance between the installation place of the relay and the fault location. The pure distance evaluation is, however, disturbed by the following factors:

a) Resistance at the fault location;
b) Load (overload) current;
c) Current- and voltage variations due to oscillations;
d) Zero-sequence interaction between parallel lines.

In case of lines that inside the basic protecting section have also an intermediate feed-in (branch, T-branch, etc.), the distorsion caused by the intermediate feed-in appears, too. Thus, the line arrangements of that kind, i.e. the phenomenon, will not be dealt with in our further discussions.

The effects occurring through points *a)*, *b)*, *c)* and *d)* which disturb the exact operation of relays, are described in many studies and articles. These papers take as a basis almost exclusively the simultaneous appearance of one or at least two phenomena. The present paper tries to develop, considering all the four disturbing factors simultaneously the formulae to be adapted in the practice.

II. Definitions

All problems related to the setting of distance protection may be reduced to the correct evaluation of an impedance seen by the relay when a fault is present at the far end of the overhead line protected, inside the protection zone, rear the opposite side. Namely the tripping must be set in the first stage with safety below this value, and the second one above this value. Though the individual protections are realized as if the faults of different types, but arising at identical distances (locations) should be seen at identical distances, all the

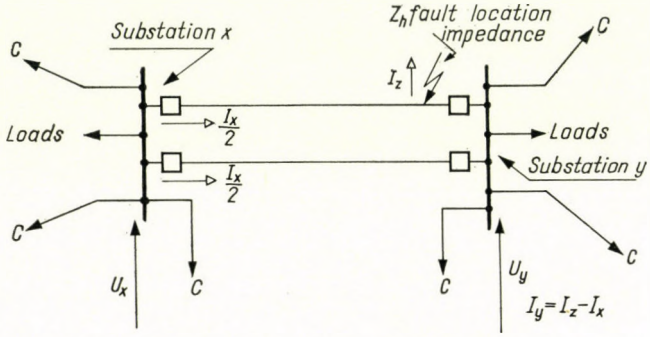

Fig. 1. Network "C" links to the other parts of the network

same this is often hindered by the disturbing factors mentioned in clause I. Accordingly, this article has to examine, what does the relay see at a short-circuit on the line end, taking all disturbing factors into account.

The network shown in Fig. 1 may be substituted by the diagram of Fig. 2. Z_{vt} involves the resultant zero-sequence impedance of the double circuit overhead line, while Z_{er} is the resistance at the fault location and eventually the combination of the resultant impedances of the negative- and zero-sequence networks, respectively (Table I). The impedance seen by the relay V may be determined, if the value of the voltages (U_x), currents (I_x), as well as symmetrical components at the installation place of relay V are known.*

For determining I_x and U_x some characteristic impedance values of the system must be known. Below the symbols and the interpretations are given (in the system the loads are included, too). The definitions refer to the system from which the faulty overhead line (one- or double-circuit) itself is taken out.

The positive sequence (50 c/s) driving point impedance at point x, with all voltage sources, as well as $n-y$ are short-circuited may be expressed by

$$Z_{xx1} = \frac{U_{x1}}{I_{x1}} \,. \tag{1}$$

* Indexes x and y denote the quantities corresponding to points x and y (see the Figures). The symmetrical component values refer always to the reference phase A.

The positive sequence driving point impedance at point y, with all voltage sources, as well as $n-x$ are short-circuited:

$$Z_{yy1} = \frac{U_{y1}}{I_{y1}} . \tag{2}$$

Transfer impedance between points $x-y$, if all voltage sources, as well as $n-y$ are short-circuited:

$$Z_{xy1} = \frac{Z_{x1}}{I_{y1}} \tag{3}$$

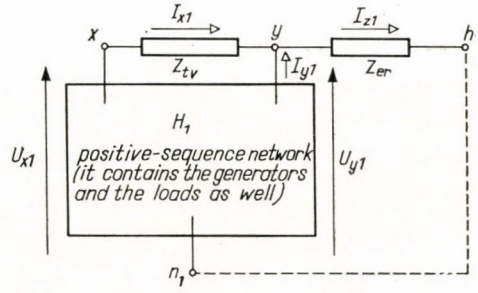

Fig. 2. Equivalent circuit (Z_{tv} : in case of double-circuit line the resultant impedance)

or, if all voltage sources, as well as $n-x$ are short-circuited:

$$Z_{xy1} = Z_{yx1} = \frac{U_{y1}}{I_{x1}} . \tag{4}$$

The values referring to the negative- and zero-sequence system may also be determined with the help of formulae (1), (2), (3) and (4), instead of index 1 stand 2 and 0.

The impedances of the overhead line: Z_{tv}, Z_{tv0} are the resultant positive (negative) and zero-sequence impedances of the overhead line discussed, or, in case of a double circuit line, those of the two lines together.

Index V denotes the quantities at the installation point of the protection.

III. Determination of the Current and Voltage of the Relay

The voltages at points x and y at the instant immediately before the short-circuit, further the voltages on the busbar under normal operational conditions, or under swinging conditions:*

$$U'_{x1} ,$$
$$U'_{y1} .$$

* Values of pre-fault state are denoted by comma.

Hence the current on the line discussed, in the state preceding the short-circuit is:*

$$I'_{x1} = -I'_{y1} = \frac{U'_{x1} + U'_{y1}}{Z_{tv}} . \tag{5}$$

From the three values (U'_{x1}, U'_{y1}, I'_{x1}) two must be known (e.g. U'_{y1}, I'_{x1}). U'_{x1}, U'_{y1} and I'_{x1} are positive sequence values.

The positive sequence network may be completed in thought with Z_{er} (Fig. 2) to determine later the current distribution by superposition: in fault-free conditions there prevails at point h the voltage U'_{y1}, as there is no current flowing on impedance Z_{er}; short-circuiting all generators and imposing on point h a voltage of $-U'_{y1}$, the value of I''_{x1} (and I''_{y1}) may be determined. Thus, the positive-sequence current flowing on the overhead line is

$$I_{x1} = I'_{x1} + I''_{x1} \tag{6}$$

and the positive-sequence current of the relay of one line, in case of a double-circuit-network is evidently half of (6):

$$I_{V1} = \frac{I_{x1}}{2} \tag{7}$$

and at a single-circuit line:

$$I_{V1} = I_{x1} . \tag{7a}$$

According to the aforementioned, short-circuiting of all generators and applying to point h a voltage of $-U'_{y1}$ the following relations may be written (Fig. 3):

$$U''_{y1} - I''_{Z1} Z_{er} + U'_{y1} = 0 ,$$

so

$$I''_{Z1} = \frac{U''_{y1} + U'_{y1}}{Z_{er}} . \tag{8}$$

$$U''_{x1} - I''_{x1} Z_{tv} - U''_{y1} = 0 ,$$

so

$$I''_{x1} = \frac{U''_{x1} - U''_{y1}}{Z_{tv}} . \tag{9}$$

$$I''_{Z1} = I''_{x1} + I''_{y1} , \tag{10}$$

$$I''_{x1} = \frac{U''_{x1}}{Z_{xy1}} - \frac{U''_{x1}}{Z_{xx1}} , \tag{11}$$

$$I''_{y1} = \frac{U''_{x1}}{Z_{xy1}} - \frac{U''_{y1}}{Z_{yy1}} . \tag{12}$$

* The capacitive and the leakage currents are neglected in the overhead line, so the results refer to lines, where this causes no considerable error.

From the five unknowns of Equs. (8)—(12) expressions I''_{x1} and I''_{Z1} [as per (10), formula I'_{y1}] are needed. After some manipulation of the equations

$$I''_{x1}\left(1+\frac{Z_{tv}+Z_{er}}{Z_{xx1}}-\frac{Z_{er}}{Z_{xy1}}\right)+ \\ +I''_{y1}\left(\frac{Z_{er}}{Z_{xx1}}-\frac{Z_{er}}{Z_{xy1}}\right)=U'_{y1}\left(\frac{1}{Z_{xx1}}-\frac{1}{Z_{xy1}}\right), \tag{13}$$

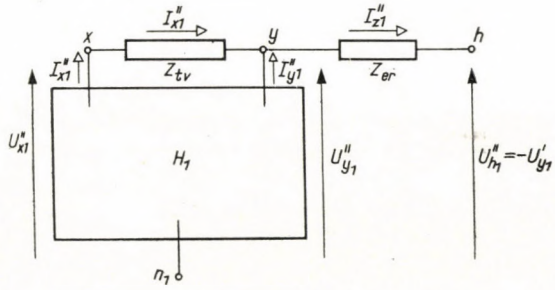

Fig. 3. Positive-sequence network

$$I''_{x1}\left(\frac{Z_{er}}{Z_{yy1}}-\frac{Z_{tv}+Z_{er}}{Z_{xy1}}\right)+ \\ +I''_{y1}\left(1+\frac{Z_{er}}{Z_{yy1}}-\frac{Z_{er}}{Z_{xy1}}\right)=U'_{y1}\left(\frac{1}{Z_{yy1}}-\frac{1}{Z_{xy1}}\right) \tag{14}$$

the solution of the equations

$$I''_{x1}=\frac{U'_{y1}\cdot Z_{xy1}\,Z_{yy1}\,(Z_{xy1}-Z_{xx1})}{a}, \tag{15}$$

$$I''_{y1}=\frac{U'_{y1}\cdot[(Z^2_{xy1}(Z_{xx1}+Z_{tv})-Z_{xx1}\,Z_{yy1}(Z_{xy1}+Z_{tv})]}{a} \tag{16}$$

where

$$a=Z^2_{xy1}(Z_{xx1}+Z_{tv})(Z_{yy1}+Z_{er})+ \\ +Z_{er}\,Z_{yy1}(Z^2_{xy1}-2\,Z_{xx1}\,Z_{xy1}-Z_{tv}\,Z_{xx1})$$

(the value of Z_{er} seen in Table I) and

$$I''_{Z1}=I''_{x1}+I''_{y1}.$$

The positive-sequence current flowing at the relay under consideration [Equs. (5), (6), (7), (7a) and (15)]:

$$I_{V1}=\mathrm{d}I_{x1}=d\,(I'_{x1}+I''_{x1}) \tag{17}$$

where $d = 1$ in case of a single-circuit-overhead line;

$d = 1/2$ in case of a double-circuit overhead line.

The positive-sequence component of the short-circuit current is:

$$I_{Z1} = I'_{Z1} + I''_{Z1}.$$

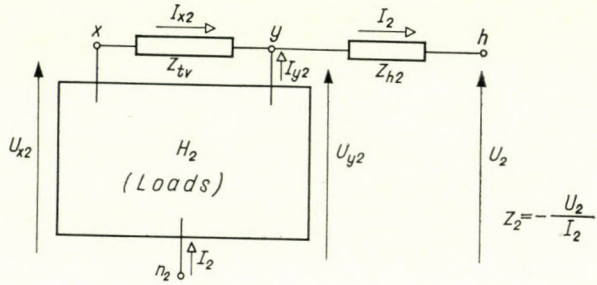

Fig. 4. Negative-sequence network

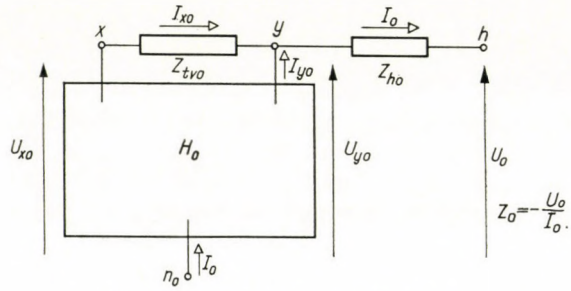

Fig. 5. Zero-sequence network

As in fault-free conditions Z_{er} is current-free,

$$I'_{Z1} = 0\,,$$

thus, on the basis of (15) and (16)

$$I_{Z1} = I''_{Z1} = I''_{x1} + I''_{y1}\,, \tag{18}$$

consequently, the load (oscillation) current does not figure in the expression.

The above equations would be sufficient for discussing a three-phase short circuit. For the case of asymmetrical faults, however, the determination of the negative- and zero-sequence currents is necessary, too.

The currents I_2 and I_0 of Figs. 4 and 5 may be determined in a generally known way depending on the sort of fault. Table I involves the values. The

values Z_2 and Z_0 indicated in the table are the resultant impedances of the system to be seen in Figs. 4 and 5 between points $n-h$. At the same time Table I includes the values of Z_{er} figuring in equations (15) and (16).

Table I

I_2 and I_0 function of the fault type

	Three-phase short-circuit $3F$	Line-to-line short-circuit $2F$	Double line-to-ground short-circuit $2FN$	Single line-to-ground short-circuit FN
Negative-sequence current	$I_2 = 0$	$I_2 = -I_{Z1}$	$I_2 = -I_{Z1}\dfrac{Z_0}{Z_2+Z_0}$	$I_2 = I_{Z1}$
Zero-sequence current	$I_0 = 0$	$I_0 = 0$	$I_0 = -I_{Z1}\dfrac{Z_2}{Z^2+Z_0}$	$I_0 = I_{Z1}$
Z_{er} as per (15) and (16), as well as (4) and (5)	$Z_{er} = Z_{h1}$	$Z_{er} = Z_{h1} + Z_2$	$Z_{er} = Z_{h1} + \dfrac{Z_2 Z_0}{Z_2+Z_0}$	$Z_{er} = Z_{h1} + Z_2 + Z_0$

Knowing the currents I_2 and I_0, respectively, thus the current of the protection tested may be determined as follows.

According to Fig. 4:

$$U_2 = -I_2 Z_2 \tag{19}$$

where I_2 may be obtained in the basis of Table I.

If in Fig. 4 U_2 is replaced by relation (19), I_{x2} may be determined. The arrangement is identical to that of Fig. 3, so I_{x2} can be obtained by Equ. (15). The difference is merely that indexes 2 come instead of indexes 1 (impedances refer to the negative sequence system), and instead of U'_{y1} the value $I_2 Z_2$, instead of Z_{er} the value of Z_{h2} are written. Consequently I_{x2} yields:

$$I_{x2} = I_2 \frac{A_2}{B_2 + C_2} \tag{20}$$

where

$$A_2 = Z_2 Z_{xy2} Z_{yy2} (Z_{xy2} - Z_{xx2}),$$

$$B_2 = Z_{xy2}^2 (Z_{xx2} + Z_{tv}) (Z_{yy\,2} + Z_{h2}),$$

$$C_2 = Z_{h2} Z_{yy2} (Z_{xy2}^2 - 2 Z_{xx2} Z_{xy2} - Z_{tv} Z_{xx2}).$$

Similar results appear on the basis of Fig. 5 as

$$U_0 = -I_0 Z_0, \tag{21}$$

$$I_{x0} = I_0 \frac{A_0}{B_0 + C_0} \tag{22}$$

where

$$A_0 = Z_0 Z_{xy0} Z_{yy0} (Z_{xy0} - Z_{xx0}),$$
$$B_0 = Z_{xy0}^2 (Z_{xx0} + Z_{tv0})(Z_{yy0} + Z_{h0}),$$
$$C_0 = Z_{h0} Z_{yy0} (Z_{xy0}^2 - 2 Z_{xx0} Z_{xy0} - Z_{tv0} Z_{xx0}).$$

In Equ. (22) Z_{tv0} is the resultant, zero-sequence impedance of the overhead line, in case of a double circuit the zero-sequence mutual impedance must be considered, too. Though when calculating positive- and negative-sequence currents, if one circuit of a double-circuit line is disconnected, one may proceed as in case of a single circuit line. The decrease of the zero-sequence impedance must be considered at the zero-sequence system, if the disconnected circuit is grounded and short-circuited, and this reduced value must be substituted for Equ. (22). However, the current of the protection must be calculated, also in this case similarly to that of the single-circuit line, consequently in Equs. (17), (20) and (24) $d = 1$.

The negative- and zero-sequence currents of the protection yield:

$$I_{V2} = d \cdot I_{x2}, \tag{23}$$

$$I_{V0} = d \cdot I_{x0} \tag{24}$$

where d is furnished by (17).

This permits the determination of the currents flowing through the protection in case of any kind of fault. With the aid of Figs. 3, 4 and 5, as well as by relations of this chapter, knowing the current distribution, the voltages prevailing at the installation place of protection may simply be determined (U_{x1}, U_{x2}, U_{x0}). Taking into account, however, the voltages and currents imposed on the protection measuring element, as well as the magnitude of the zero-sequence weighing factor, further other factors influencing the way of impedance measuring, the impedance measured may be determined.

For introducing the method, in chapter IV derivation of the general relations is given, for protections with equation for universal use, regarding the two most characteristic kinds of faults: for $3F$ and FN.

IV. Presentation of the Method for a Typical Protection, in Case of Faults 3F and FN

1. Three-phase (3F) short-circuit

In case of a three-phase short-circuit $I_2 = I_0 = 0$, $U_2 = U_0 = 0$. The positive-sequence voltage — which is identical with the phase voltage — may be determined on the basis of Fig. 2 considering that as per Table I $Z_{er} = Z_{h1}$:

$$\begin{aligned} Z_{x1} - I_{x1} Z_{tv} - I_{Z1} Z_{h1} &= 0, \\ U_{x1} = I_{x1} Z_{tv} + I_{Z1} Z_{h1}. \end{aligned} \tag{25}$$

At the majority of distance protections, in case of a fault $3F$, the line voltage and the difference of the two phase-currents are connected to the measuring element, e.g. for phase quantities $A-B$:

$$Z_M = \frac{U_A - U_B}{I_A - I_B} \,. \tag{26}$$

We may write because of the symmetry:

$$Z_M = \frac{U_A - U_B}{I_A - I_B} = \frac{(1-a^2)\,U_A}{(1-a^2)\,I_A} = \frac{U_A}{I_A}\,,$$

thus, the impedance measured is the ratio of the phase voltage and the phase current ($a = e^{j120^\circ}$).

Accordingly, the impedance seen [(17), (25) and (26)]:

$$Z_M = \frac{U_V}{I_V} = \frac{U_{x1}}{d I_{x1}} = \frac{1}{d}\,\frac{I_{x1} Z_{tv} + I_{Z1} Z_{h1}}{I_{x1}} = \frac{Z_{tv}}{d} + \frac{I_{Z1}}{d I_{x1}} Z_{h1}. \tag{27}$$

The first term of Equ. (27) is the correct and precise impedance of the overhead line seen by the relay. Namely, at a single-circuit line, when $d = 1$, the first term is Z_{vt}. At a double-circuit line, considering (17), the first term yields

$$2 Z_{tv}\,,$$

i.e. the double of the resultant impedance of the double-circuit lines, i.e. the impedance of one system.

The second term of Equ. (27) is the distortion part

$$Z\Delta = Z_{h1}\,\frac{I_{Z1}}{d I_{x1}}\,.$$

Taking Equs. (15), (16), (17) and (18) into account:

$$Z_\Delta = Z_{h1}\,\frac{Z_{xy1}^2 (Z_{xx1} + Z_{tv}) - Z_{xx1} Z_{yy1} (Z_{xy1} + Z_{tv}) + Z_{xy1} Z_{yy1} (Z_{xy1} - Z_{xx1})}{\begin{aligned} d Z_{xy1} Z_{yy1} (Z_{xy1} - Z_{xx1}) + \frac{I'_{x1}}{U'_{y1}}\, d\, [Z_{xy1}^2 (Z_{xx1} + Z_{tv})(Z_{yy1} + Z_{h1}) + \\ + Z_{h1} Z_{yy1} (Z_{xy1}^2 - 2 Z_{xx1} Z_{xy1} - Z_{tv} Z_{xx1})] \end{aligned}} \tag{28}$$

that is

$$Z_\Delta = Z_{h1}\,\frac{A}{B + C\,\dfrac{I'^1_x}{U'_{y1}}}\,, \tag{29}$$

where the values of the constants:

$$A = Z_{xy1}^2 (Z_{xx1} + Z_{tv}) - Z_{xx1} Z_{yy1} (Z_{xy1} + Z_{tv}) + Z_{xy1} Z_{yy1} (Z_{xy1} - Z_{xx1}),$$
$$B = d Z_{xy1} Z_{yy1} (Z_{xy1} - Z_{xx1}), \tag{30}$$
$$C = d\,[Z_{xy1}^2 (Z_{xx1} + Z_{tv})(Z_{yy1} + Z_{h1}) + Z_{h1} Z_{yy1} (Z_{xy1}^2 - 2 Z_{xx1} Z_{xy1} - Z_{tv} Z_{xx1})].$$

Relation (29) gives a practically good expression for the impedance perceived by the distance relay for the case of a fault $3F$, considering all factors of distortion.

2. *Simple line-to-ground short-circuit*

The great majority of the distance relay measuring elements measures at the appearance of a fault FN according to the equation given below:

$$Z_M = \frac{U_{Vf}}{I_{Vf} + k I_{V0}}, \tag{31}$$

where U_{Vf} phase voltage of phase A,
I_{Vf} phase current of phase A,
I_{V0} zero sequence current referring to the reference phase A at the installation place of the protection and

$$k = \frac{Z_{v0} - Z_{v1}}{Z_{v1}} \tag{32}$$

is a constant to be adjusted on the protection according to the data of the overhead line protected.

The phase voltage value may be determined as follows:

$$U_{Vf} = U_{x1} + U_{x2} + U_{x0}.$$

As at a short-circuit FN, at the fault location

$$U_{h1} + U_{h2} + U_{h0} = 0,$$

so

$$U_{x1} - I_{x1} Z_{tv} - I_{Z1} Z_{h1} + U_{x2} - I_{x2} Z_{tv} - I_2 Z_{h2} + U_{x0} - I_{x0} Z_{tv0} - I_0 Z_{h0} = 0$$

and

$$U_{Vf} = I_{x1} Z_{tv} + I_{x2} Z_{tv} + I_{x0} Z_{tv0} + I_{Z1} Z_h \tag{33}$$

where

$$Z_h = Z_{h1} + Z_{h2} + Z_{h0} \tag{34}$$

and as per Table I

$$I_{Z1} = I_2 = I_0 \,.$$

In the foregoing it was stipulated, but now it should again be pointed out, that Z_{tv} and Z_{tv0} are between points x and y, in case of two overhead lines, the *resultant* impedance values of the two systems!

Hence, the impedance perceived at a fault FN [(31), (33)]:

$$Z_M = \frac{U_{Vf}}{I_{Vf} + kI_{v0}} = \frac{U_{Vf}}{d\,(I_x + kI_{x0})} = \frac{I_{x1}\,Z_{tv} + I_{x2}\,Z_{tv} + I_{x0}\,Z_{tv0} + I_{Z1}\,Z_h}{d\,[I_{x1} + I_{x2} + (1+k)\,I_{x0}]}\,,$$

$$Z_M = \frac{Z_{tv}}{d} \cdot \frac{I_{x1} + I_{x2} + I_{x0}(1+k)}{I_{x1} + I_{x2} + I_{x0}(1+k)} + \frac{I_{x0}\,(Z_{tv0} - Z_{tv} - kZ_{tv}) + I_{Z1}\,Z_h}{d\,[I_{x1} + I_{x2} + (1+k)\,I_{x0}]}\,, \tag{35}$$

$$Z_M = \frac{Z_{tv}}{d} + \frac{I_{x0}\,Z_{tv}\left(\dfrac{Z_{tv0} - Z_{tv}}{Z_{tv}} - k\right) + I_{Z1}\,Z_h}{d\,[I_{x1} + I_{x2}(1+k)\,I_{x0}]}\,.$$

The first term of Equ. (35) is the same as in the Equ. (27) i.e. the correct and precise value of the impedance of the overhead line perceived by the relay. The second term of Equ. (35) is the distortion part:

$$Z_\Delta = \frac{I_{x0}\,Z_{tv}\left(\dfrac{Z_{tv0} - Z_{tv}}{Z_{tv}} - k\right) + I_{Z1}\,Z_h}{d\,[I_{x1} + I_{x2} + (1+k)\,I_{x0}]}\,. \tag{36}$$

The first term of the numerator may always be made equal to zero in case of a single-circuit line, if k is adjusted accurately, corresponding to the overhead line data [the part in brackets will be zero; see also (32)]. In case of a double-circuit line this is not possible, as the value of k ought to be made dependent on the operational conditions. Adjustment of different k values would be necessary with each of the following cases: parallel operation; at the disconnection of one line with the simultaneous grounding of the disconnected line on both ends, finally one-side disconnection of one system at a short-circuit arising in the vicinity of the disconnected end. It is an aggravating circumstance that from each of the four operating conditions mentioned above there may also follow automatic transition to the other one (e.g. by fault disconnection). Though in the interest of accurate measuring different methods are known from literature, this paper assumes the most frequently applied protection. Its equation of measuring is the (31), and so in case of double-circuit

line the first term of the numerator in Equ. (36) is generally not zero (choosing the value of k, it may be made equal to zero in one of the above four cases).

The other term of the numerator in Eq. (36) depends on the fault location impedances.

Considering the Equs. (15), (16), (17), (18), (20), (22), (23) and (24), as well as Table I, the distorting part may be written up as follows:

$$Z_{\Delta} = \frac{F}{H + M \dfrac{I'_{x1}}{U'_{y1}}} \tag{37}$$

where

$$\left.\begin{aligned}
F &= \left[\left(\frac{Z_{tv0} - Z_{tv}}{Z_{tv}} - k\right) Z_{tv} E_0 + Z_h\right] \cdot A\,; \\
H &= d \cdot Z_{xy1} Z_{yy1} (Z_{xy1} - Z_{xx1}) + d\,[E_2 + (1+k) E_0]\, A\,; \\
M &= d \cdot [Z^2_{xy1} (Z_{xx1} + Z_{tv}) (Z_{yy1} + Z_{h1} + Z_2 + Z_0) + \\
&\quad + (Z_{h1} + Z_2 + Z_0) Z_{yy1} (Z^2_{xy1} - 2 Z_{xx1} Z_{xy1} - Z_{tv} Z_{xx1})]\,; \\
&\text{here} \\
k &= \text{zero-sequence weighing factor adjusted to the protection} \\
&\quad \text{(referring to } I_0\text{) see also (32);} \\
E_2 &= \frac{Z_2 Z_{xy2} Z_{yy2} (Z_{xy2} - Z_{xx2})}{Z^2_{xy2} (Z_{xx2} + Z_{tv}) (Z_{yy2} + Z_{h2}) + Z_{h2} Z_{yy2} (Z^2_{xy} - 2 Z_{xx2} Z_{xy2} - Z_{tv} Z_{xx2})}\,; \\
E_0 &= \frac{Z_0 Z_{xy0} Z_{yy0} (Z_{xy0} - Z_{xx0})}{Z^2_{xy0} (Z_{xx0} + Z_{tv0}) (Z_{yy0} + Z_{h0}) + Z_{h0} Z_{yy0} (Z^2_{xy0} - 2 Z_{xx0} Z_{xy0} - Z_{tv0} Z_{xx0})}\,; \\
Z_h &= Z_{h1} + Z_{h2} + Z_{h0}
\end{aligned}\right\} \tag{38}$$

the value of A may be found in relations (30).

Relation (37) is similar to (29), being also treatable in practice for the general case of measuring.

The final results [(29), (37)] of the method presented give a practically treatable relation for the calculation of the way of measuring of distance relays in arbitrary conditions. One recognizes quite well the influence of the voltage (U'_{y1}: at point y in a faultfree state) and that of the load current and the current originating from oscillation (I'_{x1} is the line-current in case of a single-circuit line and is the sum of the two line-currents in case of double-circuit line) value measured by the relay.

V. Adaptation of the Results to More Simple Cases, Conclusions

1. Role of the shunt branch

The above discussions gave results for a general system. In the practice, however, assuming a more simple system arrangement, or certain neglections, the general picture may be simplified. Such a general possibility of simplification is the omission of the shunt branch.

The overhead line in question is generally not the sole interconnection between the power stations. Nevertheless, it may be assumed sometimes, or it may be even an actual case that the shunt branch does not exist practically. In the equations this means that there is no impedance Z_{xy}, $Z_{xy} \to \infty$.

Dividing the Equ. (28), valid for fault $3F$, throughout by Z_{xy1}^2 and forming a limit value ($Z_{xy1} \to \infty$), result in the following relation:

$$Z_{\Delta} = Z_{h1} \frac{Z_{xx1} + Z_{tv} + Z_{yy1}}{dZ_{yy1} + \frac{I'_{x1}}{U'_{y1}} d\,[(Z_{xx1} + Z_{tv})(Z_{yy1} + Z_{h1}) + Z_{h1} Z_{yy1}}. \tag{39}$$

Thus, the relation becomes considerably simplified.

If at the same time no current is flowing on the overhead line before the fault, so that $I'_{x1} = 0$, we obtain

$$Z_{\Delta} = Z_{h1} \left[\frac{Z_{xx1} + Z_{tv}}{dZ_{yy1}} + \frac{1}{d} \right]. \tag{40}$$

$Z_{xy1} \to \infty$ which means simultaneously that Z_{xx1} and Z_{yy1}, respectively, being the impedances of the network (without line) behind stations x and y, may be calculated directly from the short-circuit power of the substation without line.

Performing the limit transfer $Z_{xy1} \to \infty$, $Z_{xy2} \to \infty$ and $Z_{xy0} \to \infty$, for the case of a fault FN [Equs. (37) and (38)]

$$Z_{\Delta} = \frac{\beta}{\gamma} \tag{41}$$

where

$$\beta = \left[Z_{tv} \left(\frac{Z_{tv0} - Z_{tv}}{Z_{tv}} - k \right) \frac{Z_0 Z_{yy0}}{(Z_{xx0} + Z_{tv0})(Z_{yy0} + Z_{h0}) + Z_{h0} Z_{yy0}} + \right.$$
$$\left. + Z_h \right] [Z_{xx1} + Z_{tv} + Z_{yy1}]$$

$$\gamma = d\, Z_{yy1} + d\,[Z_{xx1} + Z_{tv} + Z_{yy1}] \left[\frac{Z_2\, Z_{yy2}}{(Z_{xx2} + Z_{tv})(Z_{yy2} + Z_{h2}) + Z_{h2}\, Z_{yy2}} + \right.$$

$$\left. + (1+k) \frac{Z_0\, Z_{yy0}}{(Z_{xx0} + Z_{tv0})(Z_{yy0} + Z_{h0}) + Z_{h0}\, Z_{yy0}} \right] +$$

$$+ \frac{I'_{x1}}{U'_{y1}} d\,[(Z_{xx1} + Z_{tv})(Z_{yy1} + Z_{h1} + Z_2 + Z_0) +$$

$$+ (Z_{h1} + Z_2 + Z_0)\, Z_{yy1}] .$$

The relation has become simplified here, too.

2. *Role of the Fault Location Impedance*

If in the case of a $3F$ fault the impedance at the fault location is zero, the relay can measure without distortion, that is

$$Z_{h1} = 0 ,$$

then

$$Z_{\Delta} = 0 . \tag{42}$$

If a simple line-to-ground short-circuit (FN) occurs, the situation is not always the same.

If the value of the zero-sequence weighing factor is precisely adjusted, so that k corresponds to relation (32) and $Z_h = Z_{h1} = Z_{h2} = Z_{h0} = 0$,

$$Z_{\Delta} = 0 . \tag{43}$$

Not suitably adjusting k, the bad compensation may cause an error.

It is worth mentioning that the error due to compensation may be a negative value, too ! This permits in certain cases *to neutralize the deforming effect of the fault location impedance by an over-compensation.* The condition of this, based on Equs. (37) and (38) (Z_{xy} being of finite value !) is

$$k = \frac{Z_{tv0} - Z_{tv}}{Z_{tv}} + \tag{44}$$

$$+ \frac{Z_h}{Z_{tv}} \frac{Z_{xy0}^2 (Z_{xx0} + Z_{tv0})(Z_{yy0} + Z_{h0}) + Z_{h0}\, Z_{yy0} (Z_{xy0}^2 - 2\, Z_{xx0}\, Z_{xy0} - Z_{h0}\, Z_{xx0})}{Z_0\, Z_{xy0}\, Z_{yy0} (Z_{xy0} - Z_{xx0})}$$

where

$$Z_h = Z_{h1} + Z_{h2} + Z_{h0} .$$

The value of k must be chosen corresponding to Equ. (44). It may be noted that the additional term with respect to (32) depends on the system layout variation !

The necessary measure of overcompensation expressed by current rations [Equ. (36)] is as follows:

$$k = \frac{Z_{tv0} - Z_{tv}}{Z_{tv}} + \frac{I_{Z1}}{I_{x0}} \frac{Z_h}{Z_{tv}} . \tag{45}$$

Naturally, the current values are to be substituted for the case of a fault FN occurring on the opposite end. Nevertheless, the big deviations in the fault location resistances arising along the overhead line — the end station (y side) included — may make the above method inefficient.

Among the values k, as per Equ. (45), belonging to the different possible working conditions, the lowest one must be chosen in such a way that the operation of the protection should remain selective.

The overcompensation does not affect the measuring conditions of the relay in case of fault $3F$.

3. *Feed-in from One Side Only*

If from the side of station y there is no feeding, the conditions become considerably simplified.

In this case, if a fault $3F$ exists, the value of

$$Z_{yy1} = Z_{\text{load}_1} \tag{46}$$

i. e. the impedance is to be substituted into expression (28) and (29), respectively of Z_Δ corresponding to the end-point loading.

Considering that

$$Z_{\text{load}_1} = \frac{U'_{y1}}{I'_{x1}} \tag{47}$$

as in the case of an end-point feed in only one current, corresponding to the impedance Z_{load_1}, is flowing on the overhead line, further that in this case there is no shunt branch ($Z_{xy_1} \to \infty$), Z_Δ can be got, if in Equ. (39) the value of Equs. (46) and (47) is used:

$$Z_\Delta = Z_{h1} \frac{1}{d\left(1 + \frac{Z_{h1}}{Z_{\text{load}_1}}\right)} . \tag{48}$$

This relation means that in case of an end-point feed in the value of the fault location impedance decreases and the larger the load (the smaller Z_{load_1}) the greater this decrease becomes. The physical explanation of this is that the relay measures together with the parallel connected values of the fault location

and the loading impedance a greater impedance, than the impedance of the overhead line.

In case of a fault FN, considering that $Z_{xy1} \to \infty$, $Z_{xy2} \to \infty$, $Z_{xy0} \to \infty$, see relation (41), we obtain

$$Z_{\Delta} = \frac{\delta}{\varepsilon}; \tag{49}$$

where

$$\delta = Z_{tv}\left(\frac{Z_{tv0} - Z_{tv}}{Z_{tv}} - k\right)\frac{Z_0 Z_{yy0}}{(Z_{xx0} + Z_{tv0})(Z_{yy0} + Z_{h0}) + Z_{h0} Z_{yy0}} + Z_h,$$

$$\varepsilon = d\left[\frac{Z_2 Z_{yy2}}{(Z_{xx2} + Z_{tv})(Z_{yy2} + Z_{h2}) + Z_{h2} Z_{yy2}} + \right.$$
$$+ (1 + k)\frac{Z_0 Z_{yy0}}{(Z_{xx0} + Z_{tv0})(Z_{yy0} + Z_{h0}) + Z_{h0} Z_{yy0}} +$$
$$\left. + 1 + \frac{Z_{h1} + Z_2 + Z_0}{Z_{\mathrm{load}_1}}\right].$$

Naturally, it is to be taken into account that the value Z_{yy2} is equal to the negative-sequence value of the load, which is always smaller than Z_{load_1}:

$$Z_{yy2} = Z_{\mathrm{load}_2} < Z_{\mathrm{load}_1} \tag{50}$$

and that Z_{yy0} is often furnished merely by the transformers of earthed neutral point at the y side.

4. *The Feed-in at One Side is of a Very High Value (Infinite Bus)*

Realization of this fact for e.g. the y side yields

$$Z_{yy1} = Z_{yy2} = Z_{yy0} \cong 0\,. \tag{51}$$

In case of the fault $3F$ the additional impedance measured [Equ. (28)] is:

$$Z_{\Delta 1} = \frac{1}{d}\,\frac{U'_{y1}}{I'_{x1}}\,. \tag{52}$$

This surprising result may be explained by the circumstance that because of the very great feed-in at the y side no short-circuit current (I''_{x1}) flows from the x side, but the pre-fault current I'_{x1}. Due to the infinite bus at the y side busbar voltage y remains U'_{y1}, that is, on the fault location (and loading) impedance this voltage prevails. It can also be quite simply proved, that in this case the x-side relay measures beside the overhead line impedance, also the value

determined in Equ. (52), that is, essentially the "apparent y-side loading impedance" (or the double of this) correspondig to the loading- and swing current of the overhead line before the fault. In this case the x-side protection presumably works only after the y-side circuit breaker have disconnected (cascade operation). This case occurs very rarely in the practice!

In case of a short-circuit FN [(37), (38) and (51)]:

$$Z_{\Delta} = \frac{Z_0}{Z_{h1} + Z_2 + Z_0} \frac{1}{d} \frac{U'_{y1}}{I'_{x1}} . \tag{53}$$

The result is similar to Equ.(52).The x-side relay is also seen here as an additional impedance corresponding to the overhead line load (swing) current, though a value corrected by a certain modifying factor. The x-side protection is also able in that case to work in a cascade operation, as a rule. Besides, it is true that this case is likely to occur very rarely in the practice.

If the x-side feed-in is of extremely high value, so that

$$Z_{xx1} = Z_{xx2} = Z_{xx0} = 0 , \tag{54}$$

then, in case of a fault $3F$:

$$Z_{\Delta} = Z_{h1} \frac{Z_{tv} + Z_{yy1}}{d\, Z_{yy1} + \frac{I'_{x1}}{U'_{y1}} d\, [Z_{tv}(Z_{xx1} + Z_{h1}) + Z_{h1} Z_{yy1}]} . \tag{55}$$

To draw a direct conclusion from the result is difficult. Nevertheless, one recognizes that the value Z_{Δ} is decreased (if Z_{yy} is sufficiently high, so that from the other side there is no great feed-in either). For the case of the fault FN, a similar result may be obtained.

*

One can see from the special cases presented in Chapter V that the results of this paper are useful in the majority of cases occurring in practice, and actual, as well as further, generizable results may be obtained (e.g. 2. overcompensation, 4. cascade operation, etc.).

REFERENCES

1. Warrington, A. R. van C.: Protective Relays: their Theory and Practice. Chapman & Hall, London 1962.
2. Bendes, T.: Országos villamosenergia hálózat korszerű védelmének kérdései (Relay Protection Problems of the Hungarian 120 kV Grid System). Mérnöki Továbbképző Intézet, Budapest 1954.
3. *Федосеев, А. М.:* Релейная защита электрических систем. Госэнергоиздат, Москва 1952.
4. *Атабеков, С. И.:* Релейная защита высоковольтных сетей. Госэнергоиздат, Москва 1949.

5. KIMBARK, E. W.: Power System Stability. John Wiley & Sons Inc., New York 1948.
6. MASON, C. R.: The Art and Science of Protective Relaying. John Wiley & Sons Inc., New York 1956.
7. LEWIS, W. A.—TIPPETT, L. S.: Fundamental Basis for Distance Relaying on 3-Phase Systems. *AIEE Transaction* **66** (1947), 694—700.
8. EARDER, E. L.—CUNNINGHAM, J. C.: Relay and Circuit-Breaker Application. *Westinghouse Reference Book* **2** (1950), 342—400.

DER ALLGEMEINE FALL DER DISTANZERFASSUNG DURCH SCHUTZRELAIS

P. O. GESZTI—GY. PÓKA

ZUSAMMENFASSUNG

Die Distanzerfassung durch Schutzsysteme wird durch mehrere Faktoren verzerrt, und es kann vorkommen, daß deswegen das Ansprechen nicht selektiv erfolgt oder ganz ausbleibt. Die Verfasser versuchen unter Berücksichtigung aller verzerrenden Einflüsse die allgemeine Gleichung für die Distanzmessung durch Distanzschutzeinrichtungen bzw. für die Abweichung von der genauen Distanzerfassung zu bestimmen. Der allgemein gültige Zusammenhang für einen typischen Schutz wird auf zwei charakteristische Arten von Kurzschlüssen angewendet; dann wird mit Hilfe von speziellen Fällen die praktische Anwendung des Gerätes beispielsweise dargelegt.

LE CAS GÉNÉRAL DE LA PERCEPTION PAR LES PROTECTIONS A DISTANCE

P. O. GESZTI—GY. PÓKA

RÉSUMÉ

La perception par les protections à distance est faussée par plusieurs facteurs et il peut arriver que leur fonctionnement soit non-sélectif ou qu'il y ait arrêt du fonctionnement. Les auteurs tenant compte de toutes les influences perturbatrices essaient d'établir l'équation générale de la perception par les protections à distance, c'est-à-dire de déterminer les écarts par rapport à la mesure précise de la distance. La relation générale est appliquée à une protection typique pour deux genres caracté ristiques de court-circuits et la discussion de cas spéciaux illustre ensuite l'application pratique de l'instrument.

ВОСПРИЯТИЕ ДИСТАНЦИОННЫХ ЗАЩИТ В ОБЩЕМ СЛУЧАЕ

П. О. ГЕСТИ—Д. ПОКА

РЕЗЮМЕ

Восприятие дистанционных защит искажается рядом факторов, и возможно, что из-за этого произойдет не селективное срабатывание или отказ срабатывания. Авторы делают попытку определить общее уравнение восприятия дистанционных защит при учете всех искажающих факторов, и соответственно величину отклонения от точного дистанционного восприятия. Общая зависимость применяется для типичной защиты, для двух характерных видов замыканий, а затем путем демонстрации специальных случаев дается пример практического применения прибора.

ПРОБЛЕМА ОПРЕДЕЛЕНИЯ ГОРИЗОНТОВ В ГОРНО-ПРОМЫШЛЕННЫХ ПРЕДПРИЯТИЯХ

Я. ЗАМБО
ЧЛ. КОРР. АН. ВЕНГРИИ

[Поступило 19. марта 1964.]

Автор исследует оптимальную высоту этажей в функции расходов, зависящих от этой высоты. Наиболее значительными расходами являются расходы по движению, капитальные вложения и постоянные затраты. Амортизационные затраты, происходящие от капитальных вложений, вводятся в расчет на основе принципа процентной амортизации. Записывается функция затрат, отыскивается место минимума функции, и тем самым определяется оптимальная высота этажа. На основе теоретических зависимостей могут быть сделаны практические выводы. а) Параметры функции расходов следует определить на основе регрессивной теории множества данных. б) Графическое решение кажущихся сложными математических зависимостей вполне удовлетворительно. в) Вполне достаточно выделение одного интервала, внутри которого для определения высоты этажа решающими являются горно-технические условия.

Правильный выбор расстояний между горизонтами уже давно привлекает внимание проектировщиков и строителей горно-промышленных предприятий. В рудниках прошлых столетий эта проблема не играла зчанительной роли, так как при более низкой производственной мощности горизонты требовали много более промтого оформления. Требовались погрузочные площадки гораздо меньших размеров, корридоры отдельных горизонтов, как правило, располагались по самой жиле и служили для подготовки забоев, то есть не представляли собой высокопроизводительных направляющих штреков. Таким образом, естественно, возросли капитальные затраты по отдельным этажам. Из этого следует, что вообще стремятся увеличить высоту этажей.

Высота этажа зависит от целого ряда обстоятельств. Некоторые стремятся увеличить высоту, а другие — уменьшить. Противоречивые стремления приводят к оптимальному компромиссу. Мы ставим перед собой задачу — найти это компромиссное решение и исследовать его, чтобы сделать практические выводы.

Чем больше высота этажа, тем меньше удельный амортизационный расход от капитальных вложений, при большей высоте этажей использование рудничной подъемной машины становится более выгодным, чем больше высота этажа, тем меньше число одновременно поддерживаемых этажей, большая высота этажа требует меньшего числа нарезанных в пустой породе направляющих и поперечных штреков, теоретически снижается число выбросов газа, а также снижаются потери угля или руды.

Чем меньше высота этажа, тем проще движение между двумя этажами. Под движением подразумевается, с одной стороны, перевозка людей, а с другой — транспорт продукции, пустой породы, крепежных материалов, воздуха, воды, энергии. Чем меньше расстояние между этажами, тем легче выработать шахтные пространства, связывающие два этажа (скаты, склизы, штольни), и содержать их.

За основу возьмем принцип, что высота этажа является оптимальной, если удельные затраты по этой высоте будут оптимальными. Естественно, в математической формуле невозможно учесть всех условий, но самые важные факторы можно учесть.

а) *Капитальные затраты тесно связаны с запланированной производственной мощностью поля разработки.* Эту зависимость хорошо выражает функция

$$K_{bs} = aq_0^{\nu},$$

где K_{bs} — капитальные затраты на разработку;
q_0 — производственная мощность горизонта, *т/сутки;*
ν — показатель, вообще меньше единицы.

Суточная же производительность, в свою очередь, является функцией высоты горизонта h для некоторого данного месторождения, то есть

$$q_0 = bh^{\mu},$$

где показатель μ, как правило, меньше единицы. Из этого следует:

$$K_{bs} = a\,(bh^{\mu})^{\nu} = ah^{\omega}.$$

Отношение ожидаемой глубины шахты H к высоте горизонта — дает число горизонтов. Все вырабатываемое на данной шахте количество ископаемого обозначим через Q. Тогда простые удельные амортизационные расходы можно записать в следующем виде:

$$k_{bs} = \frac{H}{h}\,\frac{ah^{\omega}}{Q}.$$

Наиболее значительная часть капитальных затрат K_{bs} падает на начальный период существования горизонта, амортизация же — в более или менее равномерном распределении — на все время существования горизонта.

Согласование проводится на основе правил расчета сложных процентов или же правил расчета прибыли. Необходимо определить такие соответственно измененные капитальные затраты (K_{br}), из которых расчетный амортизационный расход (K_{br}/n), в виде суммы прибыли через n лет, получился бы равным первоначальным капитальным затратам (K_{bs}) с процентами за

n лет. Стало быть:

$$\frac{K_{br}}{n}\,\frac{p^n-1}{p-1}=K_{bs}p^n,$$

откуда

$$K_{br}=n\,\frac{p-1}{p^n-1}\,p^n\,K_{bs},$$

где p — показатель процентов;

n — продолжительность жизни горизонта в годах;

n лет могут быть выражены в функции h:

$$n=f(h)=\frac{Qh}{Hzq_0}=\frac{Qh}{Hzbh^{\mu}}=\beta h^{1-\mu}.$$

Теперь уже можно выразить удельный амортизационный расход от капитальных затрат:

$$k_{br}=\frac{a}{zb}(p-1)\,h^{\omega-\mu}\frac{p^{\beta h^{1-\mu}}}{p^{\beta h^{1-\mu}}-1}=ch^{\omega-\mu}\frac{p^{\beta h^{1-\mu}}}{p^{\beta h^{1-\mu}}-1}\,.$$

б) *Второй важный фактор расходов, это — так называемые постоянные расходы.* Пусть суточные постоянные расходы некоторого горизонта составят K_{ns}, тогда получим удельный расход:

$$k_{ns}=\frac{K_{ns}}{q_0}=\frac{K_{ns}}{bh^{\mu}}\,.$$

в) *Также просто могут быть выражены удельные расходы по движению в пространстве между двумя горизонтами.* Обозначим расходы, падающие на *м* расстояния и на *т* вырабатываемых минералов, через k [*фор/м.т*], причем сюда входят перевозка грузов, транспортировка людей, откачка, вентиляция, ремонтные работы, а также разработка пластов между двумя горизонтами, удельные расходы по потерям энергопроводов (напр. сжатый воздух).

Расстояние между двумя горизонтами по центрам тяжести может быть просто выражено через

$$\frac{h}{2\sin\alpha_t},$$

и тогда удельные расходы по движению составят:

$$k_F=\frac{h}{2\sin\alpha_t}\sum k_f,$$

где α_t — средний уклон пласта в градусах.

В то же время удельные расходы по движению в стволе составят:

$$k_A = \frac{H+h}{2} \Sigma k_a .$$

При сложении основных факторов расходов получим:

$$k_r = k_{br} + k_{ns} + k_f + k_A = Ch^{\omega+\mu} \frac{p^{\beta h^{1-\mu}}}{p^{\beta h^{1-\mu}} - 1} + \frac{K_{ns}}{bk^{\mu}} +$$

$$+ \frac{h}{2 \sin \alpha_t} \Sigma k_f + \frac{H+h}{2} \Sigma k_a .$$

Исходя из выражения

$$\frac{\partial k_r}{\partial h} = 0 ,$$

получим следующий результат:

$$C \frac{p^{\beta h^{1-\mu}}}{p^{\beta h^{1-\mu}} - 1} \left\{ (\omega - \mu) h^{\omega-\mu-1} - \beta (1-\mu) \frac{h^{\omega-2\mu}}{p^{\beta h^{1-\mu}} - 1} \ln p \right\} -$$

$$- \frac{\mu K_{ns}}{bh^{\mu+1}} + \frac{1}{2} \left(\frac{\Sigma k_f}{\sin \alpha_t} + \Sigma k_a \right) = 0 .$$

Практическое решение данной зависимости не представляет трудностей.

Зададимся следующими данными:

$H = 600$ *м*, $Q = 54 \cdot 10^6$ *m*, $z = 300$ *суток/год*, $p = 1{,}1$,
$K_{ns} = 7500$ *Фор/сутки*, $\Sigma k_f = 0{,}036$ *Фор/м.т*, $\Sigma K_a =$
$= 0{,}014$ *Фор/м.т*, $\alpha_t = 30°$, $a = 95\,000$ *Фор/т/сутки*,
$\gamma = 0{,}7$, $b = 50$ *Фор/м.сутки*, $\mu = 0{,}9$, $\omega = 0{,}63$.

Расчетные постоянные будут:

$$a = 95\,000 \cdot 50^{0{,}7} = 1{,}469 \cdot 10^6,$$

$$\beta = \frac{54 \cdot 10^6}{600 \cdot 300 \cdot 50} = 6 ,$$

$$C = \frac{1{,}469 \cdot 10^6}{300 \cdot 50} 0{,}1 = 9{,}79.$$

Функцию же можно записать в следующем виде:

$$\varphi(h) = -9{,}79 \frac{1{,}1^{6h^{0,1}}}{1{,}1^{6h^{0,1}} - 1} \left\{ \frac{0{,}27}{h^{1,27}} + \frac{0{,}0572}{h^{1,27}(1{,}1^{6h^{0,1}} - 1} \right\} - \frac{135}{h^{1,9}} + 0{,}043 .$$

Произведем подстановки: $h = 100$, $h = 90$, $h = 80$ и полученные таким образом значения $\varphi(100)$, $\varphi(90)$, $\varphi(80)$ отложим на графике в системе h, $\varphi(h)$ (рис. 1). Кривая $\varphi(h)$ сечет абсциссу h, и точка пересечения дает ту величину h, при которой функция k_p имеет минимум ($h_{опт} = 92$ *м*).

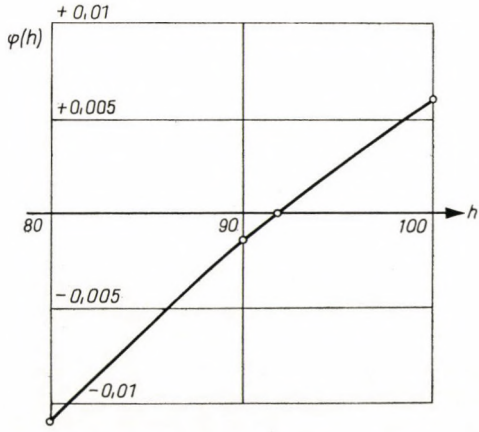

Рис. 1

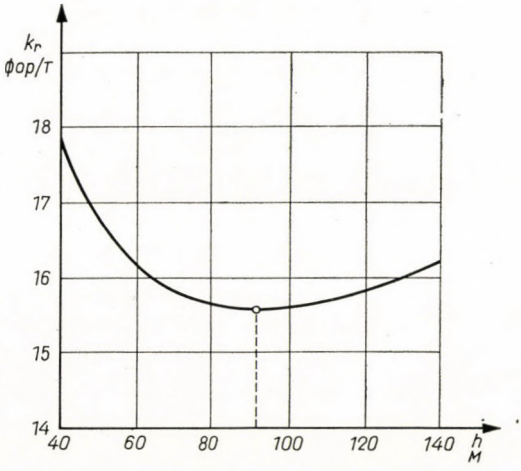

Рис. 2

Можно рассчитать также суточную производительность соответствующую оптимальному делению горизонтов

$$q_0 = = bh^{\mu} = 50 \cdot 92^{0,9} = 2927 \; m/сутки.$$

На рис. 2 изображено изменение функции k_r. Видно, что оптимальное деление горизонтов ($h_{опт} = 92$ *м*) не сопровождается значительным изменением функции k_r, то есть в этом интервале удельные расходы, зависящие от высоты этажей, возрастают лишь незначительно, если отклонение от оптимальной высоты незначительно.

Приведенный числовой пример служил только для иллюстрации метода. Выцор данных или калькуляция их в каждом отдельном случае является трудоемкой и требует тщательной работы. Чтобы избежать повторения, здесь не уделено внимания подробному описанию этой работы; дана лишь ссылка на опубликованные ранее в этом журнале работы. Это относится в первую очередь к калькуляции удельных расходов Σk_f и Σk_a; указанный метод подробно изложен ранее.

Определение расходов K_{ns} и K_{bs} как и прежде основано на регрессивном методе.

Определение постоянных суточных затрат K_{ns} регрессивным методом осуществляется относительно просто. При горной добыче, как известно, часто открывают новый горизонт. Расходы, возникающие при разработке горизонта, известны с самого начала разработок до полного их развития. Если изобразить эти расходы в функции суточной производительности, то можно легко отделить постоянные затраты (рис. 3) или же задать уравнение регрессивной прямой ($K_s = a_3 q_0 + K_{ns}$).

В данном случае используется уравнение регрессивной прямой горизонта или горизонтов, работающих при сходных условиях, оттуда и берется значение K_{ns}.

Уравнение капитальных вложений можно также определить регрессивным методом ($K_{bs} = aq_0^{\nu}$) (рис. 4). Опыт показывает, что принятая формула дает очень хорошее совпадение, плотность удовлетворительна. Показатель ν меняется в пределах $0{,}65 \div 0{,}75$, в то же время коэффициент a зависит от характера месторождения. Поскольку в горном деле образование новых горизонтов является довольно частым явлением, для точного построения регрессивной кривой в распоряжении имеется, как правило, достаточное количество данных.

Зависимость $q_0 = bh^{\mu}$ также хорошо выражает связь между высотой этажей и суточной производительностью горизонтов. Показатель μ меньше единицы, коэффициент же b является функцией производительности месторождения *(т/м²)*. Регрессивный метод и в этом случае служит для определения как показателя μ, так и коэффициента b.

Определение зависимостей

$$K_s = a_s q_0 + K_{ns},$$

$$K_{bs} = aq_0^{\nu},$$

И

$$q_0 = bh^{\mu}$$

регрессивным методом само собой представляет интересную область исследования. В этой области еще нигде не произведено более подробного исследования вопроса. В Венгрии, в Университете тяжелой промышленности в Мишкольце на Кафедре горного дела проводились такие исследования, в

первую очередь, на основе имеющихся в распоряжение советских данных. Эти исследования относятся главным образом не к полю одного горизонта, а ко всему горному предприятию. Можно было, например, установить, что зависимость между капитальными вложениями и производственной мощ-

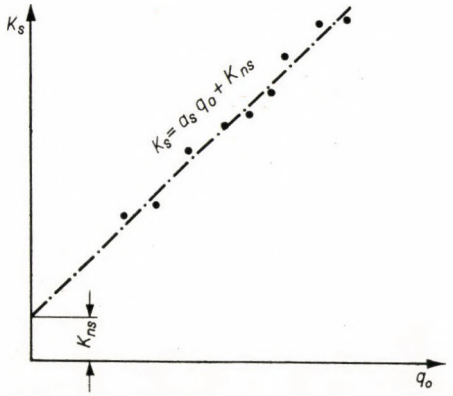

Рис. 3

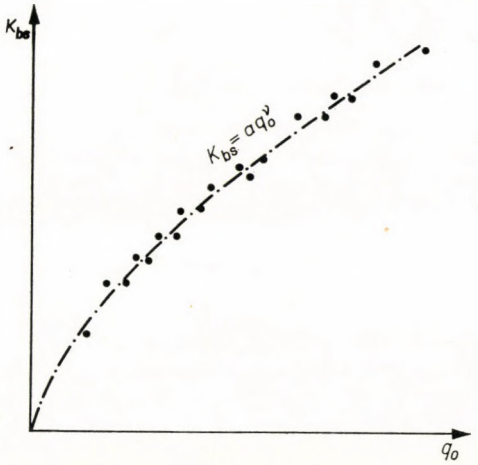

Рис. 4

ностью описывается формулой $K_{bs} = aq_0^{\nu}$ удовлетворительным для практических целей образом.

На основе изложенного можно сделать следующие выводы.

1. Прежде чем записать зависимость, определяющую оптимальное деление на горизонты, с помощью регрессивного метода необходимо исследовать множество данных. Насколько верен регрессивный метод, настолько верно можно определить оптимальную высоту этажей. Установленные

регрессивные зависимости дают не только верную основу для определения параметра или параметров, но сами по себе могут быть использованы для расчета предварительных показателей планирования производства.

2. Упрощенное графическое решение кажущихся сложными математических зависимостей вполне удовлетворяет требованиям, так как, с одной стороны, неопределенность данных намного больше, а с другой, изменение удельных затрат в районе оптимума невелико.

3. Вполне достаточно выбрать один интервал, в который попадает оптимальное расстояние между горизонтами. Целесообразно, стало быть, изобразить функцию, чтобы можно было бы определить границы интервала. Внутри интервала, при определении действительной высоты этажа, в качестве решающих факторов могут учитываться также прочие горно-технические и горно-технологические условия

ЛИТЕРАТУРА

1. *Я. Замбо:* Аналитика расположения горных предприятий. Мюсаки Кёньвкиадо, Будапешт 1960.

THE PROBLEM OF DIVISION INTO STAGES IN MINING PLANTS

J. ZAMBÓ

SUMMARY

The author examines the optimum stage level as a function of the costs related to it. The most important costs are those of movement and of transport, the investment costs and the permanent costs. The amortization costs due to the investment costs are taken into account according to the principle of amortization with an interest. The cost function is established, its minimum is determined and thus the optimum stage level can be found. From the theoretical relations, practical conclusions can be drawn: *a)* The parameters of the cost function must be determined on the basis of the regression theory of the set of data. *b)* Graphical solution of the apparently complicated mathematical relations is sufficient. *c)* It is completely sufficient to determine a range only, within which the technical requirements of mining are decisive for the determination of stage level.

DAS PROBLEM DER AUFTEILUNG AUF SOHLEN IN BERGBAUBETRIEBEN

J. ZAMBÓ

ZUSAMMENFASSUNG

Der Verfasser untersucht die optimale Sohlenhöhe als Funktion der mit der Sohlenhöhe zusammenhängenden Kosten. Die wichtigsten Kosten sind die Transportkosten, die Investitionskosten und die ständigen Kosten. Die aus den Investitionskosten stammenden Amortisationskosten werden auf Grund des Prinzips der verzinsbaren Amortisation in die Rechnungen eingeführt. Die Kostenfunktion wird angeschrieben, das Minimum der Funktion wird berechnet und auf diese Weise wird die optimale Sohlenhöhe bestimmt. Auf Grund der theoretischen Zusammenhänge können praktische Folgerungen gezogen werden: *a)* Die Parameter der Kostenfunktion müssen auf Grund der Regressionstheorie der Datenmengen bestimmt werden. *b)* Die graphische Lösung der kompliziert scheinenden mathematischen Zusammenhänge genügt. *c)* Es genügt vollkommen, einen Bereich abzugrenzen, innerhalb dessen die bergbautechnischen Bedingungen für die Bestimmung der Sohlenhöhe entscheidend sind.

LE PROBLÈME DE LA DIVISION EN ÉTAGES DANS LES EXPLOITATIONS MINIÈRES

J. ZAMBÓ

RÉSUMÉ

L'auteur examine la hauter optimum en fonction des frais dépendant de la hauteur des étages. Les plus importants de ces derniers sont les frais de mouvement et de transport, les frais d'investissement et ceux d'un caractère constant. Les frais d'amortisation résultant des frais d'investissement figurent dans les calculs suivant le principe de l'amortisation à intérêts. La fonction des frais une fois écrite, l'auteur recherche le minimum de cette fonction et détermine par là la hauteur optimum de l'étage.

Sur la base des relations théoriques, les conclusions pratiques suivantes peuvent être tirées: *a*°) Les paramètres de la fonction des frais doivent être déterminés selon la théorie de la régression des ensembles de données. *b*°) Il suffit de résoudre graphiquement les relations mathématiques qui paraissent être trop compliquées. *c*°) Il est entièrement suffisant de déterminer un seul domaine, à l'intérieur duquel les conditions de l'exploitation minière interviennent d'une manière décisive dans la détermination de la hauteur d'étage.

SOIL STABILIZATION EXPERIMENTS WITH PLASTICS

G. PETRASOVITS
CANDIDATE OF TECHNICAL SCIENCES
TECHNICAL UNIVERSITY OF BUILDING AND TRANSPORT ENG., BUDAPEST

[Manuscript received February 2, 1965]

Possibilities of stabilizing silty and pure sand soils with synthetic resins were investigated in the laboratory. A variety of synthetic resin compounds and catalytic agents were used with admixtures ranging from $5 \div 10 \div 15\%$ by weight of soil.

The effect of silt grains and lime present in the soil the extent of stabilization attained was studied experimentally, together with the relationship between initial moisture content and strength development, the significance of thermal effects and freezing, as well as their influence of strength, i.e. all effects to which stabilized soil may be exposed under natural conditions.

As revealed by the results obtained, synthetic resins are superior to sodium silicate in soil stabilization both as far as strength and range of effectiveness are concerned. At the same time cost of stabilization (Ft/cu. m) are comparable to those of the method involving the use of sodium silicate.

I. Chemical Methods for Soil Stabilization

Surface forces bonding soil particles can be permanently increased, and the permeability of the soil can be reduced by a variety of chemical methods. Soils having poor load bearing properties and a high degree of permeability can by these procedures be given mechanical and physical properties which make them suitable to meet the requirements and criteria established by the designer. A wide variety of soil stabilization methods were developed as a response to practical requirements. It is the task of the designer to select from among these the method by which any particular problem could be solved in the most sound and economical manner.

Among chemical methods it is soil stabilization with sodium silicate that comprised the most widespread application. The correctness in using sodium silicate (Na_2OnSiO_2) was corroborated by studies into cementation processes in nature, i.e., the formation of sandstone. It could be established that colloidal SiO_2 plays a significant role in natural cementation. Recognition of this fact had an appreciable influence on further research and was responsible for the trend that for a long time the greatest interest was concentrated on the selection of a suitable reacting agent. As a result of the chemical reaction which takes place between the sodium silicate solution and the reacting agent, a silicic acid (SiO_2) gel is precipitated which is insoluble in water. Therefore the problem was to select an electrolyte produced with a

sodium silicate solution, the gel of which had the highest quality. The simultaneous consideration of strength properties attained, and the economic aspects led to the widespread application of calcium chloride ($CaCl_2$) [9].

Unconfined compressive strength from $\sigma = 10 \div 30$ kg/sq.cm was obtained with sand soil, stabilized with sodium silicate having a concentration of 30 to 35 Bé^0. Owing to the high viscosity of the sodium silicate solution the application of this method is restricted to sand soils showing a permeability coefficient $k = 10^{-2} \div 10^{-3}$ cm/sec.

Methods involving the use of sodium silicate could not yield satisfactory results above the afore-mentioned limit and consequently their field of application was greatly restricted. The quest for newer stabilization materials was therefore resumed in the forties, with the aim of developing a method which has an appreciably broader range of application than that involving the use of sodium silicate and a material, which could be injected into fine-grained soils, producing a higher strength and doing this at a lower material consumption. Significant progress was achieved in the United States and in the Soviet Union, and a great number of materials were detected which meet the fundamental requirements controlling the success of soil stabilization [1—4, 10, 11].

The main requirements in up-to-date soil stabilization may be summarized as follows:

1. The stabilizing material should be cheap.
2. The necessary amount of stabilizing material to be added should not exceed 5 to 10 per cent by the weight of soil to be stabilized.
3. The stabilizing material should have a viscosity approaching that of water.
4. Stabilization should result in a greatly increased strength and reduced permeability of the soil, after the completion of the chemical reaction.
5. Bonding time should be adjustable within broad limits as required by construction technology.
6. The material should be suitable for the stabilization of several types of soil, regardless of soil moisture.
7. Equipment involved should be simple and should be easy to handle.
8. The stabilizing material should be harmless regarding operators and equipment.

A variety of organic materials of the resin type proved to be the most successful in satisfying the criteria outlined above. These materials are available in large quantities as by-products of the chemical industry, in industrially developed countries. It is for this reason that soil stabilization by plastic materials has become popular primarily in countries where the chemical industry was in the position to supply these materials at a relatively low price to the construction industry (United States of America and the Soviet Union) [5—7, 12, 13, 16].

The main advantage of soil stabilization with plastic materials over other chemical method of soil stabilization is that the resin solutions lend themselves readily to grouting even into soils having a low permeability, with permeability coefficients of $k = 10^{-5}$ cm/sec order of magnitude. Depending on the grain size distribution and mineralogical composition of the soil, unconfined compressive strengths ranging from $\sigma = 15$ to 100 kg/sq.cm were attained with the resin method of stabilization in fine grained soils, this being suitable to meet the most exacting foundation specifications [14, 15, 17].

Some of the recently developed methods yielded, from the engineering point of view, highly satisfactory results, but the resulting costs of soil stabilization are as yet excessively high owing to the high price of chemicals. Practical domestic applications are therefore confined to cases where no other alternative can be found for solving a given problem. Improved material supply and subsequently the considerable widening of the field of application of soil stabilization with plastics are expected to ensue with the growth of the chemical industry in Hungary.

Before passing on to the description and evaluating discussion of experimental studies a few words on the theoretical aspects of stabilization might be of interest.

As revealed by investigations carried out so far, the success of stabilization primarily depends on the gradation of the soil. Any reduction of particle size is accompanied by an increase of the specific surface and consequently of the number of bonds per unit volume. In view of the fact that besides the strength of individual bonds, the strength of the stabilized soil mass is also governed by the number of bonds, higher strengths are bound to occur in the case of smaller particle sizes. Since, on the other hand, the total particle surface is larger in this case, a greater quantity of stabilizing material is absorbed on this surface, leaving less to create bonds. Consequently the optimum amount of stabilizing material to be added will vary with grain size distribution.

Stabilizing materials of suitable quality and quantity will fail to produce a bond of satisfactory strength with soil particles — clay minerals — which adsorb water on their surface. In fact, adhesion of the chemical is prevented by water bonded to the surface. In soil stabilization the stabilizing effect is due to the hardened chemical, and the desired degree of stabilization cannot be achieved, unless a strong bond between soil particles and chemical is ensured.

In chemical soil stabilization hardening of the chemical may occur by one of the following processes:

precipitation,
ion exchange,
polymerization, and
oxidation.

The two last mentioned processes play the most important part in soil stabilization. Under certain conditions several substances during polymerization form giant molecules having great molecular weight. In the case of polymerization by condensation water, alcohol, or ammonia is liberated during the reaction of substances, calling for the use of acids, or bases as catalyzing agents. Coupled polymerization does not result in such a precipitation. Substances accelerating the reaction, respectively, oxydizing reagents must in these instances be added as catalyzing material.

Soil stabilization experiments using plastics carried out under the guidance of the author will be described subsequently.

II. Experiments with Different Resins

2.1. *Properties of resins used in the experiments*

Soil stabilization experiments using plastic resins were begun at the Institute for Geotechnics, Technical University for Building and Traffic Eng., Budapest, in 1962. After a thorough survey and analysis of reports published abroad, resin compounds ensuring the desired mechanical, as well as physico-chemical properties were selected. The cheapness and ready availability of the materials on the domestic market was one of the fundamental considerations. Resins were then prepared on the basis of formulae determined in this manner and partly completed by the Department for Plastics Industry, Technical University, Budapest. Urea- and melamine-base resins were selected. As is well known, resins may be produced from pure urea, or melamine with formaldehyde, but the properties of these products can be influenced by combining urea and melamine in different proportions, and can be modified, or adjusted by the addition of single- or multi-function compounds. Resin properties may be controlled to a considerable degree and may be appreciably improved by variations and modifications.

Aside from good mechanical properties, low viscosity, permanent stability at normal temperatures (20 °C), resistance to heat and no strength loss in aggressive media were also considered important requirements.

The following resin compounds were tested:

a) *Urea resin (KF—1)*
Urea: formaldehyde ratio = 1 : 1.5
The resin can be blended with unlimited quantities of water.
Solids content of the resin: 47.3%.
Viscosity at 20 °C: 6.63 cSt.

b) *Urea resin (KF—2)*
Urea: formaldehyde ratio = 1 : 2.
The resin can be blended with unlimited quantities of water.
Solids content of the resin: 43.6%.
Viscosity at 20 °C: 7.08 cSt.

c) *Melamine resin (MF—3)*
Melamine: formaldehyde ratio = 1 : 2.5.
The resin can be blended with unlimited quantities of water.
Solids content of the resin: 47.08%.
Viscosity at 20 °C: 9.02 cSt.

d) *Melamine resin (MP—4)*
Melamine: formaldehyde ratio = 1 : 2.5.
The resin can be blended with a limited quantity (1 : 7) of water.
Solids content of the resin: 51.9%.
Viscosity at 20 C°: 156 cSt.

As can be seen from the foregoing all resins with the exception of MP-4 have an extremely low viscosity, nearing that of water. Viscosity of the resin MF-4 is 156.1 cSt, so that it cannot be recommended for grouting purposes, but using a mixing process it can be made suitable for soil stabilization. Each of the four resins can be well stored and remain stable even during extended storage. Under normal conditions and at 20 °C temperature the resins can be stored for 2 ÷ 4 weeks without the deterioration of its quality. With refrigeration storage this period can be extended from 4 to 5 times the above value.

On the addition of the catalytic agent the resin hardens and assumes a cellular foam structure. Exposed to thermal effects the resins assume this cellular structure and hardening ensues even without the addition of reacting agents. For this reason the resins after a certain period become unsuitable for stabilization purposes. The rate of hardening is greatly controlled by temperature, inasmuch as a rise of about 10 °C increases the rate of hardening to about its twofold. As the heat conductivity of resin is low thus in the case of large resin masses — if heat cannot be removed — the rate of hardening is greatly accelerated. In soil-resin mixtures, however, a similar acceleration of the reaction rate does not occur any longer.

Kf-2 and MF-4 resins are less sensitive to heat.

Hardened resins are heat resistant up to temperatures between 100 and 200 °C.

Hardened resins are insoluble in acids.

Before hardening the resins are readily soluble in bases, but after hardening the dissolving effect of bases is very low. Alkalinity, respectively the carbonate content of the soil is a factor retarding, or even preventing hardening, so that a pretreatment of similar soils becomes a necessity.

Resins KF-1, KF-2 and MF-3 are readily soluble in water, but solubility of resin MF-4 in water is limited.

Hardened resins are insoluble in water, but slight amounts of mono- and oligomers — not exceeding some per cents — may be leached by flowing groundwater.

Of the above resins both urea and melamine are compounds containing nitrogen, and are thus harmless to plant and animal organisms. Slight amounts of formaldehyde may be leached from the hardened resin, but these are neutraized by organic substances present in water. Urea and melamine resins are durable.

2.2. *Hardening of resins*

Hardening of the above resins was accomplished by the addition of hydrochloric acid, ammonium chloride and oxalic acid of different concentrations. Changes in hardening time were recorded together with strength attained by adding catalytic agents of different concentration in quantities of 5, 10, 15, 20 and 25 per cent by weight. The most suitable catalytic agent and mixing ratios of the latter were selected for each resin compound on the basis of these experiments. Hardening time should be adjusted to prevent commencement of the hardening process before the resin is introduced into the soil. On the other hand, the period of grouting should not be extended over 4 to 6 hours, since the resin solution may be diluted appreciably under groundwater level, and in flowing groundwater some of the unhardened resin may be washed away, the consequence of which is that poorer stabilization results will be attained. For this reason a stabilization technology permitting the use of a catalytic agent which ensures a shorter hardening period should preferably be adopted for soil stabilization [8].

Evaluation of experiments performed with individual resin compounds can be summarized as follows:

a) *Hardening of resin KF-1.* For practical applications the use of hydrochloric acid of 7% concentration, as well as a 1 : 1 blend of 7% ammonium chloride and 3.5% hydrochloric acid was found to be the most successful for hardening resin KF-1.

When adding this catalytic agent at 20 per cent by weight hardening ensues within a period of 4 hours.

b) *Hardening of resin KF-2.* The most suitable for hardening resin KF-2 was found to be hydrochloric acid of 10% concentration and sodium chloride of 12% concentration. When adding the catalytic agent in a quantity of 10 per cent by weight, hardening was attained within 6 hours.

c) *Hardening of resin MF-3.* On the basis of experimental results for hardening resin MF-3 the use of 10% hydrochloric acid, or the 1 : 1 blend of 24% ammonium chloride and 10% hydrochloric acid can be recommended.

It should be noted that a hardening period shorter than 5 hours cannot be attained even if the reagent substance is added in larger quantities. Hardening of the resin is relatively slow, however powerful the catalytic agent may be, but other favourable properties make it well suited for practical application.

d) *Hardening of resin MF-4.* As indicated by experimental results, 10% concentration hydrochloric acid, or 12% ammonium chloride are suitable for hardening resin MF-4. When adding 10% by weight catalytic agent, a hardening period of 4 hours was observed.

The hardening period can be extended by using hydrochloric acid of 5% concentration.

2.3. *Properties of hardened resins*

The four types of resin hardened with different catalytic agents were tested for volume stability, strength and permeability, and the following results were obtained:

No volume changes of hardened KF-1 and MF-4 resins could be observed during storage under atmospheric conditions, while samples of KF-2 and MF-3 resins showed appreciable shrinkage under such conditions of storage. Shrinkage of KF-2 resin was especially pronounced.

Hardened resins showed a loss in weight even when stored underwater. This loss is due to two factors: under the influence of internal stresses developing in the resin part the water is expelled from the sample, and water-soluble components are leached by water.

The unconfined compressive strength of hardened resins varied from 30 to 60 kg/sq. cm, they showed a dense structure and were completely impervious.

III. Soil Stabilization Experiments

3.1. *Experimental procedure*

Several series of experiments were performed with the resin compounds described in the foregoing with the aim of stabilizing and waterproofing *two types of soil (Fig. 1)*.

a) One of the soils was a fine sand soil, with 80% by weight belonging to the $2 \div 0.1$ mm fraction, the rest to the $0.1 \div 0.025$ mm fraction. The uniformity coefficient of the soil was $U = 5.5$, its permeability coefficient $k = 10^{-2}$ cm/sec. The soil contained 5% $CaCO_3$.

b) The second soil was a yellow silty fine sand. The grain size distribution was: $1 \div 0.1$ mm fraction 72%, $0.1 \div 0.02$ mm fraction 23%, and silt fraction from 0.02 to 0.08 mm the remaining 5% of the soil. (All per cents by weight.) The uniformity coefficient was determined as $U = 2.5$, the permeability coefficient was $k = 3 \cdot 10^{-3}$ cm/sec. The soil contained 1.5% $CaCO_3$.

Soils treated with different resins were adjusted before each experiment to have a moisture content of $w = 0.5$ and $w = 10\%$.

Soil cylinders of 40 mm diameter and 60 mm height were prepared for each experiment uniformly. For each sample 120 grams air-dry soil was used, to which water was added to attain 10 per cent moisture in the case of moist-soil tests.

Soil samples prepared in this manner were then treated with 5, 10 and 15 per cent by weight resin compounds.

For resin KF-1, KF-2, MF-3 and MF-4 the ratio resin : catalytic agent was 9 : 1.

Catalytic agents used were 12% NH_4Cl solution and 10% HCl solution.

Soil samples made with wet soil ($w = 10\%$) by resin treatment were stored in humid air saturated to have 100% moisture, while those made with air-dry soil ($w = 0.5\%$) were stored after resin treatment under atmospheric conditions. Hardened soil samples were tested in 21 days for permeability and strength and the relationship of these properties with resin and catalyzer type, as well as with storage conditions was established.

By changing one of the above parameters at a time — two types of soil, two moisture content values, two types of catalytic agent, added in three different quantities, four types of resin — altogether 96 hardened test soil samples were made.

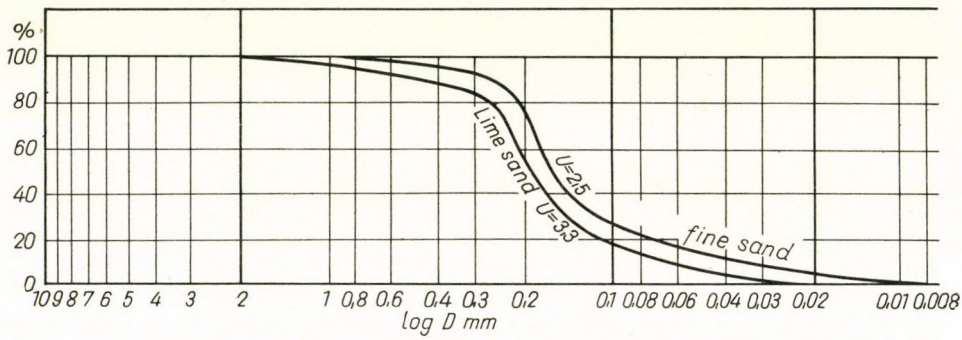

Fig. 1. Grain size distribution curves of soils used in the experiments: *a* — lime-sand; *b* — finesand

3.2. *Results of soil stabilization and waterproofing tests and discussion thereof*

From the results of tests performed on soil samples prepared as previously described the following conclusions could be arrived at on the extent of stabilization and on changes in permeability attained.

3.21. *Stabilization and waterproofing attained with resin KF-1.* results obtained in the series of tests are compiled in Figs. 2 and 3. No noteworthy strength properties were revealed by samples made with soil at $w = 10\%$ moisture and stored in humid atmosphere. Highest strength resulted from using 10% hydrochloric acid as catalytic agent, but even this value was no more than 1.5 kp/sq.cm, although 15% by weight of the catalyst was added.

Low strengths may be explained, primarily with the volume ratio of 9 : 1 of resin: catalytic agent. The resin compound, including resin and catalytic agent alike, was diluted by soil moisture to that extent, where the concentration of the catalyst was not any longer sufficient to produce hardening of the resin. This phenomenon is more pronounced in the case of lime-sand, where the hydro-

chloric acid reagent produced practically no hardening at all. Lime salts present in the soil in this case neutralized a considerable portion of hydrochloric acid added and no catalytic agent was left for hardening the resin.

Samples made with soil containing $w = 0.5\%$ moisture and stored under atmospheric conditions at room temperature ($22 \div 25$ °C) showed an appreciable gain of strength — from 22 to 38 kp/sq.cm — with both types of soil and with both resin compounds added at the rate of 15% by weight of soil. However, upon immersion into water the majority of these samples deteriorated

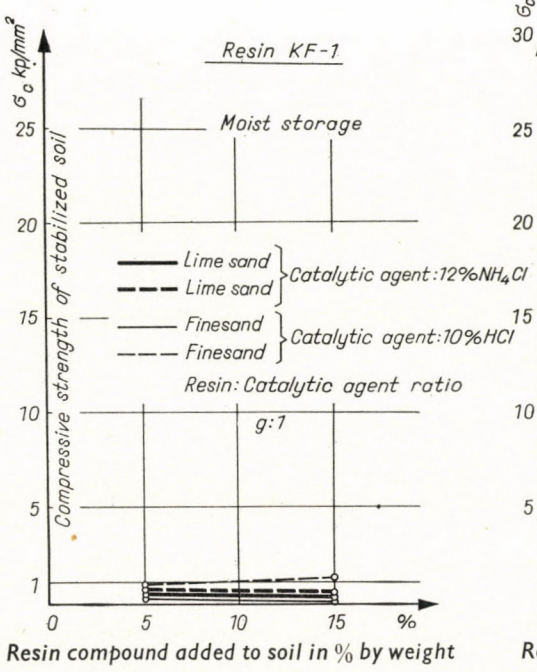

Fig. 2. Strengths developed by soil samples stored in moist atmosphere, plotted vs. quantity of KF-1 resin compound added. Initial moisture content of soil $w = 10\%$.

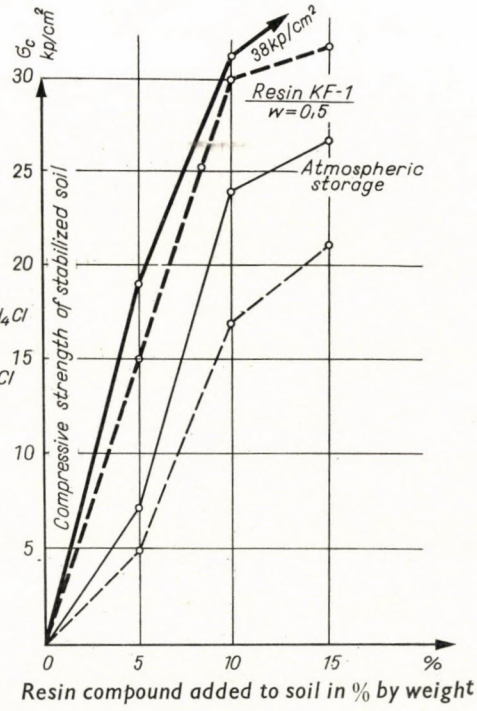

Fig. 3. Strengths developed by soil samples stored under atmospheric conditions plotted vs. quantity of KF-1 resin added. Initial moisture content of soil $w = 0.5\%$

and fell apart because some of the resin failed to react owing to the lack of adequate catalytic agent.

Unhardened resin is dissolved and leached by water.

Neither strength, nor permeability of soils treated with resin KF-1 showed any improvement at the given resin: catalyst ratio (9 : 1) and this compound was therefore classified unsuitable for practical applications. However, it would be premature to condemn the quality of the resin, in view of the favourable results obtained in stabilization experiments performed with

pure resin. With a resin : catalyst ratio of 3 : 1 satisfactory results could be expected.

3.22. *Stabilization and waterproofing attained with resin KF-2.* Stabilization results are presented in Figs. 4 and 5. Stabilization of moist soil gave results similar to those observed with resin KF-1. A slight gain in strength occurred when the resin compound was added at the rate of 15% by weight to the soil (1 kp/sq.cm).

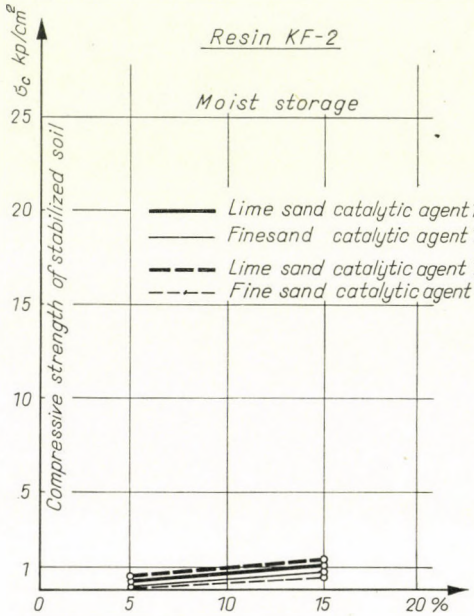

Fig. 4. Strengths developed by soil samples stored in moist atmosphere plotted vs. quantity of KF-2 resin added. Initial moisture content of soil $w = 10\%$

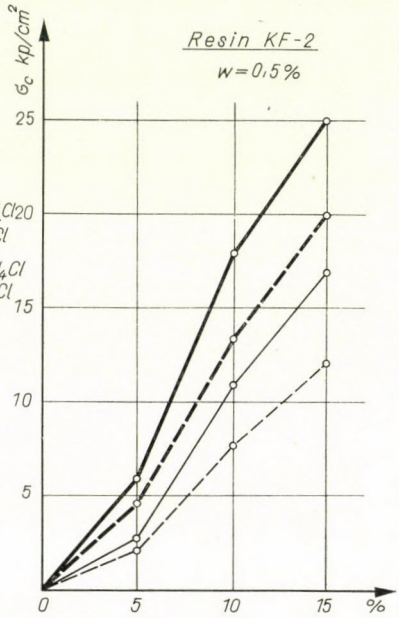

Fig. 5. Strengths developed by soil samples stored under atmospheric conditions plotted vs. quantity of resin KF-2 added. Initial moisture content of soil $w = 0.5\%$

Low strengths developed by resin KF-1 are attributed to factors identical to those listed in the previous paragraph in connection with resin KF-1. Stabilization of air-dry soil produced results which, although lower than those obtained with the resin KF-1, may still be considered satisfactory and strengths developed when the resin compound was added at 15% by weight to the soil ranged from 12 to 25 kp/sq.cm.

The change in the permeability of the soil was slight and reduced to $k = 10^{-3}$ to 7. 10^{-3} cm/sec. On the basis of preliminary experiments performed with pure resin appreciably better results may be expected from using a compound with a resin: catalyst ratio raised to 3 : 1.

3.23. *Stabilization and waterpoofing attained with resin MF-3.* Results of experiments performed with resin MF-3 are summarized in Figs. 6 and 7. Samples made with moist *lime-sand soil* and stored in humid atmosphere showed a substantial gain in strength. The unconfined compressive strength was found to be 16 kp/sq . cm when adding 15% by weight of the resin compound to the soil. The compound was mixed with 12% concentration ammonium chloride. Samples made with a compound in which 10% HCl was used as catalytic

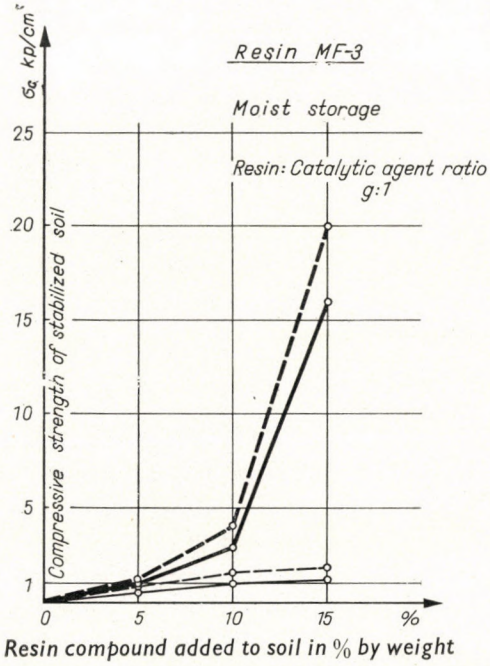

Fig. 6. Strengths developed by soil samples stored in moist atmosphere plotted vs. quantity of MF-3 resin added. Initial moisture content of soil $w = 10\%$

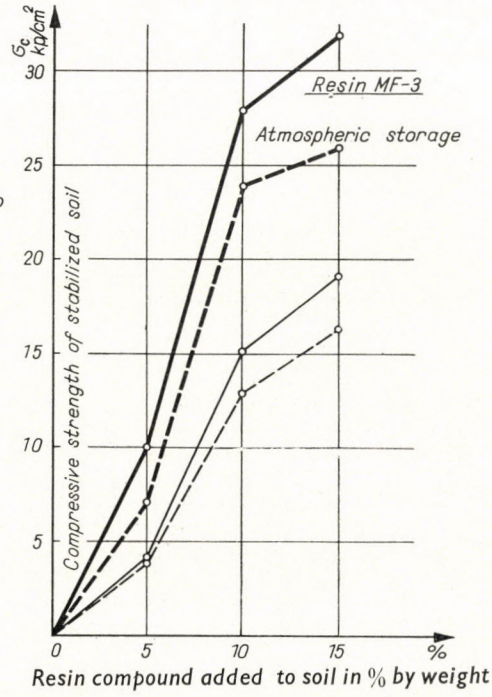

Fig. 7. Strengths developed by soil samples stored under atmospheric conditions plotted vs. quantity of MF-3 resin added. Initial moisture content of soil $w = 0.5\%$

agent showed a strength as high as 20 kp/sq.cm. The strength developed when the compounds were added at 10% by weight of soil decreased to 3 and 4 kp/sq.cm, respectively.

Aside from attaining higher strength with samples made with air-dry lime sand and stored in dry atmosphere, in this case it was the 12% NH_4Cl reagent which produced higher strength values. Conditions under which the chemical reaction takes place can be an explanation of this fact, inasmuch as the reaction during hardening is undisturbed if gases developing are given opportunity to escape, respectively there is direct contact between soil and air.

Stabilization of fine-Mo to medium sand soil in moist condition resulted in appreciably lower strength properties ($1 \div 1.8$ kp/sq.cm) than the same in dry state, where values from 16 to 19 kp/sq.cm were attained. Lower strength values attained with this type of soil are obviously attributable to the higher finesse of the gram content. According to foreign literary reports a clay fraction exceeding 3% may exert a pronounced adverse effect on strength. This loss of strength may be traced back to the hydrophile properties of the finesse. Considerable strengths attained with this type of soil ranged from 16 to 19 kp/sq.cm regardless of the catalytic agent used. An appreciable change in the permeability of the stabilized sample could be observed. The permeability coefficient k decreased from the initial value of $2 \cdot 10^{-3}$ to $k = 6 \cdot 10^{-6}$ cm/sec. On the basis of results obtained with samples stored in moist atmosphere for practical applications resin MF-3 should be added at the rate of 10 to 15% by weight of soil. Requirements of the construction industry are fully met by the resulting strength and permeability properties. Improved strengths are expected from modifying the resin: catalytic agent ratio to 1 : 3 and when the catalytic agent used is 10% HCl, sufficient amounts thereof are likely to remain in the soil even after the neutralizing effect of salts present to produce hardening of the resin. Where the resin : catalytic agent ratio is maintained at 1 : 9, the pretreatment of the soil with $3 \div 5$ % hydrochloric acid solution may produce beneficial effects.

3.24. *Stabilization and waterproofing attained with resin MF-4.* Results of experiments performed with resin MF-4 are summarized in Figs. 8 and 9. Stabilized soil samples made with moist *lime-sand* soil and stored in moist atmosphere yielded considerable strength values when the resin compound was added at a rate of 15% by weight of soil, regardless whether of 10% hydrochloric acid, or 12% NH_4Cl was used as catalytic agent. In the case of hydrochloric acid the strength developed by the sample was 21 kp/sq.cm, while with ammonium chloride it was 17 kp/sq.cm. When the resin compound was added to the lime-sand at the rate of 10% by weight, the strength observed was 5 to 6 kp/sq.cm. The same type of soil stabilized in air-dry condition and stored under atmospheric conditions developed a strength as high as $36 \div 46$ kp/sq.cm. From among the samples stored under atmospheric conditions those treated with 12% NH_4Cl developed higher strength.

Fine to medium sand soils stabilized in moist condition with 15% by weight resin compound yielded strengths from 4 to 5 kp/sq.cm, regardless which of the two catalytic agents was used. When the resin compound was added to the soil at the rate of 10% by weight, strengths of no more than 2 to 3 kp/sq.cm were observed. Appreciably lower strengths attained in the case of fine-to-medium sand soil are due to the higher finesse content of this type of soil. When stabilized in dry condition using 10 and 15% by weight

resin compound, strengths observed were $18 \div 20$ and $28 \div 32$ kp/sq.cm, respectively. The permeability coefficient of stabilized soils varied from $k = 10^{-6}$ to $9 \cdot 10^{-5}$ cm/sec.

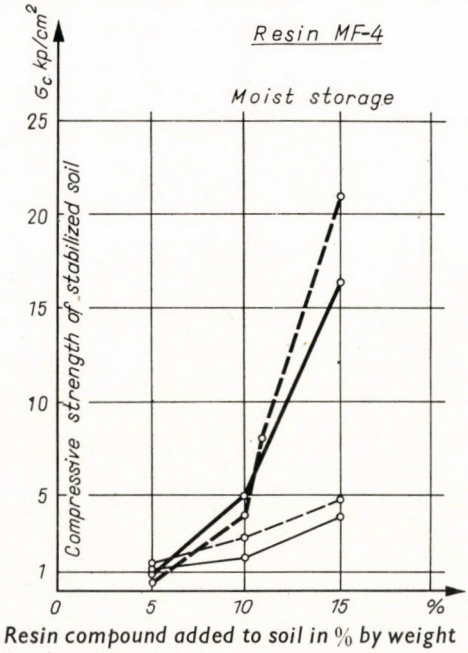

Fig. 8. Strengths developed by soil samples stored in moist atmosphere plotted vs. quantity of MF-4 resin added. Initial moisture content of soil $w = 10\%$

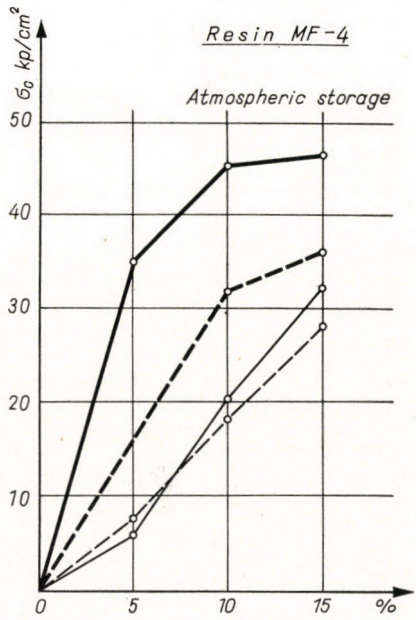

Fig. 9. Strengths developed by soil samples stored under atmospheric conditions, plotted vs. quantity of MF-4 resin added. Initial moisture content of soil $w = 0.5\%$

3.3. *Stabilization and waterproofing by sprayed resin*

In glass vessels of 10 cm diameter 4 cm thick layers were spread from the lime-sand and fine-to-medium sand soils used in these experiments.

Moisture content of the soils was $w = 0.5\%$. On both types of soil, mixtures consisting of various combinations of resins MF-3 and MF-4 as well as 10% hydrochloric acid and 12% NH_4Cl were applied by spraying. The quantity of material used for spraying corresponded to 10% by weight of a 3 cm thick soil layer. This quantity was used in two parts with a period of one hour between them. A well stabilized layer of 1.5 to 4 cm thickness developed in this manner and a coherent continuous resin crust was formed over the surface. In 14 days both soils stabilized with resin compounds containing 12% NH_4Cl developed a high degree of impermeability, high strength and a resistance ot water.

Relying on these experimental results it can be established that the spraying method is superior to the mixing one for waterproofing the surface.

The thickness of the stabilized soil layer can be reduced by introducing suitable techniques of application. By spraying the catalytic agent first on the soil, the hardening time of the resin can be shortened to 5 to 10 minutes. In this manner any deeper infiltration of the resin compound into the soil can be prevented. Should any delay in the hardening of the resin be observed, additional spraying of pure catalytic agent may be recurred to for accelerating the hardening process.

3.4. *Resistance of resin-stabilized soils to water and freezing*

3.41. *Resistance of resin-stabilized soil to water.* The influence of initial water content on the gain in strength has already been discussed in the preceding paragraph. However no mention has been made of the changes occurring on subsequent submergence. Theoretically both strength and impermeability of the soil stabilized with resin should remain unaltered even after extended underwater storage. Discrepancies — which are not related to the properties of the resin — may be due to imperfect mixing, or saturation of the soil with resin, i.e., to the insufficiency of the resin compound for creating a continuous resin film around all particles.

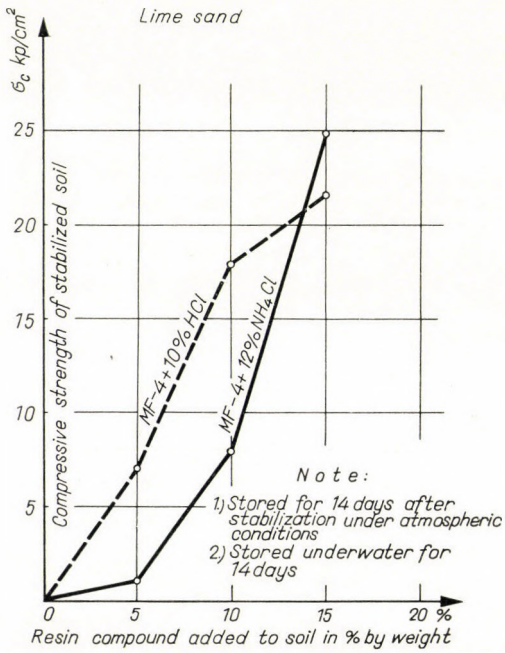

Fig. 10. Strengths developed by samples stored for 14 days after hardening., plotted vs. quantity of MF-4 resin added. Initial moisture content of soil $w = 0.5\%$
Type of soil: lime-sand

The primary aim in the series of experiments to be described below was to study the influence of the intensity of mixing. In this series soil cylinders made of lime-sand with resin MF-4 were cured for 14 days under atmospheric conditions, followed by 14 days of underwater storage. Test specimens were hereafter tested for strength and permeability. Results obtained are presented in Fig. 10. As revealed by a comparison of these results with those illustrated in Figs. 8 and 9, the loss of strength suffered by stabilized soil samples submerged after completed hardening is smaller than that of samples originally stabilized underwater, or at a high soil moisture content. Discrepancies observed are especially pronounced in the case of samples made with lower resin-compound admixtures amounting to no more than 5 to 10% by weight. The main reason for this is that in soils having a high moisture content, the resin compound is diluted before the chemical reaction could take place and poorer strengths and imperviousness are obtained in consequence thereof. The strength loss relative to samples stored under atmospheric conditions is due to the dissolution of unhardened resin and to the lack of a continuous resin film around the particles.

In cases where experiments were started by adding hydrochloric acid of 10% concentration at the rate of 5% by weight of soil to lime sand, and the soil thus pretreated was subsequently stabilized by first applying 10, then 15% resin compound, the stabilized soil samples maintained their strength at approximately the same level, regardless whether it was stored under atmospheric conditions, or submerged therein for 28 days. Maximum differences observed were 10 ÷ 15% order of magnitude.

3.42. *Resistance of resin stabilized soils to freezing.* Lime-sand soil samples stabilized with MF-4 resin compound were subjected to the freezing tests required by standard specification for soil stabilization. For cohesionless soils a weight loss of 14% related to the original weight is specified in the standard as permissible. Commonly accepted dimension of test samples are 10 cm diameter at 13 cm height. Dimensions of test samples used in the tests described below were diameter $D = 40$ mm and height $H = 60$ mm. The procedure adopted for the freezing tests was as follows:

In 21 days the soil sample was submerged for 1 ÷ 2 hours until saturation could be determined.

Thereafter it was kept at —23° C temperature for 12 hours and its weight was subsequently determined.

After storage for 12 hours at room temperature it was again weighed and the surface layer separated from the surface was removed by light brushing. Hereafter the sample was weighed repeatedly.

Samples stirred under atmospheric conditions (lefthand sample) and those subjected to 12 cycles of freezing and thawing (righthand sample) are shown

in Figs. 11a, b, c and d. Samples consisted of lime-sand soil stabilized with resin MF—4, but using different catalytic agents. The resin compound was added at a rate of 10 ÷ 15% by weight of soil. After 12 cycles of freezing and thawing stabilized soil samples revealed a weight loss from 4.5 to 5.5% regardless whether the soil was pretreated or not with hydrochloric acid, and whether 12% ammonium chloride, or 10% hydrochloric acid was added to the resin as catalytic agent. The weight loss observed was far below the value permitted

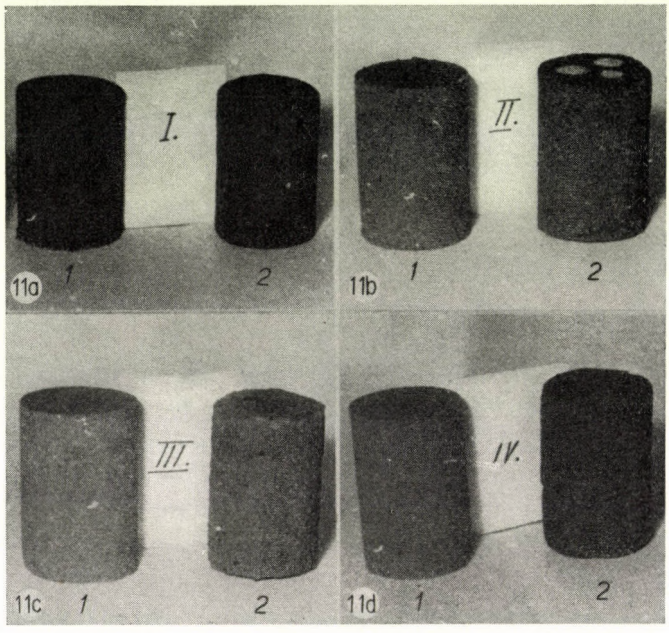

Fig. 11a — d. Fine lime sand stabilized with MF-4 resin and different catalytic agents (left sample: stored under atmospheric conditions; righthand sample: after 12 cycles of freezing and thawing)

by the standard for stabilized soils. These results may be considered especially favourable in view of the fact, that the low weight loss was obtained with samples substantially smaller than specified by the standard, which had, consequently, a much larger specific surface.

Strengths observed on samples after the freezing test are illustrated in Fig. 12. As will be perceived the strength of soil samples is considerably reduced to about 15% of those stored under atmospheric conditions, i.e., to about 4 ÷ 6 kp/sq.cm by repeated freezing and thawing. The remaining strength is still sufficient for most practical applications. The permeability coefficient of samples after the freezing test was $k = 8.5 \cdot 10^{-5}$ cm/sec, which compares favourably with the $k = 6 \cdot 10^{-6}$ cm/sec value obtained with control samples.

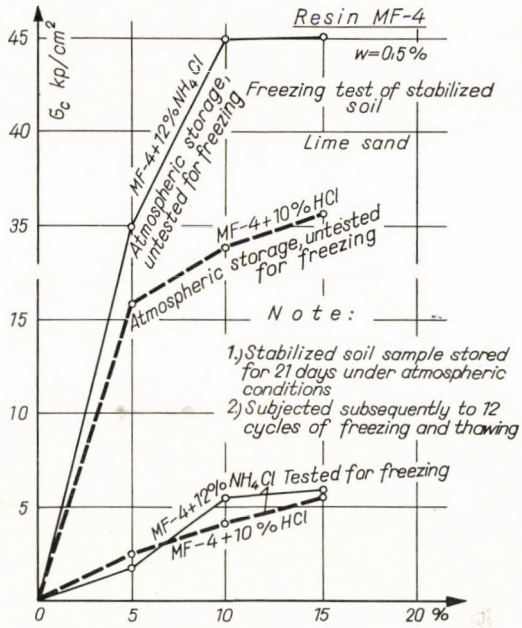

Fig. 12. Resistance of stabilized lime-sand soil to freezing plotted vs. quantity of MF-4 resin compound added. Initial moisture content of soil $w = 0.5\%$

IV. Discussion of Experimental Results Obtained with Different Resins

Owing to their outstanding engineering, as well as physical-chemical properties, plastic resins are gaining widespread application for a variety of engineering purposes including stabilization and waterproofing of soils. Plastic resins are capable of hardening at low temperatures, in the presence of organic, as well as inorganic acids and salts, and become insoluble in water.

The material structure of resins is not clearly understood as yet, any investigation thereof being made extremely difficult on the one hand by the variable conditions of the manufacturing process, and on the other by the insoluble spatial structural pattern of the hardened resin.

The successful application of resins for the stabilization and waterproofing of soils is influenced by a number of factors, most important of which are the grain-size distribution of the soil, concentration of the resin, the period of gel formation, and the pH value of the medium in which the hardening process takes place.

The effect of *grain-size distribution* on the success of soil stabilization has been experimentally demonstrated. A resin at any particular concentration

produces higher strength values in fine grained soils than in coarse ones. This may be attributed to the larger specific surface of finer particles. However, as soon as the fine particles belong to the clay fraction (kaoline, bentonite), the hardening period of sand soil is delayed, and the gain in strength is reduced. *Clay contents exceeding* 3% *were in general found to produce an appreciable strength loss*, for which the hydrophile properties of clay minerals can be offered as an explanation. The development of a strong bond between the soil particle and the resin is prevented by water adsorbed on the surface of the clay mineral.

The effect of various media was investigated and soil, respectively, groundwaters having *pH values higher than* $7 \div 8$ were found to have an adverse effect on both gain in strength and waterproofing. Experiments performed at home and abroad alike demonstrated positively the detrimental effect of *carbonates* present in the soil. A carbonate-content higher than 3% is capable of neutralizing acidic catalytic agents, or salts giving an acidic hydrolysis, and thus of preventing the hardening of the resin. Even in the case of carbonate contents below the above figure, it was found advisable to minimize carbonate effect by reducing — before the stabilization proper — the pH value of the soil, for which purpose hydrochloric acid of $3 \div 5\%$ concentration may be introduced into the soil. A hydrogen ion concentration necessary for the hardening of resin can be ensured in this manner.

Soils stabilized with urea resins were found to maintain their strength in practically all aggressive media (0.1 NaOH, 0.1 H_2SO_4, 0.1 Na_2SO_4, during air- and water storage, or alternating air-water storage). An insignificant strength loss of about 10% was observed after storage of one year under atmospheric conditions, respectively, in a medium containing sulphuric acid.

The strength and extent of waterproofing attained are also significantly influenced by the method adopted for introducing the resin into the soil. The strength obtained by *mixing* the resin with the moist soil to be stabilized is lower than that resulting if the resin compound is *grouted* into the soil. In the course of grouting the bulk of water present in the gaps of the soil is displaced by the resin compound, owing to the higher specific gravity of the latter, and the water has little opportunity during this period to dilute the resin. As a consequence strength, as well as permeability properties superior to those obtained by the mixing method can be observed. In the case of the grouting method the extent of stabilization is but little influenced by the original moisture content of the soil.

Stabilized soils were found to be resistant to corrosion and to maintain high strength for extended periods of time.

Owing to the viscosity of the resin comparable to that of water, the resin can be introduced even into fine grained soils using pressures appreciably lower than those common in cement grouting. Since plastic resin is soluble in water, the concentration of the grouting material can be controlled in advance.

No shrinkage of stabilized soil could be detected, since in the case of a proper mixing ratio of resin and soil, internal stresses developing within the resin remain small, owing to the slight thickness of the resin film enveloping the particles. Using the most favourable mixing ratio the strength of the resin stabilized soil may attain even the strength shown by the pure resin.

In the experiments described a lime-sand containing 5% $CaCO_3$ and a fine sand containing 5% silt fraction were used. Both types developed their highest strength after treatment with resins MF-3 and MF-4. The low viscosity of resin MF-3 makes it especially suitable for grouting purposes. High mechanical strength can be attained with resin MF-4, but its use for grouting is prevented by its high viscosity. Resins KF-1 and KF-2 show low viscosity and so lend themselves readily to grouting and produce high strengths in carbonate-free soils. Since both resins KF-1 and KF-2 develop strengths at a high rate even on the addition of slight quantities of the catalytic agent, soils containing $CaCO_3$ in minimal quantities (1%) are to be precured with hydrochloric acid of $3 \div 5\%$ concentration, in order to prevent neutralization of the catalytic agent by the lime present in the soil.

REFERENCES

1. Clare, K. E.: Factors Affecting the Design of Stabilized Soils. *Roads and Road Construction*, (1961), dec.
2. Grossi, F.—Woolsey, L.: Effect of fatty quaternary ammonium salts on physical properties of certain soils. *Industrial and Engineering Chemistry*, (1955), Nov.
3. Hancock, K.: Aluminium sulfate and iron sulfates as auxiliaries in bituminous stabilization of soils. *Industrial and Engineering Chemistry*, (1955), Nov.
4. Hopkins, P.: Acrylate salts or divalent metals. *Industrial and Engineering Chemistry* (1955), Nov.
5. Lauritzen, W.: Soil Stabilizers for seepage control in irrigation canals and reservoirs. *Industrial and Engineering Chemistry*. (1955), Nov.
6. Meunier, C.—Gordon, J.—Hopkins, P.: Soil-water Relationships in Calcium Acrylate Stabilized Soil. *Industrial and Engineering Chemistry*. (1955), Nov.
7. Millard, S.: The Need for Soil Stabilization. *Roads and Road Construction*, (1961), Dec.
8. Petrasovits, G.: Bodenversteinerungs- und Wasserabdichtungsversuche mit Aminoplast-Harzen. Nemzetközi Talajmechanikai és Alapozási Konferencia; Akadémiai Kiadó, Budapest 1963.
9. Petrasovits, G.: A vegyi talajszilárdítás néhány kérdéséről, és a Cebertowicz-féle eljárás gyakorlati alkalmazása (About some questions of chemical stabilization of soils and the practical application of Cebertowicz method). *Mélyépítéstudományi Szemle*, (1956), July-Aug.
10. Smith, C.: Mixing Chemicals with Soil. *Industrial and Engineering Chemistry* (1955), Nov.
11. Williams, P.: Field Control of Stabilized-Soil Construction. *Roads and Road Construction* (1961), Nov.
12. *Давыдов, В. В.:* Применение некоторых смол для укрепления горных пород. Материалы совещания по закреплению и уплотнению грунтов, Киев 1962.
13. *Ибрагимов, М. Н.:* Устройство противофильтрационной завесы в песках с помощью карбамидной смолы. Закрепление грунтов. Сборник трудов № 50, Москва 1962.
14. *Кулеев, М. Т.:* Опыт закрепления лессовых грунтов водными растворами карбамидной смолы в полевых условиях. Закрепление грунтов. Сборник трудов № 50, Москва 1962.
15. *Луканина, Т. М.—Ястребова, Л. Н.:* Применение высокомолекулярных синтетических смол для укрепления грунтов. Материалы совещания по закреплению и уплотнению грунтов, Киев 1962.

16. *Ржаницын, Б. А.:* Преобразование грунтов физико-химическими методами. Искусственное закрепление грунтов. Сборник № 17, Москва 1952
17. *Ржаницын, Б. А.:* Закрепление и уплотнение грунтов в промышленном строительстве. Материалы совещания по закреплению и уплотнению грунтов, Киев 1962.

BODENVERFESTIGUNGSVERSUCHE MIT KUNSTHARZEN

G. PETRASOVITS

ZUSAMMENFASSUNG

Im Laboratorium wurden die Möglichkeiten für die Verfestigung von schlammhaltigem und schlammfreien Boden mittels Kunstharz untersucht. Verschiedene Kunstharzgemische und Katalysatoren wurden verwendet, mit Zusätzen von 5—10—15 Gewichtsprozent.

Bei den Versuchen wurde die Wirkung der Schlammkörner und des im Boden befindlichen Kalks auf das Ausmaß der Verfestigung untersucht, sowie der Zusammenhang zwischen dem anfänglichen Wassergehalt und der erhaltenen Festigkeit, die Bedeutung des Frostes und der Wärmeeinwirkung und ihre Einflüsse auf die Festigkeit, das heißt, es wurden die Einwirkungen untersucht, denen der verfestigte Boden unter natürlichen Umständen ausgesetzt ist.

Die Ergebnisse zeigen, daß die Kunstharze höhere Festigkeit ergeben als das Wasserglas, auch ist der Ausbreitungshalbmesser größer, und dabei übertreffen die Kosten der Verfestigung (Ft/m³) nicht die Kosten des Wasserglas-Verfahrens.

ESSAIS DE STABILISATION DU SOL PAR RÉSINES SYNTHÉTIQUES

G. PETRASOVITS

RÉSUMÉ

Des recherches de laboratoire ont étudié les possibilités de stabilisation des sables limoneux et meubles par des résines synthétiques. Différents mélanges de résines et catalyseurs ont été utilisés avec des dosages de 5, 10 et 15%.

Au cours des essais ont été examinés l'influence que le limon et la chaux contenus dans le sol exercent sur le degré de stabilisation, le rapport entre le contenu initial en eau et la résistance obtenue, l'importance et l'influence du gel et de l'action thermique sur la résistance, c'est-à-dire toutes les actions pouvant s'exercer sur le sol stabilisé dans les conditions naturelles.

Les résultats ont également montré que les résines synthétiques assurent une résistance et un rayon d'action plus grands que le procédé de sylicatisation, alors que les frais de stabilisation (Ft/m³) ne dépassent point ceux de ce dernier.

ОПЫТЫ УКРЕПЛЕНИЯ ГРУНТА ИСКУССТВЕННЫМИ СМОЛАМИ

Г. ПЕТРАШОВИЧ

РЕЗЮМЕ

Лабораторные исследования были направлены на распознание возможности укрепления илистых и свободных от ила песчаных грунтов искусственными смолами. Были применены различные смеси искусственных смол и разные катализаторы, в количестве 5—10—15% от веса.

По ходу опытов исследовались влияние частиц ила и присутствующей в грунте извести на меру укрепления, зависимость между начальным содержанием воды и достигнутой прочностью, значение и влияние на прочность заморозков и теплового фактора, то есть то влияние, которое может затронуть укрепленный грунт в естественных условиях.

Результаты, впрочем, показали и то, что искусственные смолы дают большую прочность грунта чем укрепление жидким стеклом, радиус распространения больше, и в то же время расходы по укреплению грунта (Фор/м³) не превышает расходов на укрепление жидким стеклом.

COMMUNICATION METHODS USING CODES CARRYING ADDRESS AND CONTENTS OR ADDRESS ONLY

E. ÁCS
DOCTOR OF TECHN. SC.
RESEARCH INSTITUTE OF TELECOMMUNICATION, BUDAPEST

[Manuscript received March 1, 1965]

In case of communication among several subscribers on a common channel, informations concerning destination (address) and content of the message, must be transmitted. In the classical PCM the address is transmitted by the time position (serial number) of the codewords, and the contents by the codewords themselves. However, it is possible that — similarly to the method used in the computer technique — both address and contents are carried by the codewords. A further possibility is by the reverse of the classical PCM where the contents is transmitted by the position of the codewords and the address by the codeword itself. The paper deals with these last two methods, i.e. using codes carrying address and contents or address only. A review of the fundamental principles is given and possibilities of eliminating transmission errors, as well as means of band compression offered in the case of the studied method are dealt with.

I. Introduction

Any information element of the time division multi-channel transmission system is determined by two data which are independent of each other. *The first* of these characterizes the amplitude value of the sample taken from the signal function and the *second* defines that output (address) of the multi-channel transmission line where the sample should arrive.

From these two data that concerning the amplitude may be transmitted in analogous or quantized form, and that one defining the address only in quantized form, since the addresses of the outputs are integers.

The classical synchronous time division systems, with the exception of the address code system that we are dealing with here, seek to ensure the quantization of the address by the synchronization of sampling moments determined for the single channels with the transmit-receive switches. Since the uniformity of the sampling moments and the synchronization of the transmit-receive switches can be realized only approximately the quantization of the address cannot be done at present beyond $24 \div 28$ channels, and in case of free space propagation a substantial increase of the number of channels cannot be expected because of physical reasons.

The required accuracy in the transmission of the information element is considerably different for amplitude and address. While in the transmission of amplitude an uncertainty even of $1 \div 3\%$ does not cause an appreciable deterioration of quality, at the same time in PCM transmission, for instance, even in a 24 channel system a synchronism better than 0.1% is required.

It is therefore evident, that a modulation system should be developed which allows the quantization free of address synchronization, the increase of the number of channels comprised in a frame, and at the same time offers the possibility of the quantized or analogous amplitude transmission depending on the required accuracy of amplitude.

In the following the principles for both possibilities are described, that is, when besides the quantization of the address the amplitude also is quantized or the amplitude transmission is ensured by modulating the position of the address code in time. The time interval depending on the amplitude equals practically the whole sampling period, say 125 μs, irrespective of the number of channels.

As in the address code system the channels do not have fixed position in time, that is, no samples are transmitted from the inactive line, the band width is determined by the number of codes to be actually transmitted and this fact diminishes the code traffic by a $^1/_3$ or $^1/_4$ factor with respect to the PCM transmission. With the address code multi-channel transmission system integrated telephone networks can be made up, if it is ensured by *control*, that the amplitude value entering at some input can be provided *with any output address*. With regard to its main function, therefore, the telephone exchange operating on the address code principle is a time division multi-channel transmission system provided with a control. The talking paths in such an exchange are made up of the elements of the multi-channel communication link.

It follows from the principle of the system that identical amplitudes may simultaneously appear. This may lead to the congestion of addresses, or to sample loss respectively. By the use of buffer registers and design the distortions due to this can be kept within given tolerances.

II. Communication with Code Modulation

In long-distance multi-channel links there are generally a great number of repeater stations, branchings, modulating and demodulating circuits in which noises and distortions can occur. These effects, which have an unwanted influence on the quality of transmission (even on the intelligibility of speech) increase with growing distance. Therefore, the attention has become more and more focused on methods which are insensitive to the length of the transmission path. For this purpose the well-known methods of amplitude-quantization serve together with the pulse-code modulation (PCM).

The pulse-code modulation can ensure a transmission practically free of noise with very small distortion when some, by no means hard, conditions are fulfilled, even on a long transmission path including a great number of repeaters and branchings. This outstanding feature is due to the fact that the codes

transmitting the information can be regenerated if they are threatened as being unrecognizable by the superimposed noise. Consequently, it can be stated in advance that the pulse-code modulation can be made perfectly noiseless, if a communication, with regard to noise, can be said to be perfect, when only one or two clicks due to false codes occur within a period longer than the average holding time of a call (three minutes). The transmission path does not add constant hissing noise to the material to be transmitted.

As to the distortions, they also can be decreased to a practically negligible degree, only the steps used for sampling must be chosen so as to be suitably small. The fact that the number of the quantization steps is finite — practically it is between $64 \div 128$ — leads to a certain distortion, but in the case of quantizing the channels one by one the quantization error does not cause disturbance (noise) in the signal intervals.

Let us now consider in somewhat more detailed manner the noise and distortion problems of the PCM systems. A false code at the receiver output arises if any of the pulses making up the code fails due to noise, or on the contrary the receiver perceives a noise peak as a pulse. If the noise has a Gaussian distribution, then probably this happens more or less, depending on the ratio of the pulse magnitude to the effective value of noise, that the values of some noise peaks exceed the half pulse magnitude. Let us assume that this is the critical state leading to the disappearance of the pulse contained in the code or to the appearance of a false pulse. Let X_0 be the ratio of the observed value of the noise to the effective value, and $W(X_0)$ the probability that the noise amplitude exceeds a certain value X_0. For this probability we then obtain

$$W(X_0) = \frac{1}{\sqrt{2\pi}} \int_{x_0}^{\infty} e^{-|x^2/2}\, dx. \tag{1}$$

If we tabulate these probabilities in terms of the pulse amplitude — to effective value of noise ratio it can be seen that by improving the signal-to-noise ratio e.g. from 19.6 db to 23 db the error probability can be decreased from 10^{-6} (which is small enough already) to 10^{-12}. In Table I the error figure ε means how many false pulses and consequently clicks or crashes appear during the observation. The error figures were determined assuming a binary code of seven elements. As in a second eight thousand samplings are made, this means $7 \cdot 8\,000 = 56\,000$ bits/s, and multiplying the probabilities in the $W(X_0)$ column by 56 000 we obtain the number of clicks for a certain period (sec., min., hour, day, year). If some specified value of the signal-to-noise ratio, say 23 db, is referring to one repeater section and a very long transmission path is assumed with, say, 1000 repeater stations then although the error probability deteriorates from 10^{-12} to 10^{-9}, even in this case only after several hours can a click be expected in the transmitted message, for the

Table I

Binary bound Effective value of noise = $2X_0$			Probability of error, $W(X_0)$	Error figure = = 56 000 $W(X_0)$
X_0	Np	dB		
4.65	1.54	13.4	10^{-2}	560/s
7.44	2.01	17.4	10^{-4}	5.6/s
9.51	2.25	19.6	10^{-6}	3.4/min
11.2	2.45	21.0	10^{-8}	2/h
12.7	2.54	22.1	10^{-10}	0.5/day
14.1	2.64	23.0	10^{-12}	2/year

rest the transmission is perfectly noiseless or does not contain more noises than would arise in any case in the sections external to the PCM system, independent of the method of transmission.

It shall be mentioned here another of the interesting advantages of the PCM transmission, namely, that it puts low requirements on the channel filters. In code-modulated systems neither intelligible nor unintelligible cross-talk, i.e. noise will ever get over from one channel into the other if the attenuation between the two channels is no less than let us say, 12 db which is a very low requirement. Namely, in this case the noise entering the receiver has no longer a normal distribution, but gives a constant level, determined by the quality of the filter, which can be made wholly ineffective by means of threshold stages. The requirements concerning the filter however, must be strengthened if fading might also be expected. Namely, it may happen that the level of the signal decreases in the disturbed channel but at the same time not in the disturbing one.

Now let us now confine our attention to the problem of the quantization disto tion.

As mentioned above, when signal transmission does not go on (in a signal interval) the transmission is practically noiseless. The physiological effect of the quantization distortion can be evaluated on the basis of subjective experiment only.

Libois [2] made subjective experiments, namely by mixing white-noise to the message in the percentages shown in Table II. The transmission with a distortion of 5% is characterized by him as "very good". This statement can obtain approval regarding the fact that in reproducing devices (magnetic-tape recorder, gramophone etc.) the distortion of a few per cents, even including 5 per cent, can be permitted as it does not considerably deteriorate the artistic quality of the reproduction.

W. R. Bennett [3] demonstrated that in case of six-digit codes and a sampling repetition of 8000 c/s a distortion corresponding to 4 per cent (28 db)

can be attained, and using an eight-digit code the distortion will be 42 db (cc. 1 per cent).

The six-digit binary code, as is known, gives 64 and the eight-digit code 256 uniform amplitude steps between 0 and the maximum value of the information to be transmitted. (The maximum is taken to be about 12 db above the effective value of the signal.)

We do not wish to enter here into a discussion on matters concerning the use of modulation compression and expansion, it shall be only stated that taking also this possibility into consideration the transmission with cc. 60—120 amplitude steps may be looked upon in telephony as of very good quality.

Table II

Quality of conversation	Approximate ratio of the effective values of distortion and speech signal, %
Tolerable	15
Good	10
Very good	5

Summing up the above, theoretically at any rate it seems justified (also referred upon by experiences from practice) that the PCM system designed with a minimum of precaution guarantees, as may be expected, perfect transmission from the viewpoints of noise and distortion, practically with any large number of repeater stations and branchings.

However, it cannot be concealed that the free space PCM transmission involves a characteristic requirement, namely that the signal-to-noise ratio on the receiver input should never fall below 17 db, otherwise the transmission breaks down (see Table I) which means that in a high-quality radio link a minimum signal-to-noise ratio of about 20 db and on each radio track a fading reserve of 40 db (i.e. totally a signal-to-noise ratio of 60 db) are required. The problems connected with deep fading can be diminished by using diversity systems (e.g. space or frequency diversity) [4, 5].

In every time-division transmission system (also in the PCM system), especially in case of a widespread network, the difficulties of synchronization appear which should not be underestimated.

There are various obstacles in making up a large or larger number (several hundreds or thousands) of channels. The high degree of synchronization of the sampling switch at the transmitting end and the line switch at the receiving end that could enable us to make up a single time frame from a large number of channels cannot be attained yet. Because of the time jitter of the synchronizing signals the perfect synchronism of the sampling switch and the line switch between two synchronizing signals is a very difficult problem.

Even in case of a communication with no more than 120 channels, the codes consist of pulses having a length of about 0.05 μsec and the gating of such pulses at the reception, so that no false code may occur, gives to the receiver a gating task of the order of 10 nanosec at minimum. A similar uniformity is desirable in the generation of synchronizing pulses on the transmitter side.

While the latter can be realized in a relatively simple way, the former is, in case of widespread networks, theoretically and practically unrealizable, because the pulse always has a transmission delay depending on the amplifiers used on the path, on the atmospheric conditions and eventually on the motion of the transmitter or receiver with respect to each other. The random instantaneous fluctuations of the transmission delay which cannot be influenced may considerably exceed the required order of magnitude in sec, especially in the case of widespread networks.

This is perhaps the main reason why the PCM system is not yet more widely used, although apart from the problems of synchronization, the pulse engineering problems can be considered to be practically solved, not only in valve but in semiconductor electronics, too. Just for this reason, from the viewpoint of further developments in communication attention must be paid to the code-modulation methods that are insensible or only a very little sensible to the synchronism of the transmitter and receiver sides. In the following, this problem will be taken into consideration.

III. Communication with Codes Carrying Address and Contents

Let us consider a time-division-multi-channel PCM transmission. If we could observe the codes passing in succession, through the channel we might make two statements concerning them. In the first place, each code word carries information concerning an amplitude value, and second each of the codes following each other is assigned to a particular output, the assignment being determined in advance, i.e. they also carry another information concerning the output they are assigned to; the address of the output.

In the time division system the forwarding of the information element to a given address can be ensured in the following way; the input channels are scanned in turn by the sampling unit, and the line switch at the receiving end selects the corresponding single channel in the order of scanning, that is, the transmission is ensured by the synchronization of the electronic switches operating at the transmitting and receiving ends. In case of n-channel transmission it can be made understandable by using an administrative example. Let us assume that we have n items, which are observed one after the other, to be transmitted, and in order to carry it out we write these items down on separate sheets of paper, put them in order and distribute them in the same order at the output. In this way we forward information by means of letters

without addresses, the missing address being replaced by the order. This kind of transmission always involves the risk that owing to transmission errors a part of the information reaches the wrong address. If the synchronization in the time division system goes wrong, serious errors occur in the transmission.

In principle it is possible to have a time-division transmission with a number of channels greater by many orders of magnitude, which does not require the synchronization of the transmitter and receiver parts; namely when at the transmitting end a code (p_f), corresponding to the f-th output to which the coded sample is sent to, to the coded sample (r_k) of the k-th transmitter output is added.

This code, the address code, will operate only one of the output switches (the number of which may be arbitrary), the one the code is assigned to, so the amplitude sample can reach only the required output.

According to this, each code-word would be logically determined by contents and address:

$$i_{kf} = r_k + p_f \tag{2}$$

where i_{kf} means any code-word. (The following analysis will be restricted to the case of binary codes and code-words of equal length. It is assumed that every code-word consists of $r + p$ bits.)

$2^r - 1 = s$, where s is the number of quantization steps;

$2^p - 1 = n$, where n is the number of channels comprised in a frame.

The use of code-words carrying address and contents means the application and extension of a principle known in the computer technique to the problems of multi-channel transmission and exchange engineering.

From the given relations the values of r and p can be computed.

The case $f = k$ (that is the k-th input is always connected with the k-th output), corresponds to the ordinary time division multi-channel transmission, while $f \neq k$ (that is, when the k-th input may be connected to any of the outputs) is characterizing the main function of the time division electronic exchange.

The length of the binary syllable p_f carrying the address depends on the number of channels in the multi-channel communication link.* That is, e.g. in the case of 1023 channels the address can be determined by 10 binary digits. Then a code-word is determined by $i = r + p = 8 + 10 = 18$ binary digits. As at the receiving end the code-words must be clearly distinguishable from each another, a further pulse must be added to the beginning of each code word, and therefore, the binary code-word of 1023 channels including the address also must consist of 19 binary digits.

* In view of the novelty of this subject it seems convenient to demonstrate the conditions of orders of magnitude in numerical examples.

Although the number of bits to be transmitted had been increased by the factor $19/8 = 2.4$ with respect to the synchronized system, however, the problem of synchronization which according to our knowledge has been unsolvable up to now is eliminated.

Let us now consider the numerical values:

$$g_c\, 2B \cdot n(r + p + 1) = 8000 \cdot 1024 \cdot 19 = 1.56 \cdot 10^8 \tag{3}$$

where g_c is the number of bits to be transmitted in one second, and B is the sampling frequency in c/s. For the evaluation of one bit, separation of codes etc. we have only a few nanoseconds. With the actual electron valve circuits of pulse technique it is possible to carry out these tasks though the semiconductor devices (transistors, tunnel diodes, diodes) are developing so rapidly that within a reasonably short time they will also be able to solve the problems. At any rate, the actual state of development of the pulse technique concerns only the maximum number of channels which can be realized but this has no bearing on the applicability of the system.

The application of codes carrying both address and contents avoids the difficulty of synchronization but involves the increase of the band width of transmission channels with respect to the simple PCM transmission.

However, in case of using codes carrying address and contents, there is a simple possibility of applying effective methods of band compression. This possibility must also be considered when comparing the band width requirements of the synchronous and asynchronous methods.

The possibilities of band compression will be dealt with later.

IV. The Application of Codes Carrying Address Only

The application of code-words carrying both address and contents involves the broadening of the transmission band. A trivial way of diminishing the band requirement would be to transmit the address encoded and the information in the form of an amplitude-modulated pulse. In this case the asynchronous operation would be ensured and the information element would be shortened by about $6 \div 7$ bits but the transmission would remain at the PAM level and would not attain the quality of the PCM. Anyway it would by no means be easy to realize with code-words a system made up of PCM and PAM pulses.

Another solution is also possible which ensures a noise safety equal to that of methods operating with amplitude quantization without transmitting the sample taken from the amplitude of the information to be transmitted by means of a special signal on the channel.

In the known PCM transmission the switches of the transmitter and receiver sides operate synchronously and in the channel connecting these switches the codes of the amplitude samples are transmitted. In other words, in the PCM transmission the address identity of the pairs of inputs and outputs is ensured by synchronism, while the transmission of the amplitude is provided by the code transmitted on the channel.

It seems logically possible to change the terms address and amplitude, that is to use a communication system in which the amplitude identity of the pairs of inputs and outputs is ensured by synchronism and the transmission of address is provided by the code transmitted on the channel.

To clarify the above mentioned facts in a more detailed form let us compare the PCM system with the method which will be described here. In the PCM transmission a latent value which is the numerical value of the output is assigned to each amplitude, i.e. its address.

This latent value is the time interval elapsing from the beginning of the sampling period to the end of the sampling. Thus to the sample taken at the k-th input of the transmission with n channels belongs the time

$$t_k = \frac{k}{n} T$$

where T is the sampling period, e.g. 125 μsec. If at the beginning of each sampling period the transmitter emits a synchronizing signal, t_k also indicates the time after which the code of the k-th amplitude sample follows the synchronizing signal. If the line switch of the output (receiver) starts at the synchronizing signal, and switching the lines one after the other, it comes to the k-th line exactly after the time t_k, the sample will, as is known, reach the required output.

In the transmission of codes carrying the address only, the codes transmitted in succession determine the numerical value (address) of the outputs rather than the amplitudes, therefore, the latent values assigned to the codes must contain the message to be transmitted. Thus in this case, too, it belongs to the code going from the k-th input to the k-th output at the time t_k which now determines, of course, an amplitude to be forwarded to the k-th output. From this the result is that the manner of the "sampling" will be varied with respect to the PCM, namely, the sequence of the scanned input will not be 1, 2, 3, . . . k, . . . n as it usually is in time-division transmission but it will be determined by the voltage values found momentarily at the inputs: $e_p < < e_2 < e_h < e_y$ etc. (The amplitudes, in the interest of one-to-one assignment, are scanned according to a law monotone in time.) Thus, the sequence will be p, 2, k, n, y.

The k-th input at the moment t_k starts a code (address) towards the output if the instantaneous voltage e_k of the m-th input is in the specified

neighbourhood of the instantaneous voltage $E(t)$ of a local generator, that is

$$E(t) = e_k \tag{4}$$

and other inputs do not fulfil the same condition. [If the condition (4) is fulfilled at the same time by m inputs the simplest way is to forbid the $m - 1$ inputs to give addresses.]

$E(t)$ is a periodic function of time. The repetition frequency is equal to the sampling frequency. Within each period the possible amplitude values are

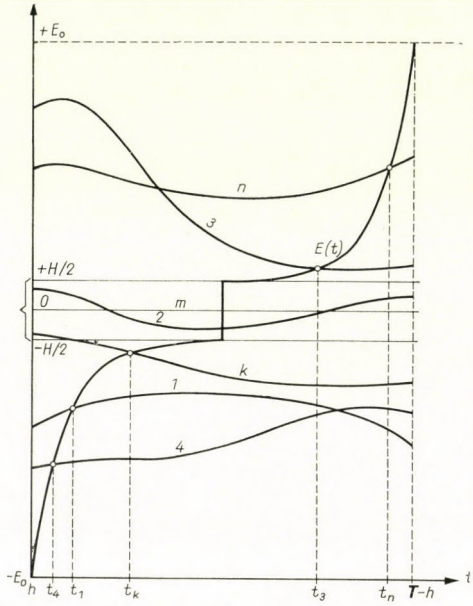

Fig. 1

scanned in a monotonously increasing order. At the beginning and end of the scanning period the value $E(t)$ is kept as a constant level for the time duration h:

$$E(t) = -E_0\,, \quad \text{if} \quad 0 = i \leqq h\,;$$
$$E(t) = \quad E_0\,, \quad \text{if} \quad T = h \leqq t \leqq T\,.$$

E_0 is a little greater than the maximum allowable modulation of the inputs.

In Fig. 1 the voltage state of the loaded inputs 1, 3, 4, n, k is shown for the interval $(0, T)$ or more exactly $(h, T - h)$. 2 and m are unloaded lines. At the moment $t = 0$ the synchronizing signal and at the moments t_4, t_1, t_k, t_3, t_n address codes are starting from the inputs.

To avoid unnecessary coincidences, in the band $\pm H/2$ round about the zero amplitude, no address is sent. The function $E(t)$ must be empirically constructed so that the sending of addresses may go on as uniformly as possible

in the time interval 0, T, but at the same time the transmission should not be too sensitive to variations in time. This is evidently possible if the probability distribution of greater and smaller amplitudes is known.

Another interesting feature of this method is that it uses only voltage comparison. Namely, the instantaneous voltage of the input under test and that of the local generator are compared. The comparison results only in a code-starting command.

Finally, at the output side the function $E(t)$ is regenerated synchronized from the input. At suitable moments the output switches controlled by the address codes, switch the local generator to the lines one after the other and the input messages will thus be transmitted to the outputs. The message transmitted is, of course, not continuous in time but it consists of discrete voltage values. If we do not consider the errors of comparison and synchronizing which can be theoretically made zero and practically negligible, we can state that the discrete values agree with the values of input voltage exactly, rather than only approximately.

In the case of the transmission of address codes alone at the input side the message to be transmitted is described by $e(t)$, the voltage values (discrete in time) arriving at the output demodulator by the function $F(t)$ and the comparison frequency is ν_0 (say 8000 c/s). Then, the two function values agree exactly ν_0-times each second. The intervals between the discrete values are filled in by the demodulator by means of a suitable interpolation method.

Let $\varphi(t)$ be the demodulated signal. In principle, the function $F(t)$ gives the samples discrete in time exactly, only in the function $\varphi(t)$ does distortion appear, depending partly on the method of sampling, partly on the realization of the demodulator.

The signal transmitted to the receiver input is amplitude-modulated, but in the simple case shown in Fig. 1, the single samples do not follow each other at regulator intervals. However, also in this case the theoretically perfect reproduction of the input signal can be ensured if $T = 1/2B$. Whether sampling is really made at irregular intervals according to Fig. 1 or from the value of the speech signals fixed at the moment $t = 0$, is not a problem of principle but is connected with the realization of the comparator and demodulator.

The comparison can be made, at least in principle, with zero error, as the pulses transmitted are not quantized quantities and so quantizing distortion does not occur. On the other hand, only an address code rather than a speech sample is transmitted and, therefore, the pulse transmitted cannot take up noise on the transmission path.

The adequate safety of the address can, in the case of suitable signal-to-noise ratio, be simply ensured.

However it may occur, that the importance of the message to be transmitted requires a higher degree of safety of the addresses. The communication

method described here places evident possibilities at our disposal for this purpose.

For evaluating the errors connected with the addresses correctly let us first state that these errors can cause two kinds of trouble. Namely, the code-word does not arrive at the wanted address, or at addresses some unwanted signals arrive.

The fact that as a consequence of failure of the address code the address does not reach the counter-station, results in sample loss only. The trouble due to this effect is unimportant even if several successive samples are missing.* A considerably greater trouble is if an address receives code-words from some foreign source, because these latter can cause trouble at the output in the signal intervals.

The probability, however, that a code-word goes to a wrong address can be diminished by orders of magnitude if the code-words are made of more bits than necessary, that is if redundancy is applied. It can be attained with suitable design that the failure of the address codes causes only sample loss and practically it does not produce false signals in foreign channels.

After this brief digression on the safety of the address let us now return to the analysis of the basic features characterizing the communication method dealt with here.

It is a peculiarity of the method analysed that the system is, as a matter of fact, position-modulated since the position of the address code within the time interval $(0,T)$ depends on the voltage amplitude at the input at the moment when emitting the code. However the substantial difference among the known systems is that while in these latter in the case of a transmission on n channels for the position-modulation a time of T/n is available, in the system transmitting only the address this time is equal to T.

For this very reason, the studied method does not need special requirements concerning the accuracy of the position of the arriving address codes.

If at the same moment the instantaneous voltages of several speech channels fall in the vicinity of the local generator voltage, then, of course, an address can be immediately forwarded, but from one source. In this case we allow the surplus address to simply get lost or we make its transmission possible with some delay. It is important that in both cases the coincidence does not cause error in the signal intervals. The appearing distortion can be eliminated by the suitable choice of the system parameters.

It may also be taken into consideration that in the case of transmitting address codes alone no pulse modulator and analogue-digital converter are necessary, contrary to all other time-division systems.

* This error, if necessary, can substantially (by orders of magnitude) be diminished by parallel connecting of channels or by repeating addresses.

Let us again consider the principle of transmission in terms of Fig. 2. In the upper part is shown the transformation of the continuous function $f(t)$ of the message to be transmitted into the function $F(t)$ containing the values for comparison and its completion in the demodulator into functions $\varphi(t)$. The function $E(t)$ for simplicity's sake is shown as sawtoothed oscillation. (The dead times and the exact law of scanning are not considered.) On the lower part of the figure the block diagram of the k-th channel of the multichannel transmission apparatus and that of the common circuit are shown. The output of the transformer belonging to the k-th channel is connected with comparator 1. With the latter also generator 2 is connected which produces

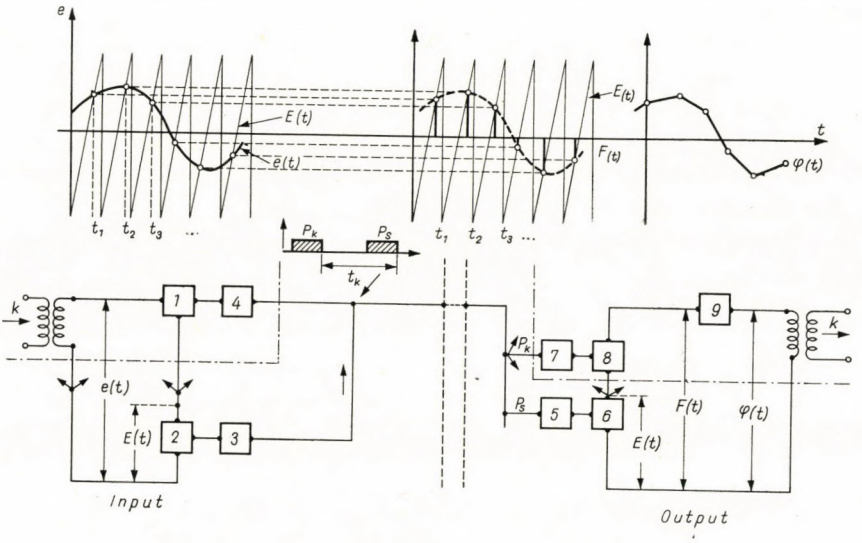

Fig. 2

function $E(t)$. Generator 2 at the beginning of each comparison period starts the address code transmitter 3, which sends the synchronizing code P_s over channel 10. At moments when $E(t) = e(t)$ hold (t_1, t_2, t_3 etc.). The comparator 1 operates the address code transmitter 4, which also sends the address code P_k given by input k over channel 10. The time between the emission of the codes P_s and P_k is t_k. The code P_s arriving at the output operates the address switch 5, which starts generator 6 of the function $E(t)$.

The code P_k starts the address switch 7. This operates switch 8 which connects generator 6 to the input of demodulator 9. Thus, to the input of the demodulator arrives a pulse train modulated in amplitude according to function $F(t)$ and at the output of the demodulator appears the continuous function $\varphi(t)$ obtained by time interpolation of the former.

V. Possibilities of Band Compression in the Case of the Transmission of Codes Carrying Address and Contents

First of all, it may be stated that within the telephone exchange the problem of band width is less critical than those concerning microwaves because it is separated from the outside world and therefore is not subjected to frequency restrictions. In the multi-channel communication link, however, the use of this method, beyond the possibilities of realizing the coding apparatus, also involves the problem of band width. As is known, the needed band width is proportional to the number of the binary digits making up the code. Thus, if the code group to be transmitted consists of 19 bits, in an ideal case, for the transmission of a speech channel a 19-fold band width is necessary compared to the usual band width of 4000 c/s of the multiplex system.

It should also be noted that in the case of PCM (and code-words of 8 bits length within it) this multiplication factor is equal to 8 and in FM systems of high capacity to $2 \div 3$. Thus, for the joint transmission of address and contents a method for narrowing the band must be applied. However, for this case relatively simple possibilities are available.

In the following three possibilities will be outlined.

Let the band narrowing factors of the single methods be α_1, α_2. (If several methods of band narrowing are jointly used we can, under the circumstances considered here, calculate with the product of the band narrowing factors.)

1. The speech channels are exploited up to 50 per cent for speech in the first rough approximation since half of the time is used for listening to the responses. In addition, the words, even the sounds are separated by intervals and sometimes a thinking time is also included between the words or sounds. Therefore, it seems justified to assume that in this sense the activity of a channel is restricted to a quarter of the time: $\alpha_1 = {}^1/_4$.*

2. The condition of good understandability is the transmission of the formants. However, their needed frequency is not always 3400 c/s. Let us, for instance, consider, the word "allover". All sounds of this word except "*v*" have their frequencies, even their fifth harmonics below 1500 c/s, if pronounced by the average voice of a man. The "*v*" needs a higher frequency but has a very short duration with respect to the whole word. In various languages the frequency and time requirements of the formants are, of course, different but it is perhaps permissible to assume the mean time value of frequency for the average speech to be about 1200 c/s, that is $\alpha_2 = {}^1/_3$.

3. It is a psychological fact (we are accustomed to it) that in peak hours there are certain difficulties, troubles, inconveniences in the street at peak traffic time, current supply, shopping etc. It is easy to presume that the telephone communication which generally guarantees the transmission of a band

* [2], p. 37.

width of 3400 c/s will deteriorate in the peak hours to only a small degree. Assuming that a network with a great number of channels is designed so that with a $^2/_3$ load it will still transmit the frequency of 3400 c/s but at a greater traffic it can react only by band compression.

Considering only the first two possibilities

$$a = a_1 a_2 = 1/12 \, .$$

The factors based on assumptions must of course be analysed theoretically and experimentally.

In the following we shall briefly survey the modulation methods allowing the band compression.

In case 1 the first condition of the exploitation of speech pauses is that no sampling from the silent lines occur. In the case of using codes transmitting address and contents (but similarly also in the system transmitting address only) this is possible since the lines missed in the sampling do not influence the receiving of the information to the right address.

For this purpose in the case of using codes carrying both address and contents a code-time transformer must be applied. This transformer lengthens the brief codes according to the average traffic. Essentially, it is a pulse amplifier lengthening the pulses passing over it as well as the pulse intervals and herewith the codes by $1/a$. This is a simple task of circuit design. This requires a buffer register, known in the computer technique, and a reader circuit whose reading frequency is smaller by the factor than the frequency of the original code pulse. The buffer register must also be suitable for storing a certain number of pulses for a short time. The code capacity of the register must be designed to a specified information loss in terms of probability calculation.

The factor a_2 (the average band need) can be realized with the transformation of the sampling circuit. This transformation can, for instance, consist in that the circuit takes a sample only when the absolute value of the first derivative of the signal function exceeds a certain threshold value. This is similar to the delta code modulation inasmuch as information is transmitted only in the case of a specified variation of the signal function, but in contrast to the case of delta modulation, the transmitted signal is the whole amplitude sample rather than only a step.

The method described here at the same time also resolves the more dense graduation of the low level signals since it equally evaluates the signals of large or small amplitude if their derivatives are equal.

Finally, it should be mentioned that the system TASI uses a similar principle for band compression. However, the method of inserting syllables (TASI is an analogous system) used there is less effective, deteriorates understandability to a higher degree and requires a more complicated apparatus.

REFERENCES

1. HÖLZLER, E.—HOLZWARTH, H.: Theorie und Technik der Pulsmodulation, Springer, Berlin 1957
2. LIBOIS, L. J.: Faisceaux Hertziens et systeme de modulation. Editions Chiron, Paris 1958
3. BENETT W. R.: Spectra of Quantized Signals, *The Bell System Technical Journal* (1948), July.
4. VAN WAMBECK, S. H.—ROSS, A. H.: Performance of Diversity Receiving Systems. *Proc. I. R. E.* (1951), March.
5. MILLER, J. Z.—BYON, L. A.: A Microwave Propagation Test. *Proc. I. R. E.* (1950), June.
6. O'NEILL, E. F.: Time Assignment Speech Interpolation. *Bell Laboratories Record* (1959), March.

VERFAHREN DER NACHRICHTENÜBERTRAGUNG MIT KODEN, WELCHE DIE ADRESSE UND DEN INHALT, ODER NUR DIE ADRESSE TRAGEN

E. ÁCS

ZUSAMMENFASSUNG

Bei der Nachrichtenübertragung zwischen mehreren Teilnehmern sollen im Kanal Informationen über den Bestimmungsort (d. h. die Adresse) der Nachricht sowie über ihren Inhalt übertragen werden. Bei dem klassischen PCM-Verfahren wird die Adresse durch die Zeitlage (Nummer) der Kodegruppen, der Inhalt aber durch die Kodegruppen selbst übertragen. Es ist jedoch möglich, daß — ähnlich wie bei dem in der Rechenmaschinentechnik verwendeten Verfahren — sowohl die Adresse wie auch der Inhalt von den Kodengruppen getragen werden. Eine weitere Möglichkeit wird durch das Umgekehrte des klassischen PCM-Verfahrens gegeben, nämlich durch das Verfahren, bei dem der Inhalt durch die Lage der Kodegruppen, die Adresse aber durch die Kodegruppe selbst übertragen wird. Die Arbeit befaßt sich mit den beiden letzten Verfahren, d. h. mit der Verwendung für Nachrichtenübertragung von Koden, die Adresse und Inhalt oder nur Adresse tragen. Es wird eine Übersicht der Grundsätze gegeben, ferner auf die Möglichkeiten der Enthebung von Übertragungsfehlern und auf die bei den erörterten Verfahren zur Verfügung stehenden Methoden der Bandverringerung hingewiesen.

MÉTHODES DE COMMUNICATIONS AVEC CODES ADRESSES ET INFORMATIONS OU CODES ADRESSES SEULEMENT

E. ÁCS

RÉSUMÉ

Si des communications entre plusieurs abonnés s'effectuent par des canaux communs, on doit transmettre des informations relatives à la destination (adresse) et au contenu du message. Dans les systèmes PCM classiques, l'adresse est transmise par la position dans le temps (n^0 d'ordre) des codes, et l'information par les codes eux-mêmes. Néanmoins, il est possible de faire porter par les codes l'adresse aussi bien que l'information, par une méthode pareille à celle employée dans la technique des machines à calculer. Une autre possibilité est offerte par le renversement du principe appliqué dans le système PCM classique, l'information étant transmise par la position chronologique des codes et l'adresse par le code même. L'auteur traite de ces deux dernières méthodes, c'est-à-dire de l'usage des codes-adresses et informations ou des codes-adresses seulement. L'auteur donnant un aperçu des principes fondamentaux et des possibilités d'élimination des erreurs de transmission, envisage également les possibilités de la compression de bande préconisée pour le système examiné dans l'étude.

МЕТОДЫ СВЯЗИ С ИСПОЛЬЗОВАНИЕМ КОДОВ, НЕСУЩИХ АДРЕС СОДЕРЖАНИЕ ИЛИ ТОЛЬКО АДРЕС

Э. АЧ

РЕЗЮМЕ

В случае связи между несколькими абонентами по каналу должны передаваться информации, относящиеся к месту назначения (т. е. к адресу) и содержанию сообщения. При обычной кодоимпульсной модуляции адрес передается временным положением (номером) кода, а содержание самим кодом. Однако, возможно, чтобы (подобно как в технике ЭМВ) коды носили как адрес, так и содержание. Дальнейшая возможность дается обращением обычной кодо-импульсной модуляции, когда содержание носит положение кодов, а адрес сам кодом. В работе рассматриваются последние два метода, т. е. использование для связи кодов, несущих адрес и содержание или только адрес. Дается обзор основных принципов. Указываются возможности устранения ошибок передачи и методы сужения полосы частот.

CALCULATION OF FACTORS INFLUENCING THE OUTPUT CHARACTERISTICS OF FLUID COUPLINGS

L. KISBOCSKÓI—F. STVRTECZKY
TECHNICAL UNIVERSITY BUDAPEST

[Manuscript received June 8, 1964]

Authors succeeded in finding a new and more exact way of calculation of the dimensions of fluid couplings, as compared to already known methods. The new formula goes as follows:

$$N = D_0^5 \, n^3_{\mathrm{p}} \, (1 - B^2) \, \gamma \, \frac{\varphi}{S} \, \Pi^3 \sqrt{2s \, \lambda^3_{Pe}} \, A \, .$$

As to the calculated values of the loss factor S according to the equation below, they proved to be in compliance with experimental results:

$$S^2 = (V_{\acute{a}} + V_{\lambda}) \left(1 + c \, \frac{u_2}{w}\right) + V_u \, .$$

The whole calculating method is based on consideration of the influence of the following factors: geometric form, blade thickness, blades number, shape of the blade tip, speed, diameter, and in addition, the physical properties of the operating fluid.

The task of projecting fluid couplings is, in most of the cases, determined by a given output N, a given engine speed n_p and a maximum of slip ($s\%$). Generally, a further stipulation is added according to which the trend of the characteristic curve is prescribed as a function of time and/or of slip.

With these preliminaries, the designer is compelled to find some auxiliary informations from scientific authorities whose work is nowadays represented by a wide and ramified literature. When we try to obtain some orientation in this field, we may state, on the whole, the following groups of papers mentioned:

a) Description of an actual construction or an example of application, at best with some additional information concerning measurements and dimensions.

b) Theoretic consideration followed by some statement of principles but not quite suitable for finding numerical relations or practical stipulations.

c) The exposition of a rather narrow, partial problem, sometimes carefully elaborated and well founded, by presenting the details of experiments and testing results.

d) Collection of experimental results obtained by tests and measurements.

At the first glance, the last type of study seems to be the most useful for the projecting designer. As will be seen, this opinion holds true only in

exceptional cases. Regrettably, authors used to communicate some diameter values and the shape of the meridional section, power, speed and the slip value, but one finds only in a few cases further data concerning the number of blades and the exact denomination of the operating fluid, perhaps its physical characteristics; and as far as data regarding blade thickness, surface conditions, form of the blade tip are concerned, the reader can seldom get true informations. (May we here refer to the curves of FÖTTINGER for which the blade number varies according to the blade type "cast" or "welded".) Neither the adopted usage to simplify informations by giving some ratio-formulas can be welcomed by designers (such as N/n, N/n^2 etc.).

In the literary resources referred to, one may find, generally, two types of formulae that are considered as useful for the calculation of the main dimensions. These are of the form:

$$N = D_0^5 n^3 s \gamma C_N , \tag{1}$$

or

$$N = D_0^5 \left(\frac{n}{100} \right)^3 k . \tag{1a}$$

(NB. Please find the explanation of symbols in the Annex at the end of this paper.)

Concerning the output factor C_N as used in equation (1), some further stipulations are usual: e.g. its validity is bound to slip limits between $0 \div 10\%$, or else the values of C_N are limited between $3 \div 8 \cdot 10^{-8}$.

Referring to formula (1a), the value of the "constant k" is determined e.g. as follows:

"Value limits of k are $0.7 \div 1.6$, and these are applicable when using light liquid oils of a density $\gamma = 800 \div 900$ kp/m^3 and when the slip value is of abt. 3%."

The quoted equations (1) and (1a) are generally followed by a remark that their application always needs further consideration, especially as far as the values to be chosen depend on special experimental results, or on some other practical informations.

Further similarity relations assumed for turbo-machines, e.g. as quoted herebelow under (2) can be applied to the calculation of fluid couplings only when the geometrical and hydraulic conditions are similar:

$$\frac{N}{N_m} = \frac{D_0^5 n^3}{D_{0m}^5 n_m^3} . \tag{2}$$

It can easily be proved that model-similarity is much more difficult to be assumed with couplings than it would be with usual hydraulic machines.

Another source of errors is the misleading — though preferred — consideration, by some authors, according to which the formula:

$$Re = \frac{nD_0}{\nu} \tag{3}$$

can be considered for fluid couplings, as the appropriate expression of Reynolds, number Re.

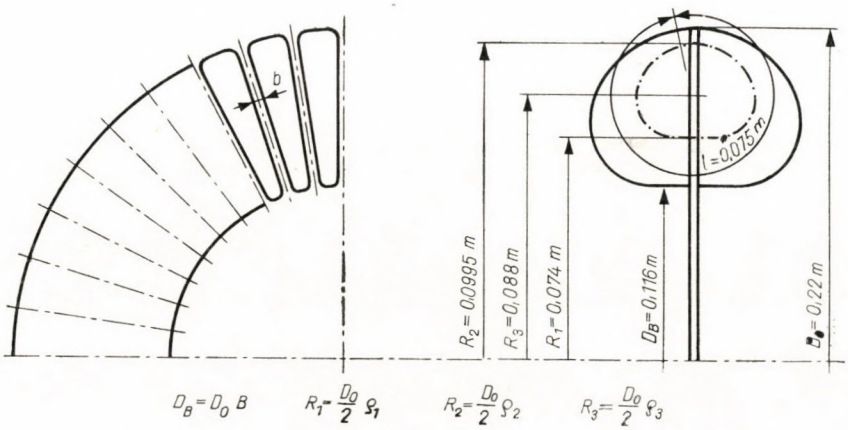

Fig. 1. Schematic diagram of the fluid-coupling, denotations

Namely, none of the authors cares for true information, how the application of the formula (2) might be influenced by the following factors:

Variation of the number of blades,

variation of the blade's thickness,

geometrical form of the blade tip,

variation of density and viscosity of the operating fluid,

dependence of the whole relations (2) on speed variation or on change of geometrical ratios, or on the possibility how the probable deviations could be estimated.

In order to eliminate all these uncertainties and to promote some nearer elucidation of the problems affected, we thought it useful to communicate the results of our experiences.

The task was to design a fluid coupling for industrial purposes, for a given output. Dimensions were determined by making use of the formula (1a) whereas for choosing the value of k we relied upon our former experiences. Taking our prototype as a basis, we have suggested to choose the value k equal to 1.67. — For an improved safety, we assumed in our calculations the value $k = 1.5$. — Dimensions and characteristics of the coupling designed are shown in Figs. 1 and 2.

The couplings once built, checking measurements were carried out. The results showed, to our greatest astonishment, a k value not exceeding 0.519.

Of course, we had to look for an acceptable reason why this deviation from the calculated value happened. After disassembling the coupling, the reasons were found. In spite of our strict prescriptions to have blades made in accordance to the variety No. I in Fig. 2, these blades corresponded to the No. III, i.e. blades of rather poor casting performance. The blades' thickness was 4 mm, instead of the prescribed 2.5 mm, they had irregularly corrugated surfaces instead of smooth ones, and the tip of the blades had a bluntish ending instead of a well rounded shape. We succeeded in making the best of

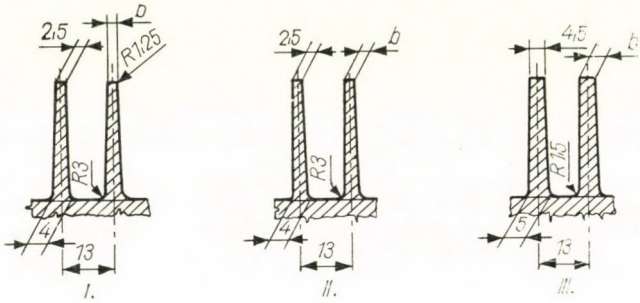

Fig. 2. Blade cross-sections of the various impeller types: I, II and III

these facts. We had on hand the opportunity to test 6 types of couplings, i.e. tests with 3 types of blades according to Fig. 2, and every type of operation with water and oil.

Our results are illustrated in Fig. 3, showing the measurements with oil, and Fig. 4, containing those obtained by using water as transmitter fluid.

The 3 types of blades are:

Type III: coupling with original blades;

Type II: coupling with blades, machined to prescribed dimensions, without rounding off the tips;

Type I: coupling having blades true to design (exactly formed blades).

As seen from the curves, in the course of measurements made with water as an operating fluid, an effect of moment break down was observed with Type I, in spite of the fact that the coupling was tested with 100% filling (equal to 0.9 part of the free volume). Of course, this section was not taken into consideration in our calculations. Table I shows the measuring results at a slip value of 3%.

In Figs 3 and 4, are the diagrams showing the output N against slip s as measured, and the relative flow velocity w, in the meridional section against slip s, as calculated according to the formula given in the following.

Fluid characteristics:

The water used is considered as having a running temperature of 35 ÷ 50° C.

The operating oil had a density of $\gamma = 865$ kp/m³ with a viscosity factor $\nu = 18 \cdot 10^{-6}$ m²/s, according to a temperature of abt. 60° C.

The disc-friction that occurs between the outer casing and the impeller has been intentionally disregarded since this portion of moment-transmission is negligible and has no bearing on practically estimated results.

Table I

Type	Operating fluid	Speed, r. p. m.	Output, HP	Slip, %	Factor, k
Designed	Oil	1440	2.32	3	1.5 (assumed)
I	oil	1440	1.45	3	0.94
II	oil	1440	1.25	3	0.812
III	oil	1440	0.8	3	0.519
I	water	1440	2.2	3	1.425
II	water	1440	1.85	3	1.2
III	water	1440	1.2	3	0.778

To start with, the value of the output N, calculated with a speed of 1440 rpm, was taken as the basic value:

$$N = \frac{wfH_p\gamma}{75} . \tag{4}$$

From this, the relative flow velocity w in the meridional section is obtained:

$$w = \frac{N\,75}{fH_p\gamma}, \tag{5}$$

where the values f (the active sectional area) and H_p (pump delivery head) were assumed on the condition that flow characteristics are obtained by considering a central stream line and an average flow velocity; this assumption is maintained through the entire course of our investigations.

The active sectional area (f) is calculated according to HELDT and TIMM as follows:

$$f = \varphi \cdot F, \tag{6}$$

where

$$F = \frac{\pi}{8} D_0^2 (1 - B^2). \tag{7}$$

Further, for the surface at the entry circumference of the turbine, by making allowance for the surface ratio determined by the blade's thickness

$$\varphi_K = 1 - \frac{Zb\left(1 - \sqrt{(1+B^2)/2}\right)}{\frac{D_0}{2}\,\frac{\pi}{2}\,(1 - B^2)}\,, \tag{8a}$$

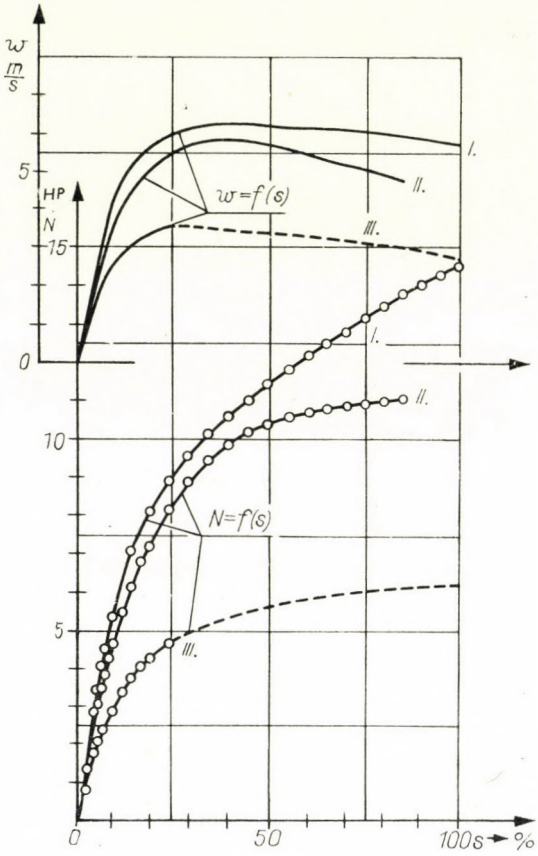

Fig. 3. Characteristics of impellers of types I, II and III, as measured on oil-filled couplings

and

$$\varphi_B = 1 - \frac{Zb\left(\sqrt{(1+B^2)/2} - B\right)}{\frac{\pi}{2}(1 - B^2)\left(\frac{D_0}{2}\right)}\,; \tag{8b}$$

further, for the pump delivery head:

$$H_p = \frac{\lambda_{Pe}\,\omega_p^2}{g}\,P^2, \tag{9}$$

where the head correction factor λ_{Pe} is taken, according to [3] and [4] from:

$$\lambda_{Pe} = \frac{1}{1 + \frac{3.6}{Z} \frac{1}{1-\tau}} . \tag{10}$$

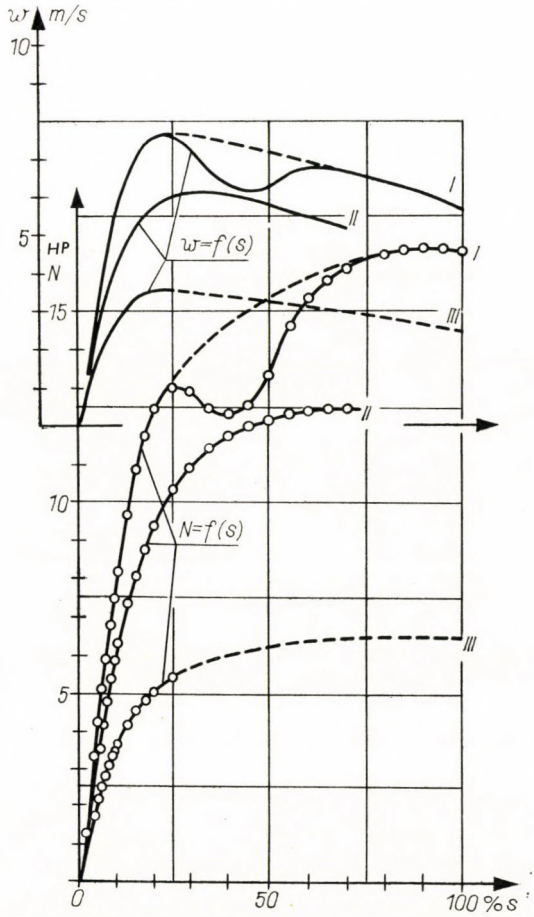

Fig. 4. Characteristics of impellers of types I, II and III, as measured on water-filled couplings

In this equation Z denotes the number of blades

and

$$\tau = \left(\frac{\varrho_1}{\varrho_2}\right)^2 ; \tag{11}$$

further

$$\varrho_1 = \frac{R_1}{D_0/2} \tag{12a}$$

and

$$\varrho_2 = \frac{R_2}{D_0/2} . \tag{12b}$$

Again, the values of ϱ_1 and ϱ_2 are to be calculated by using the deduction according to [1], as follows:

$$\varrho_1 = \sqrt[3]{\frac{[(1+B^2)/2] - B^4}{4\left(\sqrt{(1+B^2)/2} - B\right)}}, \tag{13a}$$

$$\varrho_2 = \sqrt[3]{\frac{1 - [(1+B^2)/2]^2}{4\left(1 - \sqrt{(1+B^2)/2}\right)}}. \tag{13b}$$

With the denotations used in Fig. 1, we have:

$$B = \frac{D_B}{D_0} \tag{14}$$

and, according to equation (9),

$$P = \frac{D_0}{2} \Pi, \tag{15}$$

where

$$\Pi = \sqrt{\varrho_2^2 - (1-s)\,\varrho_1^2} \tag{16}$$

expressed with the geometrical dimensions and the slip.

Power losses can be expressed, as seen from equation (4), as head losses in this form:

$$\sum h' = sH_p. \tag{17}$$

This loss, occurring in the coupling, can be expressed as the function of the relative velocity w in the meridional section which is assumed to be constant:

$$\sum h' = \frac{w^2}{2\,g} S^2, \tag{18}$$

where the loss factor S^2 is calculated, according to [5]:

$$S^2 = \zeta_0 \left(1 + c\,\frac{u_2}{w}\right) + V_u. \tag{19}$$

Here, the member cu_2/w stands as the expression of the effect of the so-called "super-turbulence" (Überturbulenz) explained by FÖTTINGER [6] and SEELIG [7].

With due consideration of the results found in [5] we can assume:

$$c = 0.18,$$

which proved a good conformity with our experimental results. As to the value of ζ_0, this consists of two distinct parts as follows:

$$\zeta_0 = V_{\acute{a}} + V_\lambda , \tag{20}$$

where the member

$$V_{\acute{a}} = V_{\acute{a}}^K + V_{\acute{a}}^B \tag{21}$$

since this shock loss is, of course, composed of two parts: $V_{\acute{a}}^K$ is the loss occurring at the pump exit and turbine entry, and $V_{\acute{a}}^B$ occurs at the turbine exit and the pump entry. Calculation of these quantities is based on the diagram to be found in [8, (Part VIII, diagrams 9 ÷ 10)].

In conformity with our research experiences, we found for

$$V_u = s^2 \left(\frac{D_0}{2}\right)^2 \varrho_1^2 \frac{\omega_p^2}{g} \frac{2g}{w^2} . \tag{22}$$

The loss caused by the fluid friction is:

$$V_\lambda = \lambda \frac{lZK_1}{4f} . \tag{23}$$

The value λ is determined by means of the commonly known curves as functions of Reynold's number Re, where for the latter the equation

$$Re = \frac{wf4}{ZK_1 \nu} \tag{24}$$

is to be used. Only this Re value cannot be constant, and this value obviously does not coincide with that one calculated according to (3), the latter being assumed as constant.

The (average) value of the wetted perimeter K_1 of the flow channel is calculated:

$$K_1 = \frac{D_0}{2} \left[(1 - B^2) + \frac{\pi (1 + B)}{Z} \right] - b . \tag{25}$$

In equation (23) the value of l is the length (in m) of the mean stream line as taken from the meridional section.

In consideration of equations (5), (9), (17) and (18), we can write:

$$w^2 = \frac{\sum h' \, 2g}{S^2} = \frac{s\lambda_{Pe} \, \omega_p^2 \, P^2}{g} \frac{2g}{S^2} = 2 \, s\lambda_{Pe} \, \omega_p^2 \frac{P^2}{S^2} . \tag{26}$$

or, therefrom we can derive:

$$w = \omega_p \frac{P}{S} \sqrt{2\, s\, \lambda_{Pe}}\,. \tag{27}$$

Now, making use of the values of N, w, H_p and f as obtained from the re-

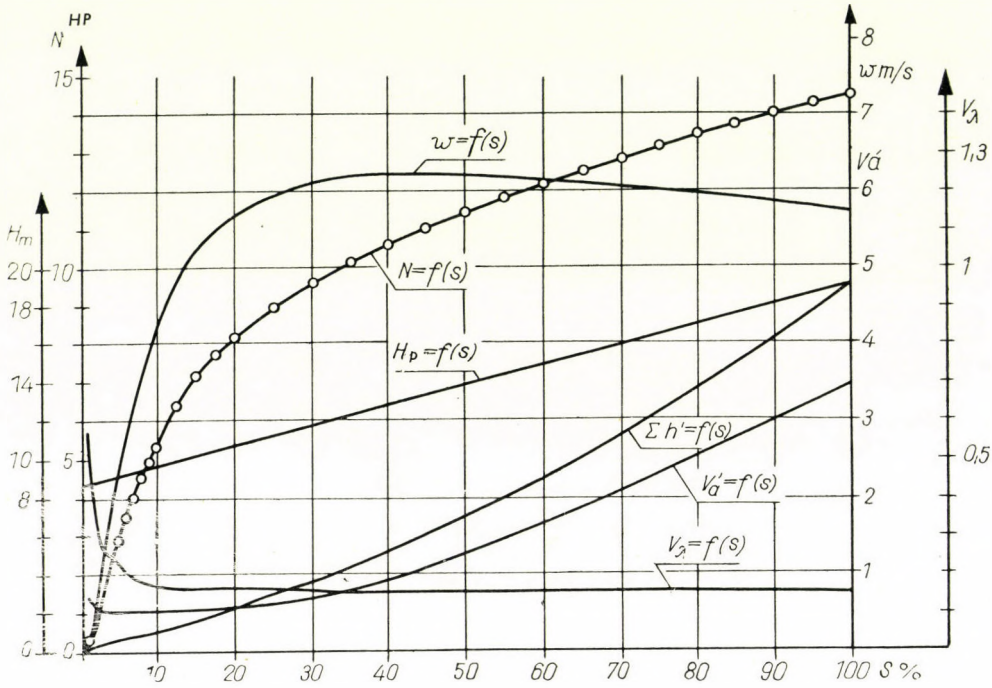

Fig. 5. Characteristics of impeller type I, calculated and measured values of an oil-filled coupling

spective equations (4), (27), (9) and (6), so the form of equation (4) will be:

$$N = D_0^5\, n_p^3\, (1 - B^2)\, \gamma\, \frac{\varphi}{S}\, \Pi^3 \sqrt{2\, s \lambda_{Pe}^3} \cdot A\,. \tag{28}$$

By adopting the usual system of units (m, kp, s, HP and rpm) and in considering the gravitational acceleration g, the value of A will be:

$$A = 7.67 \cdot 10^{-8}\ \mathrm{m/s^2}\,.$$

In Figs. 3 and 4 the w values, as calculated according to equation (5) are also plotted.

For example's sake, in Fig. 5, the characteristics of an oil fluid coupling of Type I are shown. We can state that the results of measurements and the values calculated according to the here developed method are in full coincidence. Regrettably, the immense volume of research data does not allow for a detailed communication even in tables.

Now, by equation (28) designers are aided in taking into account the effect of all the influencing factors with a greater accuracy than it would be possible by relying on the generally known formulae (1) and (1a).

This (28) equation also makes possible to determine the probable power to be transmitted by a fluid coupling manufactured by means of given technological methods, having known dimensions and built with a given number of blades.

A further advantage of this equation is the possibility of taking loss variations caused by the various forms of blades into account, and to plot the curve of the function:

$$N = f(s).$$

ANNEX

Finally, here are enumerated definitions of terms, with their symbols and units used in this paper, and as an annex, the detailed course of calculation of the loss value $V_{\acute{a}}$ according to equation (21) is given in detail.

I. Symbols

A $7.67 \cdot 10^{-8}$ [m/s²], obtained by the cumulation of constants out of (28);
b blade thickness (entry and exit), [m];
B D_B/D_0 ratio number characterising the form of the meridional section;
c 0.18 an experimental constant for Equ. 19;
C_N power factor;
D_0 nominal diameter, [m];
D_B inner diameter of blades, [m];
f active surface, [m²];
F half of the whole ring surface, [m²];
g 9.81 m/s² gravitational acceleration;
$\Sigma h'$ total head loss of the coupling, [m];
H_p pump delivery head, [m];
k power factor;
K_1 the wetted perimeter of one blade channel (as average) [m], see Equ. (23) and (24);
n r. p. m., [1/min];
N power, [HP];
P $\Pi D_0/2$;
R $\varrho D_0/2$ radius, [m];
Re Reynold's number;
s slip;
S^2 loss factor Equ. (18) and (19);
u_2 $R_2 \omega_p$ tangential velocity at the radius R_2, [m/s];
$V_{\acute{a}}$ $V_{\acute{a}}^K + V_{\acute{a}}^B$ shock loss component [confer herebelow, and Equ. (20)];
V_u $s^2(D_0/2)^2 \varrho_1 \omega_p^2/g\, 2g/w^2$ loss component, according to Equ. (22);
V_λ friction loss component according to Equ. (23);

w relative velocity, [m/s];
Z $(Z_p + Z_t)1/2$ number of blades;
γ specific weight, [kp/m³];
ζ_0 $V_{\dot{a}} + V_{\lambda}$ loss component;
λ fluid friction factor, Equ. (23);
λ_{Pe} head correction factor, Equ. (10);
φ f/F area ratio;
ν factor of kinetic viscosity, [m²/s];
Π $\sqrt{\varrho_2^2 - (1-s)\varrho_1^2}$ factor depending on the geometric form and the slip Equ. (16);
ω $n/9.55$ angular velocity, [1/s];
ϱ $R/D_0/2$;
τ $(\varrho_1/\varrho_2)^2$, according to Equ. (11);
I, II, III type designations for blades workmanship, according to Fig. 2.

II. Subscripts

0, 1, 2 according to Fig. 1;
B quantities related to the radius R_1;
K quantities related to the radius R_2;
m values referred to the small model;
p values referred to the pump impeller;
t values referred to the turbine.

Here below we will develop the method of calculation of the shock loss values based on the diagrams in [8]

$$V_{\dot{a}} = V_{\dot{a}}^K + V_{\dot{a}}^B$$

and for calculation purposes

$$V_{\dot{a}} = \sigma_1 \sigma_2 \left(\frac{a_0}{S_1}\right)^2. \tag{29}$$

To this end, the values of σ_1 are taken from the table a as function of the blade tip and the flow direction α°. Values of σ_2 are taken from the table b, equally as function of α° and the ratio a_0/S_1. Further equations:

$$\tan \alpha^K = s\frac{u_2}{w}, \qquad \tan \alpha^B = s\frac{u_2}{w} \cdot \frac{\varrho_1}{\varrho_2}; \tag{30a, b}$$

$$a_0^K = \frac{R_2 \pi}{Z} - b, \quad a_0^B = \frac{R_1 \pi}{Z} - b; \tag{31a, b}$$

$$S_1^K = \frac{R_2 \pi}{Z}, \qquad S_1^B = \frac{R_1 \pi}{Z}. \tag{32a, b}$$

REFERENCES

1. HELDT, P. M.: A Mathematical Consideration of the Fluid-Coupling. *Aut. Ind.* (1940), 360.
2. TIMM, K.: Untersuchungen an Föttinger-Kupplungen. Dissertation von T. H. Hannover, 1958.
3. BARGLAZAN, A.—DOBINDA, V.: Turbotransmisiile hidraulice. Editura Technica, Bucuresti 1957.
4. ПРОСКУРА, Б. Ф.: Kreisel- und Propellerpumpen. Gosenergoizdat, Moskwa 1962.
5. KISBOCSKÓI, L.: Über die Anderung des Strömungswiderstandes in schnell rotierende Rohrleitungen. *Acta Techn. Hung.* **22** (1958), 121—128.
6. FÖTTINGER, H.: Über die Fortbildung des Turbinenprinzips. *ZAMM.* (1925), 450.
7. SEELIG: Über das Phenomenon der „Rotationsturbulenz" in rotierenden Rohren und Kanälen. *Abhandlungen des III. Kongresses für techn. Mechanik* **1** (1930), 102.
8. ИДЕЛЬЧИК, И. Е.: Справочник, Москва. Section VIII; Diagram 8—10, pp. 299.

BERECHNUNG DES EINFLUSSES DER LEISTUNGSVERÄNDERNDEN FAKTOREN AUF DIE KENNWERTE DER HYDRODYNAMISCHEN KUPPLUNGEN

L. KISBOCSKÓI—F. STVRTECZKY

ZUSAMMENFASSUNG

Autoren haben eine Berechnungsmethode ausgearbeitet, mittels welcher die Abmessungen von hydrodynamischen Kupplungen mit einer, gegenüber der bisher üblichen größeren Genauigkeit bestimmt werden können. Der Berechnung liegt folgende Formel zu Grunde:

$$N = D_0^5 n_p^3 (1 - B^2) \gamma \frac{\varphi}{S} \Pi^3 \sqrt{2s\lambda^3 p_e} A.$$

Die laut der hier folgenden Gleichung berechneten Werte des Verlustfaktors S wurden von den Versuchsergebnissen vollauf gerechtfertigt:

$$S^2 = (V_d + V_\lambda)\left(1 + c\frac{u_2}{w}\right) + V_u .$$

In dieser Berechnung wird die Wirkung folgender Faktoren in Rechnung gezogen: geometrische Ausbildung, Schaufelstärke, Schaufelzahl, Schaufelnasform, Drehzahl, Durchmesser, physikalische Eigenschaften der Arbeitsflüßigkeit.

CALCUL DE L'INFLUENCE DES DIFFÉRENTS FACTEURS SUR LA PUISSANCE DE L'ACCOUPLEMENT HYDRODYNAMIQUE

L. KISBOCSKÓI—F. STVRTECZKY

RÉSUMÉ

Les auteurs donnent une relation pour le calcul plus précis de l'accouplement hydrodynamique, qui peut s'écrire sous la forme:

$$N = D_0^5 n_p^3 (1 - B^2) \gamma \frac{\varphi}{S} \Pi^3 \sqrt{2s\lambda^3 p_e} A .$$

Les valeurs calculées des coefficients des pertes S

$$S^2 = (V_d + V_\lambda)\left(1 + c\frac{u_2}{w}\right) + V_u$$

ont été vérifiées par des mesures de laboratoire. La méthode de calcul considère aussi l'influence de la forme géométrique, l'épaisseur et le nombre des pales, le point d'entrée de ces dernières, le nombre de tours, le diamètre et les caractéristiques physiques du fluide utilisé.

РАСЧЁТ ФАКТОРОВ, ВЛИЯЮЩИХ НА ПАРАМЕТРЫ ХАРАКТЕРИСТИКИ МОЩНОСТИ ГИДРОМУФТ

Л. КИШБОЧКОИ—Ф. ШТВРТЕЦКИ

РЕЗЮМЕ

В работе авторов приведена зависимость, применяемая для более строгого чем до сих пор расчёта гидродинамических муфт. Эту зависимость можно записать в виде:

$$N = D_0^5 n_p^3 (1 - B^2) \gamma \frac{\varphi}{S} \Pi^3 \sqrt{2 s \lambda^3 p_e} A .$$

Расчетные величины значения коэффициента потерь S подтверждены экспериментально.

$$S^2 = (V_d + V_\lambda) \left(1 + c \frac{u_2}{w}\right) + V_u .$$

Метод расчёта учитывает влияние геометриического оформления, толщины попастей, числа лопастей, оформление носовой части лопастей, числа оборотов, диаметра и физических параметров рабочей жидкости.

INDEX

Imre Rázsó 1904—1964 Имре Ражо 1904—1964 271

Ferenc Ratkovszky 1900—1965 Ференц Ратковски 1900—1965.. 273

Roboz, P.—Kovách, A.: Mass Spectrometric Studies of Additive Materials Evaporating from Tungsten Produced by Powder Metallurgical Treatment — Massenspektrometrische Untersuchung von aus pulvermetallurgisch hergestelltem Wolfram verdampfenden Zusätzen — Examen par le spectromètre de masse des additifs s'évaporant du tungstène produit par la métallurgie des poudres — *Робоз, П.—Ковач, А.:* Масс-спектроскопический анализ добавок, испаряющихся из металлокерамического вольфрама 277

Haas, A.: Stationary Temperature Distribution in Thermometer Protecting Tubes — Die stationäre Temperaturverteilung in Schutzrohren von Thermometern — La distribution stationnaire des températures dans les gaines protectrices des thermomètres — *Хаас, А.:* Распределение установившейся температуры защитных трубок термометров 291

Balázs, Gy.: Berechnung der vom Schwinden des Betons herrührenden Kräfte in Stahlbetonelementen — Analysis of Forces Due to Shrinkage — Calcul des contraintes intérieures dues au retrait du béton — *Балаж, Д.:* Расчет внутренних сил бетона, возникающих от его усадки 309

Tóth, L.: Die Wirkung des Schmierens beim Stauchen von Metallen — The Influence of Lubricants on the Deformation of a Compression Test Piece — L'influence de la lubrification dans le gonflement des métaux — *Тот, Л.:* Влияние смазки при высадке металлов 327

Visy, Z.: Moment Calculation of Continuous Reinforced Concrete Beams on Three Supports by Introducing Economical Condition — Die Berechnung der Momente von Stahlbeton-Durchlaufträgern auf drei Stützen unter der Einführung der Wirtschaftlichkeitsbedingung — Calcul des moments des poutres à trois appuis avec introduction de la condition d'économie — *Виши, З.:* Расчет момента трехопорных железобетонных балок, нагруженных постоянной и временной нагрузками, с введением условия экономичности 347

Varga, J.—Sebestyén, Gy.—Schalnew, K. K.—Tschernawskij, B. A.: Untersuchung des Maßstabeffektes der Kavitationserosion — Investigation of the Influence of the Scale Effect on the Erosion by Cavitation — Examen de l'effet d'échelle de l'érosion de cavitation — *Варга, Й.—Шебештьен, Дь. Шальнев, К. К.—Чернявский, Б. А.:* Исследование воздействия на масштаб кавитационной эрозии 361

Huszár, I.—Csizmadia, L.: Three-dimensional Photoelastic Investigation of a Twisted Bar — Räumliche photoelastische Untersuchung eines verdrehten Stabes — Photoélasticimétrie tridimensionnelle d'une barre tordue — *Хусар, И.—Чизмадиа, Л.:* Изучение крученной штанги пространственным оптическим путем 381

Geszti, P. O.—Póka, Gy.: Impedances Seen by Distance Relays in a General Case — Der allgemeine Fall der Distanzerfassung durch Schutzrelais — Le cas général de la perception par les protections à distance — *Гести, П. О.—Пока, Д.:* Восприятие дистанционных защит в общем случае 403

Замбо, Я.: Проблема определения горизонтов в горно-промышленных предприятиях — *Zambó, J.:* The Problem of Division into Stages in Mining Plants — Das Problem der Aufteilung auf Sohlen in Bergbaubetrieben — Le problème de la division en étages dans les exploitations minières 421

Petrasovits, G.: Soil Stabilization Experiments with Plastics—Bodenverfestigungsversuche mit Kunstharzen — Essais de stabilisation du sol par résines synthétiques — *Петрашович, Г.:* Опыты укрепления грунта искусственными смолами 431

Ács, E.: Communication Methods Using Codes Carrying Address and Contents or Address only — Verfahren der Nachrichtenübertragung mit Koden, welche die Adresse und den Inhalt oder nur die Adresse tragen — Méthodes de communications avec codes adresses et informations ou codes adresses s eulement — *Ач, Э.:* Методы связи с использованием кодов, несущих адрес и содержание или только адрес 451

Kisbocskói, L.—Stvrteczky, F.: Calculation of Factors Influencing the Output Characteristics of Fluid Couplings — Berechnung des Einflusses der leistungsverändernden Faktoren auf die Kennwerte der hydrodynamischen Kupplungen — Calcul de l'influence des différents facteurs sur la prissance de l'accouplement hydrodynamique — *Кишбочкои, Л.—Штвртецки, Ф.:* Расчет факторов, влияющих на параметры характеристики мощности гидромуфт 469

Printed in Hungary

A kiadásért felel az Akadémiai Kiadó igazgatója Műszaki szerkesztő: Farkas Sándor
A kézirat nyomdába érkezett: 1965. VII. 5. — Terjedelem: 18,75 (A/5) ív, 99 ábra

65.61032 Akadémiai Nyomda, Budapest — Felelős vezető: Bernát György

The Acta Technica publish papers on technical subjects in English, German, French and Russian.

The Acta Technica appear in parts of varying size, making up volumes.

Manuscripts should be addressed to

Acta Technica
Nádor u. 7.
Budapest V.
Hungary

Correspondence with the editors and publishers should be sent to the same address.

The rate of subscription to the Acta Technica is 110 forints a volume. Orders may be placed with "Kultúra" Foreign Trade Company for Books and Newspapers (Budapest I., Fő utca 32. Account No. 43-790-057-181) or with representatives abroad.

Les Acta Technica paraissent en français, allemand, anglais et russe et publient des travaux du domaine des sciences techniques.

Les Acta Technica sont publiés sous forme de fascicules qui seront réunis en volumes.

On est prié d'envoyer les manuscrits destinés à la rédaction à l'adresse suivante:

Acta Technica
Nádor u. 7.
Budapest V.
Hongrie

Toute correspondance doit être envoyée à cette même adresse.

Le prix de l'abonnement est de 110 forints par volume.

On peut s'abonner à l'Entreprise pour le Commerce Extérieur de Livres et Journaux «Kultúra» (Budapest I., Fő utca 32. Compte courant No. 43-790-057-181) ou à l'étranger chez tous les représentants ou dépositaires.

«Acta Technica» публикуют трактаты из области технических наук на русском, немецком, английском и французском языках.

«Acta Technica» выходят отдельными выпусками разного объема. Несколько выпусков составляют один том.

Предназначенные для публикации рукописи следует направлять по адресу:

Acta Technica
Nádor u. 7.
Budapest V.
Венгрия

По этому же адресу направлять всякую корреспонденцию для редакции и администрации.

Подписная цена «Acta Technica» — 110 форинтов за том. Заказы принимает предприятие по внешней торговле книг и газет «Kultúra» (Budapest I., Fő utca 32. Текущий счет № 43-790-057-181) или его заграничные представительства и уполномоченные.

54,— Ft

Index: 26.025